



THEORETICAL AND COMPUTATIONAL CHEMISTRY 13



# Energetic Materials Part 2. Detonation, Combustion

Peter Politzer  
Jane S. Murray  
editors

# Energetic Materials

## Part 2. Detonation, Combustion

THEORETICAL AND COMPUTATIONAL CHEMISTRY

SERIES EDITORS

**Professor P. Politzer**

Department of Chemistry  
University of New Orleans  
New Orleans, LA 70148, U.S.A.

**Professor Z.B. Maksić**

Rudjer Bošković Institute  
P.O. Box 1016,  
10001 Zagreb, Croatia

**VOLUME 1**

Quantitative Treatments of Solute/Solvent  
Interactions

P. Politzer and J.S. Murray (Editors)

**VOLUME 2**

Modern Density Functional Theory: A Tool for  
Chemistry

J.M. Seminario and P. Politzer (Editors)

**VOLUME 3**

Molecular Electrostatic Potentials: Concepts and  
Applications

J.S. Murray and K. Sen (Editors)

**VOLUME 4**

Recent Developments and Applications of Modern  
Density Functional Theory

J.M. Seminario (Editor)

**VOLUME 5**

Theoretical Organic Chemistry

C. Párkányi (Editor)

**VOLUME 6**

Pauling's Legacy: Modern Modelling of the Chemical  
Bond

Z.B. Maksić and W.J. Orville-Thomas (Editors)

**VOLUME 7**

Molecular Dynamics: From Classical to Quantum  
Methods

P.B. Balbuena and J.M. Seminario (Editors)

**VOLUME 8**

Computational Molecular Biology

J. Leszczynski (Editor)

**VOLUME 9**

Theoretical Biochemistry: Processes and Properties  
of Biological Systems

L.A. Eriksson (Editor)

**VOLUME 10**

Valence Bond Theory

D.L. Cooper (Editor)

**VOLUME 11**

Relativistic Electronic Structure Theory, Part 1.  
Fundamentals

P. Schwerdtfeger (Editor)

**VOLUME 12**

Energetic Materials, Part 1. Decomposition, Crystal  
and Molecular Properties

P. Politzer and J.S. Murray (Editors)

**VOLUME 13**

Energetic Materials, Part 2. Detonation, Combustion

P. Politzer and J.S. Murray (Editors)

# Energetic Materials

## Part 2. Detonation, Combustion

Edited by

**Peter Politzer**

**Jane S. Murray**

Department of Chemistry  
University of New Orleans  
New Orleans, LA 70148, USA



ELSEVIER

2003

Amsterdam – Boston – Heidelberg – London – New York – Oxford – Paris  
San Diego – San Francisco – Singapore – Sydney – Tokyo



ELSEVIER B.V.  
Sara Burgerhartstraat 25  
P.O. Box 211, 1000 AE Amsterdam, The Netherlands

© 2003 Elsevier B.V. All rights reserved.

This work is protected under copyright by Elsevier, and the following terms and conditions apply to its use:

#### Photocopying

Single photocopies of single chapters may be made for personal use as allowed by national copyright laws. Permission of the Publisher and payment of a fee is required for all other photocopying, including multiple or systematic copying, copying for advertising or promotional purposes, resale, and all forms of document delivery. Special rates are available for educational institutions that wish to make photocopies for non-profit educational classroom use.

Permissions may be sought directly from Elsevier's Science & Technology Rights Department in Oxford, UK: phone: (+44) 1865 843830, fax: (+44) 1865 853333, e-mail: [permissions@elsevier.com](mailto:permissions@elsevier.com). You may also complete your request on-line via the Elsevier homepage (<http://www.elsevier.com>), by selecting 'Customer Support' and then 'Obtaining Permissions'.

In the USA, users may clear permissions and make payments through the Copyright Clearance Center, Inc., 222 Rosewood Drive, Danvers, MA 01923, USA: phone: (+1) (978) 7508400, fax: (+1) (978) 7504744, and in the UK through the Copyright Licensing Agency Rapid Clearance Service (CLARCS), 90 Tottenham Court Road, London W1P 0LP, UK; phone: (+44) 207 631 5555; fax: (+44) 207 631 5500. Other countries may have a local reprographic rights agency for payments.

#### Derivative Works

Tables of contents may be reproduced for internal circulation, but permission of Elsevier is required for external resale or distribution of such material. Permission of the Publisher is required for all other derivative works, including compilations and translations.

#### Electronic Storage or Usage

Permission of the Publisher is required to store or use electronically any material contained in this work, including any chapter or part of a chapter.

Except as outlined above, no part of this work may be reproduced, stored in a retrieval system or transmitted in any form or by any means, electronic, mechanical, photocopying, recording or otherwise, without prior written permission of the Publisher.

Address permissions requests to: Elsevier's Science & Technology Rights Department, at the phone, fax and e-mail addresses noted above.

#### Notice

No responsibility is assumed by the Publisher for any injury and/or damage to persons or property as a matter of products liability, negligence or otherwise, or from any use or operation of any methods, products, instructions or ideas contained in the material herein. Because of rapid advances in the medical sciences, in particular, independent verification of diagnoses and drug dosages should be made.

First edition 2003

#### Library of Congress Cataloging in Publication Data

A catalog record from the Library of Congress has been applied for.

#### British Library Cataloguing in Publication Data

A catalogue record from the British Library has been applied for.

ISBN: 0 444 51519 4  
ISSN: 1380 - 7323 (Series)

Ⓢ The paper used in this publication meets the requirements of ANSI/NISO Z39.48-1992 (Permanence of Paper).  
Printed in Hungary.

## PREFACE

Our own involvement in the area of energetic materials stems from the second half of a New Orleans Saints football game in 1979, which one of us (P.P.) was attending together with Rod Bartlett (a contributor to these volumes). The Saints were losing by a large score, and with interest in the game waning, Rod spent much of the second half expounding, to a very receptive listener, the opportunities in energetic materials research. Whether this area has since been advanced or set back as a result of the Saints' ineptness that afternoon is for others to decide. What is certain, however, is that during these years we have been extremely fortunate in having the assistance, encouragement and support of a very fine group of project officers:

Dick Miller and Judah Goldwasser, ONR;  
David Squire, Ron Husk and Bob Shaw, ARO;  
Larry Davis, AFOSR;  
Jack Alster and Frank Owens, ARDEC;  
Bob McKenney, Norm Klausutis and Paul Bolduc, AFATL;  
Horst Adolph, NSWC;  
and Leonard Caveny, BMDO.

We are grateful to all of them.

In putting together these two volumes, we have greatly appreciated the enthusiastic encouragement and suggestions that we received from Betsy Rice and her willingness to prepare the overview that begins each volume, in addition to her other contribution. Finally, we want to thank Mick Coleman and Bob Murray for their much-needed help with various aspects, often tedious, of the editing process.

Peter Politzer and Jane S. Murray

This Page Intentionally Left Blank

# TABLE OF CONTENTS

## Part 1

<b>Overview of Research in Energetic Materials</b>	
<i>B. M. Rice</i> .....	1
<b>Chapter 1. A Survey of the Thermal Stability of Energetic Materials</b> .....5	
<i>J. C. Oxley</i>	
1. Introduction.....	5
2. Nitrate Esters.....	7
3. Nitroarenes.....	11
4. Nitroalkanes.....	14
5. Nitramines.....	16
6. New Energetic Materials.....	19
6.1 New Nitrogen Heterocycles.....	20
6.2 NF <sub>2</sub> Compounds.....	26
7. Energetic Salts.....	27
8. Summary of Thermal Stability and our Approach.....	30
<b>Chapter 2. Characterisation of Explosive Materials Using Molecular Dynamics Simulations</b> .....49	
<i>P. Capkova, M. Pospisil, P. Vavra and S. Zeman</i>	
1. Introduction.....	49
2. Strategy of Molecular Dynamics Simulations.....	50
3. Results and Discussion.....	53
3.1 Decomposition of RDX and $\beta$ -HMX.....	54
3.2 Decomposition of DADNE and NQ.....	56
3.3 Parameters characterizing the decomposition process.....	57
4. Conclusions.....	59
<b>Chapter 3. Nitro<math>\leftrightarrow</math><i>aci</i>-nitro Tautomerism in High-Energetic Nitro Compounds</b> .....61	
<i>P.V. Bharatam and K. Lammertsma</i>	
1. Nitro $\leftrightarrow$ <i>aci</i> -nitro tautomerism.....	61
2. Nitromethane $\leftrightarrow$ <i>aci</i> -nitromethane tautomerism.....	63
3. Tautomerism in Substituted Nitroethylenes.....	69

4. Tautomerism in Nitroaromatic Compounds.....	72
5. Tautomerism in NTO, HMX, RDX and 5-Nitro-1H-Tetrazole.....	77
<b>Chapter 4. Decomposition Mechanism of 1,1-Diamino- Dinitroethylene (FOX-7): An Overview of the Quantum Chemical Calculation.....</b>	<b>91</b>
<i>A. Gindulyte, L. Massa, L. Huang and J. Karle</i>	
1. Introduction.....	92
2. Nitroethylene Computational Details.....	95
3. Nitroethylene Results.....	96
4. DADNE Computational Details.....	97
5. DADNE Results and Discussion.....	98
5.1 Initial Step of DADNE Decomposition.....	99
5.2 Isonitrite, <b>3</b> .....	101
5.3 Hydrogen Atom Migration from NH <sub>2</sub> to NO <sub>2</sub> .....	102
5.4 HONO Elimination.....	102
5.5 CO Elimination.....	103
5.6 NH <sub>2</sub> Radical Elimination.....	103
5.7 Final Stages of DADNE Decomposition.....	103
6. Additional Check on the Accuracy of DFT Calculations.....	104
7. Concluding Remarks.....	104
<b>Chapter 5. Quantum-chemical Dynamics with the Slater-Roothaan Method.....</b>	<b>111</b>
<i>B.I. Dunlap</i>	
1. Introduction.....	111
2. Robust and Variational Fitting.....	114
3. The Slater-Roothaan Method.....	116
4. Symmetry and Balanced DFT Dynamics.....	119
5. 2-D Chemical Dynamics.....	121
6. Conclusion.....	122
<b>Chapter 6. Molecular Dynamics Simulations of Energetic Materials.....</b>	<b>125</b>
<i>D. C. Sorescu, B. M. Rice, and D. L. Thompson</i>	
1. Introduction.....	125
2. The General Method of Molecular Dynamics Simulations.....	128
3. Molecular Dynamics Studies of Energetic Materials.....	131
3.1 Gas-Phase Reactions of Energetic Materials.....	131
3.1.1 RDX: Initial Decomposition Reactions.....	132
3.1.2 HMX: Initial Decomposition Reactions.....	139
3.1.3 DMNA: A Prototypical Nitramine.....	140

3.1.4 Nitromethane Decomposition.....	142
3.1.5 Methylene Nitramine Decomposition.....	144
3.2 Non-reactive Models.....	146
3.2.1 Non-reactive Models.....	146
3.2.2 Reactive Models.....	166
3.2.3 First Principles Simulations Models.....	173
<b>Chapter 7. Structure and Density Predictions for Energetic Materials.....</b>	<b>185</b>
<i>J. R. Holden, Z. Du and H. L. Ammon</i>	
1. The Development of MOLPAK (MOLEcular PAcKing).....	188
2. Examples of Coordination Sphere Building Procedures.....	196
3. MOLPAK Overview and Structure Prediction.....	197
4. Summary and Challenges.....	211
<b>Chapter 8. X-ray Crystallography - Beyond Structure in Energetic Materials.....</b>	<b>215</b>
<i>A. A. Pinkerton, E. A. Zhurova and Y.-S. Chen</i>	
1. Introduction.....	215
2. Experimental Protocol.....	216
3. Data Reduction.....	218
4. Data Analysis.....	220
4.1 Structure Model - Spherical Atom.....	220
4.2 Structure Model - Atom Centered Multipole Model.....	221
5. Refinements.....	224
6. Electron Density Distributions.....	225
6.1 Residuals.....	225
6.2 Deformation Densities.....	225
6.3 Laplacian of the Electron Density.....	228
7. Topological Analysis.....	228
7.1 Atomic Charges.....	232
7.2 Bond Critical Point Properties.....	232
8. Properties.....	235
8.1 Electrostatic Potential.....	235
8.2 Energy Density Distribution.....	236
8.3 Energy Density Critical Points.....	237
8.4 Hydrogen Bonding.....	240
9. Conclusion.....	241
<b>Chapter 9. Computational Approaches to Heats of Formation.....</b>	<b>247</b>
<i>P. Politzer, P. Lane and M. C. Concha</i>	
1. Introduction.....	247

2. Specific Approaches to $\Delta H_f$ .....	248
3. Computational Methodologies.....	252
3.1 <i>Ab Initio</i> .....	252
3.2 Density Functional.....	253
3.3 <i>Ab Initio</i> /Empirical and Density Functional/ Empirical Combinations.....	256
4. Liquid and Solid Phase Heats of Formation.....	258
5. Applications and Discussion.....	259
5.1 Boron and Aluminum Combustion Products.....	259
5.2 H/C/N/O/F Energetic Compounds.....	260
6. Summary and Conclusions.....	271

## **Chapter 10. Thermodynamics and Mechanical Properties of HMX from Atomistic Simulations.....279**

*D. Bedrov, G. D. Smith, and T. D. Sewell*

1. Introduction.....	279
2. Force Field.....	281
2.1 General Philosophy.....	281
2.2 Quantum Chemistry.....	282
2.3 Force Field Parametrization and Validation.....	288
3. Simulations of Liquid HMX.....	292
3.1 Viscosity and Self-diffusion Coefficient.....	292
3.2 Thermal Conductivity.....	298
4. Crystalline HMX.....	302
4.1 Structural Properties.....	302
4.2 Enthalpy of Sublimation.....	306
4.3 Hydrostatic Compression.....	307
4.4 Anisotropic Elasticity.....	316
5. Conclusions.....	320

## **Chapter 11. Optical absorption in PETN and RDX.....327**

*W. F. Perger*

1. Background.....	327
2. The Approach.....	328
2.1 Optical Absorption and the Use of Crystal Program....	328
2.2 Computational Procedure.....	331
3. Results for PETN and RDX.....	332
3.1 PETN.....	333
3.2 RDX.....	333
4. Conclusions and Future Work.....	338

<b>Chapter 12. Interactions of Model Organic Species and Explosives with Clay Minerals.....</b>	<b>341</b>
<i>A. Michalkova, L. Gorb and J. Leszczynski</i>	
1. Introduction.....	341
1.1 Interactions of Energetic Materials with Soils.....	343
2. Computational Methods.....	346
3. Interactions of Clay Minerals with Water Molecules.....	348
3.1 Experimental Study.....	349
3.2 Theoretical Study.....	351
3.3 Summary.....	355
4. Interactions of Clay Minerals with Small Organic Molecules.....	356
4.1 Experimental Study.....	356
4.1.1 D-FA and D-MFA Systems.....	357
4.1.2 K-DMSO System.....	357
4.2 Theoretical Study.....	358
4.2.1 D-FA and D-MFA Systems.....	359
4.2.2 K-DMSO System.....	363
4.3 Summary.....	365
5. Interactions of Clay Minerals with Energetic Materials.....	366
5.1 Experimental Study.....	366
5.1.1 Summary.....	371
5.2 Theoretical Study.....	372
5.2.1 Interaction of 1,3,5-Trinitrobenzene with Nonhydrated Surface of Clay Minerals.....	372
5.2.2 Interaction of 1,3,5-Trinitrobenzene with Hydrated Surface of Clay Minerals.....	377
5.2.3 Summary.....	380
6. General Conclusions and Future Research Area.....	381
<b>Chapter 13. Chemistry and Applications of Dinitramides.....</b>	<b>389</b>
<i>P. Sjöberg</i>	
1. History.....	389
2. Synthetic Methods.....	390
3. Chemistry and Properties.....	392
3.1 Reactivity.....	392
3.2 Physical Properties.....	393
3.3 Chemical Stability and Compatibility.....	393
3.4 Sensitivity.....	396
4. Applications.....	398
4.1 Propulsion.....	398
4.2 Explosive Compositions.....	399



4.2.1	Phase-stabilizer in Ammonium Nitrate (AN)...	400
4.2.2	Liquid Monopropellant.....	400
4.2.3	Automotive Safety.....	401
5.	Improvement of ADN.....	401
5.1	Stabilization of ADN.....	401
5.2	Handling Properties.....	402
 <b>Chapter 14. Polynitrogens as Promising High-Energy Density</b>		
<b>Materials: Computational Design.....</b>		<b>405</b>
<i>O. Kwon and M. L. McKee</i>		
1.	Introduction.....	405
2.	Known Computational Facts of Polynitrogens.....	407
2.1	Computational Methodology.....	408
2.2	N <sub>4</sub> .....	409
2.3	N <sub>5</sub> .....	410
2.4	N <sub>6</sub> .....	411
2.5	N <sub>7</sub> .....	411
2.6	N <sub>8</sub> .....	412
2.7	N <sub>9</sub> , N <sub>10</sub> , N <sub>11</sub> and N <sub>12</sub> .....	412
2.8	Larger polynitrogens.....	413
3.	Nitrogen-rich Compounds, EN <sub>n</sub> .....	414
4.	Conclusions.....	416
 <b>Chapter 15. Electronic Structure Calculations as a Tool</b>		
<b>in the Quest for Experimental</b>		
<b>Verification of N<sub>4</sub>.....</b>		<b>421</b>
<i>T. Brinck, M. Bittererova and H. Ostmark</i>		
1.	Introduction.....	421
2.	Energetics.....	422
2.1	N <sub>4</sub> Singlet Potential Energy Surface.....	422
2.2	N <sub>4</sub> Triplet Potential Energy Surface.....	425
3.	Synthesis.....	429
3.1	Excited State N <sub>2</sub> Reactions.....	429
3.2	Nitrogen Atom Reactions.....	430
4.	Detection.....	433
4.1	IR and Raman Spectroscopy.....	433
4.2	LIF Spectroscopy.....	435
5.	Summary.....	437
 <b>Chapter 16. Changing the Properties of N<sub>5</sub><sup>+</sup> and N<sub>5</sub><sup>-</sup> by</b>		
<b>Substitution.....</b>		<b>441</b>
<i>S. Fau and R. J. Bartlett</i>		
1.	Introduction.....	441

2. Computational Methods.....	443
3. Results.....	444
3.1 $\text{CHN}_4^+$ .....	444
3.2 $\text{N}_4\text{P}^+$ and $\text{N}_3\text{P}_2^+$ .....	445
3.3 $\text{CN}_3\text{O}^+$ .....	448
3.4 Derivatives of $\text{N}_5^-$ .....	450
4. Summary and Conclusions.....	451
<b>Index for Parts 1 and 2.....</b>	<b>457</b>

## Part 2

### Overview of Research in Energetic Materials

<i>B. M. Rice</i> .....	1
-------------------------	---

### Chapter 1. Sensitivity Correlations.....5

*P. Politzer and J. S. Murray*

1. Introduction.....	5
2. Background.....	7
3. Sensitivity Correlations.....	8
4. TATB: A Case Study.....	10
5. Electrostatic Potential.....	12
6. Summary.....	18

### Chapter 2. A Study of Chemical Micro-Mechanisms of Initiation of Organic Polynitro Compounds.....25

*S. Zeman*

1. Introduction.....	25
2. Data Sources.....	27
2.1 Impact Sensitivity Data.....	27
2.2 Electric Spark Sensitivity Data.....	27
2.3 Detonation Velocity.....	27
2.4 NMR Chemical Shifts.....	27
3. Basic Mechanisms of Thermal Decomposition of Organic Polynitro and Polynitroso Compounds.....	35
4. Initiation of Polynitro Compounds.....	36
4.1 Chemical Micro-Mechanism of Initiation by Impact.....	36
4.2 Chemical Micro-Mechanism of Initiation of Detonation.....	40
4.3 Chemical Micro-Mechanism of Initiation by Electric Shock.....	43

4.4 Chemical Micro-Mechanism of Fission of Polynitro Compounds by Action of Heat and its Relation to Detonation.....	45
5. Conclusions.....	46
<b>Chapter 3. Dynamics of Energy Disposal in Unimolecular Reactions.....</b>	<b>53</b>
<i>C. Stopera and M. Page</i>	
1. Chemical Issues in the Initiation of Detonations.....	54
2. The Key Role of Unimolecular Reactions.....	54
3. Quantum Chemistry Provides Potential Energy Surface.....	56
4. Computing the Reaction Path.....	57
5. The Reaction Hamiltonian.....	61
6. Methylene Nitramine Decomposition.....	64
7. Concluding Remarks.....	68
<b>Chapter 4. Initiation and Decomposition Mechanisms of Energetic Materials.....</b>	<b>71</b>
<i>M.R. Manaa</i>	
1. Introduction.....	71
2. Initiation Models.....	72
3. Nonradiative Energy Transfer in Nitromethane.....	73
4. Effects of Pressure and Vacancies.....	75
4.1.1 Uniform Compression.....	75
4.1.2 Uniaxial Compression.....	77
4.1.3 C-H High Stretch Under Uniaxial Compression.....	79
4.2 Effect of Molecular Vacancies.....	81
4.2.1 Uniform Compression.....	83
4.2.2 Uniaxial Compression.....	85
4.3 Summary.....	86
5. Decomposition of HMX.....	87
5.1 Computational Model.....	90
5.2 Kinetics of HMX Decomposition.....	91
5.3 Summary.....	96
<b>Chapter 5. Initiation due to Plastic Deformation from Shock or Impact.....</b>	<b>101</b>
<i>C. S. Coffey</i>	
1. Introduction.....	101
2. AFM and STM Observations of the Microscopic Processes of Plastic Deformation.....	103
2.1 Micro-Indentations.....	104

2.2	Shock Response of Heavily Confined Crystals.....	105
2.3	Impact Observations.....	106
2.4	Extreme Plastic Flow.....	106
2.5	Comparison with Gold.....	107
2.6	Summary of Experimental Observations.....	107
3.	Theoretical Developments.....	108
3.1	The Deformed Lattice Potential.....	108
3.2	Plastic Flow and Energy Dissipation.....	109
3.3	Dislocation Tunneling, Particle Size Effects and Shear Band Formation.....	111
3.4	Summary of Theoretical Results.....	112
4.	Calculations.....	113
4.1	Anomalous Plastic Deformation in Impacted RDX.....	113
4.2	Estimation of Shear Band Temperatures.....	114
4.3	Yield Stress and Particle Size.....	115
4.4	Approximate Energy Dissipation Rate and $P^2 \Delta t$ Initiation Threshold.....	116
4.5	Initiation by Non-Planar Shock Waves.....	118
4.6	Initiation of Detonation.....	119
5.	Conclusions.....	120

## **Chapter 6. Fast Molecular Processes in Energetic**

	<b>Materials.....</b>	<b>125</b>
	<i>D. D. Dlott</i>	
1.	Introduction.....	125
2.	The Phenomenology of Energetic Materials.....	126
2.1	Types of Energetic Materials.....	127
2.2	Shock Waves.....	127
2.2.1	Shock Waves in Continuous Elastic Media.....	128
2.2.2	Shock Fronts in Real Materials.....	132
2.3	Detonations.....	135
2.4	Low Velocity Initiation.....	137
2.5	Shock Initiation.....	139
2.6	Sensitivity.....	141
3.	Molecular Level Structure of Energetic Materials.....	143
3.1	How Chemical Bonds are Broken.....	143
3.2	Band Structure of Molecular Solids.....	144
3.3	Molecular Crystals under Dynamic Shock Compression.....	147
3.3.1	Shock-induced Electronic Excitations.....	147
3.3.2	Shock-induced Mechanical Excitations.....	148
3.3.3	Dynamic Picture of Shock Excitation.....	150
3.4	Shock Compression of Nanometric Energetic	

Materials.....	151
4. Up-pumping, Sensitivity and Ignition.....	153
4.1 Nitromethane Shock Initiation and the Induction Time.....	154
4.2 Doorway Vibrations in Up-pumping.....	156
4.3 Up-pumping Calculations, Simulations and Sensitivity.....	160
4.4 Up-pumping and Anharmonic Defects.....	163
4.5 Up-pumping and Thermal Conductivity.....	163
4.6 Coherent Pumping of Vibrations.....	165
5. Hot Spot Formation in Porous Materials.....	168
6. Molecular Response in Detonation.....	172
7. Fast Processes in Nanometric Energetic Materials.....	175
8. Concluding Remarks.....	179

## **Chapter 7. The Equation of State and Chemistry of Detonation Products.....193**

*L. E. Fried, W. M. Howard, and J. M. Zaug*

1. Introduction.....	193
2. Computational Method.....	198
3. Fluid Equations of State.....	200
4. Condensed Equations of State.....	207
5. Application to Detonation.....	209
6. Experimental.....	210
7. Results and Discussion.....	213
8. Conclusions.....	221

## **Chapter 8. Combustion Mechanisms and Simplified-Kinetics Modeling of Homogeneous Energetic Solids.....225**

*M.Q. Brewster*

1. Introduction.....	226
2. Mathematical Model of Macroscopically Steady Combustion...	227
2.1 Condensed Phase Model.....	228
2.1.1 Governing Equations.....	228
2.1.2 Solution of Condensed Phase Equations.....	231
2.2 Gas Phase Model.....	234
2.2.1 Governing Equations.....	234
2.2.2 Solution of Gas Phase Equations.....	239
2.3 Complete Model--Gas and Condensed Phases.....	243
2.3.1 High Gas Activation Energy Solution (Intermediate Pressures).....	244
2.3.2 Low Gas Activation Energy Solution	

(Intermediate Pressures).....	244
2.3.3 High and Low Pressure Regimes (Condensed Phase Controlled Burning).....	244
2.3.4 Sensitivity Parameters.....	245
3. Results for Macroscopically Steady Combustion.....	249
3.1 Parametric (Non-Dimensional) Results for Benchmark Case.....	249
3.1.1 Burning Rate or Mass Flux.....	250
3.1.2 Surface Temperature, Heat Feedback, and Flame Standoff Distance.....	252
3.1.3 Sensitivity Parameters.....	255
3.2 Results for Common Materials.....	258
3.2.1 NC/NG Double Base Propellant.....	259
3.2.2 HMX.....	268
3.3 Summary of Steady-State Results.....	273
4. Quasi-Steady Theory of Unsteady Condition.....	273
4.1 Non-Linear Formulation.....	274
4.2 Linear Formulation.....	276
5. Results for Quasi-Steady, Oscillatory Combustion.....	278
5.1 Parametric (Non-Dimensional) Results for Benchmark Case.....	278
5.2 Results for Common Materials.....	285
5.2.1 NC/NG Double Base Propellant.....	286
5.2.2 HMX.....	286
6. Intrinsic Stability.....	288
7. Concluding Remarks.....	290

## **Chapter 9. Modeling of Nitramine Propellant Combustion and Ignition.....**

*E. S. Kim, R. Yang and V. Yang*

1. Introduction.....	297
1.1 Modeling Development of Steady-State Combustion of Nitramine Propellants.....	298
1.2. Modeling Development of Ignition of Nitramine Propellants.....	299
1.3 Modeling Development of Combustion of Nitramine/GAP Pseudo-Propellants.....	300
2. Theoretical Formulation.....	302
2.1 Steady-State Combustion of RDX Monopropellant.....	302
2.2 Laser-Induced Ignition of RDX Monopropellant.....	303
2.3 Steady-State Combustion of Nitramine/GAP Pseudo-Propellants.....	305
2.4 Conservation Equations.....	306

2.4.1	Gas-Phase Processes.....	306
2.4.2	Gas-Phase Chemical Kinetics.....	307
2.4.3	Subsurface Two-Phase Processes.....	308
2.4.4	Subsurface Chemical Kinetics and Phase Transition.....	309
2.4.5	Solid-Phase Processes.....	311
2.4.6	Radiative Heat Transfer.....	311
2.4.7	Boundary Conditions.....	313
3.	Numerical Method.....	314
4.	Discussion of Model Results.....	315
4.1	Steady-State Combustion of Nitramine Propellants.....	316
4.2	Laser-Induced Ignition of RDX Monopropellant.....	322
4.3	Steady-State Combustion of HMX/GAP and RDX/GAP Pseudo-Propellants.....	332
4.3.1	HMX/GAP Pseudo-Propellant.....	332
4.3.2	RDX/GAP Pseudo-Propellant.....	340
5.	Concluding Remarks.....	346

## **Chapter 10. Use of Kinetic Models for Solid State Reactions in Combustion Simulations.....351**

*J. Wang and C.A. Wight*

1.	Introduction.....	351
1.1	Steady Combustion Models vs. Unsteady Combustion Models.....	352
1.2	Surface Reaction Kinetics.....	353
2.	Model.....	356
3.	Results and Discussion.....	360
3.1	Validation of the Steady State Combustion with WSB Model.....	360
3.2	Ignition Time.....	361
3.3	Pressure Sensitivity and Surface Temperature.....	362
3.4	Temperature Sensitivity.....	364
3.5	Effect of Kinetic Models.....	365
3.5.1	First-order Reaction Model.....	365
3.5.2	Second-order Reaction Model.....	367
4.	Conclusion.....	369

## **Chapter 11. Towards Reliable Prediction of Kinetics and Mechanisms for Elementary Processes: Key Combustion Initiation Reactions of Ammonium Perchlorate.....373**

*R.S. Zhu and M.C. Lin*

1.	Introduction.....	374
----	-------------------	-----

2. Computational Methods.....	375
2.1 Ab Initio Calculations.....	375
2.2 Rate Constant Calculations.....	377
3. Results and Discussion.....	379
3.1 Unimolecular Decomposition of $\text{HClO}_4$ and $\text{HClO}_3$ .....	379
3.2 Reactions of H and HO with $\text{HClO}_4$ .....	382
3.2.1 $\text{H} + \text{ClO}_4$ Reaction.....	382
3.2.2 $\text{HO} + \text{HClO}_4$ Reaction.....	386
3.3 Unimolecular Decomposition of $\text{ClO}_x$ ( $x = 2 - 4$ ).....	390
3.3.1 $\text{ClOO}$ and $\text{OCIO}$ .....	390
3.3.2 $s\text{-ClO}_3$ .....	393
3.3.3 $\text{ClO}_4$ .....	394
3.4 Bimolecular Reactions of $\text{ClO}_x$ ( $x = 1-3$ ).....	395
3.4.1 $\text{HO} + \text{ClO}$ .....	395
3.4.2 $\text{HO} + \text{OCIO}$ Reaction.....	400
3.4.3 $\text{HO} + \text{ClO}_3$ .....	404
3.4.4 $\text{HO}_2 + \text{ClO}$ .....	406
3.4.5 $\text{HO}_2 + \text{OCIO}$ .....	411
3.4.6 $\text{O} + \text{ClO}$ and its Reverse Reaction, $\text{Cl} + \text{O}_2$ .....	413
3.4.7 $\text{ClO} + \text{ClO}$ .....	415
3.4.8 $\text{ClO} + \text{OCIO}$ .....	423
4. Concluding Remarks.....	436
<b>Index for Parts 1 and 2.....</b>	<b>445</b>



This Page Intentionally Left Blank

## Overview of Research in Energetic Materials

**Betsy M. Rice**

U. S. Army Research Laboratory, Aberdeen Proving Ground, MD  
21005-5069

Energetic materials encompass different classes of chemical compositions of fuel and oxidant that react rapidly upon initiation and release large quantities of force (through the generation of high-velocity product species) or energy (in the form of heat and light). Energetic materials are typically classified as explosives, propellants, pyrotechnics or incendiaries, and distinctions among the classes are usually in terms of the types of products generated and rates of reactions. These particular features have been advantageously employed in a wide variety of industrial and military applications, but often these utilizations have not been fully optimized, mainly due to the inability to identify and understand the individual fundamental chemical and physical steps that control the conversion of the material to its final products.

The conversion of the material is usually not the result of a single-step reaction, or even a set of a few simple consecutive chemical reactions. Rather, it is an extremely complex process in which numerous chemical and physical events occur in a concerted and synergistic fashion, and whose reaction mechanisms are strongly dependent on a wide variety of factors. For instance, the performance of a material is a strong function of the temperature and pressure of its environment and of its mechanical properties. The rate of energy release can be modified by additives or by varying the concentrations of fuel and oxidizer. The response of the material can be affected by the manner in which it was processed. The properties and behavior of the material can change over time. The rate of the conversion of the material is strongly dependent on the conditions of the initiation. For example, an explosive can be ignited to burn, a process that can be thought of as a reaction wave that proceeds through the material at subsonic speeds. Or it could be shock-initiated to detonation, where detonation can be described as a reaction wave that proceeds through the material at supersonic speeds. For these cases, the product concentrations and species are not the

same. Also, these processes often occur under extreme conditions of temperature and pressures, making experimental measurement difficult. These are but a few of the complexities associated with studies of reactions of energetic materials that make resolving the individual details so difficult. They are also the reason that research in the field of energetic materials is so exciting! These difficulties have required the development of a variety of innovative theoretical methods, models and experiments designed to probe details of the various phenomena associated with the conversion of energetic materials to products.

Probably the majority of experimental and theoretical efforts in energetic materials research to date have been directed toward assessing performance. The focus is often on quantifying the amount of energy that is released, identifying key reaction mechanisms, or investigating ways in which the energy release can be manipulated and controlled. However, increased environmental and safety concerns are placing new emphases on understanding other aspects of energetic materials, such as toxicity, processing emissions, combustion emissions, wear and erosion on combustion fixtures from reaction products, contamination of ground water or soil, environmentally-friendly synthesis and processing, destruction or disposal, life-span (chemical stability), storage, handling, or vulnerability to a variety of external stimuli. Naturally, models are emerging that can be used to investigate these aspects of energetic materials.

The high time and pecuniary costs associated with the synthesis or formulation, testing and fielding of a new energetic material has called for the inclusion of modeling and simulation into the energetic materials design process. This has resulted in growing demands for accurate models to predict properties and behavior of notional energetic materials before committing resources for their development. For example, in earlier times, extensive testing and modification of proposed candidate materials for military applications could take decades before the material was actually fielded, in order to assure the quality and consistent performance of the material in the desired application. Predictive models that will allow for the screening and elimination of poor candidates before the expenditure of time and resources on synthesis and testing of advanced materials promise significant economic benefit in the development of a new material.

The growing demands for predictive models of energetic materials have not eliminated the need for experimentation on energetic materials; rather, they call for increasingly detailed experimental studies to allow critical assessment, correction and enhancement of the models. This is a particularly challenging requirement, since the time and length scales of

most experiments are often many orders of magnitude larger than those of some of the models (i.e. atomistic). Nonetheless, advances are being made in designing experiments to probe behavior of energetic materials at ever-decreasing time and spatial scales; some of these are described in these volumes.

The contributions to these volumes will highlight challenges faced by researchers in the energetic materials community, as well as describe research activities directed toward fundamental characterization of properties and behavior of these interesting materials. An assortment of theoretical studies of energetic materials processes at different time and length scales and under different conditions is presented. Accompanying these are discussions of the complexity, assumptions and levels of empiricism of the models used in these studies. Also included, in order to provide perspective, are surveys of experiments designed to investigate the complex and unique chemical and physical processes occurring in energetic materials. It is hoped that the works presented in these volumes will stimulate further investigations and advances in the area of energetic materials research.

This Page Intentionally Left Blank

## Chapter 1

# Sensitivity Correlations

**Peter Politzer and Jane S. Murray**

Department of Chemistry, University of New Orleans, New Orleans, LA  
70148, USA

## 1. INTRODUCTION

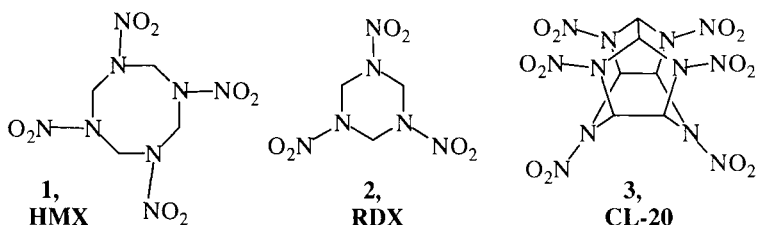
A continuing major objective in the area of energetic materials is to achieve diminished sensitivity, i.e. to reduce vulnerability to detonation initiated by unintentional external stimuli; these can include, for example, impact, shock, heat, friction and electrostatic charge [1,2]. The importance attached to this issue is seen in the establishment, by the North Atlantic Treaty Organization, of the Munitions Safety Information and Analysis Center (MSIAC, formerly NIMIC) [<http://hq.nato.int/related/nimic>]. This Center promotes efforts to decrease sensitivity and disseminates relevant information.

In general, vulnerabilities to the various types of stimuli follow roughly similar trends, although there are certainly deviations. Thus, Storm *et al* obtained satisfactory correlations, for diverse groups of compounds, between measured shock and impact sensitivities and between shock sensitivity and the critical temperature at which thermal decomposition becomes self-sustaining [3]. Zeman *et al* found somewhat more equivocal relationships involving impact and electrostatic spark sensitivity [4].

Energetic compounds are metastable. The introduction of external energy can lead to rapid decomposition, the first phase of which is endothermic but which subsequently becomes highly exothermic, releasing a great deal of energy and gaseous products at high temperatures, and giving rise to a large pressure gradient (shock front) that propagates through the compound at supersonic velocity, producing continuing self-sustaining exothermal decomposition (detonation) [1,2,5,6].

How readily this sequence of events will occur for any given compound (i.e. its sensitivity) depends of course upon its molecular structure and composition, as well as its crystal properties and physical form. Achieving greater insight into molecular factors offers a route to designing *new* less-sensitive energetic materials; understanding crystal and

designing *new* less-sensitive energetic materials; understanding crystal and physical effects may permit improvement of *existing* ones, e.g. by modification of crystallization techniques and conditions. For instance, the  $\beta$  polymorph of HMX (1) is more stable toward impact than is the  $\delta$  [7], and both are made somewhat less sensitive by grinding the crystals. Appropriate alterations of crystal shapes have diminished the shock sensitivities of several explosives, including RDX (2), HMX and CL-20 (3) [8,9].



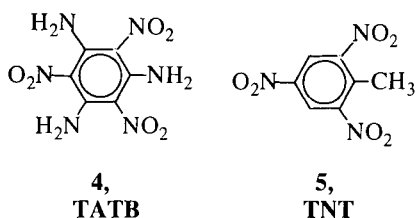
Over a period of years, considerable effort has gone into developing relationships that correlate (and hence can predict) sensitivity in terms of some molecular or crystal property, usually the former. The first problem is obtaining reliable and reproducible experimental data. These correlations most often focus upon impact sensitivity, which is normally determined by measuring the height from which a given mass, dropped on the material, has a 50% likelihood of causing detonation [1-3,10,11]. The greater is this height, designated  $h_{50}$ , the lower is the sensitivity. The results of this “drop-weight” test are very dependent upon the exact procedure that is followed and the condition of the sample, and are frequently difficult to reproduce.

A more serious problem, however, is that the initiation of detonation, as already mentioned and to be further discussed, depends upon a complex interplay of various molecular, crystal and physical factors. It can therefore be viewed as remarkable that relatively good correlations have been established between impact sensitivity and a number of different properties, although they are generally limited to a particular class of compounds, e.g. nitroaromatics. The existence of these relationships certainly does not mean that all of these properties (or perhaps any of them) play important roles in detonation initiation, as was pointed out by Brill and James [12,13]. Many of them may be symptoms of some more fundamental factor; others may happen to correlate with a more relevant property.

In this chapter, we shall present an overview of some of these sensitivity correlations. We shall try, as much as possible, to relate them to a conceptual framework.

## 2. BACKGROUND

A key concept, with respect to detonation initiation, is that of hot spots, proposed by Bowden and Yoffe [14,15]. These are small regions in the crystal lattice in which is localized some portion of the energy introduced by, for example, impact or shock. If this energy is sufficiently channeled into appropriate molecular vibrational modes, it may result in the endothermic bond-breaking or other step that leads to exothermic decomposition and detonation. For this to happen, hot spots must be large enough and hot enough that they are not prematurely dissipated by thermal diffusion. Bowden and Yoffe estimated their dimensions to be of the order of  $10^{-6}$  m, temperatures  $> 700$  K and lifetimes of  $10^{-5}$  to  $10^{-3}$  s [14,15]. Later work, cited by Tarver *et al* [16], indicated that this description roughly fits shock-induced hot spots but that those due to impact are larger and longer-lived, by factors of about  $10^3$ . More recently, however, atomic force microscopy studies of RDX have shown that the latter can be as small as  $\sim 10^{-8}$  m [17]. Using a combination of techniques (scanning electron microscopy, x-ray photoelectron spectroscopy and chemical-ionization mass spectrometry), it has been possible to identify, associated with hot spots, some of the decomposition products of TATB (**4**) and TNT (**5**) [18]. Tarver *et al* have modeled hot spots and the ignition of exothermic decomposition in HMX and TATB [16]. They found that as the hot spot becomes larger, the temperature required for ignition decreases but the time increases.



The formation of hot spots is generally attributed to the presence of lattice defects [11,17,19-23], which could include vacancies, voids, dislocations, misalignments, cracks, impurities, etc. One explanation is that defects induce strain in the lattice, which is relieved, via structural relaxation, by the externally-introduced energy; this results in a disproportionate localization of energy in the neighborhood of the defect, a portion of it being in lattice vibrations [21,22]. The thermal energy of hot spots must be efficiently transferred to appropriate molecular vibrational



modes, a process called “up-pumping” [24-27], if bond-breaking and subsequent exothermic decomposition and detonation are to be achieved. The term “trigger linkage” has been applied to the key bond or bonds that are initially ruptured [28]. Any dissipation of hot spot energy, for instance by diffusion, will lessen the likelihood of these processes. Thus Kamlet suggested that free rotation around the trigger linkage can have a desensitizing effect, since it uses energy that could otherwise go into bond-breaking vibrational modes [28,29].

The fact that solids composed entirely of very small particles are less sensitive [7,30] can now be explained on the grounds that these will have smaller hot spots and thus, as shown by Tarver *et al* [16], require higher temperatures for ignition. Once this has been achieved, however, these higher temperatures will result in more rapid reaction, as has been observed [31].

It should be noted that initiation of detonation can occur even in a homogeneous (defect-free) solid [6,24,32-36] (although this is of less practical significance since energetic compounds typically do contain lattice defects of various sorts). This can occur, for example, if there is efficient anharmonic coupling to channel energy from lattice into the critical molecular vibrations [24,25,36].

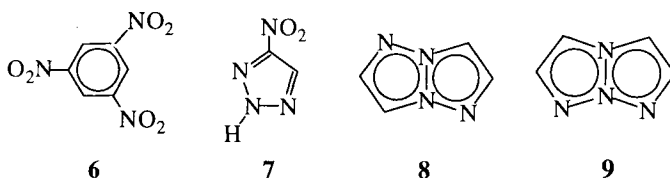
### 3. SENSITIVITY CORRELATIONS

The concepts that were outlined in the last section have suggested several approaches to developing sensitivity correlations. A popular one has been to focus upon the trigger linkage. Kamlet viewed C–NO<sub>2</sub> and N–NO<sub>2</sub> bonds as playing this role in H/C/N/O explosives, and scission of these bonds, which tend to be the weakest in the molecule [13,37-39], has indeed been shown experimentally to be the first step in the thermal decompositions of many of them [12,13,37,40-42]. Accordingly there have been a number of attempts to correlate sensitivity with properties of C–NO<sub>2</sub> and N–NO<sub>2</sub> bonds, generally some measure of their stabilities [39,43-46]. On the whole, these have been quite successful, although they are usually limited to a given class of compounds, e.g. nitramines, nitroaromatics, etc. However Owens was able to correlate with impact sensitivity the computed C–NO<sub>2</sub>, N–NO<sub>2</sub> and O–NO<sub>2</sub> bond energies of 11 molecules of different types: nitroaromatics, nitramines and nitrates [39].

An interesting variation of this emphasis upon the trigger linkage was offered by Kohno *et al* [47-49], who noted that the N–NO<sub>2</sub> distances in a group of seven nitramines (including RDX and the polymorphs of HMX) are shorter in the crystal than in the gas phase, by 0.05 – 0.08 Å. This does not occur with the C–N and N–O bonds. They suggested that this compression introduces destabilizing strain into the crystal, and were able

to correlate it approximately with the measured sensitivity. In a molecular dynamics study [49], Kohno *et al* observed intramolecular vibrational energy transfer between the N–NO<sub>2</sub> bonds, and concluded that they serve as hot spots in the crystal.

While some success has been achieved by focusing upon the strengths of C–NO<sub>2</sub> and N–NO<sub>2</sub> bonds, it is clear that other molecular factors or reactive behavior may be important in determining sensitivity. Kamlet himself recognized this when he pointed out the significance of decomposition steps that may follow N–NO<sub>2</sub> rupture in nitramines and are autocatalyzed by the NO<sub>2</sub> [28]. Brill and James have emphasized the role of reactions subsequent to C–NO<sub>2</sub> scission in the series of amino derivatives of 2,4,6-trinitrobenzene (**6**) [12,13]. In the case of TNT, there is evidence that H<sub>2</sub>C–H bond-breaking is the critical event [13,50], while the sensitivities of hydroxynitroaromatics have been related to intramolecular OH---ONO interactions [51,52]. The presence of several linked nitrogens in a molecule can be associated with instability if it allows the facile loss of N<sub>2</sub> [53]; the differing sensitivities of some picryl triazoles were explained in this manner by Storm *et al* [54], and a computational study has shown that analogous reasoning can account for the high sensitivity of the triazole **7** [55]. (On the other hand, some derivatives of the tetraazapentalenes **8** and **9** are remarkably stable [53,56,57], which we speculate may be due to the relatively positive natures of the two triply-coordinated nitrogens [58].)



Another approach to sensitivity correlations centers on the transfer of energy from the hot spot into molecular vibrational modes. Fried and Ruggiero [59] and McNesby and Coffey [27] have separately derived formulas for predicting the energy transfer rate. Both require experimental input; Fried and Ruggiero used inelastic neutron scattering data to obtain densities of lattice vibrational states, while McNesby and Coffey, whose procedure was based on bulk and molecular vibrational energy levels, determined these from Raman spectra. Both formulas produced rates of energy transfer that correlate quite well with measured impact sensitivities for two groups of seven compounds. In the present context, as well as with respect to viewing C–NO<sub>2</sub> and N–NO<sub>2</sub> as trigger linkages, it is relevant to mention the evidence indicating that the NO<sub>2</sub>

group has an enhanced capacity for accepting transferred vibrational energy [36,59,60].

Electronic excitation has sometimes been linked to sensitivity. The emphasis has often been upon valence electron promotion energies [61-63]; however Manaá and Fried suggested the possibility of ground-state vibrational excitation via intersystem crossing from higher electronic states [64]. Earlier work by Sharma *et al* can be viewed as providing some support for this [65]. Delpuech and Cherville related shock sensitivities to changes in C–NO<sub>2</sub>, N–NO<sub>2</sub> and O–NO<sub>2</sub> bond polarities in going from ground to excited electronic states [66].

Finally, there is a long history of efforts to correlate detonation-related properties, including sensitivity, explicitly with chemical composition [3,10,28,29,67-76]. Primarily H/C/N/O/F compounds have been considered, and usually each chemical type (e.g. nitramines) has been treated separately. The results, overall, have been good. The best known of these procedures is Kamlet's oxygen balance approach [28,29,70], in which sensitivity is related essentially to the number of oxygen atoms in the molecule relative to what is needed for complete conversion of hydrogens to H<sub>2</sub>O and carbons to CO. In general, the more positive is the oxygen balance, the greater is the sensitivity. There are certainly exceptions [28,29,70], for example isomers with significantly different sensitivities [10,54], and Bliss *et al* argue that the oxygen balance is simply symptomatic of the actual causes of sensitivity [10]. Its perhaps surprising success can be rationalized, as pointed out by Kamlet [28,70] and by Stine [76], that some of the key determinants of detonation properties can be expected to be similar for compounds of the same type, so that the differentiating factor, to a large extent, may be stoichiometry (upon which will depend, for example, the number of moles of gaseous products obtained per gram of compound upon decomposition, an important element in detonation performance [1,2,6]). This generalization is of course limited; thus Kamlet and Adolph found it necessary to separate nitroaromatics into two groups [29,70], depending upon whether or not they contain an  $\alpha$ -C–H linkage (as in TNT), the presence of which permits a unique decomposition route, via rupture of this bond [13,50].

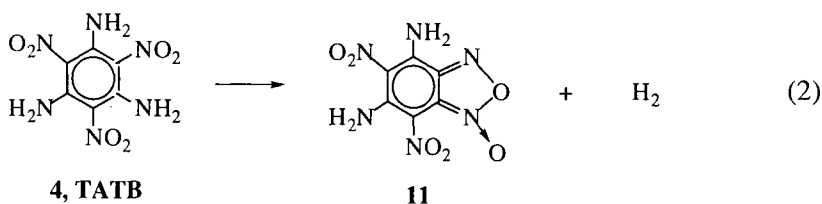
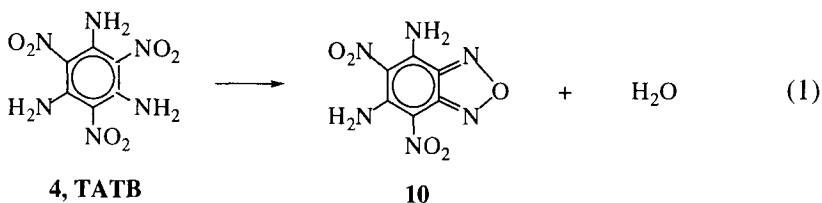
#### 4. TATB: A CASE STUDY

In the context of the various concepts that have been advanced to help elucidate detonation initiation and sensitivity, we will use TATB to illustrate the variety of molecular factors that can be involved, some having apparently opposing effects. (For an excellent discussion of TATB properties and detonation behavior, see Storm and Travis [77].) TATB (4, 1,3,5-triamino-2,4,6-trinitrobenzene) is well known for its remarkable

insensitivity; by the drop-weight method of measuring impact sensitivity, it is actually off the scale, and its  $h_{50}$  value must be estimated by extrapolation [3,77]. It has accordingly been a favorite target for investigation.

An outstanding feature of TATB is the strong and extensive hydrogen bonding, both inter- and intramolecular, between the  $\text{NO}_2$  and  $\text{NH}_2$  groups. This would be anticipated from its molecular structure, and has been confirmed crystallographically [78] and spectroscopically [79]. The intermolecular hydrogen bonding gives rise, in the solid, to a two-dimensional graphite-like network [78], to which is attributed the relatively high thermal conductivity of TATB [16,80]. In terms of the hot spot concept, this is a desensitizing factor, since it results in a more rapid dissipation of their energy through thermal diffusion; it is also one of the reasons why TATB requires a high ignition temperature [16]. On the other hand, the strong intramolecular hydrogen bonding should increase the  $\text{NO}_2$  rotational barrier, an expectation for which density functional calculations provide some support [81]. By Kamlet's reasoning [28,29], this should have a sensitizing effect, since it diminishes the loss of energy through rotation and makes more of it available to the key  $\text{NO}_2$  vibrational mode(s).

It is believed that  $\text{C}-\text{NO}_2$  homolysis is the first or one of the first steps in TATB initiation [12]. This is consistent with the idea of a trigger linkage. However the key early decomposition reactions appear to produce furazans and furoxans, e.g. **10** and **11** [12,13,18,65,77,82]:



Products **10** and **11** may undergo further internal cyclizations. Furazans and furoxans are known to be more sensitive than TATB [3,18,77,83], and their formation has been interpreted as a sensitizing event [18]. However the reactions leading to furazans and furoxans are not exothermic; eq.(2) is

actually endothermic, while eq. (1) has  $\Delta H \sim 0$  [3,16,77,82,84]. Thus these processes cannot sustain further decomposition and detonation; the required energy must be provided by subsequent steps [3,12,13,16,77,85]. Catalano and Rolon found explosion to be preceded by three stages, a slow endothermic one followed by two slow exothermic ones [85]. This delay, and the need for a series of consecutive reactions, have been viewed as a key element in TATB insensitivity [3,77].

Our purpose in this discussion is certainly not to disparage any concept or chemical or physical evidence. It is, rather, to show the number and range of valid molecular factors that can have a role in determining the sensitivity in this instance, and in others as well. The fact that it has been possible to obtain satisfactory correlations of sensitivity with individual molecular features, even though limited to specific chemical classes, suggests therefore that these features must also reflect other factors, whether directly or indirectly. It might accordingly be useful to find some way to characterize a molecule as a whole, not focusing upon any particular aspect of it, such as a certain bond, vibrational mode, etc. We shall move in this direction in the next section.

## 5. ELECTROSTATIC POTENTIAL

Hohenberg and Kohn proved in 1964 that the energy and all other properties of a system of nuclei and electrons can be obtained rigorously from its electronic density  $\rho(\mathbf{r})$  [86]. In turn,  $\rho(\mathbf{r})$  is linked by Poisson's equation [87], eq. (3), to the electrostatic potential  $V(\mathbf{r})$  that is produced by the nuclei and electrons:

$$\nabla^2 V(\mathbf{r}) = 4\pi\rho(\mathbf{r}) - 4\pi \sum_A Z_A \delta(\mathbf{R}_A - \mathbf{r}) \quad (3)$$

In eq. (3),  $Z_A$  is the charge on nucleus A, located at  $\mathbf{R}_A$ , while  $V(\mathbf{r})$  is given by,

$$V(\mathbf{r}) = \sum_A \frac{Z_A}{|\mathbf{R}_A - \mathbf{r}|} - \int \frac{\rho(\mathbf{r}') d\mathbf{r}'}{|\mathbf{r}' - \mathbf{r}|} \quad (4)$$

It follows then that the electrostatic potential can also be regarded as a fundamental determinant of a system's properties [88-90], one which may in some instances be more amenable to further analysis and application. For example, it has proven possible to derive exact expressions that relate atomic and molecular energies to  $V(\mathbf{r})$  at the positions of the nuclei [90-92]. It should be noted that  $V(\mathbf{r})$  is a physical observable, which can be

obtained experimentally, by diffraction techniques [93-96], as well as computationally.

Applications of molecular electrostatic potentials to a variety of areas – chemical reactivity and biological interactions [97-105], solvation [98,106], covalent and ionic radii [107], prediction of condensed-phase physical properties [108-110], atomic and molecular energies [89,92,111] – have been reviewed elsewhere, as indicated. Our purpose here is to relate  $V(\mathbf{r})$  to sensitivity.

We will look in particular at the detailed features of  $V(\mathbf{r})$  computed on the surfaces of energetic molecules, which is designated  $V_s(\mathbf{r})$ . This raises the question of how to define a molecular surface. In the past, this has often been done by means of fused spheres centered at the nuclear positions and having, for example, the corresponding van der Waals atomic radii [112,113]. More recently, however, there has been an increasing tendency to follow Bader *et al* [114] and take the surface to be some outer contour of the electronic density. This has the advantage that the surface then reflects the specific features of that molecule, such as lone pairs and strained bonds. We use this approach, with  $\rho(\mathbf{r}) = 0.001$  electrons/bohr<sup>3</sup>; other outer contours, e.g.  $\rho(\mathbf{r}) = 0.002$  electrons/bohr<sup>3</sup>, would serve just as well [115].

For a neutral free atom,  $V(\mathbf{r})$  is positive everywhere [116]; the effect of the nucleus dominates over that of the dispersed electrons. When atoms combine to form a molecule, the subtle charge rearrangements that occur, which give rise to bonding, also normally produce some regions of negative  $V(\mathbf{r})$ . These are often associated with lone pairs, but can also be due to the  $\pi$  electrons of unsaturated molecules, or to strained bonds. The most negative value reached in such a region is the local  $V_{\min}$ ; however, as shown by Pathak and Gadre [117], there are no local maxima,  $V_{s,\max}$ , in the three-dimensional space of the molecule other than those corresponding to the nuclei. The situation is different on the molecular surface, which is our present interest. The positive and negative portions of the surface do have both local maxima,  $V_{s,\max}$ , and local minima,  $V_{s,\min}$ , respectively.

A characteristic feature of the  $V_s(\mathbf{r})$  of nitroaromatics, nitroheterocycles and nitroalkanes is a buildup of positive potential, with a local  $V_{s,\max}$ , above the C–NO<sub>2</sub> bonds [118-120]. (See Figure 1.) This has not been observed to be associated with chemical bonds in general. It was shown that this positive buildup provides a channel for the initial approach of a nucleophile [121,122]. More relevant in the present context, however, is the fact that  $V_{s,\max}$  correlates reasonably well with the strength of the C–NO<sub>2</sub> bond, provided that the size of the molecule is taken into account [119,120]; for molecules with approximately the same surface area, the more positive is the  $V_{s,\max}$  above the C–NO<sub>2</sub> bond, the weaker is the bond.

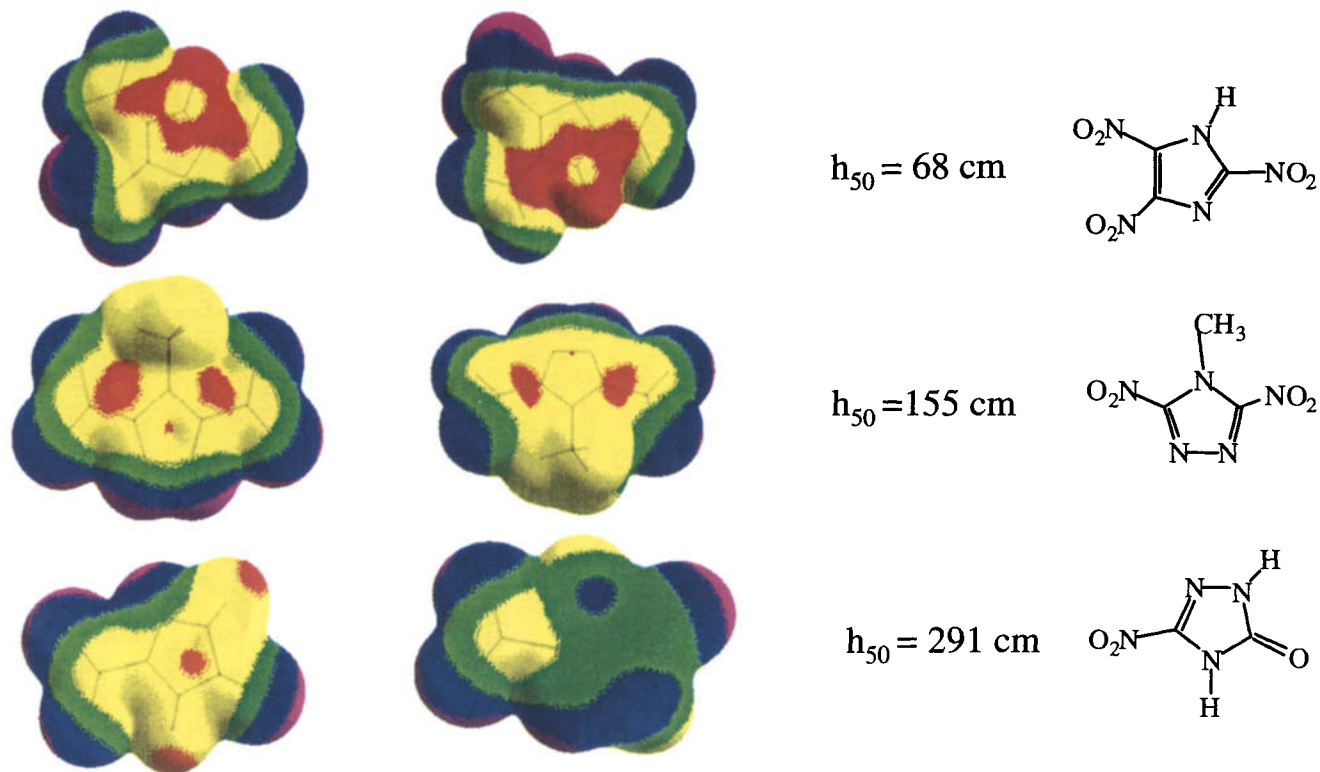


Figure 1. Electrostatic potentials, computed at the Hartree-Fock STO-5G//STO-3G level, on the front and back molecular surfaces of the three nitroheterocycles shown. Their measured impact sensitivities, taken from Storm *et al* [3], are indicated. Color ranges, in kcal/mole: red, more positive than 40; yellow, between 40 and 20; green, between 20 and 0; blue, between 0 and -20; violet, more negative than -40.

The surface potentials of energetic molecules are unusual in other respects as well. In the great majority of organic molecules, the regions of negative  $V_s(\mathbf{r})$  are smaller in area but often quite strong, while the more extensive positive regions are significantly weaker. In energetic molecules, on the other hand, the positive  $V_s(\mathbf{r})$  still cover the larger areas but now tend to be much stronger than the negative (Figure 1).

We can quantify these effects by computing the average positive and negative values of  $V_s(\mathbf{r})$ ,  $\bar{V}_s^+$  and  $\bar{V}_s^-$ , and their variances,  $\sigma_+^2$  and  $\sigma_-^2$ ; these are defined by eqs. (5) and (6):

$$\bar{V}_s^+ = \frac{1}{m} \sum_{i=1}^m V_s^+(\mathbf{r}_i) \quad \bar{V}_s^- = \frac{1}{n} \sum_{j=1}^n V_s^-(\mathbf{r}_j) \quad (5)$$

$$\sigma_+^2 = \frac{1}{m} \sum_{i=1}^m [V_s^+(\mathbf{r}_i) - \bar{V}_s^+]^2 \quad \sigma_-^2 = \frac{1}{n} \sum_{j=1}^n [V_s^-(\mathbf{r}_j) - \bar{V}_s^-]^2 \quad (6)$$

In eqs. (5) and (6),  $V_s^+(\mathbf{r}_i)$  and  $V_s^-(\mathbf{r}_j)$  are the positive and negative values of  $V_s(\mathbf{r})$ . The variances,  $\sigma_+^2$  and  $\sigma_-^2$ , are measures of the spreads or ranges covered by the positive and negative surface potentials, emphasizing their extremes because of the terms being squared. The total variance,  $\sigma_{\text{tot}}^2 = \sigma_+^2 + \sigma_-^2$ , indicates the spread of the overall  $V_s(\mathbf{r})$ . (We have found that these quantities, plus a few others that help to characterize  $V_s(\mathbf{r})$ , permit us to develop analytical representations of liquid and solid physical properties that are determined by noncovalent interactions [108-110]; two of these properties are heats of sublimation and of fusion, both of which have been mentioned as possibly relevant to detonation initiation [10,28,70].)

In Table 1 are listed the positive and negative (a) surface areas,  $A_s^+$  and  $A_s^-$ , (b) averages,  $\bar{V}_s^+$  and  $\bar{V}_s^-$ , and (c) variances,  $\sigma_+^2$  and  $\sigma_-^2$ , for 21 typical organic molecules and 5 energetic ones. These data show the trends described earlier:

- (1)  $A_s^+$  is larger than  $A_s^-$  in all except two instances, often by a factor of two or more.
- (2) For the general group, the magnitudes of  $\bar{V}_s^-$  and  $\sigma_-^2$  are nearly always larger than those of  $\bar{V}_s^+$  and  $\sigma_+^2$ ; the disparity between  $\sigma_+^2$  and  $\sigma_-^2$  is sometimes quite sizable.
- (3) For the energetic group,  $\bar{V}_s^+ > |\bar{V}_s^-|$  and  $\sigma_+^2 > \sigma_-^2$  for every molecule included.



More extensive databases confirm that these patterns are general ones [125,126].

The striking reversal in the strengths of the positive and negative surface potentials that is characteristic of energetic molecules is due to the strongly electron-attracting natures of nitro groups [127], and to a lesser extent, azine nitrogens [128]. These withdraw electronic charge from the central portions of the molecules, leaving strong and extensive positive potentials above these regions, often with more than one  $V_{s,max}$ ; the latter may be, for example, above C–NO<sub>2</sub> bonds and above phenyl rings. The only negative regions are likely to be above parts of the peripheries of the molecules, over the nitro oxygens and any azine nitrogens. These features are clearly seen in Figure 1, as well in earlier work [118] and in the recent study by Rice and Hare [129].

It should be noted that simply the presence of an NO<sub>2</sub> or azine nitrogen does not suffice to produce the effects that have been described; this is shown by several examples in Table 1. What is needed, just as for energetic performance, is that these moieties represent some critical portion of the entire molecule.

According to the “electroneutrality rule” postulated by Pauling [130,131], “....the electronic structure of substances is such as to cause each atom to have essentially zero resultant electrical charge,” [130]. This means that the tendency in a molecular system is that its electrostatic potential be as uniform and close to neutral as possible; deviations from this promote instability. This reasoning, upon which Pauling expands at length, suggests that the metastabilities of energetic compounds should be related to the typically strongly positive and variable  $V_s(\mathbf{r})$  on their molecular surfaces, and that this should provide a basis for quantifying their sensitivities.

Qualitatively, the sensitivity does tend to increase as  $V_s(\mathbf{r})$  becomes more positive and more variable, particularly within a given chemical class. This can be seen for the nitroheterocycles in Figure 1, and Rice and Hare noted this trend in their figures [129]. We proposed some time ago [125,132] that it would be reasonable to look for quantitative relationships between sensitivity and the marked imbalance between positive and negative  $V_s(\mathbf{r})$ . There are a number of ways in which this imbalance can be expressed mathematically, e.g.  $\bar{V}_s^+ - |\bar{V}_s^-|$ ,  $\bar{V}_s^+ / |\bar{V}_s^-|$ ,  $\sigma_+^2 - \sigma_-^2$ ,  $\sigma_+^2 / \sigma_-^2$ , etc. We found that different ones of these were most effective for each of the three types of energetic compounds considered: nitroaromatics, nitramines and nitroheterocycles. In each case, however, an excellent correlation with measured impact sensitivity was obtained [125,132]; the three correlation coefficients were all  $\geq 0.990$ , and the standard deviations were between 8 and 14 cm, for  $h_{50}$  values that ranged from 13 to 320 cm.

We agree with Rice and Hare [129] that it would be desirable to have all chemical classes fit a single correlation, and this continues to be one of our objectives; with this in mind, we are testing other functions of  $\bar{V}_S^+$ ,  $\bar{V}_S^-$ ,  $\sigma_+^2$  and  $\sigma_-^2$ . What is pleasing, however, is that there is a unifying concept, that applies to all of the energetic compounds that we have considered: sensitivity is related to the anomalous imbalance between the strong and variable positive surface potentials and the weaker negative ones.

## 6. SUMMARY

The molecular electrostatic potential offers a means of characterizing molecules at a fundamental level. It reveals a striking distinction between energetic nitroaromatics, nitramines and nitroheterocycles on the one hand, and the great majority of organic molecules on the other. The former are distinguished by extensive strong and variable positive surface potentials that dominate over the negative ones, i.e.  $\bar{V}_S^+ > |\bar{V}_S^-|$  and  $\sigma_+^2 > \sigma_-^2$ . This is exactly opposite to the usual  $|\bar{V}_S^-| > \bar{V}_S^+$  and  $\sigma_-^2 > \sigma_+^2$ . We have proposed that the metastabilities of energetic compounds are associated with this anomalous imbalance between positive and negative  $V_S(\mathbf{r})$ , and that it can serve as a basis for correlating and predicting sensitivity. The important point is that this is a single unifying concept, which qualitatively cuts across the differences between chemical types. Our quantitative correlations, while excellent, are currently restricted to specific classes: nitroaromatics, nitramines or nitroheterocycles. The challenge now is to unify these as well.

## ACKNOWLEDGEMENT

We greatly appreciate the financial support of the Office of Naval Research, Contract No. N00014-99-1-0393, Project Officer Dr. Judah M. Goldwasser.

## REFERENCES

- [1] S. Iyer and N. Slagg, in: J. F. Liebman and A. Greenberg (eds.), *Structure and Reactivity*, VCH Publishers, New York, 1988, ch. 7.
- [2] J. Kohler and R. Meyer, *Explosives*, 4th ed., VCH Publishers, New York, 1993.

- [3] C. B. Storm, J. R. Stine and J. F. Kramer, in: S. N. Bulusu (ed.), *Chemistry and Physics of Energetic Materials*, Kluwer, Dordrecht (The Netherlands), 1990, ch. 27.
- [4] S. Zeman, Z. Kamensky, P. Valenta and J. Jakubko, *Proceedings of the Study Days on the Sensitivity of Energetic Components and Substances to Electrostatics*, Aussois, France, 1996, 197.
- [5] P. A. Urtiew and B. Hayes, *J. Energet. Mater.*, 9 (1991) 297.
- [6] C. L. Mader, *Numerical Modeling of Explosives and Propellants*, 2nd ed., CRC Press, New York, 1998.
- [7] M. Herrmann, W. Engel and N. Eisenreich, *Propell. Expl. Pyrotech.*, 17 (1992) 190.
- [8] A. E. D. M. van der Heijden and R. H. B. Bouma, *Proceedings of the 29th ICT Conference*, Karlsruhe, 1998.
- [9] R. H. B. Bouma and A. E. D. M. van der Heijden, *Proceedings of the 32nd ICT Conference*, Karlsruhe, 2001.
- [10] D. E. Bliss, S. L. Christian and W. S. Wilson, *J. Energet. Mater.*, 9 (1991) 319.
- [11] J. E. Field, *Acc. Chem. Res.*, 25 (1992) 489.
- [12] T. B. Brill and K. J. James, *J. Phys. Chem.*, 97 (1993) 8752.
- [13] T. B. Brill and K. J. James, *Chem. Rev.*, 93 (1993) 2667.
- [14] F. P. Bowden and A. D. Yoffe, *Initiation and Growth of Explosion in Liquids and Solids*, Cambridge University Press, Cambridge, 1952.
- [15] F. P. Bowden and A. D. Yoffe, *Fast Reactions in Solids*, Butterworths, London, 1958.
- [16] C. M. Tarver, S. K. Chidester and A. L. Nichols III, *J. Phys. Chem.*, 100 (1996) 5794.
- [17] J. Sharma, C. S. Coffey, A. L. Ramaswamy and R. W. Armstrong, *Mat. Res. Soc. Symp. Proc.*, 418 (1996) 257.
- [18] J. Sharma and B. C. Beard, in: S. N. Bulusu (ed.), *Chemistry and Physics of Energetic Materials*, Kluwer, Dordrecht (The Netherlands), 1990, ch. 26.
- [19] A. W. Campbell, W. C. Davis, J. B. Ramsay and J. R. Travis, *Phys. Fluids*, 4 (1961) 511.
- [20] R. W. Armstrong, C. S. Coffey, V. F. DeVost and W. L. Elban, *J. Appl. Phys.*, 64 (1990) 979.
- [21] D. H. Tsai and R. W. Armstrong, *J. Phys. Chem.*, 98 (1994) 10997.
- [22] D. H. Tsai, *Mat. Res. Soc. Symp. Proc.*, 418 (1996) 281.
- [23] C. T. White, J. J. C. Barrett, J. W. Mintmire, M. L. Elert and D. H. Robertson, *Mat. Res. Soc. Symp. Proc.*, 418 (1996) 277.
- [24] D. D. Dlott and M. D. Fayer, *J. Chem. Phys.*, 92 (1990) 3798.
- [25] A. Tokmakoff, M. D. Fayer and D. D. Dlott, *J. Phys. Chem.*, 97 (1993) 1901.

- [26] S. Chen, W. A. Tolbert and D. D. Dlott, *J. Phys. Chem.*, 98 (1994) 7759.
- [27] K. L. McNesby and C. S. Coffey, *J. Phys. Chem. B*, 101 (1997) 3097.
- [28] M. J. Kamlet, *Proc. 6th Symp. (Internat.) Deton.*, Report No. ACR 221, Office of Naval Research, 1976, p. 312.
- [29] M. J. Kamlet and H. G. Adolph, *Proc. 7th Symp. (Internat.) Deton.*, Report No. NSWCMP-82-334, Naval Surface Warfare Center, Silver Springs, MD, 1981, p. 84.
- [30] R. E. Setchell, *Combust. Flame*, 56 (1984) 343.
- [31] S. G. Cochran and C. M. Tarver, in: J. R. Asay, R. A. Graham and G. K. Straub (eds.), *Shock Waves in Condensed Matter-1983*, Elsevier, Amsterdam, 1984, p. 593.
- [32] S. G. Lambrakos, M. Peyrard, E. S. Oran and J. P. Boris, *Phys. Rev. B*, 39 (1989) 993.
- [33] R. Bardo, in R. W. Armstrong, R. Lieb, D. H. Liebenberg, R. S. Miller and S. A. Shackelford (eds.), *Workshop on Desensitization of Explosives and Propellants*, Report No. ONREUR 92-1-W, Office of Naval Research European Office, 1992, p. 2.
- [34] R. Maffre and M. Peyrard, *Phys. Rev. B*, 45 (1992) 9551.
- [35] L. Phillips, *Mat. Res. Soc. Symp. Proc.*, 296 (1993) 155.
- [36] X. Hong, S. Chen and D. D. Dlott, *J. Phys. Chem.*, 99 (1995) 9102.
- [37] T. B. Brill, in: S. N. Bulusu (ed.), *Chemistry and Physics of Energetic Materials*, Kluwer, Dordrecht (The Netherlands), 1990, ch. 13.
- [38] C. F. Melius, in: S. N. Bulusu (ed.), *Chemistry and Physics of Energetic Materials*, Kluwer, Dordrecht (The Netherlands), 1990, ch. 3.
- [39] F. J. Owens, *J. Mol. Struct. (Theochem)*, 370 (1996) 11.
- [40] G. F. Adams and R. W. Shaw, Jr., *Annu. Rev. Phys. Chem.*, 43 (1992) 311.
- [41] T. R. Botcher and C. A. Wight, *J. Phys. Chem.*, 98 (1994) 5441.
- [42] J. C. Oxley, J. L. Smith, H. Ye, R. L. McKenney and P. R. Bolduc, *J. Phys. Chem.*, 99 (1995) 9593.
- [43] J. S. Murray and P. Politzer, in: S. N. Bulusu (ed.), *Chemistry and Physics of Energetic Materials*, Kluwer, Dordrecht (The Netherlands), 1990, ch. 8.
- [44] P. Politzer and J. S. Murray, *J. Mol. Struct.*, 376 (1996) 419.
- [45] H.-M. Xiao, J.-F. Fan, Z.-M. Gu and H.-S. Dong, *Chem. Phys.*, 226 (1998) 15.
- [46] B. M. Rice, S. Sahu and F. J. Owens, *J. Mol. Struct. (Theochem)*, 583 (2002) 69.
- [47] Y. Kohno, K. Mackawa, T. Tsuchioka, T. Hashizume and A. Imamura, *Chem. Phys. Lett.*, 214 (1993) 603.

- [48] Y. Kohno, K. Mackawa, T. Tsuchioka, T. Hashizume and A. Imamura, *Combust. Flame*, 96 (1994) 343.
- [49] Y. Kohno, K. Ueda and A. Imamura, *J. Phys. Chem.*, 100 (1996) 4701.
- [50] S. Bulusu and J. R. Autera, *J. Energet. Mater.*, 1 (1983) 133.
- [51] P. Politzer and J. M. Seminario, *Chem. Phys. Lett.*, 158 (1989) 463.
- [52] J. Fan, Z. Gu, H. Xiao and H. Dong, *J. Phys. Org. Chem.*, 11 (1998) 177.
- [53] F. R. Benson, *The High Nitrogen Compounds*, Wiley-Interscience, New York, 1984.
- [54] C. B. Storm, R. R. Ryan, J. P. Ritchie, J. H. Hall and S. M. Bachrach, *J. Phys. Chem.*, 93 (1989) 1000.
- [55] P. Politzer, M. E. Grice and J. M. Seminario, *Int. J. Quantum Chem.*, 61 (1997) 389.
- [56] R. Pflieger, E. Garthe and K. Raner, *Chem. Ber.*, 96 (1963) 1827.
- [57] R. A. Carboni, J. C. Kaner, J. E. Castle and H. E. Simmons, *J. Am. Chem. Soc.*, 89 (1967) 2618.
- [58] M. E. Grice and P. Politzer, *J. Mol. Struct. (Theochem)*, 358 (1995) 63.
- [59] L. E. Fried and A. J. Ruggiero, *J. Phys. Chem.*, 98 (1994) 9786.
- [60] X. Hong, J. R. Hill and D. D. Dlott, *Mat. Res. Soc. Symp. Proc.*, 418 (1996) 357.
- [61] J. Sharma, B. C. Beard and M. Chaykovsky, *J. Phys. Chem.*, 95 (1991) 1209.
- [62] J. Sharma and B. C. Beard, *Mat. Res. Soc. Symp. Proc.*, 296 (1993) 189.
- [63] M. M. Kuklja, E. V. Stefanovich and A. B. Kunz, *J. Chem. Phys.*, 112 (2000) 3417.
- [64] M. R. Manaa and L. E. Fried, *J. Phys. Chem. A*, 103 (1999) 9349.
- [65] J. Sharma, J. C. Hoffsommer, D. J. Glover, C. S. Coffey, F. Santiago, A. Stolovy and S. Yasuda, in: J. R. Asay, R. A. Graham and G. K. Straub (eds.), *Shock Waves in Condensed Matter-1983*, Elsevier, Amsterdam, 1984, p. 543.
- [66] A. Delpuech and J. Cherville, *Propell. Explos.*, 3 (1978) 169; 4 (1979) 61, 121.
- [67] W. C. Lothrop and G. R. Handrick, *Chem. Rev.*, 44 (1949) 419.
- [68] A. R. Martin and H. J. Yallop, *Trans. Faraday Soc.*, 54 (1958) 257.
- [69] A. Mustafa and A. A. Zahran, *J. Ind. Eng. Chem. Data*, 8 (1963) 135.
- [70] M. J. Kamlet and H. G. Adolph, *Propell. Explos.* 4 (1979) 30.
- [71] L. R. Rothstein and R. Petersen, *Propell. Explos.* 4 (1979) 56, 86.
- [72] L. R. Rothstein, *Propell. Explos.*, 6 (1981) 91.
- [73] R. Sundararajan and S. R. Jain, *Indian J. Tech.*, 21 (1983) 474.
- [74] J. Mullay, *Propell. Explos. Pyrotech.*, 12 (1987) 60.

- [75] S. R. Jain, *Propell. Explos. Pyrotech.*, 12 (1987) 188.
- [76] J. R. Stine, *J. Energet. Mater.*, 8 (1990) 41.
- [77] C. B. Storm and J. R. Travis, *Mat. Res. Soc. Symp. Proc.*, 296 (1993) 25.
- [78] H. H. Cady and A. C. Larson, *Acta Cryst.*, 18 (1965) 485.
- [79] W. M. Trott and A. M. Renlund, *J. Phys. Chem.*, 92 (1988) 5921.
- [80] R. N. Rogers, *Thermochim. Acta*, 11 (1975) 131.
- [81] M. R. Manaa, R. H. Gee and L. E. Fried, *J. Phys. Chem. A*, 106 (2002) 8806.
- [82] C. J. Wu and L. E. Fried, *J. Phys. Chem. A*, 104 (2000) 6447.
- [83] M. L. Chan, C. D. Lind and P. Politzer, *Proc. 9th Symp. (Internat.) Deton.*, Report No. OCNR-113291-7, Office of Naval Research, Arlington, VA, 1989, p. 566.
- [84] J. S. Murray, P. Lane, P. Politzer, P. R. Bolduc and R. L. McKenney, Jr., *J. Mol. Struct. (Theochem)*, 209 (1990) 349.
- [85] E. Catalano and C. E. Rolon, *Thermochim. Acta*, 61 (1983) 37, 53.
- [86] P. Hohenberg and W. Kohn, *Phys. Rev. B*, 136 (1964) 864.
- [87] R. D. Coalson and T. L. Beek, in: P. v. R. Schleyer (ed.), *Encyclopedia of Computational Chemistry*, Vol. 3, Wiley, New York, p. 2086.
- [88] P. Politzer and J. S. Murray, in: J. S. Murray and K. Sen (eds.), *Molecular Electrostatic Potentials: Concepts and Applications*, Elsevier, Amsterdam, ch. 16.
- [89] P. Politzer and J. S. Murray, *Theor. Chem. Acc.*, 108 (2002) 134.
- [90] P. Politzer, *Theor. Chem. Acc.*, in press.
- [91] P. Politzer and R. G. Parr, *J. Chem. Phys.*, 61 (1974) 4258.
- [92] P. Politzer, in: E. Brandas and E. Kryachko (eds.), *Fundamental Perspectives in Quantum Chemistry: A Tribute Volume to the Memory of Per-Olov Lowdin*, Kluwer, Dordrecht (The Netherlands), in press.
- [93] C. Lecomte, N. Ghermani, V. Pichon-Pesme and M. Souhasson, *J. Mol. Struct. (Theochem)*, 255 (1992) 241.
- [94] Z. Su and P. Coppens, *Z. Naturforsch. A: Phys. Sci.*, 48 (1993) 85.
- [95] R. F. Stewart and B. M. Craven, *Biophys. J.*, 65 (1993) 998.
- [96] D. Feil, in: J. S. Murray and K. Sen (eds.), *Molecular Electrostatic Potentials: Concepts and Applications*, Elsevier, Amsterdam, ch. 13.
- [97] E. Scrocco and J. Tomasi, *Top. Curr. Chem.*, 42 (1973) 95.
- [98] E. Scrocco and J. Tomasi, *Adv. Quantum Chem.*, 11 (1978) 115.
- [99] P. Politzer and K. C. Daiker, in: B. M. Deb (ed.), *The Force Concept in Chemistry*, Van Nostrand Reinhold, New York, 1981, ch. 6.
- [100] P. Politzer and D. G. Truhlar (eds.), *Chemical Applications of Atomic and Molecular Electrostatic Potentials*, Plenum, New York, 1981.

- [101] P. Politzer, P. R. Laurence and K. Jayasuriya, *Environ. Health Perspect.*, 61 (1985) 191.
- [102] P. Politzer and J. S. Murray, in: K. B. Lipkowitz and D. B. Boyd (eds.), *Reviews in Computational Chemistry*, Vol. 2, VCH Publishers, New York, 1991, ch. 7.
- [103] G. Naray-Szabo and G. G. Ferenczy, *Chem. Rev.*, 95 (1995) 829.
- [104] J. S. Murray and K. Sen (eds.), *Molecular Electrostatic Potentials: Concepts and Applications*, Elsevier, Amsterdam, 1996.
- [105] J. S. Murray and P. Politzer, in: A.-M. Sapse (ed.), *Molecular Orbital Calculations for Biological Systems*, Oxford University Press, New York, 1998, ch. 3.
- [106] J. Tomasi, B. Mennucci and R. Cammi, in: J. S. Murray and K. Sen (eds.), *Molecular Electrostatic Potentials: Concepts and Applications*, Elsevier, Amsterdam, 1996, ch. 1.
- [107] P. Politzer, J. S. Murray and P. Lane, *J. Comput. Chem.*, 24 (2003) 505.
- [108] J. S. Murray and P. Politzer, *J. Mol. Struct. (Theochem)*, 425 (1998) 107.
- [109] P. Politzer and J. S. Murray, *Trends Chem. Phys.*, 7 (1999) 157.
- [110] P. Politzer and J. S. Murray, *Fluid Phase Equilib.* 185 (2001) 129.
- [111] P. Politzer, in: N. H. March and B. M. Deb (eds.), *Single-Particle Density in Physics and Chemistry*, Academic, New York, 1987, ch. 3.
- [112] M. L. Connolly, *J. Am. Chem. Soc.*, 107 (1985) 1118.
- [113] Q. Du and G. A. Arteca, *J. Comput. Chem.*, 17 (1996) 1258.
- [114] R. F. W. Bader, M. T. Carroll, J. R. Cheeseman and C. Chang, *J. Am. Chem. Soc.*, 109 (1987) 7968.
- [115] J. S. Murray, T. Brinck, M. E. Grice and P. Politzer, *J. Mol. Struct. (Theochem)*, 256 (1992) 29.
- [116] H. Weinstein, P. Politzer and S. Srebrenik, *Theoret. Chim. Acta*, 38 (1975) 159.
- [117] R. K. Pathak and S. R. Gadre, *J. Chem. Phys.*, 93 (1990) 1770.
- [118] J. S. Murray, P. Lane and P. Politzer, *Mol. Phys.*, 85 (1995) 1.
- [119] P. Politzer and J. S. Murray, *Mol. Phys.*, 86 (1995) 251.
- [120] P. Politzer and J. S. Murray, *J. Mol. Struct.*, 376 (1996) 419, and early references cited.
- [121] P. Politzer, P. R. Laurence, L. Abrahmsen, B. A. Zilles and P. Sjöberg, *Chem. Phys. Lett.*, 111 (1984) 75.
- [122] J. S. Murray, P. Lane and P. Politzer, *J. Mol. Struct. (Theochem)*, 209 (1990) 163.
- [123] P. Politzer, J. S. Murray and Z. Peralta-Inga, *Int. J. Quantum Chem.*, 85 (2001) 676.

- [124] P. Politzer and J. S. Murray, in: C. Kubli-Garfias (ed.), *Biological Applications of the Quantum Chemistry Theory*, Research Signpost, Trivandrum, Kerala, India, 2002, ch. 6.
- [125] J. S. Murray, P. Lane and P. Politzer, *Mol. Phys.*, 93 (1998) 187.
- [126] J. S. Murray, T. Brinck, P. Lane, K. Paulsen and P. Politzer, *J. Mol. Struct. (Theochem)*, 307 (1994) 55.
- [127] O. Exner, *Correlation Analysis of Chemical Data*, Plenum, New York, 1988.
- [128] P. Lane, J. S. Murray and P. Politzer, *J. Mol. Struct. (Theochem)*, 236 (1991) 283.
- [129] B. M. Rice and J. J. Hare, *J. Phys. Chem. A*, 106 (2002) 1770.
- [130] L. Pauling, *J. Chem. Soc.*, (1948) 1461.
- [131] L. Pauling, *The Nature of the Chemical Bond*, 3rd ed., Cornell University Press, Ithaca, NY, 1960.
- [132] P. Politzer and J. S. Murray, in: Z. B. Maksic and W. J. Orville-Thomas (eds.), *Pauling's Legacy – Modern Modelling of the Chemical Bond*, Elsevier, Amsterdam, 1999, ch. 12.



This Page Intentionally Left Blank

## Chapter 2

# A study of chemical micro-mechanisms of initiation of organic polynitro compounds

Svatopluk Zeman

Department of Theory and Technology of Explosives, University of Pardubice,  
CZ-532 10 Pardubice, Czech Republic

### Abstract

The paper presents a brief survey of available results obtained from studies of the initiation micro-mechanisms of polynitro compounds from the point of view of organic chemistry. Attention is also paid to the basic mechanisms of low-temperature thermal decomposition of these compounds. With consideration of these results, the relationships have been specified and analyzed between the characteristics of impact and electric spark sensitivities, detonation and thermal decomposition, on the one hand, and  $^{13}\text{C}$  and  $^{15}\text{N}$  NMR chemical shifts of polynitro compounds, on the other. In the case of the impact sensitivity, the said relationships involve the NMR chemical shifts of the atoms carrying the most reactive nitro groups. In the case of the remaining stimuli studied, the  $^{15}\text{N}$  shifts of nitrogen atoms in the most reactive nitro groups themselves are involved. It has been stated that the chemical micro-mechanisms of primary fission processes of molecules of polynitro compounds in the initiation by mechanical stimuli (inclusive of the detonation course) and electric spark should be the same as in the case of their low-temperature thermal decomposition.

## 1. INTRODUCTION

The homolytic fragmentations or reactions of the  $\text{C-NO}_2$ ,  $\text{N-NO}_2$ ,  $\text{N-NO}$ , and  $\text{O-NO}_2$  groupings, or other bearers of explosibility (i.e. explosophores), are common primary fission processes of energetic materials under thermal [1-18], impact [1,3,4,6,16,19-27], shock [1,6,18,19,20,24,26-32] and electric spark stimuli [5, 32-36]. Therefore, it is natural that relationships exist between characteristics of low-temperature thermal decomposition and impact [6,37,38] or electric spark [35,39,47] sensitivities and also detonation characteristics [26,40-48,50] of polynitro compounds.

From what has been said so far it follows that chemical micro-mechanism of the primary fragmentations of explosive molecules in all the above-mentioned stimuli should be the same as in the case of their low-temperature thermal

decomposition. The similarity or identity is a topic of numerous papers [5,6,18,26,32-35,44-50]. A thermal entity of the initiation by electric spark [52] appears to be thus manifested [35,39,53]. In the case of initiation of detonation the said identity is confirmed by some striking pieces of experimental evidence. First of all, they include relationships between outputs of thermoanalytical methods and detonation characteristics of polynitro compounds [40-47,50]. By means of XPS the evidence of primary fission of N–NO<sub>2</sub> bond in 1,3,5-trinitro-1,3,5-triazacyclohexane (RDX) exposed to shock wave was obtained [51]. The same fission represents the start of thermal decomposition of RDX [6,10,13,14,17,18,26,47]. On the basis of deuterium kinetic isotope effect (DKIE) it was proved [11,54] that the rate-limiting step for the thermal decomposition of 2,4,6-trinitrotoluene (TNT) in the condensed state and that for the initiation of its detonation are identical. The presence of furoxanes and furazanes in the XPS spectrum of 1,3,5-triamino-2,4,6-trinitrobenzene (TATB) exposed to shock [55-57] provides further evidence – the pyrolysis of *ortho*-nitroanilines is a method of synthesis of benzofurazane [58] and in the case of 1,3-diamino-2,4,6-trinitrobenzene (DATB) this reaction leads to 4-amino-5,7-dinitrobenzofurazane [59]. The identity is also reflected in a relationship between the kinetics of the low-temperature thermal decomposition of the energetic materials and reaction rates in the reaction zone of their detonation [60,61].

Unfortunately, the study of impact and shock initiation processes of organic energetic materials from the point of view of physical organic chemistry recedes into background. In the last decade, molecular dynamics simulations dominate in this study [62]. Most of these simulations retain chemical micro-mechanisms of the process. Nevertheless, on the basis of molecular dynamics, Walker declared [63,64] that a shocked explosive molecule splits arbitrarily (so called “physical kinetics” [63]). On the other hand, Kohno *et al.* [27] found (by means of a kind of simulation) a defined pathway of primary fission of nitramines under impact and shock. Taking into account the knowledge about chemical mechanism of primary thermal decomposition of energetic materials, we have proved a perfect agreement between our findings [6,26] and the above-mentioned results obtained by Kohno *et al.* [27] or with our results obtained from application of semi-empirical AM1 method to the initiation of polynitro arenes [28,65]. Recently, Kuklja also showed (on the basis of quantum-chemical simulation) that changes in the molecular crystal during thermal decomposition of RDX are significant for understanding of its detonation initiation [18].

All the above-mentioned facts illustrate the significance of knowledge about low-temperature thermal reactivity of energetic materials in the study of chemical micro-mechanisms of their initiation by mechanical stimuli or electric spark. It must be stated that from among all initiation stimuli, the splitting of molecules of energetic materials by heat has been studied most thoroughly so

far. Therefore, our strategy of study of the chemical micro-mechanism of initiation of energetic materials is based on the chemistry of their primary low-temperature thermal reactions. This paper presents some recent and also brand-new results of our activity in the said sense with the exploitation of  $^{15}\text{N}$  and  $^{13}\text{C}$  NMR chemical shifts.

## 2. DATA SOURCES

### 2.1. Impact sensitivity data

The results of determination of impact sensitivity detected on the basis of sound (see the Bruceton method) were taken from literature [66-70] and are presented in Tables 1 and 2 as drop energies,  $E_{dr}$  (expressed in J). The tables also contain a survey of the polynitro compounds studied, including their code designations.

### 2.2. Electric spark sensitivity data

These data were obtained by means of an apparatus [5] developed in co-operation with Austin Detonator Co., Vsetín. They are expressed as spark energies,  $E_{ES}$ , required for 50 percent initiation probability, and were taken from Refs. [32-36]. The  $E_{ES}$  values are in linear relation with the corresponding results from Los Alamos Natl. Lab. [71] and are summarised in Tables 1 and 2 for some studied compounds.

### 2.3. Detonation velocity

The values of detonation velocity,  $D$ , of the polynitro arenes studied were calculated using the known relationships of Kamlet & Jacobs [72] for the maximum theoretical densities of crystals (i. e. for monocrystal). When the heat of formation of the substance was not available, the  $D$  values were obtained by using the relationship of Rothstein & Petersen [73]. For compounds with sulphur heteroatom in molecule the  $D$  values were taken from Ref. [40]. The  $D$  values used are summarised in Table 1.

### 2.4. NMR chemical shifts

The  $^{13}\text{C}$  NMR chemical shifts were taken from Refs. [74-76] and the  $^{15}\text{N}$  NMR chemical shifts from Refs. [6,26,77-79]. For the substances not yet prepared (i. e. DIGEN, TETROGEN and DECAGEN – see Table 2), which are of considerable theoretical interest in the chemistry of nitramines, the corresponding shift values were predicted in Refs. [26,77]. The NMR chemical shifts used are presented in Tables 1 and 2.

**Table 1**

Survey of the studied polynitro arenes and their derivatives, their code designations,  $^{13}\text{C}$  NMR chemical shifts and some sensitivity data.

Polynitro arene				$^{13}\text{C}$ NMR chemical shift [74]	
No.	chemical name and characteristics			code design.	position in molecule $\delta_{\text{C}}$ in ppm
1	1,3-Dinitrobenzene			1,3-DNB	1,3- 147.8
	spark energy, $E_{\text{ES}}$	3.15 J	[33]		2- 118.2
					4,6- 129.1
					5- 131.5
2	1,4-Dinitrobenzene			1,4-DNB	1,4- 150.7
	spark energy, $E_{\text{ES}}$	18.38 J	[33]		2,3,5,6- 125.0
3	1,3,5-Trinitrobenzene			TNB	1,3,5- 148.3
	spark energy, $E_{\text{ES}}$	6.31 J	[33]		2,4,6- 123.8
	drop energy (sound), $E_{\text{dr}}$	24.52 J	[68]		
4	2,2',4,4',6,6'-Hexanitrobiphenyl			HNB	1,1'- 126.0
	spark energy, $E_{\text{ES}}$	5.03 J	[33]		2,2'',6,6''- 148.2
	drop energy (sound), $E_{\text{dr}}$	18.64 J	[67]		3,3',5,5'- 125.2
					4,4'- 148.7
5	2,2',2'',4,4',4'',6,6',6'',6'''-Nonanitro-1,1',3',1'''-terphenyl			NONA	1,1'- 125.9
	spark energy, $E_{\text{ES}}$	16.44 J	[33]		2,2'',6,6'' 148.4
	drop energy (sound), $E_{\text{dr}}$	9.10 J	[68]		3,3'',5,5'' 125.4
					4,4'''- 148.0
					1',5'- 123.5
					2',4'- 149.2
					3'- 126.0
					6'- 149.5
6	2,4,6-tris(2,4,6-Trinitrophenyl)-1,3,5-triazine			TPT	
	spark energy, $E_{\text{ES}}$	10.61 J	[53]	benzene ring:	1- 127.8
					2,6- 148.5
					3,5- 125.3
					4- 149.1
				triazine ring:	2,4,6- 170.2
7	1,5-Dinitronaphthalene			1,5-DNN	1,5- 148.2
	spark energy, $E_{\text{ES}}$	11.20 J	[33]		2,6- 125.5
					3,7- 128.9
					4,8- 129.1
					9,10- 126.0

Table 1 continued

Polynitro arene				<sup>13</sup> C NMR chemical shift [74]	
No.	chemical name and characteristics			code design.	position in molecule $\delta_c$ in ppm
8	1,8-Dinitronaphthalene			1,8-DNN	1,8- 145.7
	spark energy, $E_{ES}$	13.99 J	[33]		2,7- 127.9
					3,6- 127.7
					4,5- 135.4
					9- 116.1
					10- 135.7
9	1,4,5-Trinitronaphthalene			TNN	1- 150.6
	spark energy, $E_{ES}$	10.97 J	[33]		2- 124.9
					3- 127.6
					4- 147.6
					5- 145.9
					6- 129.4
					7- 130.8
					8- 129.2
					9- 127.0
					10- 117.4
10	1,4,5,8-Tetranitronaphthalene			TENN	1,4,5,8- 146.9
	spark energy, $E_{ES}$	8.26 J	[33]		2,3,6,7- 128.0
					9,10- 117.9
11	1-(2,4,6-Trinitrophenyl)-5,7-dinitrobenzotriazole			BTX	
	spark energy, $E_{ES}$	6.50 J	[53]	benzene ring:	1- 129.6 <sup>a</sup>
					2,6- 145.8 <sup>a</sup>
					3,5- 125.5 <sup>a</sup>
					4- 144.8 <sup>a</sup>
				benzotriazole	4- 124.9 <sup>a</sup>
					5- 147.3 <sup>a</sup>
					6- 122.9 <sup>a</sup>
					7- 148.7 <sup>a</sup>
					8- 128.6 <sup>a</sup>
					9- 125.6 <sup>a</sup>
12	1-Methyl-2,4,6-trinitrobenzene			TNT	$\alpha$ - 15.1
	spark energy, $E_{ES}$	6.85 J	[33]		2,6- 150.9
	drop energy (sound), $E_{dr}$	39.24 J	[67]		3,5- 122.7
	detonation velocity, $D$	7.02 km s <sup>-1</sup>			4- 145.8
13	1,3-Dimethyl-2,4,6-trinitrobenzene			TNX	$\alpha$ - 13.9
	spark energy, $E_{ES}$	11.10 J	[33]		1,3- 129.2
	drop energy (sound), $E_{dr}$	10.46 J	[69]		2- 148.5
	detonation velocity, $D$	6.71 km s <sup>-1</sup>			6,4- 147.4
					5- 121.9

Table 1 continued

Polynitro arene			<sup>13</sup> C NMR chemical shift [74]	
No.	chemical name and characteristics	code design.	position in molecule	$\delta_c$ in ppm
14	1,3,5-Trimethyl-2,4,6-trinitrobenzene spark energy, $E_{ES}$ 8.98 J [33] drop energy (sound), $E_{dr}$ 20.45 J [69] detonation velocity, $D$ 6.20 km s <sup>-1</sup>	TNMs	$\alpha$ - 1,3,5- 2,4,6-	12.6 124.4 149.5
15	1-Methoxy-2,4,6-trinitrobenzene detonation velocity, $D$ 7.04 km s <sup>-1</sup> [68]	TNA	1- 2,6- 3,5- 4-	151.0 <sup>b</sup> 144.0 <sup>b</sup> 124.8 <sup>b</sup> 141.6 <sup>b</sup>
16	2,4,6-Trinitrobenzoic acid drop energy (sound), $E_{dr}$ 26.82 J [53] detonation velocity, $D$ 6.96 km s <sup>-1</sup>	TNBA	1- 2,6- 3,5- 4-	130.2 <sup>b</sup> 147.0 <sup>b</sup> 125.2 <sup>b</sup> 147.8 <sup>b</sup>
17	1-Hydroxi-2,4,6-trinitrobenzene detonation velocity, $D$ 7.57 km s <sup>-1</sup>	PA	1- 2,6- 3,5- 4-	160.2 141.9 125.4 126.4
18	1,3-Dihydroxi-2,4,6-trinitrobenzene drop energy (sound), $E_{dr}$ 10.54 J [68] detonation velocity, $D$ 7.71 km s <sup>-1</sup>	TNR	1,3- 2- 4,6- 5-	159.7 141.8 142.2 125.7
19	1-Amino-2,4,6-trinitrobenzene spark energy, $E_{ES}$ 6.85 J [33] drop energy (sound), $E_{dr}$ 43.40 J [68] detonation velocity, $D$ 7.50 km s <sup>-1</sup>	PAM	1- 2,6- 3,5- 4-	143.6 134.2 128.1 132.7
20	1,3-Diamino-2,4,6-trinitrobenzene spark energy, $E_{ES}$ 10.97 J [33] drop energy (sound), $E_{dr}$ 78.48 J [67] detonation velocity, $D$ 7.71 km s <sup>-1</sup>	DATB	1,3- 2- 4,6- 5-	145.9 122.4 122.0 131.8
21	1,3,5-Triamino-2,4,6-trinitrobenzene spark energy, $E_{ES}$ 17.75 J [33] drop energy (sound), $E_{dr}$ 120.17 J [67] detonation velocity, $D$ 7.95 km s <sup>-1</sup>	TATB	1,3,5- 2,4,6-	151.6 114.3
22	2,2',4,4',6,6'-Hexanitrodiphenylamine spark energy, $E_{ES}$ 5.02 J [33] drop energy (sound), $E_{dr}$ 11.77 J [68] detonation velocity, $D$ 7.20 km s <sup>-1</sup>	DPA	1,1'- 2,2',6,6'- 3,3',5,5'- 4,4'-	142.0 138.7 124.4 132.0

Table 1 continued

No.	Polynitro arene chemical name and characteristics			code design.	<sup>13</sup> C NMR chemical shift [74]	
					position in molecule	$\delta_C$ in ppm
23	2,2',4,4',6,6'-Hexanitrooxanilide			HNO	carbonyls	157.1
	spark energy, $E_{ES}$	14.58 J	[33]		1,1'-	128.4
	drop energy (sound), $E_{dr}$	14.22 J	[70]		2,2',6,6'-	144.7
	detonation velocity, $D$	7.34 km s <sup>-1</sup>			3,3',5,5'-	125.0
					4,4'-	143.6
24	2,4,6-tris(3-Methyl-2,4,6-trinitrophenylamino)-1,3,5-triazine			TMPM		
	spark energy, $E_{ES}$	6.84 J	[53]		benzene ring: $\alpha$ -	15.0
	detonation velocity, $D$	6.99 km s <sup>-1</sup>			1-	131.3
					2-	149.3
					3-	129.1
					4-	143.6
					5-	123.1
					6-	146.2
					triazine ring 2,4,6-	162.4
25	2,6-bis(2,4,6-Trinitrophenylamino)-3,5-dinitropyridine			PYX		
	spark energy, $E_{ES}$	8.90 J	[33]		benzene ring: 1-	136.7 <sup>a</sup>
	drop energy (sound), $E_{dr}$	15.44 J	[68]		2,6-	145.5 <sup>a</sup>
	detonation velocity, $D$	7.48 km s <sup>-1</sup>			3,5-	124.3 <sup>a</sup>
					4-	143.2 <sup>a</sup>
					pyridine ring 3,5-	148.5
					4-	123.7 <sup>a</sup>
26	1,3,7,9-Tetranitrophenothiazine-5,5-dioxide			TNPTD		
	spark energy, $E_{ES}$	5.78 J	[53]		1,9-	136.5
					2,8-	125.4
					3,7-	141.0
					4,6-	124.4
					10,12-	136.7
					13,14-	124.0
27	1,3,7,9-Tetranitrophenoxazine			TENPO		
	spark energy, $E_{ES}$	5.12 J	[53]		1,9-	141.2
					2,8-	117.3
					3,7-	144.6
					4,6-	114.3
					10,12-	142.6
					13,14-	163.4
28	2,2',4,4',6,6'-Hexanitrodiphenylsulfide			DIPS		
	spark energy, $E_{ES}$	2.56 J	[33]		1,1'-	125.7
	drop energy (sound), $E_{dr}$	7.45 J	[70]		2,2',6,6'-	144.7
	detonation velocity, $D$	7.16 km s <sup>-1</sup>			3,3',5,5'-	124.4
					4,4'-	147.8



Table 1 continued

Polynitro arene			<sup>13</sup> C NMR chemical shift [74]	
No.	chemical name and characteristics	code design.	position in molecule	δ <sub>C</sub> in ppm
29	3,3'-Dimethyl-2,2',4,4',6,6'-hexanitrodiphenylsulfide spark energy, $E_{ES}$ 8.57 J [33] detonation velocity, $D$ 6.70 km s <sup>-1</sup>	DMDIPS	α,α'- 1,1'- 2,2'- 3,3'- 4,4'- 5,5'- 6,6'-	15.1 <sup>a</sup> 122.9 <sup>a</sup> 151.2 <sup>a</sup> 131.6 <sup>a</sup> 145.5 <sup>a</sup> 123.8 <sup>a</sup> 147.9 <sup>a</sup>
30	2,2',4,4',6,6'-Hexanitrodiphenylsulfone spark energy, $E_{ES}$ 10.54 J [33] drop energy (sound), $E_{dr}$ 8.44 J [70] detonation velocity, $D$ 6.77 km s <sup>-1</sup>	DIPSO	1,1'- 2,2',6,6'- 3,3',5,5'- 4,4'-	121.1 148.5 124.1 143.5
31	2,2',4,4',6,6'-Hexanitrodiphenylmethane spark energy, $E_{ES}$ 4.10 J [33] detonation velocity, $D$ 7.14 km s <sup>-1</sup>	DPM	α- 1,1'- 2,2',6,6'- 3,3',5,5'- 4,4'-	40.0 129.5 150.5 123.9 147.0
32	1,2-bis(2,4,6-Trinitrophenyl)ethane spark energy, $E_{ES}$ 3.89 J [33] drop energy (sound), $E_{dr}$ 27.98 J [67] detonation velocity, $D$ 7.13 km s <sup>-1</sup>	DPE	α- 1- 2,6- 3,5- 4-	27.1 133.2 150.9 123.2 146.6
33	3,3'-Dimethyl-2,2',4,4',6,6'-hexanitrobiphenyl spark energy, $E_{ES}$ 4.28 J [33] drop energy (sound), $E_{dr}$ 33.14 J [67] detonation velocity, $D$ 7.10 km s <sup>-1</sup>	BITNT	α,α'- 1,1'- 2,2'- 3,3'- 4,4'- 5,5'- 6,6'-	15.4 <sup>a</sup> 122.1 <sup>a</sup> 151.2 <sup>a</sup> 133.7 <sup>a</sup> 145.3 <sup>a</sup> 124.2 <sup>a</sup> 150.1 <sup>a</sup>
34	2,2',4,4',6,6'-Hexanitrostilbene spark energy, $E_{ES}$ 6.62 J [33] drop energy (sound), $E_{dr}$ 11.50 J [68] detonation velocity, $D$ 7.27 km s <sup>-1</sup>	HNS	vinyl's C 1,1'- 2,2',6,6'- 3,3',5,5'- 4,4'-	126.3 130.7 149.6 123.4 147.2

Notes: a) the values taken from Ref. [75];

b) the values taken from Ref. [76];

**Table 2**

Survey of the studied nitramines, their code designations,  $^{15}\text{N}$  NMR chemical shifts and some sensitivity data.

No.	Nitramine		$^{15}\text{N}$ NMR chemical shift on nitrogen [6,77]		
	chemical name and characteristics	code designation	position in molecule	amino $\delta_{\text{A}}$ in ppm	nitro $\delta_{\text{N}}$ in ppm
1	1-Nitro-1-azaethylene spark energy, $E_{\text{ES}}$ 8.38 J [34]	DIGEN	1	-208.52	-23.58
2	1,4-Dinitro-1,4-diazabutane drop energy (sound), $E_{\text{dr}}$ 8.33 J [34]	EDNA	1,4	-205.47	-26.34
3	2,4-Dinitro-2,4-diazapentane spark energy, $E_{\text{ES}}$ 13.45 J [34]	OCPX	2,4	-202.61	-28.36
4	2,4,6-Trinitro-2,4,6-triazaheptane spark energy, $E_{\text{ES}}$ 8.08 J [34]	ORDX	2,6 4	-202.29 -189.90	-28.49 -32.02
5	2,4,6,8-Tetranitro-2,4,6,8-tetraazanonane spark energy, $E_{\text{ES}}$ 5.50 J [34]	OHMX	2,8 4,6	-202.25 -195.59	-28.77 -34.52
6	1,9-Diacetoxy-,4,6,8-tetranitro-2,4,6,8- tetraazanonane spark energy, $E_{\text{ES}}$ 13.93 J [34]	AcAn	2,8 4,6	-190.52 -188.06	-32.81 -33.38
7	1,3-Dinitro-1,3-diazacyclobutane spark energy, $E_{\text{ES}}$ 6.25 J [34] drop energy (sound), $E_{\text{dr}}$ 9.97 J [89]	TETROGEN	1,3	-203.62	-27.83
8	1,3,3-Trinitro-1-azacyclobutane spark energy, $E_{\text{ES}}$ 8.76 J [53] drop energy (sound), $E_{\text{dr}}$ 6.90 J [89]	TNAZ	1	-228.70	-20.50
9	1,3-Dinitro-1,3-diazacyclopentane spark energy, $E_{\text{ES}}$ 9.68 J [53]	CPX	1,3	-209.01	-31.21
10	1,4-Dinitro-1,4-diazacyclohexane spark energy, $E_{\text{ES}}$ 15.97 J [34]	DNDC	1,4	-205.49	-26.26
11	1,3,5-Trinitro-1,3,5-triazacyclohexane spark energy, $E_{\text{ES}}$ 2.49 J [34] drop energy (sound), $E_{\text{dr}}$ 5.90 J [68]	RDX	1,3,5	-198.10	-32.90
12	1,3-Endomethylene-3,7-dinitro-1,3,5,7- tetraazacyclooctane spark energy, $E_{\text{ES}}$ 17.42 J [53]	DPT	3,7	-203.70	-25.30

Table 2 - continued

No.	Nitramine chemical name and characteristics	code designatio n	<sup>15</sup> N NMR chemical shift on nitrogen [6,77]		
			position in molecule	amino $\delta_A$ in ppm	nitro $\delta_N$ in ppm
13	1,3,5,7-Tetranitro-1,3,5,7-tetraazacyclooctane spark energy, $E_{ES}$ 2.89 J [34] drop energy (sound), $E_{dr}$ 6.40 J [68]	$\beta$ -HMX	1,3,5,7	-199.10	-34.70
14	1,3,5,7,9-Pentanitro-1,3,5,7,9-pentaazacyclodecane spark energy, $E_{ES}$ 2.96 J [34] drop energy (sound), $E_{dr}$ 4.90 J [89]	DECAGEN	1,3,5,7,9	-197.38	-33.25
15	4,10-Dinitro-2,6,8,12-tetraoxa-4,10-diaza-isowurtzitane drop energy (sound), $E_{dr}$ 24.25 J [122] drop energy (first reaction) 5.10 J [a]	TEX	4,10	-197.20	-33.40
16	2,4,6,8,10,12-Hexanitro-2,4,6,8,10,12-hexaazaisowurtzitane spark energy, $E_{ES}$ 4.70 J [53] drop energy (sound), $E_{dr}$ 11.90 J [123] drop energy (first reaction) 5.38 J [6]	$\epsilon$ -HNIW <sup>b</sup>	2,6,8,12 4,10	-199.00 -179.50	-40.30 -43.40
17	2,4,6,8,10,12-Hexanitro-2,4,6,8,10,12-hexaazaisowurtzitane drop energy (sound), $E_{dr}$ 10.20 J [123]	$\alpha$ -HNIW <sup>b</sup>	2,6,8,12 4,10	-199.00 -179.50	-40.30 -43.40
18	2,5-Dinitro-2,5-diazahexane-3,4-dione spark energy, $E_{ES}$ 5.49 J [34] drop energy (sound), $E_{dr}$ 19.44 J [68]	DMNO	2,5	-166.78	-43.07
19	1-Methylnitramino-2,4,6-trinitrobenzene spark energy, $E_{ES}$ 5.49 J [34] drop energy (sound), $E_{dr}$ 7.85 J [68]	TETRYL	N	-208.80	-23.10

Notes: a) unpublished value;

b) NMR chemical shifts of the  $\alpha$ - and  $\epsilon$ -HNIWs are identical because corresponding measurements were made in solution;

### 3. BASIC MECHANISMS OF THERMAL DECOMPOSITION OF ORGANIC POLYNITRO AND POLYNITROSO COMPOUNDS

The basic problem of defining the kinetics and mechanism of the thermal decomposition of energetic materials lies in the strong dependence of the corresponding kinetic parameters on temperature, pressure, and construction materials in contact with the sample decomposed [47]. Hence the mutual compatibility of results obtained from thermal analyses of energetic materials using different methods and/or different types of apparatus of different origin is very rare [47,77,84]. So far the most reliable results in this area are both theoretical and practical findings obtained by Russian scientists on the basis of their manometric method (see Refs. [17,47] and quotations herein). The data obtained by this method are known to correspond to the non-autocatalyzed stage of thermal decomposition of the given material (i. e. to molecular structure [77]), and also to the absolute values of corresponding Arrhenius parameters. The mechanisms of primary unimolecular fragmentation in low-temperature thermal decomposition of organic polynitro and polynitroso compounds, specified mostly by the Russian authors, can be divided into [84] the following classes:

- ◆ *homolysis of C-NO<sub>2</sub>, N-NO<sub>2</sub>, O-NO<sub>2</sub> and N-NO bonds.* The homolytic fission of the first bond, particularly that connecting a sterically hindered nitro group, is characteristic for the decomposition of polynitro paraffins [17] and unsubstituted polynitro arenes [28,80]. Homolytic splitting of N-NO<sub>2</sub> bond (see Scheme 1 in paragraph 4.1) is typical of secondary nitramines [6,10,13,14,17,18,26,47], that of O-NO<sub>2</sub> bond for nitric esters [16,81], and that of N-NO bond for nitrosamines [82,83].
- ◆ *homolysis via a five-, six- or seven-membered transition state or aci-form.* Six-membered transition state (or aci form) is connected with the presence of a hydrogen atom at  $\gamma$ -position with respect to the nitro group (see Scheme 2) [7-9,17,49] in derivatives of polynitro arenes, i.e. with polynitro compounds exhibiting the so-called trinitrotoluene mechanism of thermal decomposition [7,17]. Five-membered transition state might have significance in a group of polychlorinated derivatives of TNB whose thermal decomposition represents a certain analogy with the decomposition of polymethyl derivatives of 1,3,5-trinitrobenzene [85,86]. The primary step of the thermal decomposition of chloro-derivatives could perhaps be connected with the chemical interaction between chlorine atom and oxygen of *ortho*-standing nitro group (which is also indicated by negative values of the respective activation entropy  $\Delta S^\ddagger$  [48]). An analogous interaction of this oxygen atom with sulphur atom in DIPS molecule (or its derivative – see Scheme 2 in paragraph 4.2) could also start the decomposition of this substance (again the respective  $\Delta S^\ddagger$  value is negative [48]), even though the primary homolysis of C-S bond was

originally presumed in this case [80,87]. A seven-membered transition state can be present, for example, in the first step of thermal decomposition of 1,5-dinitronaphthalene (it should begin by an interaction between oxygen atom of nitro group and hydrogen atom at *peri*-position [75,88]).

- ♦ *homolytic fragmentation without a primary participation of a nitro group.* In the case of HNAB it was assumed that its thermal decomposition is started by primary fission of the bond between carbon atom and azo-bridge [80,90]. Similarly, DIPSO and the already mentioned DIPS should be liable to C–S bond homolysis [80,87]. However, the  $\Delta S^\ddagger$  value of the corresponding decomposition is negative in all the cases [48], i.e. the reaction should proceed through a cyclic transition state (see Scheme 2 in paragraph 4.2).

Once more it is necessary to note that the above-mentioned facts are valid only for low-temperature decomposition (in the temperature range up to 600 K).

#### 4. INITIATION OF POLYNITRO COMPOUNDS

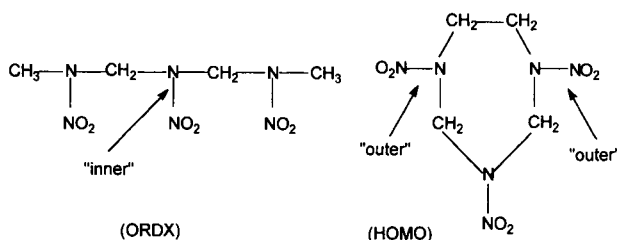
It is known that the application of  $^{15}\text{N}$  NMR chemical shifts to the study of chemical micro-mechanism of initiation of nitramines by heat [77], impact [6], shock [26] or electric spark [32] has given very valuable results. The philosophy of this approach is based on the fact that values of the shifts correspond predominantly to the electron configuration and steric conditions within the reaction centre of the molecule, i.e. in primarily reactive nitramino groups. On the basis of these findings, the approach was extended to the application of  $^{13}\text{C}$  NMR chemical shifts in polynitro arenes (see Ref. [75] and this paper). It can be argued against this approach that NMR studies in solution neglect important crystal-lattice effects that are vital in the determination of explosive properties [91]. We pointed out this possibility as early as in Ref. [92] using the particular case of 2,4,6,8,10,12-hexanitro-2,4,6,8,10,12-hexaaza-isowurtzitane. From the following text it will be seen that this fact has no fundamental significance for studies of chemical micro-mechanism of initiation of energetic materials.

##### 4.1. Chemical micro-mechanism of initiation by impact

We were engaged in study of impact sensitivity, defined as the so-called “first reaction”, in the past [6,75]. Recently we also have undertaken a study [89] of the sensitivity detected on the basis of sound (see, e.g., the Bruceton method [66-69]) and we tried to find mutual relationships between these two kinds of sensitivities [96].

Figure 1 presents a relationship between  $^{15}\text{N}$  NMR chemical shifts,  $\delta_A$ , of aza (amino) nitrogen atoms of the most reactive nitramino groups and drop energies,  $E_{dr}$ , of “the first reaction” [6]. This figure was taken from paper [6] and

shows that the impact reactivity of linear polynitramines (more than two nitramino groups in molecule) is connected with primary homolysis of "inner" N-NO<sub>2</sub> bonds in their molecules (see Scheme 1). This finding stands in accordance with the mechanism formulated for this process on the basis of molecular dynamics by Kohno *et al.* [27]. In the case of cyclic nitramines, the "outer" N-NO<sub>2</sub> bonds (see Scheme 1) are primarily homolysed by action of impact [6].



Scheme 1. Illustration of the primary splitting (homolysis) of linear (ORDX – "inner" N-N bond) and non-symmetrical cyclic (HOMO – "outer" N-N bond) nitramines by impact or shock (taken from Refs. [6,26]), but also by heat.

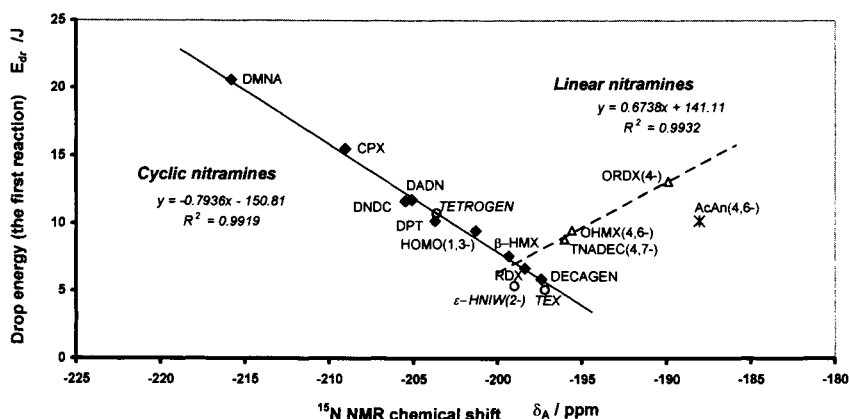


Fig. 1. Relationship between drop energy,  $E_{dr}$ , of „the first reaction“ and <sup>15</sup>N NMR chemical shifts,  $\delta_A$ , of aza nitrogen atoms carrying the most reactive nitro groups in the molecules of nitramines studied (in bracket given are the respective positions in molecule). Taken from Ref. [6] and complemented by the data of TETROGEN, HNIW and TEX.

No analogous relationships between  $E_{dr}$  values and <sup>15</sup>N NMR chemical shifts,  $\delta_N$ , of nitro-group nitrogen atoms were found [97], due to less correlation of the shifts with structural details. It must be stated that the aza (amino) nitrogen chemical shifts,  $\delta_A$ , in the nitramino groups are expected to be influenced by the nitrogen hybridisation, the size and conformation of molecule,

and the extent to which the nitrogen lone pair is involved in  $\pi$ -bonding with  $\text{NO}_2$  group [98]. As the conformation and size of molecule plays dominant role in the intermolecular interactions in the corresponding crystal, the interactions should have a significant influence on the impact sensitivity. This hypothesis is verified by Fig. 2 (taken from paper [6]), which represents a relationship between the  $E_{dr}$  values and heats of fusion,  $\Delta H_{m, tr}$ , of nitramines. As the heat represents the work needed for formation of defects in crystal lattice, the relationships found seem to stand in accordance with the ideas about the decisive role of plastic deformations of crystal played in the initiation of energetic materials by impact or shock [99-101].

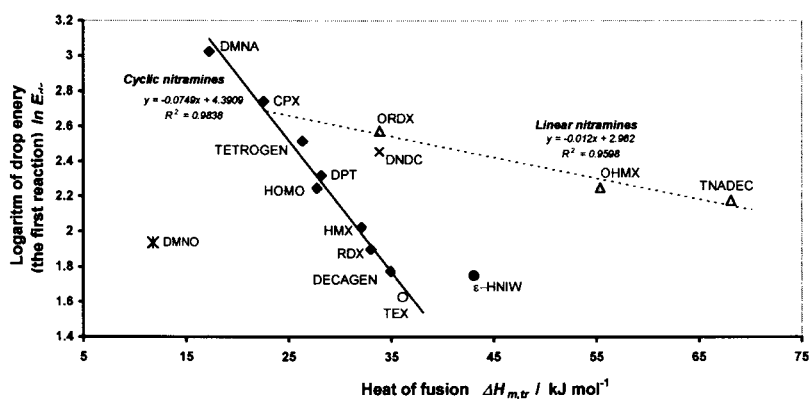


Fig. 2. Relationship between drop energy,  $E_{dr}$ , of „the first reaction“ and heat of fusion,  $\Delta H_{m, tr}$ , of nitramines; taken from Ref. [6] and complemented by data of TEX.

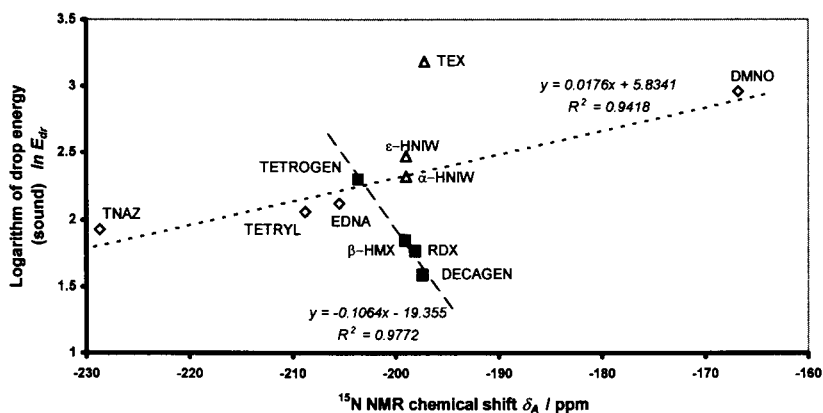


Fig. 3. Relationship between the drop energy,  $E_{dr}$ , (impact sensitivity detected by sound) and  $^{15}\text{N}$  NMR chemical shifts,  $\delta_A$ , of the aza nitrogen atoms carrying the most reactive nitro groups in the molecules of nitramines studied.

Figure 3 represents an analogous relationship between the impact sensitivity detected by sound and  $^{15}\text{N}$  NMR chemical shifts of nitramines. This relationship, in comparison with Fig. 1, is mathematically different. The difference could be interpreted by the different mechanisms of transfer of drop energy to the reaction centre of the molecule in the case of “the first reaction” as compared with the impact sensitivity detected by sound [89]. This difference is evident also in the relationship between the sensitivity and the  $\Delta H_{m,ir}$  values (see Fig. 4 taken from Ref. [89]). However, the meaning of Fig. 4 is the same as that of Fig. 2.

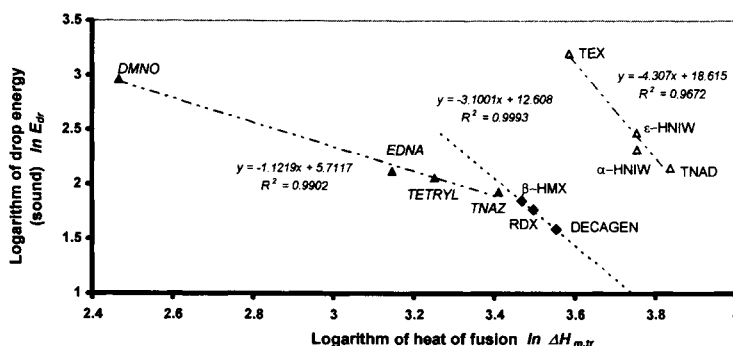


Fig. 4. Relationship between the drop energy,  $E_{dr}$  (impact sensitivity detected by sound) and heat of fusion,  $\Delta H_{m,ir}$ , of nitramines; taken from Ref. [89]; here TNAD is 1,4,5,8-tetranitro-1,4,5,8-tetraazadecaline.

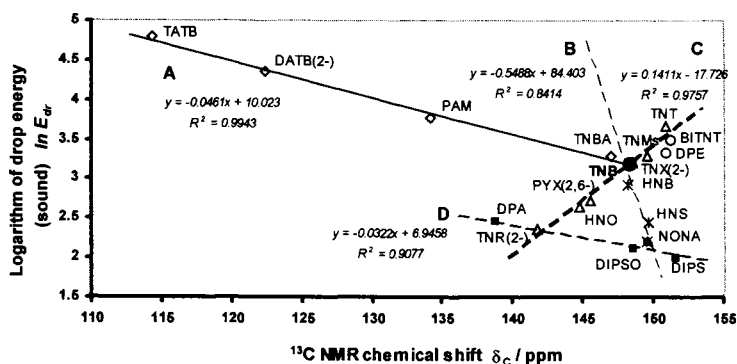


Fig. 5. Relationship between the energy,  $E_{dr}$  (impact sensitivity detected by sound) and  $^{13}\text{C}$  NMR chemical shifts,  $\delta_C$ , of the carbon atoms of aromatic system carrying the most reactive nitro groups (the numbers in brackets denote the positions in molecule).

The same shape of relationship as shown in Fig. 3 is valid for polynitro arenes in Fig. 5: here the impact sensitivity detected by sound correlates with  $^{13}\text{C}$  NMR chemical shifts of “the bearers” of the most reactive nitro groups in the molecule. According to this diagram, nitro groups in 2-positions of the



DATB, TNX, TNR and BITNT molecules and in 2- or 6-position of picryl group in the PYX molecule are found to be the most reactive. These groups are also most sterically crowded.

In the coordinate system shown in Fig. 5, the set of polynitro arenes studied falls into several classes. Classes A and C contain compounds characterised by the trinitrotoluene mechanism of primary fission in their thermal decomposition. Class B represents unsubstituted polynitro arenes (TNB, HNB and NONA) with primary homolysis of C–NO<sub>2</sub> bond in their thermal decomposition. Correlation of HNS data with this Class may be a coincidence but it may also be a result of intermolecular interaction in its crystals. Class D contains dipicryl derivatives in which the intermolecular interaction should dominate the influence on their reactivity (primary fission by heat in NONA is different from that in DIPS). The said influence occurs occasionally in larger molecules with strong intermolecular interactions and was observed in some cases of decomposition initiated by impact [36,75], electric spark [35,36] and (depending on the measurement method applied) also heat [102].

#### 4.2. Chemical micro-mechanism of initiation of detonation

By means of analogous approach as in the case of relationships in Fig. 1 we have studied mutual relationships between the characteristics of detonation and <sup>15</sup>N NMR chemical shifts of nitramines [26]. In contrast to the above-mentioned Fig. 1, the characteristics (i.e. heat of explosion or square of detonation velocity,  $D^2$ ) correlate with the <sup>15</sup>N NMR chemical shifts,  $\delta_N$ , of nitro-group nitrogen atoms. Corresponding relationships for square of detonation velocity,  $D^2$ , are presented in Fig. 6. Here the  $D^2$  values correlate with the  $\delta_N$  values of the most reactive nitro groups [26]. Therefrom it follows that, that the primary fission of nitramine molecule is the same as that in the case of initiation by impact (see Scheme 1). Again this fact perfectly agrees with the conclusions drawn by Kohn *et al.* [27] from the molecular dynamics study of impact and shock reactivity of nitramines.

An application of such approach to studies of detonation mechanism of the arenes studied is hindered by a serious problem: the unavailability of <sup>15</sup>N NMR spectra of most of them. An analogous application of the easily available <sup>13</sup>C NMR chemical shifts of “the bearers” of the most reactive nitro groups in their molecules is limited. In the case of unsubstituted polynitro arenes this application does not provide any useful relationships (the primary fission should consist in the homolysis of C–NO<sub>2</sub> bond). However, for derivatives of the said compounds it is possible to find reliable relationships if the nitro group in the reaction centre of molecule stands in perfect mesomeric interaction with the  $\pi$ -electron system of nucleus at the moment of formation of the transition state (see Scheme 2). This means that this group participates in the primary fission by one of its oxygen atoms (the trinitrotoluene mechanism of thermal

decomposition). Figure 7 corresponds to such a situation. Here the electron configuration of the “bearer” of the most reactive nitro group to a considerable extent represents the electron configuration of this group. That is why the dependences found are less close in some cases (particularly for class B compounds in Fig. 7).

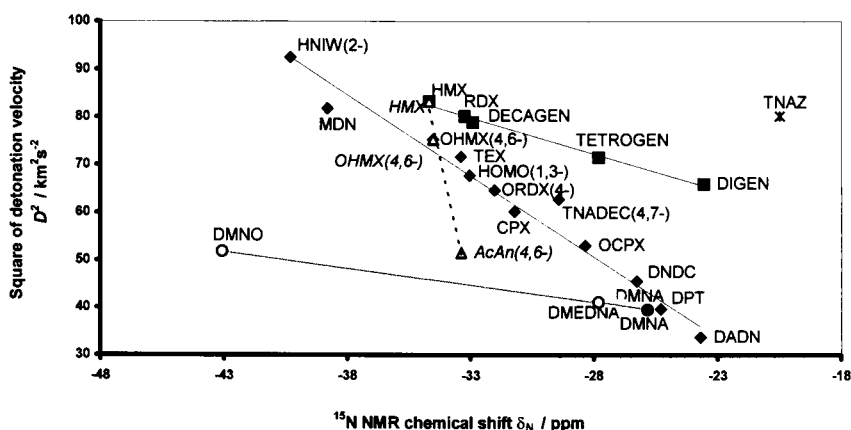


Fig. 6. Relationship between squares of detonation velocity,  $D^2$ , and  $^{15}\text{N}$  NMR chemical shifts,  $\delta_N$ , of nitrogen atoms in the most reactive nitro groups of nitramines (the numbers in brackets denote the positions in molecule); taken from Ref. [26].

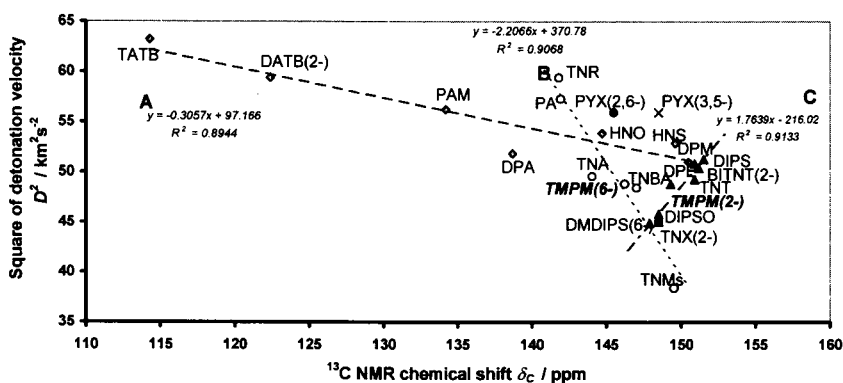
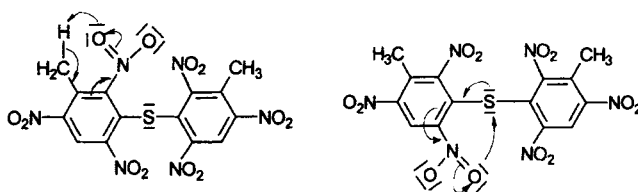


Fig. 7. Relationship between squares of detonation velocity,  $D^2$ , and  $^{13}\text{C}$  NMR chemical shifts,  $\delta_C$ , of the carbons atom of aromatic system carrying the most reactive nitro groups (the numbers in brackets denote the positions in molecule) in polynitro arenes containing amino, hydroxy, and alkyl substituents or sulphur bridge atom.

As in the case of the initiation by impact (see Fig. 5) also in the sense of Fig. 7 the most reactive nitro groups are those in 2-positions of DATB, TNX, TNR and BITNT molecules and in 2- or 6-position of picryl group in PYX

molecule. However, the PYX molecule possesses another potential reaction centre involving one of the nitro groups at 3- or 5-position of pyridine cycle (together with the bridge secondary amino group). However, the position of mutually corresponding data in the coordinate system of Fig. 7 shows that this centre is inactive in the given case. In analogy with the DMDIPS molecule, one reaction centre can be formed by methyl group and nitro group at 2-position (trinitrotoluene decomposition mechanism) or by 6-NO<sub>2</sub> group and the sulphur heteroatom (see Scheme 2). We proved the existence of the said centre as early as in the paper on impact sensitivity of polynitro arenes [75]. In Fig. 7 also the only correlating data are those belonging to the “bearer” of nitro group at 6- (or 6'-) position of the DMDIPS molecule. Two potential reaction centres are present in the TPM molecule too: namely the 2-NO<sub>2</sub> and 3-CH<sub>3</sub> groups at the benzene ring, and the 6-NO<sub>2</sub> and bridge secondary amino group at 1-position of the same ring. Figure 7 shows that these centres appear to be equivalent in the given case (their data correlate well with both group B and group C compounds in Fig. 7). For the relationships between micro-mechanisms of thermal decomposition and detonation of energetic materials see also paragraph 4.4 of this paper.



Scheme 2. Presumed mechanism of electron shifts at the beginning of low-temperature thermal decomposition of 3,3'-dimethyl-2,2',4,4',6,6'-hexanitrodiphenylsulfide with participation of nitro group at 2-position in the reaction center (typical “trinitrotoluene mechanism” – left formula) and with participation of nitro group at 6-position in the reaction center (right formula – real pathway of the fission).

The dependence type found corresponds well with the ideas about initiation of crystalline materials by impact or shock [101,103,104] (see also Refs. [26,47] and quotations herein): when a molecular crystal receives shock or impact, lattice vibrations (phonons) are excited at first. The phonon energy must then be converted into bond stretching frequencies (vibrons) with subsequent spontaneous localisation of vibrational energy in the nitro (explosophore) groupings [105,106] and then with consequential bond breaking. Conclusions of this type also correspond to an older simplified idea formulated by Bernard [107,108] on the basis of the kinetic theory of detonation: the only explosophore groups should be compressed ahead of the shock wave as a result of the activation of explosive molecules.

### 4.3. Chemical micro-mechanism of initiation by electric spark

One of the ways of specification of this mechanism can lie in study of relationships of the said sensitivity of energetic materials to their molecular structure [32], thermal reactivity [35,39,52,109-111], sensitivity to mechanic stimuli [32,109,112,113] and detonation characteristics [5,33,34,47]. As already stated, a thermal stimulus could be the basis of electric spark initiation [35,39,52,53].

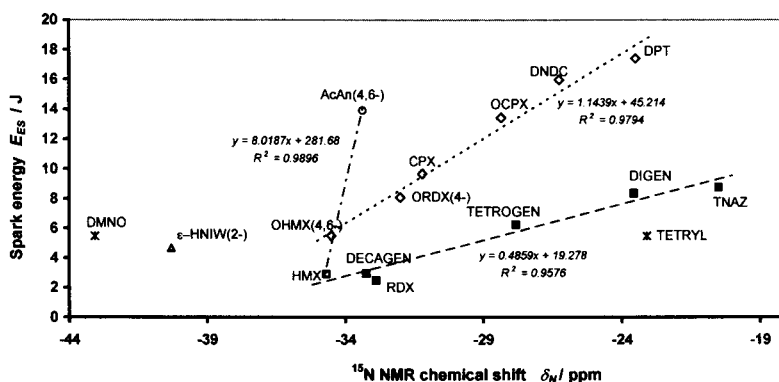


Fig. 8. Relationship between spark energy,  $E_{ES}$ , and  $^{15}\text{N}$  NMR chemical shifts,  $\delta_N$ , of nitrogen atoms of the most reactive nitro groups of (the numbers in brackets denote the positions in molecule).

An attempt at specification of the reaction centre by means of  $^{15}\text{N}$  NMR chemical shifts in the case of nitramines resulted in the dependences given in Fig. 8. In this diagram, the electric spark energy,  $E_{ES}$ , correlates with the chemical shifts,  $\delta_N$ , of nitrogen atoms of the most reactive nitro groups. The relationships in this diagram are very similar to those between the square of detonation velocity,  $D^2$ , of nitramines and their  $\delta_N$  values in Fig. 6. The mechanism of primary fragmentation should be identical in the two cases (see Scheme 1).

Due to the unavailability of  $^{15}\text{N}$  NMR spectra of the majority of polynitro arenes studied, an analogous specification was made using the  $^{13}\text{C}$  NMR chemical shifts,  $\delta_C$ , of "the bearers" of the most reactive nitro groups in their molecules. In contrast to the initiation of detonation, in this case it was possible to find relationships between the  $E_{ES}$  values and  $\delta_C$  chemical shifts even for the polynitro arenes whose decomposition should start by homolysis of the C-NO<sub>2</sub> bond. From Fig. 9 follows that these relationships are not too close for the given type of compounds nor too clear-cut from the point of view of mechanism of primary fragmentation (e.g. the presumed 7-membered transition state in decomposition of 1,5-DNN). Nevertheless, in the case of BTX they signalise the

highest reactivity of the nitro group at 7-position of benzotriazole cycle. However, if the nitro group at the reaction centre of molecule stands in perfect mesomeric interaction with the  $\pi$ -electron system of the nucleus at the moment of formation of the transition state, then close logical dependences are obtained (see Fig. 10). The described situation represents an analogy of the dependences depicted in Fig. 7, i.e. also here the “bearer” of the most reactive nitro group represents the electron configuration of this group to a considerable extent.

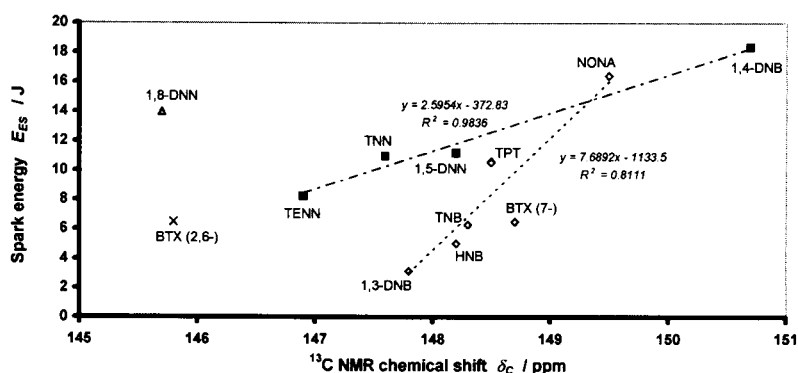


Fig. 9. Relationship between the spark energy,  $E_{ES}$ , and  $^{13}\text{C}$  NMR chemical shifts,  $\delta_C$ , of carbons atom of aromatic system carrying the most reactive nitro groups (the numbers in brackets denote the positions in molecule) in nonsubstituted polynitro arenes.

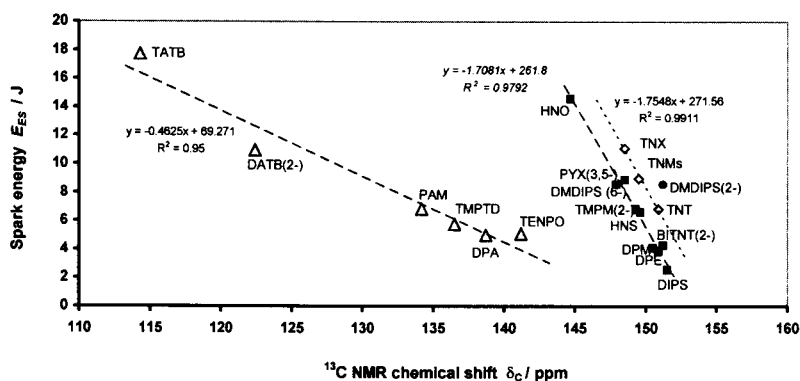


Fig. 10. Relationship between the spark energy,  $E_{ES}$ , and  $^{13}\text{C}$  NMR chemical shifts,  $\delta_C$ , of carbons atom of aromatic system carrying the most reactive nitro groups (the numbers in brackets denote the positions in molecule) in polynitro arenes containing amino, hydroxy, and alkyl substituents.

Figure 10 shows certain differences as compared with Fig. 7. In the TMPM molecule the primary reaction occurs at the centre with 2- $\text{NO}_2$  group of

benzene ring, whereas the centre with 6-NO<sub>2</sub> group should be inactive here. In the PYX molecule the primary reaction concerns 3- or 5-NO<sub>2</sub> group of the pyridine nucleus, while in the case of detonation initiation this centre should be inactive. An agreement between both diagrams is observed in the case of the reaction centre of DMDIPS molecule (i.e. the participation of 6- or 6'-NO<sub>2</sub> group).

#### 4.4. Chemical micro-mechanism of fission of polynitro compounds by action of heat and its relation to detonation

The <sup>15</sup>N NMR chemical shifts were used in analysis and prediction of the Arrhenius parameters of low-temperature decomposition of nitramines [77]. Figure 11 presents the relationship between the activation energies,  $E_a$ , of this decomposition and the aforesaid chemical shifts,  $\delta_N$ , of nitrogen atoms in the most reactive nitro groups [77]. No analogous relationship was found for the chemical shifts,  $\delta_A$ , of aza nitrogen atoms in nitramino groups. The found dependences of the type shown in Fig. 11 are discussed in detail elsewhere [77]. In this context it should be emphasised that in the sense of this diagram there appeared to exist a clearly separated group of nitramines whose primary fission does not involve the monomolecular homolysis of N–NO<sub>2</sub> bond. The group comprises monomethylnitramine (MNA) and ethylenedinitramine (EDNA), whose primary thermal decomposition should proceed by a bimolecular mechanism [114]. The thermal decomposition of RDX and HMX (from this group of nitramines) could consist in their primary depolymerisation to 1-nitro-1-azaethylene (DIGEN, see below).

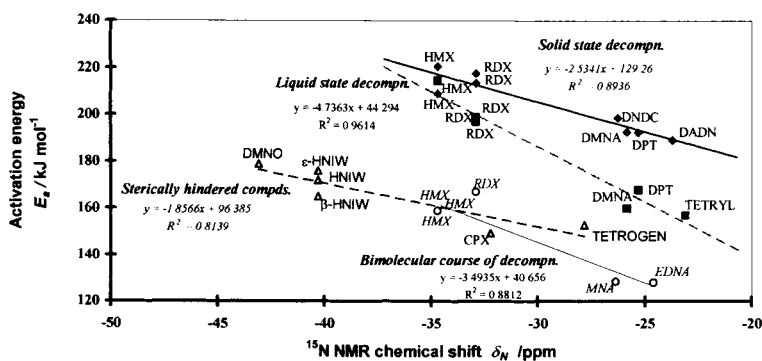


Fig. 11. Relationship between the activation energies,  $E_a$ , of low-temperature thermal decomposition and <sup>15</sup>N NMR chemical shifts,  $\delta_N$ , of nitrogen atoms in the most reactive nitro group of nitramines; taken from Ref. [77].

We also made molecular-dynamic simulation of thermal decomposition of some individual energetic materials, including RDX, at extremely high temperatures [93,94]. It turned out that the primary fragmentation mechanism at these conditions is entirely different from the low-temperature variant. In the case of the RDX unimolecular decomposition, it can be mentioned that elimination of  $\text{NO}_2$  group by homolysis of one N–N bond is observed for all reaction conditions whereas perhydrotriazine ring fission (depolymerization to 1-nitro-1-azaethylene) occurs predominantly in the gas phase thermal decomposition of this nitramine, i.e. at higher temperatures (see Ref. [95] and quotations herein).

As already mentioned there exists an inter-correlation between detonation characteristics of energetic materials and their low-temperature decomposition characteristics [40-47,50,61,83]. In particular, for the case of inorganic azides it was documented [45,47] that in this sense those activation energy values (from among the published ones) can only be adopted that correspond to the lowest temperature ranges of their thermal decomposition. This means that the effect of temperature (i.e. thermal decomposition) in classical sense has no application in the process of detonation initiation by shock or impact. The same is also true of the detonation transformation course proper in energetic materials [115]. Through complementing this statement by the findings obtained from studies of interrelations between characteristics of thermal decomposition and detonation transformation of energetic materials [40-47,50,61,83], and taking into account the views of Russian physicists about the detonation micro-mechanism [116-119] it was possible to draw the following conclusion [120]: The primary fragmentation of polynitro and polynitroso compounds in their detonation transformation proceeds at milder conditions than those present at the front of detonation wave or in its reaction zone. That means that the detonation transformation itself of the given substance should be preceded by an induction period. The course of the fragmentation mentioned is not random but is characterized by a chemical mechanism, which is most likely identical with that of the primary fragmentation of the compounds given in their low-temperature thermal decomposition. Dremin [121] postulated the necessity of such induction period also from the point of view of physics of explosion.

## 5. CONCLUSIONS

A common feature of impact, shock, electric spark and thermal sensitivities of organic polynitro compounds is the reactivity proper of C– $\text{NO}_2$ , N– $\text{NO}_2$  a O– $\text{NO}_2$  groupings in their molecules and/or molecular crystals. Besides the already existing interrelations between the characteristics of the said sensitivities [5,6,26,35,37-50] it is possible to study the micro-mechanisms of their primary chemical processes with help of the  $^{15}\text{N}$  a  $^{13}\text{C}$  NMR chemical

shifts. The values of these shifts are primarily connected with the electron configuration and steric conditions of the given atom. By comparing them with the characteristics of the aforesaid sensitivities it is possible to specify the reaction centre in a given molecule for a given type of initiation of its decomposition [6,26,32,77].

In the case of the impact sensitivity, the drop energies,  $E_{dr}$ , correlate with the  $^{13}\text{C}$  or  $^{15}\text{N}$  NMR chemical shifts of “bearer atoms” of the most reactive nitro groups. That means that besides the electron configuration of the said “bearer”, the impact sensitivity is also affected by the conformation of molecule, i.e. intermolecular effects in molecular crystal. What has been said also documents the relationship between the  $E_{dr}$  values and heats of fusion,  $\Delta H_{m,tr}$  (see also Refs. [6,89]), which is in accordance with the idea of plastic deformation of crystal in the initiation of energetic materials by impact. The relationships mentioned exist for both types of impact sensitivity but have different mathematical forms for the sensitivity as “the first reaction” and that detected by sound. This difference might be connected with differences in mechanism of transfer of drop energy to the reaction centre of molecule when the individual types of impact sensitivity are determined.

On the other hand, the characteristics of detonation, electric spark sensitivity, and thermal decomposition correlate with the  $^{15}\text{N}$  NMR chemical shifts of nitrogen atoms of the most reactive nitro groups. The basis of initiation by electric spark could lie in a thermal stimulus [35,39,52,53]. However, thermal stimuli cannot be considered in the process of detonation initiation by shock (also by impact) [115]. This also agrees with the finding that the detonation characteristics of energetic materials correlate with the characteristics of their low-temperature decomposition, which means that the primary fragmentation of polynitro compounds in their detonation transformation proceeds at milder conditions than those present at the front of detonation wave or in its reaction zone. That also means that the detonation transformation itself of the given substance should be preceded by an induction period [120].

The chemical micro-mechanisms of primary fission processes in molecules of polynitro compounds during initiation by mechanical stimuli (inclusive of the detonation course) and electric spark should be the same as in the case of their low-temperature thermal decomposition. In the case of initiation of nitramines by impact and shock, an excellent agreement in this respect was also found with the results of molecular-dynamic simulation by Kohno *et al.* [27]. The more complex molecular structure of polynitro arenes makes the problem of their primary fission somewhat complicated, too. If a molecule of these compounds contains several types of substituents, it can contain several potential reaction centres (e.g. the TMPM and PYX molecules). The initiation proper can then be realised by the molecule simultaneously participating by



several centres (the detonation of TMPM) or always by a single centre in a given type of initiation (the initiation of PYX by impact or shock versus its initiation by electric spark).

The relationships found thus focus attention on those atoms in molecules of polynitro compounds whose electron configurations and sterical conditions play a key role in the primary fission processes of these molecules during initiation by mechanic stimuli, electric spark, or heat. The findings presented are suitable pieces of starting information for molecular-dynamic or quantum-chemical simulations of initiation of energetic materials particularly by impact and shock.

## ACKNOWLEDGEMENT

This work was supported by Ministry of Industry & Commerce of the Czech Republic (research project No. FC-M2/05).

## REFERENCES

- [1] Xiao Heming, Wang Zun-Yao and Yao Jian-Min, *Acta Chim. Sinica*, 43 (1985) 14.
- [2] F. J. Owens, K. Jayasuriya, L. Abrahmsen and P. Politzer, *Chem. Phys. Letter*, 116 (1985) 434.
- [3] Fan Jianfen and Xiao Heming, *J. Mol. Struct. (THEOCHEM)*, 365 (1996) 225.
- [4] F. J. Owens, *J. Mol. Struct. (THEOCHEM)*, 370 (1996) 11.
- [5] V. Zeman and S. Zeman, in *Proc. 28<sup>th</sup> Int. Annual Conf. ICT, Karlsruhe, 1997*, p 67/1.
- [6] S. Zeman, *Propellants, Explos., Pyrotech.*, 25 (2000) 66.
- [7] V. G. Matveev, V. V. Dubikhin and G. M. Nazin, *Izv. Akad. Nauk SSSR, Ser. Khim.*, (1978) 474.
- [8] S. Bulusu and T. Axenrod, *Org. Mass Spectrom.*, 14 (1979) 585.
- [9] J. Wang and H.-Y. Lang, *Science in China, Ser. B*, 33 (1990) 257.
- [10] G. M. Nazin and G. B. Manelis, *Russ. Chem. Revs.*, 63 (1994) 313.
- [11] S. Bulusu, D. I. Weinstein, J. R. Autera, D. A. Anderson and R. W. Velicky, in *Proc. 8<sup>th</sup> Int. Symp. on Detonation, Albuquerque, NM, July 1985*.
- [12] G. J. Piermarini, S. Block and P. J. Miller, in S. N. Bulusu (Ed.), *Chemistry and Physics of Energetic Materials*, Kluwer Academic Publ., Dordrecht, 1990, p. 391.
- [13] V.P. Stepanov, A.A. Fedotov, A.N. Pavlov and G.B. Manelis, in B. N. Novozhilov (Ed.), *Khimicheskaya fizika protsessov goreniya i vzryva (Chemical Physics of the Combustion and Explosion)*, *Proc. 9<sup>th</sup> All-union Symp. Combust. Explos.*, Acad. Scienses USSR, Chernogolovka, 1989, p. 100.
- [14] M. D. Cook, *J. Energ. Mater.*, 5 (1987) 257.
- [15] R. Behrens, Jr., and S. Bulusu, *J. Phys. Chem.*, 95 (1991) 5838.
- [16] B. A. Lur'e, B. S. Svetlov and A. N. Chernyshov, in *Proc. 9<sup>th</sup> Symp. Chem. Probl. Connected Stabil. Explos.*, Sweden, May 1992, p. 119.
- [17] G. B. Manelis, G. M. Nazin, Yu. I. Rubtsov and V. A. Strunin, *Termicheskoe razloženie i goreniye vzryvchatykh veschestv i porokhov (Thermal Decomposition and Combustion of Explosives and Powders)*, Izdat. Nauka, Moscow, 1996.
- [18] M. M. Kuklja, *J. Phys. Chem.*, B 105 (2001) 10159.

- [19] F. J. Owens and P. Politzer, Shock Waves Condens. Matter, Proc. 4<sup>th</sup> Am. Phys. Soc. Top. Conf. 1985, Publ. Plenum Press, New York, 1986, pp. 857-861.
- [20] J. S. Murray and P. Politzer, in S. N. Bulusu (Ed.): Chemistry and Physics of Energetic Materials. Kluwer Acad. Publ., Dordrecht, 1990, p. 175.
- [21] P. Politzer, J. S. Murray, P. Lane, P. Sjøberg and H. G. Adolph, Chem. Phys. Letters, 181 (1991) 78.
- [22] J. S. Murray, P. Lane, P. Politzer and R. Bolduc, Chem. Phys. Letters, 168 (1990) 135.
- [23] S. Odier, in S. N. Bulusu (Ed.): Chemistry and Physics of Energetic Materials. Kluwer Acad. Publ., Dordrecht, 1990, p. 79.
- [24] M. M. Kuklja and A. B. Kunz, J. Appl. Phys., 87 (2000) 2215.
- [25] B. M. Rice and J. J. Hare, J. Phys. Chem., A 106 (2002) 1770.
- [26] S. Zeman, J. Energet Mater., 17 (1999) 305.
- [27] Y. Kohno, K. Ueda and A. Imamura, J. Phys. Chem., 100 (1996) 4701.
- [28] S. Zeman, M. Huczala and Z. Friedl, J. Energet Mater., 20 (2002) 53.
- [29] A. Delpuech and J. Cherville, Propellants Explos., 3 (1978) 169.
- [30] A. Delpuech and J. Cherville, Propellants Explos., 4 (1979) 61.
- [31] M. M. Kuklja, E. V. Stefanovich and A. B. Kunz, J. Phys. Chem., 112 (2000) 3417.
- [32] S. Zeman, V. Zeman and Z. Kamenský, in Proc. 28<sup>th</sup> Int. Annual Conf. ICT, Karlsruhe, 1997, pp. 66/1.
- [33] V. Zeman, J. Kočí and S. Zeman, HanNeng CaiLiao, 7 (1999) 127.
- [34] V. Zeman, J. Kočí and S. Zeman, HanNeng CaiLiao, 7 (1999) 172.
- [35] J. Kočí and S. Zeman, HanNeng CaiLiao, 8 (2000) 18.
- [36] J. Kočí, V. Zeman and S. Zeman, HanNeng CaiLiao, 9 (2001) 60.
- [37] S. Zeman, in Proc. 5<sup>th</sup> Int. Seminar „New Trends in Research of Energetic Materials“, University of Pardubice, April 2002, p.434.
- [38] M. A. Schrader, M. W. Leeuw and A. C. Van der Steen, Proc. 9<sup>th</sup> Int. Pyrotech. Seminar, Colorado Springs, Aug. 1984, p. 881.
- [39] D. Skinner, D. Olson and A. Block-Bolten, Propellants, Explos., Pyrotech., 23 (1997) 34.
- [40] S. Zeman, Thermochim. Acta, 41 (1980) 199.
- [41] N. M. Bhide, S. R. Naidu, E. M. Kurian and K. R. K. Rao, J. Thermal Anal., 35 (1989) 1181.
- [42] K. V. Prabhakaran, N. M. Bhide and E. M. Kurian, Thermochim. Acta, 220 (1993) 169.
- [43] P. S. Makashir and E. M. Kurian, J. Thermal Anal., 46 (1996) 225.
- [44] S. Zeman, M. Dimun and Š. Truchlík, Thermochim. Acta, 78 (1984) 181.
- [45] S. Zeman, M. Dimun, Š. Truchlík and V. Kabátová, Thermochim. Acta, 80 (1984) 137.
- [46] S. Zeman, M. Dimun, V. Kabátová and Š. Truchlík, Thermochim. Acta, 81 (1984) 359.
- [47] S. Zeman, Thermochim. Acta, 384 (2002) 137.
- [48] S. Zeman, Thermochim. Acta, 49 (1981) 219.
- [49] S. Zeman, Thermochim. Acta, 216 (1993) 157.
- [50] S. Zeman, P. Kohlíček and M. Maranda, A Study of Chemical Micromechanism Governing Detonation Initiation of Condensed Explosive Mixtures by Means of Differential Thermal Analysis Thermochim. Acta (20020, - in press
- [51] J. Owens and J. Sharma, J. Appl. Phys., 51 (1980) 1494.
- [52] M. Auzanneau and M. Roux, Propellants, Explos., Pyrotech., 20, (1995) 99.
- [53] J. Kočí, S. Zeman, J. Majzlík and J. Strnad, in Proc. 5<sup>th</sup> Int. Seminar „New Trends in Research Explosives“, University of Pardubice, April 2002, p. 110.
- [54] S. Bulusu and J. R. Autera, J. Energ. Mater., 1 (1983) 133.

- [55] J. Sharma, J. C. Hoffsommer, D. J. Glover, C. S. Coffey, F. Santiago, A. Stolovy and S. Yasuda, , in J. R. Asay, R. A. Graham and G. K. Straub (Eds.), *Shock Waves in Condensed Matter*, Elsevier Sci. Pub. B. V., Amsterdam, 1984, p. 543.
- [56] J. Sharma, J. W. Forbes, C. C. Cofey and T. P. Liddiard, *J. Phys. Chem.*, 91 (1987) 5139.
- [57] J. Sharma, in: S. C. Schmidt, R. D. Dick, J. W. Forbes and D. G. Tasker (Eds.), *Shock Compression of Condensed Matter*, Elsevier Sci. Publ. B. V., 1992, p. 639.
- [58] J. M. Prokipcak, P. A. Forte and D. D. Lennox, *Canad. J. Chem.*, 47 (1969) 2482.
- [59] T. P. Hobin, *Tetrahedron*, 24(1968) 6145.
- [60] B. N. Kondrikov, in: J. R. Bowen, N. Manson, A. K. Openheim and R. I. Soloukhin (Eds.), *Shock Waves, Explosions, and Detonations*, Vol. 87 of *Progress in Astronautics and Aeronautics*, 1983, p. 426.
- [61] S. Zeman, Š. Gazda, A. Štolcová and A. Dimun, *Thermochim. Acta*, 247 (1994) 447.
- [62] P. Politzer and S. Boyd, *Struct. Chem.*, 13 (2002) 105.
- [63] F. E. Walker, *J. Appl. Phys.*, 63 (1988) 5548.
- [64] F. E. Walker, *Propellants, Explos., Pyrotech.*, 15 (1990) 190.
- [65] S. Zeman, Z. Friedl and R. Huczala, in *Proc. 5<sup>th</sup> Int. Seminar "New Thrends in Research of Energetic Materials"*, Univ. Pardubice, April, 2002, p. 426.
- [66] M. J. Kamlet, in: A. A. Borisov (Ed.), *Detonatsiya i vzryvchatye veschestva (Detonation and Explosives)*, Izdat. Mir, Moscow, 1981, pp. 142-159. See also M. J. Kamlet, *Proc. 6<sup>th</sup> Symp. (International) on Detonation*, San Diego, Calif., 1976, *ONR Rep. ACR 221*, p. 312.
- [67] M. J. Kamlet and H. G. Adolph, *Propellants, Explos.*, 4 (1979) 30.
- [68] C. B. Storm, J. R. Stine and J. F. Kramer," in S. N. Bulusu (Ed.), *Chemistry and Physics of Energetic Materials*, Kluwer Acad. Publs., Dordrecht, 1990, pp. 605-639.
- [69] D. E. Bliss, S. L. Christian and W. S. Wilson, *J. Energ. Mater.*, 9 (1991) 319.
- [70] S. Zeman, in *Proc. 5<sup>th</sup> Int. Seminar "New Trends in Research of Energetic Materials"*, Univ. Pardubice, April 2002, p. 434.
- [71] S. Zeman, P. Valenta, V. Zeman, J. Jakubko and Z. Kamensky, *HanNeng CaiLiao*, 6 (1998) 118.
- [72] M. J. Kamlet and S. J. Jacobs, *J. Chem. Phys.*, 48 (1968) 23.
- [73] L. R. Rothstein and R. Petersen, *Propellants Explos.*, 4 (1979) 56.
- [74] S. Zeman, V. Mlynárik, I. Goljer and M. Dimun, *CS Patent 237 661* (Nov. 30<sup>th</sup>, 1987); *Chem. Abstr.* 108 (1988) 39564k.
- [75] S. Zeman and M. Krupka, in *Proc. 5<sup>th</sup> Seminar „New Trends in Research of Energetic Materials“*, Univ. Pardubice, April 2002, p. 406.
- [76] A. Lyčka, V. Macháček and J. Jirman, *Coll. Czech. Chem. Commun.*, 52 (1987) 2946.
- [77] S. Zeman, *Thermochim. Acta*, 333 (1999) 121.
- [78] S. Bulusu, T. A. Axenrod, and J. R. Autera, *Org. Magn. Reson.*, 16 (1981) 52.
- [79] M. Kaiser and B. Ditz, in *Proc. 29<sup>th</sup> Int. Annual Conf. ICT*, Karlsruhe, 1998, p. 130/1.
- [80] Yu. Ya. Maksimov and E. N. Kogut, *Tr. Mosk. Khim.-Tekhnol. Inst. Mendeleeva*, 104 (1979) 30.
- [81] B. A. Lur'e and B. S. Svetlov, *Kinet Katal.*, 35 (1994) 165.
- [82] B. A. Lur'e and B. S. Svetlov, *Tr. Mosk. Khim.-Tekhnol. Inst. Mendeleeva*, 53 (1967) 40.
- [83] A. Tall and S. Zeman, *Thermochim. Acta*, 93 (1985) 25.
- [84] S. Zeman, *Thermochim. Acta*, 290 (1997) 199.
- [85] S. Zeman, *J. Thermal. Anal.*, 17 (1979) 19.

- [86] Yu. Ya. Maksimov, N. V. Polyakova, V. F. Sapranovich, Tr. Mosk. Khim.-Tekhnol. Inst. Mendeleeva, 83 (1974) 55
- [87] V. A. Koroban and Yu. Ya. Maksimov, Khim. Khim. Tekhnol., 11 (1968) 1032.
- [88] S. Zeman, J. Thermal Anal., 21 (1981) 9.
- [89] S. Zeman and M. Krupka, in Proc. 5<sup>th</sup> Seminar „New Trends in Research of Energetic Materials“, Univ. Pardubice, April 2002, p. 415.
- [90] J. C. Hoffsommer and J. S. Feiffer, Thermal Stabilities of Hexanitroazobenzene and Hexanitrobiphenyl. Rep. NOLTR 67-74, US Naval Ordnance Lab., Silver Spring, 1967.
- [91] J. S. Clawson, M. Strohmeier, D. Stueber, A. M. Orendt, D. H. Barich, B. A. Asay, M. A. Hiskey, R. J. Pugmire and D. M. Grant, J. Phys. Chem., A 106 (2002) 6352.
- [92] S. Zeman and J. Jalový, Thermochim. Acta, 345 (2000) 31.
- [93] M. Pospíšil, P. Čapková, P. Vávra and S. Zeman, in Proc. of the 5<sup>th</sup> Int. Seminar „New Trends in Research of Energetic Materials“, University of Pardubice, April 2002, p. 262.
- [94] M. Pospíšil, P. Čapková, P. Vávra and S. Zeman, in P. Politzer (Ed.), Energetic Materials: Initiation, Decomposition and Combustion, Elsevier, Amsterdam, 2003.
- [95] D. V. Shalashilin and D. L. Thompson, J. Phys. Chem., A 101 (1997) 961.
- [96] S. Zeman, in Proc. 5<sup>th</sup> Seminar „New Trends in Research of Energetic Materials“, Univ. Pardubice, April 2002, p. 434.
- [97] S. Zeman, in Proc. 10<sup>th</sup> Symp. on Chem. Probl. Connected Stab. Explosives, Margretetrop, May 1995, p. 367.
- [98] S. Bulusu, T. A. Axenrod and J. R. Autera, Org. Magn. Reson., 16 (1981) 52.
- [99] C. S. Coffey and J. Sharma, in Proc. 11<sup>th</sup> Int. Detonation Symposium, Snowmass Village, Colorado, August 1998, p. 66.
- [100] C. S. Coffey and J. Sharma, Phys. Rev. B: Condens. Mater. Phys., 60 (1999) 9365.
- [101] K. L. McNesby and C. S. Coffey, J. Phys. Chem., B 101 (1997) 3097.
- [102] S. Zeman, J. Thermal Anal. Calorim., 65 (2001) 919.
- [103] L. E. Fried and A. J. Ruggiero, J. Phys. Chem., 98 (1994) 9786.
- [104] M. Koshi, S. Ye, J. Widiyaja and K. Tonokura, in Proc. 4<sup>th</sup> Int. Sym. on Impact Engineering, Vol. 1, July 2001, Kumamoto, Japan, p. 175.
- [105] Xiaoyu Hong, J. R. Hill and D. D. Dlott, in T. B. Brill, T. P. Russell. W. C. Tao and R. B. Wardle (Eds.), Mat. Res. Soc. Symp. Proc., 418 (1995) 357.
- [106] P. J. Haskins and M. D. Cook, in Proc. 1997 APS Conf. on Shock Waves in Condensed Matter, Amherst, USA, July 1997.
- [107] M. L. Bernard, J. Chim. Phys., 77 (1980) 243.
- [108] M. L. Bernard, Propellants, Explos., Pyrotech., 8 (1980) 46.
- [109] T. Hasegawa, E. Kawashima, K. Satoh and T. Yoshida, in Proc. 22<sup>nd</sup> Int. Pyrotech. Seminar, Fort Collins, Colorado, July 1996, p. 195.
- [110] M. Roux, A. Trevino, M. Auzanneau and C. Brassy, in Proc. 16<sup>th</sup> Annual Conf. ICT, Karlsruhe 1985, p. 3/1.
- [111] F. Hosoya, K. Shiino and K. Itabashi, Propellants, Explos., Pyrotech., 16 (1991) 119.
- [112] S. Amari, F. Hosoya, Y. Mizushima and T. Yoshida, in Proc. 21<sup>st</sup> Int. Pyrotech. Seminar, Moscow, Sept. 1995, p. 13.
- [113] F. Hosoya, Y. Wada, K. Shiino, T. Wainai, K. Itabashi, M. Tamura and T. Yoshida, Kogyo Kayaku, 53 (1992) 14.
- [114] A.N. Pavlov, A. A. Fedotov, L. L. Pavlova, Yu. V. Gameraud and F. I. Dubovitskii, in B. N. Novozhilov (Ed.), Khimicheskaya fizika protsessov goreniya i vzryva (Chemical

- Physics of the Combustion and Explosion), Proc. 9th All-union Symp. Combust. Explos., Acad. Sciences USSR, Chernogolovka, 1989, p. 103.
- [115] J. J. Gilman, Phil. Magazine, B 71 (1995) 1057.
- [116] V. Yu. Klimenko and A. N. Dremin, in Proc. 6<sup>th</sup> All-Union Symp. Combust. Explos., Sept. 1980, Alma Ata, USSR, p. 69.
- [117] A. N. Dremin, Phil. Trans. R. Soc. London, A 339 (1992) 355.
- [118] V. Yu. Klimenko, M. Ya. Yakovtsev and A. N. Dremin, Khim. Fizika, 12 (1993) 671.
- [119] V. Yu. Klimenko, Khim. Fizika, 17 (1998) 11.
- [120] S. Zeman, in Proc. 29<sup>th</sup> Int. Annual Conf. ICT, Karlsruhe, 1998, p. 141/1.
- [121] A. N. Dremin, Toward Detonation Theory. Springer-Verlag, New York, 1999.
- [122] K. Dudek, P. Mareček and P. Vávra, in Proc. 31<sup>st</sup> Annual Conf. ICT, Karlsruhe, June 2000, p. 110/1.
- [123] Ou Yuxiang, Wang Cai, Pan Zelin and Chen Boren, HanNeng CaiLiao, 7 (1999) 100.

### *Chapter 3*

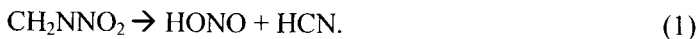
## **Dynamics of Energy Disposal in Unimolecular Reactions**

**Christopher Stopera and Michael Page**

Department of Chemistry, North Dakota State University, Fargo, North Dakota  
58105, U.S.A.

A reaction-path based method is described to obtain information from ab initio quantum chemistry calculations about the dynamics of energy disposal in exothermic unimolecular reactions important in the initiation of detonation in energetic materials. Such detailed information at the microscopic level may be used directly or as input for molecular dynamics simulations to gain insight relevant for the macroscopic processes. The semiclassical method, which uses potential energy surface information in the broad vicinity of the steepest descent reaction path, treats a reaction coordinate classically and the vibrational motions perpendicular to the reaction path quantum mechanically. Solution of the time-dependent Schroedinger equation leads to detailed predictions about the energy disposal in exothermic chemical reactions. The method is described and applied to the unimolecular decomposition of methylene nitramine.

In this chapter we outline a new semiclassical method for obtaining dynamical information about energy release in chemical reactions. We begin with some background about chemical issues related to detonation initiation and the role of unimolecular reactions. This is followed by a description of determining the steepest descent reaction pathway for a chemical reaction and determining the parameters of the Reaction Path Hamiltonian. This information, which comes from ab initio electronic structure calculations, is then used as input for a semiclassical dynamics calculation that provides information about product energy partitioning in the chemical reaction. Finally, the method is illustrated through discussion of the unimolecular decomposition of methylene nitramine,



This reaction proceeds via a five-center cyclic transition state and releases substantial energy to the product fragments.

## 1. CHEMICAL ISSUES IN THE INITIATION OF DETONATIONS

Understanding the mechanism responsible for the initiation of detonation in an energetic solid such as RDX is inherently a multidisciplinary endeavor. One important aspect of the problem is to determine how energy from various sources (shock/pressure, strain/defects, cracking, etc.) may get localized into a chemical bond or into an individual molecule to initiate some chemical event. While this is a crucial issue, successful resolution of this issue is only part of the picture. The localized energy must then initiate *sustainable* chemistry—i.e., chemistry that releases sufficient energy to drive more chemistry. With this in mind it is germane that the most widely postulated *initial* chemical event, N--NO<sub>2</sub> bond cleavage, is an *endothermic* event. It does not release energy that can drive subsequent reactions. Consequently, to understand initiation at a molecular level, we must look at steps that happen after such initial endothermic events. In particular, we must look at early subsequent *exothermic* chemical steps to have any chance of understanding initiation at a molecular level.

Thus a first step --a major step--in understanding initiation at a molecular level is to determine what unimolecular step(s) lead to substantial energy release. Furthermore, the detailed dynamics of that energy release determines whether the energy is available to drive subsequent chemistry or instead is dissipated from the site to the surrounding lattice. While the focus of the calculations presented here is isolated molecules, these calculations are designed to be relevant to dynamics of decomposition of molecules embedded in a crystal lattice.

## 2. THE KEY ROLE OF UNIMOLECULAR REACTIONS

It is tempting to look at published RDX decomposition mechanisms and pick out exothermic chemical steps to investigate. This approach is dangerous, however, because the chemistry by which most of the decomposition occurs in an established propagating detonation likely is quite different from the chemistry that initiated the detonation. One key difference between the chemistry that happens in an established detonation and initiation chemistry is that in an established detonation, chemistry is happening all around a particular site. That chemistry releases substantial energy, and that energy implies a very high local temperature. More chemistry--and more energy release--adds to that high local temperature which drives further chemistry. In other words, at this stage, there is ample energy

available and it is spread over translational and vibrational degrees of freedom. Once the detonation is fully established, the dynamics of how the energy is released in a particular elementary chemical event is all but irrelevant. But before the detonation is fully initiated, i.e., before there is a very high local heating from all around a particular site, the nature of the energy release is critical.

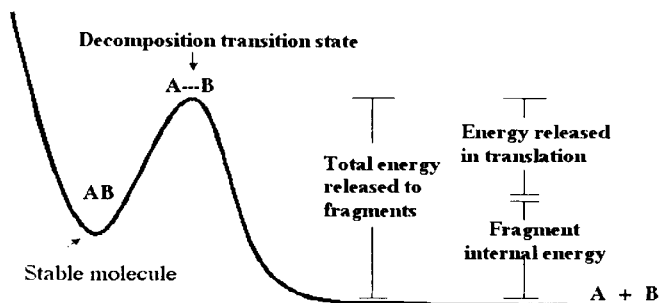


Figure 1: Schematic of Unimolecular Reaction Dynamics

Figure 1 shows a schematic of the energetic issues in an exothermic unimolecular reaction. Although the net energy released in the reaction is merely the reaction exothermicity, a decomposing molecule must have achieved a localization of potential energy sufficient to reach the decomposition transition state. Thus the dynamic energy release issue involves determining how the entire reverse barrier energy is distributed among the various modes of motion of the product fragments. Unusually high chemical energy stuck in individual vibrational modes of the product fragments (hidden energy) will be doled out to neighboring atoms in the lattice a little at a time, partly being spread out over other vibrational modes and partly leaving the reaction site as phonons. A large translational energy (available energy) release, on the other hand, can be used to surmount an activation energy for a neighboring chemical site or it can be used to disrupt the local lattice structure (i.e., a local phase change to a molten state that seems to promote initiation for RDX).



Another difference between chemistry in a propagating detonation and chemistry that might be expected at initiation is the high-temperature propagating-detonation environment has many primary and secondary decomposition products (intermediate species) around, so bimolecular reactions involving those species will be important. In the initiation environment, where less or no neighboring chemistry is going on, the profile of unimolecular steps (fragments getting enough energy to fall apart) will be raised.

Finally the nature even of the unimolecular steps may be different near initiation than in the high temperature propagation environment. In the high temperature environment, entropy drives unimolecular processes toward simple bond rupture events. Near initiation, where energy is at a premium, lower barrier more complex unimolecular steps (such as those involving cyclic transition states) will be raised in importance.

### **3. QUANTUM CHEMISTRY PROVIDES POTENTIAL ENERGY SURFACE**

To accomplish the goal of determining energy release dynamics for unimolecular chemical reactions, we bring together recent theoretical and computational advances to develop a new semiclassical dynamics model that allows the practical prediction of the dynamics of energy release from limited potential energy surface information. Most applications of quantum chemistry in the Department of Defence and elsewhere seek to address issues of molecular structure, of energetics (thermodynamics), or of chemical reaction rates (kinetics). Such issues involve the shape of molecular potential energy surfaces in only well-defined narrow areas: structures and energetics involve local minima on the surface, while rates involve properties in the transition state region. Such applications give no information at all about how the energy released in an elementary unimolecular step is distributed among the various modes of motion of the products.

Our calculations investigate a broader region of the potential energy surface in the large vicinity of a steepest descent reaction path. Our new semiclassical approach uses this information to predict the dynamics of energy disposal into product degrees of freedom. Our approach treats vibrational modes of the transition state as being correlated with vibrational modes of the product. Motion along the reaction path is treated classically, while vibrational motion perpendicular to the reaction path is treated quantum mechanically. Reaction path curvature provides a coupling (and hence an energy exchange mechanism) between the classical and quantum modes. In some reactions with substantial energy release, that energy manifests itself as internally cold product fragments

with very high translational energy. In other substantially exothermic chemical steps, product fragments come off with high vibrational excitation but low translational energy. Such distinctions are critical at initiation.

The semiclassical dynamics method discussed here can be implemented with any electronic structure technique for determining potential energy surface information. The essential requirement is that one is able to compute the matrix of force constants at many points on the potential energy surface. For this reason, it is highly desirable to choose a method for which force constants can be calculated analytically rather than by numerical difference of the analytical gradient. The essential electronic structure calculations necessary to implement the semiclassical dynamics calculations are the following: (1) locate the saddle point on the potential energy surface, (2) determine the steepest descent reaction path from the saddle point to the products, and (3) determine the matrix of force constants at many points along the reaction path. In addition, it is sometimes desirable to perform higher-level single-point energy calculations at points along the reaction path to improve the energy profile. Various quantities defined from the above information are needed along the reaction path as described below.

#### 4. COMPUTING THE REACTION PATH

The minimum energy path (MEP) in mass weighted Cartesian coordinates is the path through configuration space traced out by a hypothetical trajectory initiated at the saddle point with all inertia effects removed. It is the path that molasses would follow flowing downhill. The MEP satisfies the differential equation,

$$U(s) \equiv \frac{d\mathbf{x}}{ds}(s) = -\frac{\mathbf{g}}{\sqrt{c}}(s) \quad (2)$$

where the normalization factor,  $c$ , is defined as

$$c(s) = \mathbf{g}^t \mathbf{g} \quad (3)$$

The numerator of the right hand side of Eq. 2 is the negative of the energy gradient; it is the vector containing the forces on the atoms in each of the Cartesian directions weighted by the mass of the atom. The normalization constant in the denominator insures that the vector is of unit length, even though the magnitude of the force changes dramatically along the MEP. The solution to Eq. 2,  $\mathbf{x}(s)$ , is a vector of mass-weighted Cartesian coordinates as a function of the distance (arc

length) parameter,  $s$ . Because the energy is not known as an analytical function of the Cartesian coordinates, the solution to Eq. 2 must be determined numerically.

The most computationally intensive step in statistical or dynamical studies based on reaction path potentials is the determination of the MEP by numerical integration of Eq. (2) and the evaluation of potential energy derivatives along the path, so considerable attention should be directed toward doing this most efficiently. Kraka and Dunning [1] have presented a lucid description of many of the available methods for determining the MEP. Simple Euler integration of Eq. (2) to determine the path tends to oscillate about the true MEP. The oscillations can be reduced by using a sufficiently small stepsize, but in practice too many steps--each one of which requires an electronic structure calculation of the energy and the gradient--may be required to reach acceptable accuracy. Alternatively, constrained energy minimization can be used to return to the path [2-5].

If the reason for following a reaction path is to check for intervening minima or barriers, or simply to visualize how a molecule might change during a reaction, then the Euler-type methods may be adequate. For dynamics applications, however, accurate molecular properties are needed long the MEP in the exit valley. These properties include the energy, the 3N-7 generalized normal mode vibrational frequencies orthogonal to the path, and the 3N-7 components of the reaction path curvature.

The path dependence of the transverse vibrational frequencies and the curvature coupling elements requires knowledge of the evolution along the path of the matrix of second derivatives of the energy with respect to nuclear displacements (the force constant matrix). In practice, this dependence is determined by evaluating the force constant matrix at intervals along the path that are spaced close enough together to adequately resolve the changes in the frequencies.

The calculation of force constants at points along the MEP is often done separately from the determination of the path by numerical integration of Eq (2), but these two problems can profitably be combined. Methods recently have been proposed [6,7] that efficiently use the available force constants to better follow the path. To understand these methods and the relationship between them, consider two different Taylor series expansions about a point on the MEP. The first is the familiar expansion of the energy in the mass-weighted Cartesian coordinates,

$$E(\mathbf{x}) = E_0 + \mathbf{g}_0'(\mathbf{x} - \mathbf{x}_0) + \frac{1}{2}(\mathbf{x} - \mathbf{x}_0)' \mathbf{F}_0(\mathbf{x} - \mathbf{x}_0) + \frac{1}{6}(\mathbf{x} - \mathbf{x}_0)' [\mathbf{G}_0(\mathbf{x} - \mathbf{x}_0)] (\mathbf{x} - \mathbf{x}_0) + \dots \quad (4)$$

Here  $\mathbf{g}_0$ ,  $\mathbf{F}_0$ , and  $\mathbf{G}_0$  are, respectively, the first (gradient), second (force constants), and third energy derivatives evaluated at  $\mathbf{x}_0$ . The square brackets

indicate that the three-dimensional array of third derivatives is contracted with the vector of coordinate changes to yield a square matrix. If  $\mathbf{x}_0$  is a stationary point, i.e., a minimum, then the usual theory of small vibrations applies: the gradient term vanishes, and truncation after the second order term leads to separable, harmonic normal modes of vibration. However, on the MEP, the gradient term generally is not zero. The second relevant expansion is the Taylor series representation of the path (of the solution to Eq (2)) in the arc length parameter,  $s$ , about the same point,  $\mathbf{x}_0$ :

$$\mathbf{x}(s) = \mathbf{x}_0 + v_0^{(0)}(s-s_0) + \frac{1}{2} v_0^{(1)}(s-s_0)^2 + \dots + \frac{1}{n!} v_0^{(n-1)}(s-s_0)^n \quad (5)$$

These coefficients can also be interpreted. The first-order coefficient,  $v_0$ , is the unit vector tangent to the path and is just minus the normalized energy gradient. The second coefficient is the reaction path curvature; it is the vector that describes the change in direction of the reaction path tangent as one proceeds along the path. The key point is that the vector coefficients,  $\{v\}$ , depend only on energy derivatives evaluated at the point of expansion. Thus the coefficients in the Taylor series expansion of the path (Eq (6)) can be determined from the coefficients in the Taylor series expansion of the energy (Eq (5)). The first two terms are given by

$$v_0^{(0)} = -\frac{1}{\sqrt{c}} \mathbf{g}_0 \quad (6)$$

and

$$v_0^{(1)} = -\frac{1}{\sqrt{c}} \left( \mathbf{F}_0 - v_0^{(0)\dagger} \mathbf{F}_0 v_0^{(0)} \mathbf{I} \right) v_0^{(0)} \quad (7)$$

The higher order coefficients in the path expansion depend on higher energy derivatives, but a general formula has been derived [6]. If the path expansion is truncated at first order (after the second term in Eq (6)), then the resulting approximate path is a straight line. By substituting Eq (7) into the truncated Eq (6), stepping along the resulting straight line path can be seen to be equivalent taking an integration step by the Euler method, Eq (4). Truncating the path expansion at second order (after the third term) yields a simple quadratic approximation to the path. Determining the coefficient of the second order term requires second energy derivatives. So if force constants are available, then a quadratic step can be taken along the path. This quadratic step accounts for the curvature of the reaction path at the point of expansion and consequently allows a larger stepsize than the Euler method does for a given accuracy.

With force constants available, one can use this quadratic Taylor series method to step along the path, but it turns out that even more useful information is available from the force constants. Even though the next term in the Taylor series expansion of the path (the third order term) requires third energy derivatives, there is a contribution to this term that comes from the force constants. And in fact there is a contribution from second energy derivatives to *every* term in the Taylor series representation of the path. So if one makes a local quadratic approximation (LQA) to the *energy* (truncates Eq (5) after the second order term), then the first three terms in the Taylor series expansion of the *path* can be calculated correctly, and there is a non-zero partial contribution at every other order. Within the local quadratic approximation to the energy, Eq (2) can be solved analytically [6]. This is equivalent to summing the aforementioned approximate Taylor series expansion to infinity. The resulting method for determining the MEP, the LQA method [6], has been used to calculate the MEP for several systems of interest in energetic material decomposition [8-11].

Given partial third energy derivative information, further contributions to the coefficients in Eq (6) can be determined [7]. For example, the third order coefficient in Eq (6) requires the derivative of the force constant matrix with respect to  $s$ . This third derivative information can be estimated by a simple finite difference procedure if successive force constant matrices have been determined along the path,

$$\mathbf{F}'_0 \equiv \left( \frac{d\mathbf{F}}{ds} \right)_0 = \frac{\mathbf{F}(s_0) - \mathbf{F}(s_0 - \delta s)}{\delta s} \quad (8)$$

The evaluation of  $\mathbf{F}'$  allows a third order Taylor series expansion of the path. However, a better approach is to combine the third order Taylor series information with the LQA method. This can be done by noting that the expansion coefficient second order expansion coefficients can be split into two parts, one that depends only on second energy derivatives and is included in the LQA method and the other that contains terms that depend on the third energy derivatives,

$$\mathbf{U}_0^{(2)} = \mathbf{U}_{LQA}^{(2)} + \mathbf{U}_{correction}^{(2)} \quad (9)$$

The approximate third energy derivatives calculated as in Eq (9) from successive force constants along the path can then be used to augment the LQA step. The result is called the corrected LQA (CLQA) method [7].

$$\mathbf{x}_{CLQA}(s) = \mathbf{x}_{LQA}(s) + \frac{1}{6} \mathbf{U}_{correction}^{(2)} (s - s_0)^3 \quad (10)$$

Thus, by using a judicious combination of the LQA method and approximate evaluation of higher order terms in the Taylor-series expansion of the path, the potential energy surface information that is already available for performing statistical or dynamical calculations of the chemistry can be used to more accurately follow the path.

## 5. THE REACTION PATH HAMILTONIAN

In a pivotal development, Miller, Handy and Adams [12] derived the classical Hamiltonian for a simple potential based on the MEP. The idea of the reaction path Hamiltonian is, conceptually, to consider the potential as a trough or as a stream bed along with  $3N-7$  harmonic walls that are free to close in or widen out as one proceeds along the trough. The potential energy surface is approximated as the potential energy of the MEP  $V_0(s)$  plus a quadratic approximation to the energy in directions perpendicular to the MEP,

$$V(s, Q_1 \dots Q_{3N-7}) = V_0(s) + \sum_{k=1}^{3N-7} \frac{1}{2} \omega_k^2 Q_k^2 \quad (11)$$

Here the  $\{Q\}$  are the generalized normal coordinates and the  $\{\omega\}$  are the associated harmonic frequencies. They are obtained at each point on the path by diagonalizing the force constant matrix for which the reaction path direction as well as directions corresponding to rotations and translations have been projected out. The projected force constant matrix has seven zero eigenvalues corresponding to overall rotations, translations, and the reaction path direction. It also has  $3N-7$  nonzero eigenvalues corresponding to vibrations transverse to the path.

To obtain the reaction path potential via electronic structure calculations, one must begin at the saddle point and numerically integrate Eq. (2) as discussed previously to obtain the MEP. The force constant matrix is then needed at several points along the path in order to perform the normal mode analyses to obtain the generalized normal modes.

To obtain the Hamiltonian function for this reaction path potential, it is necessary to express the kinetic energy in terms of the momenta conjugate to the reaction path coordinates. The result, for the  $J=0$  case, is [12]

$$T_v = \frac{1}{2} \frac{\left( p_v - \sum_{i=1}^{F-1} \sum_{j=1}^{F-1} Q_i P_j B_{i,j}(s) \right)^2}{\left( 1 + \sum_{i=1}^{F-1} Q_i B_{i,i}(s) \right)^2} \quad (12)$$

and the classical reaction path Hamiltonian for the  $J=0$  case is,

$$H_{RP}^{cl}(p,s,\{P_i,Q_i\}) = \sum_{i=1}^{K-1} \left( \frac{1}{2} P_i^2 + \frac{1}{2} \omega_i^2(s) Q_i^2 \right) + V_0(s) + T, \quad (13)$$

Several approaches to obtaining both qualitative and quantitative information on polyatomic reaction dynamics via reaction path potentials have been discussed by Miller [13], Truhlar and Gordon [14], Kraka and Dunning [1], Collins [15] and Hammes-Schiffer [16].

The coupling terms that appear in the reaction path Hamiltonian can be given a geometrical interpretation. The most important coupling terms are those that couple the transverse vibrational modes directly to the reaction path. These are called the curvature coupling elements because they are a measure of the degree to which the reaction path *curves into* a particular transverse mode as the reaction coordinate is traversed. The curvature coupling element that mediates the dynamical coupling between the reaction path and the  $i^{\text{th}}$  generalized vibrational mode  $\mathbf{L}_i$  is given by

$$B_{i,F} = \left( \frac{d\mathbf{L}_i}{ds} \right)' U_0 = - \left( \frac{dU_0}{ds} \right)' \mathbf{L}_i \quad (14)$$

The curvature of the reaction path at a nonstationary point can be calculated from only the gradient and the force constants via Eq (8). Then from Eq (13), the curvature coupling elements are given by

$$B_{i,F} = U_0' \mathbf{F}_0 \mathbf{L}_i / \sqrt{c} \quad (15)$$

The curvature coupling elements are thus simply off-diagonal matrix elements of the unprojected force constant matrix in the basis of eigenvectors of the projected force constant matrix. The classical notion that a trajectory will overshoot the path and climb the wall if the path curves on the way down the hill is a reflection of this curvature coupling. Climbing the wall in a transverse direction is tantamount to exchanging energy between the reaction path and the transverse vibration.

The basic idea of our approach is to treat the reaction path degree of freedom (arc length,  $s$ , and conjugate momentum,  $p$ ) classically and treat the vibrational degrees of freedom transverse to the reaction path  $\{Q,P\}$  quantum mechanically. We neglect the direct coupling between the vibrational modes and consider only the curvature coupling. Thus each vibrational mode is coupled directly to the

reaction path degree of freedom. Neglecting the  $B_{ij}$  coupling elements and expanding the denominator in a Taylor series, the Hamiltonian becomes,

$$H_{rot} = \sum_{i=1}^{F-1} \left( \frac{1}{2} p_i^2 + \frac{1}{2} \omega_i^2(s) Q_i^2 \right) + V_0(s) + \frac{1}{2} p_s^2 - p_s^2 \sum_{i=1}^{F-1} Q_i B_{i,F}(s) \quad (16)$$

We solve Hamilton's equations for the reaction path degree of freedom using a Hamiltonian obtained by integrating over  $\{Q\}$ , the quantum coordinates,

$$H_{cl} = \frac{1}{2} p_s^2 - p_s^2 \sum_{i=1}^{F-1} B_{i,F}(s) \int \psi^*(Q_i, t) Q_i |\psi(Q_i, t) d\tau + V_0(s) + \sum_{i=1}^{F-1} \varepsilon_i \quad (17)$$

In the absence of curvature coupling, this reduces to a simple one-dimensional Hamiltonian for motion along a vibrationally adiabatic potential,

$$H_{cl} = \frac{1}{2} p_s^2 + V_0(s) + \sum_{i=1}^{F-1} \varepsilon_i \quad (18)$$

Hamilton's equations for the reaction path degree of freedom become,

$$\frac{ds}{dt} = p_s - 2 p_s \sum_{i=1}^{F-1} B_{i,F} \int \Psi^*(Q_i, t) Q_i |\Psi(Q_i, t) d\tau \quad (19)$$

and

$$\frac{dp}{dt} = -\frac{dV_0}{ds} - \sum_{i=1}^{F-1} \frac{d\varepsilon_i}{ds} + p_s^2 \sum_{i=1}^{F-1} \frac{dB_{i,F}}{ds} \int \Psi^*(Q_i, t) Q_i |\Psi(Q_i, t) d\tau \quad (20)$$

We solve the time-dependent Schrodinger equation using the following Hamiltonian for the quantum degrees of freedom,

$$\hat{H}_Q = \sum_{i=1}^{F-1} \left( \frac{-\hbar^2}{2} \frac{\partial^2}{\partial Q_i^2} + \frac{1}{2} \omega_i^2(s) Q_i^2 \right) - p_s^2 \sum_{i=1}^{F-1} Q_i B_{i,F}(s) \quad (21)$$

This is a sum of harmonic oscillator Hamiltonians plus a coupling induced by the curvature.

$$\hat{H}_Q = \sum_{i=1}^{F-1} \hat{h}_i(Q_i) + \hat{H}' \quad (22)$$



Once again, in the absence of curvature coupling, this reduces to a sum of independent harmonic oscillator Hamiltonians. The wavefunction is written as a product of one-dimensional functions each expanded in a harmonic oscillator basis.

$$\Psi(Q_1, Q_2, \dots) = \Phi_1(Q_1)\Phi_2(Q_2)\Phi_3(Q_3)\dots \quad (23)$$

where

$$\Phi_k = \sum_{i=1}^N c_{i,k} \chi_i^k(Q_k) = \sum_{i=1}^N (\alpha_{i,k} + i\beta_{i,k}) \chi_i^k(Q_k) \quad (24)$$

The time-dependent Schrodinger equation leads to the following equations for the expansion coefficients

$$\hbar \frac{\partial}{\partial t} [\alpha_{ik}(t)] = \beta_{ik}(t) \varepsilon_{ik} + \sum_{j=0}^{\infty} \beta_{ij}(t) H'_{jk} \quad (25)$$

$$-\hbar \frac{\partial}{\partial t} [\beta_{ik}(t)] = \alpha_{ik}(t) \varepsilon_{ik} + \sum_{j=0}^{\infty} \alpha_{ij}(t) H'_{jk} \quad (26)$$

These equations are solved numerically using a leap-frog algorithm. The classical and quantum parts of the problem are solved simultaneously. Each provides information at each time step necessary to the other. The expansion coefficients give the final state populations for the product vibrational modes.

## 6. METHYLENE NITRAMINE DECOMPOSITION

As an illustrative example of the semiclassical reaction path dynamics method, we discuss the HONO elimination pathway for the unimolecular decomposition of methylene nitramine,



This reaction proceeds through a five-center cyclic transition state and has an activation barrier of approximately 30 kcal/mol [17]. Because the reaction is about 20 kcal/mol exothermic, there is about 50 kcal/mol of energy released to the product fragments [18]. The issue we address is how this 50 kcal/mol is distributed amongst the various modes of motion of the products HCN and HONO [19].

If there was no curvature coupling, motion along the steepest descent reaction path would be uncoupled from the internal vibrational degrees of freedom.

The reaction path degree of freedom becomes, far in the exit valley, simply a separation of the product fragments. Therefore in the absence of coupling, the entire 50 kcal/mole would be manifest as relative translation of the product fragments. This is the vibrationally adiabatic picture.

To see qualitatively why the vibrationally adiabatic picture breaks down, consider HX elimination from haloethane,  $\text{H}_3\text{C}-\text{CH}_2\text{X} \rightarrow \text{H}_2\text{C}=\text{CH}_2 + \text{HX}$ . Here the reaction path motion in the vicinity of the four-center cyclic transition state is predominantly the H-atom approaching the halogen atom. As one proceeds along the reaction path towards products, the energy goes down rapidly and the H and X atoms therefore accelerate toward one another. The H and X atoms cannot continue to move toward one another, and partway down this exit valley, the reaction path changes direction to become the incipient HX molecule repelling the distorted ethylene fragment. The inertia from the initial portion of the reaction path thus causes the H and X atoms to slap into one another. To a first approximation, the energy from the transition state down to the region of this reaction path curvature goes into HX vibration, and the energy from the curvature region to the product asymptote goes into relative translation. Calculations using the semiclassical method discussed here are in good agreement with experiment for  $\text{X}=\text{F}$  and for  $\text{X}=\text{Cl}$  [20].

The five-center cyclic transition state for the HONO elimination reaction is shown in Figure 2. Like in the haloethane case, reaction path motion near the transition state is predominantly the transferring H-atom approaching the O-atom of the  $\text{NO}_2$  group for incipient bond formation. Because the product asymptote is over 50 kcal/mol lower in energy than this transition state, it is reasonable to surmise significant energy will go into the OH stretching vibration of HONO. However that is not the case.

Analysis of the HONO elimination reaction indicates the dynamics are substantially different from the haloethane dynamics. The primary differences can be understood by looking at the results of the dynamics calculations in Figure 3 in conjunction with the structures along the reaction path. Figure 3 shows the reaction path potential energy falling from approximately 53 kcal/mol at the transition state ( $s=0.0$ ) to zero at the products. The dashed line in Figure 3 is the overall curvature of the reaction path. This is what couples the reaction path energy to the internal vibrations. The curvature has a substantial peak around  $s=0.6$ . This is where the reaction path direction changes from that shown by the arrows in Figure 2. After this point, the path changes from the H-atom approaching the O-

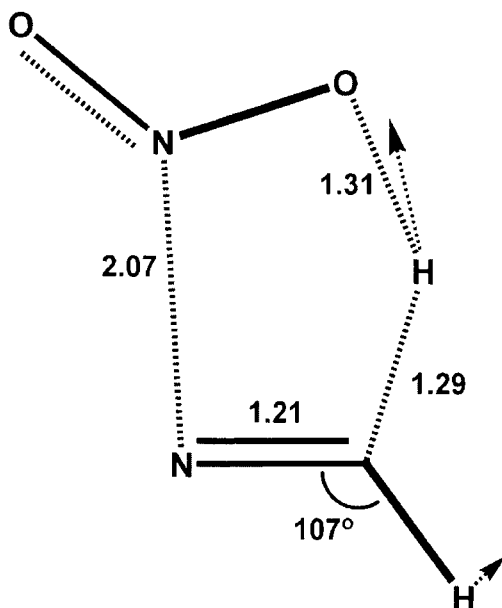


Figure 2. Transition State Structure ( $s=0.0$ ) for  $\text{H}_2\text{CNNO}_2 \rightarrow \text{HCN} + \text{HONO}$ . Arrows represent motion tangent to the reaction path.

atom to the H-atom moving perpendicular to the newly formed OH bond, increasing the NOH bond angle. Essentially the H-atom transfers to the O-atom early in the exit valley. While this curvature allows energy transfer to the OH stretch, this curvature happens very early, and there is little reaction path kinetic energy to transfer. As a result, only about 2.5 kcal/mol goes into the OH stretch, in striking contrast to the haloethane cases. Figure 4 shows the reaction path tangent at  $s=1.0$ . As can be seen in Figure 3, this is a point just after the large curvature peak. There is nearly 40 kcal/mol yet to be released to the products after this point.

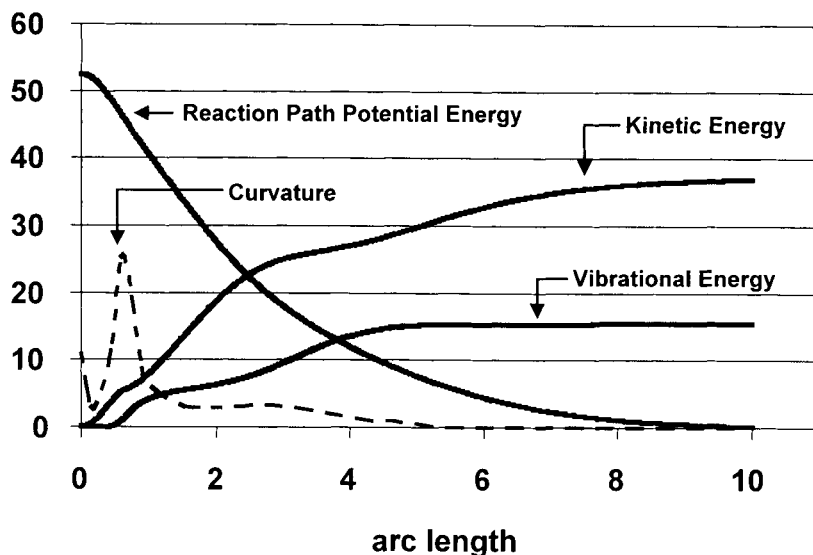


Figure 3: Reaction Path Energy, Curvature, and dynamical results along the reaction path for  $\text{H}_2\text{CNNO}_2 \rightarrow \text{HCN} + \text{HONO}$

Significantly, the HCN fragment is quite bent after the H-atom transfers. It is the small second curvature peak, with a maximum around  $s=3$ , that is responsible for most of the vibrational excitation in the products. In the end, only about 2.5 kcal/mol goes into the OH stretch, while over 10 kcal/mol gets deposited in to the HCN bending vibration. The total vibrational energy of the product fragments is about 16 kcal/mol. While this is significant vibrational excitation, this leaves about 38 kcal/mole for relative translation of the product fragments.

It is this 38 kcal/mol translational energy that is available immediately in the local region to be transferred to neighboring molecules and thus initiate more chemistry. For initiation to succeed, energy released in exothermic reactions such as this one must promote subsequent chemistry rather than be dissipated to the surrounding lattice as phonon modes.

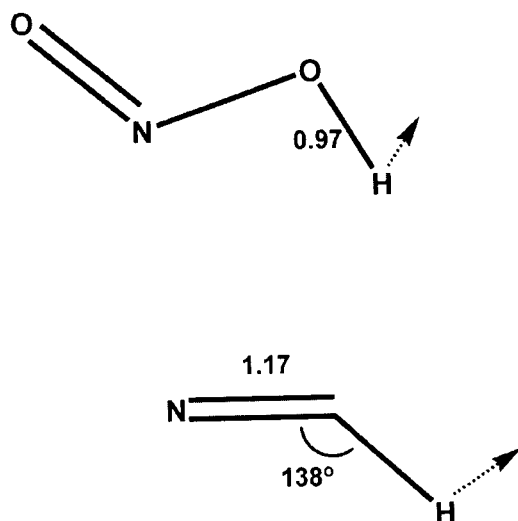


Figure 4: Structure at  $s=1.0$  for  $\text{H}_2\text{CNNO}_2 \rightarrow \text{HCN} + \text{HONO}$ . Arrows represent motion tangent to the reaction path.

## 7. CONCLUDING REMARKS

A first step --a major step--in understanding initiation at a molecular level is to determine what unimolecular step(s) lead to large translational energy release. If certain key steps could be identified, one could in principle make a material less sensitive by some chemical modification that raises the (activation) energy barriers for those key steps.

Another important issue is that large-scale molecular dynamics simulations are not poised to get this energy partitioning right without being "taught" the dynamical information that comes from the kinds of calculations discussed here.

That is, for the molecular dynamics simulations that include energy release chemistry steps to be realistic, these chemical steps must have two features. They must have an endothermic component such that initial chemical events remove rather than release energy, and they must have exothermic steps that release a fraction rather than all the chemical energy into product translation. That fraction must come from calculations such as those discussed in this chapter. These two features are the MD-simulation equivalent of chemical induction times in fluid dynamics simulations.

The dynamical methods presented in this chapter may be used in conjunction with electronic structure methods such as Density Functional Theory that can be used on various RDX fragments as well as on RDX itself. A key feature of the reaction path based methods is that the calculation does not scale unfavorably with the number of atoms, making the prospect of performing these calculations to get valuable dynamical information for larger systems tractable.

## REFERENCES

1. Kraka, E. and Dunning, T. H., in *Calculating and Characterizing Molecular Potential Energy Surfaces, Advances in Molecular Electronic Structure Theory*, JAI press, Greenwich, CT, 1990, p. 129-173.
2. Ishida, K., Morokuma, K., Komornicki, A., *J. Chem. Phys.*, **66**, 2153 (1977).
3. Schmidt, M. W., Gordon, M. S., Dupuis, M., *J. Am. Chem. Soc.*, **107**, 2585 (1985).
4. K. Muller, L. D. Brown *Theor. Chim. Acta.*, **53** 75 (1979).
5. Gonzalez, C., Schlegel, H. B., *J. Chem. Phys.*, **90**, 2154 (1989).
6. M. Page, J. W. McIver, Jr. *J. Chem. Phys.*, **88**, 922 (1988).
7. M. Page, C. Doubleday, and J. W. McIver, Jr., *J. Chem. Phys.*, **93**, 5634 (1990).
8. B. C. Garrett, M. Koszykowski, C. F. Melius and M. Page, *J. Phys. Chem.*, **94**, 7096 (1990).
9. M. R. Soto and M. Page, *J. Phys. Chem.*, **94**, 3242 (1990).
10. M. R. Soto, M. Page, and M. McKee, *Chem. Phys.*, **153**, 415 (1991).
11. M. R. Soto and M. Page, *J. Chem. Phys.*, **97**, 7287 (1992).
12. Miller, W. N., Handy, N. C., Adams, J. A., *J. Chem. Phys.*, **72**, 99 (1980).
13. W. H. Miller in *The Theory of Chemical Reaction Dynamics*, (D. Deidel 1986) D. C. Clary (ed.) p. 27-45.

14. D. G. Truhlar, M. S. Gordon, *Science*, **249**, 491 (1990). From Force Fields to Dynamics: Classical and Quantal Paths.
15. M. A. Collins, *Adv. Chem. Phys.*, **93**, 389 (1996)
16. S. Hammes-Schiffer, S. R. Billeter, *Int. Rev. Phys. Chem.*, **20**, 591 (2001)
17. R. C. Mowrey, M. Page, G. F. Adams, B. H. Lengsfeld, *J. Chem. Phys.*, **93**, 1857 (1990)
18. B. M. Rice, G. F. Adams, M. Page, D. Thompson, *J. Phys. Chem.*, **99**, 5016 (1995).
19. C. Stopera, W. Thweatt, M. Page, *manuscript in preparation*.
20. W. Thweatt, Ph.D. Thesis, North Dakota State University, 2003.

## *Chapter 4*

# **Initiation and decomposition mechanisms of energetic materials**

**M. R. Manaa**

Lawrence Livermore National Laboratory, Energetic Materials Center  
P.O. Box 808, L-282, Livermore, California 94551

## **1. INTRODUCTION**

Under shock propagation or impact, energetic materials undergo rapid heating to a few thousand degrees and are subjected to a compression of hundreds of kilobars, [1] resulting in almost 30% volume reduction. Complex chemical reactions are initiated, and a dense, highly reactive supercritical fluid is established behind the propagating detonation front. Several experimental results suggest the existence of strong correlations between the applied mechanical stress and shocks, the local heterogeneity and defects (dislocations, vacancies, cracks, impurities, etc.), and the onset of chemical reactions. [2-7] Computational investigations aspire to unravel the role of these parameters, with the objective of constructing accurate and predictive models of performance and sensitivity for the development of new energetic materials.[8]

The experimental and theoretical studies of defects in energetic materials lends support to the theory of "hot spot" formation, according to which the ignition starts in localized regions of highly concentrated energy associated with defects.[9-11] The nature of these hot spots is still an unresolved issue. Dlott and Fayer [10] have proposed that the anharmonic coupling between phonons and low-frequency molecular vibrations is strong at such hot spots, and hence causes defect molecules to transiently attain high vibrational temperatures; these temperatures favor chemical reactions that normally do not occur in the bulk. However, no widely agreed upon microscopic model exists to describe how the size, morphology, and density of the defects in the crystalline solid affect the overall rate of the reaction energy release.

Chemical decomposition models are critical ingredients in order to predict, among others, the measured times to explosion and the conditions for ignition of hot spots.[12] While decomposition mechanisms could be proposed based on



the experimental results, reaction rate constants are only attainable for the simplest of reactions, and at combustion conditions. Chemical kinetic rates of condense-phase energetic materials at detonation conditions are virtually non-existent.

## 2. INITIATION MODELS

The initial response of a heterogeneous energetic molecular solid to a sudden compression attracted widespread interest. Coffey [11, 13-15] postulated that the initiation process is due to tunneling of dislocations in a solid; when the shock velocities are sufficiently high, the dislocations can have energy adequate to directly pump the internal vibrational modes of the constituent molecules. The vibrational energy up-pumping model [10] suggests that the shock wave produce a bath of excited phonons absorbed by the lowest vibrational modes of molecules that make up the crystal. Increased phonon absorption and intramolecular vibrational energy redistribution (IVR) lead to excitation of higher frequency modes, eventually reaching an equilibrium transition state, and proceeding to chemical bond breakage and the subsequent chemical reactions. A simple formula for the total energy transfer rate into a given vibron band in terms of the density of vibrational states and the vibron-phonon coupling was subsequently derived. [16] The phonon upconversion rates, based on small cubic anharmonic terms, were shown to correlate with the sensitivity in such explosives as TATB, HMX and lead styphnate. Tarver [17] discussed multiple roles of highly vibrationally excited molecules in the reaction zones of detonation waves for his model of the nonequilibrium Zeldovich-von Neumann-Doring theory of self-sustaining detonations. [18-20]

In contrast, several other proposals considered models associated with electronic processes. According to Williams, [21] initiation of detonation in solids can occur through changes induced in the Fermi level because of a double electron and positive hole injection followed by chemical reactions. This is an interesting idea that would lend itself to scrutiny through computational treatment: The tremendous compression assault at the shock front induces changes in the band-gap structure of the material right behind the front. More recently, Dremin and co-workers [22] made an attempt to explain why molecules lying in the shock front dissociate; his proposed dissociation mechanism directly involves electronic excitations. In the same spirit, Gilman [23-25] suggested that the compression due to the pressure wave front causes local metallization when the bending of certain covalent bonds reduces the energy gap between the highest occupied (HOMO) and the lowest unoccupied molecular orbitals (LUMO). This effect in turn favors chemical decomposition, in compliance with a criterion given in the 1920s by Herzfeld [26] for crystals with dense structures. According to this criterion, a material becomes metallic if its molar refractivity, which is proportional to polarizability and hence

approximately proportional to the inverse of the optical gap, exceeds the molar volume.

Simulations of band-gap properties of imperfect energetic molecular solids, such as the cyclotrimethylene trinitramine (RDX) And pentaerythritol tetranitrate (PETN) crystals with vacancies and dislocations, have been attempted recently by Kuklja and Kunz. [27-31] Their results have indicated that compression of the RDX crystal in the presence of single [28-30] and dimmer [27,30] vacancies reduces the optical gap of this material appreciably, thus decreasing the excitation energy needed for the insulator-metal phase transition. Specifically, these calculations showed that the edge dislocations cause a dramatic reduction of the optical gap due to the splitting of the local electronic states from both the valence and conduction bands. These findings have in turn prompted a mechanism based on electronic excitations induced by the impact wave propagating through the crystal. [32] According to this hypothesis, the pressure exerted by the impact wave front causes the dramatic reduction of the band gap to nearly zero values and results in the breakage of the N-NO<sub>2</sub> chemical bond in RDX, thus initiating detonation and chemical chain reactions.

Conclusive experimental evidence is still lacking in support of any of the models. The complexity of the process under shock or impact for solid materials is at best a multiscale event in time and space. Current atomistic computational studies, first principle approaches, are thus limited by the size of the system of interest, and/or by the duration of the process. These limitations usually restrict the investigation to individual effects, such as pressure, shear, and vacancies.

### 3. NONRADIATIVE ENERGY TRANSFER IN NITROMETHANE

Intuitively, one would expect dramatic changes in the atomic and electronic properties of a heterogeneous molecular solid under a violent assault. One plausible mechanism is electronic excitation: electrons are light, fast and quantal, thus responding first to exterior perturbations. Following electronic excitation, however, several processes could be at play to induce chemical reactions. These include dissociation on the excited state surface, radiative processes, and nonradiative energy deactivation.

In a recent study, we have considered the topology of the ground and first excited states of the nitromethane molecule, [33] to investigate the feasibility of metallization through molecular bond bending as proposed by Gilman. [23-25] The equilibrium geometry of the triplet state (the first electronically excited state) of the molecule is such that the ONO bond makes an angle of about 50 degree relative to the C-N bond (Fig.1), markedly different from the equilibrium geometry of the ground state where  $\gamma$  is zero. An adiabatic barrier to dissociation on this first excited state with respect to the C-N bond was determined to be about 33 kcal/mol, using highly correlated ab initio

multireference configuration interaction methodology. [34] The existence of this barrier should presumably allow the triplet state to support a few vibrational levels, and owing to a different spin multiplicity that forbids decaying, to be long lived. Intersystem crossing, however, provides a nonradiative deactivation channel, and such a crossing has been located by determining the minimum energy crossing point (MECP) on the singlet-triplet surface of intersection. [33] This point is located 13 kcal/mol above the equilibrium geometry of the triplet state, thus establishing a second barrier for energy redistribution that is more than half of the adiabatic one. It is expected, therefore, that thermal activation along the nitro bending mode to permit efficient energy transfer from the triplet state to higher vibrational levels of the ground surface. There are no experimental measurements on the triplet formation for nitromethane, but a recent study on nitrobenzene [35] showed that the triplet formation is very efficient with a quantum yield of  $\geq 80\%$ , and that this state has a lifetime of  $\leq 500$  ps. An earlier study [36] established a very short nonradiative lifetime of about one picosecond for the excited singlet state of nitromethane, with efficiency of 76% in energy deactivation. Vibrationally hot ground-state molecules could thus be generated by fast internal conversion (singlet-singlet) and intersystem (singlet-triplet) crossings. The excess, nonradiative (kinetic: heat) energy could then be supplied to near shell molecules and speed up the decomposition process.

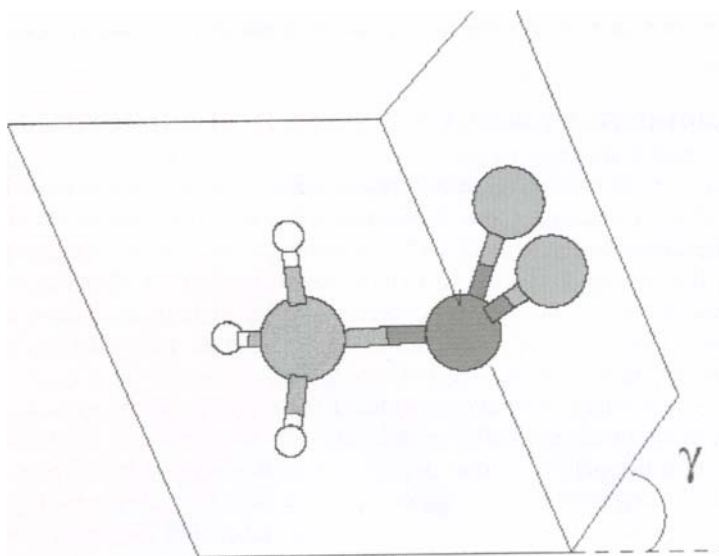


Fig. 1. The bending of  $\text{NO}_2$  group out of the CNOO plane ( $\gamma \sim 53^\circ$ ) leads closure of the HUMO-LUMO gap. This structure is also near the equilibrium geometry of the first electronically excited state of nitromethane.

## 4. EFFECTS OF PRESSURE AND VACANCIES

The effect of bending of the nitro group indicates *how* a band-gap closure can be achieved. The question remains, however, whether appreciable bending of the NO<sub>2</sub> group inside the nitromethane crystal can be achieved within the experimentally accessible pressure range. This can be addressed through electronic structure calculations on the effect of static pressure, uniform and uniaxial, on the optical gap of nitromethane. The pressure effect is also studied with the presence of molecular vacancies to examine the combined pressure vacancy effect on the band-gap structure.

Briefly, the electronic structure calculations are based on the self-consistent charge density-functional tight binding (SCC-DFTB) scheme.[37] This is an extension of the standard tight binding approach [38] in the context of DFT, [39] and self-consistently describes total energies, atomic forces, and charge transfer. An essential element of our analysis is that, for each fixed set of lattice parameters, all interatomic positions are determined by total energy minimization, i.e., the atoms are fully relaxed. The tight-binding character of the SCC-DFTB makes it feasible to study large supercells, containing up to 32 molecules, with concentrations of molecular vacancies ranging from 3.125% to 25%. The present study [40] therefore differs with respect to computational tools and system sizes from recent first-principles calculations, which considered smaller supercells with more demanding, first-principles computations.[41] The two methods give very similar results for the band gap of systems accessible to both.

### 4.1.1. Uniform compression

To simulate the effect of uniform strain on solid nitromethane, the initial lattice parameters were successively decreased by keeping their ratio fixed. The pressure  $P$  is estimated by using the low-temperature formula  $P = \partial E_{tot} / \partial V$ . For hydrostatic compression up to 50% of the original volume  $V_0$ , the pressure rises to about 50 GPa, while the HOMO-LUMO gap dropped by 0.6 eV, i.e., by 13% of its original value. This compression results in a simultaneous increase of the HOMO and the LUMO energies, while the decrease of the HOMO-LUMO gap is almost monotonic in the volume strain, as depicted in Fig.2. The change induced in the band gap by very high hydrostatic compression is shown in Fig.3 for strain equal up to 70%.

It is of interest to note that the mutual orientations of the C-N axes vary smoothly with the strain,  $(V_0 - V)/V_0$ , when this is less than 40%, with the corresponding pressure not exceeding 20 GPa. When  $V/V_0$  is between 58% and 60% and  $P$  is estimated to lie between 15 and 25 GPa, the atomic configuration undergoes an abrupt change accompanied by rotations of the methyl (CH<sub>3</sub>) groups, in agreement with first-principles calculations; [41] a similar transition

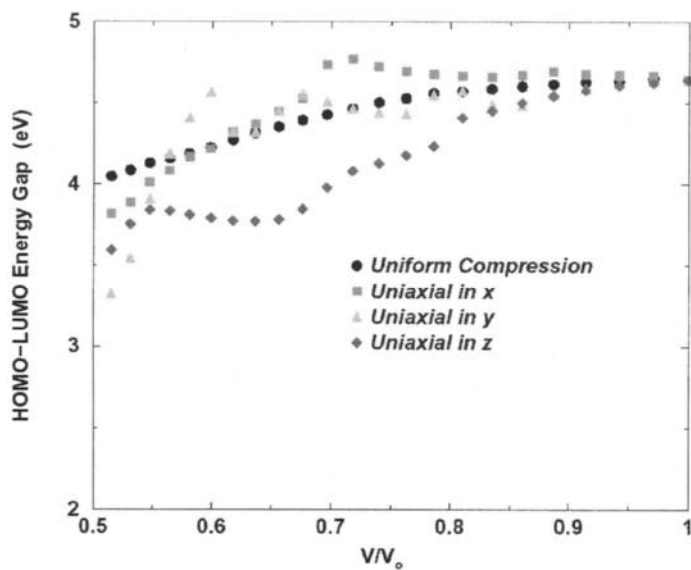


Fig.2. HUMO-LUMO energy gap of the perfect nitromethane crystal under uniform and uniaxial compression of the primitive unit cell.

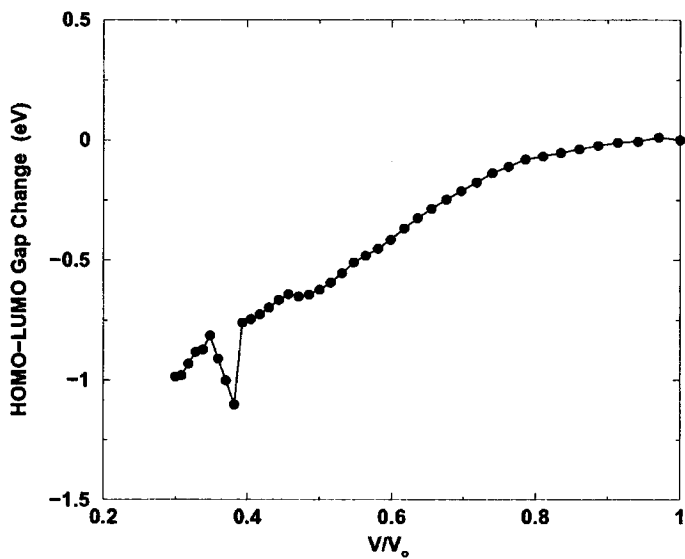


Fig.3. HUMO LUMO gap change under uniform compression. The sudden drop in the gap corresponds to the reported high C-H bond stretching.

was observed in that work for  $V/V_0$  between 59% and 77% and  $P$  in the range 10-30 GPa. This transition is expected because the barrier for the rotation of the methyl group is known to be very low. [42]

The following changes of the bond lengths and bond angles were observed as the strain varied from 0 to 50%. While practically no bending of the nitro group in the molecules took place, the C-N bond lengths were invariably shortened at most by 6%. In contrast, the eight N-O bond lengths in the unit cell exhibited different variations, with a maximum deviation of 61% from their equilibrium values. The bond angles involving the nitro group in each molecule remained practically intact. A few of the C-H bonds were stretched up to 2% of their initial values. No significant change in the bond angles involving the nitro group was noticed even as the uniform strain was increased from 50% to 70%. However, two of the C-H bonds were highly stretched when the strain was extended to values above 60%. The same effect on the C-H bond in all molecules of the unit cell was also observed under uniaxial stress, yet the estimated pressure is appreciably lower. This case is discussed in more detail below.

#### 4.1.2. Uniaxial compression

Compared to uniform compression, uniaxial strain along one of the lattice vectors is more likely to lead to detonation. Dick has proposed [43] that detonation initiation in nitromethane is favored by shock-wave propagation in specific directions related to the orientation-dependent steric hindrance to the shear flow. This proposal is based on a model according to which the sterically hindered shear process causes preferential excitation of optical phonons strongly coupled with vibrons.

We applied uniaxial compression along each of the  $x$ ,  $y$ , and  $z$  axes, and tracked the HOMO-LUMO gap as a function of the volume change, for strains not exceeding 50% and corresponding estimated pressures as high as 100 GPa (see Fig. 2). Among the three types of compression, the ones in  $x$  and  $y$  yielded the highest estimated pressure. The gap was decreased at most by 1.4 eV (a 30% reduction of the original value) under stress in  $y$ . This drop is higher than in the case with uniform strain, while the gap behavior here is not strictly monotonic, i.e., the gap does not continuously decrease as the uniaxial strain increases. The strains in  $x$  and  $y$  seem to cause a similar overall behavior of the gap. The compression in  $y$ , however, causes a steeper reduction of the gap as  $V/V_0$  approaches 50%. In contrast, the compression in  $z$  reduces the energy gap more drastically for intermediate values of  $V/V_0$ , roughly between 65% and 80%. This last effect can be visualized as follows. The molecules approach each other in  $z$  by bringing the methyl group of one close to the nitro group of the next, while the cell lattice parameter  $c$  approaches the intermolecular distance. Consequently, the electron densities of the HOMO and the LUMO, which are

localized near the nitro group, are distorted more than in any other type of compression of similar magnitude and the band gap is reduced more rapidly for this type of uniaxial strain.

A closer look at the atomic configurations reveals structural transitions which are triggered preferentially by pressure anisotropy. The most frequent transition in the  $x$  compression involves of course molecule translations, rotations of the methyl groups (which occur even for  $V/V_0$  close to 1) and reorientations of the molecules, primarily via relative translations and rotations around their C-N axes. Two such abrupt transitions are observed when  $V/V_0 = 67-70\%$  and the estimated pressure is 25-30 GPa, and  $V/V_0 = 59-62\%$  with an estimated pressure of 45-55 GPa. In the  $z$  compression the methyl groups seem to undergo smoother transitions as each molecule's center-of-mass is translated in  $z$ . In contrast, the  $y$  compression causes abrupt transitions when  $V/V_0 = 76-81\%$  and  $63-66\%$  and the pressure is estimated to lie in the ranges 2-5 and 13-16 GPa, respectively.

Notably, the dramatic stretching of four C-H bonds, one in each nitromethane molecule of the unit cell, occurs under stress in  $y$  when  $V/V_0$  is between 59% and 62%, with an estimated pressure of 25-40 GPa; more precisely, these bond lengths are stretched by more than 10-12% of their original values in this case. The increase of strain in  $y$  above 50% causes these bonds to be stretched further and leads to the abstraction of their protons. This indication of proton dissociation corresponds to the steep part of the curve in Fig. 2, and renders the  $y$  and  $x$  compressions qualitatively different.

The C-N bond lengths are again invariably shortened, at most by 6%, 9%, and 2-3% of their initial values under  $x$ ,  $y$ , and  $z$  compression, respectively. In contrast, the N-O bond lengths exhibit positive or negative deviations from their equilibrium values that depend both on the location of the corresponding molecules and the direction of compression. It is worthwhile noting that only the compression in  $y$  causes the N-O bond length to be continuously stretched in all molecules at most by 3% of the initial value. The bond angles do not exhibit any change worthy of reporting for this range of compression.

#### 4.1.3. C-H high stretch under uniaxial compression

As mentioned previously, the SCC-DFTB calculations predict a high stretching of the C-H bond that leads to proton abstraction under  $y$  compression when the strain becomes of the order of 40% or higher; for uniform compression, the corresponding strain takes the significantly higher values, in the range 60-62%, at estimated pressure of 150-180 GPa. One of the intermediate atomic configurations leading to the proton dissociation in the former case of uniaxial strain is shown in Fig.4. Note that the high stretching of the C-H bond is visualized graphically by enlarging the symbols that correspond to each abstracted acidic hydrogen atom (the atomic sizes in these figures are proportional to the van der Waals radius of the ionized form).

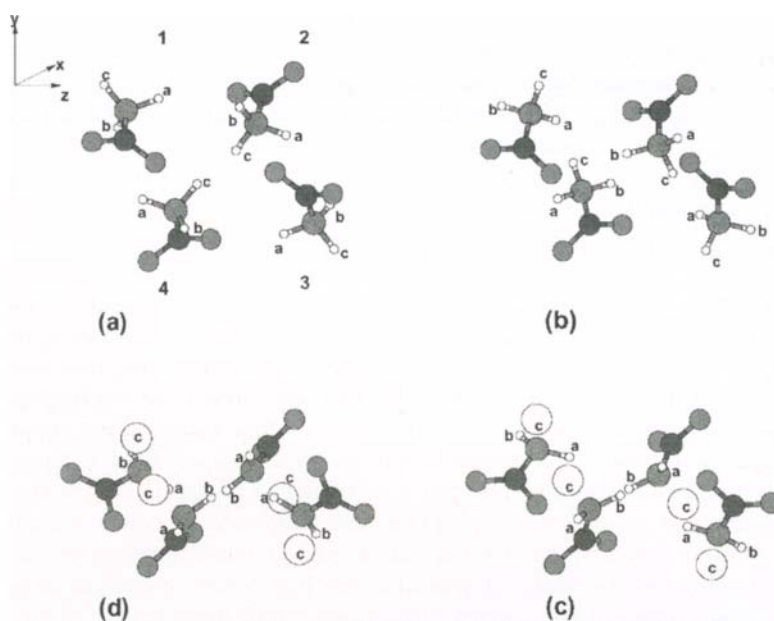


Fig.4. Atomic configurations of the unit cell for uniaxial compression along  $b$  direction, leading to H-abstraction. (a) Original cell at  $V = 281.7 \text{ \AA}^3$ . (b) Molecular reorientation and methyl rotation at  $V/V_0 = 0.79$ . (c) C-H bond stretch by 12% at  $V/V_0 = 0.60$ . (d) Configuration at  $V/V_0 = 0.51$ . In (c) and (d) the abstracted protons are shown in larger circles.



A physical picture of the C-H bond stretching is the following: upon contraction of the initially single C-N covalent bond, electronic charge is transferred to the region of space between the C and N atoms. Consequently, the C-N bond becomes stronger and its character approaches that of a double covalent bond. The adjacent C-H bonds act as sources of the electronic charge; at least one of these H atoms is deprived of some electronic charge and its bond is weakened. On the other hand, the orbitals localized near the NO<sub>2</sub> group are not significantly distorted by the compression. The Mulliken charge changes given in Table 1 are in agreement with this picture. The total Mulliken charge loss of the H atoms is found to increase monotonically with uniaxial strain in each molecule, being dominated for high strain by the charge pertaining to the markedly stretched C-H bonds (shown in Fig. 4), as expected. While these values follow closely the Mulliken charge gain of the C atoms for low uniaxial strain, they start to deviate significantly as the strain approaches 50%.

These findings imply that chemical reactions and transitions from covalent to ionic C-H bonds prior to detonation in nitromethane are more likely to start *before* the closure of the optical gap. Roughly speaking, an actual precursor to detonation appears to be the proton dissociation and not the hypothesized metallization induced by drastic changes in the bond angles. [23] Interestingly, energetic materials can therefore be considered as more sensitive to their chemistry under uniaxial rather than uniform compression, in agreement with Dick's results that invoke a steric hindrance model for nitromethane. [43]

There have been numerous experimental studies of the reaction kinetics that may lead to detonation of liquid nitromethane. Most of these studies are concerned with the nature of chemical products that may speed up detonation. Shaw *et al.*, [44,45] for example, measured the effect of the concentration of protonated compounds within the energetic material on the time needed until explosion. Their experiments indicated that a reaction involving hydrogen atoms or protons is involved in the first steps of this fast-reaction process. This suggestion was later corroborated by Blais *et al.* [46] by more direct measurements, who also referred to a sequence of previous investigations by Engelke and co-workers. [47,48] Our zero-temperature, static calculations point to similar conclusions for the nitromethane molecular crystal. A similar prediction for this material was also reached concurrently via ongoing first principles, molecular-dynamics simulations at high densities (1.5-2.5 g/cm<sup>3</sup>) and high temperatures ( $T = 2000-4000$  K). [49]

Table 1

Mulliken charges changes of carbon and hydrogen of the nitromethane molecules 1 and 2 in the unit cell under uniaxial compression along **b**.

$V/V_0$	C <sub>1</sub>	H <sub>1a</sub>	H <sub>1b</sub>	H <sub>1c</sub>	C <sub>2</sub>	H <sub>2a</sub>	H <sub>2b</sub>	H <sub>2c</sub>
0.79	0.012	-0.010	0.016	0.016	0.012	-0.010	0.016	0.020
0.60	0.126	-0.016	-0.026	-0.026	0.108	-0.019	-0.008	-0.155
0.51	0.294	-0.014	-0.074	-0.074	0.168	-0.051	-0.030	-0.245

#### 4.2. Effect of molecular vacancies

In view of Dick's [43] proposal and the persistence of uniaxial strain following shock propagation, the cases of uniform and uniaxial compression are herein presented separately. In order to simulate vacancies of desired densities in the nitromethane crystal, we first superimposed two, four, and eight unit cells in order to create  $2 \times 1 \times 1$ ,  $2 \times 2 \times 1$ , and  $2 \times 2 \times 2$  supercells where the numbers express multiples of the primitive unit cell dimensions. More precisely, a vacancy concentration of 25% was formed in two different ways: first, by removal of one entire molecule from the primitive unit cell and, second, by removal of two molecules from the  $2 \times 1 \times 1$  supercell. Vacancy concentrations of 12.5%, 6.25%, and 3.125% were also modeled by removal of one molecule from the  $2 \times 1 \times 1$ ,  $2 \times 2 \times 1$ , and  $2 \times 2 \times 2$  supercells, respectively. In the following, unless it is stated otherwise, there is no lattice relaxation and the initial supercell structure merely stems from a multiple of the starting primitive cell along the  $x$ ,  $y$ , and  $z$  axis.

The  $2 \times 1 \times 1$  supercell models are shown in Figs. 5(a) and 6(a) with their HOMO-LUMO gaps depicted in Figs. 5(b) and 6(b). The unit cell and larger supercells are not shown. A pair of vacancies in the  $2 \times 2 \times 1$  supercell is created by removing the molecules nearest to the endpoints of the cell diagonal. To realize some of the underlying complexity, it suffices to mention that a  $2 \times 2 \times 2$  supercell with one molecular vacancy contains 31 nitromethane molecules, which amounts to 217 atoms with 744 valence electrons. Each supercell is strained up to 50% of its original volume.

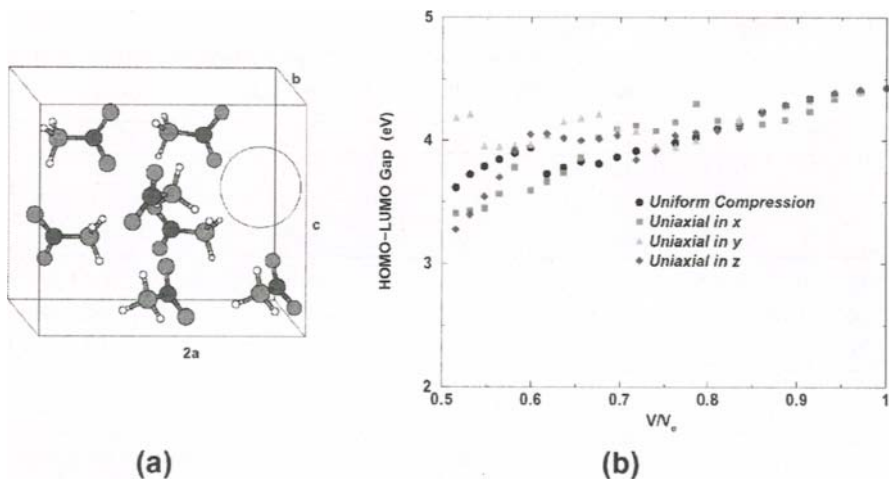


Fig.5. (a) 2×1×1 supercell with 1 molecular vacancy, corresponding to 12.5% vacancy concentration. (b) HOMO-LUMO gap (in eV) for uniform and uniaxial compression.

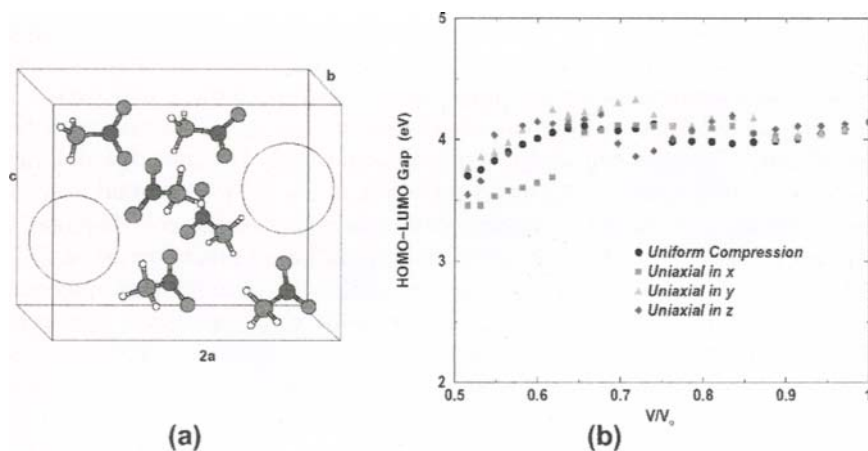


Fig.6. (a) 2×1×1 supercell with 2 molecular vacancies, corresponding to 25% vacancy concentration. (b) HOMO-LUMO gap (in eV) for uniform and uniaxial compression.

#### 4.2.1. Uniform compression

A comparison with Fig. 3(b) shows that the band gap with one molecular vacancy (a concentration of 25%) in the primitive unit cell (not shown) exhibits a tendency to remain flat for a wider range of the volume strain in the presence of a vacancy. The overall drop, however, is about the same as in the case with no vacancy, i.e., 0.6 eV. This resistance of the gap to changes induced by stress stems from the increase in the size of the effective free space that each molecule experiences because of the vacancy. The gap reduction is so small that it cannot allow for considerable electron excitations from the HOMO to the LUMO. The molecules reorient themselves so that the structure relieves the applied stress; roughly speaking, the molecules tend to take positions that are closest to those of minimum pressure for the given lattice parameters. The most frequent structural change observed is again the rotation of the methyl group, yet the variation in the atomic positions appears to be smoother in the presence of a vacancy.

The effect of vacancy concentrations of 12.5% and 25% on the HOMO LUMO gap are shown in Figs. 5(b) and 6(b) on the basis of a  $2 \times 1 \times 1$  supercell. With  $V/V_0$  varying from 100% to 50%, the estimated pressure reaches almost 30 GPa for concentration of 12.5% and 10 GPa for concentration of 25%. Again, no appreciable narrowing of the band gap is found. The small jumps appearing in the simulation data for the band gap correspond to abrupt structural transitions involving relative reorientations of the C-N axes and rotations of the methyl groups, especially of the molecules that lie in close proximity to the vacancies.

In Fig. 7 the HOMO-LUMO gap of the  $2 \times 1 \times 1$  supercell is depicted for vacancy concentrations of 12.5% and 25%, with the inclusion of partial optimization of the initial lattice parameters. Accordingly,  $V_0$  is now the volume that corresponds to the relaxed supercell in each case. Notably, any two of these curves intersect. In other words, for any fixed  $V/V_0$ , the gap is not a strictly monotonic function of the vacancy concentration. The pressures at the intersection points for the perfect crystal are estimated to be 5 GPa and 18 GPa (from right to left). In Fig. 8 the gaps are shown for vacancy concentrations of 12.5% and 6.25% from the  $2 \times 2 \times 1$  supercell, and 3.125% from the  $2 \times 2 \times 2$  supercell, where the starting point ( $V/V_0 = 1$ ) is that of the minimum pressure for the given vacancy concentration and hydrostatic compression. The curves are well-separated now. For any fixed volume strain, the gap is roughly a monotonically decreasing function of the density. In all these cases, the gap is reduced at most by 1.3 eV, dropping to 3.25 eV. The smallest decrease in the gap occurs when the vacancy concentration is the highest, i.e., equal to 25%.

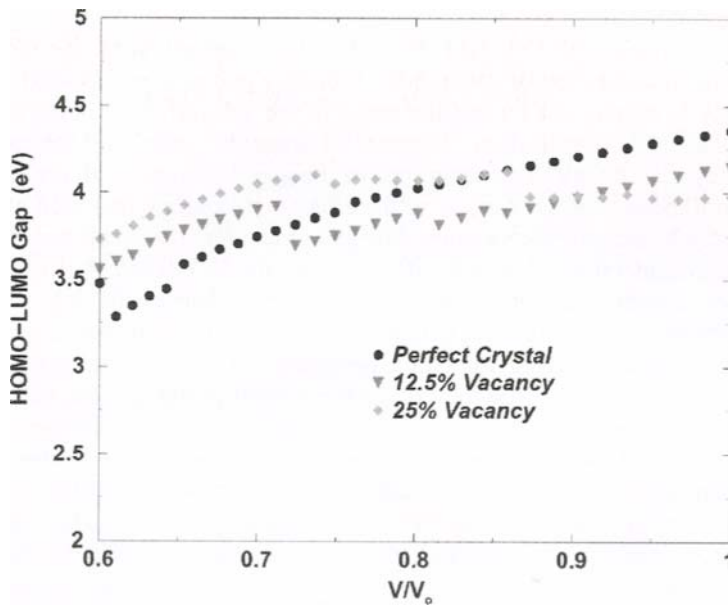


Fig.7. HUMO-LUMO gap (in eV) for uniform compression and vacancy concentration of 0, 12.5, and 25% in  $2 \times 1 \times 1$  supercell.

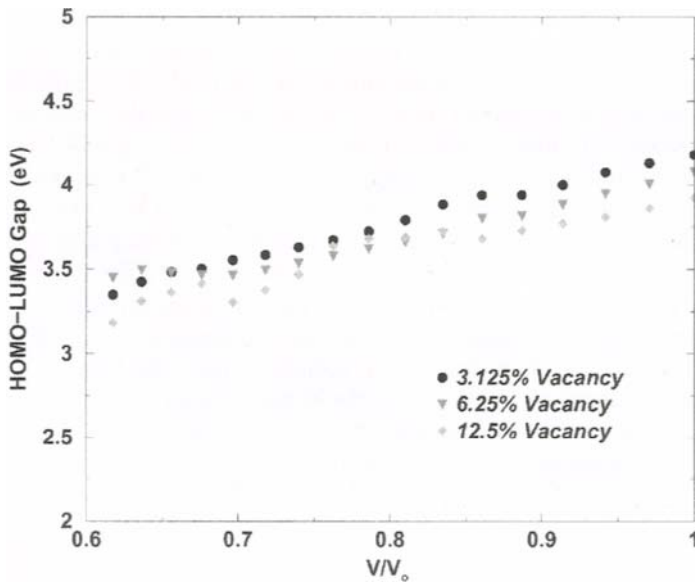


Fig.8. HUMO-LUMO gap (in eV) for uniform compression and vacancy concentration of 3, 6.25, and 12.5% in the  $2 \times 2 \times 1$  and  $2 \times 2 \times 2$  supercells.

#### 4.2.2. Uniaxial compression

Application of uniaxial strain does not alter the order of magnitude of the HOMO-LUMO gap reduction, as shown in Figs. 5(b), 6(b), and 9 where only strain in the  $x$  direction is considered. In fact, for this uniaxial compression the gap is reduced at most by 1 eV. The unstrained structure of Fig. 9 corresponds to the minimum pressure for the given compression in  $x$  by starting with the nonoptimized lattice parameters of the unit cell. In each set of curves in Fig.9 the smallest change in the gap is again observed when the vacancy density is the highest, 25%. In Fig.9 one sees that the gap decreases with the vacancy density, and thus the curves appear to be more distinct, compared to the case with uniform strain.

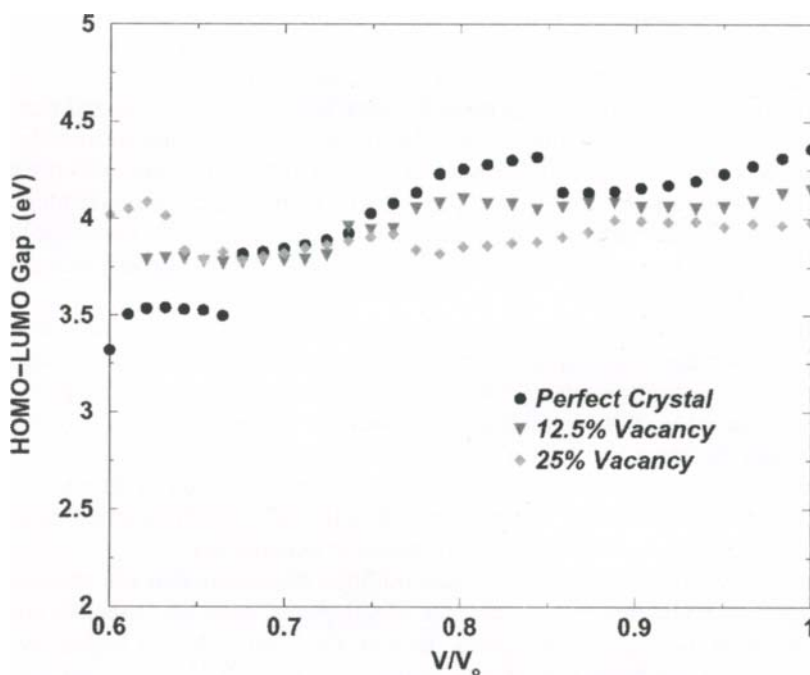


Fig.9. HOMO-LUMO gap (in eV) for uniaxial compression and vacancy concentration of 0, 12.5, and 25% in the  $2 \times 1 \times 1$  supercell.

### 4.3. Summary

The applied uniform and uniaxial compression to the nitromethane crystal, with and without molecular vacancies demonstrated only a slight reduction of the HOMO-LUMO gap for hydrostatic pressures up to 150 GPa or higher. This small reduction essentially prohibits any consideration of electron excitations, and hence of nonradiative transitions due to the crossing of adjacent energy surfaces of molecules.[33] The band-gap drop is most likely attributed to the relatively weak intermolecular interactions, as the molecules tend to maintain positions that yield the lowest possible pressure in the crystal. Accordingly, no appreciable bending of the nitro group is observed for this range of volume strains.

The constituent molecules undergo changes in their bond lengths, relative orientations of the C-N axes, and rotations of their methyl groups in order to relieve the applied stress. What configuration prevails of course depends on how the energy landscape evolves under adiabatic compression, and therefore on how high the barriers are for transitions to neighboring local minima of other configurations. The most common structural transition observed in our simulations is the rotation of the methyl group. It should be emphasized that it is crucial to be able to describe accurately the atomic forces and to include full atomic relaxation, an essential feature of the SCC-DFTB method, which makes it possible to capture this effect. This aspect of the calculations renders the reported results distinctly different from that by Kuklja *et al.*, [32] who applied a "rigid molecule approximation" and thus calculated a large decrease of the band gap in the RDX crystal.

Because of the crystal anisotropy, on the other hand, the sequence and the frequency of phase transformations depend on the character of compression. For example, the compression in  $z$  forces the molecules to develop more rapidly electrostatic interactions, which in turn affect the electronic charge of the nitro group and therefore result in a steeper decrease of the band gap with applied pressure. Since charge transfer is important in the description of atomic forces, we expect that its realistic description within the SCC-DFTB method captures the general features of the molecular response to external stress.

It follows from the physical picture outlined previously that the stress relief is in general facilitated by the presence of vacancies, since the effective size of free space in the unit cell increases. Indeed, the results show a higher overall persistence of the band gap of the crystal with vacancy defects with applied pressure. It should be pointed out, however, that the present model of periodically distributed vacancies is restricted in its applicability; in real materials the vacancies follow an inhomogeneous, and even random, distribution.

One interesting result of the reported calculation was to show that the C-H bond was highly stretched, and its proton most likely dissociates, in the perfect crystal under both uniform and uniaxial strain in the  $y$  direction. Under uniaxial

compression, the requisite pressure to induce this behavior is estimated to be significantly lower, lying in the accessible regime of 20-40 GPa. We interpreted this effect as being associated with the induced electron-charge transfer from the hydrogen to the region between the carbon and the nitrogen, since the C-N bond is noticeably contracted and its character is progressively modified from a single to a double covalent bond.

These results point to the preliminary conclusion that the chemistry prior to detonation is strongly dependent on the pressure anisotropy, and starts before any band-gap closure, i.e., metallization which would be caused by bending of covalent bonds involving the nitro group. Accordingly, further decrease of the band gap seems to be favored by the formation of protons in the crystal. It remains to check this hypothesis by applying a more accurate, first-principles method. Because the formation of a free-electron gas is favored under very high pressure, it can be argued that Local Density Approximation (LDA) within DFT should suffice to produce reliable results for this regime. It is remarkable that reported results, being derived under adiabatic compression and for zero temperature, are in qualitative agreement with ongoing first-principles, molecular-dynamics simulations at both high density and temperature. Specifically, these last simulations also predict that the C-H bond is highly stretched at an early stage of the compression. [8,49]

## 5. DECOMPOSITION OF HMX

HMX (1,3,5, 7-tetranitro-1, 3,5,7-tetraazacyclooctane) is widely used as an ingredient in various explosives and propellants. A molecular solid at standard state, it has four known polymorphs, one of which, the  $\delta$  phase is comprised of six molecules per unit cell, as depicted in Fig.10. We study the chemical decomposition of the dense fluid of this phase by conducting a high-density and temperature ( $\rho = 1.9 \text{ g/cm}^3$ ,  $T = 3500 \text{ K}$ ) quantum mechanical based molecular dynamics simulation. [50] To our knowledge, this is the first reported ab initio based/molecular dynamics study of an explosive material at extreme conditions for extended reaction times of up to 55 picoseconds, thus allowing the formation of stable product molecules.



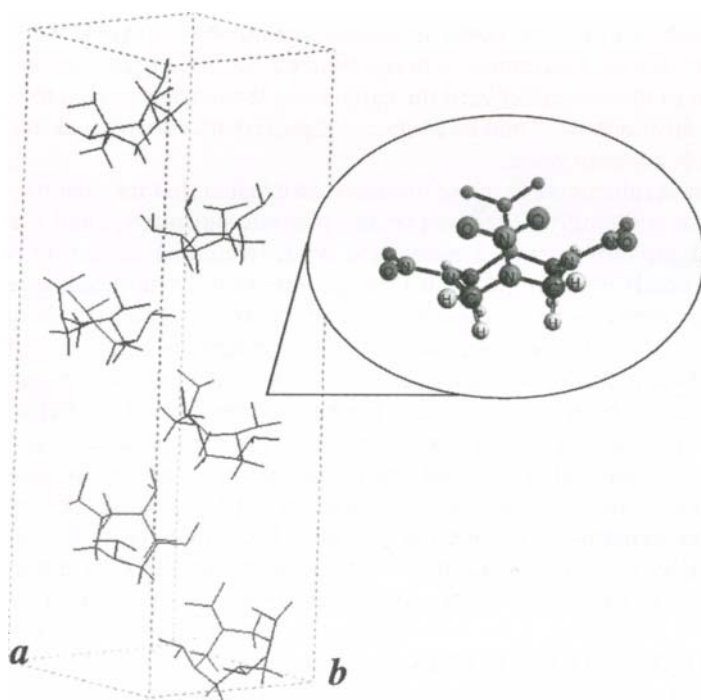


Fig.10. Crystal and molecular (insert) configurations of HMX in the  $\delta$  phase.

Experimental characterizations at low temperatures (i.e.  $< 1000$  K, well below detonation temperature) of decomposition products of condensed-phase HMX have been numerous. [51-63] These studies tend to identify final gas products (such as  $\text{H}_2\text{O}$ ,  $\text{N}_2$ ,  $\text{H}_2$ ,  $\text{CO}$ ,  $\text{CO}_2$ , etc.) from the surface burn, and aspire to establish a global decomposition mechanism. The early thermal decomposition study using mass spectrometry at  $T=503$ ,  $527$ , and  $553$  K of Syryanarayana et al. [51] identified a concerted decomposition into four methylenenitramine ( $\text{CH}_2\text{N}_2\text{O}_2$ ), which can further decompose into  $\text{CH}_2\text{O}$  and  $\text{N}_2\text{O}$ . At  $448$ - $548$  K, Farber and Srivastava [53] identified a major decomposition product with  $m/e=148$  and proposed a homolytic cleavage of HMX to two  $\text{C}_2\text{H}_4\text{N}_4\text{O}_4$  fragments that might further decompose to form methylenenitramine via  $\text{C}_2\text{H}_4\text{N}_4\text{O}_4 \rightarrow 2 \text{CH}_2\text{N}_2\text{O}_2$ .  $\text{CH}_2\text{N}$  and  $\text{NO}_2$  were later detected as decomposition products from the  $\text{CH}_2\text{N}_2\text{O}_2$  intermediate in an electron spin resonance pyrolysis study. [54] Recent experiments using thermogravimetric modulated beam mass spectrometry and isotope scrambling identified gaseous pyrolysis products such as  $\text{H}_2\text{O}$ ,  $\text{HCN}$ ,  $\text{CO}$ ,  $\text{CH}_2\text{O}$ ,  $\text{NO}$ , and  $\text{N}_2\text{O}$  between  $483$  and  $508$  K. [56-58] Brill et al. have analyzed rate

measurements for the early stage of HMX thermal decomposition, [60] revealing the existence of an approximate linear relationship between the Arrhenius prefactor,  $\ln A$ , and the apparent activation energy,  $E_a$ . Brill later suggested two competing global mechanisms for thermal decomposition, the first leading to 4HONO and 4HCN, while the second leads to the formation of 4CH<sub>2</sub>O and 4N<sub>2</sub>O. [61]

The above noted experimental work on thermal decomposition of condensed phase HMX is largely restricted to relatively low temperature (~550 K) and pressure (0.1 GPa) regimes. Similar experimental observations at detonation conditions (temperatures 2000-5000 K, and pressure 10-30 GPa), however, have not been realized to date. While recent applications of ultrafast spectroscopic methods [64] hold great promise for determining such decomposition mechanisms in the foreseeable future, at present, computer simulations provide the best access to the short time scale processes occurring in these regions of extreme conditions of pressure and temperature. [65] In particular, simulations employing many-body potentials, [66,67] or tight-binding based methods have emerged as viable computational tools, the latter has been successfully demonstrated in the studies of shocked hydrocarbons. [68,69]

Previous theoretical studies have included electronic structure calculations of various decomposition channels of the gas-phase HMX molecule. [70-72] Melius used the Bond-Additivity-Corrected (BAC) MP4 method to determine decomposition pathways for nitramine compounds, HMX and RDX. [70] The initial step in his decomposition scheme is N-NO<sub>2</sub> bond breaking, which subsequently causes a significant weakness in the second-nearest-neighbor bond breaking energies (18 kcal/mol for the C-N bond dissociation), leading to HCN, NO<sub>2</sub>, and H as the net products for rapid thermal heating. In the condensed phase, however, Melius made the observation that alternative decomposition mechanisms can occur. The deposited NO<sub>2</sub> fragment can recombine as a nitride, which can then decompose by breaking the O-N bond to form NO, or attract weakly hydrogen atoms and form HONO. The HONO molecules can then rapidly equilibrate to form water via the reaction  $2\text{HONO} \rightarrow \text{H}_2\text{O} + \text{NO}_2 + \text{NO}$ .

Lewis et al. [71] calculated four possible decomposition pathways of the  $\alpha$ -HMX polymorph: N-NO<sub>2</sub> bond dissociation, HONO elimination, C-N bond scission, and the concerted ring fission. Based on the energetics, it was determined that N-NO<sub>2</sub> dissociation was the initial mechanism of decomposition in the gas phase, while they proposed HONO elimination and C-N bond scission to be favorable in the condensed phase. The more recent study of Chakraborty et al. [72], using the DFT(B3LYP) method, reported detailed decomposition pathways of the  $\beta$ -HMX, the stable polymorph at room temperature. It was concluded that consecutive HONO elimination (4HONO) and subsequent decomposition into HCN, OH and NO are energetically the most favorable pathways in the gas phase. The results also showed that the formation of CH<sub>2</sub>O and N<sub>2</sub>O could occur preferably from secondary decomposition of

methylenenitramine. While these studies concentrated on gas phase decomposition mechanisms, to date no computational treatment of condensed phase reaction mechanisms exist. Other theoretical studies were concerned with the derivation of a force field from first principle calculations, [73] and the application of classical molecular dynamics as in simulating pressure effects on crystal packing. [74,75]

### 5.1. Computational model

To directly simulate the condensed-phase chemical reactivity of HMX, we use the SCC-DFTB method to determine the interatomic forces and simulate the decomposition at constant-volume and temperature conditions. The initial condition of the simulation included six HMX molecules in a cell, corresponding to the unit cell of the  $\delta$  phase of HMX (Fig. 10) with a total of 168 atoms. It is well known [76] that HMX undergoes a phase transition at 436 K from the  $\beta$  phase (two molecules per unit cell with a chair molecular conformation, density = 1.89 g/cm<sup>3</sup>) to the  $\delta$  phase (with boat molecular conformation, density=1.50 g/cm<sup>3</sup>). We thus chose the  $\delta$  phase as the initial starting structure so as to include all the relevant physical attributes of the system prior to chemical decomposition. The calculation started with the experimental unit cell parameters and atomic positions of  $\delta$  HMX. The atomic positions were then relaxed in an energy minimization procedure. The resulting atomic positions were verified to be close to the experimental positions.

The volume of the cell was then reduced to the final density of the simulation. The atomic structure was subsequently fully optimised at the corresponding cell volume. Our intention is to study the high- pressure and high- temperature chemistry of HMX in general, so the exact density and temperature used in our simulation is somewhat arbitrary. We used a density of 1.9 g/cm<sup>3</sup> and a temperature of 3500 K. This state is in the neighborhood of the Chapman-Jouget state of  $\beta$ -HMX (3500 K, 2.1g/ cm<sup>3</sup>) as predicted through thermochemical calculations described later. The closest experimental condition corresponding to our simulation would be a sample of HMX, which is suddenly heated under constant volume conditions, such as in a diamond anvil cell.

The molecular dynamics simulation was conducted at constant volume and constant temperature. Periodic boundary conditions, whereby a particle exiting the cell on one side is reintroduced on the opposing side with the same velocity were imposed. Constant temperature conditions were implemented through simple velocity rescaling. The probability to rescale atom velocities was chosen to be 0.1 per time step. A dynamic time-step of 0.5 fs was used, and snapshots at 2.5 fs steps were collected.

A procedure was implemented to identify the product molecules of interest: H<sub>2</sub>O, N<sub>2</sub>, CO<sub>2</sub>, and CO. Covalent bonds were identified according to bond distance. This is motivated by the difference between covalent (1 - 1.7 Å) and

van der Waals bond distances ( $\sim 3 \text{ \AA}$ ). We chose maximum bond distances of:  $R(\text{O-H})=1.3$ ,  $R(\text{CO})=1.7$ , and  $R(\text{N-N})=1.5 \text{ \AA}$  in the molecule identification procedure. The results of the molecular identification procedure were confirmed through visual examination of representative simulation steps. We note that the procedure may incorrectly identify transition states as being molecular species. Since transition states are short lived, and since we apply the procedure to small molecules, this problem should not significantly affect the time averaged concentrations reported here.

## 5.2. Kinetics of HMX decomposition

We first discuss the overall chemical process predicted, followed by a discussion of reaction mechanisms. Under the simulation conditions, the HMX was in a highly reactive dense fluid phase. There are important differences between the dense fluid (supercritical) phase and the solid phase, which is stable at standard conditions. Namely, the dense fluid phase cannot accommodate long-lived voids, bubbles, or other static defects, since it has no surface tension. Instead numerous fluctuations in the local environment occur within a timescale of 10s of femtoseconds. The fast reactivity of the dense fluid phase and the short spatial coherence length make it well suited for molecular dynamics study with a finite system for a limited period of time. Under the simulation conditions chemical reactions occurred within 50 fs. Stable molecular species were formed in less than a picosecond. We report the results of the simulation for up to 55 picoseconds. Figs. 11 (a-d) display the product formation of  $\text{H}_2\text{O}$ ,  $\text{N}_2$ ,  $\text{CO}_2$  and  $\text{CO}$ , respectively. The concentration,  $C(t)$ , is represented by the actual number of product molecules formed at the corresponding time  $t$ . Each point on the graphs (open circles) represents a 250 fs averaged interval. The number of the molecules in the simulation was sufficient to capture clear trends in the chemical composition of the species studied. These concentrations were in turn fit to an expression of the form:  $C(t) = C(1 - e^{-bt})$ , where  $C$  is the equilibrium concentration and  $b$  is the effective rate constant. From this fit to the data, we estimate effective reaction rates for the formation of  $\text{H}_2\text{O}$ ,  $\text{N}_2$ ,  $\text{CO}_2$ , and  $\text{CO}$  to be 0.48, 0.08, 0.05, and  $0.11 \text{ ps}^{-1}$ , respectively.

It is not surprising that the rate of  $\text{H}_2\text{O}$  formation is much faster than that of  $\text{N}_2$ . Fewer reaction steps are required to produce a triatomic species like water, while the formation of  $\text{N}_2$  involves a much more complicated mechanism. [70] Further, the formation of water (Fig. 11-a) starts around 0.5 ps and seems to have reached a steady state at 10 ps, with oscillatory behavior of decomposition and formation clearly visible. We expect this trend to continue until chemical equilibrium is reached, well beyond the current simulation time. The formation of  $\text{N}_2$  (Fig. 11-b), on the other hand, starts around 1.5 ps and is still progressing (slope of the graph is slightly positive) after 55 ps of simulation time, albeit at small variation.

Due to the lack of high-pressure experimental reaction rate data for this (and other) explosive(s) with which to compare with, we produce in Fig.12 a comparison of dominant species formation for decomposing HMX obtained from entirely different theoretical approach. The concentration of species at chemical equilibrium can be estimated through thermodynamic calculations, as implemented within the Cheetah thermochemical code. [77,78] For HMX, the molecules  $N_2$ ,  $H_2O$ ,  $CO_2$ ,  $HNCO$ , and  $CO$  were predicted to be present in quantities greater than 1 mol/kg HMX. The species  $CO$ ,  $NH_3$ ,  $H_2$ ,  $CH_4$ ,  $H$ ,  $CH_3OH$ ,  $NO$ , and  $C_2H_4$  were also predicted to be present in quantities greater than 0.0001 mol/kg HMX. The species  $N_2O$ ,  $C_2H_2$ ,  $N$ ,  $O$ ,  $O_2$ ,  $NO_2$ ,  $HCN$ , atomic  $C$ , and  $O_3$  were not predicted to have significant concentrations. Carbon in the diamond phase was predicted to be in equilibrium with the other species at a concentration of 4.9 mol/kg HMX. The thermochemical calculations predict a pressure for fully reacted HMX of 16 GPa, or 160 kBar.

As can be noticed in Fig. 12, the results of our present simulation compare very well with the formation of  $H_2O$ ,  $N_2$ , and  $HNCO$ . The relative concentration of  $CO$  and  $CO_2$ , however, is reversed at the limited time of our simulation. No condensed carbon was found in the current simulation. Several other products and intermediates with lower concentrations, common to the two methods, have also been identified. These include  $HCN$ ,  $NH_3$ ,  $N_2O$ ,  $CH_3OH$ , and  $CH_2O$ . It is hoped that interplay between the two vastly different approaches could be established at much longer simulation time. The goal will be to expand the product molecule set of the thermochemical code with important species determined from our ab initio based simulations for kinetic modelling.

One expects more  $CO_2$  than  $CO$  as final products, as predicted by Cheetah (Fig. 12). The results displayed in Figs. 11 (c-d) show that, at simulation time of 40 ps, we are still in the second stage of reaction chemistry. At this stage, the  $CO$  concentration is still rising and has not yet undergone the water gas shift reaction ( $CO + H_2O \rightarrow CO_2 + H_2$ ) conversion. Interestingly, this shift seems to occur at around 50 ps of the simulation, with  $CO_2$  molecules are being formed while  $CO$  concentration is correspondingly diminishing. The simulation is currently being extended several more tens of picoseconds to monitor this behavior, and to eventually reach a steady state production.

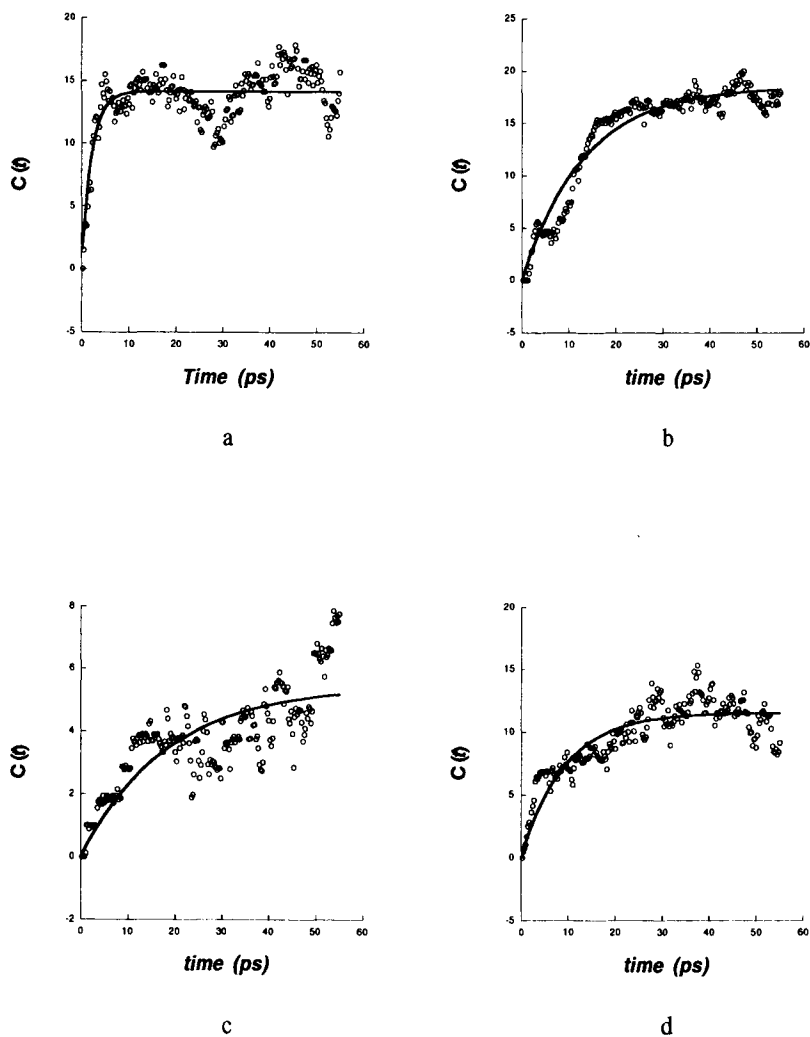


Fig. 11. Product particle-number formations as a function of time of (a)  $H_2O$ , (b)  $N_2$ , (c)  $CO_2$ , and (d)  $CO$ .

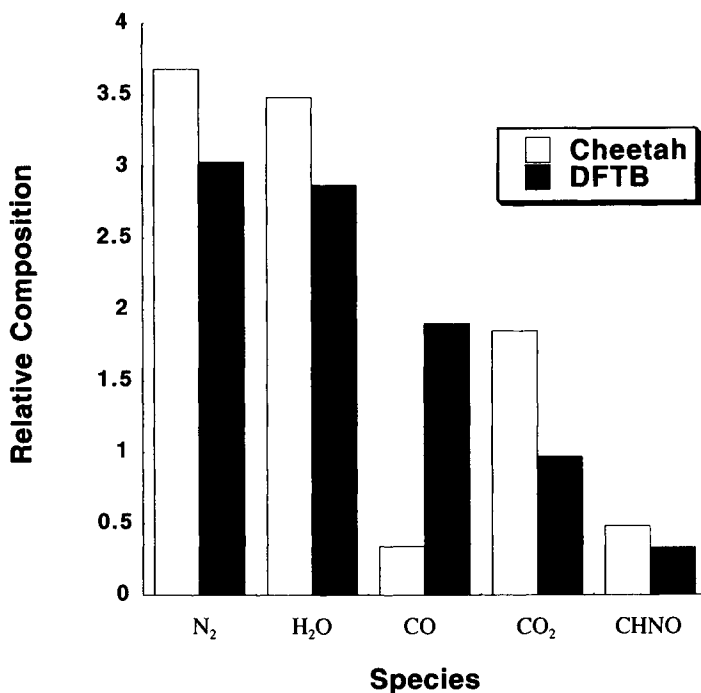
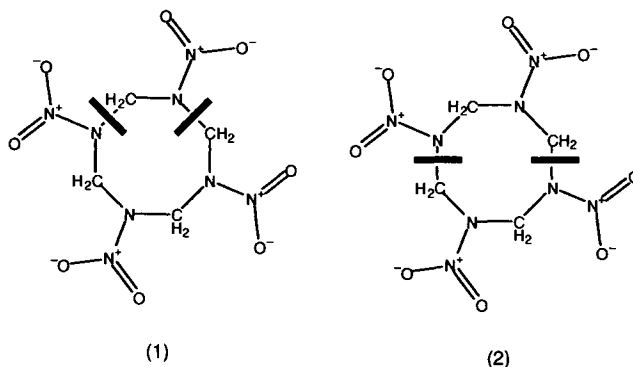


Fig.12. Comparison of relative composition of dominant species determined from current DFTB simulation (dark boxes) and from a thermodynamical calculation (empty boxes).

The current simulation should allow for the construct of a global reaction mechanism for the decomposition of HMX at the stated physical conditions. Here, we only report the initial steps of the decomposition pathways, deferring detailed mechanisms of this and similar simulations at different conditions for future publications. The first chemical event in our simulation is the breaking of the N-NO<sub>2</sub> bond and the dissociation of NO<sub>2</sub> fragments. At 200 fs of simulation time, the number of NO<sub>2</sub> fragments is 10, out of a possible total of 24, with some being successive elimination from the same HMX molecule. This preference to bond rupture is consistent with the recent observation that the energetic barriers for the cleavage of N-NO<sub>2</sub> bond in the solid phase of the nitramine RDX vary depending on the location of the molecule in the crystal.[79] At this stage of the

simulation, the C-N bond breaking is also exhibited, occurring in two ways: the first (1) producing methylenenitramine ( $\text{CH}_2\text{N}_2\text{O}_2$ ), while the symmetric breaking (2) leads to the formation of two  $\text{C}_2\text{H}_4\text{N}_4\text{O}_4$  moieties, as shown below.

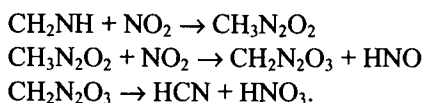


Seven  $\text{CH}_2\text{N}_2\text{O}_2$  species have been formed at around 200 fs of simulation time. These results are similar to those identified in thermal decomposition experiments. [51,53] A further N- $\text{NO}_2$  bond breaking then follows the decomposition (1) and (2) above. From (1), this leads to the formation of  $\text{CH}_2\text{N}$  and  $\text{NO}_2$ . These pathways are remarkably similar to those predicted previously by Melius from the decomposition of nitramines at fast heating rates. [70]

As the radical  $\text{CH}_2\text{N}$  is formed, the production of HCN occurs via the reaction:



Another source for the formation of HCN follows from a series of complex reactions that also produce nitric acid,  $\text{HNO}_3$ :



The schematic mechanism for these reactions is illustrated in Fig. 13. We also note that formaldehyde,  $\text{CH}_2\text{O}$ , is first formed from a reaction involving large intermediate fragments. The formation occurs from the reaction of the  $\text{C}_2\text{H}_4\text{N}_4\text{O}_4$  moiety, which is produced from the symmetric bond scission of the



HMX molecule as in (2) above, with HNO. The reaction leads to the production of  $\text{CH}_2\text{O}$  and a larger intermediate fragment that undergoes further decomposition.

### 5.3. Summary

We conducted a quantum-based molecular dynamics simulation of HMX at a density of  $1.9 \text{ g/cm}^3$  and temperature of 3500 K for up to 55 picoseconds has been conducted. These are conditions similar to those encountered at the Chapman-Jouget detonation state. Thus, although we do not model the entire shock process, we can provide some insight into the nature of chemical reactivity under similar conditions. Under the simulation conditions HMX was found to be in a highly reactive dense supercritical fluid state. We estimated effective reaction rates for the production of  $\text{H}_2\text{O}$ ,  $\text{N}_2$ ,  $\text{CO}_2$ , and  $\text{CO}$  to be 0.48, 0.08, 0.05, and  $0.11 \text{ ps}^{-1}$ , respectively. The simulation is being extended until a steady state for the production of these products is reached. The simulation can serve as a basis for the construction of a global decomposition mechanism of HMX that, lacking experimental data, can be validated through standard ab initio quantum mechanical methods. The reported results can be more fully validated through comparison with experimental findings at similar conditions, which we hope this study will motivate.

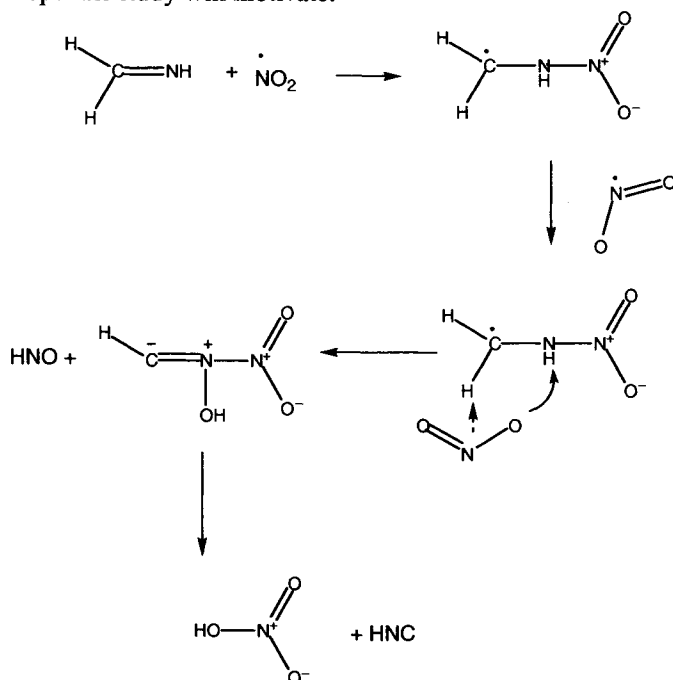


Fig.13. Mechanistic scheme for the formation of HCN.

Since the SCC-DFTB method can be implemented in parallel mode [35] with great efficiency, the size of the system can be increased to a few thousands atoms without imposing severe limitations on the simulation time. Overcoming the shortcoming of system size will allow us to consider solid carbon formation, which is not accounted for in our current simulation due to the limited system size and simulation time. The reaction rates were implemented in a three-step chemical/ hydrodynamic/thermal model of flame propagation, allowing for better agreement with recent experimental results on the flame speed.[36] Further, we find reasonable agreement for the concentration of dominant species with those obtained from thermodynamic calculations.

Although the present work sheds much needed light on the chemistry of energetic materials under extreme conditions, there are methodological shortcomings that need to be overcome in the future. The demanding computational requirements of the present method limit the simulation time to less than 100 ps. In fact, the simulations reported here took over one year of simulation time on a modern workstation. This limits the method's applicability to short times and corresponding high temperature conditions. Due to experimental difficulty, however, most work that resolves chemical speciation is done at significantly lower temperatures. A second issue is that the SCC-DFTB method is not as accurate as more elaborate *ab initio* methods. The high temperature conditions of the present work ameliorate this difficulty. For instance, at 3500K a 10 kcal/mol error in a reaction barrier leads to a factor of 4 error in the reaction rate. This is an acceptable error for qualitative study. At 600K, however, a comparable error in the barrier would lead to a factor of 4000 error in the reaction rate. There is no quantum molecular dynamics technique currently accurate enough to provide reliable reaction rates at 600K. Nonetheless, we find the present approach to be a promising direction for future research on the chemistry of energetic materials.

## ACKNOWLEDGMENTS

This work was performed under the auspices of the U.S. Department of Energy by the University of California, Lawrence Livermore National Laboratory under contract No. W-7405-Eng-48.

## REFERENCES

- [1] Y. B. Zel'dovich and Y. P. Raiser, *Physics of Shockwaves and High Temperature Hydrodynamics Phenomena*, Academic Press, New York, 1966.
- [2] A. W. Campbell, W. C. Davis, J. B. Ramsay, and J. R. Travis, *Phys. Fluids*, 4 (1961) 511.
- [3] N. S. Enikolopyan, *Dokl. Akad. Nauk SSSR*, 283 (1985) 612.
- [4] M. H. Miles and J. T. Dickinson, *Appl. Phys. Lett.*, 41 (1982) 924.
- [5] A. N. Dremin, S. D. Savrov, V. S. Trofimov, and K. K. Shvedov, *Detonation Waves in Condensed Matter*, Nauka, Moscow, 1970.
- [6] W. L. Elban, R. W. Armstrong, K. C. Yoo, R. G. Rosemeier, and R. Y. Yee, *J. Mater. Sci.*, 24 (1989) 1273.
- [7] G. I. Kanel, S. V. Razorenov, A. V. Utkin, and V. E. Fortov, *Impact-Wave Phenomena in Condensed Matter*, Yanus-K, Moscow, 1996.
- [8] L. E. Fried, M. R. Manaa, P. F. Pagoria, and R. L. Simpson, *Annu. Rev. Mater. Res.*, 31 (2001) 291.
- [9] F. P. Bowden and A. D. Yoffe, *Initiation and Growth of Explosion in Liquids and Solids*, Cambridge University Press, London, 1952.
- [10] D. D. Dlott and M. D. Fayer, *J. Chem. Phys.*, 92 (1990) 3798.
- [11] C. S. Coffey, *Phys. Rev. B*, 24 (1981) 6984.
- [12] C. M. Tarver, S. K. Chidester, and A. L. Nichols III, *J. Phys. Chem.*, 100 (1996) 5794.
- [13] C. S. Coffey, *Phys. Rev. B*, 32 (1984) 5335.
- [14] C. S. Coffey, *J. Appl. Phys.*, 70 (1991) 4248.
- [15] C. S. Coffey, *Structure and Properties of Energetic Materials*, D. H. Liebenberg, R. W. Armstrong, and J. J. Gilman, (eds.), *Materials Research Society*, Boston, MA, 1993, pp. 63-73.
- [16] L. E. Fried and A. J. Ruggiero, *J. Phys. Chem.*, 98 (1994) 9786.
- [17] C. M. Tarver, *J. Phys. Chem. A*, 101 (1997) 4845.
- [18] C. M. Tarver, *Combust. Flame*, 46 (1982) 111.
- [19] C. M. Tarver, *Combust. Flame*, 46 (1982) 135.
- [20] C. M. Tarver, *Combust. Flame*, 46 (1982) 157.
- [21] F. Williams, *Adv. Chem. Phys.*, 21 (1971) 289.
- [22] A. N. Dremin, V. Y. Klimenko, O. N. Davidova, and T. A. Zoludeva, *Ninth Symposium (International) on Detonation*, OCNR, Portland, 1989, pp. 724-729.
- [23] J. J. Gilman, *Philos. Maga. B*, 71 (1995) 1057.
- [24] J. J. Gilman, *Czech. J. Phys.*, 45 (1995) 913.
- [25] J. J. Gilman, *Science*, 274 (1996) 65.
- [26] K. F. Herzfeld, *Phys. Rev.*, 29 (1927) 701.
- [27] M. M. Kuklja and A. B. Kunz, *J. Phys. Chem. B*, 103 (1999) 8427.
- [28] M. M. Kuklja and A. B. Kunz, *J. Appl. Phys.*, 86 (1999) 4428.
- [29] M. M. Kuklja and A. B. Kunz, *J. Appl. Phys.*, 87 (2000) 2215.
- [30] M. M. Kuklja and A. B. Kunz, *J. Phys. Chem. Solids*, 61 (2000) 35.
- [31] M. M. Kuklja and A. B. Kunz, *J. Appl. Phys.*, 89 (2001) 4962.
- [32] M. M. Kuklja, E. V. Stefanovich, and A. B. Kunz, *J. Chem. Phys.* 112 (2000) 3417.
- [33] M. R. Manaa and L. E. Fried, *J. Phys. Chem. A*, 103 (1999) 9349.
- [34] M. R. Manaa and L. E. Fried, *J. Phys. Chem. A*, 102 (1998) 9884.
- [35] M. Takezaki, N. Hirota, and M. Terazima, *J. Phys. Chem. A* 101, 3443 (1997).
- [36] C. Rajchenbac, J. Gediminas, and C. Rulliere, *Chem. Phys. Lett.*, 231 (1995) 467.
- [37] M. Elstner, D. Porezag, G. Jungnickel, J. Elsner, M. Hauk, T. Frauenheim, S. Suhai, and G. Seifert, *Phys. Rev. B*, 58 (1998) 7260.

- [38] J. C. Slater and G. F. Koster, *Phys. Rev.*, 94 (1954) 1498.
- [39] P. Hohenberg and W. Kohn, *Phys. Rev.*, 136 (1964) B864.
- [40] D. Margetis, E. Kaxiras, M. Elstner, Th. Frauenheim, and M. R. Manaa, *J. Chem. Phys.* 117, (2002) 788.
- [41] E. J. Reed, J. D. Joannopoulos, and L. E. Fried, *Phys. Rev. B*, 62 (2000) 16500.
- [42] S. F. Trevino and W. H. Rymes, *J. Chem. Phys.*, 73 (1980) 3001.
- [43] J. J. Dick, *J. Phys. Chem.*, 97 (1993) 6193.
- [44] R. Shaw, P. S. Decarli, D. S. Ross, E. L. Lee, and H. D. Stromberg, *Combust. Flame*, 35 (1979) 237.
- [45] R. Shaw, P. S. Decarli, D. S. Ross, E. L. Lee, and H. D. Stromberg, *Combust. Flame*, 50 (1983) 123.
- [46] N. C. Blais, R. Engelke, and S. A. Sheffield, *J. Phys. Chem. A*, 101 (1997) 8285.
- [47] R. Engelke, W. L. Earl, and C. M. Rohlfiing, *J. Phys. Chem.*, 90 (1986) 546.
- [48] R. Engelke, D. Schiferl, C. B. Storm, and W. L. Earl, *J. Phys. Chem.*, 92 (1988) 6815.
- [49] M. R. Manaa and L. E. Fried, in preparation.
- [50] M. R. Manaa, L. E. Fried, C. F. Melius, M. Elstner, and T. Frauenheim, *J. Phys. Chem. A*, 106 (2002) 9024.
- [51] B. Suryanarayana, R. J. Graybush, and J. R. Autera, *Chem. Ind. London*, 52 (1967) 2177.
- [52] S. Bulusu, T. Axenrod, and G. W. A. Milne, *Org. Mass. Spectr.*, 3 (1970) 13.
- [53] M. Farber and R. D. Srivastava, 16th JANNA Combust. Meeting, Vol. 308, CPIA pub., 1979, pp. 59.
- [54] C. V. Morgan and R. A. Bayer, *Combust. Flame*, 36 (1979) 99.
- [55] R. A. Fifer, *Progress in Astronautics and Aeronautics*, K. K. Kuo and M. Summerfield (eds.), AIAA Inc., New York, 1984, pp. 177.
- [56] R. Behrens, *Int. J. Chem. Kinet.*, 22 (1990) 135.
- [57] R. Behrens, *J. Phys. Chem.*, 94 (1990) 6706.
- [58] R. Behrens and S. Bulusu, *J. Phys. Chem.*, 95 (1991) 5838.
- [59] J. C. Oxley, A. B. Kooh, R. Szekers, and W. Zhang, *J. Phys. Chem.*, 98 (1994) 7004.
- [60] T. B. Brill, P. E. Gongwer, and G. K. Williams, *J. Phys. Chem.*, 98 (1994) 12242.
- [61] T. B. Brill, *J. Prop. Power*, 11 (1995) 740.
- [62] C.-J. Tang, Y. J. Lee, G. Kudva, and T. A. Litzinger, *Combust. Flame*, 117 (1999) 170.
- [63] C.-J. Tang, Y. J. Lee, and T. A. Litzinger, *J. Prop. Power*, 15 (1999) 296.
- [64] D. D. Dlott, *Ann. Rev. Phys. Chem.*, 50 (1999) 251.
- [65] P. Politzer and S. Boyd, *Struct. Chem.*, 13 (2002) 105.
- [66] C. T. White, D. H. Robertson, M. L. Elert, and D. W. Brenner, *Microscopic Simulations of Complex Hydrodynamic Phenomena*, M. Mareschal and B. L. Holian (eds.), Plenum Press, New York, 1992, pp. 111.
- [67] D. W. Brenner, D. H. Robertson, M. L. Elert, and C. T. White, *Phys. Rev. Lett.*, 70 (1993) 2174.
- [68] S. R. Bickham, J. D. Kress, and L. A. Collins, *J. Chem. Phys.*, 112 (2000) 9695.
- [69] J. D. Kress, S. R. Bickham, L. A. Collins, B. L. Holian, and S. Goedecker, *Phys. Rev. Lett.*, 83 (1999) 3896.
- [70] C. F. Melius, *Chemistry and Physics of Energetic Materials*, D. N. Bulusu (ed.), Kluwer, Dordrecht, 1990.
- [71] J. P. Lewis, K. R. Glaesemann, K. Van Opdorp, and G. A. Voth, *J. Phys. Chem. A*, 104 (2000) 11384.
- [72] D. Chakraborty, R. P. Muller, S. Dasgupta, and W. A. Goddard III, *J. Phys. Chem. A*, 105 (2001) 1302.
- [73] G. D. Smith and R. K. Bharadwaj, *J. Phys. Chem. B*, 103 (1999) 3570.
- [74] D. C. Sorescu, B. M. Rice, and D. L. Thompson, *J. Phys. Chem. B*, 102 (1998) 6692.

- [75] D. C. Sorescu, B. M. Rice, and D. L. Thompson, *J. Phys. Chem. B*, 103 (1999) 6783.
- [76] A. G. Landers and T. B. Brill, *J. Phys. Chem.*, 84 (1980) 3573.
- [77] L. E. Fried and W. M. Howard, *J. Chem. Phys.*, 109 (1998) 7338.
- [78] L. E. Fried and W. M. Howard, *Phys. Rev. B*, 61 (2000) 8734.
- [79] M. M. Kuklja, *J. Phys. Chem. B*, 105 (2001) 10159.

## *Chapter 5*

# **Initiation Due to Plastic Deformation From Shock or Impact**

**C. S. Coffey**

Indian Head Division, Naval Surface Warfare Center, Indian Head, MD 20640

This chapter concerns the initiation of chemical reaction in explosive crystals as they undergo plastic deformation due to shock or impact. The energy dissipated by shear induced plastic deformation is hypothesized to be the source of the energy required to initiate reactions in the explosive crystals. A brief review is presented of Atomic Force Microscope (AFM) observations that show that crystals subjected to plastic flow experience semi-permanent deformation in both their lattice and molecular structures. The resolution of the AFM is approximately  $10^{-11}$  m. which allows the AFM to detect lattice and molecular distortions at levels that reflect quantum effects. This has lead to the development of a deformed lattice potential which when combined with a quantum mechanical description of plastic deformation determines the response of a crystal to shock or impact. These results account for AFM observations of extreme plastic flow, shear band formation and the extrusion of molten flows from these shear bands in shocked or impacted RDX and in impacted gold. Calculations of the energy dissipated in the shear bands suggest that the shear bands are a likely source of hot spots from which initiation starts. A brief account is given of experiments in which sinusoidal shock wave fronts were generated and used to distinguish between initiation due to shock pressure and initiation due to shear stress.

## **1. INTRODUCTION**

The intent of this chapter is to identify and understand the mechanisms responsible for initiation of chemical reactions in crystalline explosives as they undergo shock or impact. Guidance for this effort has been obtained from the observations of shocked or impacted explosive crystals using the Atomic Force Microscope (AFM). The AFM has a spatial resolution of about  $10^{-11}$  m which allows changes in the lattice or molecular structures of shocked or impacted crystals to be detected at the

molecular and sub-molecular levels. The AFM images only the surface of the deformed solid making it necessary to infer the state of interior of the deformed solid from the surface images. In the case of most shocked or impacted crystals the deformation extends throughout the crystals. For severe deformation, as occurs in shear bands, the assumption is made that the severely deformed surfaces features extend throughout the corresponding severely deformed regions in the interior of the crystal. It will be shown that this assumption yields reasonable results not possible in a classical analysis.

Often it is necessary to determine the response of crystalline explosives to shock or impact. For shocks, this response is usually determined by engineering calculations that use macroscopic experimental data to estimate the shock initiation pressure of the explosive of interest. Such calculations are empirical and provide no insights into why a particular explosive responds as it does. For example, both the particle size and internal damage state of the explosive crystals have major roles in determining initiation sensitivity to shock amplitude and duration. Seldom are these effects known or measured during explosive testing and consequently are generally not taken into account in calculations of initiation sensitivity. Further, it is well known that if plastic deformation is reduced or prevented by pressing an explosive charge to near its crystal density and confining the charge so that it can undergo little if any plastic flow, initiation does not occur at any shock pressure level even those in excess of the CJ detonation pressure. Known as "Dead Pressing", this technique has often been used to control or attempt to control shock sensitivity [1,2]. In the same way, it is likely that some amount of inadvertent "Dead Pressing" is responsible for the occasional failure of some explosive charges to initiate properly.

Predicting the initiation threshold due to impact also presents major problems. Often the energy of the impact is insufficient to raise the bulk temperature of the explosive sample to its initiation level. Further, the effects of crystal size and internal damage state are just as important for impact initiation as for shock initiation. Usually it is postulated that the localized hot spots that form during impact are the sources responsible for initiation. However, hot spot formation and the associated initiation process have been only poorly understood. It has been shown experimentally that during impact the hot spots and initiation sites are due to plastic deformation of the explosive [3,4]. It has also been shown that pressure by itself has little or no direct role to play in this process. Initiation only occurs in regions of high rate plastic flow regardless of the pressure amplitude. This behavior is similar to that of "Dead Pressing" observed during shock initiation.

Section (1) of the Chapter briefly reviews the large data base that has been obtained from Atomic Force Microscopy of shocked or impacted crystalline solids.

Much of this data has been or will be published elsewhere [5-10]. The data shows that the lattice and molecules of plastically deformed crystals experience significant and semi-permanent deformation. From this, insights are obtained that permit the development of an approximate deformed lattice potential for shocked or impacted crystals. Shear bands have been observed in shocked or impacted crystals. Some of shear bands show that molten material had been extruded from deep within the bands. These are possibly the source of the hot spots thought to be responsible for initiation during shock or impact. On the basis of these and other experimental observations it is concluded that energy dissipation and localization during plastic deformation is likely to be responsible for initiation of chemical reaction.

Section (2) develops a theoretical account of plastic deformation and energy dissipation at the atomic or molecular level. The AFM observations show that plastic deformation of shocked or impacted crystals can significantly deform both the crystal lattice and its molecular components. These molecular and sub-molecular scale processes require a quantum mechanical description and necessarily involve the lattice and molecular potentials of the deforming crystals. A deformed lattice potential is developed which when combined with a quantum mechanical account of plastic flow in crystalline solids will be shown to give reasonably complete and accurate descriptions of the plastic flow and initiation properties of damaged and deformed explosive crystals. The deformed lattice potential allows, for the first time, the damaged state of the crystal lattice to be taken into account when determining crystal response to shock or impact.

The remaining sections employ the deformed lattice and quantum picture of plastic flow to account for shear band formation as a means of achieving the energy localization and hot spot temperatures necessary for initiation of crystalline explosives by shock or impact. Also briefly examined will be the role of the deformed lattice potential in causing particle size effects and its effect on the plastic deformation and energy dissipation rates. Finally, the dependence of the energy dissipation rate on shear stress will be shown to imply that reaction initiation will be dependent on the shape of the shock wave or impact stimulus. These predictions will be compared with experiment.

## **2. AFM AND STM OBSERVATIONS OF THE MICROSCOPIC PROCESSES OF PLASTIC DEFORMATION**

The Atomic Force Microscope and the Scanning Tunneling Microscope, STM, offer major improvements in spatial resolution over optical and Scanning Electron Microscopes, (SEM). The AFM and STM allow a maximum spatial resolution of



about  $2$  or  $3 \times 10^{-11}$  m. For comparison, the lattice spacing of the molecular explosive crystal RDX ( $\text{C}_3\text{H}_6\text{N}_6\text{O}_6$ ) is approximately  $5.8 \times 10^{-10}$  m. The spatial resolution of the SEM is typically several times this distance. This illustrates the superior capability of the AFM and STM to determine the changes in molecular and crystal lattice structures in shocked or impacted RDX or similar crystals. The AFM and STM microscopes measure surface phenomena so that the distortions that occur in the interior of the crystals must be inferred from the surface distortions. The SEM and similar microscopes probe the interior of the crystals. However, their results are averaged over all of the atoms or molecules that lie on the path of the electron beam through the crystal. Local changes in the lattice structure due to distortions are quickly averaged away in a mostly perfect crystal. The analysis used here for the AFM data examines the surface distortion data from severely deformed portions of a shocked or impacted crystal where the deformation is known to extend through the crystal. In this way it is often possible to infer the likely state of the interior of the crystal.

Most of the AFM data presented here is on shocked or impacted crystals of the explosive RDX. Other explosives have been examined to lesser degrees and these show similar results to RDX. Because RDX is a non-conducting molecular crystal the AFM must be used to examine its deformation properties. For contrast with a very different material the results of a series of impacts on gold are also presented. Prior to shock or impact AFM and STM observations were made on well prepared RDX crystals and gold samples. These yielded the known molecular and lattice structures of RDX and the lattice structure of gold.

The AFM data shows that the deformed molecular and crystal lattice states persist for long times. For RDX, the semi-permanent higher energy deformed states persist for at least five years, which is the time that had elapsed between when some of the RDX shock and impact experiments were done and when they were examined by the AFM. The time elapsed between the impacts on gold and the AFM examination was about 2 to 3 months. Annealing is likely to be the only way to return all of the lattice and molecules to their lowest energy level state.

## 2.1 Micro-Indentations

In a series of experiments, nanometer size, conical indenters were used to examine the nature of micro-deformation in RDX crystals [9]. When the indenter was pushed only slightly into an undeformed RDX crystal to a diameter of about 10 nanometers, plastic deformation appeared to be mainly associated with the RDX molecules both distorting them and pushing them out of their equilibrium lattice configuration and

into a mound about the indenter. It was only when the indenter was pushed farther into the crystal that pits indicative of dislocations were observed. Further indentation to where the conical diameter at the crystal surface was about 70 nanometers, revealed large numbers of pits,  $\approx 10^{13} \text{ m}^{-2}$ , in the mounded region around the indenter. These were the first signs of plastic flow due to the creation and motion of dislocations and indicate that in the sequence of permanent deformation the molecules deform first followed by the lattice. This pattern appears to prevail throughout the deformation of RDX and likely applies to deformation of similar molecular solids. In the case of RDX the permanent deformation displacement between adjacent molecules often approached 20 % of the molecular spacing of the undeformed lattice. This permanent distortion is the combination of the molecular and lattice deformations and occurs for all deformation by shock or impact.

## 2.2 Shock Response of Heavily Confined Crystals

Extensive AFM observations have been made on a collection of single RDX crystals each of which had been individually enclosed in containers that limited their plastic deformation during shock. Each crystal and its container were subjected to a high amplitude shock. In several cases single RDX crystals were subjected to shocks of 12.9 GPa. pressure and duration of approximately  $2 \times 10^{-6} \text{ s}$  and were recovered intact. Had this form of "Dead Pressing" not been employed and the crystals allowed to deform they would have been detonated by a similar shock but at about a 1 GPa. shock pressure. As it was, many RDX crystals in this series of experiments were inadequately confined and did detonate at high shock pressures. The AFM scans of the recovered crystals have shown the existence of extensive plastic flow including shear bands several of which showed the presence of exuded flows of what had been molten RDX [5]. The very short,  $2 \times 10^{-6} \text{ s}$  duration of the shock appears to preclude the much slower classical process of shear band formation due to limited plastic flow followed by localized thermal heating causing lattice softening and further localized plastic flow, additional thermal heating and so forth, eventually resulting in shear band formation. The thickness of the shear bands was measured to be approximately a few times  $10^{-7} \text{ m}$ . It is unlikely that thermal conduction in such narrow shear bands would permit the classical shear band formation process. The shear bands extended along the slip plane directions for many hundreds of nanometers. The AFM observations showed little if any evidence of surface subsidence about the many places where the molten RDX had been extruded from the shear bands. It can be inferred from this that the melting had occurred deep within the shear bands in the interior of the crystal and that the local temperature in

the interior of the shear bands must have been at or above the 209 °C melting point of RDX. It is possible that chemical reaction did not occur because the size of the molten RDX regions was less than the critical size needed to start the reactions.

In summary, the RDX molecular and lattice structures were significantly distorted by shock induced deformation, especially on the surface of the shear bands. The amplitude of the lattice potential as measured by the AFM was most reduced in the highly deformed shear band regions. The presence of molten RDX extruded from deep within the interior of the shear bands indicates that the deformed lattice extended deep into the crystal.

### **2.3 Impact Observations**

AFM observations of impacted RDX crystals showed a very similar behavior to that of shocked RDX. When plastic flow occurred, large deformations were observed in the crystal lattice and molecules. As with shocks, plastic deformation so distorted the RDX molecules and lattice that there appeared no recognizable indication of the lowest energy configurations of the RDX molecules or lattice. Chemical reaction did not occur when the impacted crystal was at or near its maximum density and confined to prevent plastic flow.

For very severe deformation, shear bands were observed and frequently these showed that molten RDX had been extruded from the shear bands in a fashion entirely similar to that observed in severe deformation due to strong shock. The shear band thickness was a few times  $10^{-7}$  m. and the flow patterns of what had been molten RDX emanating from the shear bands were essentially identical to those emanating from the shear bands in shocked RDX. The shear bands and melting were only observed in the regions of maximum shear deformation which were always located near the outer edge of the impacted sample disc. Chemical reaction always first initiates in crystals located in these highly deformed outermost regions [3-5].

### **2.4 Extreme Plastic Flow**

Most unusual and initially most surprising was the amount of plastic strain measured in impacted RDX crystals. RDX is usually regarded as a brittle crystal which fractures at about 10 % strain. Impact on 50 to 100 mg of poly-crystalline RDX samples by a 10 kg free falling drop weight released from a height of about .2 m formed disc shaped samples about 15 mm in diameter and .1 mm thick. The surfaces of the impactor and the anvil on which the sample was placed were

moderately roughened so that substantial friction and shear existed in the sample during impact. AFM scans showed that the plastic deformation varied considerably across the impacted sample disc. At the center of the sample disc where the shear from the impact was zero the AFM showed little or no plastic strain but all of the crystals were fractured by the impact. With increasing distance from the center the plastic strain increased until at the outer edge of the impacted sample disc the RDX crystals experienced plastic strains of up to 2000 % or more [10]. The AFM showed that these crystals were intact and elongated in the radial direction of plastic flow and showed significant shear banding and evidence of melting within the shear bands. Due to the large amount of plastic flow, plastic deformation extended throughout the crystals in the perimeter region of the sample disc.

## **2.5 Comparison With Gold**

To compare the results obtained from the molecular crystal RDX with a very different material, gold was impacted by the 10 kg impactor released from free fall heights of .1 m and 1 m [10]. The gold was .999 pure, annealed and initially in the form of spheres about 2 mm in diameter which were sandwiched between two layers of molecularly flat mica sheets or between polished stainless steel shim stock. After impact the gold was in the form of flat discs about 5 to 6 mm in diameter. These were examined by the AFM and STM. In the case of the .1 m free fall height the gold lattice retained its hexagonal structure with slip along the {111} planes and showed only moderate lattice disruption. However, when the impactor was released from a height of 1 m the gold in the high shear regions near the outer part of the impacted sample disc assumed a cubic lattice structure with slip along the {100} planes. As with impacted RDX, shear bands were often observed from which molten gold had been extruded. These shear bands were very similar in size and appearance to the shear bands in shocked or impacted RDX. The shear band thickness was approximately a few times  $10^{-7}$  m and they extended for distances of hundreds of nanometers along the slip planes.

## **2.6 Summary of Experimental Observations**

While the above experiments are only a part of the AFM observations on shocked or impacted RDX and gold they lead to the conclusion that plastic deformation occurs due to shear and extends through out most of the solid. In the case of deformations due to higher energy shock or impact, the amplitude of the lattice potential decreases especially in the shear band regions where it appears that the lattice is reduced to a

random collection of atoms or distorted molecules. The deformed lattice likely represents a continuum of higher conformational energy states.

### 3. THEORETICAL DEVELOPMENTS

The AFM data reveals that the deformation of the crystal lattice and molecules occurs on a scale associated with quantum effects. On this basis the hypothesis of a deformed lattice potential has been introduced to describe the deformed lattice produced by plastic flow [12]. The deformed lattice potential,  $U$ , is constructed from an expansion about the undeformed potential,  $U_0$ . The second term in the expansion leads to a correction to the lattice potential that gives the Hall-Petch particle size-crystal strength dependence. The third term is more difficult because it attempts to describe the lattice potential in regions of large deformation far from the undeformed lattice potential. The AFM observations show that this term must be negative because severe plastic deformation reduces the amplitude of the lattice potential. The third term must account for the ability of the lattice to undergo the extreme plastic deformation measured in impacted RDX and other molecular crystals, the formation of shear bands in RDX in times approaching  $10^{-6}$  s, why the shear bands measured in shocked and impacted RDX and in impacted gold all appear similar and the appearance of a transition from the lowest energy configuration of the hexagonal atom arrangement of the gold lattice to a higher energy configuration of a square lattice structure during impact.

In the theoretical developments that follow, two of the standard assumptions of conventional plastic flow are retained. It will be assumed that plastic flow occurs by the creation and motion of dislocations and that to first order the length of the crystal slip planes does not change during plastic deformation. The development of a deformed lattice potential will be undertaken first and then incorporated into a quantum mechanical approach to plastic deformation required to describe plastic deformation due to shock or impact.

#### 3.1 The Deformed Lattice Potential

The deformed lattice potential,  $U$ , can be written as an expansion about the undeformed potential,  $U_0$  in terms of the number of dislocations,  $N$ , on an active slip plane [12].

$$U \approx U_0 + \frac{dU_0}{dN} N + \frac{d^2U_0}{dN^2} \frac{N^2}{2!} + \text{higher order terms.} \quad (1)$$

The second term can be expanded as  $dU_0/dN = (dU_0/dx)(dx/dN)$ . The quantity  $dU_0/dx$  is a measure of the lattice damage due to the deformation. Let  $l$  be the length of the crystal along the slip direction and  $d$  be the atomic/molecular spacing of the undeformed lattice. Then  $l/d$  is the number of atoms/molecules on a line in the slip direction of the slip plane. Since the length of the slip planes is assumed constant during plastic deformation, the quantity  $l/d$  is the number of molecules along the slip plane that must share the fixed crystal length with the  $N$  dislocations. Let  $\delta$  be the displacement introduced on the slip plane by a single dislocation. Assume that this displacement is shared equally by all of the molecules/atoms on the slip plane, so that  $dx/dN \approx \delta d/l$ . The deformed lattice potential becomes

$$U \approx U_0 + \frac{dU_0}{dx} \frac{\delta d}{l} N + \frac{d^2 U_0}{d^2} \frac{N^2}{2!} + \text{higher order terms} . \quad (2)$$

From stability arguments, the damage must initially act to increase the lattice potential so that the quantity  $dU_0/dx$  must be positive. The third term becomes important during severe plastic deformation. With increasing plastic flow the AFM studies show that the lattice and the molecular potentials increasingly deform and decrease in amplitude [6,9]. This implies that for a highly deformed crystal the third term is negative and can reduce the deformed lattice potential causing the crystal to soften and even fail. The lattice deformation due to severe plastic flow observed by the AFM is so extensive and complicated that a simple continuation of the expansion from the undeformed potential is not warranted nor is it needed for the present purposes.

### 3.2 Plastic Flow and Energy Dissipation

It is assumed that plastic flow occurs by the creation and motion of dislocations. The classical approach to dislocation motion holds that thermal fluctuations help carry the dislocations over the lattice potential barriers [13,14]. However, at normal temperatures the thermal fluctuations occur at rates of only  $10^{10}$  rad/s to perhaps  $10^{11}$  rad/s while the dislocations responsible for the plastic wave due to shock or impact travel at speeds from about .1 km/s to  $> 10$  km/s depending on the amplitude of the shock or impact. These dislocations must encounter and overcome the lattice potential barriers at rates often in excess of  $10^{13}$  rad/s [15]. Thus, energy transfer to the dislocations by thermal fluctuations occurs at rates at least two to three orders of magnitude slower than needed to overcome the lattice potential barriers and support the plastic wave component of a shock or impact.

In order to overcome the difficulty that thermal processes cannot support the plastic wave due to a shock or severe impact, it has been suggested that dislocation motion occurs by quantum tunneling [15,16]. The dislocation velocity,  $v(\tau, U)$ , can be written as

$$v(\tau, U) = v_0 T(\tau, U) , \quad (3)$$

where  $v_0$  is the shear wave sound speed in the crystal and  $T(\tau, U)$  is the probability that a dislocation encountering a lattice potential barrier,  $U$ , in response to an applied shear stress  $\tau$  will tunnel through the barrier. The plastic deformation rate,  $d\gamma/dt$ , can be written as the quantum mechanical equivalent of the Orowan relation

$$\frac{d\gamma}{dt} = v_0 \frac{2T(\tau, U) b p_c(\tau) N_s l}{l_0} . \quad (4)$$

Here,  $b$  is the Burgers length appropriate to the crystal,  $p_c(\tau)$  is the probability of creating a dislocation with the available shear stress energy and the quantity  $l_0$  is the average thickness of the dislocation source.  $N_s$  is the number of active dislocation sources whose dislocations appear on the crystal surface and has dimensions of  $(\text{length})^{-2}$ .

It is often convenient to let  $N_s = \zeta_s / (w \cdot l)$  where  $\zeta_s$  is the number of dislocation sources whose dislocations intercept the shear region of width  $w$  and length  $l$ . Equation (4) reduces to

$$\frac{d\gamma}{dt} = v_0 \frac{2T(\tau, U) b p_c(\tau) \zeta_s}{w l_0} . \quad (5)$$

If the dislocations do not cross slip onto other slip systems but project directly onto the shear surface, then  $w \approx l_0$ .

Energy dissipation occurs in a crystal undergoing plastic flow because the moving dislocations interact with and locally perturb the lattice. The high energy phonons resulting from these interactions in turn interact with the naturally occurring anharmonicities of the lattice potential and, in the well known manner, quickly cascade down to a thermal equilibrium distribution. Since energy is conserved throughout these processes, the same amount of energy transferred to the lattice by the moving dislocations appears in the final thermal equilibrium state. The rate of energy dissipation,  $dE/dt$  per unit length of dislocation, due to  $N$  dislocations moving on an active slip plane is [17,18]

$$\frac{dE}{dt} \approx AN v_0 T(\tau, U) + \prod_l \frac{B_l}{[E_l - E_{l-1} - T(\tau, U) \frac{\hbar v_0}{d}]^2 + \Gamma_l^2} \quad , \quad (6)$$

where  $A$  and  $B_l$  are constants and  $\Gamma_l$  is the width of the  $l$ -th internal molecular vibrational level and  $\hbar$  is Planck's constant divided by  $2\pi$ . The first term above applies to lower rate deformation due to mild shock or impact where  $T(\tau, U) < 1$  and resembles the empirical expression for the energy dissipation rate due to moving dislocations. In the quantum derivation

$$A = \left[ \frac{1}{32\pi^2(1-\nu)^2} \cdot \frac{(RGb)^2}{\rho d^3} \cdot v_0^{-2} \right] \quad , \quad (7)$$

$R$  is the effective radius of the dislocation core,  $\rho$  is the density of the crystal,  $G$  is the shear modulus,  $\nu$  is the Poisson ratio. The second term in Equation (6) applies to very rapid deformation processes due to strong shock loading and is dominated by the resonant condition  $E_l - E_{l-1} \approx T(\tau, U)v_0\hbar/d$  that occurs as  $T(\tau, U) \rightarrow 1$ . This term leads to resonant multi-phonon molecular excitation and dissociation associated with detonation and is discussed elsewhere [18].

### 3.3 Dislocation Tunneling, Particle Size Effects and Shear Band Formation

The AFM records show that shear bands form during shock or impact and have a major role in determining the plastic response of a crystal to these stimuli. The deformed lattice potential and its role in the tunneling probability determine shear band formation. The simplest picture of shear band formation is that of a dislocation source, of thickness  $l_0$ , responding to a strong shear stress by creating copious numbers of dislocations on the slip planes intersected by the source. It will be assumed that the dislocation source creates a nearly equal number of dislocations on each slip plane it intersects. The dislocations created on a slip plane must share the fixed length of the slip plane with all of the atoms or molecules on that slip plane which results in a locally deformed lattice associated with the slip plane. Taken together these slip planes form a band of intense shear deformation in the portion of the lattice intersecting the dislocation source.

When a crystal is subjected to large plastic deformation due to shock or impact the local dislocation sources produce extremely large numbers of dislocations. These so distort and reduce the amplitude of the lattice potential in the bands of slip



planes that intersect each source that it is possible for the amplitude of the deformed lattice potential to decrease to energies equal to or less than that of the applied shear stress energy of the dislocations. In this case, the third term in the deformed lattice potential, Equation (1), acts to decrease the amplitude of the deformed potential causing the dislocation tunneling probability to approach unity and shear bands to dominate plastic flow and energy dissipation. Creation of shear bands occurs very rapidly because in this picture only the dislocations are involved in shear band formation and these move at or near the local shear wave speed. The AFM observations support such a picture because they show that the amplitude of the deformed lattice potential decreases with increasing plastic deformation and that shear bands dominate large plastic flow.

### 3.4 Summary of Theoretical Results

The above expressions illustrate the central role that the tunneling probability has in determining the quantum mechanical elements of plastic flow. The tunneling probability,  $T(\tau, U)$ , contains all of the dependencies of the applied shear stress, temperature and lattice potential that effect plastic deformation.

As developed here  $T(\tau, U)$  contains, for the first time, a lattice potential that accounts for the effects of crystal deformation. Recall that the tunneling probability is a sensitive function of the difference between the shear stress energy,  $\varepsilon(\tau)$ , of a dislocation and the lattice potential,  $U$ ,  $T(\tau, U) = f(\varepsilon(\tau) - U)$  [19]. Usually the barrier potential  $U$  is held constant while  $\varepsilon(\tau)$  is allowed to vary. Here, the deformed lattice potential,  $U$ , is a function of the crystal damage so that the tunneling probability will be determined in part by crystal deformation. Thus, the plastic response of the crystal to an applied shear stress will be dependent on the damaged state of the crystal. Severe crystal deformation will reduce the lattice potential and increase the tunneling probability towards unity causing shear bands to form. When the tunneling probability nears unity the shear bands will dominate plastic flow and energy dissipation in the crystal.

The tunneling probability allows a number of simplifications. For example, because the effective mass of a dislocation is large, the shape of the complicated lattice potential often is not important and can be approximated by a square well potential which has analytic solutions. This will be used to simplify the prediction of the initiation probability due to an applied shear stress.

## 4. CALCULATIONS

In this section calculations will be under taken to illustrate the ability of the above theory to account for the experimental observations. The first of these to be addressed is the surprising plastic deformation behavior of RDX.

### 4.1 Anomalous Plastic Deformation in Impacted RDX

Recall that RDX, normally considered a brittle material, when subjected to rapid high amplitude shear exhibited very large permanent plastic strain often in excess of 2000%. The AFM showed that the deformed RDX crystals were intact but severely deformed and elongated in the direction of plastic flow with significant shear band formation. The plastic deformation of the crystals was so great, it appears certain that the crystals were deformed throughout with the most severe deformation occurring in the shear bands. Had the application of the shear stress been at lower amplitude and slower rates the formation of shear bands and the associated lattice softening would not have occurred and brittle failure would have taken place.

To estimate the plastic deformation, assume that the deformation occurs mainly in the shear bands. Introduce into the plastic deformation rate, Equation (5) nominal characteristic values for RDX,<sup>20</sup> so that the plastic deformation rate reduces to  $d\gamma/dt \approx 2T(\tau, U)p_c(\tau) \times 10^7 \text{ s}^{-1}$ . Approximating  $d\gamma/dt \approx \Delta\gamma/\Delta t$  and letting  $\Delta t \approx 5 \times 10^{-4} \text{ s}$ , which is the measured time of the impact, gives  $\Delta\gamma \approx T(\tau, U)p_c(\tau) \times 10^4 \text{ s}^{-1}$ . It will be shown in the following paragraph that for mild impacts slightly less than that required for initiation of chemical reaction in RDX,  $T(\tau, U)p_c(\tau) \approx 10^{-3}$  in crystals at the outer perimeter of the impacted sample. The plastic strain is  $\Delta\gamma \approx 10$  which is close to the measured values of  $\Delta\gamma \approx 10$  to 20, (1000% to 2000%).

In a recent series of impact tests the plastic deformation rates required to initiate chemical reaction were measured at the reaction site for 10 different explosive materials ranging from the sensitive explosives RDX and HMX to the insensitive explosives PBXN-128 and PBX 9502 [21]. The measured plastic deformation rate ranged from  $\Delta\gamma/\Delta t \approx .7 \times 10^4 \text{ s}^{-1}$  for RDX or HMX to  $\Delta\gamma/\Delta t > 3 \times 10^5 \text{ s}^{-1}$  PBXN-128 to PBX-9502. Substituting these measured plastic deformation rates into the expression for the calculated plastic deformation rate in the previous paragraph implies that first reaction occurs in the impact tested materials when  $10^{-3} < T(\tau, U)p_c < 10^{-2}$ . As shown above,  $T(\tau, U)p_c \approx 10^{-3}$  predicts the observed plastic strain in RDX crystals just prior to the initiation threshold.

Consider next the plastic deformation rate that occurs in a crystal during a very high amplitude shock. For very large plastic deformation the amplitude of the

deformed lattice potential in the shear bands has been observed to decrease and in the limit where  $U < e(\tau)$ , the tunneling probability approaches unity within the shear band. In this same limit of large deformation due to very high amplitude shock the probability of generating a dislocation also approaches unity,  $p_c \rightarrow 1$ . Using the same representative crystal characteristic values as above [20], the plastic deformation rate is approximately  $d\gamma/dt \approx 10^7 \text{ s}^{-1}$ . This closely approximates the plastic deformation rates measured by A. D. Sakharov and co-workers in various metals and crystalline solids at shock strengths of 10 GPa or greater [22,23,24].

## 4.2 Estimation of Shear Band Temperatures

The AFM records show that melting can occur in the shear bands implying that the shear bands are possibly the local hot spots where chemical reaction can start. For the 12.9 GPa. amplitude and  $10^{-6}$  s duration shock discussed above the temperature in the shear bands in RDX can be estimated from the energy dissipation rate, Equation (6). Equation (7) accounts for the constants appearing in the interaction between the moving dislocations and the lattice [15,16]. Typical values are given in Reference (25). Substituting these inputs into Equation (7) gives  $A \leq 6.5 \times 10^{-2} (\text{Nt s})^2/(\text{kg m}^3)$ .

The number of moving dislocations,  $N$ , can be estimated by noting that shear bands are regions of large plastic flow. For RDX crystals the average density of dislocations in regions of large plastic flow approaches  $10^{12}$  to  $10^{13}$  dislocations/ $\text{m}^2$ . These dislocations are usually localized in the shear bands where heating and melting occur. In the shocked RDX crystal the nominal surface area of the shear band is determined by the product of the shear band thickness, approximately .1 micron, and a nominal length of 1 m. Assume an averaged dislocation density of  $10^{13}$  dislocations/ $\text{m}^2$  so that in a nominal shear band there existed an average of  $10^6$  dislocations that were moving and dissipating energy during the applied shock.

The energy dissipation rate for the moving dislocations is given by the first term of Equation (6) so that when the above values are substituted into Equation (6) the total energy dissipation rate for  $N = 10^6$  moving dislocations becomes

$$\frac{dE}{dt} \leq 1.3 \times 10^8 T(\tau, U) \text{ J/s} \quad . \quad (8)$$

The time duration of the applied shock that generated the shear bands in Reference (5) is estimated to be  $\Delta t \approx 10^{-6}$  seconds so that the total energy dissipated by the moving dislocations in the shear band was  $\Delta E \leq 1.3 \times 10^2 T(\tau, U) \text{ J}$ . The AFM records indicate that this energy was localized in shear bands to a space about .1

micron high so that the energy density within the band was  $\Delta E/m^3 \leq 1.3 \times 10^9 T(\tau, U) \text{ J/m}^3$ . The temperature,  $\Delta\Theta$ , within the shear band is just  $\Delta\Theta = E(\text{J/m}^3)\rho^{-1} (\text{m}^3/\text{Kg}) C_V^{-1} (\text{Kg}^\circ\text{K/J})$ . For RDX,  $C_V \approx 1.2 \times 10^3 \text{ J/(Kg }^\circ\text{K)}$ , thus the temperature increase in the hot portion of the shear band is  $\Delta\Theta \leq 600 T(\tau, U) ^\circ\text{K}$ . Estimating the tunneling probability to be about .3 to .4 for the partially confined crystal subjected to a 12.9 GPa shock, the temperature increase in the shear band of the shocked RDX is 180 °C to 240 °C. The ambient temperature of experiment was about 23 °C so that the temperature in the shear bands was about 203 to 263 °C. Molten RDX was observed flowing from the shear bands in this experiment. The melting temperature of RDX is 209 °C.

In the same way it is possible to estimate the temperature of the shear bands in 2 mm diameter gold spheres impacted by a 10 Kg mass falling from a height of 1 m an initial impact velocity of 4.427m/s. The shear bands were located near the edge of the impacted sample disc where shear is a maximum. Molten gold was observed to have been exuded from portions of the shear bands [9]. The shear bands in impacted gold were essentially identical to the shear bands in shocked RDX. The nominal physical property inputs for gold given in Reference (26) were used. The approximate temperature in the shear bands is  $\Delta\Theta \approx 2 \times 10^3 T(\tau, U) ^\circ\text{K}$ . Setting  $T(\tau, U) = .5$  gives the temperature in the shear bands as  $\Delta\Theta \approx 10^3 ^\circ\text{K}$ . The melting temperature of gold is 1063 °C.

While the agreements between the calculated shear band temperatures and the melting temperatures for RDX and gold are satisfying, it should not be overlooked that some of the inputs to the calculations are only reasonable estimations. For example, it was estimated that the dislocation number density of gold in highly deformed regions was  $10^{14}$  dislocations/m<sup>2</sup>. Had a number density of  $2 \times 10^{14}$  dislocations/m<sup>2</sup> been used the tunneling coefficient would be reduced to 0.35.

#### 4.3 Yield Stress and Particle Size

A quantity of interest is the yield strength,  $\tau_Y$ , of crystals as a function of crystal size, damage and temperature. Due to the relatively large effective mass of the dislocation core, a sensible amount of tunneling and plastic flow only begins to occur when the dislocation energy approaches the height of the lattice potential barrier,  $\epsilon \approx U$ . The dislocation energy is

$$e = \frac{t^2 V}{2G} + \frac{k\Theta}{2} \quad (9)$$

$\Theta$  is the temperature,  $k$  is Boltzmann's constant and  $V$  is the volume of the dislocation core.

Combining Equations (2) and (9) the crystal yield stress is

$$\tau \approx \tau_y \approx \left[ \frac{2G}{V} \left( U_0 + \frac{dU_0}{dx} \frac{N\delta\ell}{\ell} + \frac{1}{2} \frac{d^2U_0}{dN^2} N^2 - \frac{1}{2} k\Theta \right) \right]^{1/5}. \quad (10)$$

This result gives the dependence of crystal yield strength on particle size and work hardening due to the creation and movement of  $N$  dislocations during plastic flow. In the limit of small particle size,  $\ell < 20$  microns, where typically  $dU_0/dx (N\delta\ell)\ell^{-1} \gg U_0$  and the third order correction term is small, the yield stress behaves as  $\tau_y \propto (N/\ell)^{1/5}$ . This prediction accounts for the observed increased yield strength of small crystals and forms the basis of the specialty iron and steel industry [26,27]. It is also likely to be the reason why the shock and impact sensitivity decrease with crystal size as  $\ell^{-5/5}$ .

#### 4.4 Approximate Energy Dissipation Rate and the $P^2 \Delta t$ Initiation Threshold

Because of the large effective mass of a dislocation, the shape of the lattice potential often is not important which allows the lattice potential to be approximated by rectangular potential barriers. For modest shear stress levels, where the dislocation energy is less than the lattice potential,  $\varepsilon < U$ , the probability that a dislocation of energy  $\varepsilon$  will tunnel through a rectangular potential barrier of height  $U$  is [19]

$$T(\tau, U) = \frac{4\varepsilon(U - \varepsilon)}{4\varepsilon(U - \varepsilon) + U^2 \sinh^2 \chi(U - \varepsilon)^{5/2} W}, \quad (11)$$

where  $\chi = (2m/\hbar^2)^{1/2}$ ,  $m$  is the effective mass of the dislocation and  $W$  is the width of the barrier. This expression has well known solutions when the lattice potential remains constant. However, the AFM observations show that with increased deformation the amplitude of the lattice potential decreases suggesting that the third term in the lattice potential, Equation (1), is increasing in magnitude. Currently, a complete description of the third term of the deformed lattice potential for an arbitrary amount of plastic deformation and crystal particle size is not known. But it is possible to approximate Equation (11) when  $\varepsilon < U$  by observing that for this

condition generally  $T(\tau, U) < 1$  so that  $U^2 \sinh^2 \chi (U - \varepsilon)^{1/2} W > 4\varepsilon(U - \varepsilon)$ . Substituting this approximation into Equation (6) estimates the total energy dissipation rate in crystalline solids undergoing plastic deformation as

$$\frac{dE}{dt} \approx v_0 \frac{4A N^* \varepsilon}{U \sinh^2 \chi W U^5} \quad , \quad (12)$$

where  $A$  is given by Equation (7) and  $N^*$  is the total number of moving dislocations in a crystal of length  $l$  and molecular spacing  $d$ ,  $N^* = Nl/d$ . The dislocation energy,  $\varepsilon$ , is given by Equation (9).

Usually in shock and impact experiments the applied pressure,  $P(r, t)$ , is measured. The shear stress can be determined as the spatial gradient of the applied pressure,  $\tau = \text{grad } P(r, t) \cdot d\mathbf{r}$ . The shear inducing component of the pressure can be written as  $P(r, t) = P_0 \pi(r, t)$  where  $P_0$  is the pressure amplitude of  $P(r, t)$  and  $\pi(r, t)$  contains the spatial and temporal components of  $P(r, t)$  [29]. Then the shear stress in the sample is  $\tau \approx P_0 \text{grad } \pi(r, t) \cdot d\mathbf{r}$ . From Equations (6), (9) and (12), the average energy dissipation rate due to plastic deformation in the crystal is

$$\frac{dE(\vec{r}, t)}{dt} \approx P_0^2 (\vec{\nabla} \pi(\vec{r}, t) \vec{dr})^2 \bullet \text{constant} \quad , \quad (13)$$

where the constant is just the remaining terms from Equations (2), (6), (7), (9) and (12).

It is difficult to measure the local energy dissipation rate within most crystals as they undergo plastic deformation due to shock or impact. However, for crystalline explosives the critical energy density required for initiation can be estimated by determining when shear bands form and become hot spot-reaction initiation sites in the manner described above. However, shear bands are but a small part of the crystal and most of the energy dissipation occurs in the bulk of the crystal prior to shear band formation and is given by Equation (13). The critical energy for initiation can be approximated as the energy dissipated in the bulk of the crystal up to the moment of shear band formation and the establishment of local hot spot-initiation sites. This critical energy can be estimated by integrating the bulk energy dissipation rate of Equation (13) for a time interval  $\Delta t$  from the start of crystal deformation until hot spots and initiation sites form.

Usually, in the routine tests used to determine the shock initiation threshold of explosives,  $\pi(r, t)$  is determined by the test geometry. Generally this does not change, and just the pressure amplitude of the applied shock is measured. Thus, it is appropriate to estimate the average energy dissipated in the bulk of the explosive

crystals required to initiate of chemical reaction

$$\Delta E(\vec{r}, t)_{\text{initiation}} \approx P_0^2 \Delta t \int \bar{\Delta} \pi(\vec{r}, t) \bullet \bar{dr} \cdot \text{constant} \quad , \quad (14)$$

where  $\Delta t$  is duration of the shock required for initiation to occur. The  $P_0^2 \Delta t$  form of the threshold relation is well known from experimental observations of the energy required to initiate chemical reactions in all common crystalline explosives and is the basis of most empirical models of explosive initiation [30]. Occasionally, small corrections to the  $P_0^2 \Delta t$  behavior are sought and these maybe due to the amount that the lattice potential deviates from the rectangular lattice barrier approximation. Finally, when  $\text{grad } \pi(\vec{r}, t) \approx 0$ , energy dissipation and, consequently, initiation do not occur. This is responsible for the "Dead Pressing" behavior referred to above. These results imply that initiation of crystalline explosives occurs by shear and that the role of pressure is to create the shear stress necessary for sufficient plastic flow and heating to occur for reaction to take place.

#### 4.5 Initiation by Non-Planar Shock Waves

Equation (14) suggests that the shock initiation threshold levels can be controlled by generating non-uniform shock waves to produce shear stress waves. Consider for example, a Sakharov type sinusoidal shock wave front advancing in the  $z$  direct but with a sinusoidal shape in the  $x$  direction and the necessary corrugations in the  $y$  direction. Such a wave front contains only small amounts of shear stress in the peak and trough regions of the sine wave while the mid regions, where the slope of the sine wave is steepest, contain the maximum shear component. A crystal located in the path of the advancing shock but at the peak of the sine wave would experience mainly compression from the locally nearly flat shock wave. A similar crystal located in the path of the advancing shock but in the region of maximum slope would experience larger shear stress in the  $z$  direction as the advancing shock wave first encountered one side of the crystal and sequentially progressed across the crystal in the  $x$  direction until the entire crystal was engulfed.

The shear stress is easily estimated. Let the shock pressure be  $P(x, y, z, t) = P_0 \sin(2\pi x/\lambda) u(z-vt, y)$  where  $P_0$  is the shock wave pressure and  $\lambda$  is the wave length. The shear stress is then  $\tau(x, y, z, t) = \text{grad } P(x, y, z, t) \cdot dr \approx (2\pi/\lambda) P_0 \cos(2\pi x/\lambda) l$  where  $l$  is the average crystal particle size. Determination of the local energy dissipation rate can be obtained from Equation (14). It is predicted that initiation will first occur where the shear stress and the energy dissipation rate are greatest so that initiation will first occur at  $x = \pm m\lambda/2$ , where  $m = 0, 1, 2$ , etc. On the  $x, y$  plane first initiation

will appear as long lines of reacting material in the y direction. Each reaction line will be separated from its nearest neighbors in the x direction by a distance  $x = \lambda/2$ . Eventually these linear regions of reacting material will grow, coalesce and consume the entire explosive. Such a behavior has been observed in recent experiments in which both sinusoidal and trapezoidal shock wave fronts were generated and produced the results predicted above [31,32].

The above result can be generalized on the basis of the inequality,  $\text{grad } P_{\text{curved wave}}(x,t) \cdot \vec{u}_z > \text{grad } P_{\text{plane wave}}(x,t) \cdot \vec{u}_z$ . Because of this inequality, Equation (14) predicts that a plane shock wave of amplitude  $P_0$  will dissipate less energy than a strongly curve shock wave of the same amplitude  $P_0$ . For example, if the amplitude of the plane shock wave is just below the shock level needed for initiation then a curved shock wave of the same amplitude will dissipate a greater amount of energy and is more likely to produce initiation.

#### 4.6 Initiation of Detonation

Initiation of chemical reaction in explosive crystals occurs due to the local energy dissipated in the crystals during plastic flow arising from shock or impact. For mild shock or impact the energy dissipation rate is given by the first term of Equation (6). In the case of very high amplitude shocks the second term of the energy dissipation rate of Equation (6) offers the possibility of a very different, singular, behavior. Here, the denominators in the second term can approach zero,  $E_i - E_{i-1} - T(\tau, U) \hbar \nu_0 d^{-1} \approx 0$ , and result in an extremely fast energy dissipation rates. The case of resonance excitation combined with maximum energy separation between molecular vibration levels requires  $T(\tau, U) \approx 1$ . The rapid resonant energy dissipation results in a very rapid multi-phonon excitation subsequent dissociation of the explosive molecules. The chemical energy released by molecular dissociation augments the energy dissipated by the moving dislocations causing further molecular dissociation and chemical reaction. These processes together with energy localization are likely to be responsible for detonation. If somehow the plastic flow in the explosive crystals is stopped, even during full detonation, the energy dissipation due to plastic flow and the chemical energy release also stop regardless of the applied pressure. This is the Dead Pressing discussed earlier.

The transition to detonation occurs as the dislocation tunneling probability approaches unity. While the molecular excitation and dissociation processes are entirely quantum mechanical processes the detonation velocity is accessible through classical means. The detonation velocity,  $D$ , is the velocity of the plastic wave where energy dissipation and molecular dissociation take place,  $D = v$ . But  $v =$



$T(\tau, U) v_0$  where  $v_0$  is the local shear wave speed in the detonation wave. At high shear stress levels,  $T(\tau, U) \approx 1$  while  $v_0$  is reasonably well approximated by semi-empirical means. Thus, while multi-phonon molecular excitation and dissociation occur in times of  $10^{-12}$  s, reaction propagation only occurs at the local shear wave speed in the detonation wave, typically 5 to 10 km/s.

## 5. CONCLUSIONS

The unprecedented spatial resolution of the Atomic Force Microscope makes it possible to examine the plastic deformation of shocked or impacted solids at the atomic or molecular levels. At these levels the molecular and lattice behaviors are determined by quantum mechanics. While the AFM is limited to imaging only the surface of the deformed solid, in many if not most shocked or impacted solids the deformation extends throughout the sample. It is necessary to infer the deformation in the interior of the sample from the surface information. In the case of severe deformation as found in shear bands the assumption has been made that the severely distorted surface features extend throughout the similar severely distorted regions in the interior of the solid. This assumption yields reasonable results not accessible by a classical analysis.

The recent AFM experimental data concerning plastic flow place severe restrictions on possible theoretical accounts of plastic deformation in crystalline solids due to shock or impact. The high spatial resolution of the AFM,  $\approx 2 \times 10^{-11}$  m, reveals substantial plastic deformation in shocked or impacted crystal lattices and molecules. Understanding how this occurs and its effect on plastic flow requires a quantum mechanical description. The semi-permanent lattice deformation has necessitated the development of a deformed lattice potential which, when combined with a quantum mechanical theory of plastic deformation, makes it possible to describe many of the features found in the AFM records. Both theory and the AFM observations indicate that shock and impact are similar shear driven processes that occur at different shear stress levels and time durations. The role of pressure is to provide an applied shear stress sufficient to cause initiation.

Finally, there is no evidence in the AFM records that plastic flow in crystals occurs by classical physics processes over distances smaller than about  $10^{-6}$  to  $10^{-7}$  m. Rather, the AFM observations indicate substantial semi-permanent lattice and molecular deformation throughout crystals subjected to shock or impact. This raises serious questions about efforts to calculate the response of even an atomic solid to a shock or impact using the classical physics of rigid masses and spring type forces. In this regard, the relatively mild impact experiments on gold show shear banding and

melting, partial height dislocation steps, and indicate substantial distortion of the atomic lattice as well as a transition from the normal body centered cubic lattice to a semi-permanent cubic lattice at relatively low level impacts.

## ACKNOWLEDGEMENTS

The author wishes to acknowledge the support of the Office of Naval Research and in particular to thank Mr. C. W. Anderson of ONR for his support of this research. He also wishes to acknowledge the contributions that Dr. J. Sharma has made towards understanding the physics of initiation and plastic deformation with his seminal work on shocked and impacted crystals using the Atomic Force Microscope.

## REFERENCES

1. S. J. Jacobs, Unpublished Report, in **Third Symposium on Detonation**, Office of Naval Research Rept. ACR-52, p. 784, (1960).
2. G. B. Kistiakowsky, Unpublished Report, **Proceedings of the Third International Symposium on Combustion Flame and Explosion Phenomena**, Williams and Wilkins, Baltimore, p. 560, (1949).
3. C. S. Coffey and V. F. DeVost, *Propellants, Explosives and Pyrotechnics*. **20**, 105,(1995).
4. C. S. Coffey, M. J. Frankel, T. P. Liddiard and S. J. Jacobs, in *Seventh Symposium on Detonation*, 970, (1981).
5. C. S. Coffey and J. Sharma, *J. of Appl. Phys.*, **89**, 4797 (2001).
6. J. Sharma and C. S. Coffey, in **Shock Compression of Condensed Matter**, edited by S. C. Schmidt and W. C. Tao (AIP Press, Woodbury, NY, 1995), p. 811.
7. J. Sharma and C. S. Coffey, in **Decomposition, Combustion and Detonation Chemistry of Energetic Materials**, edited by T. B. Brill, T. P. Russell, W. C. Tao and R. B. Wardle, MRS Symposia Proceedings No. 418 (Materials Research Society, Pittsburgh, 1995), p. 257.
8. J. Sharma, S. M. Hoover, C. S. Coffey, A. S. Tompa, H. W. Sandusky, R. W. Armstrong, and Elban, W. L. in **Shock Compression of Condensed Matter-1997**, AIP Conf. Proc. **429**, 563 (1997).
9. J. Sharma, R. W. Armstrong, W. L. Elban and C. S. Coffey, *Appl. Phys. Lett.*, Feb. (2001).
10. J. Sharma, C. S. Coffey, W. L. Elban and S. M. Hoover, To be published in *Proceedings of the TMS Meeting*, March 2003.

11. J. Sharma, C. S. Coffey, R. W. Armstrong, W. L. Elban and S. M. Hoover, in Proc. Shock Compression of Condensed Matter, M. D. Furnish, N. N. Thadhani and Y. Horie, Eds. AIP Press, 837, (2002).
12. C. S. Coffey and J. Sharma, Phys. Rev. B **60**, 9365 (1999).
13. U. F. Kocks, A. S. Argon, and M. F. Ashby, "Thermodynamics and Kinetics of Slip" in **Progress in Material Science**, B. Chalmers, J. W. Christian and T. B. Massalski eds Pergamon Press, 1975.
14. A. V. Granato, K. Lucke, J. Schlipf and L. J. Teutonico, J. Appl. Phys. **35** 2732, (1964).
15. C. S. Coffey, Phys. Rev. B **49**, 208 (1994).
16. C. S. Coffey, in **Mechanics of Deformation at High Rates**, edited by R. Graham (Springer-Verlag, Berlin, 1996), Vol. 3.
17. C. S. Coffey, Phys. Rev. B **24**, 6984 (1981).
18. C. S. Coffey, Phys. Rev. B **32**, 5335 (1984).
19. A. Messiah, in **Quantum Mechanics** (North-Holland, Amsterdam, 1962), Vol. 1.
20. For a nominal shear wave speed of RDX,  $v \approx 2 \times 10^3$  m/s, a Burgers length  $b \approx 5 \times 10^{-10}$  m, a dislocation source thickness measured to be approximately  $w \approx l_0 \approx 3 \times 10^{-7}$  m and one dislocation source per shear band,  $\zeta = 1$ .
21. J. Namkung and C. S. Coffey, in **Shock Compression of Condensed Matter-2001**, Editors, M. D. Furnish, N. N. Thadhani and Y. Horie, American Institute of Physics, 1003, (2002).
22. A. D. Sakharov, R. M. Zaidel', V. N. Mineev and A. G. Oleinik, Soviet Physics-Doklady, **9**, 1091, (1965).
23. V. N. Mineev and E. V. Savinov, Soviet Physics JETP, **25**, 411, (1967).
24. V. N. Mineev and R. M. Zaidel', Soviet Physics JETP, **27**, 874, (1968).
25. For RDX the Poisson ratio is approximated as  $\nu \approx .5$ . The length  $d$  is the molecular spacing,  $d = 5.8 \times 10^{-10}$  m, and the Burgers length,  $b \approx d$ .  $R$  is the radius of the dislocation core which is taken as  $R \approx 2d$ . The shear wave speed is  $v_0 \approx 2 \times 10^3$  m/s and the density of RDX is  $\rho \approx 1.8 \times 10^3$  kg/m<sup>3</sup>. The nominal shear modulus for RDX is  $G \approx 4$  GPa. Within the heavily deformed shear bands the lattice potential will be reduced which will reduce the shear modulus so that the calculation will over estimate the energy dissipation and temperature in the shear band.
26. For gold, the thickness of the bands was approximately  $10^{-7}$  m and the number of dislocations in the heavily deformed shear bands was taken as  $10^{14}$  dislocations/m<sup>2</sup>. The shear modulus,  $G \approx 3.95$  GPa, Poisson ratio  $\nu \approx .5$ , the inter-atomic spacing  $d \approx$

$2.3 \times 10^{-10}$  m, the Burgers length  $b \approx d$ , the dislocation radius  $R = 2d$ , the shear wave speed  $v_0 = 1.5$  km/s, the specific heat of gold  $C_v = .13 \times 10^3$  J/ (Kg °K), density  $\rho = 19.8 \times 10^3$  Kg/m<sup>3</sup>.

27. E. O. Hall, Proc. Phys. Soc. London, Sect B **64**, 747 (1951).

28. N. J. Petch, J. Iron Steel Inst., London **174**, 25 (1953).

29. C. S. Coffey, in **Decomposition, Combustion, and Detonation Chemistry of Energetic Materials**, Editors, T. B. Brill, T. P. Russell, W. C. Tao and R. B. Wardle. Mat. Res. Soc. Symp. Proc. Vol. 418, p. 331, (1996).

30. E. L. Lee and C. M. Tarver, Phys. Fluids, 23, 2362 (1980).

31. R. J. Lee, C. S. Coffey, E. J. Cart and P. K. Gustavson, To be published in the Proceedings of the APS Shock Physics Conference, July 20 - 25, 2003.

32. J. A. Campos, I. Plaksin, J. Direito, D. Braga and C. S. Coffey, To be published in the Proceedings of the APS Shock Physics Conference, July 20 - 25, 2003.

This Page Intentionally Left Blank

## Chapter 6

# Fast molecular processes in energetic materials

Dana D. Dlott\*

School of Chemical Sciences, University of Illinois at Urbana-Champaign, Box 01-6 CLSL, 600 S. Mathews Ave., Urbana, IL 61801.

## ABSTRACT

This chapter describes experimental and theoretical approaches for understanding shock compression, low velocity initiation, hot spot formation, shock initiation and detonation of energetic materials and nanotechnology energetic materials on the femtosecond time scale and at the level of individual molecules. Particular attention is paid to models that combine chemistry, mechanics and quantum behavior. Suggestions are made for future work in key areas.

## 1. INTRODUCTION

This chapter describes approaches for understanding energetic materials at the level of individual molecules. An individual molecule is about one nanometer (10Å). Energetic mechanical stimuli such as crack or shock front propagation move at or above the speed of sound, 3-9 km/s or equivalently 3-9 nanometers per picosecond [1]. Thus an individual molecule in an energetic material sees a fast mechanical stimulus. If we take the shock front to be a few molecules in width (*vide infra*) then molecules see ultrafast mechanical excitation occurring on the picosecond time scale. Whereas molecules are associated with nanometers and picoseconds, detonations are associated with millimeters and microseconds. Thus there are two significant problems associated with these fast phenomena: understanding the fast microscopic phenomena themselves and bridging the tremendously disparate time and length scales.

Quite a few different approaches have been tried. One popular approach (CJ and ZND theories, Section 2.3) explicitly states that in a detonation, the chemical reaction kinetics and pathways do not matter at all. All that matters are physical and mechanical properties such as the Hugoniot of the unreacted

---

\* Electronic mail: [dlott@scs.uiuc.edu](mailto:dlott@scs.uiuc.edu)

material. Not surprisingly, most proponents of this approach are mechanical engineers and physicists. On the other hand, many popular approaches to the problem of explosive sensitivity to impact or other stimuli state that sensitivity can be understood from single-molecule properties alone, such as inner-core electronic levels or the locations of lower frequency vibrational levels, and mechanics and physics do not matter at all. Not surprisingly, most proponents of this approach are chemists. An approach whose popularity today has been steamrolling is molecular dynamics, where a bunch of theoretical molecules are observed in a theoretical shock front. Since virtually all simulations use classical mechanics, most proponents of this approach think they can get along perfectly well without quantum mechanics.

In this chapter, I will present some models for understanding a range of energetic material behavior. These models are heuristic, that is they were created primarily in an attempt to teach us something. They combine, in a perhaps somewhat *ad hoc* manner, concepts from mechanics and chemistry and they attempt to model quantum behavior in a realistic way [2], at least in the regimes where quantum mechanics ought to be important. The late Harry G. Drickamer described this approach as “Gedanken Theory” for experimentalists. He often said, “We know what a *gedanken* experiment is. That is where you say, ‘if I could actually do this experiment what would result?’. A *gedanken theory* is where you say, ‘if I could actually *do this theory* what would result?’”.

To the end users of energetic materials--mechanical engineers, construction engineers, soldiers, etc., the only relevant quantities are macroscopic—mainly the detonation velocity, the CJ pressure and the heat of explosion. So sometimes it is questioned whether a molecular-level understanding is even needed. However there clearly are problems that seemingly cannot be solved by ordinary engineering. The first nagging problem has been with us from the beginning: preventing accidents based on a fundamental understanding of what causes energetic material sensitivity to small insults. A second problem is newer and very exciting. Now that nanotechnology has begun to be applied to energetic materials, the possibility has arisen for *de novo* design of new nanoenergetic materials based on engineering every atom into an optimized nano and microstructure.

## 2. THE PHENOMENOLOGY OF ENERGETIC MATERIALS

The phenomenology of energetic materials is described in every good explosives handbook. Nevertheless I wish to describe some of the relevant phenomena once again. As a physical chemist trained in molecular dynamics and molecular interactions, it took a long time for me to be able to communicate effectively with researchers in the mainstream of the energetic materials area. This section is intended primarily for the quick education of physical chemists and molecular

physicists who are interested in connecting molecular dynamics and condensed matter physics with the field of energetic materials.

## 2.1. Types of energetic materials

Energetic materials are classed as *primary* or *secondary* [3]. *Initiation* means the onset of the first reaction or set of reactions. *Ignition* means the first appearance of light and heat. A primary consists of crystals of unstable molecules such as the silver fulminate from the caps in little toy guns or the baby poppers on the 4<sup>th</sup> of July, lead azide, mercury fulminate or lead styphnate. Rather weak stimuli such as percussion can cause the crystallites to rub together, initiating the decomposition of these unstable molecules into smaller fragments plus energy. With primaries, the initiating step is also the ignition step. A *secondary* such as PETN, RDX, HMX, nitromethane (NM) or TATB consists of stable molecules. All high-performance energetic materials are secondaries. Without giving it much thought, one might imagine that a molecule of NM or RDX could explode violently, but in fact an isolated molecule of NM or RDX does nothing extraordinary. These are rather stable molecules with sizeable barriers to reaction. The initiating steps are *endothermic*. A good deal of energy has to be input to break down these stable materials into smaller reactive fragments. It is in a series of subsequent steps where these fragments combine to produce small stable molecules [4] such as NO<sub>2</sub>, CO, H<sub>2</sub>O, HCN and HONO that ignition occurs and energy is released—usually a great deal more energy than primaries. There are several kinds of secondary energetic materials. *Homogeneous* materials are great for fundamental studies but they are not generally used in practical applications. Two examples are liquid NM and large single crystals of PETN. *Inhomogeneous* materials are great for practical applications. Usually these are practiced formulations of engineered crystallites of secondaries plus a sticky binder (plastic-bonded explosives or PBX). For instance C4 is a composite of 91% RDX and 9% polyisobutylene, PBX 9501 consists of 95% HMX, 2.5% dinitropropyl acrylate-furmarate and 2.5% estane, and PBX 9502 consists of 95% TATB plus 5% Kel-F binder [3]. *Nonideal* materials consist of separate fuels and oxidizers, for example powdered Al plus powdered ammonium perchlorate, or hydroxy-terminated polybutadiene plus liquid oxygen. These are cheap and are used in a variety of propellant and undersea explosive applications where fast energy release is not desirable or not needed. *Nanoenergetic* materials are nonideal materials where the fuel component and possibly the oxidizer component is present as a nanoparticle or nanostructure.

## 2.2 Shock waves

In this section I first describe an idealized shock wave in a continuous elastic medium, and then explain how things change in real materials such as a



metal slab, a molecular crystal and a molecular material that is disordered by having random pores.

### 2.2.1 Shock waves in continuous elastic media

It is usual to consider 1D shock compression by a planar shock front, since considerable but pedestrian mathematical complexities become involved in 3D shocks [5]. Imagine a heavy plate falling at velocity  $U_p$  onto a block of density  $\rho_0$ , as depicted in Figs. 1a-c [6]. When  $U_p$  is small, an acoustic wavefront is launched, which moves through the sample at speed of sound  $c_0$ . With an acoustic wave, the density  $\rho_0$  is the same ahead and behind the front. The acoustic front generated by a collision between parallel flat surfaces would initially be very steep, since the interaction potential between the atoms in the plate and the atoms in the sample has a very short range of  $\sim 0.1$  nm. However this acoustic wavefront composed of a broad range of acoustic frequencies would spread out quickly due to acoustic dispersion. When  $U_p$  is large (here “large” means a significant fraction of  $c_0$ ), a shock front is launched (Fig. 1c). The plate-sample interface begins to move (in fluid mechanics the sample begins to “flow”). For simplicity the flow velocity is ordinarily assumed to match the plate velocity  $U_p$ , which is approximately true when the plate has a much higher

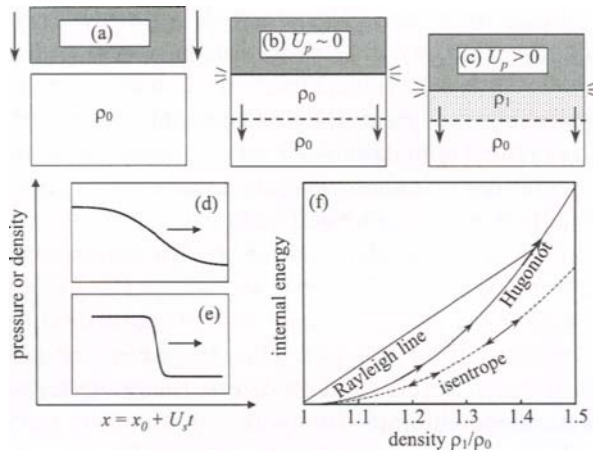


Fig. 1. (a) A heavy plate is dropped at velocity  $U_p$  on a sample with density  $\rho_0$ . (b) When  $U_p$  is small, an acoustic wave is launched. The density on both sides of the front remains  $\rho_0$ . (c) When  $U_p$  is larger, a shock wave is launched with velocity  $U_s$ . The density  $\rho_1$  behind the front is larger than  $\rho_0$ . (d) and (e) A gradually rising shock front is a nonlinear excitation that steepens up as it runs, because the higher pressure components move at a higher speed. (f) A reversible adiabatic compression follows the curve labeled isentrope. A single-stage shock is an irreversible adiabatic compression that follows a Rayleigh line until it intercepts the Hugoniot. The Hugoniot is not a path, but rather it is the locus of all points accessible by a single-stage shock. Adapted from ref. [6]

density [1,5]. When the sample material velocity is equal to  $U_p$ , the shock velocity  $U_s$  is about equal to  $U_p + c_0$ . The density  $\rho_1$  behind the shock front is greater than  $\rho_0$ . For instance when  $U_p = 0.1c_0$ , then  $U_s \approx 1.1c_0$  and  $\rho_1 \approx 1.1\rho_0$ . In words, a plate moving 1/10 of the sample's sound velocity produces about 10% compression. Elementary considerations of conservation of mass, momentum and energy lead to the Hugoniot-Rankine relations [7],

$$\rho_1 = \rho_0 \left( 1 - \frac{U_p}{U_s} \right)^{-1}, \quad (1)$$

$$P_1 - P_0 = \rho_0 U_s U_p, \quad (2)$$

and

$$E_1 - E_0 = \frac{1}{2}(P_1 + P_0)(V_0 - V_1), \quad (3)$$

where  $P_0$  is the initial pressure ( $P_0 \approx 0$ ),  $P_1$  is the shock pressure,  $V_0 = 1/\rho_0$  and  $V_1 = 1/\rho_1$ . Shock pressures are usually given in GPa units (SI), where 1 GPa = 10 kilobars (kB)  $\approx 10^4$  atm.

An amazing feature of shock compression is illustrated in Figs. 1d-e. A *driven shock front steepens up as it runs*, in contrast to acoustic waves that disperse as they run [1]. Imagine a shock front that is not initially steep (Fig. 1d). Think of the front as a higher pressure wave trailing a lower pressure wave. Equation (2) above shows the trailing wave moves faster. In an ideal continuous elastic medium, the shock front steepens until it becomes an abrupt discontinuity. The shock front risetime  $t_r \rightarrow 0$ .

The closest approximation to a continuous elastic medium is a simple liquid that does not freeze during shock compression. Whenever the time resolution of measurement techniques improve, the shock front risetime in liquids has appeared faster. Some very interesting but indirect measurements have been made in water. It is reportedly impossible to freeze water with a single-stage shock [8], although multistage shocks that produce less heating can freeze water above  $\sim 3$  GPa [9]. In 1984, Harris and Presles [10] measured the shock-induced electrical polarization of water and inferred a shock front risetime  $t_r = 1$  ps. Subsequent measurements in R. Alfano's lab [11] that looked at stimulated optical scattering of a picosecond light pulse from a laser-driven shock front in water were also consistent with  $t_r = 1$  ps. Water is not a simple liquid at the nanometer length scale—it is a complicated hydrogen-bonded network of triatomic molecules. So it is difficult to know if the 1 ps risetime is simply limited by measurement techniques or is an intrinsic value determined by

the molecular structure. In solids, the shock front develops a more complicated and extended structure as it propagates, as discussed below.

Shock compression is an *irreversible* adiabatic compression that heats the material behind the front [1]. The temperature rise can be divided into two parts. The minimum temperature rise would result if shock compression were slow enough that it approximated a reversible adiabatic compression from  $V_0$  to  $V_1$ . This process, where  $\Delta S = 0$ , is also called an isentropic compression [1]. Due to the irreversible nature of shock compression, an additional rise is produced that results from the entropy increase  $\Delta S_{irr}$  across the shock front. This additional rise depends on the detailed nature of the shock front. Shock compression is hotter than isentropic compression. The new temperature  $T_1$  cannot be determined from the Hugoniot-Rankine equations alone. Some kind of equation of state (EOS) is also needed (for state-of-the art examples see Refs. [12-14]), and the usual choice is a Grüneisen equation of state. The temperature  $T_1$  is given by [1],

$$T_1 = \Delta T_{rev} + \Delta T_{irr} = T_0 e^{\Gamma \Delta V} + \Delta T_{irr}, \quad (4)$$

where  $\Delta V = 1 - V_1/V_0$ , and  $\Gamma$  is the Grüneisen coefficient [15]. The Grüneisen coefficient  $\Gamma$  determines how much of the shock energy goes into compression and how much goes into heat. The temperature jump  $\Delta T_{rev}$  is greater for more compressible materials and for materials with larger Grüneisen coefficients, which are associated with more anharmonic potential energy surfaces. The second term in Eq. (4) is path dependent. Figure 1f [16] shows the isentropic path of the internal energy from density  $\rho_0$  to  $\rho_1$ . Along this path,  $\Delta T_{irr} = 0$ . For a single-stage shock compression, the internal energy follows a linear path from the initial state to the final state as shown by Eq. (3) and in Figure 1f. This linear path is termed a *Rayleigh line* [1]. The final state of the (unreacted) shocked material is where the Rayleigh line intersects the Hugoniot curve. Hugoniot is a term used for a family of relations between the shock velocity, pressure and density. The Hugoniot is fundamentally different from thermodynamic pathways such as adiabats and isotherms. A shocked sample does not follow the Hugoniot curve. The Hugoniot is the locus of all points representing final states accessible by single-stage shock compression. In the special case of single-stage shock compression at pressure  $P$ , Eq. (4) becomes,

$$T_1 = T_0 e^{\Gamma(V_0 - V_1)} + \int_{V_0}^{V_1} \frac{f(V) e^{\Gamma V}}{C_V} dV, \quad (5)$$

where  $C_v$  is the constant-volume heat capacity and  $f(V) = \left[ \frac{1}{2}(V_0 - V_1) \frac{dP}{dV} + \frac{1}{2}P \right]$ . Shock heating of crystalline materials may be quite dependent on the direction of shock propagation. This anisotropy problem can be handled by molecular dynamics simulations of shocks in different directions [17,18] or by considering the tensor nature of the Grüneisen coefficient and the tensor nature of the compressibility [12,14,19,20]. In the latter case the direction-dependent temperature jump can be determined using Eqs. (4) or (5) and the appropriate elements of the Grüneisen and compressibility tensor. For instance, Jindal and Dlott calculated the shock-induced temperature rise using Eq. 4 for a naphthalene crystal with shock compression along the crystal  $a$ ,  $b$ , or  $c$ -axes, as shown in Fig. 2 [20]. Naphthalene, although not an energetic material, was chosen because it is a model system for molecular crystal studies [21,22] and a high quality anharmonic potential energy surface was available [23]. The direction-dependent Grüneisen parameter was largest for compression along the  $c$ -axis, but naphthalene is more incompressible in this direction [20]. Thus the temperature increase is considerably greater for shocks along the  $a$  and  $b$ -axes. Recently Gupta and co-workers have directly measured the shock-induced temperature increase for shock compression along two different crystallographic planes of ammonium perchlorate [12,14]. Even rather small direction-dependent effects may be significant. Since chemical reaction rates are typically exponentially sensitive to temperature, even a relatively small orientation dependence of shock-induced heating can have a substantial effect on chemistry.

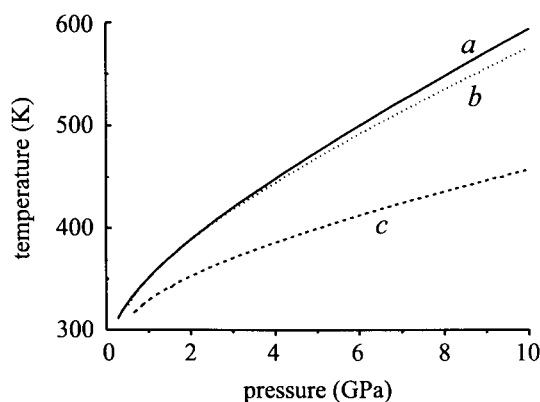


Fig. 2. Shock heating of a molecular crystal depends on the direction of shock propagation. The calculated anisotropy of shock-induced heating in a naphthalene crystal shows that  $c$ -axis compression leads to a smaller temperature rise than the  $a$ -axis or  $b$ -axis, because the crystal is less compressible along  $c$ . Reproduced from ref. [20].

### 2.2.2 Shock fronts in real materials

In real materials a shock front develops a structure and a finite risetime due to processes that convert the directed energy of the shock front into a variety of mechanical excitations that do not propagate [1,5]. Thus there is no such thing as “the shock front risetime”. As discussed below, the shock front risetime in Al can be 6 ps or 6 ns. In casual conversation a lot of sentences will begin with “The shock front risetime is ....,” so beware! The risetime  $t_r$  will depend on the shock pressure, the material, its homogeneity or lack thereof, and the shock run distance. In phenomenological theories, shock front broadening processes are characterized by a “shock viscosity”  $\eta_{sh}$  [24]. There is not yet a good atomic-level model for shock viscosity, although recent nonequilibrium molecular dynamics simulations are intriguing [25]. The shock viscosity concept might be viewed as an extension of ordinary viscosities to extremely large strain rates (i.e. large amplitudes and high frequencies), for instance 20% compression in 10 ps giving a strain rate  $\Delta x/x \approx 2 \times 10^{11} \text{ s}^{-1}$ . We know quite a bit about viscosity increases at higher frequencies from acoustic attenuation measurements [26], but little about the *large-amplitude effects* at high frequency.

One important difference between liquids and solids is that the latter can support shear for a long time. The ability to support shear is termed “strength”. To illustrate the effects of strength, consider the atomic solid with a cubic lattice (representing for instance a homogeneous slab of Al metal) depicted in Fig. 3 subjected to a fast uniaxial compression along  $z$ . This solid can be viewed as inertially confined along  $x$  and  $y$  during the early stages of shock compression

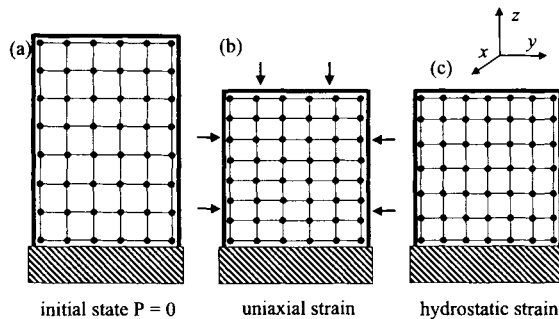


Fig. 3. Effects of fast uniaxial compression along the  $z$ -axis, illustrated with a simple cubic lattice. (a) For short times the lattice is inertially confined along  $x$  and  $y$ ; that is illustrated by the confining cylinder walls. (b) Uniaxial strain compresses the lattice along  $z$  but not along  $x$  and  $y$ . The resulting force vectors (*small arrows*) show that a combination of longitudinal and shear forces result. If the material strength exceeds the shear force, the uniaxial strain is maintained. (c) If the sample is a fluid that does not support shear or if the shock strength exceeds the material strength, the lattice material relaxes to a state of hydrostatic compression by rearranging and breaking interatomic bonds (an atom in the second row has moved to the first row). Adapted from Chapter XI of ref. [1].

[1]. In Fig. 1 this lateral inertial confinement is shown schematically by the device of drawing thick walls of a confining cylinder. As the atomic planes are driven together by the shock front, the compression process is initially *uniaxial* and *elastic*. The lattice constant along  $z$  is reduced while the  $x$  and  $y$  lattice constants are unaffected. If the shock strength is less than the material strength, the material remains in a state of uniaxial compression (Fig. 3b), whereas a liquid would rapidly relax to a state of hydrostatic pressure by driven diffusive motion of some of the liquid's atoms or molecules. However when the shock strength exceeds the strength of the lattice, *plastic deformation* results. Atoms are ripped from their lattice sites, and they go over barriers to new sites. With a sufficiently strong shock wave, the microscopic structure of the solid is destroyed and a state of hydrostatic compression is generated (Fig. 3c). The shock strength necessary to create a fluid-like state of hydrostatic compression is termed the Hugoniot Elastic Limit (HEL) [27]. The HEL concept is tempting, since it allows mechanical engineers to treat solids with the much simpler formalisms appropriate to fluid mechanics [27]. However it might be worthwhile resisting this temptation, since in real solids there is usually some strength remaining even with quite strong shocks. In that case the relaxation from uniaxial to hydrostatic compression is not complete. A beautiful illustration of this is seen in the atomistic simulations of Holian and co-workers (e.g. see Fig. 2 of ref. [17]).

Shock fronts in Al have been studied extensively. The risetimes are measured as the shock front emerges at an Al-air or Al-window interface, using a fast laser interferometer (usually a VISAR [5,28]) to watch the displacement of the Al surface. With a 4 GPa shock in 12 mm Al, in 1969 Johnson and Barker saw a two-part structure [29]. The leading part is termed the *elastic precursor*. The elastic part disperses as it runs through the lattice, so the elastic precursor has a slower risetime ( $\sim 100$  ns) which increases with run distance. The steep trailing shock front had a  $< 10$  ns risetime. These 10-100 ns times are a far cry from the 1 ps mentioned above. A variety of factors might account for these nanosecond risetimes. These might include experimental problems such as a tilted impact between plate and sample [30], but more likely these measured values result from shock propagation through many millimeters of a polycrystalline metal sample undergoing large-scale plastic deformation [31].

The VISAR results leave open the question of the risetime of a shock propagating through a very thin and highly homogeneous slab of Al. In 2002, Gahagan et al. [32-34] set out to measure the intrinsic shock rise time in Al using a femtosecond laser. A femtosecond laser-generated shock removes any broadening that might be caused by tilt or flatness of an impactor. The sample was a homogeneous vapor-deposited thin film only 1  $\mu\text{m}$  thick. A novel laser interferometer set up was developed that had femtosecond time resolution. Their results at 4 GPa are shown in Fig. 4. One complicating factor is that the probe

laser pulse does not see just the Al surface; it actually penetrates the surface down to a depth of a few nm. Correcting for this, a rise time  $t_r = 6.25$  ps was determined. We might imagine that a perfectly generated shock front in a thick slab of Al might start with a 6 ps risetime and spread out to 6 ns in 1 cm of propagation.

Based on this discussion we might expect shock front risetimes in homogeneous energetic materials to be quite short, but for practical energetic materials, the most significant issue is shock propagation through composites containing polycrystals of large molecules. Although shock propagation over macroscopic distances in lumpy impedance-mismatched composites is unlikely to support a planar shock front with a picosecond risetime, the question of whether thin layers of polycrystalline molecular materials can support fast risetimes was settled in 1997 [35,36]. The Dlott group used vibrational spectroscopy to measure the shock front risetime at 4 GPa in a 700 nm thick layer of polycrystalline anthracene ( $C_{14}H_{10}$ ), as depicted in Fig. 5. Anthracene is a brittle molecular crystal that appears to approximate a fluid above the Hugoniot Elastic Limit, so the anthracene vibrational response is fast and nonviscous. Coherent anti-Stokes Raman spectroscopy (CARS) was used to study the most intense Raman-active transition, denoted  $\nu_4$  (a symmetric ring-breathing mode) [35,36]. At ambient conditions this transition is located at  $1404\text{ cm}^{-1}$  with a FWHM of  $4\text{ cm}^{-1}$ . The temperature and pressure response of  $\nu_4$  was calibrated with a high pressure and high temperature cell [37]. Pressure causes a blueshift and temperature causes broadening. Figures 5a and 5e show the CARS

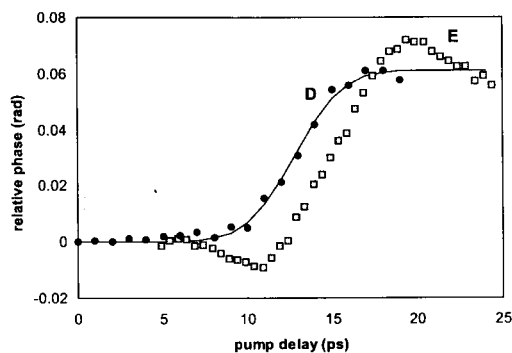


Fig. 4. Rise time of a 4 GPa shock in a thin film of Al generated by a femtosecond laser pulse. The open squares are the experimentally measured phase shift of interference fringes generated by a pair of femtosecond probe pulses monitoring shock breakout at the free Al surface. The solid circles are the data corrected for changes in the optical properties of Al. The shock front rise time  $t_r = 6.25$  ps. Reproduced with permission from ref. [32].

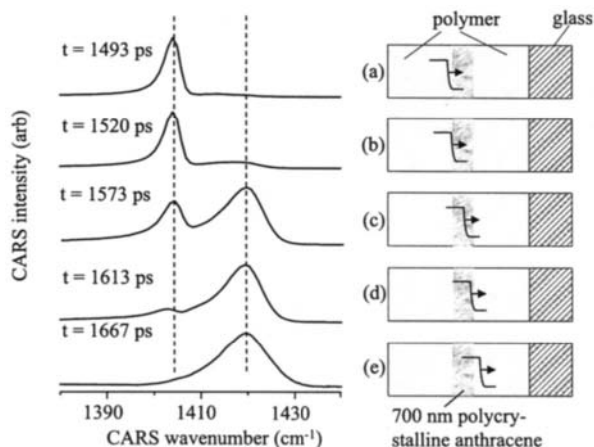


Fig. 5. Shock front rise time in a 700 nm thick sample of polycrystalline anthracene. (a)-(e) Coherent Raman (CARS) spectra of the  $\nu_4$  transition, which blueshifts and broadens when shocked at 4 GPa. The cartoons at right illustrate the progress of the shock front through an impedance-matched sandwich. When the shock front is midway through the anthracene layer, two separate peaks are seen in the CARS spectrum, representing ambient and shocked anthracene. The shock front risetime is considerably shorter than the shock transit time of 180 ps through the 700 nm layer. Detailed analysis shows that  $t_r < 25$  ps. Adapted from ref. [35].

spectrum of  $\nu_4$  of the thin layer of anthracene just before (Fig. 5a) and just after shock compression (Fig. 5e). The shock-induced blueshift gives the pressure as 4.2 GPa. A 4 GPa shock travels across 700 nm of anthracene in 180 ps. If the shock front had a gradual rise, then as it passed through the polycrystalline layer the pressure would build up gradually, and the CARS spectrum would gradually blueshift. If the shock front had a sudden rise, it would split the layer into two parts, as shown in the right hand side of Fig. 5. The spectrum at any time is observed to consist of two peaks, representing the shocked and unshocked parts of the layer. That immediately showed that the shock front risetime was  $\ll 180$  ps. The lineshapes in Fig. 5 were subjected to a rigorous mathematical analysis using the techniques of singular-value decomposition to show that the shock front risetime in this polycrystalline molecular crystal layer was  $< 25$  ps [35,36].

### 2.3 Detonations

A detonation refers to a shock wave in an energetic material that runs at a steady velocity driven by chemical reactions initiated at the shock front [38,39]. Due to damping at edges and surfaces, the detonation state can occur only if the sample is larger than the critical failure diameter [3]. With a few exceptions, the critical diameter is typically in the mm to cm range, so detonations are associated with macroscopic loads of energetic materials and are extremely powerful. For HMX, the detonation velocity is 9.1 km/s, the pressure is 39 GPa,



and the heat of explosion is  $\Delta H_{\text{expl}} = 11.1 \text{ kJ/cm}^3$  [3]. A 39 GPa pressure is enough to compress typical organic solids by a factor of about two [7,40].

The most remarkable feature of detonations is how (with a few problematic exceptions) each energetic material detonates at a characteristic constant velocity. In other words, detonation is a complex phenomenon but a dynamically stable state that can be described by a very few variables [38]. The first explanation of this was proposed by Chapman and Jouguet (CJ) around 1900. During a detonation (see Fig. 6) an energetic material changes from the unreacted state, say a cold molecular crystal, to the reacted state—a hot stew of small molecule gases. The CJ plane behind the shock front (Fig. 6a) is the location where the reaction is just complete. The region between the shock front and the CJ plane is the *reaction zone*. In the case of PBX 9501 (mostly HMX) detonation, the reaction zone is 0.1-1.0 mm wide, corresponding to a reaction time of 10-100 ns. CJ argued that a point of stability was found where the detonation velocity was equal to the shock velocity in this plane, i.e. the particle velocity plus the acoustic velocity of the reacted material. The velocity that satisfied this condition was the stable detonation velocity. In 1940 Zel'dovich, von Neumann and Doering (ZND) extended the model to include a gradual and smooth transition from unreacted material at the shock front to the CJ plane. Figure 6b shows the hypothetical Hugoniot of an unreacted and reacted

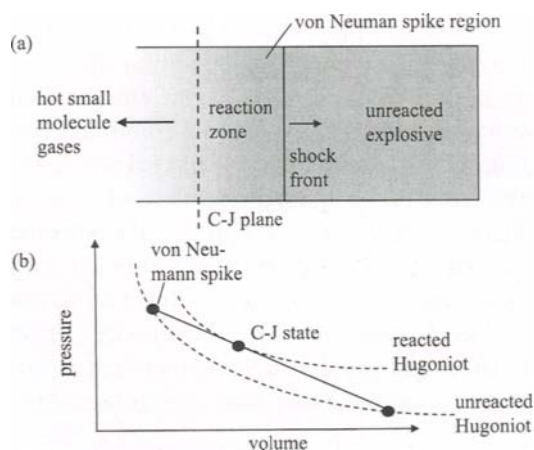


Fig. 6. Detonation in a slab of energetic material. (a) The detonation shock front runs at a constant velocity, driven by fast expansion of chemical reaction products. The highest pressure is in the von Neumann spike region just behind the front. At the Chapman Jouguet (C-J) plane the reaction is just complete. (b) Shock compression follows the indicated Rayleigh line to where it intersects the unreacted Hugoniot at the von Neumann spike. The point where this Rayleigh line is tangent to the reacted Hugoniot is the C-J state of stable detonation velocity.

material. For chemical decomposition of a larger molecule into many smaller molecules, the pressure at any given volume is greater in the reacted material. For a detonation to be stable, the shock front in the unreacted material must follow a particular Rayleigh line in Fig. 6b that is tangent to the reacted Hugoniot. Behind the shock front as the reacted material expands and does work, the pressure decreases. The pressure is highest just behind the shock front. This region of highest pressure is termed the “von Neumann spike”. The lower pressure at the CJ plane is the equilibrium detonation pressure. The CJ and ZND models describe the detonation state adequately [38]. The big problem in applying these models besides the complete absence of chemistry or molecular dynamics, is a lack of knowledge of these two Hugoniot [41]. It is difficult to obtain the unreacted Hugoniot at higher pressure because energetic materials want to detonate, but imagine detonating a material, collecting all the products, compressing and heating them to a high temperature and pressure and then performing shock experiments to measure the reacted Hugoniot. However a variety of theoretical methods have been developed for this problem, so the ZND model has proven to be an accurate description of 1D steady detonation waves. Around 1980 several efforts commenced, notably the work of Craig Tarver [42,43], to create a nonequilibrium ZND model that describes the detailed states of reacting molecules and vibrational excitations between the shock front and the CJ plane.

## 2.4 Low velocity initiation

Energetic materials can be made to react violently by relatively minor insults such as dropping a hammer a few feet [3,44-46]. This low velocity initiation (LVI) process can be unpredictable and is difficult to understand. LVI is often studied using a drop-hammer apparatus to determine a minimum height needed for a 50% chance of LVI of a particular energetic material ( $H_{50}$ ). The peak stress in a drop-hammer test is thought to be  $\sim 1$  GPa lasting for  $\sim 250$   $\mu$ s [46]. Some problematic observations are that LVI can be dramatically altered by changing the crystallite size, the binder composition and even by applying an organic monolayer to a metal drop hammer [41]. In fact different labs routinely obtain quite different results due to differences in hammer or experimental design [46,47]. Developing a deeper understanding of LVI is urgently needed to prevent dangerous or fatal accidents among workers who handle energetic materials. McNesby and Coffey [48] point out that a typical drop hammer impact adds enough energy to raise the equilibrium temperature of a bulk sample by only a few tens of degrees. Clearly low velocity initiation involves some process of localizing the drop hammer energy in small volumes of the sample that temporarily become much hotter than the bulk. This poorly understood process termed “hot spot formation” is ubiquitous in energetic material initiation [44,45]. Hot spots, originally proposed by Bowden and Yoffe in 1952 [44], are

formed by a variety of mechanisms that cause localization of some of the shock front energy in a small volume. These mechanisms include adiabatic compression of trapped gas in voids, friction involving sliding or impacting surfaces, shear band formation caused by mechanical failure, sparks, triboluminescence, heating at crack tips [44,45,49], and phonon pooling at anharmonic defects [50,51]. Due to the competition between heat loss and chemical ignition, a small colder hot spot might die out before it ignites its surroundings, whereas a larger hotter hot spot might grow and ignite an entire charge [52]. Thermal explosion theory has been applied by many authors to determine the range of critical hot spot sizes and temperatures that lead to unchecked growth [53]. When growing hot spots are generated, the impacted material will undergo widespread ignite. Although the existence of hot spots has been postulated for decades, direct observations have been few until relatively recently [52]. Direct observational methods see hot spots that are typically in the 0.1 to 10 mm range. A notable advance in the study of macroscopic hot spot behavior was the introduction of IR emission techniques. Miller et al. in 1985 [54] used a high speed IR detector to observe localized heating in crystalline solids during LVI, and Woody and co-workers [55,56] used a high speed IR imaging array.

Very little is known about the molecular mechanics associated with hot spot formation. Some insights have been provided by molecular dynamics simulations of lattices with purposely introduced defects [57-62]. A truly remarkable observation was made by Coffey and Sharma in 2001 [63]. They used an atomic-force microscope (AFM) for *post mortem* studies of crystals of RDX following hammer impact. Figure 7a is an AFM image of the RDX surface prior to the drop, showing a perfect array of individual molecules. Figure 7b shows the surface after an impact from a height well below  $H_{50}$ . The permanent damage observed consists of molecules that are displaced and reoriented in all directions. Images obtained from drop hammer and shock

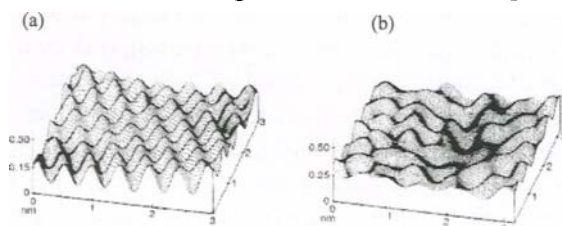


Fig. 7. Atomic force microscope (AFM) images of an RDX crystal. (a) A perfect crystal lattice is observed on a smooth cleavage plane surface. (b) After drop-hammer impact from a height well below  $H_{50}$ , individual molecules are displaced and reoriented. Reproduced with permission from ref. [63].

experiments have been analyzed to make estimates of local heating rates on the nanometer length scale. These images hint at some of the complexities that will be needed to describe hot spot formation starting from individual molecules and continuing to at least the mm length scale either by combining nanoscale molecular dynamics with mesoscale material simulations, or by combining analytical and numerical models [53,64].

## 2.5 Shock initiation

Shock initiation is used to reproducibly cause detonation in explosive devices [38]. Most practical devices use a sensitive primary that can be triggered electronically or by impact to send a shock wave into the secondary that results in a steady detonation. Ordinarily the initiating shock is much smaller than the steady detonation pressure, which is termed an “underdriven” initiation. The minimum shock initiation threshold pressure is usually obtained from a gap test [46]. A calibrated charge is used to launch a shock through varying thicknesses of PMMA plates (gaps) to the explosive packed to 90% of theoretical maximum density. The threshold pressure  $P_{90}$  is that which detonates 50% of the samples. The value of  $P_{90}$  increases with decreasing shock duration, and in fact the usual initiation criterion is that  $P^2t = \text{constant}$  [41]. For typical microsecond shock initiation of useful energetic materials,  $P_{90}$  is usually in the 0.5-5 GPa range. Two classic papers published in 1961 by W. C. Davis and co-workers [65,66] used a large body of accumulated experimental results to explain how the basic initiation phenomenon was fundamentally different in homogeneous and heterogeneous composite solid explosives. The fundamental differences are illustrated in Fig. 8.

Underdriven shock initiation of homogeneous explosives (Fig. 8a-d) is well-described by a thermal explosion model. When a shock enters a homogeneous explosive, it starts to grow weaker. Ignition in the compressed liquid first occurs where the shock entered, where the explosive has been hot for the longest time. The time between shock entry and ignition is termed the *induction time*, which may be several microseconds. Ignition leads to *deflagration*, defined as widespread rapidly propagating chemical reactions, which transitions into a *superdetonation* in the compressed material. A superdetonation is a detonation in a material that has already been compressed. The superdetonation in the compressed liquid behind the shock front catches up with the initiating shock front (Fig. 8c) and they combine and relax along the Rayleigh line in Fig. 6b to form a steady-state detonation. A beautiful illustration of this process was obtained by C. S. Yoo and co-workers in 1995 [67,68], who used a fast calibrated emission apparatus to measure the blackbody radiation from two different homogeneous explosives, liquid NM and large single crystals of PETN. In those studies the detonation was overdriven—the initiating shock front was actually larger than the steady detonation. Overdriven

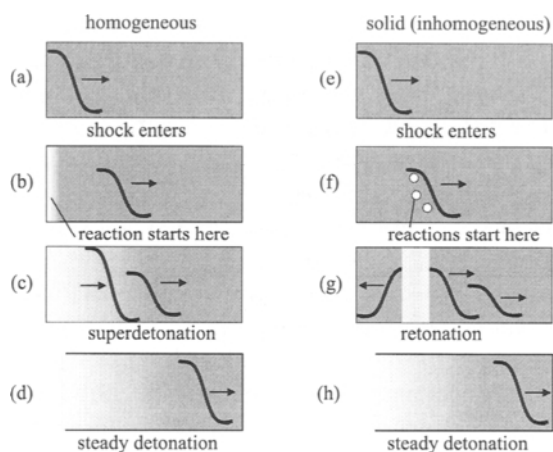


Fig. 8. Schematic of shock initiation of energetic materials, based on refs. [65] and [66]. In a homogeneous material such as liquid NM (a)-(d), ignition begins first at the entry face which has been hot for the longest time. The delay between shock entry and ignition is termed the induction time. A fast reaction in the compressed material (superdetonation) runs up to the shock front, eventually relaxing to a stable detonation state. In an inhomogeneous material (e)-(h), ignition begins first at hot spots behind the shock front. Generation of a stable detonation wave is accompanied by a backwards detonation (retonation) that consumes the unreacted material near the entry face.

initiation was used to minimize delays and assure a rapid transition to detonation. With NM shocked at 10.7 GPa, the temperature rose to 2800K in the ignition zone near the shock entrance. The superdetonation temperature was 4300K, and when a steady detonation was achieved, the CJ temperature was 3800K. A similar superdetonation with somewhat different temperatures was also observed in PETN single crystals. More recently, these prototype homogeneous explosives NM and PETN have been studied in detail by Gupta and co-workers as a function of shock conditions. They measured NM emission, Raman spectra and temperature [13,69-73], and PETN emission and absorption [74,75].

Shock initiation of inhomogeneous explosives (Fig. 8e-h) is generally associated with the formation of hot spots behind the shock front. Hot spots large enough to grow will ignite the material just behind the shock front. A rapidly moving deflagration front is launched in both the forward and backward direction (Fig. 8g). The backward moving wave transitions into a *retonation*. The forward moving wave catches up with the initiating shock to transition into a steady detonation (Fig. 8h). As mentioned above, hot spots are notoriously difficult to observe directly [52], so until recently most of the evidence for hot spots came from the increase in shock sensitivity caused by purposely adding voids or defects.

## 2.6. Sensitivity

Sensitivity is a term that refers to a material's tendency to explode under conditions that are often considered safe. Sensitivity depends simultaneously on three rather complicated factors, the nature of the *stimulus*, the *chemical composition* and the *physical or mechanical state*. The dependence on stimulus has given rise to a large number of sensitivity measurements, including several variants of the drop hammer and gap tests mentioned above, and measurements of the critical failure diameter. The claim is often made that impact sensitivity is highly correlated with shock sensitivity [46], which if true would be a great simplification. While this may be true in some cases, and a rough correlation certainly exists, the actual evidence for a strong correlation is flimsy [47]. Sensitivity is not solely a function of the chemical composition. Two samples with the same chemical composition may have vastly different sensitivities. For instance a single bubble in a beaker of NM can lower its shock sensitivity by an order of magnitude [44]. Pressed TNT can have four times the shock sensitivity of cast TNT [3], so TNT could be either more or less sensitive than RDX. Different isomorphous forms of HMX crystals have dramatically different sensitivities [3]. Shock initiation of large single crystals of PETN, RDX, NM and HMX depends a great deal on the direction of shock propagation [76-78]. Plastic explosives with larger crystallites are more sensitive but less powerful. On the other hand certain materials are clearly less sensitive than others regardless of physical state. For instance there appears to be no way to make a TATB formulation be less sensitive than a PETN formulation.

The urgent need to develop a reliable predictor of a material's sensitivity has given rise to a sizeable literature on the subject, and the quality of much of this literature is quite poor. Many researchers in the field appear to believe that there is a Raman spectrometer or an Auger or NMR spectrometer or a quantum computer code package that, if only used properly, would in one fell swoop characterize an energetic material's sensitivity. However this search for a "magic bullet" is totally illogical in light of the abovementioned discussion--that a science of sensitivity must take into account the simultaneous dependence on stimulus, chemical composition and mechanics. Some of the properties that have been claimed to be quality predictors of sensitivity include the thermal conductivity [44,45], the carbon Auger line shape [79], shake-up promotion energy from XPS spectra [80], the C-NO<sub>2</sub> bond length and its electrostatic potential [81], the HOMO-LUMO gap [82], the density of hydrogen bonds [79], the density of vibrational states near 425 cm<sup>-1</sup> [48,83,84], and so on.

Brill and James [47] wrote a beautiful yet cynical paper that examined the problem of low quality or illogical correlations between molecular properties and sensitivity. They focused on a set of four closely related amino-substituted trinitrobenzenes that are often used as model compounds [46] in the sensitivity

studies listed above. They examined the correlations between various measures of sensitivity and many properties claimed to be sensitivity predictors. Many claims in the literature were found to be contradictory and many were chemically absurd. For example, many predictors involve C-NO<sub>2</sub> bond properties. It should then follow that low-temperature thermal decomposition experiments that measure the initial step of C-NO<sub>2</sub> bond cleavage should also be a good predictor of sensitivity, which turns out to be wrong [47]. That is because in these systems the later reaction steps and chemistry at defects and surfaces play a more important role in sensitivity.

One of the most significant problems with the search for sensitivity predictors lies in the *misuse of correlation analysis*. It is a fundamental rule of statistical analysis that *the data that are used to infer a correlation cannot be used to prove its existence*. So if a study of these four substituted benzene compounds suggested that sensitivity is correlated with some spectroscopic transition or some bond parameter, then the existence of this correlation can only be proven by examining its validity using a large number of other materials not used to infer the correlation's existence. A true theory of sensitivity that resulted should be better than one which simply reaffirms the position of four compounds on a sensitivity plot—it should be equally able to tell us the relative sensitivities of new and different explosive compounds and in addition that nonexplosive compounds such as sodium chloride or liquid nitrogen will not explode.

A useful theory of sensitivity must seamlessly combine stimulus, chemistry and mechanics. Of course the stumbling block for this and for many problems in materials science is the high degree of difficulty of determining which structures will have a desired property or function. A useful approach might be to consider what qualities an ideal insensitive explosive might have. First of all, there must be an absence of mechanisms that tend to concentrate energy, for instance the mechanical structure should disfavor the creation of hot spots. A larger heat capacity and a larger thermal conductivity helps suppress hot spot formation. Second, shock-induced heating should be minimal, which Eq. (4) shows happens when materials are less compressible and have a smaller Grüneisen parameter. This particular criterion is especially useful, inasmuch as the relationships between molecular structure and compressibility and anharmonicity are reasonably well understood [22]. For instance an extensive hydrogen-bonded network lowers the compressibility which might help explain the insensitivity of TATB and NTO. Third, the chemical reaction scheme that runs up to initiation should feature several highly endothermic initial steps with high reaction barriers so that the exothermic steps leading to explosive runaway occur later rather than sooner [85].

### 3. MOLECULAR LEVEL STRUCTURE OF ENERGETIC MATERIALS

In this section I will briefly review the molecular levels of energetic materials and discuss some of the consequences for shock-induced chemistry and shock initiation. The emphasis will be on processes that break the first bonds of relatively stable molecules. Discussions of the highly complicated chemistry that follows the initiation step can be found in many reviews, but are outside the scope of this chapter.

#### 3.1. How chemical bonds are broken

Chemical reactions occur in molecules that are activated by vibrational excitations, electronic excitations or some combination of both. It is also possible to have chemistry by direct mechanical breaking of bonds (tribochemistry). Figure 9 is a simplified molecular level diagram, that represents a slice of the Born-Oppenheimer potential energy surface along a particular coordinate that could be identified with the reaction coordinate. A large molecule with  $N$  atoms will have  $3N-6$  vibrational coordinates. In the ground electronic state, the minimum energy required to break a bond is  $D_0$ . It is possible to do this purely by mechanics. With today's nanotechnology, a large molecule can be attached to two macroscopic objects, say two polymer beads, and the two beads pulled apart until the weakest bond breaks [86]. A sharp knife

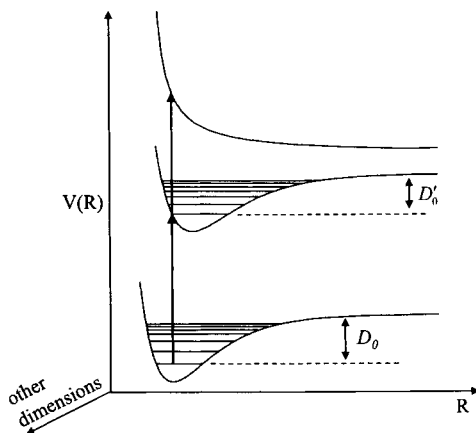


Fig. 9. Potential energy diagram for breaking chemical bonds in an energetic molecule. The specific coordinate  $R$  shown here is identified as the reaction coordinate. In ascending energy these levels are the electronic ground state, a bound excited state and a dissociative excited state. Thermal cleavage of a bond in the electronic ground state requires a minimum energy  $D_0$ . In bound electronic states the bond dissociation energy  $D_0'$  is usually smaller than  $D_0$ , so thermochemistry often has a lower barrier electronic excited states. Chemical bonds can also be broken by electronic excitation to predissociative or dissociative electronic states.



or band saw cutting an extended polymeric solid such as a piece of plastic tubing will break  $\sim 10^{14}$  bonds per second [41]. This knife chemistry works for extended polymers, but it might not work for molecular crystals. The knife most likely would cut between the molecules, and would only rarely break a chemical bond.

Thermal decomposition studies of energetic materials with relatively low heating rates represent a huge literature [39]. Low heating-rate studies of energetic materials are highly relevant to situations where slow heating (cookoff) leads to accidental explosions [85]. There has been some effort devoted to measuring higher heating-rate processes. The complex scheme of chemical reactions that characterizes thermal decomposition, ignition or detonation of large organic molecules can change quite a bit with heating rate, even at relatively low heating rates of 100K/s. So there is spirited debate about the relevance of low-heating rate studies to fast processes such as shock initiation [47].

Conventional models of thermochemistry envision a molecule in contact with a thermal bath which is chemically active along a particular coordinate (the "reaction coordinate"). For isolated molecules the bath is the other  $3N-5$  vibrations, and for condensed phase molecules the bath consists of these  $3N-5$  intramolecular states plus a vast number of states of the other molecules. In order to break a bond, the molecule has to have an internal energy termed the "activation energy"  $\Delta E^*$ . The value of  $\Delta E^*$  is usually somewhat greater than the energy to break the bond  $D_0$  because it is statistically improbable for all the energy in the molecule to be temporarily concentrated in the reaction coordinate. For instance, for HMX  $D_0$  for breaking a C-NO<sub>2</sub> bond is  $\sim 140$  kJ/mol [87] and  $\Delta E^*$  from low-heating rate experiments is 218 kJ/mol [88].

Electronic excitations may become involved in two ways. In the bound electronic states (Fig. 9) often the activation energy  $\Delta E^*$  is smaller than in the ground electronic state, so thermochemistry is usually easier in electronic excited states. In predissociative states there is a barrier to dissociation, but it is minimal compared to the translational energy imparted by electronic excitation. In dissociative states (Fig. 9), electronic excitation leads directly to bond breaking without any thermal energy at all. The electronic states and photochemistry of the molecules that compose many energetic materials, including RDX have been studied using molecular beam techniques, notably by Chris Capellos [89] and in the laboratory of Elliot Bernstein [90].

### 3.2 Band structure of molecular solids

A molecular crystal consists of a individual molecules held together by nonbonded interactions [22]. The fundamental concept that is used in essentially all theories of molecular solids is that there are *two quite different types of bonds*. There are strong intramolecular bonds that hold together the atoms in

individual molecules, and weaker intramolecular bonds that hold the molecules together in a crystal. This is not the case in ionic or metallic crystals. If we look into a benzene ( $C_6H_6$ ) crystal and we find a carbon and a hydrogen atom, we can know with certainty whether they are a bonded pair on the same molecule or a nonbonded pair on two different molecules. This concept is expressed quantum mechanically in the form of a zeroth-order Hamiltonian that describes a bunch of isolated noninteracting molecules, and a perturbation Hamiltonian that describes their intermolecular interactions [21]. The eigenstates of this zeroth-order Hamiltonian are simply the energy levels of the individual molecules—translations, rotations and electronic states. When weak coupling between these molecules on an infinite periodic lattice is added, molecular translations and rotations become extended states called *phonons*, molecular vibrations become *vibrons* and electronic excitations become *excitons*. The nature of phonons and vibrons depends on whether the molecules are rigid or flexible. A rigid molecule is one that will not vibrate no matter how hard you shake it. A flexible molecule is one that flops around when you shake it, meaning lower frequency vibrations associated with bending motions of larger molecular groups become excited. Flexibility is expressed in quantum mechanics by incorporating *anharmonic corrections* in the Hamiltonian, that is terms which contain products of phonon and vibrational coordinates [21]. A rigid molecule has two totally independent sets of harmonic energy levels corresponding to translations and vibrations. A flexible molecule has a degree of anharmonic coupling between the translations and vibrations. These concepts and their effects on band structure are illustrated in Fig. 10.

Figure 10a shows a 1D lattice of diatomic molecules. In the extreme case of totally rigid molecules, exciting the phonons (shaking the molecule) cannot excite molecular vibrations (vibrations along the chemical bond). There will be a large gap between the phonon cut-off frequency (Debye frequency) and the vibron energy [91]. The vibron band has dispersion, that is the energy is independent of the wavevector  $k$ , because a vibration on any molecule would not care what its neighbors were doing. If we now add some realism, namely a bit of flexibility to the molecules, several interesting things happen. First the translational motion associated with the acoustic phonons becomes mixed with vibrational motion. In other words the chemical bond stretches a little bit when the molecules are shaken. A molecule translates a little bit when it vibrates, so the vibrational energy acquires a dependence on the vibration of neighboring molecules. This creates a vibron band with a degree of dispersion. Molecular flexibility causes the gap between the phonon band and the vibron band to narrow.

Two new dynamical processes become possible in the diatomic lattice shown in Fig. 10a as a result of molecular flexibility, as represented by anharmonic coupling between phonons and vibrations. First, a vibrationally

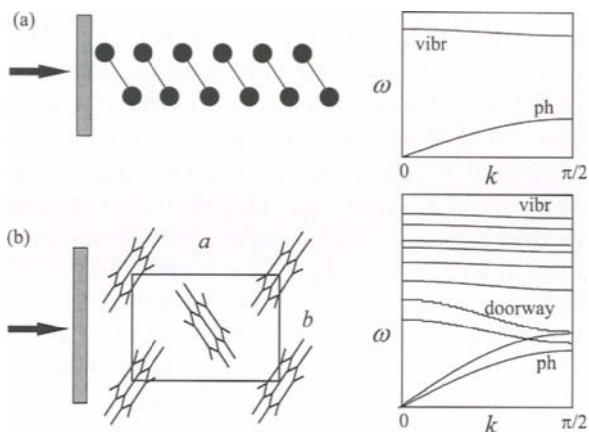


Fig. 10. (a) A 1D lattice of rigid diatomic molecules. The dispersion curve for acoustic phonons that result from translations runs from zero frequency to a cut-off termed the Debye frequency. The vibron has no dispersion. Adding flexibility to the molecules introduces dispersion in the vibron state and narrows the gap between vibrons and phonon as shown at right. (b) A 3D lattice of flexible naphthalene molecules. The 12 phonons overlap significantly with the two or three lowest energy vibrations, termed doorway modes. Doorway modes are coupled to both phonons and higher frequency vibrations associated with bond breaking. Adapted from ref. [91].

excited molecule can lose its energy by simultaneous emission of phonons. The order of this multiphonon relaxation process (the number of phonons) is approximately equal to the vibrational frequency divided by the Debye frequency. This process is termed *vibrational energy relaxation* (VER) [92-94]. Second, a similar number of phonons can combine to produce a vibrational excitation. This phonon-to-vibration process is termed *multiphonon up-pumping* [50].

Figure 10b depicts the case of a 3D lattice, once again the model system naphthalene [22]. Naphthalene with 2 molecules per unit cell, has 3 acoustic and 9 optic phonon branches, whose direction-dependent dispersion curves have been measured via neutron scattering and calculated using lattice-dynamics methods [95]. The 48 normal modes of vibration fall into three distinct classes. Many higher frequency vibrational modes such as C-H stretching ( $\sim 3000 \text{ cm}^{-1}$ ) or symmetric C-C stretching ( $500\text{-}1600 \text{ cm}^{-1}$ ) closely approximate rigid molecule behavior. Other higher frequency modes such as C-H bending ( $1500\text{-}1600 \text{ cm}^{-1}$ ), which would properly be viewed as vibrons, evidence a small but measurable dispersion that indicates an interaction of a few  $\text{cm}^{-1}$  between adjacent molecules. The two or three lowest energy vibrations, including the  $\sim 175 \text{ cm}^{-1}$  “butterfly” vibration of the two coupled rings and the  $\sim 212 \text{ cm}^{-1}$  twisting mode, are strongly mixed with higher frequency phonons [96]. In other

words, shaking naphthalene causes the rings to flap and twist. Such special lower energy vibrations are termed “doorway vibrations” [50]. The term “doorway vibrations” is applied to vibrations that have a significant degree of coupling to both phonons and the higher energy vibrations. They are the doorway for energy transfer from shock waves outside the molecule to the higher energy vibrations inside the molecule associated with bond breaking. In energetic materials, characteristic doorway vibrations are associated with C-NO<sub>2</sub> bending and NO<sub>2</sub> rocking [83].

### 3.3. Molecular crystals under dynamic shock compression

In this section we discuss how shock compression produces electronic and vibrational excitations that can cause chemical reactions. It is an outline for a theory that connects the fluid-mechanical picture of shock compression to the quantum mechanical picture of chemical reaction dynamics.

#### 3.3.1 Shock-induced electronic excitations

Shock-induced electronic excitation is simple in fluids but problematic in solids. The theory described in Zel’dovich’s book [1] to describe strong shocks in air shows that shock-induced electronic excitations become significant when the temperature behind the shock front  $T_1$  becomes large enough to create electronic excitations (thermoelectronic excitation). The probability of a molecule being electronically excited is simply proportional to the Boltzmann factor  $\exp(-E_{el}/k_B T_1)$ , where  $E_{el}$  is the energy of the lowest electronically excited state, keeping in mind that  $E_{el}$  tends to decrease with increasing pressure. Typically the energy of the first electronically excited state of a stable closed-shell molecule such as N<sub>2</sub> is several eV, several times 10,000 cm<sup>-1</sup>, or equivalently several thousand degrees K. Many open-shell molecules such as O<sub>2</sub> have low-lying electronic states that are easily excited by shock compression, but these low-lying multiplets are generally not associated with chemical reactions. Shock compression of air readily produces electronic excitations due to the high compressibility of gases. But in condensed matter which is much less compressible, the high temperatures that lead to electronic excitations (in the absence of high-energy chemical reactions) are difficult to produce. Recently Fried, Joannopoulos and co-workers used powerful advanced quantum molecular dynamics techniques to look at shock-induced electronic excitation in NM [97] and HMX [98]. They showed that in an unreactive solid, the shock pressures needed for electronic excitation were on the order of 100 GPa, which is quite a bit beyond any CJ detonation pressure.

If this argument appears to show that electronic excitations are irrelevant to LVI or shock initiation of solids, think again. A series of observations dating back to the Renaissance [99] shows that the simple theory of thermoelectronic excitation in fluids does not explain an important process in solids, termed

triboluminescence or fracture-induced emission. Merely grinding sugar with a mortar and pestle can produce blue light generated by electronic excitations in the  $\sim 3\text{eV}$  region [99]. There is a sizeable descriptive literature on fracture-induced emission, but the fundamental mechanisms remain cloudy. Fractured solids (even pure ice) can emit photons, electrons, ions, and neutral molecules [100,101]. Although the ability of rather small mechanical insults or shocks to generate visible and UV light is poorly understood, clearly some energy concentration mechanisms are at work. These are generally associated with low-probability charge generation at moving crack interfaces [102]. The combination of excess charge and large amplitude motion can lead to large electric fields and a variety of electron-impact processes that can generate both light and energetic chemical species. The combination of energetic materials with low probability high energy events is a volatile one that is difficult to handle theoretically. These high energy processes are never seen in molecular simulations because simulations are poorly equipped for studying unlikely but significant events, particularly if these are molecular events resulting from large amplitude mechanical motion. The problem—and it is an enduring one—is the vast disparities of length and time scales that are required to understand energetic material dynamics. Simulations of shock-induced electronic excitations have to start with fracture on the mesoscale (length scales of perhaps 0.1 to 100  $\mu\text{m}$ ), but each finite-volume element has to seamlessly incorporate nanoscale quantum mechanical molecular properties needed to properly describe electronic excitation and field ionization. More effort along these lines coupled with well-characterized experiments is needed.

### 3.3.2 Shock induced mechanical excitations

Rapid compression by a very steep shock front traveling in a particular direction in an anisotropic molecular solid will not excite all mechanical states equally. For instance consider Fig. 10b, which depicts a shock moving along the  $b$ -axis of naphthalene [20]. Figure 10b suggests that a shock front will preferentially excite translational phonons with wavevectors along the  $b$ -axis, along with librons in the  $ac$  plane. Higher frequency motions such as C-H stretching vibrations seem unlikely to be excited directly. How can we determine which specific states are initially excited by the shock front? The Grüneisen parameter  $\Gamma$  in Eq. 4 characterizes the change in internal energy (heat) with changes in volume. It is well known that  $\Gamma$  can be written in terms of the individual phonon and vibron states [15],

$$\Gamma = \frac{\sum_i \gamma_i (C_v)_i}{\sum_i (C_v)_i}, \quad (6)$$

where  $C_v$  is the constant volume heat capacity, and  $\gamma_i$  is the Grüneisen coefficient of mode  $i$ . These mode-Grüneisen coefficients are given by [15],

$$\gamma_i = \frac{\partial \ln \omega_i}{\partial \ln V}. \quad (7)$$

Extending Eqs. (6) and (7) one step further, Jindal and Dlott [20] introduced a *uniaxial mode-Grüneisen parameter*,

$$\gamma_{qi}^x = -\frac{\partial \ln \omega_{qi}}{\partial \ln x}. \quad (8)$$

The uniaxial mode-Grüneisen parameter is a direct measure of how much energy is transferred from a shock propagating along a particular direction to a particular mode. For instance in Eq. (8),  $\gamma_{qi}^x$  is the Grüneisen parameter for compression along the  $x$ -direction, for mode labeled  $j$  with wavevector  $\mathbf{q}$ .

Knowing the values of these uniaxial mode-Grüneisen parameters for all the states of a molecular crystal provides tremendous insight into the nature of the initial shock excitation. Quite a bit is known about mode-Grüneisen parameters from vibrational spectroscopy (IR or Raman) of crystals subjected to hydrostatic compression. In fact numerous studies of high pressure frequency shifts in molecular crystals show that phonons have the largest mode-Grüneisen parameters, followed by doorway vibrations and distantly trailed by higher frequency vibrations [22,95,103]. Little is known about the uniaxial mode-Grüneisen parameters since it is much more difficult to measure vibrational spectra with uniaxial strain. Craig Eckhardt [104,105] has developed a piezomodulated Raman spectroscopy technique that is useful in this regard, however piezomodulation experiments are always in the elastic limit, and large-amplitude measurements more relevant to shock compression do not exist. Accurate calculation of mode-Grüneisen parameters from first principles is difficult. Grüneisen parameters are a property of the anharmonic interactions, and so they are sensitive to minute details of the potential energy surface. Jindal and Dlott [20] calculated uniaxial mode-Grüneisen parameters for crystalline naphthalene, using a well-known high-quality potential energy surface that is known to accurately reproduce experiments such as neutron scattering measurements of direction-dependent phonon dispersions [95]. Knowing the uniaxial mode-Grüneisen parameters for every state of the crystal, Jindal and Dlott were able to calculate the bulk Grüneisen parameter and the bulk Grüneisen tensor for naphthalene and to determine the temperature rise as a function of shock propagation direction shown in Fig. 2.

### 3.3.3 Dynamic picture of shock excitation

We can now outline a dynamic picture of the way a planar shock front produces vibrational excitations in molecular crystals that are needed for the initial endothermic steps of thermochemical bond breaking. As a shock front moves through a molecular solid, it deposits its energy preferentially into states with larger uniaxial mode-Grüneisen parameters. These will primarily be phonons whose wavevector runs parallel to the axis of shock propagation. For larger flexible molecules, doorway vibrations may also be excited, for instance wagging of  $\text{NO}_2$  groups oriented parallel to the shock front. Then as a result of anharmonic coupling, the energy will be redistributed among all the other states of the crystal until thermal equilibrium is attained at a new higher temperature  $T_1$  given by Eq. (4) or Eq. (5). Based on the two quite different kinds of chemical bonds in molecular materials, this redistribution process can be divided into *two phases*. First the specific phonons excited at the shock front equilibrate with the rest of the phonons. This is the faster phase because the largest anharmonic couplings are the couplings among phonons. It has often been suggested that phonon equilibrium occurs within about 1 ps [106-108]. Supporting evidence for this view comes from anharmonic lattice calculations of naphthalene [23]. For two states to exchange energy within 1 ps, the anharmonic coupling must be on the order of  $15 \text{ cm}^{-1}$ . For most higher frequency phonons of naphthalene (in the  $50\text{-}150 \text{ cm}^{-1}$  range), 10-30% of the phonon frequency is due to anharmonic terms in the Hamiltonian [23]. Second the equilibrated phonons excite molecular vibrations via multiphonon up-pumping, which is the slower process because molecular vibrations are ordinarily quite a bit less anharmonic than phonons.

The key parameter in this two-phase model is  $t_r/\tau_{up}$ , where  $t_r$  is the rise time of the shock front and  $\tau_{up}$  is the time constant for multiphonon up-pumping. For gradually rising shock fronts,  $t_r/\tau_{up} > 1$ . In this case redistribution is faster than the gradual rise of the shock front so all the phonons and vibrons heat up together, always remaining in thermal equilibrium as the temperature gradually rises from  $T_0$  to  $T_1$ . For steeply rising shock fronts,  $t_r/\tau_{up} < 1$ . In this case the shock front produces a highly nonequilibrium mechanical state consisting of a dense sea of extremely hot mobile delocalized phonons which persists for a few multiples of  $\tau_{up}$ . After this time phonons and vibrations are in equilibrium at temperature  $T_1$ . The thin phonon-rich layer behind the shock front where multiphonon up-pumping is rapid and efficient has a width  $\ell_{up}$  given by  $\ell_{up} = U_s \tau_{up}$  [50,51].

With slow up-pumping only a time-dependent thermodynamic temperature  $T(t)$  is needed to describe the state. In a nonequilibrium system where phonons and vibrations are pumped at different rates, a much larger number of parameters are needed to specify the state. Dlott and Fayer simplified

this problem by assuming that phonon-phonon and vibration-vibration equilibration processes are fast [50]. In that case only two time-dependent variables, termed quasitemperatures, are needed to describe these two thermal baths. The phonon quasitemperature  $\theta_{ph}$  is the effective temperature of the shock-excited phonons, and the vibration quasitemperature  $\theta_{vib}$  is the effective temperature of the molecular vibrations. Passage of a shock front causes an immediate jump in  $\theta_{ph}$  and a delayed jump in  $\theta_{vib}$ . A shock that raises the temperature from  $T_0$  to  $T_1$  deposits an amount of energy per unit volume equal to [50,51],

$$E_1 - E_0 = \int_{T_0}^{T_1} C_v(T) dT = \int_{T_0}^{T_1} [C_{v,ph} + C_{v,vib}(T)] dT. \quad (9)$$

If all the energy  $E_1 - E_0$  is initially input to the phonons only, then the initial phonon quasitemperature  $\theta_{ph}(0) = (E_1 - E_0)/C_{v,ph}$  will be much greater than the final temperature  $T_1$ , because the phonon heat capacity  $C_{v,ph}$  in Eq. (9) is much smaller than the total heat capacity of phonons plus vibrations,  $C_v(T)$  [50]. For instance with a shock that heats naphthalene by 400K, the initial phonon quasitemperature  $\theta_{ph}(0)$  is nearly 2400K [51].

The up-pumping model says that instead of the molecule's vibrations becoming activated right at the shock front, there is a brief delay before vibrational activation occurs. This might be a trivial and unimportant feature of shock excitation—just an irrelevant brief delay—unless the nonequilibrium conditions that persist during this brief time play a significant role in shock initiation. Several possible ways that up-pumping can affect explosive sensitivity are discussed in the next section.

### 3.4 Shock compression of nanometric energetic materials

Nanometric energetic materials are a novel type of nonideal energetic materials containing metal particle fuels with diameters in the 20-1,000 nm range [109]. The attraction of nanometric materials are the potential for high energy release and the possibility of applying precision supermolecular engineering to explosives design. It has long been recognized that two-component explosives consisting of metal particle fuels and oxidizers can produce more than twice as much as high-performance molecular explosives such as HMX [109], where the heat of explosion is 11.1 kJ/cm<sup>3</sup>. For instance Al + (poly)-tetrafluoro ethylene (PTFE) is predicted to release 22 kJ/cm<sup>3</sup>. A variety of widely used undersea explosives and rocket propellants [110] have been developed, containing Al particles typically 30  $\mu$ m average diameter with a wide size distribution. These materials have a number of problems including relatively slow energy release and poor fuel consumption efficiency [110]. Moving to nanometer-scale metal particles seems enticing, to provide faster



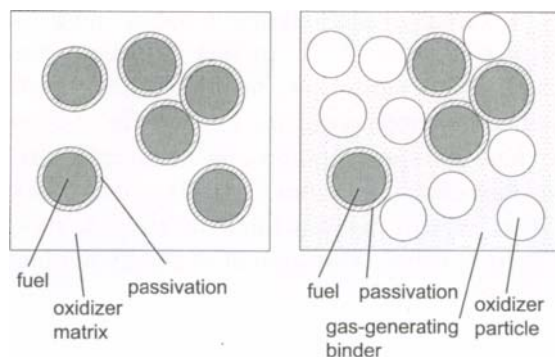


Fig. 11. Schematics of nanoenergetic materials. (*left*) A trinary system of nanometric metal particle fuel protected by a passivation layer, suspended in a uniform bulk oxidizer matrix. (*right*) Both fuel and oxidizer are nanoparticles, and a binder is used to generate gas that provides a working fluid.

energy release and better control over material homogeneity and material properties, and new nanometric formulations have recently been tested as propellants [111,112] and explosives [113].

Figure 11 shows that nanometric energetic materials have at minimum three different parts [114]. The fuel portion consists of nanoparticles of zero-valent metals, especially Al and B. The oxidizer portion may be either a continuous polymer such as a fluoropolymer [115], or oxidizer nanoparticles such as  $\text{MoO}_3$  [109,116]. A key feature is the fuel's passivation layer that keeps the fuel from oxidizing prior to ignition. Usually this layer is the native oxide 3–5 nm thick that forms spontaneously on the surface of Al or B particles upon exposure to air. Another possibility suggested by the broad usage of self-assembled monolayers (SAMs) is a dense organic monolayer [117], perhaps with long fluoroalkane tail groups, whose properties could be tailored using the techniques of synthetic organic chemistry. Nanoenergetic formulations may also contain a gas-generating component to provide working fluid for the rapid expansion. Fluoropolymers or energetic materials such as HMX have been used for this purpose.

Initiation of nanoenergetic materials requires a break down of the passivation layer to bring a bare metal surface into contact with oxidizer. Although the growth of oxides on Al clusters has been investigated by high-quality molecular simulations [118], the dynamic depassivation process has not been studied much. Microphotographic evidence exists to show that with slow heating rates the metal core begins to melt, and the volume expansion associated with heating and phase transitions can produce cracks in the oxide shell [119], allowing the liquid metal to leak out. This melting and cracking mechanism is probably not important for shock initiation. Systems such as those depicted in

Fig. 11 present a significant nanoscale spatial variation in shock impedance. For instance in an Al/PTFE composite, the ratio of shock impedance Al/PTFE is about six (the shock impedance is the product of the sound velocity and the density [5]). With this level of impedance mismatch, the pressure transmitted to Al from shocked PTFE would be only ~30% of the incident pressure [5]. Thus a steep shock front would undergo multiple scattering by the metal nanoparticles embedded in a polymer, causing the shock front risetime to increase significantly [120]. Since PTFE is quite a bit more compressible than metals, the initial temperature of PTFE behind a shock front will be quite a bit higher than Al. Thus we should think of shock initiation not in terms of fast mechanical activation processes with up-pumping, but as the result of an attack of hot oxidizer on the passivation layer of colder metal particles. Some insights into the molecular basis for this attack process might be obtained by looking at experiments where passivated metal surfaces in vacuum are bombarded by energetic particles or molecules.

#### 4. UP-PUMPING, SENSITIVITY AND IGNITION

In this section we will explore the relationships between the multiphonon up-pumping rate and explosive sensitivity to low velocity impact or initiating shock initiation. We focus on up-pumping because it is a key process that allows the seamless fully quantum mechanical connection of large amplitude mechanical processes such as cracking, dislocation formation, moving edge dislocations and shock compression to the initiation chemistry. The idea of this section is to explore the effects of weaker mechanical insults that lead to ignition, rather than the chemistry behind a strong detonation wave that will be discussed below. Given a relatively weak stimulus, we must concentrate on processes that can localize energy in a small volume such as a thin layer behind a shock front or at a defect. If the dynamic up-pumping process is to be relevant, there must be a fast component to these stimuli, that is they should obey the criterion  $t_r/\tau_{up} < 1$ , otherwise up-pumping is nothing more than an irrelevant brief delay in the heating process. For instance, accidental ignition of explosives caused by slow stimuli such as a slowly rising temperature due to a fire would not be expected to be sensitive to the up-pumping rate.

The structure of shock fronts in simple molecular gases such as  $N_2$  and  $O_2$  has been studied since the 1950's [1,121]. Kinetic theory provides a powerful framework for analyzing gas-phase shock fronts, and a wealth of data exists to characterize collisional processes in gases. Kinetic theory provides a characteristic length scale to describe the shock front, the mean-free path  $\lambda = 2^{1/2}\rho\sigma$ , where  $\sigma$  is the collision cross-section. For  $N_2$  at STP,  $\lambda = 65$  nm and the average time between collisions is 140 ps. The undisturbed molecules ahead of the shock front are hit by a stream of molecules having a net velocity along the

shock propagation axis. It takes a few collisions with the undisturbed molecules to get them up to speed, so the shock front is a thin layer whose width is a few multiples of the mean-free path. However it takes more collisions to bring the rotational temperature and the translational temperature into equilibrium, typically 10's of collisions for rotations and 1,000's of collisions for vibrations [1]. Thus the vibrational temperature rise in a gas-phase shock might be delayed by hundreds of microseconds. In condensed phases there is no fundamental length scale corresponding to the mean-free path [1]. Together with the quantum mechanical nature of molecular vibrations, this has hampered progress in this area a great deal.

#### 4.1 Nitromethane shock initiation and the induction time

The original attempts to understand shock wave induced up-pumping and relate it to energetic material initiation began about 20 years ago, when the first calculations were made on NM. Provided all bubbles are carefully removed [65] NM is a homogeneous liquid, so the only mechanisms for energy localization involve the special thin layer just behind the shock front. The central idea in NM studies was to calculate the rate of phonon activation of the C-N stretch that is needed to break the C-N bond. Several authors also extended or extrapolated their NM calculations to speculate about what happens with RDX or HMX.

In 1979, Pastine *et al.* outlined the basic problem for shock wave-induced molecular excitation [122], including the separation of phonon and vibron states and the need to excite vibrations before chemistry could occur. Their formalism for calculating  $\tau_{up}$  for shocked NM turned out to be extremely sensitive to the values of parameters that were not well known. They estimated the time for phonon excitation of lower frequency bending modes (doorway vibrations) to be 700 ps, and the time for doorway-to-CN-stretch conversion to be many microseconds. This microsecond time constant is similar to the duration of typical initiating shocks and the NM induction time mentioned in Section 2.5 and Fig. 8(a)-(d). It was suggested that phonon up-pumping behind the shock front might be the cause of the induction time and thus the rate-determining step in NM initiation. In other words up-pumping caused a lengthy delay in vibrational activation behind the shock front, resulting in the microsecond induction time of NM.

In 1984, Zerilli and Toton [106] returned to the NM up-pumping problem using a quantum mechanical model that is well known in the context of radiationless transitions. This calculation again relies critically on a poorly-known parameter, namely the magnitude of the anharmonic coupling between phonons and vibrations. To determine this phonon-vibration coupling, they turned to an established theory for coupling between electronic excitations and vibrations characterized by the Huang-Rhys factor. They extended the Huang-Rhys formalism for electron-vibration coupling to the problem of phonon-

vibration coupling. Attempts were made to extract the magnitude of phonon-vibration anharmonic coupling from IR spectra of NM. These attempts relied on phonon-vibration energy exchange being the dominant influence on the vibrational lineshape. However in retrospect, we now know that other (pure dephasing) mechanisms are responsible for the vibrational lineshape in liquids [123], so an accurate determination of the anharmonic coupling from such spectra is impossible. Zerilli and Toton calculated that phonon pumping of NM doorway vibrations at 5 GPa occurred in 10 ns, and phonon pumping of C-N stretching was in 1 ms [106]. This extremely slow time constant for C-N activation, clearly at odds with observed induction times [65,68], was used to argue that conventional mechanisms of shock front heating of molecules could not explain shock initiation of NM. A new mechanism involving coherent excitation behind the shock front was proposed, which is discussed below.

In 1986 and 1989, Bardo [124,125] used radiationless transition models to calculate the time constant for shock wave pumping of the C-N stretch of NM to its dissociation limit. Bardo's calculations were based on recent developments in the field of collisionless intramolecular vibrational energy redistribution of large molecules [126], which alleviated the problem of trying to extract anharmonic couplings from vibrational spectra. He obtained a value for CN stretch activation of 100 ns, and suggested that phonon up-pumping was indeed the rate limiting step that determined the NM induction time.

The huge variations in these theoretical results for the up-pumping time, ranging from 100 ns to 1 ms, motivated my group to attempt a direct measurement using laser spectroscopy. In 1994, Chen, Tolbert and Dlott [127] used a picosecond laser pulse to excite a dye termed a "molecular heater" dissolved in the NM. Ultrafast radiationless relaxation of this dye generated a burst of phonons that heated the NM by 30K. Due to this rapid isochoric heating, the pressure also rose by ~0.05 GPa. Vibrational energy dynamics were probed using incoherent anti-Stokes Raman scattering. With an anti-Stokes probe, all Raman-active vibrational transitions can be monitored simultaneously, and the intensity of each transition will be proportional to its instantaneous population [128]. The population rise was monitored in two doorway vibrations at 480  $\text{cm}^{-1}$  and 657  $\text{cm}^{-1}$  that involve  $\text{NO}_2$  bending and rocking, and the 918  $\text{cm}^{-1}$  C-N stretch, as shown in Fig. 12. Chen, Tolbert and Dlott found that doorway vibration pumping occurred within the apparatus time response <25 ps, with C-N stretch pumping occurring about 30 ps later. Although these measurements are performed near ambient pressure, higher pressures would be expected to increase the up-pumping rate [51]. Thus shock wave up-pumping in NM is expected to occur in about 10 ps. This ~10 ps time scale is also observed in modern molecular simulations [129], and in vibrational energy relaxation studies of liquid NM [130]. There is no possible way that picosecond time scale up-pumping could account for the induction time in NM.

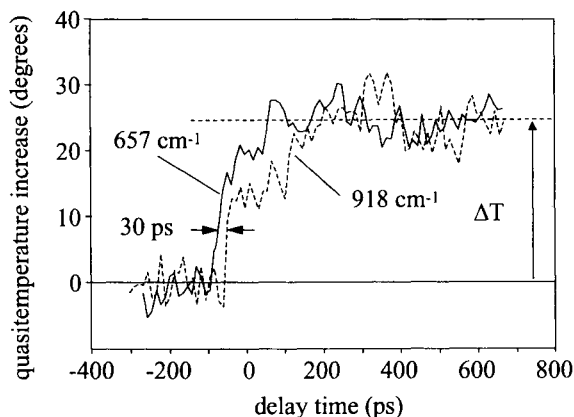


Fig. 12. Experimental measurement of multiphonon up-pumping in nitromethane (NM), reproduced from ref. [127]. Phonons are generated using a picosecond pulse to excite a dye molecular heater. Anti-Stokes Raman spectroscopy is used to monitor population changes that can be converted to vibrational quasitemperatures. The  $657\text{ cm}^{-1}$  doorway vibration is pumped faster than the instrument resolution of 25 ps. The  $918\text{ cm}^{-1}$  C-N stretch, which must be activated to break a C-N bond, is excited 25 ps later.

#### 4.2. Doorway vibrations in up-pumping

Although the quantum mechanical formalisms used to calculate the up-pumping rates in NM were quite complicated, there is a simple explanation for why early NM calculations gave times for up-pumping that were many orders of magnitude too slow. Although some of the too-slow rate is due to misestimation of critical parameters, most of it is due to using the wrong mechanism. The calculations cited above were based upon early theories of vibrational energy transfer in molecules, which were based on studies of diatomic molecules. With a diatomic, there is a large gap between the top of the phonon band the vibron band (see Fig. 10a), so phonon-to-vibron up-pumping requires a high-order multiphonon process involving the simultaneous absorption of  $n$  phonons, where  $n$  is typically 10–40 [131–133]. In general the transition rates for multiphonon processes *decrease exponentially with  $n$*  [134], so high-order multiphonon absorption is highly inefficient. In polyatomic molecules with many vibrational levels, the gap between phonons and lower frequency vibrations is much smaller (Fig. 10b), so  $n$  is much smaller as well—typically 2 or 3. A much more efficient mechanism for phonon-to-vibration transfer, via the doorway vibrations, exists in polyatomic molecules as shown in Fig. 13.

In Fig. 13, the continuous energy levels on the right hand side represent the phonon states of a solid. In a liquid such as NM there are no true phonons, but there is a band of collective excitations of the lower energy continuum that

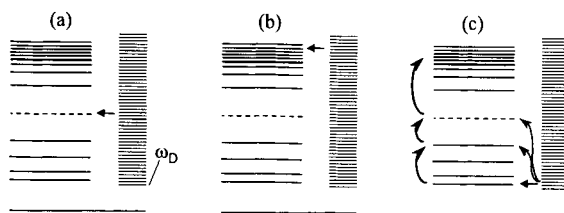


Fig. 13. Multiphonon and doorway mode models for phonon pumping of vibrations. The continuous states at right represent phonons. States from zero frequency to  $\omega_D$  (lighter color) represent phonon fundamentals; higher energy states are phonon combinations and overtones. (a) Excitation of a vibrational fundamental (dashed line) by multiphonon pumping. (b) Excitation of the same vibrational mode to the dissociation limit by a much higher-order multiphonon process. (c) Excitation to the dissociation limit by a sequence of several lower-order processes involving phonon-to-doorway mode and doorway-to-vibration pumping.

plays the same role as phonons [135]. The lower energy states of this continuum are the fundamental excitations [136], that range from zero energy to the Debye cut-off  $\omega_D$ . In liquid NM this fundamental cut-off is  $\sim 150 \text{ cm}^{-1}$ , which increases somewhat with increasing pressure [127]. The higher energy states of this continuum are overtone and combination states (multiphonon excitations). Direct multiphonon up-pumping of a specific vibrational fundamental (e.g. the CN stretch) is shown in Fig. 13a. Direct multiphonon up-pumping of the same vibrational excitation to the dissociation limit is shown in Fig. 13b. The former process requires the simultaneous action of several phonons and the latter requires simultaneous absorption of many phonons. For instance in NM, pumping the  $918 \text{ cm}^{-1}$  CN stretch fundamental involves the simultaneous absorption of no fewer than six phonons, with twelve or more phonons involved in pumping the first overtone, etc. Pumping to the dissociation limit requires about  $12,000 \text{ cm}^{-1}$ , or about 80 phonons. These pumping processes involving simultaneous absorption of 10 to 100 phonons are the slower processes discussed in early up-pumping theories that required times in the 10 ns to 1 ms range.

The doorway model for polyatomic molecules [50] is shown in Fig. 13c. The lowest doorway modes of larger polyatomic molecules require the simultaneous action of only two or three phonons. Once a doorway vibration is excited, continuing the up-pumping up to the specific vibration or to overtones of that vibration involves *sequential steps with a small number--typically one--phonon at a time*. Thus up-pumping in the doorway model involves a first slower step with two or three phonons, and then a *sequence of highly efficient steps* involving one or perhaps two phonons at a time. Each of these lower-order processes occurs on the picosecond time scale, and the total time constant for up-pumping or bond breaking is approximately the number of phonons required—10 to 100—times a few picoseconds. The result is that doorway vibrations

become excited by initiating shock fronts on the 10 ps time scale, higher energy vibrations become activated on the 10 ps time scale, and bond dissociation energies can be input on the 10-100 ps time scale. This general statement should be qualified. It really means that up-pumping behind an initiating shock front might take 100 ps in extreme cases involving rigid polyatomic molecules where the doorway vibrations are higher frequency, and it might take just a few picoseconds for floppy molecules that couple more strongly to the phonons.

Dlott and Fayer's doorway model of phonon pumping [50] suggested two essentially equivalent methods for determining the rate of phonon pumping of doorway vibrations for large polyatomic molecules where only two phonons are needed to pump a doorway vibration. The anharmonic term in the Hamiltonian responsible for two-phonon doorway mode pumping is a cubic anharmonic term of the form [21,50],

$$V^{(3)} = \frac{1}{3!} \sum_{\psi} \frac{\partial^3 V(\{\psi\})}{\partial \psi_1 \partial \psi_2 \partial \psi_3} \bigg|_{\{\psi\}_0} \psi_1 \psi_2 \psi_3 \quad (10)$$

In Eq. (10),  $V(\{\psi\})$  is the potential energy surface for the molecular crystal with a set of normal coordinates  $\{\psi\}$ , and the partial derivative is evaluated at the equilibrium position  $\{\psi\}_0$ . Cubic anharmonic terms are dominant in lattice-dynamic expressions for thermal expansion and for the Grüneisen coefficient [21]. In addition cubic anharmonicity gives rise to a variety of dynamical interactions among phonons and between phonons and vibrations. Due to wavevector matching constraints and density of states arguments, two-phonon pumping of a doorway vibration at frequency  $\Omega$  is most efficient when both phonons have about one-half the energy,  $\Omega/2$  [50,137]. The rate constant for this up-pumping process is [50,135],

$$k_{2ph \rightarrow vib} = \frac{36\pi^2}{\hbar} \langle V^{(3)}(V) \rangle^2 \rho^{(2)}(\Omega) [n_{ph}(T, V) - n_{vib}(T, V)], \quad (11)$$

where  $\langle V^{(3)}(V) \rangle$  is a shorthand for the specific volume-dependent matrix element of the operator in Eq. (10),  $\rho^{(2)}(\Omega)$  is the two-phonon density of states at the doorway mode frequency  $\Omega$ , and  $n_{ph}(T, V)$  refers to the Planck occupation factor of phonons of frequency  $\omega = \Omega/2$ ,  $n_{\omega}(T, V) = \{\exp(\hbar\omega(V)/k_B T) - 1\}^{-1}$ . Thus the first approach discussed by Dlott and Fayer was a direct calculations using techniques of lattice dynamics described in Califano's book [21]. The matrix element  $\langle V^{(3)} \rangle$  and the density of states in Eq. (11) can be calculated provided the potential is accurately known. However this may be problematic because

most model potential energy surfaces are optimized to reproduce structures [95] and do not necessarily reproduce anharmonicity with high fidelity.

The second approach to calculating the rate constant in Eq. (11) was semi-empirical. Although it is quite difficult to measure the up-pumping rate directly, the reverse process of doorway vibration decay into two phonons has been studied in several cases using either ultrafast spectroscopy [130,138] or dynamic vibrational lineshape analysis [139,140]. Lineshape analysis fails for ambient liquids where the lineshape is dominated by pure dephasing processes [141], but it can be successfully applied to low temperature perfect crystals where the lineshape is dominated by energy relaxation processes [142]. The rate constant for the relaxation that is the reverse of up-pumping is denoted  $k_{vib \rightarrow 2ph}$ , which can be related to  $k_{2ph \rightarrow vib}$  using microscopic reversibility, knowing the density of states at both  $\Omega$  and  $\Omega/2$ . These parameters are well known for naphthalene, based on low temperature lineshape analysis of the data of Hess and Prasad [139], which served as a basis for the original Dlott and Fayer calculations. The density of states of a number of useful energetic materials is accurately known as a result of neutron scattering measurements or lattice calculations, but the anharmonic coefficients are not. Several groups have argued that the anharmonic couplings are similar in a variety of primary and secondary explosives [48,83], so that although the up-pumping rates cannot be calculated with accuracy, the *relative rates* of different energetic substances can be calculated [84].

In the high-temperature limit, the Planck occupation factors  $n_\alpha(T)$  can be approximated as  $n_\alpha(T) \propto k_B T / \hbar \omega$ . Therefore the up-pumping rate is proportional to the difference in quasitemperatures, that is  $n_{ph}(T) - n_{vib}(T) \propto (\theta_{ph} - \theta_{vib})$  [50]. Then the time dependence of the phonon and vibrational quasitemperatures can be described by the differential equations [50]

$$\frac{\partial \theta_{ph}}{\partial t} = \frac{\kappa(V)}{C_{v,ph}} [\theta_{vib} - \theta_{ph}] \quad (12a)$$

$$\frac{\partial \theta_{vib}}{\partial t} = \frac{\kappa(V)}{C_{v,vib}(\theta_{vib})} [\theta_{ph} - \theta_{vib}], \quad (12b)$$

where the vibrational heat capacity  $C_{v,vib}(\theta_{vib})$  is dependent on the vibrational quasitemperature. To solve Eqs. (12) two parameters are needed, the initial phonon quasitemperature which is determined using Eq. (9), and the parameter  $\kappa(V)$ , which is the specific volume-dependent energy transfer parameter that characterizes the rate of phonon-pair conversion to vibration. The value of  $\kappa(V_0)$  can be calculated given  $\tau(0)$ , the measured lifetime of a doorway mode at low temperature [50],



$$\kappa(V_0) = \frac{j\hbar\Omega}{\tau(0)\Theta_e}, \quad (13)$$

where  $j$  is the number or degeneracy of doorway modes. In this equation,  $\Theta_e$  is the equivalence temperature, the temperature at which the rate of up-pumping into the doorway mode is equal to the low temperature rate of relaxation of the doorway mode by two phonon emission. Methods for estimating the increase of  $\kappa(V)$  with increasing pressure or decreasing specific volume have been discussed by Tokmakoff, Fayer and Dlott [51].

The calculation of up-pumping parameters for naphthalene relies on the determination of  $\tau(0)$  from low temperature Raman measurements of doorway vibration transitions. Quite recently Ye et al., used this experimental method to study RDX and  $\beta$ -HMX single crystals [140]. Generally speaking, their lineshapes gave values of  $\tau(0)$  that were quite similar to was seen by Hess and Prasad with naphthalene. Thus the naphthalene model for up-pumping appears quite reasonable for RDX and HMX as well. The principle differences are that HMX and RDX have floppy  $\text{NO}_2$  groups that naphthalene does not, so in Eq. (13) these energetic materials have a few more doorway modes.

#### 4.3. Up-pumping calculations, simulations and sensitivity

Tokmakoff, Fayer and Dlott solved Eqs. (12) for shock up-pumping of naphthalene [51]. To solve Eqs. (12), the parameters needed are heat capacities which are easily determined from tables or from statistical mechanics, the energy transfer parameter  $\kappa(V)$  and the initial phonon quasitemperature  $\theta_{ph}(0)$ . The timescale of the up-pumping process is essentially determined from the Hess and Prasad [139] low-temperature Raman measurements of the lineshapes of doorway vibrations at 175 and 212  $\text{cm}^{-1}$ , which gives  $\tau(0)$ . Equation (13) can then be used to determine the value at ambient pressure  $\kappa(V_0) = 2.7 \text{ J}\cdot\text{mol}^{-1}\cdot\text{K}^{-1}\cdot\text{ps}^{-1}$  [50]. The specific-volume dependence of  $\kappa(V)$  was determined from the shape of the intermolecular potential energy surface, as described in ref [51]. The initial phonon quasitemperature  $\theta_{ph}(0)$  was calculated using Eq. (9) for a range of shock pressures  $P$  by calculating the equilibrium final temperature  $T_I$  using Eq. (5). Some representative results are shown in Fig. 14. In this calculation the compression ratio  $V_I/V_0 = 0.80$ , corresponding to a shock pressure of  $P = 4.7 \text{ GPa}$ . The phonons start with an initial quasitemperature  $\theta_{ph}(0) \approx 2500\text{K}$ , and end up in equilibrium with the vibrations, which heat up from the initial temperature of 300K to a final temperature  $T_I \approx 760\text{K}$ . One of the important results is the much faster cooling of the phonons compared to the vibrations. The rate constant for phonon cooling from Eq. (12a),  $\kappa C_{ph}$  is much larger than the rate constant for vibrational heating from Eq. (12b),  $\kappa C_{vib}$

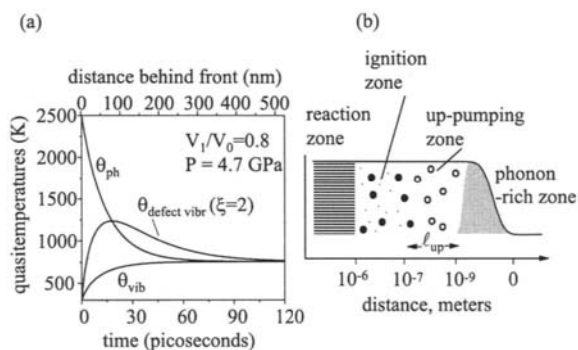


Fig. 14. (a) Calculated time-dependent phonon and vibration quasitemperatures  $\theta_{ph}$  and  $\theta_{vib}$  for naphthalene shocked at 4.7 GPa (20% compression). The defect vibrational quasitemperature is calculated for an anharmonic enhancement  $\xi = 2$ , and the vibrational temperature at the defect overshoots the vibrational temperature in the bulk by ~500K. (b) Schematic structure of the shock front. Adapted from ref. [51].

because  $C_{vib} \gg C_{ph}$ . Figure 14 shows that the time scale for multiphonon up-pumping is a few tens of ps. Most of the rapid rise in vibrational quasitemperature is complete by 30 ps, and the system has reached the thermal equilibrium temperature,  $T_j$ , by approximately 70 ps. The calculated width of the up-pumping zone is shown in Fig. 15 [51]. There are offsetting effects. As the pressure rises, the up-pumping rate becomes faster but the shock front also runs faster. The up-pumping zone width  $\ell_{up}$  in this calculation ranges only from 100-170 nm for pressures from 0-10 GPa. Tokmakoff, Fayer and Dlott estimated that typical explosives such as HMX should not differ from the naphthalene results by more than a factor of two [51].

Molecular simulations seem to be a good way of studying up-pumping behind a shock front, at least for the lower frequency vibrations that are more accurately represented in classical simulations. It has been remarked that the first simulations of detonation in molecular crystals [143] showed no up-pumping at all. However in order to develop enough chemical energy to drive a shock wave on the picosecond time scale of those simulations, hypothetical molecules were invented that had minimal barriers to reaction and enormous energy release. In the simulation by Carter White and co-workers, the potential barrier height of the reactant molecules was  $640\text{ cm}^{-1}$  whereas the vibrational frequency was  $1064\text{ cm}^{-1}$  [143]. Thus these extremely reactive molecules described by a REBO (reactive empirical bond-order) potential have no bound vibrational excited states at all, and it is no surprise that they dissociate before phonons can pump much energy into vibrations. Since 1994, several simulations of larger molecules with potentials more representative of secondary explosives

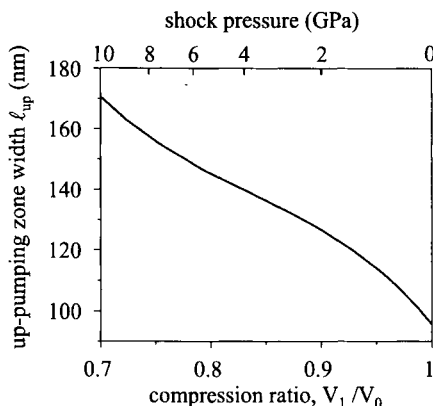


Fig. 15. Calculated up-pumping zone width, adapted from ref. [51]. As the shock pressure increases, the up-pumping rate increases but the shock moves faster, so the zone width changes by less than a factor of two for shocks in the 0-10 GPa range.

have shown clear evidence for up-pumping on the picosecond time scale. Carter White and co-workers observed picosecond up-pumping of diatomic molecules in a 3D simulation [59]. Vibrational hot spots (*vide infra*) associated with void collapse were observed near defect sites. Belak's simulations of 10 GPa shocks in liquid butane showed a high initial translational (phonon) quasitemperature, followed by up-pumping on the picosecond time scale [129]. Preliminary results for NM gave an up-pumping time constant of about 10 ps [129]. Fried, Tarver and co-workers have observed shock-initiated up-pumping that occurs in about 10 ps in simulations of HMX and TATB.

In 1994, Fried and Ruggerio [83] looked at up-pumping in seven primary, secondary or insensitive explosives. Using neutron scattering data obtained by S. Trevino, they determined the two-phonon density of states used in Eq. 11. They then assumed that the anharmonic coupling per molecule was the same for all the explosive compounds, which allowed them to compute the *relative* up-pumping rates as a function of doorway vibration frequency for all seven compounds. The data showed a general trend suggesting that faster up-pumping was associated with more sensitive materials. A plot of the up-pumping rate at for doorway vibrations near  $425\text{ cm}^{-1}$  versus drop-hammer sensitivity suggested an approximately linear relationship between high sensitivity to low velocity impact and up-pumping rate. It was suggested this relationship might also apply to shock initiation. In 1997, McNesby and Coffey [48] performed a similar but even simpler analysis, where the relative up-pumping rates of seven secondary explosives were estimated by counting the number of doorway states determined from Raman spectra in the doorway region. Once again there was a general trend of higher drop-hammer sensitivity being associated with faster up-

pumping. Quite recently, Ye et al., extended this analysis to several more secondary explosives and observed a similar correlation [84]. As discussed above, none of these purported associations or correlations meets even lower quality tests of statistical significance. Nevertheless these works do suggest a deeper look at ways that *fast up-pumping* might increase explosive sensitivity.

#### 4.4. Up-pumping and anharmonic defects

The Dlott-Fayer model proposed a link between high sensitivity and *slower* up-pumping. They reasoned that in explosives with slow up-pumping, where a superhot sea of delocalized phonons persisted for a longer time, there were opportunities to concentrate the shock energy at defect sites [50]. The existence of anharmonic defects or defect-perturbed domains was proposed, where the anharmonic coupling in Eq. (11) was somewhat greater than the bulk anharmonic coupling. An anharmonic defect might result from the presence of a vacancy, as in the Carter White simulations [59], an impurity molecule that can produce a defect-perturbed domain, or defects sown in the wake of the shock front itself [50] such as those seen in Fig. 7b. Figure 14a shows that the defect vibrational quasitemperature can temporarily overshoot the bulk vibrational quasitemperature by a significant amount, even if the total amount of anharmonic enhancement is not particularly large. In Fig. 14a, the defect is modeled as a region where the anharmonic coupling is twice the bulk. Shock compression heats the bulk crystal to  $\sim 750\text{K}$ , but the peak temperature at the defect is more than  $1200\text{K}$  for  $\sim 30$  ps. Since energetic material ignition is highly sensitive to the peak temperature, it was possible to show that this type of hot spot could lead to local ignition of energetic materials such as HMX and RDX which could ultimately ignite the bulk [51]. The shock-induced up-pumping model with anharmonic defects is described schematically in Fig. 14b. Immediately behind the shock front is a phonon-rich region. The phonons preferentially pump vibrations at the defect. Since vibrations do not move very fast, this process localizes the shock energy in a small volume producing hot spots in the  $\sim 150$  nm thick region behind the front.

#### 4.5 Up-pumping and thermal conductivity

One very interesting suggestion to relate fast up-pumping to explosive sensitivity involves the thermal conductivity. As illustrated in Fig. 3, when a hammer is dropped on a crystalline material, a large shear force develops that results in high shear-rate deformation processes such as cracking or moving edge dislocations (crystal planes sliding against each other at quite high velocities). In 1952, Bowden and Yoffe [44] gave the following expression for the temperature rise at the interface between two rubbing solids,

$$\Delta T = \frac{\mu W V}{4\alpha J} \frac{1}{k_1 + k_2}, \quad (14)$$

where  $\mu$  is the coefficient of friction,  $W$  the load between the surfaces,  $V$  the sliding velocity,  $\alpha$  the radius of the region of contact,  $J$  the heat capacity and  $k_1$  and  $k_2$  are the two solids' thermal conductivities. Initiation occurs if  $\Delta T$  reaches a critical thermal explosion temperature. Equation (14) is characterized by the product of two terms, the first representing heat generation and the second heat dissipation.

A microscopic picture of the heat generation process has been discussed by several authors, and in the context of hot spot generation by Coffey, who calculated the velocity of moving edge dislocations in a crystalline solid and the rate of phonon generation [144-146]. Coffey points out that dislocation velocities can easily be several nm/ps (1 nm/ps = 1 km/s). For typical 1 nm molecules the dislocation velocity is several molecular diameters per picosecond, and the generated phonon frequencies can easily reach several multiples of  $10^{12}$ /s, or 100-200  $\text{cm}^{-1}$ . This nonequilibrium population of predominantly higher frequency phonons launched predominantly along the direction of motion of the moving edge dislocations are among the most efficient phonons for exciting molecular vibrations via multiphonon up-pumping. Several estimates have been made of the density of phonons near a crack or moving edge dislocation. Coffey's method relies on several estimates for parameters that are difficult to judge or confirm. Holmes, Francis and Fayer [147] looked at this problem as well. They calculated initial phonon quasitemperatures starting from experimental measurements or estimates of temperatures at crack surfaces, and estimated initial phonon quasitemperatures at crack surfaces of RDX to be as high as 4000K, which is similar to the initial phonon temperatures calculated by Tokmakoff et al. [51] in the shock-induced up-pumping model.

Adding the possibility of up-pumping to the heat dissipation problem brings in some new physics. The usual theory of lattice thermal conductivity says that heat is carried by phonons. On shorter length scales phonon propagation is ballistic, but on larger length scales heat conduction becomes diffusive, where the key length scale is the phonon mean-free path. In the diffuse case the thermal conductivity is given by [137],

$$\kappa = \frac{1}{3} \sum_i C_i v_i \ell_i, \quad (15)$$

where the sum is over all phonon modes, and  $C$ ,  $v$  and  $\ell$  are the phonon heat capacity, velocity and mean-free path. In crystalline solids, the thermal

conductivity is usually dominated by the acoustic phonons that have a smaller heat capacity but a larger mean-free path. The phonon mean-free path is usually determined by scattering from impurities or infrequent Umklapp processes [137].

Under conditions where large amplitude mechanical perturbations create a dense sea of phonons, especially phonons near the zone edge, the mean-free path in Eq. (15) may be decreased due to phonon-phonon anharmonic coupling. In other words there is a second-order correction to Eq. (15) that reduces the thermal conductivity at higher phonon concentrations. For instance terms where two phonons efficiently combine to pump a doorway vibration drastically reduce the thermal conductivity by converting a mobile pair of phonons into an essentially immobile vibration. Similarly, interactions that convert faster acoustic phonons into slower optic phonons also reduce the mean-free path.

Under conditions of shock compression, moving edge dislocations or crack formation, the thermal conductivity in Eq. (14) should also contain higher order terms that decrease as the phonon concentration increases. In that case the temperature at a moving surface could become catastrophically higher than predicted by Eq. (14) as the thermal conductivity dropped off when the phonon concentration became sufficiently large. The onset of this catastrophic behavior would occur at lower phonon concentrations when the anharmonic coupling is large and up-pumping is fast. Thus the sensitivity to LVI might increase in materials characterized by fast up-pumping. This connection between fast up-pumping and poor thermal conductivity was first (to my knowledge) suggested by Fried and Ruggerio [83], and it plays an essential role in the crack propagation heating model of Holmes, Francis and Fayer [147].

#### 4.6. Coherent pumping of vibrations

So far the up-pumping models discussed above describe the behavior of molecules in a thermalized field of *incoherent phonons*. With incoherent vibrational up-pumping, the vibrational population grows linearly in time until the populations (Eq. 11) or quasitemperatures (Eq. 12) equalize [50].

There is a formal similarity in the mathematics used to describe vibrational transitions pumped by a resonant radiation field [148] and vibrational transitions pumped by phonons in a crystal lattice. In the lowest-order approximations, the radiation field and the vibrational transition are coupled by a transition dipole matrix element that is a linear function of a coordinate. The transition dipole describes charge displacement that occurs during the transition. Some of the cubic anharmonic coupling terms described by Eq. (10) result in a similar coupling between vibrational transitions and a phonon coordinate. These generally have the form  $\psi_{\text{vib}}^2 \psi_{\text{ph}}$ , so that the energy of the vibration with normal coordinate  $\psi_{\text{vib}}$  is linearly proportional to the phonon coordinate  $\psi_{\text{ph}}$ . Thus either an incoherent photon field or an incoherent phonon field can result in incoherent

vibrational pumping. The analogy between photon and phonon pumping is not perfect because at high intensities photons in a vacuum behave differently from phonons in a lattice.

Coherent pumping by photons--and by extension phonons—is possible if the source is coherent and the pumping rate is faster than processes that destroy molecular coherence such as vibrational dephasing [141]. A coherent radiation source is one in which there is a well-defined phase relationship between the photons [148]. Usually a coherent radiation field can be treated as a classical wave with a well-defined phase. In coherent pumping, it is the vibrational *amplitude* that initially grows linearly with time. The initial increase in vibrational population *grows quadratically with time*. Although incoherent pumping can at best result in saturation, that is equal populations in ground and excited states, coherent pumping can produce highly inverted states where the excited-state population greatly exceeds the ground state population [148]. Resonant coherent pumping is an exceedingly fast and efficient way of creating high levels of vibrational excitation.

Much of the theory of coherent vibrational pumping was stimulated by multiphoton IR laser dissociation experiments on molecules such as SF<sub>6</sub> in the gas-phase in the 1970's [149]. Ordinarily when gas phase molecules are irradiated by incoherent IR light, they heat up until the weakest bond dissociates. The goal of multiphoton dissociation experiments was to achieve control over which bond breaks by tuning a coherent source into different vibrational transitions. For instance with the molecule CH<sub>2</sub>ClF, tuning a laser into the C-F stretch or the C-Cl stretch might cause the different bonds to dissociate. In multiphoton IR experiments, individual molecules were pumped to dissociation by absorbing 30-50 IR photons, but the thermal dissociation product was always obtained and laser control of chemical reaction pathways appeared to be a failure [149]. Although the early stages of the multiphoton pumping process were found to involve highly efficient coherent pumping up to a level of perhaps 10 vibrational quanta, above these levels fast intramolecular relaxation processes destroyed the coherence, leading to thermochemical rather than laser-specific reaction pathways. In the past 30 years a much more sophisticated view of laser control has been developed that includes strategies for overcoming the effects of intramolecular vibrational relaxation and laser control of bond-breaking has been achieved in a few celebrated cases [150].

There are several unresolved issues in the problem of coherent vibrational pumping by shock fronts. These include: (1) to what degree can a shock front be viewed as a coherent phonon source? (2) can a shock front coherently drive vibrational excitations, and (3) could shock front coherent pumping cause selective bond breaking, especially bonds other than those broken by ordinary thermochemical reactions? One way to look at the first issue is to look at the shock front as a superposition of phonons. Since phonons form a complete set

of states, any mechanical excitation of a lattice can be described as a superposition of phonons. However phonons are extended excitations and a shock front is localized, so this type of expansion is problematic and will not converge rapidly. An extremely complicated superposition of extended phonon states is required. Nevertheless to describe a steep shock front, all these phonons must interfere destructively in the undisturbed region ahead of the front, and then suddenly come into phase right at the front. Far behind the shock front the phonons will have random phases and look like heat. Because a well-defined phase relationship must exist among these phonons at the shock front, some degree of phonon coherence will exist. The highest degree of coherence will be present when the shock front is the steepest. In addition, very steep shock fronts contain more of the higher frequency zone-edge phonons that pump vibrations most efficiently. However vibrational dephasing processes in large hot polyatomic molecules destroy coherence on the 0.1-1.0 ps time scale [94,141], so coherent pumping would be significant only for molecules within a few nanometers of even a very steep shock fronts.

Quite a few authors have suggested that large amplitude mechanical perturbations associated with the initiation of solid explosives might result in direct fracture or scission of chemical bonds. This process is sometimes called shear-induced chemical decomposition. For instance J. Dick [151] has tried to explain the orientation dependence of shock sensitivity in PETN and NM single crystals in terms of which directions are more efficient in shearing NO<sub>2</sub> groups off the molecule. F. Walker [41,108] argued that a molecule in a 5 GPa shock front just a few angstroms thick will feel a shear force that can be greater than what is needed to break C-N or N-O bonds. Molecular dynamics simulations using crude models for simple molecules also see what appears to be bond scission at a shock front [108,152,153], although simulations of larger molecules with greater realism (e.g. [154]) have not yet shown this type of behavior.

In 1977, Dancz and Rice [155] showed that model one-dimensional lattices with anharmonic potentials, particularly the Morse potential, can under certain conditions support large amplitude coherent motion. In 1982, Coffey and Toton [107] extended Pastine's model [122] of up-pumping behind a shock front to include the possibility of coherent multiphonon dissociation. They used formalisms developed to treat multiphoton IR dissociation experiments and concluded that direct multiphonon dissociation of RDX could be extremely rapid and even more efficient than thermal dissociation, efficient even for relatively weak compressive waves. The very fast multiphonon pumping rates of Coffey and Toton turn out in retrospect to be unrealistic because the transition rate matrix elements used were unrealistically large. More recently this problem has been investigated by the group of C. Martens [156,157]. High quality molecular dynamics simulations were made of nanoscale shock waves generated by photodissociation of I<sub>2</sub> molecules in rare gas matrices. These shock waves could



propagate intact for many molecular diameters and could possibly cause bond cleavage at a distance [156]. More recently simulations were made of a diatomic impurity in a monatomic lattice. A shock wave propagating through the monatomic lattice induced coherent excitation (but not dissociation) of the diatomic [157].

At the present time the tangible evidence for shear-induced bond scission is not compelling but the possibility cannot be dismissed. Even the possibility of highly selective shear-induced bond scission, for instance cutting  $\text{NO}_2$  groups off of energetic materials remains a possibility. However the proposals and studies so far have not presented a reasonable quantum-mechanical treatment of this problem that is compatible with what is known about ultrafast intramolecular vibrational energy redistribution. Resonant coherent vibrational pumping by phonons at a shock front appears to be a worthwhile area for future studies.

## 5. HOT SPOT FORMATION IN POROUS MATERIALS

In inhomogeneous energetic composites, shock and low velocity impact sensitivity is often associated with hot spots formed at pores and voids. A void is the most compressible region in a material, so the temperature jump associated with fast compression ought to be largest there. Most experiments are quite indirect, looking, for instance, at sensitivity increases caused by purposely introducing voids. A great deal has been written from the mechanical engineering perspective about hot spot formation in voids or pores [52,158], which is outside the scope of this chapter. However much less is known about fast events at the molecular level, and most of that comes from molecular dynamics simulations of pores a few molecules in diameter.

In 2001, Hambir, Kim, Dlott and Frey [120] used picosecond laser spectroscopy to look at shock-induced collapse of nanometer pores with real-time optical probes that were sensitive to fast molecular dynamics. Both pore collapse and the shape of the transmitted shock front were studied. The schematic experimental arrangement is shown in Fig. 16, which depicts one element of a shock target array that is rapidly scanned through the focus of a 100 pulse per second laser. This set up is similar to what was used to generate the data shown in Fig. 5, except now the 4.2 GPa, <25 ps shock passes through a nanoporous polymer, poly-methyl methacrylate (PMMA) before it reaches the anthracene gauge layer. CARS spectroscopy is used to monitor both the nanoporous layer and the downstream anthracene gauge. When the PMMA layer was prepared, some polystyrene (PS) coils ~100 nm in diameter were introduced. The randomly distributed 100 nm PS coils have a somewhat greater shock impedance than PMMA, so with PS present the sample is a “nanoscattering” sample. Shock fronts are expected to undergo multiple but weak scattering from the PS coils. The PS in the phase-separated PS/PMMA

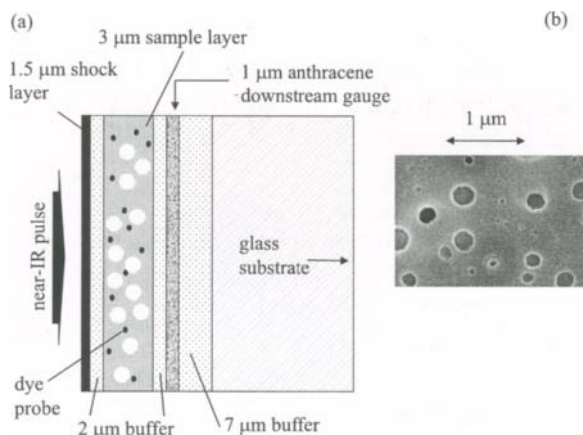


Fig. 16. Schematic of experiment to study shock-induced nanopore collapse in real time. (a) One element of a shock target array. A near-IR laser pulse generates shock waves by ablation of an absorbing surface layer. The shock front steepens up to  $<25$  ps in the buffer layer. CARS spectroscopy is used to probe dye molecules in the nanoporous layer, which monitor strain and temperature, and a thin anthracene downstream gauge which monitors changes in the risetime of the shock front caused by pore collapse. (b) Scanning electron micrograph of the surface of the nanoporous layer. The pore size distribution is  $100 \text{ nm} \pm 10\%$ . The distribution appears broader in the image, since it sees only the pore cross-section in the surface plane. Reproduced from ref. [120].

layer can also be solvent etched [159], leaving behind a “nanoporous” layer containing voids of  $\sim 100 \text{ nm}$  diameter with a  $\pm 10\%$  size distribution. About 60% of the PMMA volume consisted of these  $100 \text{ nm}$  voids. An electron micrograph of the nanoporous layer is shown in Fig. 16. A dye probe molecule (R640 dye) is embedded in the PMMA. High pressure causes a dye vibrational transition to blueshift whereas high temperature causes it to redshift [160,161].

The basic questions concerning shock void collapse are outlined in Fig. 17. Analytical models of pore collapse follow two approaches, termed *hydrodynamic* [162] or *viscoplastic*. In Mader’s hydrodynamic model [162] (Fig. 17a), a steep planar shock front hits the upstream surface of an empty spherical pore of diameter  $d$  (for nanopores, gas inside the pore can be neglected [52,162]), it accelerating the free surface to velocity  $2U_p$  [5]. The pore’s free surface undergoes hydrodynamic focusing [61,162]. A material spike strikes the downstream surface, causing impact heating. In molecular dynamics simulations, individual molecules from the upstream surface are observed to break off and strike the downstream surface [61,163]. The *hydrodynamic time constant* for pore collapse is approximately the material transit time across the pore,

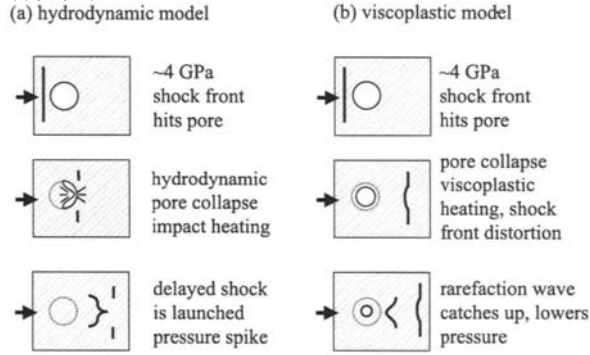


Fig. 17. Hydrodynamic and viscoplastic models for pore collapse. (a) Hydrodynamic collapse is much faster. Heat is generated when the upstream surface impacts the downstream surface. A pressure spike is generated by hydrodynamic focusing. (b) Viscoplastic collapse occurs more slowly, behind shock front. Heat is generated by viscoplastic work. Both collapse processes break up and attenuate the shock front, and generate time-delayed shocklets. Reproduced from ref. [120].

$$\tau_h = d/2U_p. \quad (16)$$

The part of the shock front that hit the pore arrives downstream delayed by  $\sim\tau_h$ . The transmitted shock front also has a transient pressure spike caused by hydrodynamic focusing [162]. Using tabulated Hugoniot data for PMMA [7], the shock velocity  $U_s = 4$  km/s and the material velocity is  $U_p = 0.8$  km/s. Recalling that 1 km/s = 1 nm/ps, the hydrodynamic collapse time for 100 nm pores is expected to be,

$$\tau_h \approx 60 \text{ ps}.$$

In the viscoplastic model of Carroll and Holt [49], later extended by Khasainov et al., [52] Butler et al., [158] and Frey [164] (Fig. 17b), pores in a viscous material collapse slowly behind the shock front via 1D (radial) plastic deformation. Heating results from viscoplastic work. In the small Reynolds number limit (see below), the *viscous time constant*  $\tau_{vis}$  is independent of pore diameter [52]:

$$\tau_{vis} = \frac{4\eta_{sh}}{P}, \quad (17)$$

where  $\eta_{sh}$  is the shock viscosity [158]. The principal problem in using this model is knowing  $\eta_{sh}$ . The ordinary viscosity of PMMA, which here is a tough

rigid supercooled liquid below its glass-transition temperature, is greater than  $10^{12}$  Pa·s. In laser-driven shock experiments, Kim et al. have measured the shock viscosity  $\eta_{sh}$  for PMMA with 3.7 GPa shocks, using CARS spectroscopy of the R640 dye probe mentioned above [160,161]. In viscoelastic media, the shock front develops a two-part structure consisting of a steep rise due to elastic compression and a more gradual rise due to viscous plastic deformation [165-167]. The time constant for the more gradual part is equal to the shock viscosity divided by the bulk modulus [168,169]. The shock viscosity was determined to be 3 Pa·s [160], about the viscosity of glycerol at 15 °C. In other words, with a 4 GPa shock the effective viscosity of solid PMMA is reduced by twelve orders of magnitude and shocked PMMA flows like sugar syrup. Using this  $\eta_{sh}$ , the Reynolds number  $R = d(\rho P)^{1/2}/8\eta_{sh} = 0.1$ , so Eq. (17) is valid. The viscoplastic pore collapse time  $\tau_{vis}$  was found to be [120],

$$\tau_{vis} \approx 3 \text{ ns.}$$

Experimental results [120] are shown in Fig. 18. Figure 18a shows the CARS frequency shift of the anthracene downstream shock gauge. After passing through the nanoscattering layer, the steeply rising ( $t_r < 25$  ps) 4.2 GPa shock front is attenuated to 3.7 GPa. After passing through the nanoporous layer the front is attenuated much more, to 2.7 GPa. The attenuation in the porous layer is due to rarefaction waves created as the pores collapse.

The dye response in the PMMA sample layer, Fig. 18b, is considerably different. In the nanoscattering layer there is a fast rise of the blueshift, limited by the shock transit time of  $\sim 750$  ps through the 3  $\mu\text{m}$  thick layer. After the shock is over, there is a small residual redshift that arises from the heat left over after the cycle of compression and expansion [37,170]. In the nanoporous layer, the blueshift is much smaller, even though the incident shock pressure is the same. That is because there is extra heat generated in the sample due to pore collapse, which offsets the pressure blueshift with a heat redshift. After the shock is over, this heat-induced redshift continues to increase with an  $\sim 3$  ns time constant, which is identified with the pore collapse process. This 3 ns pore collapse time supports the viscoplastic model and is inconsistent with the hydrodynamic pore collapse model. Thus these nanoscale hot spot experiments are real-time measurements of viscoplastic pore collapse. Keep in mind that the sample is a high molecular weight polymer, so there is no reason to suppose the same behavior would occur if the void were inside a molecular crystal such as RDX. On the other hand, the observed void collapse ought to be a good model for void collapse in the plastic-bonded regions between molecular crystals in composite energetic materials.

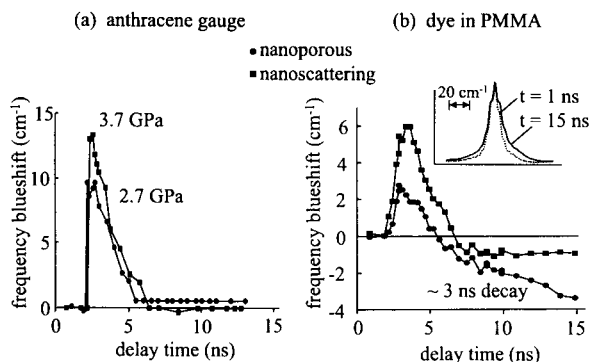


Fig. 18. Time dependent frequency shifts from CARS spectra of (a) 1  $\mu\text{m}$  thick downstream anthracene gauge, and (b) dye probe in 3  $\mu\text{m}$  thick nanoscattering or nanoporous PMMA. The incident 4.2 GPa shock front is attenuated to 3.7 GPa and 2.7 GPa by the scattering and porous samples. After the shock is over (about  $t = 6$  ns), the dye probe shows a persistent residual redshift associated with heat generated by shock compression. In the porous sample, this redshift is larger and it develops more slowly, over  $\sim 3$  ns, which is the time constant for pore collapse. The extra heat generated by pore collapse results in CARS lineshape broadening (inset). Reproduced from ref. [120].

## 6. MOLECULAR RESPONSE IN DETONATION

Now we consider fast processes occurring at molecules in a detonation front. In contrast to Section 4, which dealt with initiating pressures of a few GPa, detonation pressures are typically tens of GPa. Understanding the dynamics of molecules under these extreme conditions presents a great challenge. Detonation experiments are difficult and expensive. Most dynamic experiments measure time-velocity histories either at free surfaces or with embedded gauges that can disrupt the detonation flow. These provide at best an indirect view of the molecular dynamics. Molecular spectroscopy measurements are hindered by the difficulty of penetrating the dense detonating condensed matter, and optical probes may be swamped by huge light output. Nobody has directly measured a rise time of a detonation shock front in a high explosive. The fastest particle velocity measurements to date show risetimes less than the  $\sim 300$  ps time resolution of the VISAR measurement apparatus [171,172]. Even the most modern high-speed instrumentation has been unable to adequately resolve the von Neumann spike [171]. Many techniques have been used to measure the detonation temperature, but only quite recently have high-accuracy temperature measurement become possible. Blackbody emission techniques have undergone substantial improvements recently [68,173], but emission techniques are generally sensitive only to the highest temperature regions in the explosive. Despite massive experimental difficulties, time-resolved x-ray diffraction

techniques have been coupled to shock compression experiments [174-177] to study lattice dynamics of metals, and silicon, phase transitions in salts [178,179], and uniaxial strain in salts [180,181]. Recently picosecond time resolution has been achieved in x-ray diffraction of shocked silicon [182], and iron [183]. Although ultrafast x-ray diffraction has not yet been applied to shocked molecular materials, picosecond x-rays have been used to image shock fronts in liquid deuterium [184,185]. Another exciting development has been the use of neutron resonance spectroscopy [186] to determine the spatial distribution of the temperature of tungsten atom probes loaded into the explosive. Some advances have also been made in using proton radiography to image larger scale features of the detonation front [187]. Another exciting area has been the development of high repetition rate femtosecond laser shock experiments on thin films of energetic materials, which have the high time resolution and connection to spectroscopic probes such as vibrational spectroscopy that are needed to understand energetic molecules behind the shock front. One significant problem encountered so far in the development of these methods has been the inability to generate shocks that are large enough to initiate chemistry within a few picoseconds [188,189], although new improvements in femtosecond pulse shaping are quite promising [190]. Molecular dynamics of detonation fronts seems to be one of those areas where theory holds a great advantage over experiment.

Some very interesting theoretical proposals have been made to describe molecules in a detonation front. In 1978, Eyring proposed the idea of "starvation kinetics" [191]. Eyring noted that although transition-state theory predicts that molecules at sufficiently high temperatures can react at rates up to  $10^{13} \text{ s}^{-1}$ , in an actual detonation the overall rate of molecular reactions is closer to  $10^6 \text{ s}^{-1}$ . Recall that in ordinary thermochemistry, bond breaking at temperature  $T$  results from a fluctuation that temporarily concentrates into a single reaction coordinate an amount of energy from the bath equal to the activation energy. This type of temporary concentration cannot occur if the other molecules in the bath are all trying to react at the same time [42], because the bath does not have enough heat capacity to activate all these molecules. Even though the molecules are at a high temperature, they are starved for enough vibrational energy to activate many reactions simultaneously. We cannot view the hot dense stew of molecules at the detonation front as a canonical ensemble at constant temperature, but instead we must treat the system as a microcanonical ensemble where a fixed amount of energy flows around from molecule to molecule breaking chemical bonds as it moves, but at a greatly reduced rate.

Several authors, including F. Walker [41,108], J. J. Gilman [192] and A. B. Kunz [193,194] have argued that detonation fronts simply disintegrate molecules, reducing them to a sea of dense hot atoms. These assertions are motivated both by simulations and estimates of the forces and energies in the

detonation front. For instance the particle velocity in detonating HMX can be as great as 5 km/s. The heavy atoms C, N and O will therefore have a kinetic energy of 150-200 kJ/mol, and when these moving atoms slam into stationary molecules, each atom alone has almost enough energy to break a C-C or C-N bond (the bond energies are typically 300-350 kJ/mol) [41,108]. Similar estimates can be made for the shear forces at the shock front [192]. However this type of analysis seems a bit superficial, so a deeper examination appears to be warranted.

The quantum mechanical picture of molecular disintegration arises from the theory of metal-insulator transitions. Crystals of closed-shell molecules are insulators. As density is increased, electrons move from the stronger covalent bonds to the weaker intermolecular bonds, which weakens the intramolecular bonds and strengthens the intermolecular bonds. At a critical density the distinction between intramolecular and intermolecular bonding is lost, the bonding electrons become delocalized over all atoms and the insulator metallizes. However very recent calculations on NM and TATB using highly accurate quantum mechanical methods show that metallization in detonation fronts is highly unlikely [87,195]. Typical pressures required for metallization are 120-180 GPa (compared to 40 GPa detonation pressures). Even consideration of possible effects of uniaxial compression [195] or enhancements at defects [194] appears to put metallization out of the range of detonation fronts.

Recently two related theoretical approaches have been used to study the behavior of HMX and RDX under extreme conditions pertinent to detonation. Although neither simulation treats the complete quantum mechanical problem, each incorporates some quantum realism but in two different ways. Fried and co-workers used quantum molecular dynamics techniques to simulate six molecules of HMX at 3500K at a density of  $1.9 \text{ g/cm}^3$ , which is close to C-J conditions [196]. Quantum molecular dynamics means that at each step in a classical simulation an approximate Schrödinger equation is solved for the potential surface used for the next step. Goddard and co-workers simulated the passage of a steep shock front through an RDX crystal [154] using a classical mechanical force field ReaxFF, which was derived by fitting the potential for RDX thermochemistry computed using high-level quantum calculations [197]. Besides the difficulties associated with doing such massive calculations, an important basic problem is interpreting the results. The output of simulations is a large number of atomic coordinates and momenta. To be understandable, these have to be converted somehow into the spatial and temporal concentrations of recognizable chemical species. For instance, somewhere in the simulation there may be an O and an H atom nearby, but this might or might not be an OH molecule. Phase-space analysis has proven helpful here, monitoring both position and momenta simultaneously to establish whether atoms are moving in

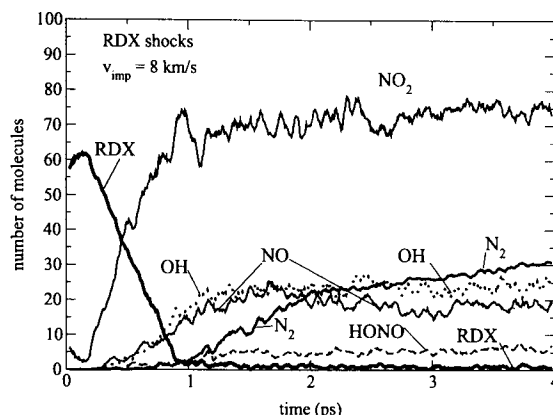


Fig. 19. Results of a simulation of RDX shocked at pressures near the C-J pressure. The RDX decays within  $\sim 0.5$  ps, which is equivalent to about 50 vibrational periods of C-N or N-O groups.  $\text{NO}_2$  is the first product to appear followed by  $\text{N}_2$ , OH and  $\text{N}_2$ . Reproduced with permission from ref. [154].

a correlated way expected for stretching vibrations of a chemically bonded species [154].

Both types of simulations show the parent RDX or HMX molecule decomposing rapidly into smaller fragments. In Fried's hot HMX simulation [196],  $\text{H}_2\text{O}$  was the first product formed, with a time constant of  $\sim 2$  ps. Figure 19, provided by Goddard and co-workers [154], shows results from a shock RDX simulation when the shock velocity was comparable to the C-J detonation velocity. In the shocked RDX simulation, RDX decomposed with an  $\sim 0.5$  ps time constant.  $\text{NO}_2$  was the first product to appear followed by  $\text{N}_2$ , OH and  $\text{N}_2$ . The reader should not attach too much significance to the slightly different chemistries observed in these simulations, since the conditions are somewhat different and the potentials are slightly different. A striking similarity is that RDX or HMX decomposition takes about 1 ps. The heavy-atom stretching vibrations such as C-N and N-O are usually in the  $1000\text{--}1500\text{ cm}^{-1}$  range, so a vibrational period is 20-30 fs. That means there are perhaps fifty periods of vibration before a chemical bond is broken, which is totally inconsistent with the picture of molecular disintegration or shear-induced chemical decomposition, despite the fact that the shock simulations use an idealized shock front that is just one molecule wide.

## 7. FAST PROCESSES IN NANOMETRIC ENERGETIC MATERIALS

Explosives and propellants containing conventional metal particles, where the metal particle diameter is typically  $30\text{--}100\text{ }\mu\text{m}$  with a broad size distribution, have been in practical use for decades. The general rule is that combustion of



these larger particles is rate-limited by diffusive mixing of the fuel and oxidizer [198,199]. Nanoparticles will burn much faster than conventional formulations. As the particle size is decreased diffusion chemistry becomes faster, so it might be possible with nanoparticles to reach a limit where diffusion is no longer rate-limiting and rates become controlled by chemical reaction dynamics. R. Armstrong and co-workers [112] have studied burning rates of various propellants containing nano aluminum, and find deviations from conventional behavior when the particle size drops below  $\sim 200$  nm.

An important practical question involves finding appropriate formulations of metal nanoparticles which detonate with high velocity and high energy release. A fast energy release rate is needed to sustain a detonation, so a related fundamental question is what processes ultimately limit the energy release process. As a measure of the needed energy release rate, we note that in HMX the reaction zone is 0.1-1.0 mm wide behind a detonation front propagating at 9 mm/ $\mu$ s, so energy release occurs on the 10-100 ns time scale [42]. By contrast, in conventional Al explosives  $\text{Al}_2\text{O}_3$  has been observed to form at rates of  $\mu\text{m}$  per  $\mu\text{s}$  [200], which is indicative of energy release in  $\sim 100$   $\mu\text{s}$ , about  $10^3$  times slower than in HMX.

Dlott and co-workers [114,201] have used fast laser spectroscopy to study chemical reactions in nanoenergetic materials consisting of Al particles in the 50-200 nm size range embedded in a nitrocellulose (NC) oxidizer. A 100 ps duration near-IR pulse was used to heat the Al particles. At this pulse duration there is enough time for heat to spread uniformly throughout the Al particles, so that chemistry results from the reaction between uniformly heated Al particles and the surrounding NC. Depending on the laser intensity, the initial temperature of Al particles ranged from the melting point 933K to the boiling point 2470K. To simplify interpretation and to obtain optical access to the interior of the samples, the experiments were done in the limit of low Al nanoparticle concentration. With flash laser heating, a general scheme for the chemistry can be written as follows [114,201],

flash heating of Al  $\rightarrow$  activation/depassivation  $\rightarrow$  oxidizer attack  
 $\rightarrow$  hot nascent species  $\rightarrow$  radiative and nonradiative energy release  
 $\rightarrow$  propagation  $\rightarrow$  termination.

Figure 20 [201] shows optical emission spectra from nanoaluminum/NC samples as a function of laser fluence. The lowest fluence  $J = 0.4 \text{ J/cm}^2$  is just enough to melt the Al particles, and the highest fluence  $J = 5.2 \text{ J/cm}^2$  is just enough to totally vaporize the particles. The first observable light emission is detected near the melting point. It is broad and structureless and is consistent with a blackbody type emission. At fluences where the Al starts to vaporize, a

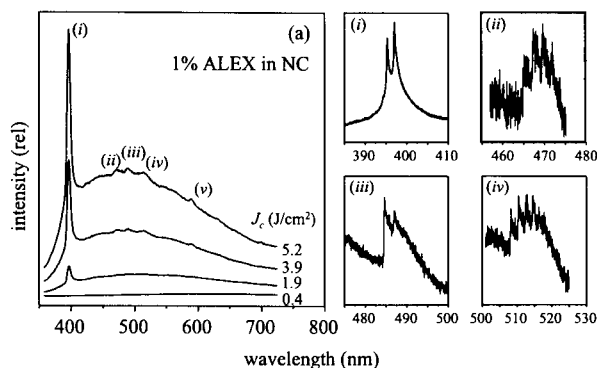


Fig. 20. (left) Optical emission spectra from a suspension of Al nanoparticles in nitrocellulose oxidizer (NC) after laser flash heating at the indicated fluences. Higher resolution spectra of the features indicated by (i)-(iv) are shown in the insets. These features are attributed to AlO emission at surfaces or gas pockets. Reproduced from ref. [201].

broad nonthermal emission that peaks near 480 nm is observed. This emission is attributed to the  $B \rightarrow X$  transition of condensed phase AlO. Most likely there is also unresolved emission from other oxides of aluminum such as  $AlO_2$ . On top of the emission are some sharp features shown in the insets. These are identified as originating from hot Al atoms and various vibronic transitions of AlO. The sharp features that are also observed in ablation of Al surfaces in air [202] are probably due to Al at the surface or in a gas pocket.

Figure 21 shows some images taken after a nanoenergetic Al/NC sample was exposed to a single 100  $\mu\text{m}$  diameter flash-heating pulse at the indicated fluence. At lower laser fluence such as 0.4  $\text{J}/\text{cm}^2$ , the ignition reaction is confined to a sprinkling of spots which ignite and extinguish without igniting the entire irradiated region. These small ignited regions are hot spots formed by Al nanoparticles plus a nearby shell of NC oxidizer. At fluences above  $\sim 1.5 \text{ J}/\text{cm}^2$ , the entire irradiated region is ignited and consumed, which indicates that individual hot spots become hot enough and large enough to ignite the NC that lies between the nanoparticles. Figure 21 also shows the time-dependence of the emission shown in Fig. 20, integrated over all wavelengths. At the lowest fluence the nanoparticles are just melted, and a weak light burst is observed whose duration is shorter than the apparatus time resolution of  $\sim 1 \text{ ns}$ . Increasing the fluence to the regime where hot spots are created and die out produces a more intense light burst whose duration is  $\sim 2 \text{ ns}$ . Further increasing the fluence to the regime where the reaction spreads to the NC between the hot spots produces an even more intense light burst whose duration is even longer,  $\sim 3.5 \text{ ns}$ . Thus 2 ns is the time for energy release in this Al/NC sample, and 3.5 ns is the time for the reaction to propagate throughout the sample [201].

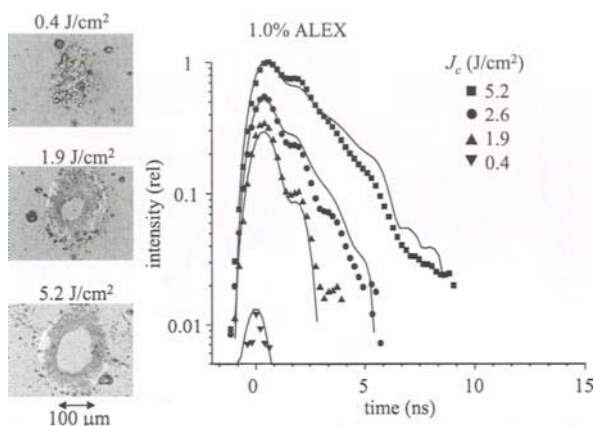


Fig. 21. (left) Images of samples of nanoaluminum in nitrocellulose (NC) exposed to single flash-heating pulses at the indicated fluences. At the lower fluence, thermochemical reactions are confined to hot spots created in regions near an Al particle. At higher fluences the entire sample is ignited and consumed. (right) Time-dependence of the light burst emitted after flash-heating. Oscillations in the signal are caused by ringing in the fast detector. In the lower fluence regime where hot spots ignite and go out, the burst lasts 2 ns. In the higher fluence regime where reactions spread to the NC between hot spots, the burst lasts 3.5 ns. Adapted from ref. [201].

Figure 22 shows the time dependence of  $\text{NO}_2$  disappearance in a flash-heated nanoaluminum sample [201].  $\text{NO}_2$  disappearance is measured using CARS spectroscopy to monitor the  $\text{ONO}_2$  totally symmetric stretching transition near  $1300\text{ cm}^{-1}$ . At the lowest fluence there is practically no  $\text{NO}_2$  consumption, but at higher fluences,  $\text{NO}_2$  consumption is seen to occur in two phases. The faster phase is characterized by an  $\sim 300\text{ ps}$  time constant, and the amplitude of the faster phase increases with laser intensity. The slower phase occurs over  $\sim 2\text{ ns}$ . The faster phase is associated with consumption of the shell of  $\text{NO}_2$  near each nanoaluminum particle. The slower phase is associated with  $\text{NO}_2$  consumption between the hot spots.

Figures 21 and 22 together show that initiation, defined as the onset of  $\text{NO}_2$  consumption, occurs in  $\sim 300\text{ ps}$  whereas ignition and energy release as measured by light output occurs in  $\sim 2\text{ ns}$  [114,201]. Referring to the reaction scheme above, we can conclude that neither the activation/passivation stage nor the oxidizer attack stage is the rate limiting step in energy release. Instead the  $\sim 2\text{ ns}$  energy release rate for nanoparticles and their associated oxidizer shell is limited by nonradiative relaxation of the hot nascent chemical reaction products including  $\text{AlO}$ . The  $3.5\text{ ns}$  energy release for the sample itself is even a bit slower than the  $2\text{ ns}$  time constant for an individual Al nanoparticle and its surrounding NC shell, since there is an additional contribution from reaction propagation into the regions between the hot spots.

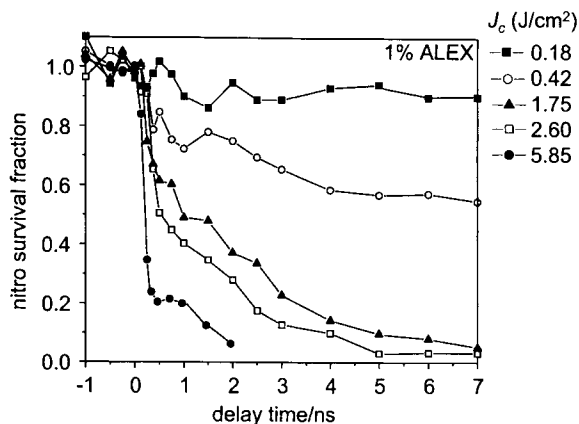


Fig. 22. CARS measurements of nitro consumption by hot nanoaluminum particles in NC. The faster  $\sim 300$  ps phase is identified with nitro consumption in a shell surrounding hot nanoaluminum. The slower  $\sim 2$  ns phase is identified with nitro consumption in the NC between the nanoparticles. Reproduced from ref. [201].

## 8. CONCLUDING REMARKS

Throughout this chapter, I have tried to stress concepts for understanding fast processes in energetic materials that attempt to combine mechanics, chemistry and quantum mechanics. One might ask what is the ultimate goal of studies of this sort, especially from the perspective of the end user of energetic materials. From the theoretical point of view, the ultimate goal might be a computer model that can be used to design highly efficient explosive or propulsion devices because it works on the larger space and time regimes pertinent to applications, say  $10^{-2}$ - $10^2$  m and  $10^{-6}$ - $10^{-3}$  s. However in contrast to the semiempirical models used today, which are not very robust in the sense that they cannot reliably deal with unforeseen circumstances and cannot accurately calculate anything that was not originally input, this ultimate model would be extremely robust since every step of the calculation would have a firm basis in fundamental principles. From the experimental point of view, the ultimate goal might be the ability to construct supermolecular engineered energetic materials from the ground up, that is to say every atom is in the right place, with the knowledge that a particular assembly would function in a desired manner. For instance one might imagine a material consisting of parallel arrays of nanometer diameter cylinders of metal oxide glasses (sol gel oxidizers [109,113,203]) packed with 1-D chains of nanoscale metal clusters that store both chemical energy and structural energy, which might deliver several times the energy of HMX concentrated along the direction of the cylinder axis, in the same way that electronic energy moves in 1-D down nanometer silica glass cylinders [204]. Although this vision might seem

futuristic or outlandish, it is particularly useful in that it suggests a roadmap for future experimental and theoretical efforts.

In the experimental realm, several areas can be identified for future work. To better understand sensitivity, we need a better idea of what happens when energetic materials are subjected to mild insults. For example, more studies of what happens in a drop-hammer test seem warranted. These might include sub-critical experiments such as the studies of Sharma and co-workers [63,205] who analyzed the chemical composition and molecular structure of samples after sub-threshold drop hammer impact, or real time IR imaging of hot spot formation such as the studies of Woody and co-workers [55,56]. For some reason, sub-critical experiments seem not very popular in the energetic materials community; perhaps missing out on the big explosion is not satisfying enough.

A related area involves detailed real-time studies of materials with sub-critical shock compression, to investigate the details of multiphonon up-pumping, the initial events in shock-induced chemistry, and the detailed nature of the shock front, including the behavior of common material properties such as thermal conductivity and viscosity under high dynamic strain rates. Similarly, real-time studies of molecular dynamics in detonation fronts are needed. However there are many experimental obstacles that need to be overcome to make such studies possible. The sub-critical shock measurements are simpler, and in the last few years there have been several successful demonstration experiments with picosecond time resolution, as described above. Real-time detonation measurements are much more problematic, both from the standpoint of high repetition rate detonation generation and spectroscopic probes that can see molecules inside a detonating solid. Right now there are several competing approaches to this problem. One approach uses essentially single-shot shock experiments with a gas gun [30] or national laser facility [206]. However single-shot ultrafast spectroscopy techniques [207-209] and their synchronization to single-shot shock generation [30] require more development. Another approach uses a conventional table-top laser system that has extraordinary high repetition rate spectroscopic capabilities [189]. However this approach has not yet been able to deliver powerful laser-driven shock waves with long enough duration to initiate much chemistry [16,188,189]. One approach that might be worthwhile is the combination of laser-launched miniflyer plates [210-214] that make very powerful shocks with high repetition rate techniques in ultrafast spectroscopy.

Finally I would mention the application of advanced nanotechnology techniques to the design and synthesis of new energetic materials. Some truly impressive nanotechnology techniques have been developed for ordinary materials that can be adapted to energetic materials. The obstacles in this area are the difficulties of scaling up these techniques to produce kilogram quantities of materials, and of knowing which structures are desired, that is understanding

the relationships between nanoengineered structures and energetic material performance.

In theory, several new directions can be suggested. The problems of obtaining theoretical models of sensitivity were discussed in Section 2.6. More sophisticated theoretical models of up-pumping seem worthwhile, for instance calculations using realistic molecules and anharmonic potential energy surfaces that look at the dependence of up-pumping on specific excitations or specific directions of shock propagation, and the effects of up-pumping in determining the structure of the shock front. Phonon generation and up-pumping under conditions of LVI could be investigated, where one obstacle is accurately describing the localized generation of phonons under LVI conditions. The possibility of coherent phonon pumping needs further examination. Finally, a great challenge is better incorporation of quantum effects in simulations. On the nanoscale, quantum mechanics is needed to more accurately describe chemical reaction pathways and excited states. On larger length scales, quantum mechanics is needed to describe infrequent events leading to infrequent high energy photon or particle generation at crack surfaces.

## 9. ACKNOWLEDGEMENT

This material is based upon work supported by the US Army Research Office under award number DAAD19-00-1-0036, the Air Force Office of Scientific Research under awards F49620-00-1-0049 and F49620-03-1-0032, and the Department of Energy, Division of Materials Sciences under Award No. DEFG02-91ER45439, through the Frederick Seitz Materials Research Laboratory at the University of Illinois at Urbana-Champaign. I thank Prof. Y. M. Gupta for introducing me to molecular dynamics of shock compression, Prof. M. D. Fayer and Prof. A. Tokmakoff, valued collaborators in the multiphonon up-pumping studies, Dr. R. Frey for teaching me about pore collapse, Prof. Hackjin Kim for his superb work on shock compression of polymers, the much-appreciated support from Dr. Robert Shaw and Dr. David Mann of ARO and Dr. Michael Berman of AFOSR, and the many students, postdocs and visitors who have worked over the years on these projects in my laboratory.

## REFERENCES

- [1] Y. B. Zel'dovich and Y. P. Raiser, *Physics of Shock Waves and High-temperature Hydrodynamic Phenomena* (Academic Press, New York, 1966).
- [2] Y. M. Gupta, in: *Shock Compression of Condensed Matter - 2001*, eds. M. D. Furnish, N. N. Thadhani, and Y. Horie (American Institute of Physics, New York, 2002), p. 3.

- [3] J. Köhler and R. Meyer, *Explosives*, fourth edition (VCH Publishers, New York, 1993).
- [4] C. F. Melius, *J. Phys. (Paris)* C4 (1987) 341.
- [5] J. Cagnoux, P. Chartagnac, P. Hereil, and M. Perez, *Ann. Phys. Fr.* 12 (1987) 451.
- [6] D. D. Dlott, *Acc. Chem. Res.* 33 (2000) 37.
- [7] S. P. Marsh, *LASL Shock Hugoniot Data* (University of California Press, Berkeley, CA, 1980).
- [8] J. M. Walsh and M. H. Rice, *J. Chem. Phys.* 26 (1957) 815.
- [9] K. Tödheide, in: *Water, A Comprehensive Treatise*, Vol. 1, eds. F. Franks (Plenum Press, New York, 1972), p. 463.
- [10] P. Harris and H.-N. Presles, *J. Chem. Phys.* 77 (1982) 5157.
- [11] K. P. Leung, A. G. Doukas, P. H. Jones, D. Papadimitriou, R. R. Alfano, and P. Harris, *Phys. Rev. B* 31 (1985) 8329.
- [12] J. M. Winey, Z. A. Dreger, Y. A. Gruzdkov, B. J. Jensen, and Y. M. Gupta, in: *Shock Compression of Condensed Matter - 1999*, eds. M. D. Furnish, L. C. Chhabildas, and R. S. Hixson (American Institute of Physics, New York, 2000), p. 231.
- [13] J. M. Winey, G. E. Duval, M. D. Knudson, and Y. M. Gupta, *J. Chem. Phys.* 113 (2000) 7492.
- [14] J. M. Winey, Y. A. Gruzdkov, Z. A. Dreger, B. J. Jensen, and Y. M. Gupta, *J. Appl. Phys.* 91 (2002) 5650.
- [15] N. W. Ashcroft and N. D. Mermin, *Solid State Physics* (Holt, Reinhart and Winston, New York, 1976).
- [16] D. D. Dlott, S. Hambir, and J. Franken, *J. Phys. Chem. B* 102 (1998) 2121.
- [17] T. C. Germann, B. L. Holian, and P. S. Lomdahl, *Phys. Rev. Lett.* 23 (2000) 5351.
- [18] S. V. Zybin, M. L. Elert, and C. T. White, *Phys. Rev. B* 66 (2002) 220102.
- [19] J. M. Winey and Y. M. Gupta, *J. Appl. Phys.* 90 (2001) 1669.
- [20] V. K. Jindal and D. D. Dlott, *J. Appl. Phys.* 83 (1998) 5203.
- [21] S. Califano, V. Schettino, and N. Neto, *Lattice Dynamics of Molecular Crystals* (Springer-Verlag, Berlin, 1981).
- [22] A. I. Kitaigorodskii, *Molecular Crystals and Molecules* (Academic Press, New York, 1973).
- [23] R. G. Delle Valle, P. F. Fracassi, R. Righini, and S. Califano, *Chem. Phys.* 74 (1983) 179.
- [24] J. W. Swegle and D. E. Grady, *J. Appl. Phys.* 58 (1985) 692.
- [25] B. R. Holian, *J. Chem. Phys.* 117 (2002) 9567.
- [26] T. A. Litovitz and C. M. Davis, in: *Physical Acoustics. Principles and Methods*, eds. W. P. Mason (Academic Press, New York, 1965), p. 282.
- [27] R. A. Graham, *Solids Under High-Pressure Shock Compression. Mechanics, Physics and Chemistry* (Springer-Verlag, New York, 1993).

- [28] L. M. Barker and R. E. Hollenbach, *J. Appl. Phys.* 43 (1972) 4669.
- [29] J. N. Johnson and L. M. Barker, *J. Appl. Phys.* 40 (1969) 4321.
- [30] M. D. Knudson, K. A. Zimmerman, and Y. M. Gupta, *Rev. Sci. Instrum.* 70 (1999) 1743.
- [31] F. E. Prieto and C. Renero, *J. Appl. Phys.* 44 (1973) 4013.
- [32] K. T. Gahagan, D. S. Moore, D. J. Funk, R. L. Rabie, S. J. Buelow, and J. W. Nicholson, *Phys. Rev. Lett.* 85 (2000) 3205.
- [33] K. T. Gahagan, J. H. Reho, D. S. Moore, D. J. Funk, and R. L. Rabie, in: *Shock Compression of Condensed Matter - 2001*, eds. M. D. Furnish, N. N. Thadhani, and Y. Horie (American Institute of Physics, New York, 2002), p. 1351.
- [34] K. T. Gahagan, D. S. Moore, D. J. Funk, J. H. Reho, and R. L. Rabie, *J. Appl. Phys.* 92 (2002) 3679.
- [35] G. Tas, S. A. Hambir, J. Franken, D. E. Hare, and D. D. Dlott, *J. Appl. Phys.* 82 (1997) 1080.
- [36] G. Tas, J. Franken, S. A. Hambir, and D. D. Dlott, *Phys. Rev. Lett.* 78 (1997) 4585.
- [37] S. A. Hambir, J. Franken, D. E. Hare, E. L. Chronister, B. J. Baer, and D. D. Dlott, *J. Appl. Phys.* 81 (1997) 2157.
- [38] W. Fickett and W. C. Davis, *Detonation* (University of California Press, Berkeley, CA, 1979).
- [39] S. N. Bulusu, *Chemistry and Physics of Energetic Materials* (Kluwer Academic Publishers, Dordrecht, 1990).
- [40] R. H. Warnes, *J. Chem. Phys.* 53 (1970) 1088.
- [41] F. E. Walker, "The initiation and detonation of explosives--an alternative concept," Report No. UCRL-53860 (1988).
- [42] C. M. Tarver, *J. Phys. Chem. A* 101 (1997) 4845.
- [43] C. M. Tarver, in: *Shock Compression of Condensed Matter 2001*, eds. M. D. Furnish, N. N. Thadhani, and Y. Horie (American Institute of Physics, New York, 2002).
- [44] F. P. Bowden and A. D. Yoffe, *Initiation and Growth of Explosion in Liquids and Solids* (University Press, Cambridge, 1952).
- [45] F. P. Bowden and A. D. Yoffe, *Fast Reactions in Solids* (Academic Press Inc., New York, 1958).
- [46] C. B. Storm, J. R. Stine, and J. F. Kramer, in: *Chemistry and Physics of Energetic Materials*, eds. S. N. Bulusu (Kluwer Academic Publishers, Dordrecht, 1990), p. 605.
- [47] T. B. Brill and K. J. James, *J. Phys. Chem.* 97 (1993) 8752.
- [48] K. L. McNesby and C. S. Coffey, *J. Phys. Chem. B* 101 (1997) 3097.
- [49] M. M. Carroll and A. C. Holt, *J. Appl. Phys.* 43 (1972) 1626.
- [50] D. D. Dlott and M. D. Fayer, *J. Chem. Phys.* 92 (1990) 3798.



- [51] A. Tokmakoff, M. D. Fayer, and D. D. Dlott, *J. Phys. Chem.* 97 (1993) 1901.
- [52] B. A. Khasainov, A. V. Attetkov, and A. A. Borisov, *Chem. Phys. Reports* 15 (1996) 987.
- [53] C. M. Tarver and A. L. Nichols III, in: *The Twelfth Symposium (International) on Detonation*, Vol. in press, eds. J. M. Short and J. L. Maienschein (OCNR, Arlington, VA, 2003), p. 599.
- [54] P. J. Miller, C. S. Coffey, and V. F. DeVost, *J. Appl. Phys.* 59 (1985) 913.
- [55] D. L. Woody, *J. Appl. Phys.* 72 (1992) 783.
- [56] D. Woody, J. Davis, and S. Coffey, in: *Shock Compression of Condensed Matter 1991*, eds. S. C. Schmidt, R. D. Dick, F. J. W., and D. G. Tasker (Elsevier Science Publishers B. V., Amsterdam, 1991), p. 729.
- [57] J. W. Mintmire, D. H. Robertson, D. W. Brenner, and C. T. White, in: *Shock Compression of Condensed Matter 1991*, eds. S. C. Schmidt, D. R. D., J. W. Forbes, and D. G. Tasker (Elsevier Science Publishers B. V., New York, 1991), p. 147.
- [58] D. H. Tsai, *J. Chem. Phys.* 95 (1991) 7497.
- [59] J. W. Mintmire, D. H. Robertson, and C. T. White, *Phys. Rev. B* 49 (1994) 14859.
- [60] C. T. White, J. J. C. Barrett, J. W. Mintmire, M. L. Elert, and D. H. Robertson, in: *Shock Compression of Condensed Matter--1995*, Vol. 370, eds. S. Schmidt and W. C. Tao (American Institute of Physics, New York, 1995), p. 187.
- [61] B. L. Holian, T. C. Germann, J.-B. Maillet, and C. T. White, *Phys. Rev. Lett.* 89 (2002) 285501.
- [62] D. H. Tsai, in: *Chemistry and Physics of Energetic Materials*, eds. S. N. Bulusu (Dordrecht, 1990), p. 229.
- [63] C. S. Coffey and J. Sharma, *J. Appl. Phys.* 89 (2001) 4797.
- [64] C. M. Tarver, S. K. Chidester, and A. L. Nichols III, *J. Phys. Chem.* 100 (1996) 5794.
- [65] A. W. Campbell, W. C. Davis, and J. R. Travis, *Phys. Fluids.* 4 (1961) 498.
- [66] A. W. Campbell, W. C. Davis, J. B. Ramsay, and J. R. Travis, *Phys. Fluids.* 4 (1961) 511.
- [67] C. S. Yoo, N. C. Holmes, and P. D. Souers, in: *Decomposition, Combustion, and Detonation Chemistry of Energetic Materials*, Vol. 418, eds. T. B. Brill, T. P. Russell, W. C. Tao, and R. B. Wardle (Materials Research Society, Pittsburgh, 1996), p. 397.
- [68] C. S. Yoo, N. C. Holmes, and P. C. Souers, *AIP Confer. Proc.* 370 (1996) 913.
- [69] Y. A. Gruzdkov and Y. M. Gupta, *J. Phys. Chem. A* 102 (1998) 8325.
- [70] X. Hong, S. Chen, and D. D. Dlott, *J. Phys. Chem.* 99 (1995) 9102.
- [71] G. I. Pangilinan and Y. M. Gupta, *J. Phys. Chem.* 98 (1994) 4522.

- [72] J. M. Winey and Y. M. Gupta, *J. Phys. Chem. B* 101 (1997) 10733.
- [73] J. M. Winey and Y. M. Gupta, *J. Phys. Chem.* 101 (1997) 9333.
- [74] Y. A. Gruzdkov, Y. M. Gupta, and J. J. Dick, in: *Shock Compression of Condensed Matter - 1999*, eds. M. D. Furnish, L. C. Chhabildas, and R. S. Hixson (American Institute of Physics, New York, 2000), p. 929.
- [75] Z. A. Dreger, Y. A. Gruzdkov, and Y. M. Gupta, in: *Shock Compression of Condensed Matter - 1999*, eds. M. D. Furnish, L. C. Chhabildas, and R. S. Hixson (American Institute of Physics, New York, 2000), p. 933.
- [76] J. J. Dick, R. N. Mulford, W. J. Spencer, D. R. Pettit, E. Garcia, and D. C. Shaw, *J. Appl. Phys.* 70 (1991) 3572.
- [77] J. J. Dick, *J. Phys. Chem.* 97 (1993) 6193.
- [78] A. M. Frank, in *Microphotography of shocks in crystals*, Victoria, B.C., Canada, 1992.
- [79] J. W. Rogers Jr., H. C. Peebles, R. R. Rye, J. E. Houston, and J. S. Binkley, *J. Chem. Phys.* (1984) 4513.
- [80] J. Sharma, B. C. Beard, and M. Chaykovsky, *J. Phys. Chem.* 95 (1990) 1209.
- [81] F. J. Owens, *J. Mol. Struct.* 121 (1985) 213.
- [82] T. Luty, P. Ordon, and C. J. Eckhardt, *J. Chem. Phys.* 117 (2002) 1775.
- [83] L. E. Fried and A. J. Ruggerio, *J. Phys. Chem.* 98 (1994) 9786.
- [84] S. Ye, K. Tonokura, and M. Koshi, *J. Jpn. Explosive Soc.* 63 (2002) 104.
- [85] R. Behrens Jr., *J. Phys. Chem.* 94 (1990) 6706.
- [86] M. Grandbois, M. Beyer, M. Rief, H. Clausen-Schaumann, and H. E. Gaub, *Science* 283 (1999) 1727.
- [87] C. J. Wu and L. E. Fried, in: *The Eleventh Symposium (International) on Detonation*, eds. J. E. Kennedy and J. M. Short (OCNR, Arlington, 1999), p. 490.
- [88] S. Zeman, M. Dimun, and S. Truchlik, *Thermochim. Acta* 78 (1984) 181.
- [89] C. Capellos, in: *The Twelfth Symposium (International) on Detonation*, eds. J. M. Short and J. L. Maienschein (OCNR, Arlington, VA, 2003), p. 813.
- [90] H.-S. Im and E. R. Bernstein, *J. Chem. Phys.* 113 (2000) 7911.
- [91] D. D. Dlott, *Ann. Rev. Phys. Chem.* 37 (1986) 157.
- [92] A. Nitzan and J. Jortner, *Molec. Phys.* 25 (1973) 713.
- [93] A. Nitzan, S. Mukamel, and J. Jortner, *J. Chem. Phys.* 60 (1974) 3929.
- [94] D. W. Oxtoby, in: *Photoselective Chemistry Part 2*, Vol. 47, eds. J. Jortner, R. D. Levine, and S. A. Rice (Wiley, New York, 1981), p. 487.
- [95] A. J. Pertsin and A. I. Kitaigorodsky, *The Atom-Atom Potential Method: Applications to Organic Molecular Solids* (Springer-Verlag, Berlin, 1987).
- [96] É. L. Bokhenkov, E. M. Rodina, E. F. Sheka, and I. Natkaniec, *Phys. Status Solidi B* 85 (1978) 331.
- [97] E. J. Reed, J. D. Joannopoulos, and L. E. Fried, *Phys. Rev. B* 62 (2000) 16500.

- [98] E. J. Reed, M. R. Manaa, J. D. Joannopoulos, and L. F. Fried, in: *Shock Compression of Condensed Matter - 2001*, eds. M. D. Furnish, N. N. Thadhani, and Y. Horie (American Institute of Physics, New York, 2002), p. 385.
- [99] E. N. Harvey, *A History of Luminescence. From the Earliest Times Until 1900* (American Philosophical Society, Philadelphia, 1957).
- [100] T. I. Quickenden, B. J. Selby, and C. G. Freeman, *J. Phys. Chem. A* 102 (1998) 6713.
- [101] J. T. Dickinson, L. C. Jensen, M. R. McKay, and F. Freund, *J. Vac. Soc. Technol. A* 4 (1986) 1648.
- [102] D. E. Hare, N. C. Holmes, and D. J. Webb, *Phys. Rev. B.* 66 (2002) 014108.
- [103] W. Häfner and W. J. Kiefer, *J. Chem. Phys.* 86 (1987) 4582.
- [104] K. M. White and C. J. Eckhardt, *Phys. Rev. Lett.* 39 (1987) 574.
- [105] T. Luty and C. J. Eckhardt, *J. Chem. Phys.* 82 (1984) 1515.
- [106] F. J. Zerilli and E. T. Toton, *Phys. Rev. B* 29 (1984) 5891.
- [107] C. S. Coffey and E. T. Toton, *J. Chem. Phys.* 76 (1982) 949.
- [108] F. E. Walker, *J. Appl. Phys.* 63 (1988) 5548.
- [109] L. E. Fried, M. R. Manaa, P. F. Pagoria, and R. L. Simpson, *Annu. Rev. Mater. Res.* 31 (2001) 291.
- [110] E. W. Price, in: *Fundamentals of Solid-Propellant Combustion, Progress in Aeronautics and Astronautics, Vol. 90*, eds. K. Kuo and M. Summerfield (AIAA, New York, 1984), p. 479.
- [111] J. T. DeSena and K. K. Kuo, *J. Propul. Power* 15 (1999) 794.
- [112] R. W. Armstrong, B. Baschung, D. W. Booth, and M. Samirant, *Nano Lett.* in press (2003) .
- [113] T. M. Tillotson, A. E. Gash, R. L. Simpson, L. W. Hrubesh, J. Satcher, J. H., and J. F. Poco, *J. Non Cryst. Solids* 2001 (2001) 338.
- [114] S. Wang, Y. Yang, Z. Sun, and D. D. Dlott, *Chem. Phys. Lett.* 368 (2002) 189.
- [115] L. J. Parker, H. D. Ladouceur, and T. P. Russell, *AIP Conf. Proc.* 505 (2000) 941.
- [116] S. F. Son, in: *Shock Compression of Condensed Matter - 2001*, eds. M. D. Furnish, N. N. Thadhani, and Y. Horie (American Institute of Physics, New York, 2002), p. 1059.
- [117] D. L. Alara and R. G. Nuzzo, *Langmuir* 1 (1985) 52.
- [118] T. Campbell, R. K. Kalia, A. Nakano, P. Vashishta, S. Ogata, and S. Rogers, *Phys. Rev. Lett.* 82 (1999) 4866.
- [119] C. E. Aumann, G. L. Skofronick, and J. A. Martin, *J. Vac. Sci. Technol. B* 13 (1995) 1178.
- [120] S. A. Hambir, H. Kim, D. D. Dlott, and R. B. Frey, *J. Appl. Phys.* 90 (2001) 5139.

- [121] E. F. Greene and J. P. Toennies, *Chemical Reactions in Shock Waves* (Academic Press, New York, 1964).
- [122] D. J. Pastine, D. J. Edwards, H. D. Jones, C. T. Richmond, and K. Kim, in: *High-pressure Science and Technology*, Vol. 2, eds. K. D. Timmerhaus and M. S. Barber (Plenum, New York, 1979), p. 264.
- [123] A. Tokmakoff, D. Zimdars, B. Sauter, R. S. Francis, R. S. Kwok, and M. D. Fayer, *J. Chem. Phys.* 101 (1994) 1741.
- [124] R. D. Bardo, *Int. J. Quantum Chem.: Quantum Chem. Symp.* 20 (1986) 455.
- [125] R. D. Bardo, in: *Proceedings of the Ninth Symposium on Detonation*, Vol. Volume I, eds. J. M. Short (1989), p. 235.
- [126] J. D. McDonald, *Annu. Rev. Phys. Chem.* 30 (1979) 29.
- [127] S. Chen, W. A. Tolbert, and D. D. Dlott, *J. Phys. Chem.* 98 (1994) 7759.
- [128] A. Laubereau and W. Kaiser, *Rev. Mod. Phys.* 50 (1978) 607.
- [129] J. Belak, in: *High-Pressure Science and Technology - 1993*, Vol. 309, eds. S. C. Schmidt, J. W. Shaner, G. A. Samara, and M. Ross (American Institute of Physics, Woodbury, NY, 1994), p. 1063.
- [130] J. C. Deak, L. K. Iwaki, and D. D. Dlott, *J. Phys. Chem. A* 103 (1999) 971.
- [131] S. A. Egorov and J. L. Skinner, *J. Chem. Phys.* 103 (1995) 1533.
- [132] S. A. Egorov and J. L. Skinner, *J. Chem. Phys.* 105 (1996) 7047.
- [133] K. F. Everitt, S. A. Egorov, and J. L. Skinner, *Chem. Phys.* 235 (1998) 115.
- [134] A. Nitzan, S. Mukamel, and J. Jortner, *J. Chem. Phys.* 63 (1975) 200.
- [135] V. M. Kenkre, A. Tokmakoff, and M. D. Fayer, *J. Chem. Phys.* 101 (1994) 10618.
- [136] P. Moore, A. Tokmakoff, T. Keyes, and M. D. Fayer, *J. Chem. Phys.* 103 (1995) 3325.
- [137] P. G. Klemens, in: *Solid State Physics*, Vol. 7, eds. F. Seitz and D. Turnbull (Academic Press, New York, 1958), p. 1.
- [138] C. M. Aubuchon, K. D. Rector, W. Holmes, and M. D. Fayer, *Chem. Phys. Lett.* 299 (1999) 84.
- [139] L. A. Hess and P. N. Prasad, *J. Chem. Phys.* 78 (1983) 626.
- [140] S. Ye, K. Tonokura, and M. Koshi, *J. Jpn. Explosive Soc.* 63 (2002) 49.
- [141] D. W. Oxtoby, *Adv. Chem. Phys.* 40 (1979) 1.
- [142] P. L. Decola, R. M. Hochstrasser, and H. P. Trommsdorff, *Chem. Phys. Lett.* 72 (1980) 1.
- [143] D. W. Brenner, D. W. Robertson, M. L. Elert, and C. T. White, *Phys. Rev. Lett.* 70 (1993) 2174.
- [144] C. S. Coffey, *Phys. Rev. B* 24 (1981) 6984.
- [145] C. S. Coffey, *Phys. Rev. B* 34 (1986) 5674.
- [146] C. S. Coffey, *J. Appl. Phys.* 62 (1987) 2727.

- [147] W. Holmes, R. S. Francis, and M. D. Fayer, *J. Chem. Phys.* 110 (1999) 3576.
- [148] S. Mukamel, *Principles of Nonlinear Optical Spectroscopy* (Oxford University Press, New York, 1995).
- [149] P. A. Schulz, A. S. Sudbø, D. J. Krajnovich, H. S. Kowk, Y. R. Shen, and Y. T. Lee, *Annu. Rev. Phys. Chem.* 30 (1979) 379.
- [150] F. F. Crim, *Annu. Rev. Phys. Chem.* 44 (1993) 397.
- [151] J. J. Dick and J. P. Ritchie, *J. Appl. Phys.* 76 (1994) 2726.
- [152] A. M. Karo, F. E. Walker, T. M. DeBoni, and J. R. Hardy, *Acta. Astronaut.* 5 (1978) 1041.
- [153] M. Peyrard, S. Odier, E. Oran, J. Boris, and J. Schnur, *Phys. Rev. B.* 33 (1986) 2350.
- [154] A. Strachan, A. van Duin, D. Chakraborty, S. Dasgupta, and W. A. Goddard III, *Phys. Rev. Lett.* in press (2003) .
- [155] J. Dancz and S. A. Rice, *J. Chem. Phys.* 67 (1977) 1418.
- [156] D. Kohen and C. C. Martens, *J. Chem. Phys.* 111 (1999) 4343.
- [157] D. A. Rose and C. C. Martens, *J. Phys. Chem. A* 101 (1997) 4613.
- [158] J. Kang, P. B. Butler, and M. R. Baer, *Combust. Flame* 89 (1992) 117.
- [159] S. Walheim, E. Schäffer, J. Mlynek, and U. Steiner, *Science* 283 (1999) 520.
- [160] H. Kim, S. A. Hambir, and D. D. Dlott, *J. Phys. Chem. B* 104 (2000) 4239.
- [161] H. Kim, S. A. Hambir, and D. D. Dlott, *Phys. Rev. Lett.* 83 (1999) 5034.
- [162] C. L. Mader, *Phys. Fluids.* 8 (1965) 1811.
- [163] R. S. Sinkovits, L. Phillips, E. S. Oran, and J. P. Boris, in: *Decomposition, Combustion, and Detonation Chemistry of Energetic Materials*, Vol. 418, eds. T. B. Brill, T. P. Russell, W. C. Tao, and R. B. Wardle (Materials Research Society, Pittsburgh, 1993), p. 161.
- [164] R. B. Frey, in: *Proceedings of the Seventh Symposium (International) on Detonation* (Naval Surface Weapons Center, Annapolis, MD, 1981), p. 36.
- [165] K. W. Schuler, *J. Mech. Phys. Solids* 18 (1970) 277.
- [166] K. W. Schuler and J. W. Nunziato, *Rheol. Acta* 13 (1974) 265.
- [167] K. W. Schuler, J. W. Nunziato, and E. K. Walsh, *Int. J. Solids Structures* 9 (1973) 1237.
- [168] M. A. Berg, *J. Phys. Chem. A* 102 (1998) 17.
- [169] M. A. Berg and H. W. Hubble, *Chem. Phys.* 233 (1998) 257.
- [170] S. A. Hambir, J. Franken, and D. D. Dlott, *High Pressure Sci. Technol.* 7 (1998) 891.
- [171] R. L. Gustavsen, S. A. Sheffield, and R. R. Alcon, in: *The Eleventh Symposium (International) on Detonation*, eds. J. E. Kennedy and J. M. Short (OCNR, Arlington, 1999), p. 821.
- [172] S. A. Sheffield, D. D. Bloomquist, and C. M. Tarver, *J. Chem. Phys.* 80 (1984) 3831.

- [173] C. S. Yoo, N. C. Holmes, P. C. Souers, C. J. Wu, F. H. Ree, and J. J. Dick, *J. Appl. Phys.* 88 (2000) 70.
- [174] J. S. Wark, N. C. Woolsey, and R. R. Whitlock, *Appl. Phys. Lett.* 61 (1992) 651.
- [175] J. S. Wark, R. R. Whitlock, A. Hauer, J. E. Swain, and P. J. Solone, *Phys. Rev. B* 35 (1987) 9391.
- [176] J. S. Wark, R. R. Whitlock, A. A. Hauer, J. E. Swain, and P. J. Solone, *Phys. Rev. B* 40 (1989) 5705.
- [177] J. S. Wark, D. Riley, N. C. Woolsey, G. Keihn, and R. R. Whitlock, *J. Appl. Phys.* 68 (1990) 4531.
- [178] T. d'Almeida and Y. M. Gupta, *Phys. Rev. Lett.* 85 (2000) 330.
- [179] M. D. Knudson and Y. M. Gupta, *Phys. Rev. Lett.* 81 (1998) 2938.
- [180] P. A. Rigg and Y. M. Gupta, *Phys. Rev. B* 63 (2001) 094112.
- [181] P. A. Rigg and Y. M. Gupta, *Appl. Phys. Lett.* 73 (1998) 1655.
- [182] H. Kishimura, A. Yazaki, H. Kawano, Y. Hironaka, K. G. Nakamura, and K. Kondo, in: *Science of Superstrong Field Interactions*, eds. K. Nakajima and M. Deguchi (American Institute of Physics, New York, 2002), p. 247.
- [183] D. Batani, A. Morelli, M. Tomasini, A. Benuzzi-Mounaix, F. Philippe, M. Koenig et al., *Phys. Rev. Lett.* 88 (2002) 235502.
- [184] G. W. Collins, L. B. Da Silva, P. Celliers, D. M. Gold, M. E. Foord, R. J. Wallace et al., *Science* 281 (1998) 1178.
- [185] L. B. Da Silva, P. Celliers, G. W. Collins, K. S. Budil, N. C. Holmes, J. Barbee, T. W. et al., *Phys. Rev. Lett.* 78 (1997) 483.
- [186] D. J. Funk, B. W. Asay, B. I. Bennett, J. D. Bowman, R. M. Boat, P. M. Dickson et al., in: *Shock Compression of Condensed Matter -- 1997*, Vol. AIP Conference Proceedings 429 (American Institute of Physics, Woodbury, NY, 1998), p. 887.
- [187] J. D. Zumbro, K. J. Adams, K. R. Alrick, J. F. Amann, J. G. Boissevain, M. L. Crow et al., in: *The Twelfth Symposium (International) on Detonation*, eds. J. M. Short and J. L. Maienschein (OCNR, Arlington, VA, 2003), p. 54.
- [188] D. S. Moore, D. J. Funk, K. T. Gahagan, J. H. Reho, G. L. Fisher, S. D. McGrane et al., in: *Shock Compression of Condensed Matter - 2001*, eds. M. D. Furnish, N. N. Thadhani, and Y. Horie (American Institute of Physics, New York, 2002), p. 1351.
- [189] D. D. Dlott, *Annu. Rev. Phys. Chem.* 50 (1999) 251.
- [190] S. D. McGrane, D. S. Moore, D. J. Funk, and R. L. Rabie, *Appl. Phys. Lett.* 80 (2002) 3919.
- [191] H. Eyring, *Science* 199 (1978) 740.
- [192] J. J. Gilman, *Science* 274 (1996) 65.
- [193] M. M. Kuklja, E. V. Stefanovich, and A. B. Kunz, *J. Chem. Phys.* 112 (2000) 3417.

- [194] M. M. Kuklja and A. B. Kunz, in: *Shock Compression of Condensed Matter - 1999*, eds. M. D. Furnish, L. C. Chhabildas, and R. S. Hixson (American Institute of Physics, New York, 2000).
- [195] C. J. Wu, L. H. Yang, L. E. Fried, J. Qunneville, and T. J. Martinez, *Phys. Rev. B* in press (2003) .
- [196] M. R. Manaa, L. E. Fried, C. F. Melius, M. Elstner, and T. Frauenheim, *J. Phys. Chem. A* 106 (2002) 9024.
- [197] D. Chakraborty, R. P. Muller, S. Dasgupta, and W. A. Goddard, III, *J. Phys. Chem. A* 104 (2000) 2261.
- [198] B. Baschung, D. Grune, H. H. Licht, and M. Samirant, in *Combustion phenomena of a solid propellant based on aluminum powder*, Stresa, Italy, 2000, p. 81.
- [199] *Fundamentals of Solid-Propellant Combustion*; Vol. 90, edited by K. K. Kuo and M. Summerfield (AIAA, New York, 1984).
- [200] D. J. Pastine, M. Cowperthwaite, J. M. Solomon, and J. W. Enig, in: *The Twelfth Symposium (International) on Detonation*, Vol. in press, eds. J. M. Short and J. L. Maienschein (OCNR, Arlington, VA, 2003), p. 204.
- [201] Y. Yang, Z. Sun, S. Wang, and D. D. Dlott, *J. Phys. Chem.* in press (2003) .
- [202] G. I. Pangilinan and T. P. Russell, *J. Chem. Phys.* 111 (1999) 445.
- [203] T. M. Tillotson, L. W. Hrubesh, R. L. Simpson, R. S. Lee, R. W. Swansiger, and L. R. Simpson, *J. Non Crystal. Solids* 225 (1998) 358.
- [204] T.-Q. Nguyen, J. Wu, V. Doan, B. J. Schwartz, and S. H. Tolbert, *Science* 288 (2000) 652.
- [205] T. P. Liddiard, J. W. Forbes, J. W. Watt, R. N. Baker, J. Sharma, and B. C. Beard, in: *Tenth Symposium (International) on Detonation*, Boston MA (Office of Naval Research, Silver Spring MD, 1993).
- [206] G. W. Collins, P. M. Celliers, L. B. Da Silva, R. Cauble, D. M. Gold, M. E. Foord et al., *Phys. Rev. Lett.* 87 (2001) 165504.
- [207] J. T. Fourkas, L. Dhar, K. A. Nelson, and R. Trebine, *J. Opt. Soc. Am. B* 12 (1995) 155.
- [208] L. Dhar, J. T. Fourkas, and K. A. Nelson, *Opt. Lett.* 19 (1994) 643.
- [209] G. P. Wakeham and K. A. Nelson, *Opt. Lett.* 25 (2000) 505.
- [210] T. Sekine, M. Yoshida, and K. A. Tanaka, in: *Proceedings of 3rd NIRIM Intern. Symp. on Advanced Materials*, eds. M. Akaishi (NIRIM, Tsukuba, 1996), p. 29.
- [211] W. M. Trott, in: *High-Pressure Science and Technology -- 1993*, eds. S. C. Schmidt, J. W. Shaner, G. A. Samara, and M. Ross (American Institute of Physics, Woodbury, NY, 1993), p. 1655.
- [212] W. M. Trott and K. D. Meeks, *J. Appl. Phys.* 67 (1990) 3297.

- [213] W. M. Trott, R. E. Setchell, and A. V. Farnsworth Jr., in: *Shock Compression of Condensed Matter - 2001*, eds. M. D. Furnish, N. N. Thadhani, and Y. Horie (American Institute of Physics, New York, 2002), p. 1347.
- [214] H. He, T. Kobayashi, and T. Sekine, in: *Shock Compression of Condensed Matter - 2001*, eds. M. D. Furnish, N. N. Thadhani, and Y. Horie (American Institute of Physics, New York, 2003), p. 1339.



This Page Intentionally Left Blank

## *Chapter 7*

# **The equation of state and chemistry of detonation products**

**Laurence E. Fried, W. Michael Howard, and J. M. Zaug**

Lawrence Livermore National Laboratory, University of California,  
Livermore, CA 94551, USA

## **INTRODUCTION**

The energy content of an energetic material often determines its practical utility. An accurate estimate of the energy content is essential in the design of new materials [1] and in the understanding of quantitative detonation tests [2]. The useful energy content is determined by the anticipated release mechanism. Since detonation events occur on a microsecond timeframe, any chemical reactions slower than this are not relevant when considering a detonation. Another way of looking at energy release mechanisms is through thermodynamic cycles. Detonation can be thought of as a cycle that transforms the unreacted explosive into stable product molecules at the Chapman-Jouget state [3]. This is simply described as the slowest steady shock state that conserves mass, momentum, and energy. Similarly, the deflagration of a propellant converts the unreacted material into product molecules at constant enthalpy and pressure. The nature of the Chapman-Jouget and other special thermodynamic states important to energetic materials is strongly influenced by the equation of state of stable detonation products.

Understanding energy release in terms of thermodynamic cycles ignores the important question of the time scale of reaction. The kinetics of even simple molecules under high pressure conditions is not well understood. Diamond anvil cell and shock experiments promise to provide insight into chemical reactivity under extreme conditions.

Despite the importance of chemical kinetic rates, chemical equilibrium is often nearly achieved when energetic materials react. This is a consequence of the high temperatures produced by such reactions (up to 6000 K). We will begin our discussion by examining thermodynamic cycle theory as applied to high explosive detonation. This is a current research topic because high explosives produce detonation products at extreme pressures and temperatures: up to 40 GPa and 6000 K. Relatively little is known about material equations of state under these conditions. Nonetheless, shock experimentation on a wide range of materials has generated sufficient information to allow reasonably reliable thermodynamic modeling to proceed.

One of the attractive features of thermodynamic modeling is that it requires very little information regarding the unreacted energetic material. The elemental composition, density, and heat of formation of the material are the only information needed. Since elemental composition is known once the material is specified, only density and heat of formation need to be predicted.

Chapman-Jouget (C-J) detonation theory [3] implies that the performance of an explosive is determined by thermodynamic states--the Chapman-Jouget state and the connected adiabat. Thermochemical codes use thermodynamics to calculate these states, and hence obtain a prediction of explosive performance. The allowed thermodynamic states behind a shock are intersections of the Rayleigh line (expressing conservation of mass and momentum), and the shock Hugoniot (expressing conservation of energy). The C-J theory states that a stable detonation occurs when the Rayleigh line is tangent to the shock Hugoniot.

This point of tangency can be determined, assuming that the equation of state  $P = P(V,E)$  of the products is known. The chemical composition of the products changes with the thermodynamic state, so thermochemical codes must simultaneously solve for state variables and chemical concentrations. This problem is relatively straightforward, given that the equation of state of the fluid and solid products is known.

One of the most difficult parts of this problem is accurately describing the equation of state of the fluid components. Despite its simplicity and lack of rigorous derivation, the Becker-Kistiakowski-Wilson (BKW) is used in many practical energetic material applications. There have been a number of different parameter sets proposed for the BKW EOS [5-8]. Kury and Souers [9] have critically reviewed these equations of state by comparing their predictions to a database of detonation tests. They

concluded that BKW equations of state could not adequately model the detonation of a copper lined cylindrical charge. The BKWC parameter set [10] partially overcame this deficiency through more aggressive parametrization techniques. BKWC is not reliable when applied to explosives very high in hydrogen content, however.

It has long been recognized that the highly empirical nature of the BKW equation of state limits the accuracy achievable in detonation calculations. This is particularly important when designing new materials that may have unusual elemental compositions. Efforts to achieve better equations of state have largely been based on the concept of model potentials. With model potentials, molecules interact via idealized spherical pair potentials. Statistical mechanics is then employed to calculate the equation of state of the interacting mixture of effective spherical particles. Most often, the exponential-6 potential is used for pair interactions:

$$V(r) = \frac{\epsilon}{\alpha - 6} [6 \exp(\alpha - \alpha r / r_m) - \alpha (r_m / r)^6]$$

Here,  $r$  is the distance between particles.  $r_m$  is the minimum of the potential well.  $\epsilon$  is the well depth, and  $\alpha$  is the softness of the potential.

The JCZ3 EOS was the first successful model based on a pair potential that was applied to detonation [11]. This EOS was based on fitting Monte Carlo simulation data to an analytic functional form. Hobbs and Baer [12] have recently reported a JCZ3 parameter set called JCZS. JCZS employs some of the parametrization techniques used in the construction of BKWC. It achieves better accuracy for the detonation of common high explosives than BKW equations of state. Since it is extensively parametrized to detonation, it has difficulty in reproducing reactive shock Hugoniot of hydrocarbons and other liquids [13].

Ross proposed a soft-sphere perturbation theory for the equation of state of the exponential-6 fluid [14]. Ross, Ree and others successfully applied this equation of state to detonation and shock problems [15-18]. Kang et al. also derived a fluid perturbation theory designed to work at high-density [19]. Computational cost is a significant difficulty with equations of state based on fluid perturbation theory. W. Byers Brown [20] developed an analytic representation of Kang et al.'s equation of state using Chebyshev polynomials. The accuracy of the above equations of state has been recently evaluated; those authors concluded that Ross's approach is the most reliable [21]. More recently, Fried and Howard have used a

combination of integral equation theory and Monte Carlo simulations to generate a highly accurate equation of state for the exponential-6 fluid [22].

The exponential-6 model is not well suited to molecules with a large dipole moment. Ree [23] has used a temperature-dependent well depth  $\epsilon(T)$  in the exponential-6 potential to model polar fluids and fluid phase separations. Fried and Howard have developed an effective cluster model for HF [24]. The effective cluster model is valid to lower temperatures than the variable well-depth model, but it employs two more adjustable parameters. More progress needs to be made in the treatment of polar detonation product molecules.

Efforts have been made to develop equations of state for detonation products based on direct Monte Carlo simulations instead of analytical approaches [25]. This approach is promising given recent increases in computational capabilities. One of the greatest advantages of direct simulation is the ability to go beyond van der Waals 1-fluid theory [26]. Kerley has advocated the ideal mixing approximation as an alternative to 1-fluid theory [27].

In most cases, interactions between unlike molecules are treated with Lorentz-Berthelot combination rules [28]. Non-additive pair interactions have been used for  $N_2$  and  $O_2$  [18]. The resulting  $N_2$  model accurately matches double shock data, but is not accurate at lower temperatures and densities [22]. A combination of experiments on mixtures and theoretical developments is needed to develop reliable unlike-pair interaction potentials.

Many materials produce large quantities of solid products upon detonation. The most common solid detonation product is carbon, although some explosives produce aluminum and aluminum oxide [29]. Uncertainties in the equation of state and phase diagram of carbon remain a major issue in the thermochemical modeling of detonation. van Thiel and Ree have proposed an accurate Mie-Gruneisen equation of state for carbon [30]. Fried and Howard [31] have developed a simple modified Murnaghan equation of state for carbon that matches recent experimental data on the melting line of graphite. There is considerable uncertainty regarding the melting line of diamond. Fried and Howard argue based on reanalysis of shock data that the melting line of diamond should have a greater slope. Shaw and Johnson have derived a model for carbon clustering in detonation [32]. Viccelli and Ree have derived a carbon-clustering model for use in hydrodynamic calculations [33,34].

In the present chapter, we apply an accurate and numerically efficient equation of state for the exp-6 fluid based on Zerah and Hansen's hypernetted-mean spherical approximation (HMSA)[22] equations and Monte Carlo calculations to detonation, shocks, and static compression. We present a library of parameters for fluid and condensed high pressure molecules in Ref. [35]. We call this library "EXP6".

EXP6 supports a wide range of elements and condensed detonation products. We have applied a Murnaghan[24] equation of state (EOS) form to a variety of metals, metal oxides and other solids. We have also matched phase transition data for many of these solids. For example, this form has recently been applied to the EOS of carbon[31]. Thermal effects in the EOS are included through the dependence of the coefficient of thermal expansion on temperature, which can be directly compared to experiment. We find that we can replicate shock Hugoniot and isothermal compression data for a wide variety of solids with this simple form.

The exp-6 potential has also proved successful in modeling chemical equilibrium at the high pressures and temperatures characteristic of detonation. However, in order to calibrate the parameters for such models, it is necessary to have experimental data for molecules and mixtures of molecular species at high temperature and pressure. Static compression data, as well as sound speed measurements, provide important data for these models.

We validate EXP6 through several independent means. We consider the shock Hugoniots of liquids and solids in the "decomposition regime" where thermochemical equilibrium is established. We argue that this regime is reached for most organic materials above 50GPa shock pressures. We also validate the code against high explosive overdriven shock Hugoniots, and more traditional metrics such as the detonation velocity and pressure. Overall, we find that EXP6 offers a highly accurate representation of high pressure equation of state properties with no empirical fitting to detonation data.

While there exists an extensive body of experimental techniques and experience on computational methods appropriate to ambient conditions, the

regime of strong repulsive interactions at very high densities has not been as extensively investigated. The experiments discussed here are aimed both at enlarging the family of properties conveniently measured at high pressure and, principally, at providing the data appropriate to a critical test of the theory of the internuclear potential in simple substances at high density.

## COMPUTATIONAL METHOD

Cheetah is a thermochemical code that is used to predict detonation performance for solid and liquid explosives. Cheetah solves thermodynamic equations between product species to find chemical equilibrium for a given pressure and temperature. Chapman-Jouget (C-J) theory says that the detonation point is a state in thermodynamic and chemical equilibrium, so Cheetah can predict the properties of this state. From these properties and elementary detonation theory the detonation velocity and other performance indicators are computed.

Thermodynamic equilibrium is found by balancing chemical potentials, where the chemical potentials of condensed species are just functions of pressure and temperature, while the potentials of gaseous species also depend on concentrations. In order to solve for the chemical potentials, it is necessary to know the pressure-volume relations for species that are important products in detonation. Moreover, it is necessary to know these relations at the high pressures and temperatures that typically characterize the CJ state. Thus, there is a need for improved high-pressure equations of state for fluids, particularly for molecular fluid mixtures. The exponential-6 (exp-6) potential model defines the energy of interaction of a classical fluid composed of identical spherical particles. This model has been used with considerable success to describe the equation of state of many materials over a wide range of pressure and temperature[36].

We now specify the equation of state used to model detonation products. For the ideal gas portion of the Helmholtz free energy, we use a polyatomic model including electronic, vibrational, and rotational states. Such a model can be conveniently expressed in terms of the heat of formation, standard entropy, and constant pressure heat capacity of each species.

The heat capacities of many product species have been calculated by a direct sum over experimental electronic, vibrational, and rotational states. These calculations were performed to extend the heat capacity model beyond the 6000K upper limit used in the JANAF thermochemical tables. Chebyshev polynomials, which accurately reproduce the heat capacities, were generated.

The HMSA/MC equation of state was used to describe the excess Helmholtz free energy. An extended Lorentz-Berthelot approximation was used to generate the interaction between unlike species.

$$\begin{aligned}\varepsilon_{ij} &= \sqrt{\varepsilon_{ii}\varepsilon_{jj}} \\ r_{m,ij} &= k_{ij}(r_{m,ii} + r_{m,jj})/2 \\ \alpha_{ij} &= \sqrt{\alpha_{ii}\alpha_{jj}}\end{aligned}$$

The parameter  $k_{ij}$  is a non-additive interaction parameter. In nearly all cases we use  $k_{ij} = 1$ . Our goal is to derive a model for supercritical fluids applicable to a very wide range of states and properties. In order to do so, we have developed an automatic optimization procedure to match a variety of experimental data.

Experimental observables were placed into categories. We took the first category to be the volume along the shock Hugoniot and reshocked states. The second was the temperature along the shock Hugoniot and reshocked states. The third was the volume under static compression. The last category was the sound speed under static compression. For each category, we determined an average error.

The figure of merit is a weighted average of the category errors. We assigned a weight of 40% to shock volumes, 25% to shock temperatures, 25% to static volumes, and 10% to the speed of sound. The optimization procedure is weighted more to shocks than static measurements, although we find below that we reproduce both well. A stochastic optimization algorithm was employed to minimize the figure of merit function. Our final parameters are listed in Ref. [35]. In the following subsections we analyze the performance of the resulting equation of state in reproducing a wide range of experimental measurements. Results for nitrogen are fully discussed in [22]. Although the



parameters in that work are slightly different than those used here, the comparison to experiment is similar.

Other workers[36,37] have shown that a chemical equilibrium model of hydrocarbons based on an exponential-6 fluid model using Ross's soft-sphere perturbation theory is successful in reproducing the behavior of shocked hydrocarbons. Our model of the supercritical phase includes the species  $H_2$ ,  $CH_4$ ,  $C_2H_6$ , and  $C_2H_4$ . We have chosen model parameters so as to match both static compression isotherms and shock measurements wherever possible. The ability to match both types of experiments well increases confidence in the general applicability of our high pressure equation of state model.

We now specify the sources of experimental data used in the calculations that follow. The shock Hugoniot data for polyvinylchloride (PVC), polychlorotrifluoroethylene (PCTFE),  $CH_2Cl_2$ ,  $CHCl_3$ ,  $CCl_4$ , polyethylene, n-hexane, cyclohexane, benzene, PVF<sub>2</sub>, and PTFE comes from Marsh[38] and for  $CH_4$  from Nellis et al.[39]. Shock Hugoniot and shock temperature data for  $H_2$  comes from a variety of sources[40-42]. We use static compression data for  $CH_2F_2$ ,[43]  $HF$ [44],  $C_2H_4$ [45,46],  $CH_4$ [47,48], and  $C_2H_6$ [49,50].

Calibration began with  $H_2$ , which was matched to measured shock Hugoniot and shock temperatures. The same parameters were used for  $H_2$  and  $D_2$ , because of the identical potential energy of interaction of the two isotopes. This served to further constrain the  $H_2$  equation of state.

Next parameters for  $CH_4$ ,  $C_2H_6$ , and  $C_2H_4$  were determined by matching a combination of static and shock compression data for the materials,  $CH_4$ ,  $C_2H_6$ ,  $C_2H_4$ , benzene, n-hexane, and cyclohexane. We found agreement to within roughly 1% between the measured and calculated equation of state properties.

## FLUID EQUATIONS OF STATE

In Figure 1 we show the shock Hugoniot of polybutene as calculated with the current modeling system. We find good agreement with reshock experiments up to 210 GPa in this material as well. In Figure 2 we compare

calculated and experimental isotherms of  $C_2H_6$ . Note that a high level of accuracy is found even at moderate (MPa) pressures.

We next discuss the fluorocarbon model. To our knowledge, high pressure equation of state measurements have not been performed on  $F_2$ . We use exp-6 parameters for  $F_2$  estimated by Zerilli and Jones [51]. We considered the shock behavior of PTFE in order to determine parameters for  $CF_4$ .

We predict that PTFE decomposes into a fluid phase composed mostly of  $CF_4$ , and carbon in the diamond phase. We found an unusually high value of the potential steepness parameter  $\alpha$ . We note that Zerilli and Jones[51] also obtained a very steep potential for  $CF_4$  by spherically averaging a Lennard-Jones potential.

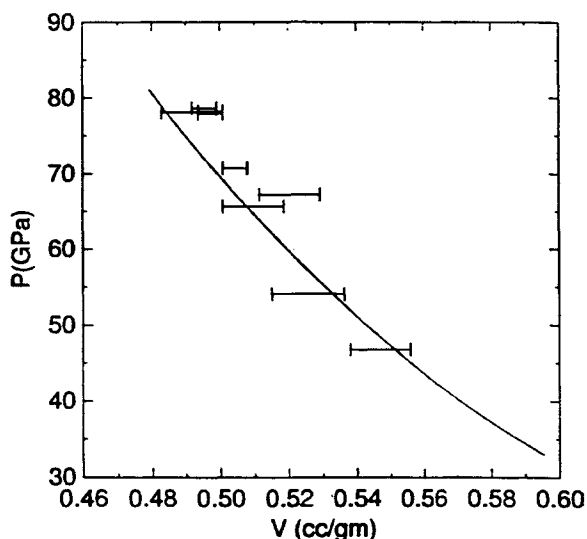


**Figure 1.** Measurements of the reactive shock Hugoniot of polybutene (error bars) are compared to calculations of the present model (line)

HF is known to strongly associate[52], in the gaseous, liquid, and fluid phases. We have determined a simple HF association model that matches both high and low pressure data.

There is insufficient experimental data on HF to uniquely determine the exp-6 parameters of each associated species. Instead, we use simple scaling rules to relate the properties of the clusters to that of HF.

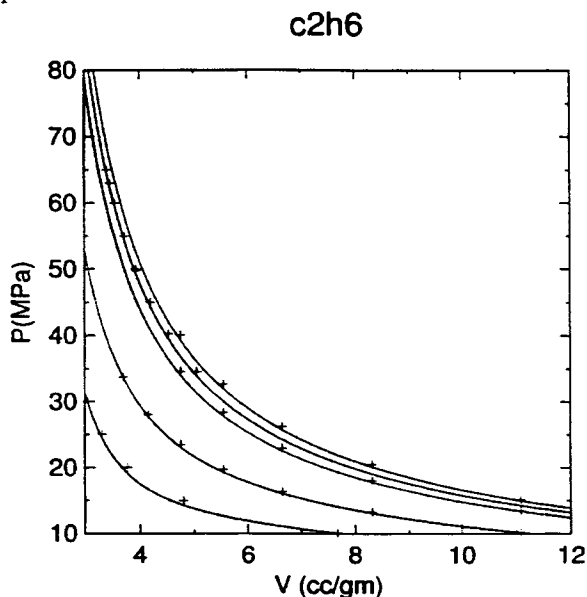


Figure 2. Measurements of the isotherms of  $C_2H_6$  at 400, 473, 573, and 600K (points) are compared to calculations of the present model (lines)

The motivation for the cluster model is to determine the simplest possible model that will match both the low pressure static compression of supercritical HF, and the shock Hugoniot of PVF2. The current model succeeds in this regard, although we cannot claim that the description of individual cluster species is quantitatively accurate. We have found that it is possible to match the shock Hugoniot of PVF2 without the association model, but the static compression requires an explicit treatment of association. We decided to limit our model to only those clusters described by JANAF.

We show the calculated isotherms of HF in Figure 3. The calculated shock Hugoniot of PVF2 is shown in Figure 4. In our calculations PVF2

dissociates to HF and carbon. The HF model is seen to work equally well in the experimental pressure range of 0.01 to 75 GPa.

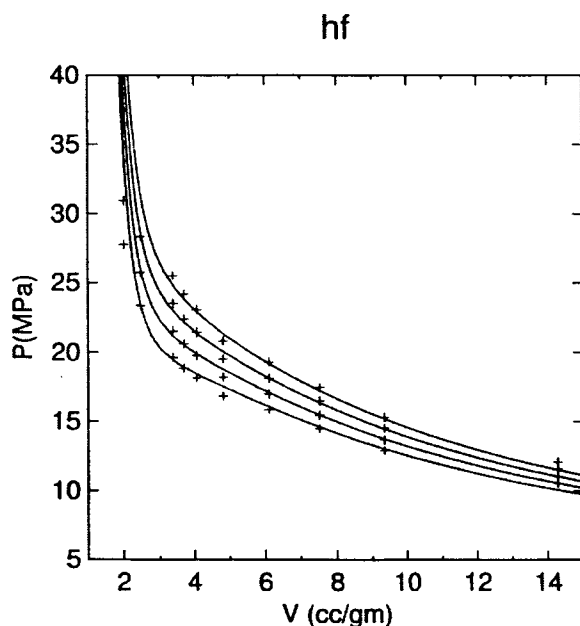


Figure 3: Measurements of the isotherms of HF at 543, 553, 563, and 573K (points) are compared to calculations of the present model (lines)

There is more shock data available on chlorocarbons than the fluorocarbons. This allows for more extensive testing of the validity of the present model. We note that Dremov and Modestov[53] have reported effective exponential-6 parameters for chlorinated methanes. We find their parameters to be inaccurate when used within the current modeling framework, which uses the recently developed HMSA/MC equation of state[22], and a product set including hydrocarbons and condensed carbon. Parameters for fluid  $\text{CCl}_4$  were matched to the shock Hugoniot of liquid  $\text{CCl}_4$ .

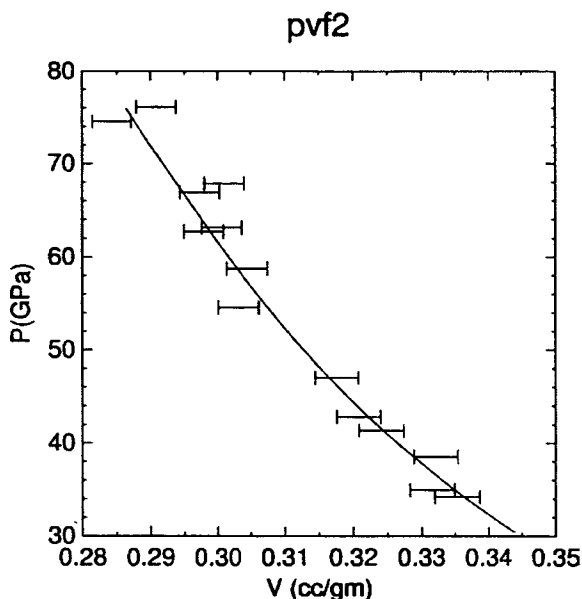


Figure 4. Measurements of the shock Hugoniot of PVF2 (error bars) are compared to calculations of the present model (line)

$\text{H}_2\text{O}$  is a major detonation product. A simple exp-6 potential model, however, does not naturally represent the hydrogen-bonded tetrahedral structure of water. We find that an effective two-species model is effective in representing the equation of state of supercritical water over a wide range of conditions. In the two-species model, we represent water by two species in chemical equilibrium: non-associated water ( $\text{H}_2\text{O}$ ) and associated water:  $\text{H}_2\text{O}(\text{a})$ . The non-associated water has standard state parameters given by gaseous water. In associated water, however, standard state parameters are chosen closer to that of liquid water: the standard enthalpy and entropy are both less than that of gaseous water.

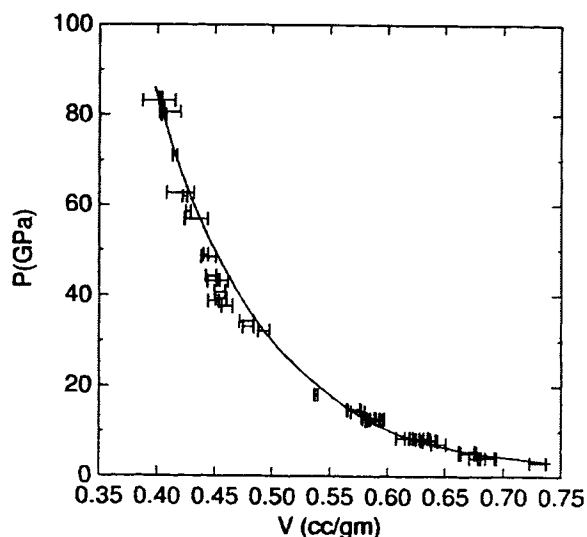


Figure 5: Measurements of the shock Hugoniot of  $\text{H}_2\text{O}$  (error bars) are compared to calculations of the present model (line)

In the limit of high temperatures and low density, chemical equilibrium favors the non-associated species. For temperatures close to the critical temperature, associated water is favored. This models the increasingly strong nature of the interactions between water molecules as hydrogen bonding is established in the fluid.

In Figure 5 we compare our model to the shock Hugoniot of liquid water. Good agreement is seen. In particular, we successfully reproduce the low-density tail of the shock Hugoniot while using the (correct) energy of formation for liquid water in the shock Hugoniot relations ( $E_0$ ). In this region a single exp-6 species fails to accurately model the experimental data. In fact, solutions to the Hugoniot equation do not exist for low compressions with a single species model. In Figure 6 we compare the predictions of the EXP6 model for  $\text{H}_2\text{O}$  to experimental PVT data taken between 1600 and 500K[54]. The model is in good agreement with experiment, even in the difficult region near the critical temperature.

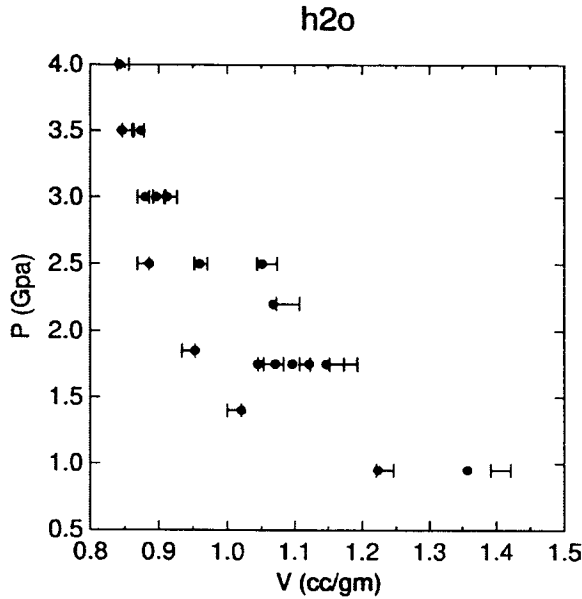


Figure 6: PVT measurements of water between 500 and 1600K (error bars) are compared to calculations of the present model (points).

Most commercially used explosives and propellants have roughly a 1:1 carbon/oxygen ratio. Thus, CO is expected to be a major detonation product. The modeling of CO presents some challenges. The shock Hugoniot of CO reaches very high temperatures. In order to model this accurately, we calculated extended  $C_p$  functions for CO, O<sub>2</sub> and CO<sub>2</sub> valid up to 20,000K. A comparison between our calculated shock Hugoniot and the experimental shock Hugoniot of CO is shown in Figure 7. The accurate modeling of the CO shock Hugoniot required the specification of non-additive pair interaction parameters between O and CO<sub>2</sub>. We set  $k_{\text{CO}_2,\text{O}} = 0.897$ . This is the only non-additive interaction parameter used in EXP6.

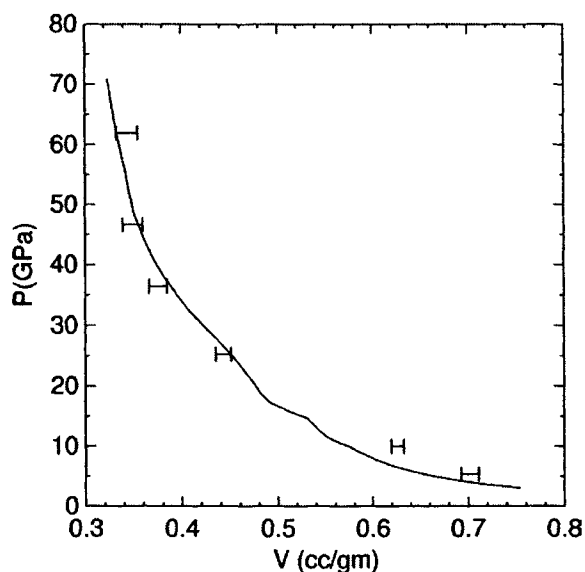


Figure 7: Measurements of the shock Hugoniot of CO(error bars) are compared to calculations (line)

We have also calibrated the CO model to static compression data. In Figure 8 we compare isotherms of CO to experimental data. Good agreement is found.

## CONDENSED EQUATIONS OF STATE

We used the Murnaghan equation of state model described in Ref. [24] for all condensed materials except for carbon. The parameters for the equation of states of these materials is given in Ref. [35].

Carbon is also a major detonation product. A successful thermochemical library must include an accurate equation of state for carbon. Our carbon equation of state [13] is based on an explicit functional form for  $G(P,T)$ . It is more often the case that the pressure of a system is known than its volume. This makes a  $(P,T)$  equation of state very convenient in practical application.



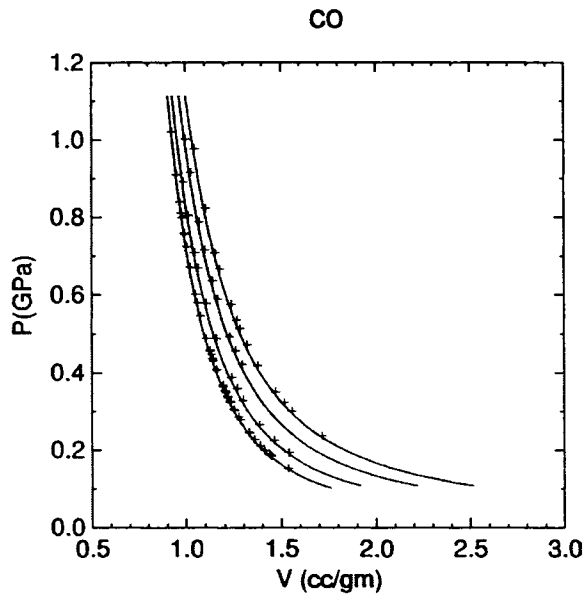


Figure 8. Measurements of the isotherms of CO(crosses) at 308K, 373K, 473K, and 573K are compared to calculations (lines)

Aluminum is a major ingredient in many detonation products. It reacts to form primarily  $\text{Al}_2\text{O}_3$  in detonations. We have derived multiphase models for Al and  $\text{Al}_2\text{O}_3$  based on the Murnaghan equation of state. Parameters are given in Ref. [35]. We show the shock Hugoniot of  $\text{Al}_2\text{O}_3$  as an example in Figure 9.

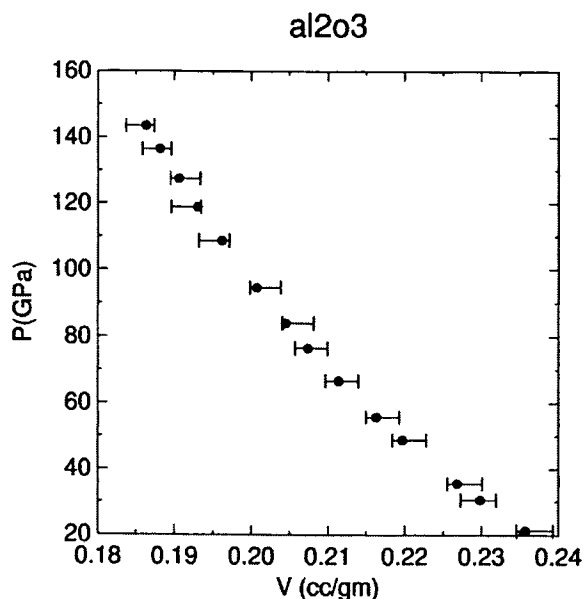


Figure 9. Measurements of the shock Hugoniot of Al<sub>2</sub>O<sub>3</sub> (error bars) are compared to calculations (Dots).

## APPLICATION TO DETONATION

We now consider how the equation of state described above predicts the detonation behavior of condensed explosives. The overdriven shock Hugoniot of an explosive is an appropriate equation of state test. The overdriven Hugoniot tests the EOS across a broad range of thermodynamic states. The Hugoniot of PETN is shown in Figure 10. We have calculated the Hugoniot with the EXP6 model presented here and also with the JCZS [12] product library. JCZS calculations were performed without liquid water, since the temperatures reached in these simulations were far above the liquid region.

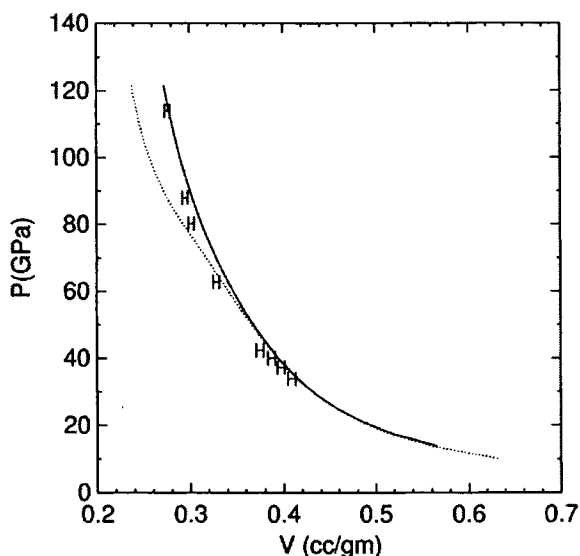


Figure 10: The shock Hugoniot of PETN as calculated with EXP6 (solid line) and the JCZS library (dotted line) vs. experiment (error bars).

In Figure 11 we calculate the shock Hugoniot of HMX/TATB (49% HMX, 47% TATB, 4% Estane) to experiment. Good agreement is seen with both product libraries.

We have applied the equation of state to numerous formulations containing the elements C, H, N, and O. We find that the EXP6 equation of state library improves significantly on previous BKW libraries. Its average error in the detonation velocity is somewhat higher than that of JCZS. EXP6, however, is not fit to any detonation data, whereas many adjustable parameters in JCZS were fit to detonation data.

## EXPERIMENTAL

New experiments are needed to further our understanding of the equation of state and kinetics of detonation products. The optical Impulsive Stimulated Light Scattering (ISLS) technique is discussed in general in Ref.

[55,56] and specifically in the context of the DAC in Refs. [57-59]. Briefly, two successive "excitation" pulses, (30  $\mu\text{J}$ , 60  $\mu\text{m}$  diameter,  $\sim 100$  ps duration)

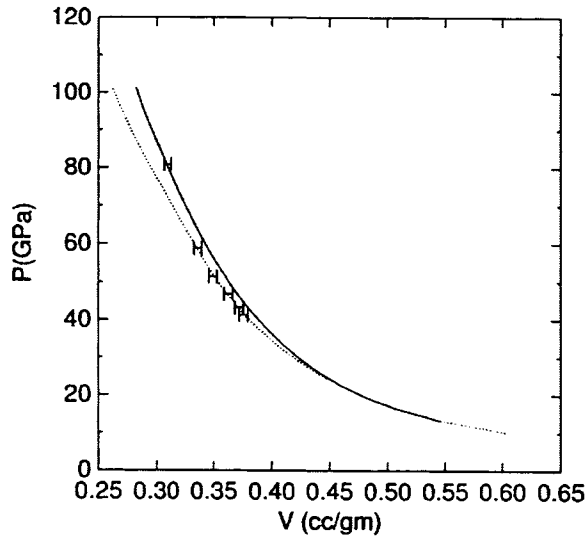


Figure 11. The shock Hugoniot of HMX/TATB as calculated with EXP6 (solid line) and the JCZS library (dotted line) vs. experiment (error bars).

are selected from the output train of a Q-switched (500 Hz), mode-locked Nd:YAG laser and recombined in the sample at an angle  $2\theta$ , but otherwise coincident in space and time. Interference establishes a periodic distribution of intensity and, in a sample that absorbs in the near infrared, a (spatially) periodic variation in the temperature and pressure ensues. The coupling between laser light and the excited material modes is such that the local temperature rise remains "impulsive." The associated thermal pressure launches counter-propagating acoustic waves. The acoustic wavelength,  $d$ , in this case equal to the period of the optical grating, may be expressed in terms of the excitation wavelength,  $\lambda_E = 1.064 \mu\text{m}$ , and  $\theta$  as

$$d = \lambda_A = \frac{\lambda_E}{2 \sin \theta}$$

In a fluid sample one longitudinal wave is excited. The impulsively excited acoustic wave induces a temporally and spatially periodic variation in the index of refraction of the sample. A third pulse ( $\sim 1 \mu\text{J}$ ,  $20 \mu\text{m}$  diameter,  $\sim 80$  ps duration) selected from the same Q-switched envelope as the excitation pulses is frequency doubled ( $\lambda_p = 0.532 \mu\text{m}$ ) and delayed by a combination of time of flight and mode lock pulse selection to generate the "probe." Observation of the intensity of the Bragg scattering of the probe, by the acoustic or thermo-acoustic grating, as a function of probe delay serves to determine the frequency ( $\nu$ ), and hence the adiabatic velocity ( $c = d\nu$ ) of the acoustic waves.

In practice, grating spacings are determined by making the same measurement on a piece of glass with a known speed of sound and which gives a strong, stable signal suitable for a calibrant. The glass was in turn calibrated against water and fused silica [60-62]. The velocity is typically determined with a precision of  $< \pm 0.2\%$ .

Pressure determinations were made by monitoring the wavelength of the fluorescence (excited by a He-Cd laser or by the 488-nm  $\text{Ar}^+$  laser line) of ruby chips that surround or are embedded in the sample. Rubies after grinding to tens of microns have residual strains which are often large enough to offset pressure measurements by  $\sim 0.05$  GPa, and occasionally as much as 0.2 GPa. Annealing at  $\sim 1000^\circ \text{C}$  for several hours decreases both the magnitude and frequency of these deviations yet it is still common to find rubies which differ reproducibly by the equivalent of 0.02 GPa. The most precise work completed has been on the melting curve of  $\text{O}_2$ , in which the relative wavelengths of rubies were recorded at 0 GPa and the high-pressure results corrected by the same amounts. The reference rubies at 0 GPa were kept in the same temperature controlled housing as were the samples, because wavelength shifts equivalent to 0.01 GPa are generated by temperature differences of  $0.5^\circ \text{C}$  and in order to match as closely as possible the two spectral line shapes. With hydrostatic samples one can measure pressures with a precision of slightly better than 0.01 GPa. A 1/4m spectrometer (1200 grooves/mm grating) and 750 bin CCD ( $11 \mu\text{m}$  pixel width) gave a dispersion of  $2.3 \times 10^{-3} \text{ \AA/bin}$ . Micro FTIR spectra were taken on a Bruker Optics vector-33 FTIR spectrometer ( $4\text{cm}^{-1}$  resolution).

Liquid formaldehyde is not available commercially, and exists only at low temperatures. Our chemical procedure for producing liquid formaldehyde was as follows: Into a dried 500 mL 3-necked round-bottomed fitted with a N<sub>2</sub> inlet and outlet, thermocouple, and surrounded by a heating mantle was placed approximately 80g of paraformaldehyde (fills flask 2/3 full). The mixture was heated to decompose the paraformaldehyde with the internal temperature controlled with a thermocouple connected to a temperature controller set at 150°C. The formaldehyde was initially collected (under a slow N<sub>2</sub> flow) in a small condensing trap cooled at CO<sub>2</sub>/ acetone temperature to insure removal of residual water and any low boiling impurities. After about 5 mL of formaldehyde was collected in the trap the outlet tube was connected to the diamond anvil apparatus, which was kept under a N<sub>2</sub> atmosphere and cooled to dry ice/ acetone temperatures. Enough formaldehyde was collected to completely cover the diamond anvil cell (~20 mL). The cell was opened and then closed to encapsulate the sample. A rhenium gasket was used to radially confine the diamond anvil cell samples.

## RESULTS AND DISCUSSION

The sound velocity of pure methanol (MeOH) was measured along a 250°C isotherm up to 3.9 GPa. After each data point was taken the sample was cooled and the velocity was again measured and compared to previous measurements of uncooked MeOH [63]. No appreciable velocity difference between data sets was observed. The measured sound speeds for MeOH are given in Table I.

P(GPa)	c(km/s)
.561	2.194
.987	2.720
1.424	3.000
1.633	3.219
2.640	3.771
3.160	4.023
3.890	4.255

Table I: Measured sound speed for CH<sub>3</sub>OH at 250 °C.

A comparison of ISLS experimental data and Cheetah computational results is given in Figure 12. The exp-6 potential model used was based on the shock Hugoniot of methanol. The  $\sim 3\%$  difference between data sets shows the utility of Cheetah and the consistency between static and dynamic equation of state measurements. The exp-6 parameters for species considered here are given in Table II.

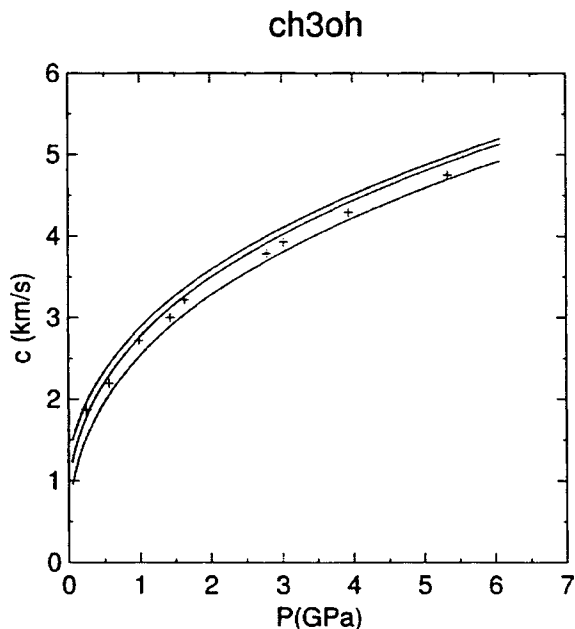


Figure 12: Measured sound speed for  $\text{CH}_3\text{OH}$  at 300, 200, and 94 degrees C (crosses) versus calculations.

Species	$H_0$	$S_0$	$r_m$	$\epsilon$	$\alpha$
$\text{CH}_2\text{O}$	-116	0.219	3.72	350	13.0
$\text{CH}_2\text{Oa}$	-119	0.217	5.64	350	13.0
$\text{CH}_3\text{OH}$	-201	0.240	4.24	507	13.0

Table II: Heat of formation ( $H_0$ : kJ/mol), standard entropy ( $S_0$ : kJ/mol-K), exp-6 potential minimum ( $r_m$ : Å), well depth ( $\epsilon$ : K) and steepness parameter ( $\alpha$ ) for species studied in this work.

An attempt was then made to measure the velocity of MeOH at 5 GPa, but at this pressure MeOH froze. The sample was then brought up to 325°C where it promptly began to phase separate into immiscible supercritical reaction products (Figure 13). Upon cooling, brownish platelet looking forms were observed at 315°C. Some of the smaller bubbles contained diamond.

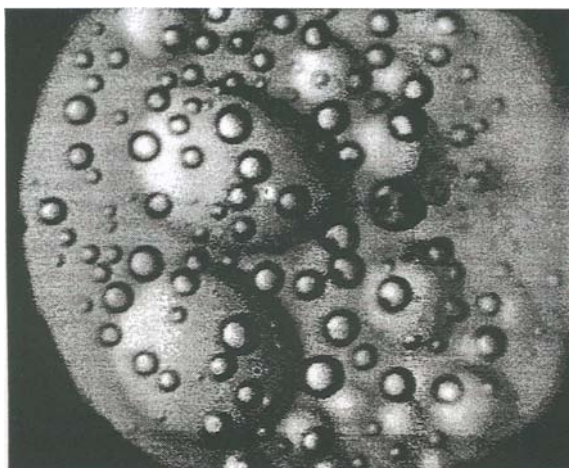


Figure 13: MeOH product bubbles at 232°C and 5 GPa.



Heat was again applied, and the formation of tendrils (possibly rhenium oxide) began at 331°C. These tendrils retreated at 325°C. Upon further cooling brown platelets re-appeared at 316°.



Figure 14: MeOH products frozen at 110°C and 5 GPa. A spot at the 9 o'clock position is ruby used to optically measure pressure.

At this point the furnace was removed from the optical table and placed on a microscope stage where digital micro-graphs were taken of the bubbles as they dissipated and eventually froze, Figure 14.

We compared FTIR spectra of the frozen sample to MeOH at ambient conditions. The results are shown in Figure. 15. When pure methanol is loaded to 5 GPa the ensuing temperature induced reaction proceeds without forming bubbles. We have studied each reproducible reaction process and have determined from FTIR experiments conducted at the National Synchrotron Light Source at Brookhaven National Laboratory (Beam Line U2a) that pure MeOH reacts to form water and carbon dioxide. Methanol subjected to 532nm and 1064 nm 100 ps pulses reacts to form supercritical water, carbon dioxide, ethane, and perhaps methane (see Figures 15, 16, and 17). These same products are predicted by the CHEETAH thermo-chemical code if no carbon, in the form of diamond, is produced.

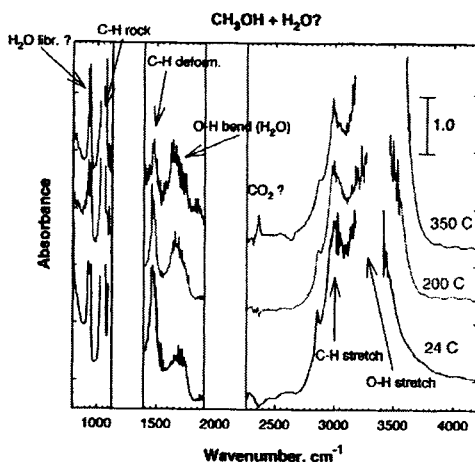


Figure 15. FTIR spectrum of MeOH in the water-rich product region of the DAC showing the formation of both water and  $\text{CO}_2$ .

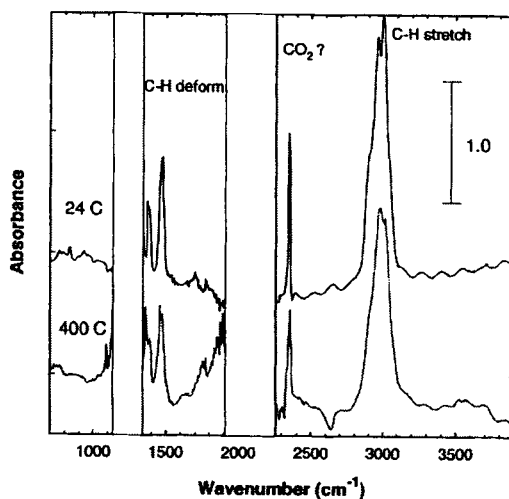


Figure 16. FTIR spectrum of MeOH in the ethane-rich product region of the DAC showing the formation of both ethane and  $\text{CO}_2$ .

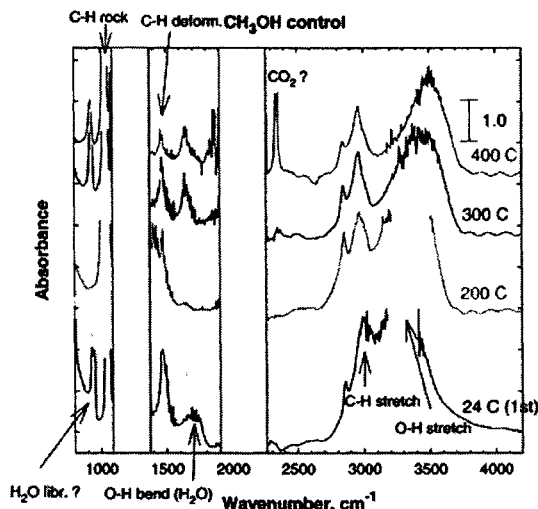


Figure 17. FTIR spectrum of non laser-treated MeOH showing only water and CO<sub>2</sub> products. The 24 C spectrum is from the laser-treated sample prior to reaction.

We have not verified if product molar volume equivalents between experiment and computation match. We can also conduct Raman and FTIR studies on these materials as the fluids freeze.

ISLS measurements of the sound speed in CH<sub>2</sub>O were also performed. The same procedures were followed as for CH<sub>3</sub>OH. The experimental results are given in Table III. CH<sub>2</sub>O is not in the current default product set for the Cheetah library. Parameters were estimated using simple corresponding states theory. These gave results with an average absolute error of 42%. The CH<sub>2</sub>O parameters used with the JCZS product library were also compared to the experimental data. A 33% average absolute error was found. CH<sub>2</sub>O is a polar molecule. We have found that a two-species description of polar associated fluids can dramatically increase the accuracy of the exp-6 model. In the present case, we use species CH<sub>2</sub>O and CH<sub>2</sub>Oa. CH<sub>2</sub>Oa is associated formaldehyde. CH<sub>2</sub>Oa has lower standard energy and entropy than CH<sub>2</sub>O. Parameters for CH<sub>2</sub>O and CH<sub>2</sub>Oa are given in Table II. A comparison between the two species model and the experimental data are given in Figure 18. Good agreement is seen, with an average error of 6%.

P(Gpa)	T(C)	C(km/s)
0.821, 0.822	24	2.484
1.505, 1.466	247	2.626
		2.608
		2.614
0.350, 0.342	250	1.227
0.984, 0.855		2.353
		2.332
1.968, 2.023		3.072

Table III: Sound speed measurements for CH<sub>2</sub>O. Pressure pairs were taken before and after sound speed determinations. Repeated values are blank.

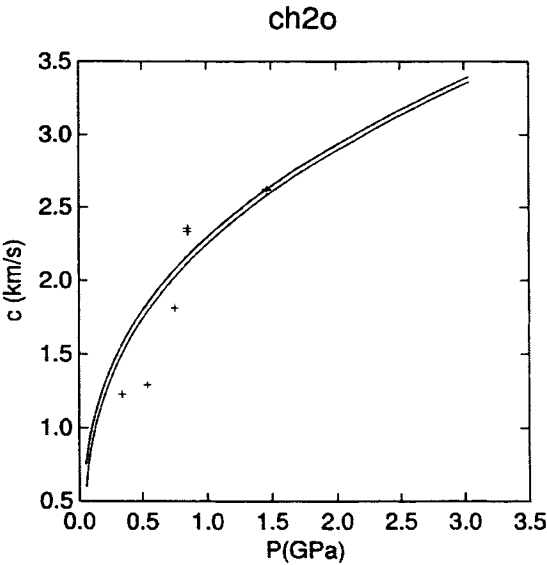


Figure 18: Measured sound speed for CH<sub>2</sub>O at 250 and 300 °C vs. calculations.

We have applied the present refinements to the EXP6 product library used in Cheetah. With the refined parameters, we can examine the nature of chemical composition at Chapman-Jouget (CJ) detonation states. The CJ states of three common explosives, HMX, RDX, and NM, were determined with the Cheetah program. Results are shown in Figure 19.  $\text{CH}_2\text{O}$  is predicted to be present in significant concentrations at the C-J state, but  $\text{CH}_3\text{OH}$  is not.

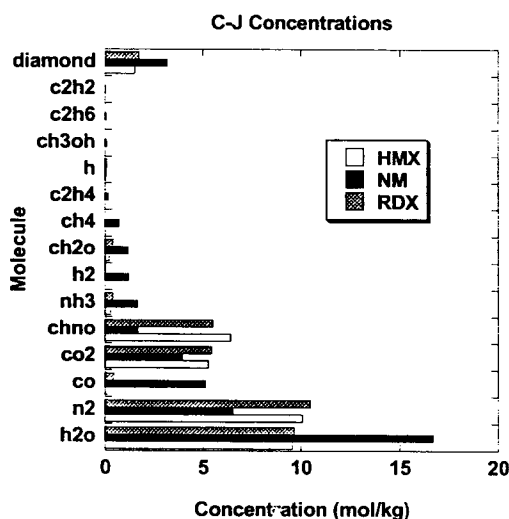


Figure 19: Concentrations at the Chapman-Jouget state of HMX, RDX, and NM using the EXP6 product library.

## CONCLUSIONS

In the present chapter we have reviewed a numerically efficient and accurate equation of library state for high pressure fluids and solids. Thermodynamic cycle theories allow us to apply this model profitably to the reactions of energetic materials. The equation of state is based on HMSA integral equation theory, with a correction based on extensive Monte Carlo simulations. We have also shown that our equation of state can be used to accurately model the properties of molecular fluids and detonation products. The accuracy of the equation of state of polar fluids is significantly enhanced by using a multi-species or cluster representation of the fluid.

Our ability to model the behavior of shocked fluorocarbons and chlorocarbons helps to unify data that was previously apparently unrelated; the behavior of this class of materials under shocks over 35 GPa are now related to the properties of a small set of simple decomposition products.

We have measured the sound speed of supercritical MeOH at 250 °C up to 3.9 GPa. MeOH froze at 5 GPa. An attempt to carry on the sound speed study along a 325°C isotherm was thwarted by chemical reaction toward products that may include water, ethane, methane, diamond, and perhaps formaldehyde. Nonetheless, the diamond anvil cell provides a unique opportunity to study the chemical kinetics of fluids under extremely high pressures.

We predict that  $\text{CH}_2\text{O}$  is found in appreciable quantities in the C-J state of the explosives found. This is a somewhat surprising result. Successful thermochemical treatments of detonation have been developed either with or without  $\text{CH}_2\text{O}$ . We compared the accuracy of detonation velocities for a database of explosives containing C, H, N, and O. The inclusion of  $\text{CH}_2\text{O}$  made little difference in the overall accuracy of the results.

We also note that  $\text{CH}_3\text{OH}$  is found in only trace quantities in our C-J calculations. This species may play a more important role in kinetic mechanisms of energetic material decomposition.

Another interesting observation is that HNCO (isocyanic acid) is a major detonation product. The exp-6 model for this species is currently based on

estimates used in the JCZS product library. Closer experimental investigation of the chemical species formed by reacting energetic materials is called for.

## ACKNOWLEDGEMENTS

The authors thank Dr. A. Goncharov and Dr. Z. Liu for assistance in collecting  $\mu$ -FTIR data at the National Synchrotron Light Source, and A. Goncharov for data analysis. We also thank Dr. J. Crowhurst for CH<sub>2</sub>O sound velocity data.

\*This work performed under the auspices of the U.S. Department of Energy by the Lawrence Livermore National Laboratory under contract number W-7405-Eng-48.

## REFERENCES

- [1] LE Fried, MR Manaa, PF Pagoria, RL Simpson: *Ann. Rev. Mat. Sci.* 31 (2001) 291-321.
- [2] PC Souers, JW Forbes, LE Fried, S Anderson, S Dawson, P Vitello, R Garza: *Propellants Explosives Pyrotechnics* 26 (2001) 180-90.
- [3] W Fickett, WC Davis, University of California Press, Berkeley, 1979.
- [4] GB Kistiakowsky, EB Wilson. Office of Scientific Research and Development, 1941.
- [5] M Finger, E Lee, FH Helm, B Hayes, H Hornig, R McGuire, M Kahara, M Guidry, Sixth Symposium (International) on Detonation. Office of Naval Research, Coronado, CA, 1976, p. 710-22.
- [6] CL Mader, University of California Press, Berkeley, CA, 1979.
- [7] SA Gubin, VV Odintsov, VI Pepekina: *Sov. J. Chem. Phys.* 3 (1985) 1152.
- [8] ML Hobbs, MR Baer, Tenth International Detonation Symposium, Boston, MA, 1993, p. 409-18.
- [9] PC Souers, JW Kury: *Propellants, Explosives, Pyrotechnics* 18 (1993) 175.
- [10] LE Fried, PC Souers: *Propellants, Explosives, Pyrotechnics* 21 (1996) 215-23.
- [11] M Cowperthwaite, WH Zwisler, Sixth Detonation Symposium, 1976, p. 162.
- [12] ML Hobbs, MR Baer, BC McGee: *Propellants, Explosives, Pyrotechnics* 24 (1999) 269-79.
- [13] LE Fried, 2000.
- [14] M Ross: *J. Chem. Phys.* 71 (1979) 1567.
- [15] M Ross, FH Ree: *J. Chem. Phys.* 73 (1980) 6146-52.
- [16] FH Ree: *J. Chem. Phys.* 81 (1984) 1251.
- [17] M van Thiel, FH Ree: *J. Appl. Phys.* 62 (1987) 1761-67.
- [18] M van Thiel, FH Ree: *J. Chem. Phys.* 104 (1996) 5019-25.

- [19] HS Kang, CS Lee, T Ree, RF H.: J. Chem. Phys. 82 (1985) 414.
- [20] W Byers Brown: J. Chem. Phys. 87 (1987) 566.
- [21] F Charlet, ML Turkel, JF Danel, L Kazandjian: J. Appl. Phys. 84 (1998) 4227-38.
- [22] LE Fried, WM Howard: J. Chem. Phys. 109 (1998) 7338-48.
- [23] FH Ree: J. Chem. Phys. 84 (1986) 5845-56.
- [24] LE Fried, WM Howard: J. Chem. Phys. 110 (1999) 12023-32.
- [25] MS Shaw: J. Chem. Phys. 94 (1991) 7550-53.
- [26] TW Leland, JS Rowlinson, GA Sather: Trans. Faraday Soc. 64 (1947) 1447.
- [27] GI Kerley in J.M. Short (Ed.), Eighth Symposium (International) on Detonation. Naval Surface Weapons Center, Albuquerque, NM, 1985, p. 540-45.
- [28] TM Reed, KE Gubbins, McGraw-Hill, New York, 1973.
- [29] HD Jones, FJ Zerilli: J. Appl. Phys. 69 (1991) 3893-900.
- [30] M van Thiel, FH Ree: Int. J. of Thermophysics 10 (1989) 227-36.
- [31] LE Fried, WM Howard: Phys. Rev. B 61 (2000) 8734-43.
- [32] MS Shaw, JD Johnson: J. Appl. Phys. 62 (1987) 2080-85.
- [33] JA Viecelli, FH Ree: J. Appl. Phys. 86 (1999) 237-48.
- [34] JA Viecelli, FH Ree: J. Appl. Phys. 88 (2000) 683-90.
- [35] LE Fried, WM Howard, PC Souers in J.L.M.a.J.M. Short (Ed.), 12th Symposium (International) on Detonation. NSWC, Indian Head, San Diego, CA, 2002.
- [36] FH Ree: J. Chem. Phys. 70 (1979) 974.
- [37] WJ Nellis, FH Ree, RJ Trainor, AC Mitchell, MB Boslough: J. Chem. Phys. 80 (1984) 2789.
- [38] SP Marsh, University of California Press, Berkeley, 1980.
- [39] WJ Nellis, FH Ree, M van Thiel, AC Mitchell: J. Chem. Phys. 75 (1981) 3055.
- [40] RD Dick, GI Kerley: J. Chem. Phys. 73 (1980) 5265.
- [41] WJ Nellis, AC Mitchell, M van Thiel, GJ Devine, RJ Trainor: J. Chem. Phys. 79 (1983) 1480.
- [42] NC Holmes, M Ross, WJ Nellis: Phys. Rev. B 52 (1995) 15835.
- [43] PF Malbrunot, PA Meunier, GM Scatena, WH Mears, KP Murphy, JV Sinka: J. Chem. Eng. Data 13 (1968) 16.
- [44] VEU Franck, W Spalthoff: Z. Elektrochem. 61 (1957) 348.
- [45] HJ Achtermann, HD Baehr, TK Rose: J. Chem. Thermodynamics 21 (1989) 1023.
- [46] DR Douslin, RH Harrison: J. Chem. Thermodynamics 8 (1976) 301.
- [47] PJ Kortbeek, JA Schouten: International Journal of Thermophysics 11 (1990) 455.
- [48] G Handel, R Kleinrahm, W Wagner: J. Chem. Thermodynamics 24 (1992)?
- [49] DR Douslin, RH Harrison: J. Chem. Thermodynamics 5 (1973) 491.
- [50] RC Prasad, JES Venart: Int. J. of Thermophys. 5 (1984) 367.
- [51] FH Zerilli, HD Jones in J.W.S. S. C. Schmidt, G. A. Samara, M. Ross (Ed.), High pressure science and technology. American Institute of Physics, 1993, p. 113-16.
- [52] ML Klein, IR McDonald: J. Chem. Phys. 71 (1979) 298.
- [53] VV Dremov, DG Modestov: Chem. Phys. Rep. 17 (1998) 781.
- [54] NH Erokin, BI Kalyanov: Thermal Engineering 27 (1980) 634.
- [55] YX Yan, LT Cheng, KA Nelson, in J.H.C.a.R.E. Hester (Ed.), Advances in Non-linear Spectroscopy. John Wiley Ltd., London, 1987.



- [56] MD Fayer: IEEE J. Quantum Electronics 22 (1986) 1444.
- [57] JM Brown, LJ Slutsky, KA Nelson, LT Cheng: Science 241 (1988) 65.
- [58] JM Zaug, EH Abramson, JM Brown, LJ Slutsky, in Y.S.a.M. Manghnani (Ed.), High Pressure Research: Applications to Earth and Planetary Sciences. American Geophysical Union, Washington, DC, 1992, p. 157-66.
- [59] JM Zaug, JM Brown, LJ Slutsky: J. Phys. Chem. 98 (1994) 6008-16.
- [60] M Greenspan, CE Tschiegg: J. Acoust. Soc. Am. 31 (1959) 75-76.
- [61] WD Wilson: J. Acoust. Soc. Am. 31 (1959) 1067-72.
- [62] A Handbook, McGraw-Hill, New York, 1957.
- [63] JM Zaug, University of Washington, Seattle, WA, 1994.

## *Chapter 8*

# **Combustion Mechanisms and Simplified-Kinetics Modeling of Homogeneous Energetic Solids**

**M. Q. Brewster**

Department of Mechanical and Industrial Engineering, University of Illinois at Urbana-Champaign, Urbana, IL 61801, The United States of America

The combustion mechanisms of homogeneous energetic solids, such as double-base propellant, are considered in the framework of simplified-kinetics modeling. The framework is the classical approach of quasi-steady gas and condensed-phase reaction zones, homogeneous solid, and one-dimensional heat feedback and flame structure. The primary system performance parameter of interest is the burning rate or regression rate of the solid. The effect of important environmental parameters such as pressure, temperature, and radiative heat flux, as well as intrinsic system parameters such as temperature sensitivity of condensed- and gas-phase reaction zones, are considered. Validation of modeling assumptions is addressed via comparison of theoretical predictions with experimental observations both for steady state and quasi-steady, time-dependent conditions for the common materials NC/NG and HMX. The approach is to seek a balance between theoretical complexity and physical fidelity (*i.e.*, predictive capability) that achieves some sort of optimum between these competing interests. For example, complexity for its own sake, *e.g.*, in detailed chemistry (particularly if it is uncertain), is not included if it cannot be justified by demonstrated improvement in macroscopic system performance simulation capability. Similarly, mathematical simplicity is not retained for its own sake if it entails serious deleterious effects in physical fidelity. The result of this approach is a simplified mathematical (usually analytical) model that has the ability to elucidate some important fundamental mechanisms as well as simulate both steady and unsteady behavior of these

complex chemically reacting dynamic systems with surprising fidelity, given the simplicity of the assumptions. The results illustrate the stark contrast that exists between the limiting assumptions of an asymptotically high gas-phase activation energy versus a vanishingly small one. The former approach, which is the more common one, is actually shown to be less accurate in simulating the macroscopic combustion behavior of common homogeneous energetic solids. Where possible, connections are also made between global modeling parameters and fundamental ones, such as decomposition activation energies and bond strengths.

## 1. INTRODUCTION

The term homogeneous energetic solid or homogeneous solid propellant refers to energetic solids that burn in a manner such that ingredient heterogeneity or unmixedness does not appreciably influence the burning rate or flame structure. This definition is thought to apply to most single-component energetic solids such as cyclo-tetramethylene-tetranitramine (HMX), cyclo-trimethylene-trinitramine (RDX), and ammonium perchlorate AP (<13 MPa), to molecularly mixed multi-component materials such as nitrocellulose/nitroglycerine (NC/NG) double-base propellant, and to certain molecularly unmixed or composite propellants, such as RDX- or HMX-composite modified double base (CMDDB) propellants. In these systems the condensed phase (solid and surface liquid layer) decomposition zone and gas flame structure (often referred to collectively as the combustion wave) are essentially one-dimensional spatially; composition and temperature variations are important only in the direction normal to the burning surface. One-dimensionality simplifies mathematical analysis of these materials considerably and has made it possible for significant progress to be made in modeling combustion of homogeneous propellants. Yet, while significant progress has been made in mathematically describing combustion of homogeneous propellants and thereby deducing their combustion mechanisms, many unsolved questions remain. The objectives of this chapter are to review the progress that has been made in simplified-kinetics modeling homogeneous propellant combustion, to summarize the mechanisms that are well established and agreed upon, and to note points of recent progress that are still under debate as well as areas of active research. The framework for doing this is the presentation of (a) a simplified, classical analysis

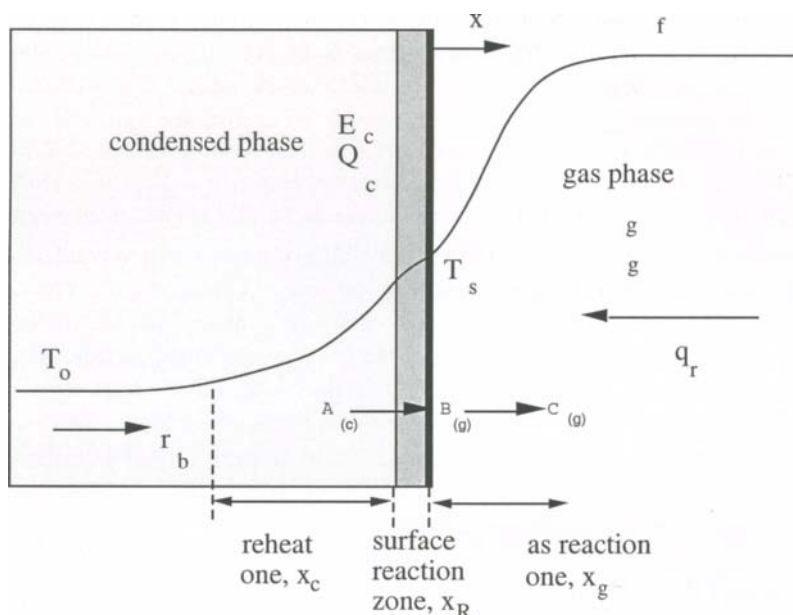


Fig. 1 Problem schematic for burning homogeneous propellant showing condensed phase (surface) reaction zone, gas phase reaction zone and corresponding steady-state temperature profiles. Propellant is fed from left at surface regression rate  $r_b$ . Simplified kinetics description has propellant (A) decomposing in condensed phase to intermediate species (B) via zero-order, high activation energy, irreversible single-step reaction, and (B) reacting to (C) in gas phase via second-order (overall), irreversible single-step reaction.

of steady-state combustion of homogeneous energetic solids and (b) a comparison of the theoretical results with experimental observations for the common materials NC/NG and HMX.

## 2. MATHEMATICAL MODEL OF MACROSCOPICALLY STEADY COMBUSTION

A schematic diagram of the system being studied is shown in Fig. 1. The system consists of the condensed phase region (solid plus any surface liquid layer) and the

gas phase region. The two regions are separated by an interface referred to as the burning surface or just surface which is assumed to be planar. An  $x$ -coordinate origin is fixed at the surface with positive sense into the gas phase. The surface is imagined to be stationary, with the propellant being fed in from the left-hand side at the steady regression rate,  $r_b$ , or in other words, the frame of reference translates with the burning surface. The initial propellant temperature is  $T_o$ , the surface temperature is  $T_s$ , and the final flame temperature is  $T_f$ . Two distinct chemical reaction zones are recognized: a high-density, condensed phase reaction zone near the surface and a low-density, gas phase reaction zone. The density difference between the condensed phase and gas phase reaction zones is one of the key differences that require separate treatment of the gas and condensed phases. This is particularly important for unsteady combustion due to the much larger thermal mass in the condensed phase. Other differences are species mobility, which is more limited in the condensed phase, thermophysical properties such as thermal conductivity, which is typically larger in the condensed phase, and basic chemical kinetics differences, which are discussed below.

## 2.1. Condensed Phase Model

### 2.1.1. Governing Equations

The propellant is assumed to undergo an irreversible thermal decomposition process in the condensed phase. The simplest description of this process is a single-step, unimolecular reaction with the initial reactant species-A (formula weight  $W$ ) going to intermediate species-B (same formula weight  $W$ ) as shown in Fig. 1,



with a zero-order Arrhenius reaction rate,

$$\Omega_c = \rho_c A_c \exp\left[\frac{-E_c}{RT}\right], \quad (2)$$

converting  $Q_c$  units of chemical to sensible enthalpy per unit mass reacted. The reaction rate is assumed to be independent of reactant mass fraction and only a function of temperature. The activation energy  $E_c$  corresponds roughly to the

energy required to initiate the process, which is either the bond strength of the initial bond breaking homolysis reaction or the activation energy for formation of an activated complex in the case of decomposition by a transition state. In reality, many decomposition reactions occur simultaneously but their activation energies are often similar in magnitude and large enough ( $E_a/RT \gg 1$ ), at least for useful propellants, that the material is relatively stable. Once initiation has occurred, recombination reactions rapidly follow which usually liberate chemical energy. The net effect of the endothermic initiation and exothermic recombination reactions is a condensed-phase process that can be either slightly exothermic or endothermic overall and therefore may be characterized as overall relatively neutral energetically (compared to the gas phase) with decomposition energy  $Q_c$  ( $>0$ , exothermic;  $<0$ , endothermic). The detailed, elementary chemical reactions in the condensed phase, particularly the reactions following the initiation process, are still not well known for most energetic materials. Thus it is difficult to predict  $Q_c$  just from knowledge of the material molecular structure; empirical measurements must be relied on for quantitative values of  $Q_c$ . In this regard thermocouple measurements have been useful. This simplified, single-step decomposition model, though only an approximation of a much more complicated process, is nevertheless a useful and appropriate description, given the absence and uncertainty of detailed condensed phase chemistry information presently. This simple model includes the two most important parameters that characterize the condensed phase process: the temperature sensitivity of the initiation reaction(s),  $E_c$ , and the overall thermochemical energy release of the condensed phase processes,  $Q_c$ .

Based on this single-step mechanism, the one-dimensional, steady conservation of mass (A+B), species-A, and energy equations for the condensed phase ( $x < 0$ ) can be written as

$$\text{mass (A + B): } m = \rho_c r_b = \text{constant} \quad (3)$$

$$\text{species-A: } m \frac{dY}{dx} = -\Omega_c; \quad Y(0^-) = 0, \quad Y(-\infty) = 1 \quad (4)$$

$$\text{energy: } mC \frac{dT}{dx} = k_c \frac{d^2T}{dx^2} + Q_c \Omega_c + q_r K_a \exp(K_a x); \quad T(0) = T_s, \quad T(-\infty) = T_o \quad (5)$$

$$\text{where } T_s = T_o + \frac{1}{mC} [mQ_c + q_c + q_r]; \quad q_c = k_g \left. \frac{dT}{dx} \right|_{0+}. \quad (6)$$

The condensed phase density  $\rho_c$ , specific heat  $C$ , thermal conductivity  $k_c$ , and radiation absorption coefficient  $K_a$  are assumed to be constant. The species-A equation includes only advective transport and depletion of species-A (generation of species-B) by chemical reaction. The species-B balance equation is redundant in this binary system since the total mass equation,  $m = \text{constant}$ , has been included; the mass fraction of B is  $1-Y$ . The energy equation includes advective transport, thermal diffusion, chemical reaction, and in-depth absorption of radiation. Species diffusion ( $d^2Y/dx^2$  term) and mass/energy transport by turbulence or multi-phase advection (bubbling) which might potentially be important in a sufficiently thick liquid layer are neglected. The radiant flux term  $q_r$  represents the net radiant heat flux absorbed by the propellant for a collimated, monochromatic radiant flux (such as laser radiation). For broadband, diffuse, thermal radiation from hot combustion products the absorption coefficient should be multiplied by a factor of 1.5 to 2 to account for obliquity of the diffuse rays (mean beam length effect) and a suitable spectral integration should be done to represent the spectral variation of the incident radiant flux and the propellant optical properties (reflectivity and absorption coefficient). Thermal emission and radiative scattering by the propellant are neglected. The boundary condition  $Y(-\infty)=1$  represents pure reactant, A, far upstream of the burning surface and  $Y(0^-)=0$  corresponds to the assumption of complete conversion of A to B at the surface (the notation  $0^-$  indicates the condensed-phase side of the interface). The boundary condition  $T(-\infty)=T_o$  represents the prescribed initial temperature of the energetic material and  $T(0)=T_s$  represents the unknown surface temperature. The expression for  $T_s$  comes from a control volume energy balance on the condensed-phase region, which introduces the unknown conductive heat feedback from the gas phase,  $q_c$ .

By introducing a reference mass flux  $m_r$  and the following non-dimensional parameters and variables,  $\tilde{T} = T/(T_f - T_o)$ ,  $\tilde{x} = xm_r C / k_c$ ,  $\tilde{A}_c = \rho_c A_c k_c / Cm_r^2$ ,  $\tilde{E}_c = E_c / R(T_f - T_o)$ ,  $\tilde{\Omega}_c = \Omega_c k_c / Cm_r^2$ ,  $\tilde{K}_a = K_a k_c / m_r C$ ,  $\tilde{q}_{c,r} = q_{c,r} / m_r C(T_f - T_o)$ ,  $\tilde{Q}_c = Q_c / C(T_f - T_o)$ , the condensed phase conservation equations can be re-written

in non-dimensional form, resulting in an important reduction in the number of parameters:

$$\Omega_c = \tilde{A}_c \exp\left[\frac{-\tilde{E}_c}{\tilde{T}}\right] \quad (7)$$

$$\tilde{m} = \frac{m}{m_r} = \frac{r_b}{r_{b_r}} \quad (8)$$

$$\tilde{m} \frac{dY}{d\tilde{x}} = -\Omega_c; Y(0^-) = 0, Y(-\infty) = 1 \quad (9)$$

$$\tilde{m} \frac{d\tilde{T}}{d\tilde{x}} = \frac{d^2\tilde{T}}{d\tilde{x}^2} + \tilde{Q}_c \Omega_c + \tilde{q}_r \tilde{K}_a \exp(\tilde{K}_a \tilde{x}); \tilde{T}(0) = \tilde{T}_s, \tilde{T}(-\infty) = \tilde{T}_o \quad (10)$$

$$\text{where } \tilde{T}_s = \tilde{T}_o + \tilde{Q}_c + \tilde{q}_c/\tilde{m} + \tilde{q}_r/\tilde{m}. \quad (11)$$

The last equation, which is an energy balance on the condensed phase, can be written as

$$\frac{\tilde{Q}_c}{\tilde{T}_s - \tilde{T}_o} + \frac{\tilde{q}_c}{\tilde{m}(\tilde{T}_s - \tilde{T}_o)} + \frac{\tilde{q}_r}{\tilde{m}(\tilde{T}_s - \tilde{T}_o)} = 1 \quad (12)$$

where the respective terms on the left-hand side represent the fractions of energy going to raise the temperature from  $T_o$  to  $T_s$  supplied by condensed phase heat release, conductive heat feedback from the gas phase, and radiation. Typically the  $Q_c$  and  $q_c$  terms dominate. The condensed phase equations are over-constrained in that two boundary conditions are imposed on  $Y$  whereas the species equation is only first order. This means that system will only be satisfied by a unique value of mass flux;  $\tilde{m}$  is an eigenvalue of the problem. It is also possible to formulate and obtain solutions for this problem for reaction orders other than zero and surface mass fractions other than zero [1,2].

### 2.1.2. Solution of Condensed Phase Equations

The condensed phase energy equation, being decoupled from the species



equation by the zero-order reaction rate assumption can be solved independently for the burning mass flux eigenvalue  $\tilde{m}$  as a function of  $\tilde{T}_s$ . This has been done for  $\tilde{E}_c \gg 1$  (which is a realistic approximation for most stable, usable energetic materials and propellants) using Activation Energy Asymptotics, AEA [2,3]. The procedure involves splitting the problem into an inert, convective-diffusive preheat zone (dropping the  $\tilde{Q}_c \tilde{\Omega}_c$  term) and a thin, reactive-diffusive zone (dropping the  $m d\tilde{T}/d\tilde{x}$  term). The characteristic length scale of the convective-diffusive zone is  $x_c = k_c/mC = \alpha_c/r_b$ , which is the ratio of the thermal diffusivity and convective velocity. The characteristic length scale of the reactive-diffusive zone is  $x_c$  reduced by a factor of the non-dimensional condensed phase activation energy,  $x_R = x_c/(\tilde{E}_c/2\tilde{T}_s)$  [3] (typically,  $\tilde{E}_c/2\tilde{T}_s > 5$ ). A new parameter  $f_r$  is introduced which is the fraction of  $q_r$  transmitted through the thin reactive-diffusive zone or surface reaction layer. The relation

$$f_r = \exp\left(\frac{-2\tilde{K}_a\tilde{T}_s}{\tilde{m}\tilde{E}_c}\right), \quad (13)$$

which is simply Beer's law applied over the pathlength  $x_R$  has been shown to be a reasonable representation for this parameter [3,4]. The term  $\tilde{K}_a/\tilde{m}$  is the optical thickness of the relatively thick, convective-diffusive zone and  $2\tilde{K}_a\tilde{T}_s/\tilde{m}\tilde{E}_c$  is the optical thickness of the thin, reactive-diffusive layer. The solution for temperature profile from the inert, convective-diffusive equation is

$$\frac{\tilde{T} - \tilde{T}_o}{\tilde{T}_s - \tilde{T}_o} = \left[1 - \left(\frac{f_r J}{1 - \tilde{K}_a/\tilde{m}}\right)\right] \exp(\tilde{m}\tilde{x}) + \left(\frac{f_r J}{1 - \tilde{K}_a/\tilde{m}}\right) \exp(\tilde{K}_a\tilde{x}) \quad (14)$$

where  $J = \tilde{q}_r/\tilde{m}(\tilde{T}_s - \tilde{T}_o)$  is another form of dimensionless absorbed radiant flux, which represents the fraction of energy required to raise the propellant temperature from  $T_o$  to  $T_s$  that is provided by the radiant flux. Typically most of this required energy is supplied by conductive heat feedback from the gas phase and condensed phase heat release with  $J < 0.1$ . Thus the temperature profile is usually dominated by the first term on the right-hand side, the convective-diffusive term. This equation defines an exponential temperature profile in the inert preheat zone that has a characteristic length scale of  $x_c = k_c/mC = \alpha_c/r_b$  as shown in Fig. 1. In the

exceptional case of propellant decomposition driven by a strong external radiative flux with a propellant very translucent to that radiation, it is conceivable that the temperature profile could be dominated by the second term, *i.e.*, the radiative in-depth absorption term; however, this is unlikely under typical propulsion-combustion operating conditions.

The solution for  $\tilde{m}$  from the reactive-diffusive equation is

$$\tilde{m}^2 = \frac{\tilde{A}_c \tilde{T}_s^2 \exp(-\tilde{E}_c/\tilde{T}_s)}{\tilde{E}_c(\tilde{T}_s - \tilde{T}_o - \tilde{Q}_c/2 - f_r \tilde{q}_r/\tilde{m})}; \quad f_r = \exp\left(\frac{-2\tilde{K}_a \tilde{T}_s}{\tilde{m} \tilde{E}_c}\right) \quad (15)$$

or, in dimensional form [3],

$$r_b^2 = \frac{A_c \alpha_c \exp\left(\frac{-E_c}{RT_s}\right)}{\frac{E_c}{RT_s} \left(1 - \frac{T_o}{T_s}\right) \left[1 - \frac{Q_c}{2C(T_s - T_o)} - f_r J\right]}; \quad f_r = \exp\left(\frac{-2K_a \alpha_c RT_s}{r_b E_c}\right). \quad (16)$$

An approximate expression which is widely used instead is

$$r_b = A_s \exp\left(\frac{-E_s}{RT_s}\right). \quad (17)$$

These equations are commonly called *pyrolysis* relations, in reference to the thermal (as opposed to a possibly chemical or photonic) nature of the initiating step(s) in the condensed phase decomposition process. It can be seen that while the second, simpler pyrolysis expression with constant coefficient ( $A_s$ ) preserves the important Arrhenius exponential temperature dependent term, it ignores the effect of the initial temperature, condensed phase heat release and thermal radiation parameters present in the more comprehensive zero-order pyrolysis relation. These terms ( $T_o$ ,  $Q_c$ , and  $q_r$ ) make a significant difference when it comes to sensitivity parameter and unsteady combustion considerations. It is also important to note the factor of 2, which relates the apparent "surface" activation energy  $E_s$  to the actual "bulk" activation energy  $E_c$ ,  $E_s \approx E_c/2$ . Failure to recognize this factor of two hindered progress in some cases as attempts were

begun to relate apparent activation energies (*i.e.*,  $E_s$  values obtained from Arrhenius plots) to realistic activation energies ( $E_c$  values) as indicated by reasonably well known chemical bond energies (*e.g.*, the 40 kcal/mol CO-NO<sub>2</sub> bond energy in NC/NG). This can be seen in many early papers where the difference between the two is not recognized or at least not acknowledged. When this difference is properly recognized, it is reasonable to expect good agreement between apparent activation energies from Arrhenius plots and realistic bond homolysis energies.\*

The pyrolysis equations above are based on an assumed  $T_s$  which is not generally known from condensed phase considerations alone. To proceed further and obtain a solution for mass flux requires information about the conductive heat feedback to the surface from the gas phase  $q_c$  which must be supplied by the gas phase analysis.

## 2.2. Gas Phase Model

### 2.2.1. Governing Equations

The gas phase species that evolve into the gas phase as products of the condensed phase decomposition process consist of many reactive intermediates, some of which are probably short-lived radicals. The detailed chemistry of the gas phase reaction zone (as for the condensed phase reaction zone) is an area of active research. At the present time, it is not possible to predict the gaseous composition at the burning surface or to say with confidence that a given postulated detailed chemical mechanism accurately represents the gas phase chemistry for any given energetic material, although progress has been made, particularly for H-C-N-O materials like nitrate esters (NC/NG) and nitramines (HMX, RDX). Not only is the detailed chemistry still somewhat uncertain but even the basic nature of the mechanism, *e.g.*, chain reaction versus thermal decomposition seems not to be universally established. Therefore, relatively simple chemical kinetic mechanisms are still being investigated for the gas-phase processes with the expectation that the results of these simplified mechanisms can help clarify the nature of the chemistry in this important region near the surface where a substantial amount of the exothermic reaction occurs that drives the combustion. (In the formulation described here, it is assumed that if there is net exothermicity in the condensed

---

\* The author and several colleagues are indebted to Dr. Guy Lengelle for instruction on this point during AGARD visits to ONERA

phase, it is a small fraction of the exothermicity of the near-surface, gas-phase reactions, which is the usual case for energetic solids.)

What can be said of the gas-phase chemistry with some confidence is that bimolecular reactions probably play an important role under most conditions. The simplest description of gas-phase chemistry that incorporates bimolecular interactions is a single-step, irreversible, bimolecular reaction with intermediate species-B (formula weight  $W$ ) going to product species-C (same formula weight  $W$ ),



with a second-order (overall) Arrhenius reaction rate,

$$\Omega_g = B_g \rho_g^2 Y T^2 \exp\left(-\frac{E_g}{RT}\right), \quad (19)$$

which converts  $Q_g$  units of chemical to sensible enthalpy per unit mass reacted. The reaction rate is assumed to be first order with respect to reactant (species-B, mass fraction  $Y$ ) and second order overall. The  $T^2$  term in the prefactor allows for simple mathematical solutions. This is not in exact agreement with kinetic theory ( $T^{0.5}$ ) but is not a significant assumption in the present context since the assumed value of  $E_g$  is much more important with regard to the temperature dependence of the reaction rate. With the assumption of ideal gas behavior,

$$\rho_g = \frac{P}{(R/W)T}, \quad (20)$$

the reaction rate can also be written as

$$\Omega_g = A_g P^2 Y \exp\left(-\frac{E_g}{RT}\right); \quad A_g = \frac{B_g}{(R/W)^2}. \quad (21)$$

The molecular weight dependence implied here for collision frequency ( $W^2$ ) is again not in exact agreement with kinetic theory ( $W^{0.5}$ ) but this approximation is inconsequential in a simplified kinetic representation. The mechanistic interpretation of the gas reaction and the meaning of species-M will be deferred.

Unlike the condensed phase process, for which the large activation energy, thermal decomposition mechanism ( $E_a/RT \gg 1$ ) has been established by a large amount of evidence, a similar consensus has not developed for the gas phase. A range of activation energies for the gas phase from very large ( $E_g/RT \gg 1$ ) to very small ( $E_g/RT \ll 1$ ) can be reasonably postulated. Since the interpretation of the reaction equation depends on the value of  $E_g$ , mechanistic interpretation will come later in connection with solutions corresponding to various values of  $E_g$  that have been obtained.

The one-dimensional, steady conservation of mass (B+C), species-B, and energy equations for the gas phase ( $x > 0$ ) are

$$\text{mass (B+C): } m = \rho_g u = \text{constant} \quad (22)$$

$$\text{species-B: } m \frac{dY}{dx} = \rho_g D \frac{d^2 Y}{dx^2} + \Omega_g; \quad Y(0^+) = Y_s, \quad Y(\infty) = 0 \quad (23)$$

$$\text{where } Y_s = 1 + \left. \frac{\rho_g D}{m} \frac{dY}{dx} \right|_{0^+} \quad (24)$$

$$\text{energy: } mC \frac{dT}{dx} = k_g \frac{d^2 T}{dx^2} + Q_g \Omega_g; \quad T(0) = T_s, \quad T(\infty) = T_f \quad (25)$$

$$\text{where } T_s = T_o + \frac{1}{mC} [mQ_c + q_c + q_r]; \quad q_c = k_g \left. \frac{dT}{dx} \right|_{0^+} \quad (26)$$

$$\text{and } T_f = T_o + \frac{1}{C} \left[ Q_c + Q_g + \frac{q_r}{m} \right]. \quad (27)$$

The species-B balance equation includes advective transport, Fickian diffusion, and depletion by chemical reaction. The binary diffusion coefficient  $D$  represents downstream diffusion of reactant species-B relative to upstream diffusion of product species-C. The expression for  $Y_s$ , the surface mass fraction of B (gas side), is obtained from a species balance at the surface on B which includes advective transport of pure B to the interface on the condensed phase side and both advective and diffusive transport of B away from the surface on the gas side. The downstream condition  $Y(\infty) = 0$  represents the assumption of complete conversion

of species-B to species-C far from the surface. The species-C balance equation is redundant in this binary system since the total mass equation,  $m = \text{constant}$ , has been included; the mass fraction of C is  $1-Y$ . The energy equation includes advection, diffusion (conduction), and chemical reaction. Radiation absorption and emission are neglected in the gas phase. The expression for  $T_s$  is obtained from an energy balance on the condensed phase region. The expression for  $T_f$  is obtained from an energy balance on the entire system, including both the condensed and gas phase regions. The gas phase specific heat ( $C_p$ ) is assumed equal to the condensed phase specific heat  $C$  and constant; thermal conductivity  $k_g$  is also assumed to be constant. The ratio  $k_g/C$  is assumed equal to the product  $\rho_g D$  ( $Le = k_g/C\rho_g D = \alpha_g/D = 1$ ), although  $\rho_g$  and the gas binary diffusion coefficient  $D$  are not assumed constant but allowed to vary in the  $x$ -direction, as they are both strong functions of temperature which varies in the  $x$ -direction. Gas density varies as  $P/T$  via the ideal gas equation. Thus the assumption of constant  $\rho_g D$  implies that  $D$  is assumed to vary as  $T/P$  which is a fair approximation of the kinetic theory result for binary diffusion which holds that  $D$  varies as  $T^{1.5}/P$ .

The momentum equation is not included above because it gives the simple result that pressure  $P$  is essentially constant. More specifically it says that  $P$  drops by an amount equal to  $m$  times the increase in  $u$ . The gas accelerates away from the surface due to the increasing temperature and decreasing density. However, the drop in  $P$  is typically so small ( $-\Delta P = m\Delta u \ll P$ )--on the order of a few Pascals whereas  $P$  is typically of order MPa--that  $P$  can be treated as constant.

Due to the similarity of the energy and species equations and their boundary conditions, the Shvab-Zeldovich relation between temperature and mass fraction holds,

$$Y = (T_f - T)/Q_g C, \quad (28)$$

and the species and energy equations are equivalent.

By introducing the following non-dimensional parameters and variables,  $\tilde{T} = T/(T_f - T_o)$ ,  $\tilde{x} = xm_r C/k_g$ ,  $D_g = P^2 k_g A_g / C m_r^2$ ,  $\tilde{E}_g = E_g / R(T_f - T_o)$ ,  $\tilde{\Omega}_g = \Omega_g k_g / C m_r^2$ ,  $\tilde{Q}_g = Q_g / C(T_f - T_o)$ ,  $Le = k_g / C\rho_g D = \alpha_g / D = 1$ , the gas phase conservation equations can be re-written in non-dimensional form,

$$\tilde{\Omega}_g = D_g Y \exp \left[ \frac{-\tilde{E}_g}{\tilde{T}} \right] \quad (29)$$

$$\tilde{m} = \frac{m}{m_r} = \frac{r_b}{r_{br}} \quad (30)$$

$$\tilde{m} \frac{dY}{d\tilde{x}} = \frac{d^2 Y}{d\tilde{x}^2} - \tilde{\Omega}_g; \quad Y(0^+) = Y_s, \quad Y(\infty) = 0 \quad (31)$$

$$\text{where } Y_s = 1 + \frac{1}{\tilde{m}} \frac{dY}{d\tilde{x}} \Big|_{0^+} \quad (32)$$

$$\tilde{m} \frac{d\tilde{T}}{d\tilde{x}} = \frac{d^2 \tilde{T}}{d\tilde{x}^2} + \tilde{Q}_g \tilde{\Omega}_g; \quad \tilde{T}(0) = \tilde{T}_s, \quad \tilde{T}(\infty) = \tilde{T}_f \quad (33)$$

$$\text{where } \tilde{T}_s = \tilde{T}_o + \tilde{Q}_c + \frac{\tilde{q}_c}{\tilde{m}} + \frac{\tilde{q}_r}{\tilde{m}}; \quad \tilde{q}_c = \frac{d\tilde{T}}{d\tilde{x}} \Big|_{0^+} \quad (34)$$

$$\text{and } \tilde{T}_f = \tilde{T}_o + 1; \quad (\tilde{Q}_g = 1 - \tilde{Q}_c - \tilde{q}_r/\tilde{m}) \quad (35)$$

with the Shvab-Zeldovich relation

$$Y = (\tilde{T}_f - \tilde{T})/\tilde{Q}_g. \quad (36)$$

The non-dimensional gas phase heat release  $\tilde{Q}_g$  is not an independent parameter if non-dimensional condensed phase heat release and radiative flux are specified; it can be found from the overall energy balance,

$$\tilde{Q}_g + \tilde{Q}_c + \tilde{q}_r/\tilde{m} = 1. \quad (37)$$

The three terms on the left-hand side represent the respective fractions of energy going to increase the temperature from  $T_o$  to  $T_f$  supplied by gas phase heat release,

condensed phase heat release, and external radiation. Typically the  $\tilde{Q}_g$  term dominates.

### 2.2.2. Solution of Gas Phase Equations

Analytical solutions for the simplified gas equations above have been published only for limiting values of large and small activation energy,  $\tilde{E}_g \gg 1$  [3,5] and  $\tilde{E}_g \ll 1$  [6,7] but these limiting cases are sufficient for demonstrating the important parametric dependencies.

#### 2.2.2.1. High Gas Activation Energy

The classical large activation energy ( $\tilde{E}_g \gg 1$ ) solution obtained by activation energy asymptotics [5] is

$$\tilde{m}^2 = \frac{2D_g \tilde{T}_f^4}{\tilde{E}_g^2 \tilde{Q}_g^2} \exp\left(\frac{-\tilde{E}_g}{\tilde{T}_f}\right); \quad \tilde{T}_f = \tilde{T}_o + 1 \quad (38)$$

$$m^2 = \frac{2k_g A_g R^2 C T_f^4 P^2}{E_g^2 Q_g^2} \exp\left(\frac{-E_g}{RT_f}\right); \quad T_f = T_o + \frac{1}{C} \left[ Q_c + Q_g + \frac{q_r}{m} \right] \quad (39)$$

$$\tilde{q}_c / \tilde{m} = \tilde{Q}_g \exp(-\tilde{x}_g \tilde{m}) \quad (40)$$

$$\frac{\tilde{T} - \tilde{T}_s}{\tilde{T}_f - \tilde{T}_s} = 1 - \frac{Y}{Y_s} = \frac{\exp(\tilde{x} \tilde{m}) - 1}{\exp(\tilde{x}_g \tilde{m}) - 1}; \quad \tilde{x} \leq \tilde{x}_g. \quad (41)$$

This solution defines a flame structure analogous to the condensed phase: an inert, convective-diffusive preheat zone of thickness  $x_g$ , followed by a thin, reactive-diffusive flame zone or flame sheet. Equations (38) and (39) give the mass flux or burning rate directly; the mass flux is controlled by gas phase kinetics. Condensed-phase reaction kinetics only influences the surface temperature, which is given by the condensed-phase pyrolysis relation. Equation (40) gives the flame standoff distance  $x_g$ , where the conductive heat feedback comes from the energy



balance  $\tilde{T}_s = \tilde{T}_o + \tilde{Q}_c + \tilde{q}_c/\tilde{m} + \tilde{q}_r/\tilde{m}$ . And Eq. (41) gives the temperature/species profile in the convective-diffusive zone.

The interpretation of the gas phase kinetic mechanism for  $\tilde{E}_g \gg 1$  is as follows. In the reaction  $B + M \rightarrow C + M$ , species-M is any species, which in this binary gas system formally means B or C. The gas reaction is interpreted as thermal decomposition of species-B by high-energy collision with either itself or species-C. Reaction is initiated by collision between two molecules that are relatively unreactive chemically (compared to radicals); only a tiny fraction ( $\exp(-\tilde{E}_g/\tilde{T}_f)$ ) of the collisions that occur lead to reaction, those involving the most thermally energetic molecules. This is consistent with the assumption of the reaction rate being second order overall, but first order with respect to reactant species-B. The mass fraction of the other collision partner, species-M, which does not appear in the reaction rate expression, is implicitly taken to be constant at a value of unity.

The prefactor  $B_g$  or  $A_g$  can be converted to units of 1/s ( $A_g P^2/\rho_g = B_g P^2 W^2/R^2 \rho_g = B_g P T W/R$ ) to compare with collision frequencies from kinetic theory. As noted above, the temperature dependence of  $B_g P T W/R$  is not in exact agreement with kinetic theory ( $\sim P T^{-0.5} W^{-0.5}$ ), nor is the molecular weight dependence (although the pressure dependence is). Therefore close agreement with kinetic theory is not expected; however, order-of-magnitude agreement is expected. At a pressure of 5 MPa,  $A_g P^2/\rho_g$  is of order  $10^{13}$  1/s for NC/NG (Table 2), as obtained by matching measured regression rates, which agrees with kinetic theory. For NC/NG double base propellant combustion, species-B would represent the reactants of the primary flame, such as  $\text{NO}_2$  and  $\text{CH}_2\text{O}$ , while species-C would represent the products of the primary flame,  $\text{NO}$ ,  $\text{CO}$ , and  $\text{H}_2\text{O}$ . The secondary flame, which produces final thermodynamic products  $\text{N}_2$  and  $\text{CO}_2$ , does not occur close enough to the propellant surface to contribute to the regression rate below 10 MPa, and is not included in the model. The assumed final flame temperature corresponds to the dark zone temperature of around 1300 to 1600 K.

More complicated interpretations of  $B + M \rightarrow C + M$  in the limit  $\tilde{E}_g \gg 1$  can be made that still fall in the realm of simplified modeling, for example, the two-step Lindemann mechanism,  $B + M \rightleftharpoons B^* + M$ ;  $B^* \rightarrow C$  [8]. However, such interpretations haven't been shown to lead to better agreement with observations for homogeneous energetic solids than the single step, irreversible reaction and since they represent an additional level of complexity they are not considered here.

### 2.2.2.2. Low Gas Activation Energy

The low activation energy ( $\tilde{E}_g < 1$ ) solution [6,7,9] is

$$\tilde{m}^2 = 4D_g \frac{1}{\left\{ 2\Lambda \tilde{Q}_g (\tilde{T}_s - \tilde{T}_o - \tilde{Q}_c - \tilde{q}_r/\tilde{m}) - 1 \right\} + 1\}^2 - 1} \quad (42a)$$

$$m^2 = \frac{4P^2 k_g A_g}{C} \frac{1}{\left\{ 2\Lambda Q_g (C(T_s - T_o) - Q_c - q_r/m) - 1 \right\} + 1\}^2 - 1} \quad (42b)$$

$$\tilde{x}_g = 2\Lambda \left( \sqrt{\tilde{m}^2 + 4D_g} - \tilde{m} \right) \quad (43a)$$

$$\tilde{q}_c/\tilde{m} = \tilde{Q}_g \left( \tilde{x}_g \tilde{m} + 1 \right) \quad (43b)$$

$$\frac{\tilde{T} - \tilde{T}_f}{\tilde{T}_s - \tilde{T}_f} = \frac{Y}{Y_s} = \exp \left( -\frac{\tilde{x}}{\tilde{x}_g} \right). \quad (44)$$

Using Eq. (11), the ratio involving  $Q_g$  in Eq. (42) can be shown to be the positive-definite  $Q_g/(q_c/m)$ , which for low pressures is much less than unity and with increasing pressure approaches unity. This solution describes a broadly distributed reaction zone that is convective, diffusive, and reactive in nature with a characteristic length scale of  $x_g$ . Equation (42) must be solved simultaneously with the condensed-phase solution, Eqs. (11) and (15), for  $m$  and  $T_s$ . An important distinction from the large gas activation energy solution is that the condensed-phase kinetics also contribute to determining the mass flux in addition to gas phase kinetics.

The interpretation of the gas phase kinetic mechanism for  $\tilde{E}_g \ll 1$  is as follows. In the reaction  $B + M \rightarrow C + M$ , species-M can be interpreted as representing a pool of unspecified chain carriers whose concentration is negligibly small compared to that of B and C and spatially constant (*i.e.*, steady-state approximation). Species-B is an intermediate, representative of species like  $\text{NO}_2$ ,  $\text{HONO}$ , and  $\text{CH}_2\text{O}$  in NC/NG and HMX/RDX. Species-C is interpreted kinetically as products formed by the primary flame, such as  $\text{NO}$ ,  $\text{CO}$ , and  $\text{H}_2\text{O}$ . The process

is assumed to be a bimolecular exchange reaction. Potentially important chain carriers include N, H, OH, etc. Potentially important elementary reactions represented by  $B + M \rightarrow C + M$  include  $\text{NO}_2 + \text{H} \rightarrow \text{NO} + \text{OH}$ ,  $\text{NO}_2 + \text{N} \rightarrow 2\text{NO}$ , and  $\text{NO}_2 + \text{OH} \rightarrow \text{NO} + \text{HO}_2$ . Because the chain carrier concentration is so small, it is not necessary to make a distinction between the M species that appear on the left- and right-hand sides even though they would, in general, be different and these species need not be included in the species equation. Again the prefactor in units of 1/s ( $A_g P^2 / \rho_g = B_g P^2 W^2 / R^2 \rho_g = B_g P T W / R$ ) can be compared with kinetic theory predictions with the expectation of at least order of magnitude agreement. These frequency factor values, as obtained by matching measured regression rates, are typically of order  $10^5$  to  $10^8$  1/s in the pressure range of 1 to 5 MPa for NC/NG (Table 2) and HMX/RDX, which is five to eight orders of magnitude smaller than the kinetic theory collision frequency. This discrepancy might appear to be indicative of a flaw in the low- $\tilde{E}_g$  theory. However, the mass fraction of the second collision partner, species-M, which has been assumed constant, would, in the case of a chain reaction mechanism, be expected to be quite small for radicals, of order  $10^{-5}$  to  $10^{-8}$ . This small chain carrier mass fraction has been effectively incorporated into the prefactor  $A_g$ , reducing its value by that amount from the kinetic collision frequency. Therefore, the mechanism is consistent with the assumption of the reaction rate being second order overall, but first order with respect to reactant species-B. The mass fraction of the other collision partner, species-M, which does not appear in the reaction rate expression, is implicitly taken to be constant at a very small value and incorporated into  $B_g$  or  $A_g$ .

Of the two limiting representations, the high- $\tilde{E}_g$  thermal decomposition theory has been the most commonly assumed model for several decades. However, recently the low- $\tilde{E}_g$  chain reaction theory has been shown to give good agreement with a wide range of increasingly accurate experimental measurements. The low- $\tilde{E}_g$  model was developed in an effort to resolve discrepancies between high- $\tilde{E}_g$  theory and experimental observations of gas-phase temperature profile and burning rate temperature sensitivity in HMX. This effort led to an assumption of vanishingly low  $\tilde{E}_g$  and a corresponding interpretation of the near-surface, gas-phase processes having more the character of chain reaction than that of thermal decomposition. As it turns out this idea was proposed as early as 1950 (for double-base propellant) by Rice and Ginell [10], but was largely forgotten in favor of

high- $\tilde{E}_g$  thermal decomposition and activation energy asymptotics. In 1982 Miller [11] revisited Parr and Crawford's [12] mathematically equivalent (but mechanistically different) constant-temperature-reaction-rate version and in 1997 Ward, Son, and Brewster "re-discovered" essentially the original Parr and Crawford, low- $\tilde{E}_g$  version [6,7,9,13].

### 2.3. Complete Model--Gas and Condensed Phases

The mathematical problem outlined above can be expressed in a variety of ways. Non-dimensional form allows the problem to be expressed in terms of the minimum number of parameters and independent variables.

Dependent variables:  $\tilde{m}, \tilde{T}_s, \tilde{x}_g$

Independent variables:  $D_g, \tilde{T}_o, \tilde{q}_r$

Parameters:  $\tilde{E}_g, \tilde{A}_c, \tilde{E}_c, \tilde{Q}_c, \tilde{K}_a$

The primary dependent variable of importance is the mass flux. The independent variables, in order of decreasing importance, are pressure, initial temperature, and radiant flux. Pressure enters as an independent variable through  $D_g$ , which also plays the role of a gas phase kinetic parameter (collision frequency or Arrhenius prefactor,  $A_g$ ). In contrast, the number of dimensional parameters is roughly twice the non-dimensional number.

Dependent variables:  $m, T_s, x_g$

Independent variables:  $P, T_o, q_r$

Parameters:  $A_g, E_g, Q_g, k_g, A_c, E_c, Q_c, k_c, \rho_c, C, K_a$

One of the key issues is the dependence of mass flux on the various parameters. Not all parameters have a strong influence on mass flux in all regions of parameter space. The dependence of mass flux on various parameters in different limiting

regions of parameter space is discussed next in the context of the complete solution of the coupled condensed and gas phase problems.

### 2.3.1 High Gas Activation Energy Solution (Intermediate Pressures)

The primary result of the high gas activation energy limiting solution is Eq. (38). This relation gives the mass flux directly without coupling to the condensed phase solution, and can be expressed functionally as

$$\tilde{m} = \tilde{m}(\tilde{D}_g, \tilde{E}_g, \tilde{Q}_g, \tilde{T}_o) \quad (45)$$

or, in dimensional terms,

$$m = m(P, T_o, q_r; A_g, E_g, Q_g, k_g, Q_c) . \quad (46)$$

Condensed phase parameters do not influence the mass flux (except that  $Q_c$  appears in the thermodynamic role of contributing to  $T_f$ ).

### 2.3.2. Low Gas Activation Energy Solution (Intermediate Pressures)

In the low gas activation energy limit, gas kinetics still have a strong influence as represented through  $D_g$  and  $A_g$  but not a controlling one. Condensed phase kinetic parameters also appear.

$$\tilde{m} = \tilde{m}(\tilde{D}_g, \tilde{A}_c, \tilde{E}_c, \tilde{Q}_c, \tilde{T}_o, \tilde{q}_r, \tilde{K}_a) \quad (47)$$

$$m = m(P, T_o, q_r; A_g, Q_g, k_g, A_c, E_c, Q_c, k_c, \rho_c, C, K_a) \quad (48)$$

### 2.3.3. High and Low Pressure Regimes (Condensed Phase Controlled Burning)

In the limits of high and low  $D_g$  (high and low pressure) the model outlined here approaches condensed phase controlled burning regimes, independent of  $E_g$ . That is, both  $\tilde{E}_g \gg 1$  and  $\tilde{E}_g \ll 1$  models converge to the same set of equations. In the low  $D_g$  (low pressure) limit, gas conductive heat feedback becomes negligible compared with condensed phase heat release and/or radiative heat feedback, and  $m$  and  $T_s$  are given by Eqs. (11) and (15) with  $q_c \rightarrow 0$  ( $x_g \rightarrow \infty$ ).

$$D_g \ll 1: \quad \tilde{m}^2 = \frac{\tilde{A}_c \tilde{T}_s^2 \exp(-\tilde{E}_c/\tilde{T}_s)}{\tilde{E}_c(\tilde{T}_s - \tilde{T}_o - \tilde{Q}_c/2 - f_r \tilde{q}_r/\tilde{m})}; \quad \tilde{T}_s = \tilde{T}_o + \tilde{Q}_c + \tilde{q}_r/\tilde{m} \quad (49a)$$

$$\tilde{m} = \tilde{m}(\tilde{A}_c, \tilde{E}_c, \tilde{Q}_c, \tilde{T}_o, \tilde{q}_r, \tilde{K}_a) \quad (49b)$$

In the high- $D_g$  (high-pressure) limit, the surface temperature approaches the gas flame temperature and  $m$  is given by Eq. (15) with  $T_s \rightarrow T_f$ ,

$$D_g \gg 1: \quad \tilde{m}^2 = \frac{\tilde{A}_c \tilde{T}_f^2 \exp(-\tilde{E}_c/\tilde{T}_f)}{\tilde{E}_c(\tilde{T}_f - \tilde{T}_o - \tilde{Q}_c/2 - f_r \tilde{q}_r/\tilde{m})}; \quad \tilde{T}_f = \tilde{T}_o + 1, \quad (50a)$$

$$\tilde{m} = \tilde{m}(\tilde{A}_c, \tilde{E}_c, \tilde{Q}_c, \tilde{T}_o, \tilde{q}_r, \tilde{K}_a). \quad (50b)$$

#### 2.3.4. Sensitivity Parameters

Another key issue is the sensitivity of the mass flux or burning rate and surface temperature to the independent variables,  $P$ ,  $T_o$ ,  $q_r$ . The sensitivity of burning rate to pressure and initial temperature is obviously important for internal ballistics and rocket motor performance prediction for quasi-static operation. The sensitivity of surface temperature is not quite as obvious but is related to the unsteady combustion behavior through Zeldovich-Novozhilov (ZN) theory. The sensitivity parameters are derivatives of the steady equations as defined in the nomenclature. Equation (15) or (16) can be differentiated with respect to initial temperature ( $T_o$ ), pressure ( $D_g$ ), and radiative flux ( $q_r$ ) to give

$$r = \frac{k[2 - \tilde{Q}_c(\tilde{T}_s - \tilde{T}_o) - f_r J] - 1}{(2 + \tilde{E}_c/\tilde{T}_s)(\tilde{T}_s - \tilde{T}_o - \tilde{Q}_c/2 - f_r \tilde{q}_r/\tilde{m})/\tilde{T}_s - 1} \quad (51)$$

$$\delta = \frac{-n}{(2 + \tilde{E}_c/\tilde{T}_s)(\tilde{T}_s - \tilde{T}_o - \tilde{Q}_c/2 - f_r \tilde{q}_r/\tilde{m})/\tilde{T}_s - 1} \quad (52)$$

$$\delta_q = \frac{-n_q + k f_r J}{(2 + \tilde{E}_c/\tilde{T}_s)(\tilde{T}_s - \tilde{T}_o - \tilde{Q}_c/2 - f_r \tilde{q}_r/\tilde{m})/\tilde{T}_s - 1}. \quad (53)$$

which apply for any value of  $\tilde{E}_g$ . Differentiating Eq. (38) with respect to initial temperature ( $T_o$ ), pressure ( $D_g$ ), and radiative flux ( $q_r$ ) gives, for  $\tilde{E}_g \gg 1$ ,

$$k = \frac{(\tilde{T}_s - \tilde{T}_o)(2 + \tilde{E}_g/2\tilde{T}_f)/\tilde{T}_f}{1 + \tilde{q}_r/\tilde{m}\tilde{Q}_g} \quad (\tilde{E}_g \gg 1) \quad (54)$$

$$\nu = \frac{1}{1 + \tilde{q}_r/\tilde{m}\tilde{Q}_g} \quad (\tilde{E}_g \gg 1) \quad (55)$$

$$\nu_q = \frac{\tilde{q}_r/\tilde{m}\tilde{Q}_g}{1 + \tilde{q}_r/\tilde{m}\tilde{Q}_g} \quad (\tilde{E}_g \gg 1) \quad (56)$$

and differentiating Eqs. (11), (15), (42), (43), and (44) gives, for  $\tilde{E}_g \ll 1$ ,

$$k = \frac{1 + J \left[ (2 + \tilde{E}_c/\tilde{T}_s)(\tilde{T}_s - \tilde{T}_o - \tilde{Q}_c/2 - f_r\tilde{q}_r/\tilde{m})/\tilde{T}_s - 1 \right]}{2 - \tilde{Q}_c(\tilde{T}_s - \tilde{T}_o) - f_r J} \frac{2\tilde{x}_g\tilde{m}\tilde{Q}_g(\tilde{T}_s - \tilde{T}_o)}{(2 + \tilde{E}_c/\tilde{T}_s)(\tilde{T}_s - \tilde{T}_o - \tilde{Q}_c/2 - f_r\tilde{q}_r/\tilde{m})/\tilde{T}_s - 1} + J \quad (57)$$

$$\nu = \frac{2\tilde{x}_g\tilde{m}\tilde{Q}_g \left[ (\tilde{T}_s - \tilde{T}_o)(1 + \tilde{x}_g\tilde{m})(2 + \tilde{x}_g\tilde{m}) \right]}{2 - \tilde{Q}_c(\tilde{T}_s - \tilde{T}_o) - f_r J} \frac{2\tilde{x}_g\tilde{m}\tilde{Q}_g(\tilde{T}_s - \tilde{T}_o)}{(2 + \tilde{E}_c/\tilde{T}_s)(\tilde{T}_s - \tilde{T}_o - \tilde{Q}_c/2 - f_r\tilde{q}_r/\tilde{m})/\tilde{T}_s - 1} + J \quad (58)$$

$$\nu_q = \frac{J \left\{ 1 + f_r \left[ (2 + \tilde{E}_c/\tilde{T}_s)(\tilde{T}_s - \tilde{T}_o - \tilde{Q}_c/2 - f_r\tilde{q}_r/\tilde{m})/\tilde{T}_s - 1 \right] \right\}}{2 - \tilde{Q}_c(\tilde{T}_s - \tilde{T}_o) - f_r J} \frac{2\tilde{x}_g\tilde{m}\tilde{Q}_g(\tilde{T}_s - \tilde{T}_o)}{(2 + \tilde{E}_c/\tilde{T}_s)(\tilde{T}_s - \tilde{T}_o - \tilde{Q}_c/2 - f_r\tilde{q}_r/\tilde{m})/\tilde{T}_s - 1} + J \quad (59)$$

In the low- $D_g$  limit, the sensitivity parameters become

$$k = \frac{(1 - \tilde{T}_o/\tilde{T}_s)(1 + \tilde{E}_c/2\tilde{T}_s)}{1 + J(1 - \tilde{T}_o/\tilde{T}_s)(1 + \tilde{E}_c/2\tilde{T}_s)} \quad (60)$$

$$v = 0 \quad (61)$$

$$r = 1 - kJ \quad (62)$$

$$\delta = 0 \quad (63)$$

and in the high- $D_g$  limit,

$$k = (1 - \tilde{T}_o/\tilde{T}_s)(1 + \tilde{E}_c/2\tilde{T}_s) \quad (64)$$

$$v = 0 \quad (65)$$

$$r = 1 \quad (66)$$

$$\delta = 0. \quad (67)$$

A variation of the  $\tilde{E}_g \gg 1$  model arises from the gas flame approximation originated by Michelson [14, Eq. (2.11)]. Michelson proposed an approximate formula for laminar flame thickness in a gas, which was refined by Linan and Williams for high- $\tilde{E}_g$  conditions (see Eqs. (2.11)-(2.15) of [14]) and can be written as

$$\tilde{x}_g = \tilde{m}Z^2/\tilde{Y}_s D_g \exp(-\tilde{E}_g/\tilde{T}_f); \quad Z = \tilde{E}_g(\tilde{T}_f - \tilde{T}_s)/\tilde{T}_f^2; \quad Y_s = (\tilde{T}_f - \tilde{T}_s)/\tilde{Q}_g \quad (68)$$

where  $\tilde{T}_s$  for a gas flame would be replaced by the initial gas temperature. It can be shown that this formula is a good approximation of the rigorous  $\tilde{E}_g \gg 1$  solution for a burning solid when the surface temperature  $\tilde{T}_s$  is used instead of the initial gas temperature in the Zeldovich number,  $Z$ , as shown in Eq. (68). Replacing Eq. (38) by (68) in the  $\tilde{E}_g \gg 1$  solution gives a model that is nearly



Table 1  
Material Properties and Combustion Parameters for Benchmark Case

	$\tilde{E}_g \gg 1$	$\tilde{E}_g \ll 1$
<b>Condensed phase parameters</b>		
$\tilde{E}_c$	10	10
$\tilde{A}_c$	1e17	1e17
$\tilde{Q}_c$	0.1	0.1
$\tilde{K}_a$	0	0
$\tilde{q}_r$	0	0
$\tilde{T}_o$	0.15	0.15
<b>Gas phase parameters</b>		
$\tilde{E}_g$	10	0
$D_g$	1.384e7	7.881
$\tilde{Q}_g$	0.9	0.9
$\tilde{T}_f$	1.15	1.15
<b>Results</b>		
$\tilde{T}_s$	0.312	0.312
$\tilde{m}$	10	10
$\tilde{x}_g$	0.268	1.36
$\tilde{q}_c$	0.616	0.616
$\nu (=n)$	1.0	0.84
$\nu q$	0	0
$k (= \sigma_p (T_s - T_o))$	0.89	1.38
$r$	0.021	0.081
$\delta$	-0.089	-0.075
$\delta q$	0	0

equivalent to the original  $\tilde{E}_g \gg 1$  solution and is essentially that used in the monopropellant flame of the BDP model [15,16].

### 3. RESULTS FOR MACROSCOPICALLY STEADY COMBUSTION

#### 3.1. Parametric (Non-Dimensional) Results for Benchmark Case

The most efficient way to illustrate the effect of various parameters (although not always the most physically insightful) is through non-dimensional parameters. A baseline case for illustrating the effect of various non-dimensional parameters on steady regression behavior is selected as shown in Table 1. The value of  $D_g$  is selected so that the mass fluxes are the same between the two cases  $\tilde{E}_g \gg 1$  and  $\tilde{E}_g \ll 1$  (the different  $D_g$  values compensate for the different  $\tilde{E}_g$  values), and therefore the surface temperatures and conductive heat feedback terms are the same. The temperature and volumetric heat release profiles are shown in Fig. 2. The effect of large  $\tilde{E}_c$  is to concentrate the condensed phase heat release in a narrow zone at the surface,  $\tilde{x}_g = 0$ . Similarly, the effect of large  $\tilde{E}_g$  is to

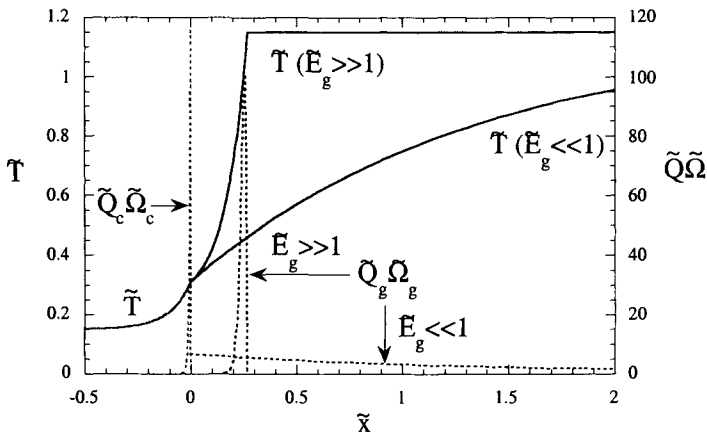


Fig. 2 Non-dimensional temperature profiles and volumetric heat release rates for benchmark case (Table 1). Condensed-phase heat release is concentrated near surface due to  $\tilde{E}_c \gg 1$  assumption. Large- $\tilde{E}_g$  case concentrates gas-phase heat release in a flame sheet at  $\tilde{x}_g = 0.27$ . Small- $\tilde{E}_g$  case distributes gas-phase heat release broadly over a region with characteristic  $(1/e)$  length scale of  $\tilde{x}_g = 1.4$ .

concentrate all the gas phase heat release in a flame sheet at  $\tilde{x}_g = 0.27$ . However, the effect of small  $\tilde{E}_g$  is to distribute the gas phase heat release broadly, with a  $1/\epsilon$  characteristic length scale of  $\tilde{x}_g = 1.4$ . Since these two models represent extreme (opposite) limiting conditions in terms of  $\tilde{E}_g$ , the actual heat release profile in real materials is probably an intermediate case between these two extremes. Experimental evidence, however, suggests that most materials are closer to the  $\tilde{E}_g \ll 1$  limit than  $\tilde{E}_g \gg 1$ .

### 3.1.1. Burning Rate or Mass Flux

The variation of mass flux with  $D_g \exp(\tilde{E}_g / \tilde{T}_f)$  is shown in Fig. 3. The Damkohler number  $D_g$  can be thought of as a non-dimensional pressure. The

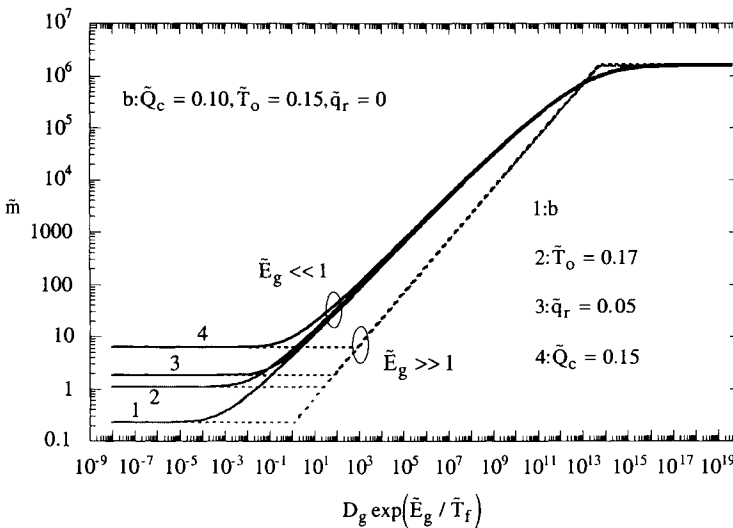


Fig. 3 Non-dimensional mass flux for benchmark (1) case (Table 1) showing effect of non-dimensional initial temperature (2), absorbed radiant flux (3), and condensed phase heat release (4). Horizontal axis (Damkohler number by Arrhenius factor) represents non-dimensional pressure. Low- and high- $D_g$  regions represent condensed-phase controlled (pressure independent) burning regimes. Typical operating conditions correspond to horizontal axis values of  $10^1$  to  $10^3$ .

benchmark case (labeled "b" in Fig. 3) has the same parameters as Table 1 except  $D_g$  is allowed to vary. Thus Fig. 3 can be thought of as a plot of mass flux or burning rate as a function of pressure, or more accurately  $P^2$ , with the effect of  $\tilde{E}_g$  being represented by the two extreme limits of asymptotically large  $\tilde{E}_g$  and vanishingly small  $\tilde{E}_g$ . Substitution of dimensional values for the parameters would show that the calculations in Fig. 3 are extended to pressures beyond ideal-gas range; nevertheless the essential features and trends would not be significantly different upon introduction of non-ideal gas compressibility. Similarly, the low- $D_g$  limit extends to pressures lower than those at which many energetic materials burn stably. Still, the low pressure (low  $D_g$ ) limit is useful to consider for illustrating the effect of  $\tilde{E}_g$  on the burning behavior; in addition, many energetic materials, particularly ones with larger exothermicity of the condensed phase reaction, do burn at low pressures. For the baseline case in Fig. 3 ( $b: \tilde{Q}_c = 0.10, \tilde{T}_o = 0.15, \tilde{q}_r = 0$ ) both limiting  $\tilde{E}_g$  cases show a strong dependence of burning rate on  $D_g$  or pressure over an intermediate pressure range that covers most practical situations. The pressure sensitivity or so-called pressure exponent  $\nu$  or  $n$  is 1 for the large  $\tilde{E}_g$  case and less than one (0.84 for the benchmark conditions of Table 1) for the small  $\tilde{E}_g$  case. In this pressure ( $D_g$ ) regime, the gas reaction zone makes an important contribution to determining the regression rate for any  $\tilde{E}_g$  value. Indeed for  $\tilde{E}_g \gg 1$ , the gas reaction kinetics completely determine the burning rate (at least to the degree  $\tilde{Q}_g$  is uncoupled from condensed phase chemistry). For  $\tilde{E}_g \ll 1$ , the condensed phase kinetic parameters still play a role. Away from the intermediate, pressure-sensitive region in Fig. 3, at extremely high and low  $D_g$  values, there are regions of pressure-insensitive, condensed phase kinetically controlled burning. The transition to these regions occurs gradually in the low- $\tilde{E}_g$  case. In the high- $\tilde{E}_g$  case, the transition occurs abruptly. In the low- $D_g$  limit, as pressure decreases the surface temperature gradient (and hence conductive heat feedback) approaches zero; the gas flame is blown away from the surface. For  $\tilde{E}_g \ll 1$ , this condition is approached gradually as pressure is reduced; but for  $\tilde{E}_g \gg 1$ , it occurs abruptly. In the high- $D_g$  limit, as pressure increases the surface temperature approaches the flame temperature, a "surface flame" is achieved [17]. For  $\tilde{E}_g \ll 1$ , this condition is approached gradually as

pressure is increased; but for  $\tilde{E}_g \gg 1$ , it occurs abruptly. These results show that at extremely high and low pressures there is a predicted transition to condensed phase kinetically controlled burning for any  $\tilde{E}_g$  value. Results for intermediate  $\tilde{E}_g$  values would fall between the two limiting cases shown in Fig. 3. Three cases showing parametric variations away from the benchmark case ( $b: \tilde{Q}_c = 0.10, \tilde{T}_o = 0.15, \tilde{q}_r = 0$ ) are also shown in Fig. 3:  $\tilde{Q}_c = 0.15$ ,  $\tilde{T}_o = 0.17$ , and  $\tilde{q}_r = 0.05$ . The effect of each of these non-dimensional condensed phase parameters is to increase the mass flux, more noticeably so at lower pressures (lower  $D_g$  values) and lower  $\tilde{E}_g$  values.

3.1.2. Surface Temperature, Heat Feedback, and Flame Standoff Distance

The non-dimensional surface temperature  $\tilde{T}_s$  and conductive heat feedback  $\tilde{q}_c$  are shown in Fig. 4 for the benchmark case (Table 1) as a function of  $D_g \exp(\tilde{E}_g / \tilde{T}_f)$ . As pressure ( $D_g$ ) increases, surface temperature increases from the minimum value at the blowoff limit, namely  $\tilde{T}_o + \tilde{Q}_c + \tilde{q}_r / \tilde{m}$  ( $= 0.25$ ) to the

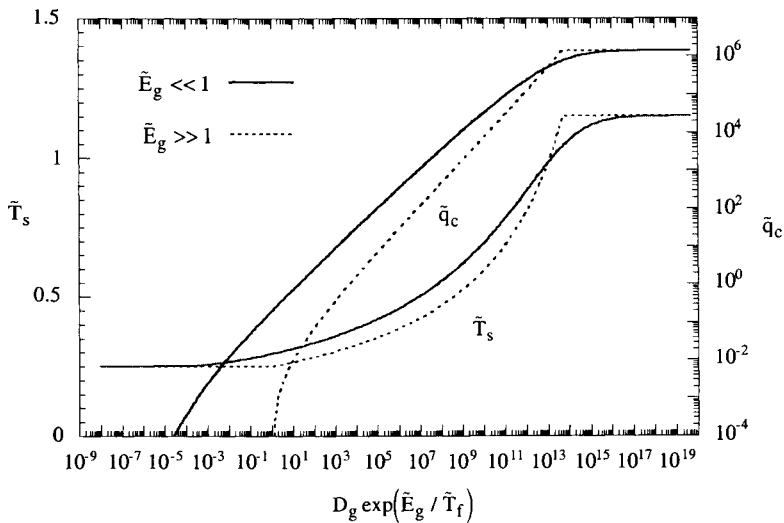


Fig. 4 Non-dimensional surface temperature and conductive heat feedback from gas phase to surface for benchmark case (Table 1).

maximum value, at the surface flame limit, or  $\tilde{T}_f (= 1.15)$ . Conductive heat feedback from the flame to the surface  $\tilde{q}_c$  increases as a power function over the intermediate pressure regime of interest. This is due to the inverse power function decrease in non-dimensional flame standoff distance  $\tilde{x}_g$  as shown in Fig. 5. The curves for  $\tilde{x}_g$  decrease with a nearly constant slope of -2 in Fig. 5 in the intermediate pressure regime. This indicates that dimensional flame standoff distance  $x_g$  varies approximately as  $1/P$ . As pressure increases, gas-phase heat release rate increases due to pressure-sensitive bimolecular reactions; the flame is pushed closer to the surface ( $x_g$  decreases) and the temperature gradient and hence conductive heat feedback increase, even to the extent of overcoming the increasing mass blowing effect associated with increasing  $\tilde{m}$ . As for comparing the flame standoff distance for the two limits of large and small  $\tilde{E}_g$ , the results of Fig. 5 are somewhat misleading. It would appear from Fig. 5 that  $x_g$  is larger for large  $\tilde{E}_g$  than for small  $\tilde{E}_g$  over most pressures, at least based on the same  $D_g \exp(\tilde{E}_g / \tilde{T}_f)$

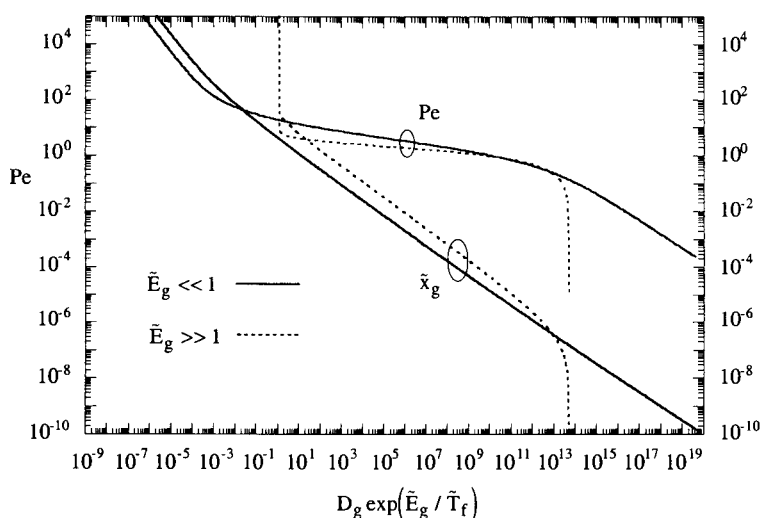


Fig. 5 Non-dimensional flame standoff distance and Peclet number based on flame standoff distance (ratio of bulk-to-diffusion velocity) for benchmark case (Table 1). Note that in dimensional terms  $x_g$  for small  $\tilde{E}_g$  is actually greater than that for large  $\tilde{E}_g$  for comparable conditions.

value. However, the comparison should be done as in Table 1, for equivalent mass fluxes and conductive heat feedbacks (different  $D_g \exp(\tilde{E}_g / \tilde{T}_f)$  values). As shown in Table 1 and Fig. 2, for  $\tilde{m} = 10$  the flame standoff distance is about a factor of five bigger (1.36 compared with 0.27 in terms of  $\tilde{x}_g$ ) for the small- $\tilde{E}_g$  case. This is one instance where non-dimensional results obscure the dimensional trends. In general, for the same mass flux,  $\tilde{x}_g$  is bigger for small  $\tilde{E}_g$  for equivalent mass flux and conductive heat feedback conditions.

Figure 5 also shows the Peclet number based on the flame standoff distance,  $Pe = \tilde{x}_g \tilde{m}$ , which can be interpreted as the ratio of the bulk convective velocity to diffusion velocity ( $Pe = u/(D/x_g) = u/(\alpha_g/x_g)$ ). In the intermediate pressure regime where axial back-diffusion of heat is a strong contributor in driving the bulk convective flow,  $Pe$  is of order one and relatively constant. This can be seen from the form  $u/(D/x_g)$ . Recall that  $D$  and  $\alpha_g$  are assumed to vary as  $T/P$ . Therefore as  $P$  decreases,  $D$  increases. However,  $x_g$  also varies approximately as

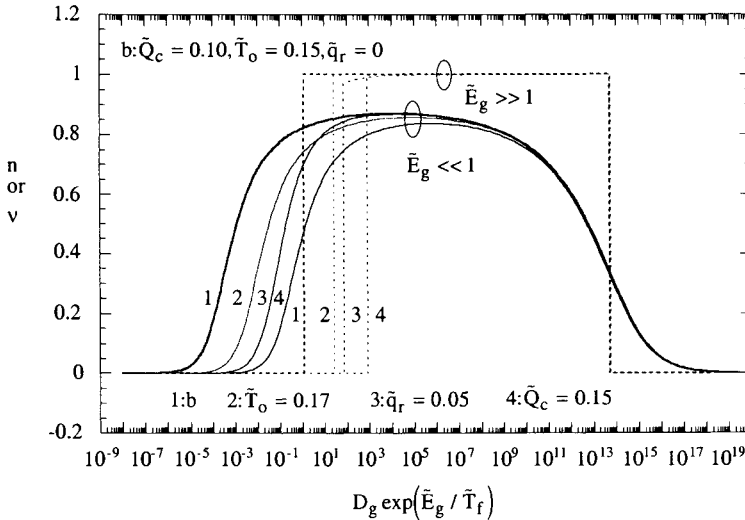


Fig. 6 Pressure sensitivity of burning rate for benchmark (1) case (Table 1) showing effect of non-dimensional initial temperature (2), absorbed radiant flux (3), and condensed phase heat release (4).

$1/P$  at intermediate pressures; therefore, the diffusion velocity  $D/x_g$  is nearly independent of  $P$ . Yet  $u = \rho_c r_b / \rho_g$  varies as  $P^{n-1}$  and at intermediate pressures,  $n$  is of order one (slightly less than one for  $\tilde{E}_g \ll 1$ ) so  $Pe$  and  $u$  are relatively constant, decreasing slightly with increasing  $P$ . In the low- and high-pressure limits where condensed phase heat release takes on more importance as the mass flux driving force,  $n$  decreases toward zero, the sensitivity of  $x_g$  to  $P$  increases, depending on  $\tilde{E}_g$  (more so for bigger  $\tilde{E}_g$ ), and therefore the sensitivity of  $Pe$  to  $P$  increases.

### 3.1.3. Sensitivity Parameters

The pressure exponent or pressure sensitivity parameter ( $\nu$  or  $n$ ) is shown in Fig. 6. At very high and low pressures, the condensed-phase kinetically controlled regimes seen earlier in Fig. 3 are also apparent in Fig. 6 where the pressure sensitivity goes to zero. The low-pressure transition point can be seen to be sensitive to  $\tilde{T}_o$ ,  $\tilde{q}_r$ , and  $\tilde{Q}_c$ , increasing with each of those parameters, whereas the high-pressure transition point is not. In the important intermediate pressure range, the pressure sensitivity is relatively constant at around 0.8 for small  $\tilde{E}_g$  and 1 for large  $\tilde{E}_g$ . The transition between the intermediate pressure regime and the high- and low-pressure regimes is more precipitous for larger  $\tilde{E}_g$  values.

The burning-rate temperature-sensitivity parameter ( $k$ ) is shown in Fig. 7. The usual dimensional temperature sensitivity  $\sigma_p = k/(T_s - T_o)$  can be obtained by dividing the plotted non-dimensional  $k/(\tilde{T}_s - \tilde{T}_o)$  value by an assumed value for  $(T_f - T_o)$ . For  $D_g \exp(\tilde{E}_g / \tilde{T}_f)$  values above  $10^4$  (intermediate and high pressures),  $k/(\tilde{T}_s - \tilde{T}_o)$  is relatively small and independent of  $D_g$  (pressure),  $\tilde{T}_o$ ,  $\tilde{q}_r$ , and  $\tilde{Q}_c$ . For lower pressures  $k/(\tilde{T}_s - \tilde{T}_o)$  increases significantly and becomes a strong function of pressure,  $\tilde{T}_o$ ,  $\tilde{q}_r$ , and  $\tilde{Q}_c$ . The low-pressure behavior (*i.e.*, high  $k/(\tilde{T}_s - \tilde{T}_o)$  values sensitive to  $\tilde{T}_o$ ,  $\tilde{q}_r$ , and  $\tilde{Q}_c$ ) reflects the fact that the condensed phase reaction has a strong influence on the regression rate and that the condensed phase reaction rate is itself quite temperature sensitive (due to large- $\tilde{E}_c$  thermal decomposition). In the intermediate pressure region where the gas phase reaction kinetics have a strong influence on burning rate, the value of  $\tilde{E}_g$  has a strong influence on the  $k/(\tilde{T}_s - \tilde{T}_o)$  behavior. The  $\tilde{E}_g \gg 1$  expression indicates that



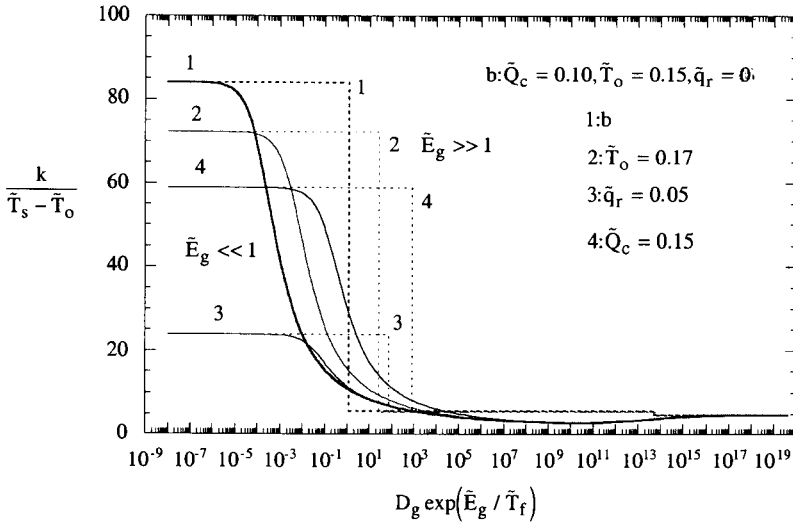


Fig. 7 Temperature sensitivity of burning rate for benchmark (1) case (Table 1) showing effect of non-dimensional initial temperature (2), absorbed radiant flux (3), and condensed phase heat release (4).

$k/(\tilde{T}_s - \tilde{T}_o)$  is very sensitive to the selected value of  $\tilde{E}_g$  and not dependent on  $\tilde{E}_c$  (gas phase kinetically controlled). Higher  $\tilde{E}_g$  values yield higher temperature sensitivity. The  $\tilde{E}_g \ll 1$  value of  $k/(\tilde{T}_s - \tilde{T}_o)$  is low in this pressure range because the gas reaction rate, which by definition is temperature insensitive, is having a strong influence on the burning rate. In the range of  $D_g \exp(\tilde{E}_g / \tilde{T}_f)$  values from 10 to  $10^3$  where gas kinetics are still playing a strong role in determining burning rate, the value of  $\tilde{E}_g$  is seen to have a strong effect on  $k/(\tilde{T}_s - \tilde{T}_o)$ . The  $\tilde{E}_g \gg 1$  value of  $k/(\tilde{T}_s - \tilde{T}_o)$  stays constant all the way down to the low- $D_g$  transition at which point it jumps to the much larger, low-pressure values discussed above. However, the  $\tilde{E}_g \ll 1$  value begins increasing to make a gradual transition to the low-pressure limit. The practical implication is that the  $\tilde{E}_g \ll 1$  model indicates a strong dependence of  $k/(\tilde{T}_s - \tilde{T}_o)$  on pressure,  $\tilde{T}_o$  and  $\tilde{Q}_c$  at pressures below 1

MPa, which has been observed in HMX combustion data, whereas the  $\tilde{E}_g \gg 1$  model does not. The reason is that as pressure drops below 1 MPa, the burning rate for  $\tilde{E}_g \gg 1$  becomes increasingly sensitive to condensed phase reaction kinetics and does so in a continuous fashion. One trend that is obscured by using non-dimensional variables as presented here is that dimensional temperature sensitivity  $\sigma_p = k/(T_s - T_o)$  is also sensitive to radiant flux  $q_r$  in the range of  $D_g \exp(\tilde{E}_g / \tilde{T}_f)$  values from  $10^{-1}$  to  $10^3$  whereas the dimensionless parameter seems to suggest otherwise. The difference between the dimensional and non-dimensional representations has to do with the effect  $q_r$  has on flame temperature;  $q_r$  increases the value of  $(T_f - T_o)$ , which must be divided into  $k/(\tilde{T}_s - \tilde{T}_o)$  to obtain  $\sigma_p$ . Therefore, increasing  $q_r$  actually often decreases  $\sigma_p$ , especially at low pressures.

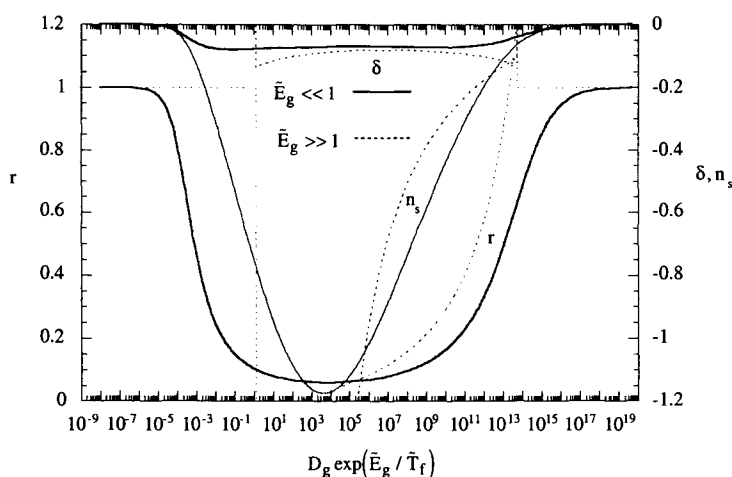


Fig. 8 Remaining ZN sensitivity parameters for benchmark case (Table 1): sensitivity of surface temperature to initial temperature ( $r$ ) and Jacobian parameters ( $\delta$  and  $n_s$ ). Note that  $n_s$  is negative (the nonphysical singularity in  $n_s$  for  $\tilde{E}_g \gg 1$  corresponding to  $r < 0$  has been omitted).

The remaining sensitivity parameters,  $r$  (sensitivity of  $T_s$  to  $T_o$ ) and  $\delta$  (Jacobian parameter) are shown as a function of non-dimensional pressure  $D_g \exp(\tilde{E}_g / \tilde{T}_f)$  in Fig. 8. The  $r$ -parameter is generally positive, except for a region of  $D_g \exp(\tilde{E}_g / \tilde{T}_f)$  between 1 and 100 for the  $\tilde{E}_g \gg 1$  case. The  $\delta$ -parameter is generally negative since the pressure exponent is positive, as indicated by Eq. (52). These parameters have significance for unsteady combustion as discussed elsewhere. For steady combustion, the ratio of these two parameters,  $n_s = \delta r$ , has a unique significance. Several decades ago a simple pyrolysis relation of the form

$$r_b = A_s P^{n_s} \exp\left(\frac{-E_s}{RT_s}\right) \quad (69)$$

was proposed with the hope of better matching experimental results [18,19,20]. The idea had merit; assuming the right value of  $n_s$  was selected (varying with  $P$  and  $T_o$ ) it should be possible to imitate experimental behavior or that of a more rigorous pyrolysis relation, such as zero-order, high activation energy, at least for linear response or sensitivity parameter behavior. However, for many years only positive values of  $n_s$  were considered to be physically meaningful, presumably because it was assumed that if  $n_s$  was negative an increase in pressure would result in an increase in  $r_b$ . At the time, the equivalence  $n_s = \delta r$  had not yet been recognized [21]. As Fig. 8 shows, however, for zero-order, high-activation energy decomposition, the  $n_s$ -parameter is generally negative [22] (except for the seemingly unphysical region of negative  $r$ -parameter for the  $\tilde{E}_g \gg 1$  case which gives a  $\infty$  to  $+\infty$  singularity that has been omitted from Fig. 8). The reason a negative Jacobian parameter does not result in a decrease in  $r_b$  with increasing  $P$  is that  $T_s$  increases at a fast enough rate that the exponential term offsets the  $P^{n_s}$  term. Unsteady combustion experiments have also recently verified that negative Jacobian parameter values are more realistic than positive ones.

### 3.2 Results for Common Materials

The steady combustion behavior of two common energetic materials are discussed in the context of the foregoing simplified model: uncatalyzed NC/NG double base propellant and cyclo-tetramethylene-tetranitramine (HMX).

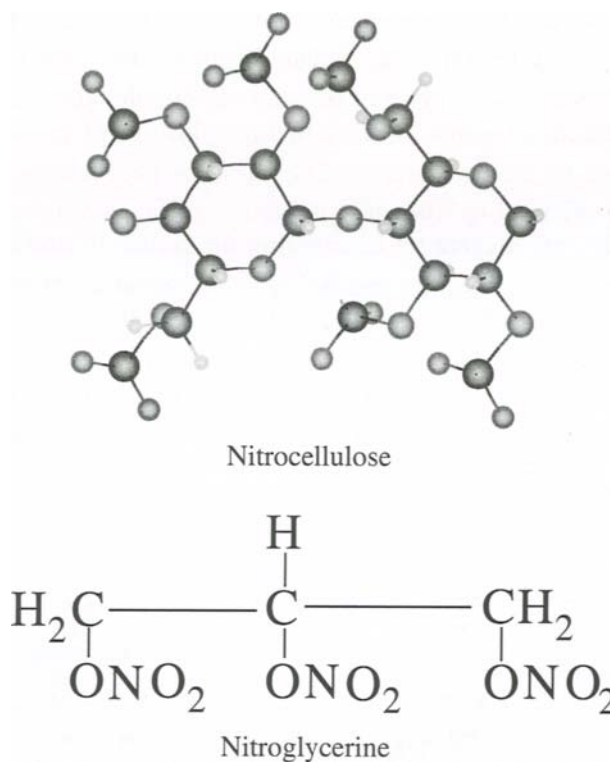


Fig. 9 Nitrocellulose (NC) and nitroglycerine (NG) molecules comprising double base propellant.

### 3.2.1. NC/NG Double Base Propellant

#### 3.2.1.1. Condensed phase decomposition zone

Nitrocellulose/nitroglycerine (NC/NG) double base propellant burns with a nominally single-stage decomposition region and a two-stage gas flame at pressures below 10 MPa. Decomposition is thought to be initiated by thermal homolysis of CO-NO<sub>2</sub> bonds in NC and NG (see Fig. 9), requiring about 40 kcal/mol. This endothermic initiation step is followed by rapid recombination reactions, which are presently not well understood but are probably exothermic, resulting in a condensed phase process which is overall slightly net exothermic at most pressures. Accordingly, reasonable single-step decomposition parameter

values are  $E_c = 40$  kcal/mol (corresponding to the CO-NO<sub>2</sub> bond strength),  $A_c = 1e17$  1/s, and  $Q_c = 20$  to 100 cal/g. Figure 10 shows that these parameters fit the decomposition behavior of variety of uncatalyzed double base propellants under a variety of conditions in terms of an Arrhenius plot ( $\ln(r_b)$  vs.  $1/T_s$ ) where  $T_s$  is usually measured by thermocouples. The variation between the data points and theoretical lines seen in Fig. 10 is not of major significance and could possibly be accounted for to some degree by considering the actual  $T_o$  and  $q_r$  values for the various experimental conditions and the variation between those values and the assumed model values of  $T_o = 300$  K and  $q_r = 0$ . Also, experimental error in determining the actual surface location plays a role. The most important result of Fig. 10 is that the putative CO-NO<sub>2</sub> bond energy  $E_c = 40$  kcal/mol shows good correlation with measurements over such a wide range of pressures, regression rates, and surface temperatures.

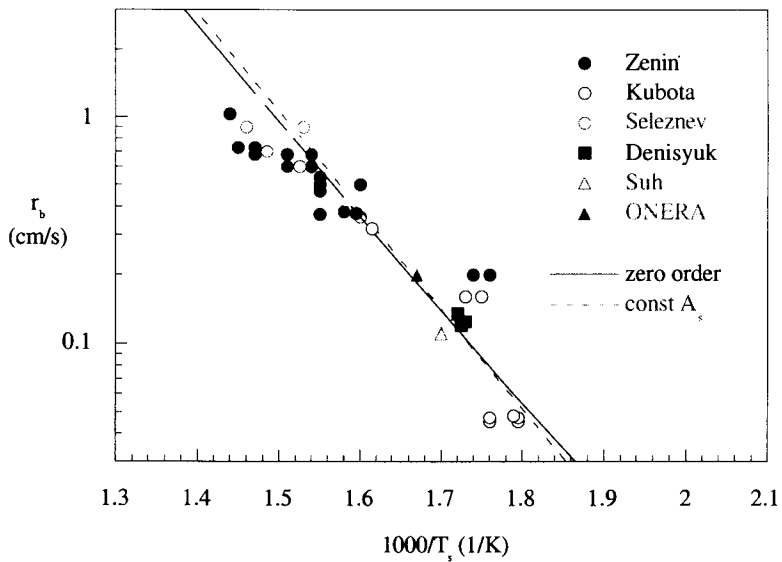


Fig. 10 Arrhenius plot for uncatalyzed double base propellant. The constant- $A_s$  curve is Eq. (17) with  $A_s = 3.82e6$  cm/s and  $E_s = 20$  ( $E_c = 40$ ) kcal/mol. The zero-order curve is Eq. (16) for  $A_c = 1e17$  1/s,  $E_c = 40$  kcal/mol,  $Q_c = 100$  cal/g,  $q_r = 0$ ,  $C = 0.35$  cal/g-K,  $T_o = 300$  K,  $\alpha_c = 1.2e-3$  cm<sup>2</sup>/s.

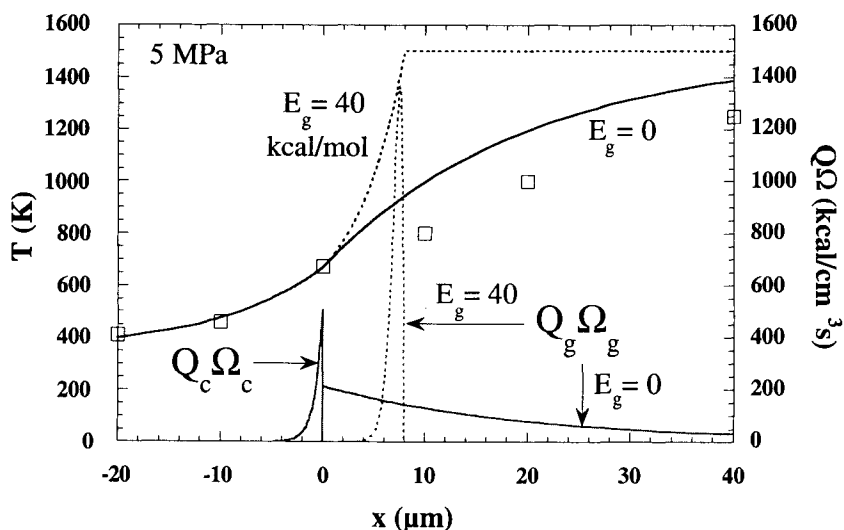


Fig. 11 Temperature profiles and volumetric heat release for double base NC/NG propellant-N (uncatalyzed, medium heat of explosion) along with model predictions for  $\tilde{E}_g \gg 1$  and  $\tilde{E}_g \ll 1$ . Thermocouple measurements (squares) are from [23]. A secondary flame (unimportant for burning rate) occurs at  $500 < x < 800 \mu\text{m}$  where the temperature increases from 1500 K to over 2400 K.

### 3.2.1.2. Gas phase reaction zone

Figure 11 shows near-surface, gas phase temperature measurements for steady burning of uncatalyzed, medium energy NC/NG propellant (designated propellant-N following Russian notation) at 5 MPa (50 atm) from thermocouples [23]. At this pressure there is a distinct two-stage gas flame structure but only the primary stage closest to the surface, where temperature increases from  $T_s = 668 \text{ K}$  to around 1500 K, is important for determining regression rate (only the primary stage is shown in Fig. 11). In the primary flame species like  $\text{NO}_2$ ,  $\text{HONO}$ , and  $\text{CH}_2\text{O}$  which evolve from the surface as decomposition products are converted to  $\text{NO}$ ,  $\text{CO}$ , and  $\text{H}_2\text{O}$ , with a significant liberation of chemical energy,  $Q_g$ . The secondary flame occurs between 500 and 2000  $\mu\text{m}$  from the surface at this pressure; the temperature increases from 1500 to 2400 K. In this latter flame  $\text{CO}$  and  $\text{NO}$  are converted to  $\text{N}_2$  and  $\text{CO}_2$ .

Model predictions based on realistic thermophysical and thermochemical parameters (see Table 2) are also shown in Fig. 11 for both  $\tilde{E}_g \gg 1$  ( $E_g = 40$  kcal/mol) and  $\tilde{E}_g \ll 1$  ( $E_g = 0$ ). Both models exhibit exponential temperature profiles,  $\tilde{E}_g \gg 1$  concave-up and  $\tilde{E}_g \ll 1$  concave-down. At the surface,  $dT/dx$  is the same for both models due to the regression rates being the same. Comparing the predictions with thermocouple measurements [23], it can be seen that the  $\tilde{E}_g \ll 1$  model overpredicts the thermocouple measurements somewhat but is much closer qualitatively and quantitatively than the  $\tilde{E}_g \gg 1$  model. The discrepancy may be partly due to thermocouple lag error, which becomes more pronounced as pressure (regression rate) increases. The general shape of Zenin's measured temperature profiles is closer to that predicted by the  $\tilde{E}_g \ll 1$  model than by  $\tilde{E}_g \gg 1$ . The characteristic flame standoff distance  $x_g = 8 \mu\text{m}$  predicted by the  $\tilde{E}_g \gg 1$  model is clearly too small and the temperature profile is not correct. Interestingly, however, the  $\tilde{E}_g \gg 1$  model has been the most popular simple kinetics model considered in the past few decades.

Application of the BDP model (which is essentially equivalent to the  $\tilde{E}_g \gg 1$  model described here) to NC/NG propellant combustion has been previously reported [15,16]; however, the results are not entirely consistent with the present calculations. The reported BDP flame thickness, is generally higher than the  $\tilde{E}_g \gg 1$  model calculations using Table 2 values; for example,  $x_g$  has been reported as 20 to 30  $\mu\text{m}$  at 50 atm [16]. Figure 11 show that these values are closer to Zenin's data which is surprising given that BDP is essentially equivalent to the  $\tilde{E}_g \gg 1$  model. The reason has to do with the value of gas thermal conductivity  $k_g$  used in the BDP model, which is reported as 0.002 cal/cm-s-K [16]. This value is an order of magnitude larger than what has been reported for NC/NG propellant based on analysis of the thermal properties of the anticipated gas species in the primary flame ( $\sim 0.0002$  cal/cm-s-K) [23,24]. Therefore, an erroneous (high)  $k_g$  value can compensate for an incorrect temperature profile (high  $E_g$  value) by allowing a reduced  $dT/dx$  at the surface but still maintaining the correct conductive heat feedback  $q_c = k_g dT/dx$ . To see how an erroneous  $k_g$  value can compensate for an incorrect temperature profile ( $E_g$  value), consider this simple example. If  $k_g$  were increased by a factor of 2.5 from 0.0002 to 0.0005 and  $B_g$  decreased by the same factor to maintain the same  $m$ ,  $T_s$ , etc., the  $\tilde{E}_g \gg 1$  model temperature profile in

Fig. 11 would shift such that  $x_g$  would increase by a factor of 2.5 from 8 to 20  $\mu\text{m}$ . At the same time  $dT/dx$  at the surface would drop by the same factor such that  $q_c (= k_g dT/dx)$  would remain constant (in fact, all computed results would remain constant except  $x_g$  because other than in the expression for  $x_g$ , Eq. (40),  $k_g$  enters the problem only through Eq. (39) as a product with  $A_g$  or  $B_g$ ). Thus an erroneously high gas thermal conductivity can compensate for an unrealistically large  $E_g$  value to give realistic  $x_g$  and  $k_g dT/dx$  values. (Of course it cannot compensate for the curvature of  $T(x)$  which remains qualitatively different from observations.)

Figure 11 also shows the calculated volumetric heat release rates due to chemical reaction ( $Q_c \Omega_c$  and  $Q_g \Omega_g$ ). For  $\tilde{E}_g \gg 1$  the effect of large  $E_g$  is to concentrate all the gas phase heat release in a flame sheet relatively close to the surface ( $x_g = 8 \mu\text{m}$ ). For  $\tilde{E}_g \ll 1$ , the effect of small  $E_g$  is to distribute the heat release broadly over a thicker zone (characteristic  $1/e$  distance,  $x_g = 20 \mu\text{m}$ ). Since

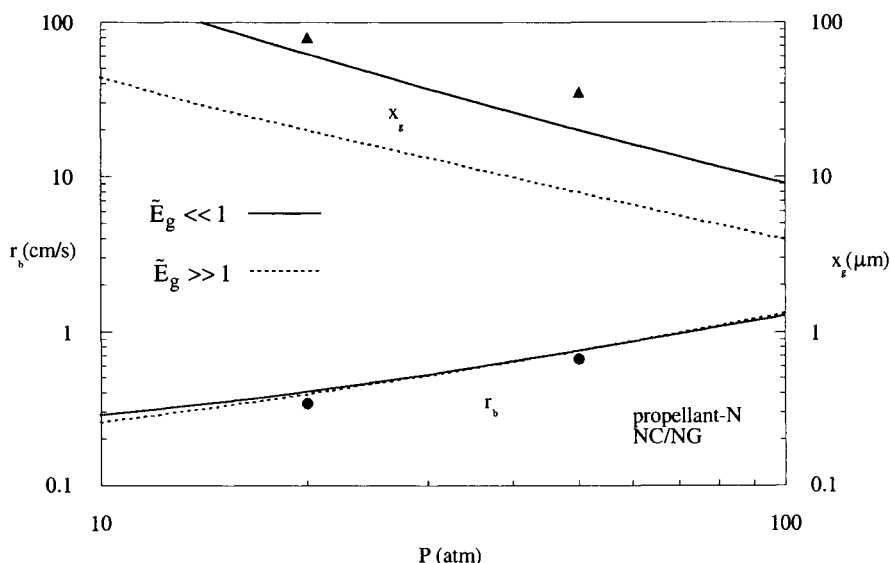


Fig. 12 Effect of pressure on burning rate and flame thickness for NC/NG propellant-N. Measurements from Zenin [23]; model based on parameters in Table 2.



these two models represent extreme (opposite) limiting conditions in terms of  $E_g$ , the actual heat release profile in a material such as NC/NG is probably an intermediate case somewhere between these two extremes. The temperature measurements, however, suggest that the real case is probably closer to the small  $E_g$  limiting representation than the large  $E_g$  case. Based on more detailed kinetics and numerical simulations Lengelle, *et al.* [25] have suggested values in the range of 5 to 10 kcal/mol as being appropriate.

3.2.1.3. *Burning rate and primary flame length scale*

Figure 12 shows  $r_b$  and  $x_g$  as functions of pressure for propellant-N. Experimental data points are from Zenin [23] and calculations are for  $\tilde{E}_g \gg 1$  and  $\tilde{E}_g \ll 1$  using the parameters in Table 2. Among the input parameters only the gas phase kinetic terms  $E_g$  and  $B_g$  are different between the two models, with  $B_g$  being adjusted to match burning rate at the baseline condition (50 atm, 300 K).

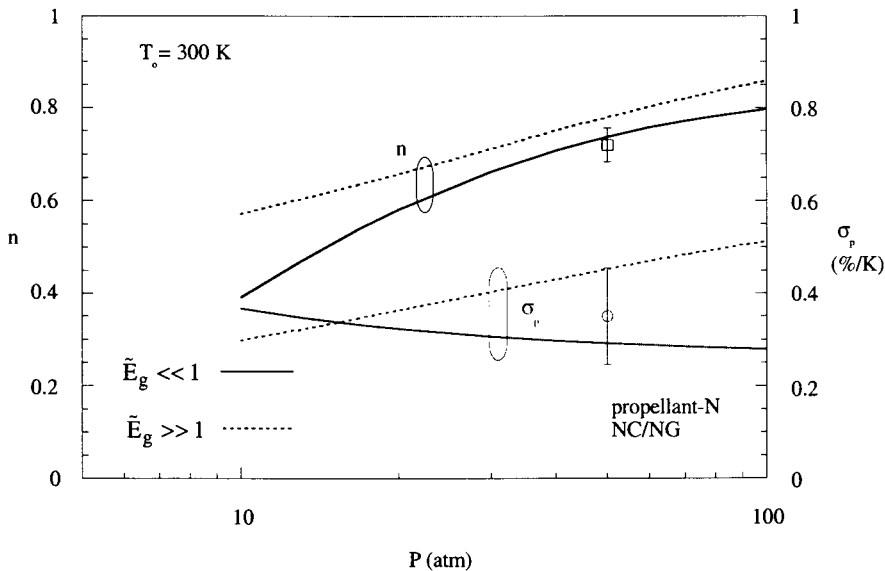


Fig. 13 Temperature sensitivity and pressure exponent vs. pressure for propellant-N. Experimental data are from Lengelle, *et al.* [25] for  $n$  and Ibricu and Williams [3] for  $\sigma_p$ . Model based on parameters in Table 2.

Across the range of pressures, burning rates are similar with  $\tilde{E}_g \gg 1$  showing a slightly higher pressure sensitivity ( $n$ ). Both models exhibit a decreasing trend of  $x_g$  with pressure ( $\sim p^{-1}$ ); however, the  $\tilde{E}_g \gg 1$  value of  $x_g$  is significantly less than the experimental data and the  $\tilde{E}_g \ll 1$  model results.

### 3.2.1.4. Pressure and temperature sensitivity parameters

The pressure sensitivity ( $n$ ) and temperature sensitivity ( $\sigma_p$ ) are shown in Figs. 13 and 14. Most reported measurements indicate  $n$  values between 0.6 and 0.8, increasing with pressure (Fig. 13). Conceivably  $n$  could vary with  $T_o$  and  $q_r$  also but well controlled measurements are scarce. Most reported measurements of  $\sigma_p$  at  $T_o = 300$  K are between 0.5 and 0.6 %/K, independent of pressure, at least within measurement uncertainty. With increasing  $T_o$  (Fig. 14),  $\sigma_p$  definitely shows an increasing behavior. The experimental data points in Figs. 13 and 14 are from [3]. Their value of  $\sigma_p = 0.35$  %/K (relatively independent of pressure) is low

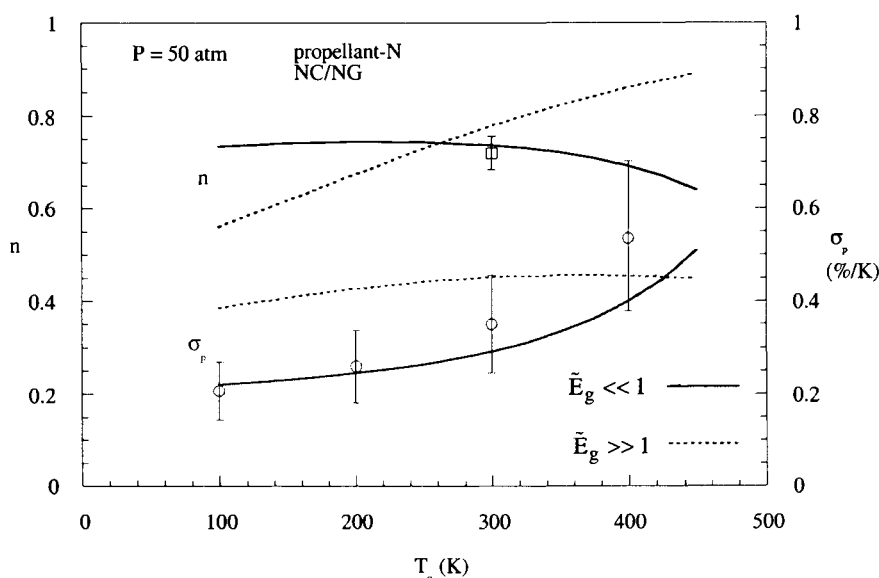


Fig. 14 Temperature sensitivity and pressure exponent vs. temperature for propellant-N. Experimental data are from Lengelle, *et al.* [25] for  $n$  and Ibricu and Williams [3] for  $\sigma_p$ . Model based on parameters in Table 2.

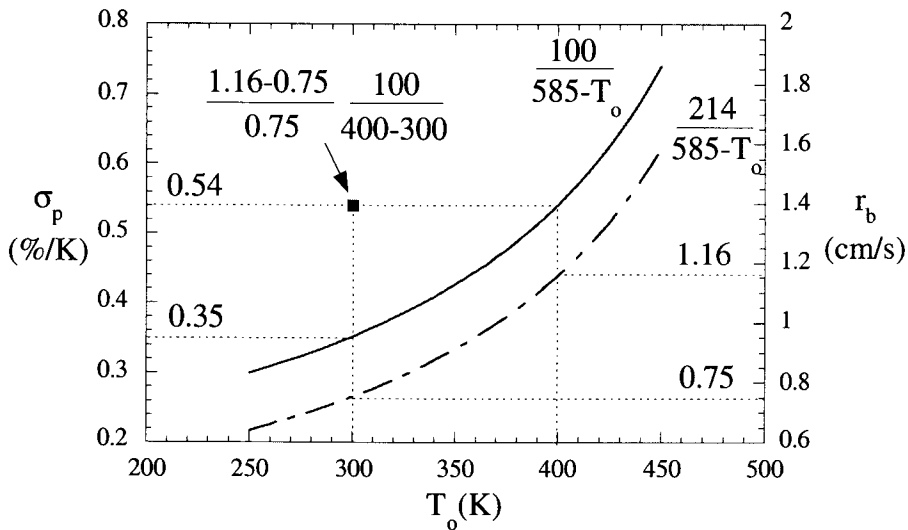


Fig. 15 Example calculation of temperature dependence of temperature sensitivity for double base propellant-N showing the difference between continuous functional representation of  $\sigma_p(T_o)$  (solid line) and finite difference representation (data point at 300 K); for increasing  $\sigma_p$  with  $T_o$ , the latter over-estimates the former as shown by the single data point value at 300 K, 0.54 %/K, relative to the continuous function value at the same temperature, 0.35 %/K.

compared with the majority of reported values. However, Ibricu and Williams [3] accounted for  $\sigma_p(T_o)$  variations whereas most measurements do not. The significance of this is illustrated by a simple example.

As reported by Ibricu and Williams [3],  $\sigma_p(T_o)$  may be approximated for propellant-N by  $\sigma_p = 1/(585 - T_o)$  or  $\sigma_p(\%/K) = 100/(585 - T_o)$ , as shown in Fig. 15. Therefore, by integration the general burning rate relation using a reference value of  $r_b(300 \text{ K}) = 0.75 \text{ cm/s}$  is  $r_b = 214/(585 - T_o)$ , giving  $\sigma_p(300 \text{ K}) = 0.35$ ,  $\sigma_p(400 \text{ K}) = 0.54$ , and  $r_b(400 \text{ K}) = 1.16 \text{ cm/s}$ , as shown in Fig. 15. The finite difference value of  $\sigma_p(300 \text{ K})$  inferred from the two burning rates normalized by 0.75 cm/s would be 0.54, as shown by the single data point in Fig. 15, whereas the actual (continuous functional representation) value as indicated by the solid line is 0.35. This example shows that  $\sigma_p$  values obtained from burning rate measurements at

elevated temperatures using a finite difference calculation are higher than the actual values based on a continuous functional representation for propellants with this type of  $\sigma_p(T_o)$  dependence. The higher  $T_o$  is above ambient, the larger the inferred  $\sigma_p$  (finite difference) value will be. The finite difference calculation is not necessarily inappropriate; when the reverse procedure is used to estimate the effect of elevated  $T_o$  on burning rate, the correct estimate will result if the same  $T_o$  interval is used in a finite difference calculation (*i.e.*,  $(0.75)(0.0054)(400-300) + 0.75 = 1.16$ , the correct burning rate at 400 K). But for the purpose of comparing with model predictions the continuous variation of  $\sigma_p(T_o)$  should be recognized, which suggests the values reported by Ibiricu and Williams are more appropriate. This may also explain why the most commonly reported values of temperature sensitivity for double base propellant are in the range of 0.5 to 0.6 %/K, because NC/NG temperature sensitivity is an increasing function of temperature.

The error bars in Figs. 13 and 14 are a reflection of the uncertainty with which a given quantity can be measured for a given propellant (5% for  $n$ , 30% for  $\sigma_p$ ). They do not indicate the range of variation for different propellants, which might be larger depending on the energy (heat of explosion) of the propellant; nor do they represent the range of reported values for propellants of supposedly similar compositions. As noted above, the method of determining  $\sigma_p$  from measurements can introduce significant variation. Radiative flux can also have an effect on  $\sigma_p$  which means the environment (motor vs. strand) can have a large influence as has been observed.

### 3.2.1.5. NC/NG Properties

Some comments are in order about the assumed Table 2 property values in relation to values reported in the literature. The assumed  $Q_c$  value (40 cal/g) is somewhat smaller than Zenin's reported results [23]. This is based on the observation for similar measurements in HMX that the thermocouple technique seems to introduce a systematic, pressure-dependent error in the gas temperature profile, which underestimates  $q_c$  and overestimates  $Q_c$  at high pressures. Some degree of variation in  $Q_{c,g}$  and radiative heat feedback,  $q_r$ , with pressure undoubtedly exists and can be included if model fine tuning is desired. However, there is justification for ignoring, in the first approximation, the pressure dependence of these terms relative to  $q_c$ , the conductive heat feedback from the gas phase, due to the strong pressure dependence of the gas reaction kinetics. In order to focus on the major flame structure effects (*e.g.*, gas phase reaction temperature

sensitivity,  $E_g$ ), variations in  $q_r$  (radiation) and  $Q_{c,g}$  with pressure can be ignored. The solid thermal diffusivity ( $0.0008 \text{ cm}^2/\text{s}$ ) is slightly smaller than values commonly used in the past ( $0.0012 \text{ cm}^2/\text{s}$ ). Recent measurements of N5 propellant by Parr and Hanson-Parr [26] indicate a value of  $0.0012 \text{ cm}^2/\text{s}$  at room temperature, decreasing to  $0.0010$  at  $100 \text{ deg C}$ . Thus there is some justification for extrapolating to  $0.0008$  since the average heated layer temperature  $0.5(T_o + T_s)$  is about  $200 \text{ deg C}$ .

### 3.2.2. HMX

HMX, shown in Fig. 16, is considered next. Under normal conditions the extended dark zone (two-stage gas flame structure) evident in NC/NG is not as readily apparent with HMX. Hence for many conditions, HMX can be treated as a single-stage decomposition zone followed by a single-stage gas flame going to the final equilibrium products. Relevant property estimates for simulating HMX using the simplified kinetics model are given in Table 2. Gas thermal radiation accounts for the assumed value of  $q_r$ . The value of  $E_c$  ( $42 \text{ kcal/mol}$ ) is close to the estimated bond strength of the  $\text{N-NO}_2$  bond (see Fig. 16), rupture of which is thought to initiate decomposition. The prefactors  $A_c$  and  $B_g$  were determined by matching  $r_b$  ( $0.38 \text{ cm/s}$ ) and  $T_s$  ( $733 \text{ K}$ ) at  $20 \text{ atm}$  and  $298 \text{ K}$ . Comparisons of the model results and some experimental observations follow.

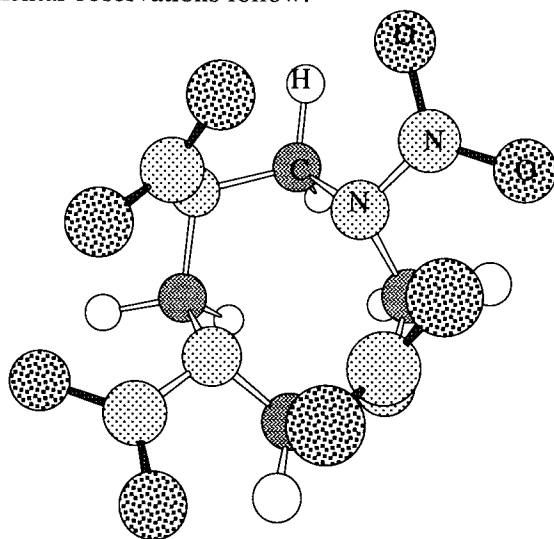


Fig. 16 HMX ( $\text{CH}_2\text{N}_2\text{O}_2$ )<sub>4</sub>

Table 2

Material Properties and Combustion Parameters for NC/NG Double-Base Propellant-N ( $P < 100$  atm) and HMX

	NC/NG		HMX	
	$\tilde{E}_g \ll 1$	$\tilde{E}_g \gg 1$	$\tilde{E}_g \ll 1$	$\tilde{E}_g \gg 1$
$P$ , atm	50	50	70	70
$q_n$ , cal/cm <sup>2</sup> -s	20	20	4.8	4.8
$T_o$ , K	300	300	298	298
<b>Condensed phase parameters</b>				
$\rho_c$ , g/cm <sup>3</sup>	1.55	1.55	1.8	1.8
$C$ , cal/g-K	0.35	0.35	0.335	0.335
$\alpha_c$ , cm <sup>2</sup> /s	8e-4	8e-4	7.9e-4	7.9e-4
$E_c$ , kcal/mol	40	40	42	42
$A_c$ , s <sup>-1</sup>	1e17	1e17	9e15	9e15
$Q_c$ , cal/g	40	40	60	60
$K_a$ , cm <sup>-1</sup>	50	50	5670	5670
<b>Gas phase parameters</b>				
$k_g$ , cal/cm-s-K	2e-4	2e-4	1.67e-4	1.67e-4
$E_g$ , kcal/mol	0	40	0	40
$B_g$ , cal <sup>2</sup> /atm <sup>2</sup> -g-s-K <sup>2</sup> -cm <sup>3</sup>	2.00e-3	1.88e5	2.22e-3	4.20e2
$B_g P^2 W^2 / R^2 \rho_g^*$ 1/s	5.47e4	7.12e12	1.39e5	4.08e10
$Q_g$ , cal/g	363	363	758	758
$T_f$ , K	1500	1500	2750	2750
$W$ , g/mol	24	24	24	24
<b>Results</b>				
$T_s$ , K	668	668	793	800
$r_b$ , cm/s	0.75	0.75	1.15	1.29
$x_g$ , $\mu$ m	20	8	15	4
$\sigma_p$ , K <sup>-1</sup>	2.9e-3	4.5e-3	2.0e-3	2.0e-3
$q_c$ , cal/cm <sup>2</sup> -s	84	84	215	246
$v$ , $n$	0.74	0.78	0.88	0.99
$k$	1.07	1.66	0.99	1.02
$r$	0.058	0.137	0.046	0.050
$\delta$	-0.063	-0.067	-0.065	-0.073
$n_s$	-1.1	-0.49	-1.4	-1.5

\*based on  $0.5(T_s + T_f)$  for  $\tilde{E}_g \ll 1$  and  $T_f$  for  $\tilde{E}_g \gg 1$

### 3.2.2.1. Temperature profile

Figure 17 shows calculated temperature profiles at 1, 10, and 70 atm. At the surface,  $dT/dx$  is nearly the same for both models due to the regression rates being

nearly the same. As pressure increases, the response of the second-order gas kinetics causes the temperature profile to shift toward the surface. Zenin [27] has recently reported microthermocouple measurements for HMX at 1, 5, 20 and 70 atm. These data show the same qualitative behavior as the  $\tilde{E}_g \ll 1$  model, *i.e.*, concave down temperature profile. Zenin's 5 and 20 atm data are re-plotted in Fig. 17. The 5 atm Zenin data lie nearly on top of the 10 atm WSB model curve. By assuming that 10 atm measurements would fall halfway between the 5 and 20 atm data, it can be seen that the  $\tilde{E}_g \ll 1$  model at 10 atm underpredicts the thermocouple measurements somewhat, but is closer qualitatively and quantitatively than the  $\tilde{E}_g \gg 1$  model. The 70 atm  $\tilde{E}_g \ll 1$  profile rises faster than Zenin's (not plotted) but this may be partly due to thermocouple lag error which becomes more pronounced as pressure (regression rate) increases. Microthermocouple measurements in HMX have also been reported by Parr and Hanson-Parr [28] at 1 atm with laser-augmentation. These data appear similar to Zenin's except for a more pronounced initial concave-up curvature, which may be associated with a melt layer plateau or an effect of the laser augmentation used.

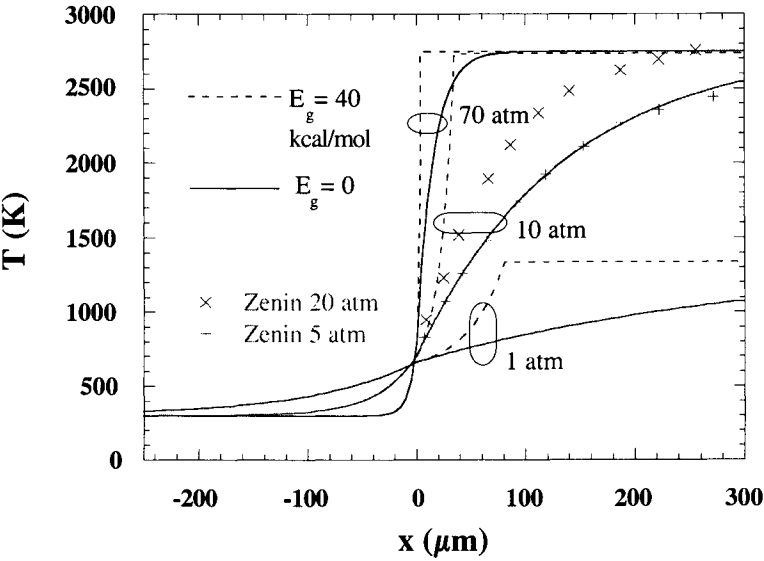


Fig. 17 Temperature profile for HMX. Experimental data from Zenin [27]. Model predictions based on parameters in Table 2.

With laser augmentation at 1 atm, HMX will exhibit a dark zone temperature plateau similar to NC/NG at 1300 to 1500 K. In this case, the single-step gas reaction can be applied to the primary flame; the secondary flame will have no appreciable effect on steady burning rate, as in NC/NG. If it is desired to simulate the secondary flame, a more complex kinetic mechanism (at least two-step) must be considered. Complex chemical kinetics models have shown the ability to simulate the two-stage gas flame structure of RDX under laser irradiation. (However, complex chemistry models still have difficulty in predicting the correct temperature sensitivity of HMX, as noted below.)

### 3.2.2.2. Burning rate and temperature sensitivity

Figure 18 shows steady burning rate for HMX as a function of pressure for six initial temperatures, ranging from 198 K to 423 K [29,30,31]. The data above and below 298 K have a multiplier applied as shown to separate the data and make

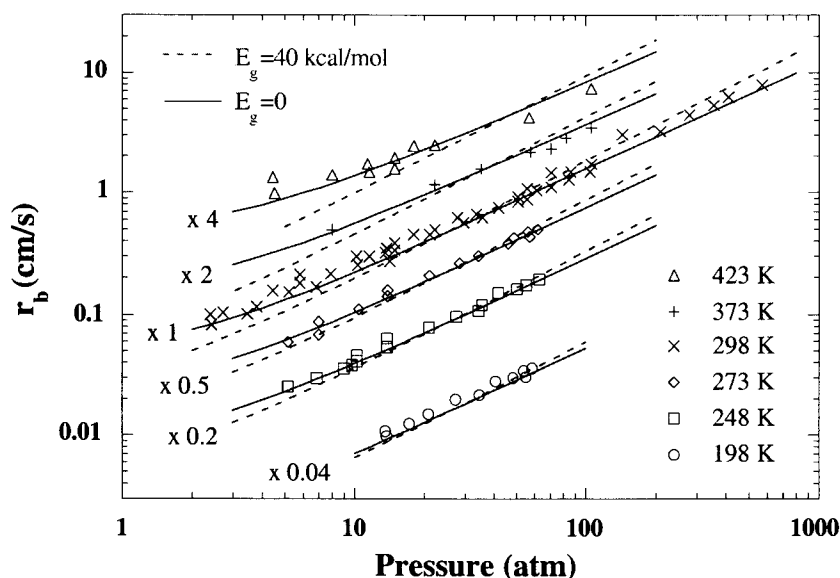


Fig. 18 Burning rate for HMX. Experimental data from Boggs, *et al.* [29]; Boggs [31]; Parr, *et al.* [30].



comparison with models easier. Large  $E_g$  overpredicts the pressure exponent; small  $E_g$ , however, predicts the correct pressure exponent. The 423 K data also show that large  $E_g$  underpredicts burn rate at low pressures and high temperatures. This shortcoming manifests itself in the temperature sensitivity, which is plotted in Fig. 19. The experimental data of Fig. 19 have been obtained from the Boggs-Parr data of Fig. 18 by curve fitting and analytically differentiating. This amplifies any error that may have existed in the original data. Nevertheless clear trends are evident showing that  $\sigma_p$  increases with temperature and decreases with pressure. These same observed trends are predicted by small  $E_g$  whereas large  $E_g$  predicts  $\sigma_p$  is relatively independent of both pressure and temperature. To put Fig. 19 in perspective, it is important to realize that currently comprehensive HMX combustion models with hundreds of reactions cannot yet predict the experimentally observed trends of  $\sigma_p(T_o, P)$ .

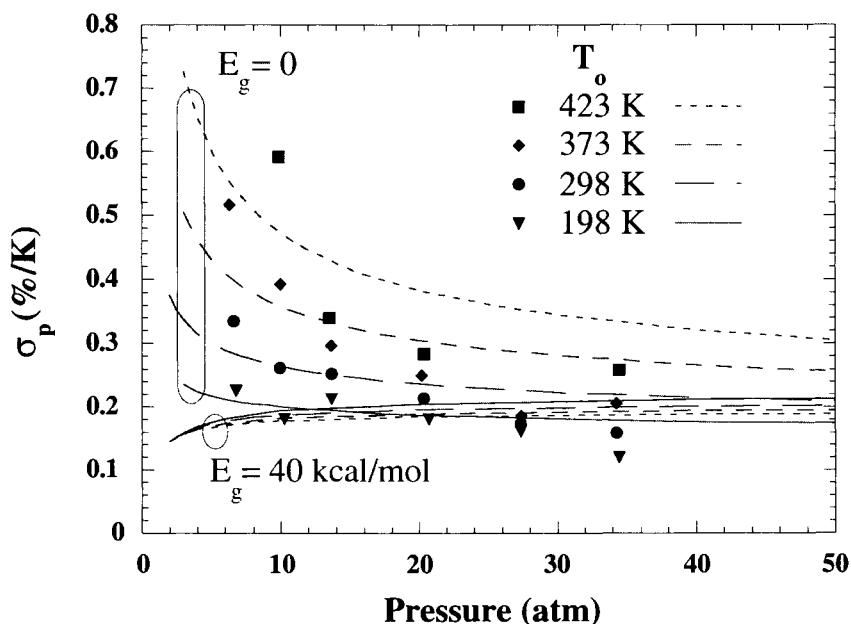


Fig. 19 Burning rate temperature sensitivity for HMX. Experimental data from Boggs, *et al.* [29]; Boggs [31]; Parr, *et al.* [30].

### 3.3. Summary of Steady-State Results

Simplified kinetics combustion modeling can lead to significant understanding of combustion mechanisms in homogeneous propellants, both in terms of estimates of global parameters from comparison with measurements and in terms of sensitivity analysis. Insight developed from simplified modeling includes estimates of the partitioning of heat release between condensed- and gas-phase regions, estimates of reaction-rate temperature sensitivity of condensed- and gas-phase reaction zones, and sensitivity of regression rate to condensed- and gas-phase chemical kinetic and transport processes. Still there is a need for detailed chemical kinetics combustion modeling. Although detailed chemistry models currently fall short in predicting some burning-rate sensitivity parameters, this is due to temporary lack of information; ultimately a more detailed approach should provide the more accurate description necessary to simulate complex phenomena such as ignition and multiple stage flame structure.

## 4. QUASI-STEADY THEORY OF UNSTEADY COMBUSTION

For describing unsteady combustion, the classical theory of quasi-steady (QS) combustion of homogeneous energetic materials can be applied using the steady-state models outlined above, within certain limitations on frequency or time-constant of imposed changes. The QS theory is based on the assumption of quasi-steady behavior (unsteady terms vanish,  $\partial()/\partial t \rightarrow 0$ ) in *both* the gas phase and the condensed-phase reaction zone. In the U.S. and Europe this theory (also called QSHOD for quasi-steady, homogeneous, one-dimensional) was developed in the context of the flame modeling (FM) approach whereas in the former Soviet Union the phenomenological Zeldovich-Novozhilov (ZN) approach was used. The two approaches are essentially equivalent. Within this common framework, thermal relaxation in the inert condensed phase, with time scale  $t_c$ , is the only non-quasi-steady process. The condensed-phase reaction layer and the gas phase region are considered to respond instantly to changing external conditions. This formulation implicitly assumes that condensed-phase reactions are confined to a thin region near the surface of the condensed phase (i.e., surface reaction) which is justified only if two conditions are met. First, the effective activation energy of the condensed-phase decomposition must be large enough that a relatively thick inert convective-diffusive zone develops, followed by a thin reactive-diffusive zone

( $E_c/RT \gg 1$ ;  $x_c = \alpha_c/r_b \gg x_R = x_c/(E_c/2RT_s)$ ). Typical values of  $E_c/2RT_s$  for energetic materials are 5 to 15. For steady burning, even the smallest realistic values ( $\sim 5$ ) are large enough that AEA formulas (leading term only) such as Eq. (15) are accurate to within a few percent. This does not guarantee similar accuracy for oscillatory burning, however, which depends on the frequency of the imposed perturbation. Therefore, the second necessary condition is that the frequency of the perturbation be less than the characteristic frequency of the reaction layer ( $f \ll f_R$ ). It is to be expected that at some sufficiently large frequency, the QS model will fail by virtue of non-QS (*i.e.*, distributed) reaction effects in the condensed phase, if not by some other mechanism.

#### 4.1. Non-Linear Formulation

Consistent with steady-state solution discussed earlier, we will consider the surface reaction (QS) approximation for unsteady behavior. Accordingly, the chemical heat release term is removed from the energy differential equation and placed in the surface boundary condition and a fraction of the absorbed radiant flux ( $1-f_r$ ) is deposited in the surface layer:

$$\text{energy: } \rho_c C \frac{\partial T}{\partial t} + mC \frac{\partial T}{\partial x} = k_c \frac{\partial^2 T}{\partial x^2} + q_r K_a \exp(K_a x); \left. \frac{\partial T}{\partial x} \right|_{0^-, t} = f_s(t), T(-\infty, t) = T_o \quad (74)$$

$$\text{where } f_s = \frac{1}{k_c} ((1-f_r)q_r + q_c + mQ_c); q_c = k_g \left. \frac{\partial T}{\partial x} \right|_{0^+}. \quad (75)$$

The Zeldovich-Novozhilov (ZN) method provides a convenient alternative for representing the conductive heat feedback from the quasi-steady gas phase as opposed to solving the quasi-steady gas phase differential equations. The method consists of using the steady burning laws and integral energy equations to transform the steady burning laws to a form that is valid for unsteady burning. The steady burning laws can be represented functionally as

$$\bar{m} = \bar{m}(T_o, \bar{P}, \bar{q}_r) \quad (76)$$

$$\bar{T}_s = \bar{T}_s(T_o, \bar{P}, \bar{q}_r) \quad (77)$$

where the indicated functionalities can be either in the form of analytic flame modeling equations (FM approach) or empirical data (ZN approach). (An overbar represents time-independent or time-mean conditions.) Using the steady integral energy equation

$$\bar{f}_s = \frac{\bar{r}_b}{\alpha_c} (\bar{T}_s - T_o) - \frac{f_r \bar{q}_r}{k_c} \quad (78)$$

the steady burning laws can be transformed to eliminate  $T_o$  in favor of  $\bar{f}_s$ :

$$\bar{m} = \bar{m}(\bar{f}_s, \bar{P}, \bar{q}_r) \quad (79)$$

$$\bar{T}_s = \bar{T}_s(\bar{f}_s, \bar{P}, \bar{q}_r). \quad (80)$$

These functional relationships have been shown to be valid on a time-dependent basis [32] under the quasi-steady assumption, giving,

$$m = m(f_s, P, q_r) \quad (81)$$

$$T_s = T_s(f_s, P, q_r). \quad (82)$$

Using the time-dependent integral energy equation for surface reaction

$$f_s = \frac{r_b}{\alpha_c} \left( T_s - \left[ T_o - \frac{1}{r_b} \frac{\partial}{\partial t} \int_{-\infty}^0 T dx \right] \right) - \frac{f_r q_r}{k_c} \quad (83)$$

an apparent initial temperature  $T_{oa}$  can be defined to include the unsteady energy accumulation in the condensed phase region

$$T_{oa} = T_o - \frac{1}{r_b} \frac{\partial}{\partial t} \int_{-\infty}^0 T dx \quad (84)$$

$$f_s = \frac{r_b}{\alpha_c} (T_s - T_{oa}) - \frac{f_r q_r}{k_c} \quad (85)$$

and the unsteady burning laws can be written as

$$m = m(T_{oa}, P, q_r) \quad (86)$$

$$T_s = T_s(T_{oa}, P, q_r). \quad (87)$$

These final relations, which are obtained either from a steady model (FM) or steady-state  $r_b$  and  $T_s$  measurements (ZN), when combined with the unsteady differential energy equation above allow solution of the unsteady temperature field in the condensed phase  $T(x, t)$  and the unsteady burning-rate eigenvalue  $m(t)$  for a prescribed unsteady  $P(t)$  or  $q_r(t)$ . This solution can be numerical, in which case nonlinear behavior can be simulated, or, in the case of small amplitude linear behavior, analytic representation is possible. The linear analytic solution is more commonly reported; nonlinear simulations have not been reported much outside of the Russian literature.

#### 4.2 Linear Formulation

In the linear approximation, an analytical solution of the QS problem can be obtained. Linearization means that the amplitude of the disturbance ( $P$  or  $q_r$ ) is small enough that the corresponding burning mass flux output it produces is small enough in amplitude relative to the mean mass flux that nonlinear terms are negligible; the consequence of this condition is that the output is linearly proportional to the input. Consider the case of oscillatory burning and, more specifically, the burning response to a harmonic input. The input is a sine wave with circular frequency  $\omega$  ( $= 2\pi f$ ) and amplitude  $\Delta P$  or  $\Delta q_r$ .

$$P(t) = \bar{P} + P'(t) = \bar{P} + \Delta P \exp(i\omega t) \quad \text{or} \quad q_r(t) = \bar{q}_r + q'_r(t) = \bar{q}_r + \Delta q_r \exp(i\omega t) \quad (88)$$

For a linear response, the corresponding mass flux response and temperature field will also be harmonic at the same frequency

$$m(t) = \bar{m} + m'(t) = \bar{m} + \Delta m \exp(i(\omega t + \phi)) \quad (89)$$

$$T(x, t) = \bar{T}(x) + T'(x, t) = \bar{T}(x) + \Delta T(x) \exp(i(\omega t + \varphi(x))). \quad (90)$$

where  $\Delta m$  is the amplitude of the mass flux response output and  $\phi$  is the phase between the output and input (lead  $\phi > 0$ , lag  $\phi < 0$ ). In the linear approximation,  $\Delta m \ll \bar{m}$  and  $\Delta T \ll \bar{T}$  such that nonlinear terms such as  $m' \partial T' / \partial x$  are negligible. This allows analytic solutions to be obtained, which can be represented in terms of frequency response function defined as

$$R_p = (m'/\bar{m})/(P'/\bar{P}) \quad \text{or} \quad R_q = (m'/\bar{m})/(q'_r/\bar{q}_r) \quad (91)$$

where the response function is independent of the input amplitude.

The QS frequency response functions for pressure-perturbed burning (constant radiant flux) and radiation-perturbed burning (constant pressure) have been obtained as

$$R_p = \frac{\nu + \delta(\lambda - 1)}{\lambda r + k/\lambda - (r + k) + 1 - \frac{k f_r J(\lambda - 1)}{\lambda(\beta + \lambda - 1)}} = \frac{nAB + n_s(\lambda - 1)}{\lambda + A/\lambda - (1 + A) + AB - \frac{A f_r J(\lambda - 1)}{\lambda(\beta + \lambda - 1)}} \quad (92)$$

$$R_q = \frac{\nu_q + \delta_q(\lambda - 1) - \frac{k f_r J(\lambda - 1)}{\beta + \lambda - 1}}{\lambda r + k/\lambda - (r + k) + 1 - \frac{k f_r J(\lambda - 1)}{\lambda(\beta + \lambda - 1)}} = \frac{\nu_q AB + n_q(\lambda - 1) - \frac{A f_r J(\lambda - 1)}{\beta + \lambda - 1}}{\lambda + A/\lambda - (1 + A) + AB - \frac{A f_r J(\lambda - 1)}{\lambda(\beta + \lambda - 1)}} \quad (93)$$

Equations (92) and (93) assume  $f_r$  (the surface reaction layer transmissivity) is a constant parameter. The steady-state sensitivity parameters,  $k$ ,  $r$ ,  $\nu$ ,  $\delta$ ,  $\nu_q$ , and  $\delta_q$  are obtained from the steady solutions discussed previously (FM) or steady-state measurements (ZN). The latter form ( $A$ ,  $B$ ,  $n$ ,  $n_s$ ) was derived under the FM formalism developed in the U.S. and Europe [20,33] while the former ( $k$ ,  $r$ ,  $\nu$ ,  $\delta$ ) was derived under the ZN approach in Russia [32]. Both approaches were recognized as being similar several years ago in terms of underlying assumptions. The complete mathematical equivalence of the ZN and FM approaches at a term-by-term level ( $A = k/r$ ,  $B = 1/k$ ,  $n = \nu$ ,  $n_s = \delta/r$ , or  $n_q = \delta_q/r$ ), including the Jacobian parameters ( $n_s = \delta/r$ ,  $n_q = \delta_q/r$ ), was demonstrated in 1993 [21,22]. Before 1993, the equivalence of the  $n_s$  parameter appearing in the *ad hoc* FM Arrhenius surface pyrolysis relation

$$\bar{r}_b = A_s \bar{P}^{n_s} \bar{q}_r^{n_q} \exp(-E_s/RT_s) \quad (94)$$

and the ZN Jacobian parameter  $\delta$  had apparently not been recognized due to a subtle difference in linearization. Furthermore, while rigorous results for AEA-decomposition (*e.g.*, Eq. (16)) had been available for many years, they apparently have not been applied to unsteady combustion of solids until recently. Instead, Eq. (94) has been almost universally assumed in FM studies, usually with  $n_s = 0$  and  $n_q = 0$ . However, recent results for double base propellants have shown that the simple but formally derived AEA formula based on single-step, zero-order decomposition Eq. (16) with its negative pressure Jacobian parameter,  $n_s < 0$ , is superior to the constant coefficient surface pyrolysis formula ( $n_s = n_q = 0$ ) for describing oscillatory burning. This has renewed interest in applying Eq. (94) with a negative pressure Jacobian parameter,  $n_s < 0$  [34], now that such values appear to be formally justified.

## 5. RESULTS FOR QUASI-STEADY, OSCILLATORY COMBUSTION

Results for oscillatory combustion assuming quasi-steady gas and condensed phase reaction zone (surface reaction approximation) are presented in two groups. First, general characteristics of oscillatory combustion are discussed in the context of the non-dimensional formulation, similar to the steady-state benchmark problem of Table 1. Second, specific results for the common materials NC/NG and HMX are presented.

### 5.1. Parametric (Non-Dimensional) Results for Benchmark Case

The non-dimensional benchmark case ( $\tilde{E}_g \ll 1$ ) in Table 1 is selected for illustrating general behavior and parametric variations. The same parameters as the small- $E_g$  case in Table 1 are used except  $\tilde{Q}_c = 0.07$  instead of 0.1. The following set of dimensional parameters corresponds to this set of non-dimensional parameters, although, obviously, not uniquely so:  $P = 10$  atm,  $T_o = 300$  K,  $T_f = 2300$  K,  $Q_c = 42$  cal/g,  $Q_g = 558$  cal/g,  $C = 0.3$  cal/g-K,  $E_c = 39,740$  kcal/mol,  $A_c = 1e17$  1/s,  $\alpha_c = 8e-4$  cm<sup>2</sup>/s,  $\rho_c = 1.6$  g/cm<sup>3</sup>,  $W = 24$  g/mol,  $k_g = 2e-4$  cal/cm-s-K,

$B_g = 1.66\text{e-}2 \text{ cal}^2/\text{atm}^2\text{-g-s-K}^2\text{-cm}^3$ ,  $r_{br} = 0.02828 \text{ cm/s}$ ,  $r_b = 0.2322 \text{ cm/s}$ ,  $T_s = 617.8 \text{ K}$ .

Figure 20 shows the time-domain burning rate response to a sinusoidal variation in pressure with 1% amplitude. This amplitude is small enough that the linear approximation is reasonably valid, i.e., output is proportional to input.

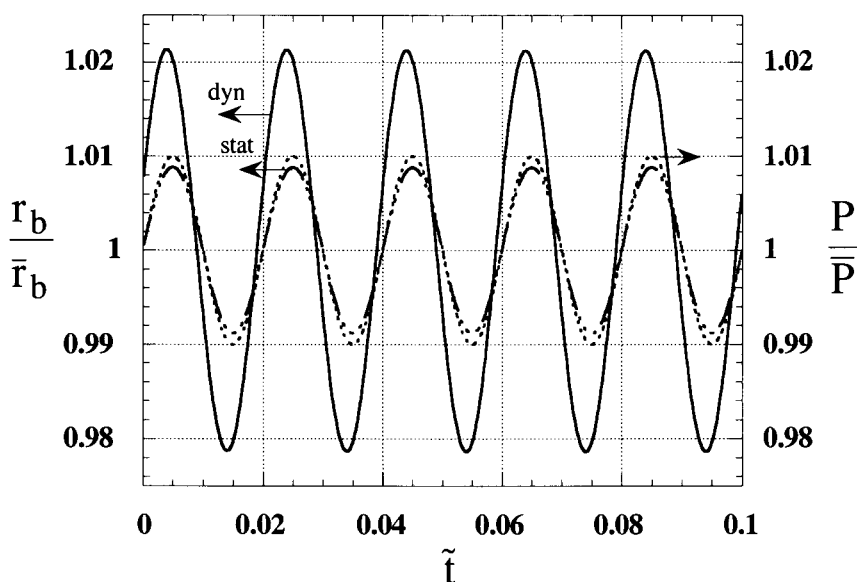


Fig. 20 Small amplitude (linear) burning rate response (dyn) to sine wave variation in pressure with 1% amplitude. Mean input parameters are nominally those of non-dimensional case ( $\tilde{E}_g \ll 1$ ) in Table 1 except  $\tilde{Q}_c = 0.07$  instead of 0.1. Non-dimensional frequency is  $\omega\alpha_c / r_b^2 = 4.66$  or  $\omega\alpha_c / r_{br}^2 = 2\pi(50)$ . The static response (stat) is included to show the result if thermal conduction inertia in the condensed phase were ignored, i.e., if  $r_b = aP^n$  ( $n = 0.883$ ) were applied. Note the correspondence with the response function of Fig. 22. The non-dimensional frequency is to the left of the response peak where the phase is positive (lead). The burning rate response amplitude is 2.1%.



Therefore a sinusoidal pressure input gives a nearly sinusoidal burning rate output. Non-dimensional frequency is  $\omega\alpha_c/r_b^2 = 4.66$  or  $\omega\alpha_c/r_{br}^2 = 2\pi(50)$ . (The dimensional frequency is  $f = 50$  Hz according to the parameter list above which specifies a characteristic time of  $\alpha_c/r_{br}^2 = 1$  s.) The burning rate response at this frequency has an amplitude of 2.1% of the mean burning rate and leads the driving pressure by 18 degrees. The magnitude of the response function is therefore  $|R_p| = (\Delta r_b/\bar{r}_b)(\Delta P/\bar{P}) = 0.021/0.01 = 2.1$ . The fact that burning rate can lead the pressure at relatively low frequencies sometimes seems counterintuitive but this result has in fact been verified by measurements. The reason has to do with the storage of internal energy via thermal conduction in the solid and how the amount of stored energy varies with burning rate. Consider first steady burning conditions at different pressures. There is greater internal energy present in the heated layer

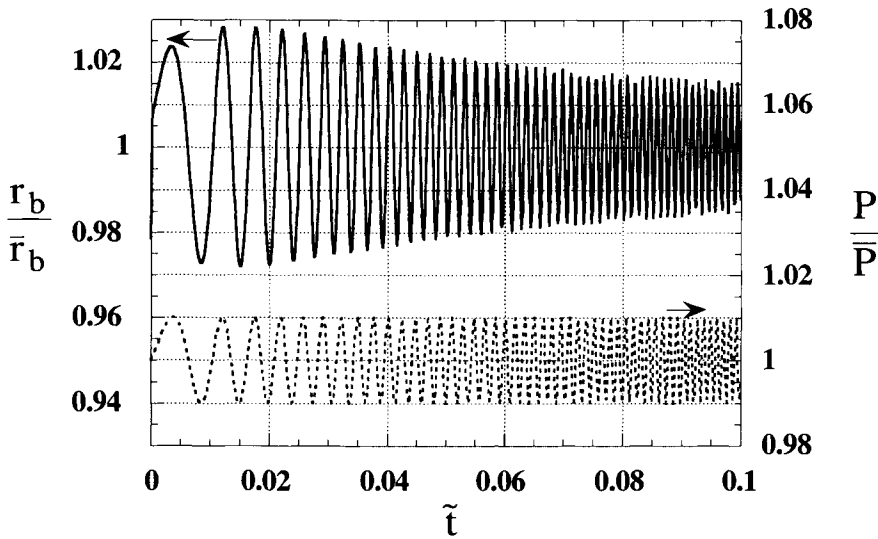


Fig. 21 Small amplitude (linear) burning rate response to sine sweep variation in pressure with 1% amplitude. Mean input parameters are nominally those of non-dimensional case ( $\tilde{E}_g \ll 1$ ) in Table 1 except  $\tilde{Q}_c = 0.07$  instead of 0.1. The initial non-dimensional frequency is slightly to the left (low frequency) side of the peak. Note the correspondence with the response function of Fig. 22: as frequency increases the amplitude of the burning rate response increases and then decreases, while the phase changes from positive (lead) to negative (lag).

of the solid at low pressures and low steady burning rates due to the thicker thermal profile in the solid (bigger  $x_c$ ) established by the convective-diffusive balance (notwithstanding the fact that  $T_s$  is lower at lower burning rates). Under higher pressures,  $T_s$  is higher but the heated zone is thinner such that the deeper layers are cooler and the total internal energy of the solid is lower. Now consider burning under harmonically oscillating pressure. When the frequency is not too large (not greater than the frequency corresponding to time for burn off of the heat layer  $x_c$ ) the decomposing surface reaction zone will respond nearly instantaneously to an increase or decrease in pressure (*i.e.*,  $q_c$ ) to increase or decrease the burning rate by a certain amount. But in addition, the extra surplus or deficit of stored internal energy in the material being convected to the surface will also contribute to either increasing or decreasing the burning rate. During a pressure upswing, the surplus of stored internal energy in the solid augments the burning rate and the result is that the instantaneous burning rate (see "dyn" for dynamic in Fig. 20) is greater than what it would have been if the same instantaneous pressure had been imposed under steady conditions ("stat" for static in Fig. 20). During a pressure downswing, the deficit of stored internal energy diminishes the burning rate below what it would have been if the same instantaneous pressure had been imposed under steady conditions. This translates into a phase lead of burning rate relative to pressure.

Now consider the effect of frequency. As frequency increases from the case considered in Fig. 20, it will eventually reach a value where the period of the pressure oscillation corresponds to the time for burn off of the heated layer. At approximately this frequency, a resonance condition occurs. The burning rate exhibits a maximum amplitude and zero phase, *i.e.*, in-phase with driving pressure. As frequency is increased further, beyond the resonance value, the burning rate amplitude decreases and phase goes negative (lags pressure). This behavior can be seen in Fig. 21, which shows the response of burning rate to a linear sine sweep of frequencies. Initially the frequency is below the resonance value and the burning rate response slightly leads the pressure. As frequency increases, burning rate response amplitude goes through a maximum (where phase is nearly zero) and then decreases. On the high frequency side of the resonance condition, the burning rate response increasingly lags the pressure (negative phase). This behavior can be plotted succinctly in the form of the linear frequency response function as shown in

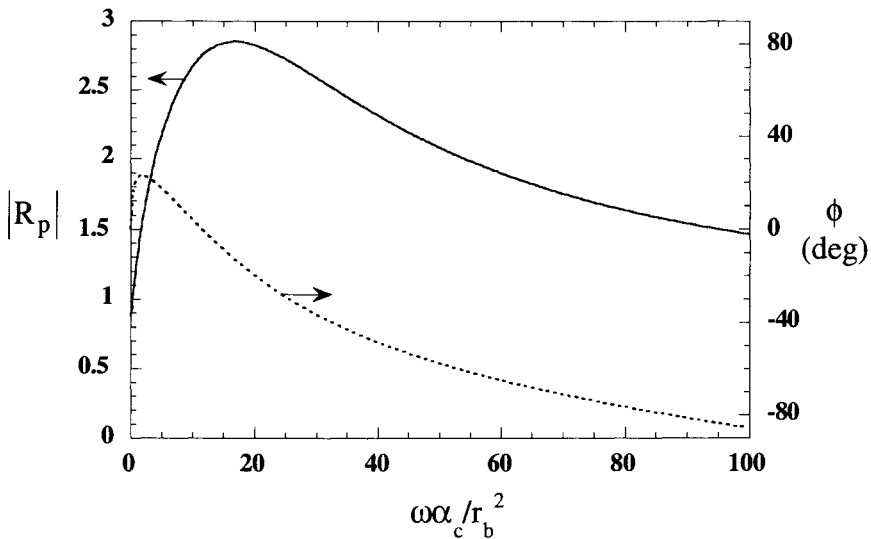


Fig. 22 Linear, pressure-coupled burning rate response function, magnitude and phase. Mean input parameters are nominally those of non-dimensional case ( $\tilde{E}_g < 1$ ) in Table 1 except  $\tilde{Q}_c = 0.07$  instead of 0.1.

Fig. 22 which shows both magnitude and phase of the burning rate response as a function of non-dimensional frequency.

Now consider the effect of amplitude of the oscillating input pressure. Figure 23 shows the time-domain burning-rate response to a sinusoidal variation in pressure with 40% amplitude for the same frequency as Fig. 20. This amplitude is large enough that the linear approximation is not valid, *i.e.*, output is not proportional to input. Therefore even though the driving pressure is sinusoidal, the burning rate response is non-sinusoidal. This is a result of the nonlinear terms such as  $m' \partial T' / \partial x$  becoming non-negligible. The nonlinear result shows that some of the response that would have been converted to output at the same frequency as the input had the response been linear is being instead converted to other frequencies. It is possible to spectrally analyze the output and characterize the response in terms of spectral content. Indeed a frequency-domain response function can still be calculated. However, this response will be different from, and should not be

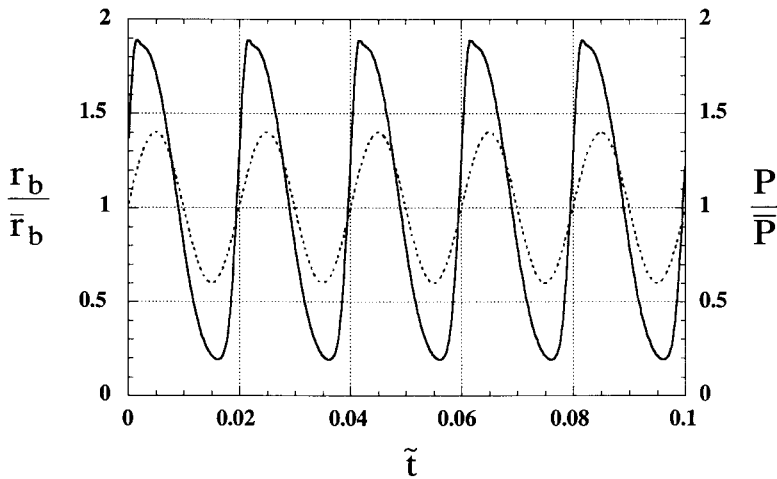


Fig. 23 Large-amplitude (nonlinear) burning rate response to sine wave variation in pressure with 40% amplitude. Mean input parameters are nominally those of non-dimensional case ( $\tilde{E}_g \ll 1$ ) in Table 1 except  $\tilde{Q}_c = 0.07$  instead of 0.1. Non-dimensional frequency is  $\omega\alpha_c/r_b^2 = 4.66$  or  $\omega\alpha_c/r_{b_r}^2 = 2\pi(50)$ . Note the non-sinusoidal, steep-fronted, burning rate output.

confused with, the *linear* response function considered above. For nonlinear behavior, unlike linear behavior, the response is dependent on the amplitude and waveform of the input. That is, for small amplitude, linear behavior, the same response function will be obtained whether the input is pure sinusoidal, sine sweep, or pulsed (in the latter two cases spectral analysis via FFT gives the response function), whereas for large amplitude, nonlinear behavior different waveforms and amplitudes will give different frequency-domain response functions. While simulation of realistic time-dependent rocket chamber internal ballistics requires consideration of nonlinear behavior (not only nonlinear combustion response but nonlinear gas dynamics as well), the linear limit is always a useful starting point and is considered first in assessing the stability of a given system.

The quantity of interest in a first-order, linear internal ballistics stability analysis is the component of the pressure-coupled response function that is in-phase with the pressure, i.e., the real part of  $R_p$ ,  $\text{Re}\{R_p\} = |R_p|\cos\phi$ , because this is the part that feeds acoustic energy into the acoustic field in the chamber. The real part is often simply referred to as the response function, although technically the response function is the complex quantity,  $R_p$ . Figure 24 shows  $\text{Re}\{R_p\}$  for the conditions of Fig. 22 ( $\tilde{Q}_c = 0.07$ ) and also the responses for  $\tilde{Q}_c = 0.09$  and 1.0. The strong effect of condensed phase heat release is quite evident. Temperature sensitivity ( $k$ -parameter) has a strong effect on the response function and the  $k$ -parameter is quite sensitive to  $Q_c$  as shown in Fig. 7. With increased  $Q_c$ ,  $k$  increases and so does the response magnitude (and real part, near resonance). This indicates that measuring dynamic combustion response is an effective way of accurately quantifying  $Q_c$ , which is otherwise quite difficult. It also indicates that condensed-phase chemistry plays a strong role in determining the stability of an energetic material.

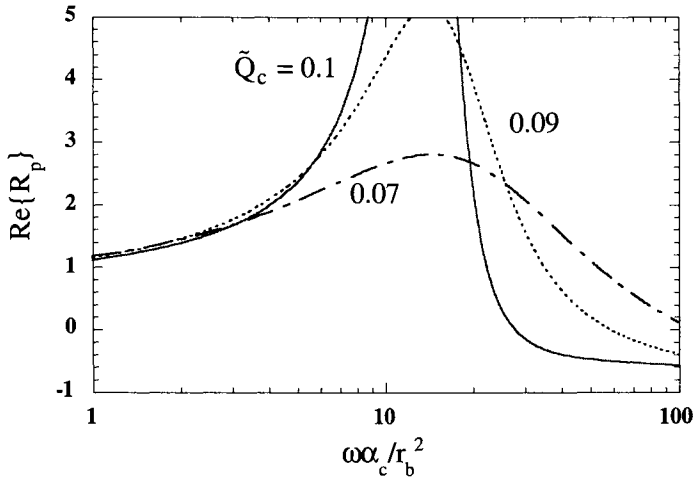


Fig. 24 Linear, pressure-coupled burning rate response function, in-phase (real) component. Mean input parameters are nominally those of non-dimensional case ( $\tilde{E}_g \ll 1$ ) in Table 1.

In passing it is noted that the results presented in Figs. 20 through 23 were calculated using a finite difference numerical code. This is not necessary for the linear response results (Figs. 20, 21, 22 and 24) where the analytic solution could be used; however, as a validation of the numerical solution it is good practice to show that the linear analytic results can be obtained in the limit of small amplitude disturbances.

### 5.2 Results for Common Materials

As a companion to the steady-state results presented above, oscillatory combustion results and model comparisons are also presented for NC/NG and HMX. The model parameters are those given in Table 2. Thus a unified, coherent steady and unsteady theory is considered.

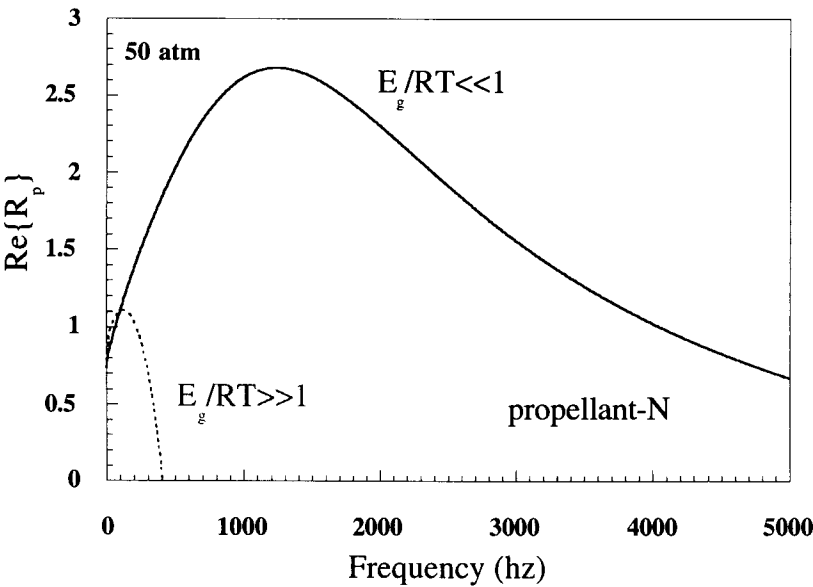


Fig. 25 In-phase component of pressure-coupled response function for propellant-N (50 atm). Shaded region represents T-burner measure-ments Horton and Price [35]; NWC [36]. Model calculations are for quasi-steady model using parameters of Table 2. Condensed-phase reaction zone characteristic frequency is estimated to be  $f_R = 10,000$  Hz; quasi-steady assumption should be valid up to at least 3000 Hz.

### 5.2.1 NC/NG Double Base Propellant

Figure 25 shows the pressure-coupled response function (real component) for propellant-N. Experimental data have been obtained from T-burners [35,36]. These measurements involve a significant degree of uncertainty partly due to assumptions made in reducing the data. The shaded region in Fig. 25 represents the measurements of propellants N4 and JPN from [36] with an uncertainty interval of  $\pm 100\%$  added in order to include the results for JPN reported by Horton and Price which are about a factor of two higher. This large degree of uncertainty tempers any conclusions drawn by comparison with models. Nevertheless, the experimental data are still useful. As can be seen in Fig. 25, the  $\tilde{E}_g \ll 1$  model (Table 2 parameters) falls well within the shaded region up to about 3500 Hz, at which point it is likely that the quasi-steady approximation begins to break down ( $f_R = 10,000$  Hz) by underpredicting phase. The  $\tilde{E}_g \gg 1$  model begins to fall out of the range of measurements at a rather low frequency (about 400 Hz). Clearly, the measured responses are better represented by low- $E_g$  theory and parameters, even with the uncertainty in the experimental data, as the quasi-steady theory should be valid up to at least 3000 Hz for these conditions. The quasi-steady theory assuming low- $E_g$  has also shown good agreement with laser-induced oscillatory combustion data for double-base propellant.

It should be noted that it is difficult to match  $\text{Re}\{R_p\}$  over the appropriate frequency range using realistic parameters unless the full decomposition relation, Eq. (16), and a negative Jacobian parameter,  $n_s < 0$ , are used. If Eq. (69) is used with  $n_s = 0$  (Eq. (17)), agreement is unsatisfactory over the 0 to 3000 Hz interval [37]. This again illustrates that dynamic combustion response measurements are an effective way of accurately quantifying combustion parameters, such as  $n_s$  or  $\delta$ , which are otherwise quite difficult to measure.

### 5.2.2 HMX

Figure 26 shows the pressure-coupled response function (real component) for HMX at two pressures 10 and 70 atm. Experimental data have been obtained from T-burners [38] at 14 and 68 atm. Pipe length and heat loss considerations limited the T-burner measurements to above 300 Hz (for long pipes heat loss limits the accuracy of the analysis used in the data reduction). The peak of the response at 10 atm is predicted to occur between 100 and 200 Hz while at 70 atm the peak is predicted to occur between 3000 and 4000 Hz. Neither set of measurements, 14 or

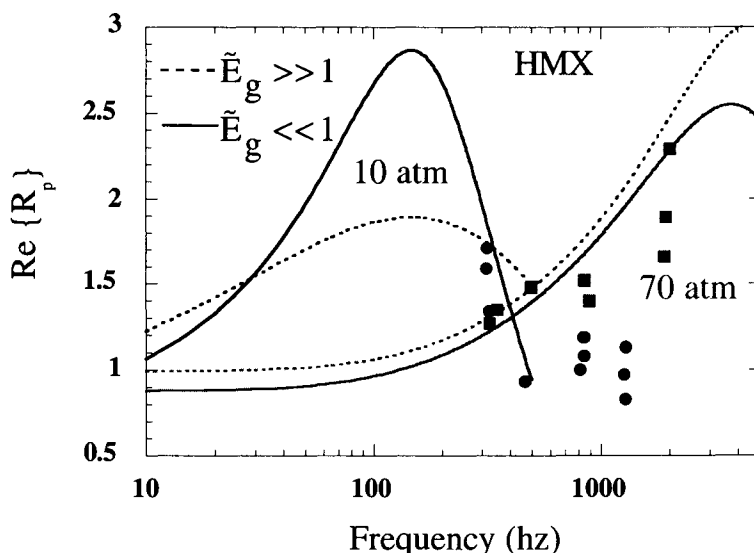


Fig. 26 In-phase component of pressure-coupled response function for HMX. Data points represents T-burner measurements at 14 and 68 atm from Finlinson and Stalnaker [38]. Model calculations are for quasi-steady model using parameters of Table 2 at 10 and 70 atm (predicted before T-burner measurements) Brewster, *et al.* [13]. Condensed-phase reaction zone characteristic frequency is estimated to be  $f_R = 900$  and 22,000 Hz; quasi-steady assumption should be valid up to at least 300 and 5000 Hz.

68 atm, covers the respective frequency range where the peak would be expected to occur. The predicted low-pressure peak is below the 300 Hz T-burner data; and the predicted high-pressure peak is above the 2000 Hz T-burner data. Nevertheless, the experimental data show the appropriate trends and illustrate an important general feature of  $R_p$  data: as pressure increases the response peak frequency increases approximately as  $r_b^2$ , according to the scaling arguments discussed earlier. To reiterate, the peak or resonance condition occurs when the driving disturbance period is approximately the same as (within a factor of two of) the time for burn-off of the heated layer,  $t_c = \alpha_c / r_b^2$ , *i.e.*, when frequency is approximately  $f_c = r_b^2 / \alpha_c$ . For the 10 and 70 atm conditions,  $f_c$  calculated by this



scaling is 60 and 1660 Hz, respectively ( $r_b$  is 0.22 and 1.15 cm/s and  $\alpha_c$  is estimated in Table 2), so the predicted peak frequencies are approximately a factor of two higher than the simple  $f_c$  scaling indicates, but this amount of deviation is not unusual.

As frequency increases above  $f_c$  and begins approaching  $f_R$  (which is greater than  $f_c$  by a factor of the non-dimensional activation energy  $E_c/2RT_s$ ), the quasi-steady approximation begins to break down. The condensed phase reaction zone characteristic frequency is estimated to be  $f_R = 900$  and 22,000 Hz at 10 and 70 atm, respectively; the quasi-steady assumption should be valid up to at least 300 Hz (10 atm) and 5000 Hz (70 atm). Thus for the 10 atm case, only the lowest frequency data (300 to 500 Hz) would be expected to correspond to the quasi-steady theory. It seems to be typical of quasi-steady theory to predict the phase lag to be too large as frequency approaches  $f_R$ . This translates into underprediction of  $\text{Re}\{R_p\}$  which appears to be the case for the low- $E_g$  model at 10 atm for  $f > 500$  Hz. At 70 atm, both models show good agreement with the limited data available, with the low- $E_g$  case slightly better. Additional oscillatory experiments have been conducted with HMX at 1 atm using laser energy to perturb combustion, which show better agreement with the low- $E_g$  model. In fact, the parameters for HMX in Table 2 were developed from the laser-recoil response function experiment and used to predict the pressure-coupled response before the T-burner measurements were actually made [13]. Further and more recent success of this simplified-kinetics approach in predicting pressure response of HMX can be seen in [39].

The degree of agreement in HMX response function is suggestive of a corresponding degree of accuracy in the model's representation of the actual complex combustion process. In particular, it is noteworthy that the decomposition energy barrier, 42 kcal/mole, corresponds to either of two competing initiation processes that might be expected for HMX decomposition, N-NO<sub>2</sub> bond scission and HONO elimination.

## 6. INTRINSIC STABILITY

Apart from the question of linear stability of a coupled burning propellant-gas chamber system, there is the question of linear or intrinsic stability of a burning propellant as an isolated system in a constant pressure environment. The mathematical model presented above exhibits solutions that are intrinsically

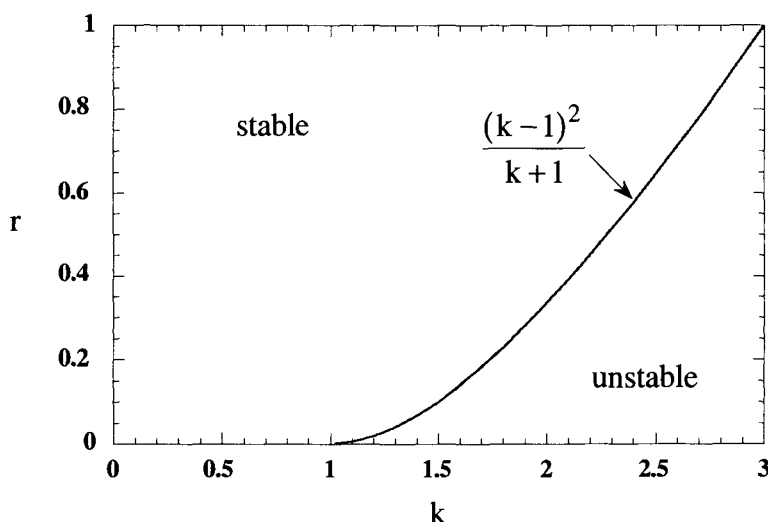


Fig. 27 Intrinsic stability map for homogeneous solid with quasi-steady gas and surface reaction, negligible radiation absorption ( $q_r = 0$ ) or surface absorption of radiation ( $f_r = 0$ ).

unstable for certain values of parameters. In the ZN formulation [32], the relation for intrinsic stability is

$$r > \frac{(k-1)^2}{k+1} \quad (q_r = 0 \text{ or } f_r = 0) \quad (95)$$

and the stable and unstable regimes are shown in Fig. 27. For  $r$ - $k$  parameter combinations in the unstable region, the analytic solution may give a result for steady burning rate but it is an unstable solution; a numerical simulation using the same parameters will diverge. If a numerical simulation of either steady or unsteady burning is diverging, it is advisable to check the  $r$ - $k$  parameters for intrinsic stability. As a case in point, the low- $E_g$  case in Table 1 is in fact linearly unstable. If the non-dimensional condensed phase heat release parameter is reduced from 0.1 to 0.07, the burning propellant becomes linearly stable. Many energetic materials exhibit regimes of unstable or erratic combustion or non-

burning behavior such as at low pressure. For example, HMX does not burn well at 1 atm and lower pressures. This behavior has been attributed to intrinsic instability but the evidence in that regard is still sparse. The anomalous combustion behavior of AP at pressures between 135 and 300 atm has also been attributed to intrinsic instability, again, without conclusive evidence. Because this type of instability has to do with the propellant as an isolated system (no acoustic cavity is necessary), it has also been referred to as non-acoustic instability.

## 7. CONCLUDING REMARKS

Simplified kinetics combustion modeling can lead to significant understanding of combustion mechanisms in homogeneous propellants. Both steady-state and unsteady combustion offer useful information. New understanding comes both in terms of estimates of global parameters from comparison with measurements and in terms of sensitivity analysis. Insight developed from simplified modeling includes estimates of the partitioning of heat release between condensed- and gas-phase reaction zones, and sensitivity of regression rate to condensed- and gas-phase chemical kinetic and transport processes. Still there is a need for detailed chemical kinetics combustion modeling. Although detailed chemistry models currently fall short in predicting some burning rate sensitivity parameters and therefore in predicting unsteady behavior [39], this is due to temporary lack of information; ultimately a more detailed approach should provide the more accurate description necessary to simulate complex phenomena such as ignition and multi-stage flame structure.

## ACKNOWLEDGMENTS

The author would like to acknowledge the financial support of ONR for many years while this work was being conducted and the technical insights of Dr. Guy Lengelle (ONERA), Dr. Steve Son (Los Alamos National Laboratory), and Prof. Atsushi Ishihara (Saitama Institute of Technology).

## NOMENCLATURE

### Dimensional Parameters

$A_c$	= condensed phase reaction rate prefactor
$A_g$	= gas phase reaction rate prefactor ( $= B_g/(R/W)^2$ )
$B_g$	= gas phase reaction rate prefactor
$C$	= specific heat, $C_p$ , or generic product species
$D$	= binary diffusion coefficient in gas phase
$E_c$	= activation energy of condensed phase reaction
$E_s$	= $E_c/2$ (when $n_s = 0$ )
$f$	= frequency (Hz)
$f_{c,R}$	= $1/t_{c,R}$
$K_a$	= radiation absorption coefficient of condensed phase
$k_{c,g}$	= thermal conductivity
$M$	= generic third body species in gas phase reaction
$m$	= mass flux, $\rho_c r_b$
$m'$	= $\Delta m \exp[i(2\pi ft + \phi)]$
$P$	= pressure
$P'$	= $\Delta P \exp[i2\pi ft]$
$q_r$	= absorbed radiant heat flux in condensed phase
$q_c$	= conductive heat flux to surface from gas phase
$q_r'$	= $\Delta q_r \exp[i2\pi ft]$
$Q_{c,g}$	= heat release (positive exothermic)
QS	= quasi-steady gas and condensed phase reaction zone assumption
$R$	= universal gas constant, 1.987 cal/mol-K
$r_b$	= burning rate
$t_{c,R}$	= characteristic times, $x_{c,R}/r_b$
$T_{o,s,f}$	= initial, surface, or final flame temperature
$W$	= molecular weight
$x$	= coordinate normal to surface, positive into gas phase
$x_c$	= solid convective-diffusive length scale, $\alpha_c/r_b$
$x_R$	= condensed phase reaction zone length scale, $x_c/(E_c/2RT_s)$
$x_g$	= gas flame characteristic thickness
$\alpha_{c,g}$	= thermal diffusivity
$\Delta$	= amplitude of fluctuating quantity
$\rho_{c,g}$	= density

$$\sigma_p = k/(T_s - T_o)$$

$$\Omega_{c,g} = \text{reaction rate}$$

### Non-Dimensional Parameters

$$\tilde{A}_c = \rho_c A_c k_c / C m_r^2$$

$$A = (T_s - T_o)(\partial \ln r_b / \partial T_s)_{p,q_r} (=k/r) \text{ or generic reactant species}$$

$$B = 1/[(T_s - T_o)(\partial \ln r_b / \partial T_o)_{p,q_r}] (=1/k) \text{ or generic intermediate species}$$

$$D_g = P^2 k_g A_g / C m_r^2$$

$$\tilde{E}_{c,g} = E_{c,g} / R(T_f - T_o)$$

$$f_r = \exp(-K_a x_R), \text{ fraction of } q_r \text{ absorbed below surface reaction zone}$$

$$J = q_r / m C (T_s - T_o) = \tilde{q}_r / \tilde{m} (\tilde{T}_s - \tilde{T}_o)$$

$$k = (T_s - T_o)(\partial \ln r_b / \partial T_o)_{p,q_r}$$

$$\tilde{K}_a = K_a k_c / m_r C$$

$$Le = k_g / C \rho_g D = \alpha_g / D = 1$$

$$\tilde{m} = m / m_r$$

$$n_q = (\partial \ln r_b / \partial \ln q)_{T_s,p} (= \delta_q / r)$$

$$n_s = (\partial \ln r_b / \partial \ln P)_{T_s,q_r} (= \delta' / r)$$

$$n = (\partial \ln r_b / \partial \ln P)_{T_o,q_r} (=v)$$

$$\tilde{q}_{c,r} = q_{c,r} / m_r C (T_f - T_o)$$

$$\tilde{Q}_{c,g} = Q_{c,g} / C (T_f - T_o)$$

$$R_p = \text{pressure-driven frequency response function}$$

$$= (m'/m)/(P'/P) \text{ at constant } q_r$$

$$R_q = \text{radiation-driven frequency response function}$$

$$= (m'/m)/(q_r'/q_r) \text{ at constant } P$$

$$r = (\partial T_s / \partial T_o)_{p,q_r}$$

$$\tilde{T} = T / (T_f - T_o)$$

$$\tilde{x} = x m_r C / k_{c,g}$$

$$Y = \text{mass fraction of A (condensed) or B (gas)}$$

$$\delta, \delta_q = \text{Jacobian parameters, } v_r - \mu k, \quad v_q r - \mu_q k$$

$$\lambda = 1/2 + (1/2)(1 + 4i\Omega)^{1/2}$$

$$\mu = [1/(T_s - T_o)](\partial T_s / \partial \ln P)_{T_o,q_r}$$

$$\mu_q = [1/(T_s - T_o)](\partial T_s / \partial \ln q_r)_{T_o,p}$$

$$v = (\partial \ln r_b / \partial \ln P)_{T_o,q_r} \text{ (same as } n)$$

$$\nu_q = (\partial \ln r_b / \partial \ln q_r)_{T_o, p}$$

$$\tilde{\Omega}_{c,g} = \Omega_{c,g} k_{c,g} / C m_r^2$$

$\Omega$  = dimensionless frequency:  $2\pi f \alpha_c / r_b^2$

### Subscripts and Superscripts

c = condensed phase, convective-diffusive, or conduction

g = gas phase

r = radiation or reference (mass flux)

R = reaction zone in condensed phase

s = surface

$\bar{\phantom{x}}$  = steady condition or mean value

$\tilde{\phantom{x}}$  = nondimensional quantity

$\hat{\phantom{x}}$  = complex fluctuating quantity

## **REFERENCES**

- [1] A. G. Merzhanov and F. I. Dubovitskii, Proceedings of the USSR Academy of Science 129:1, 153-156 (1959).
- [2] G. Lengelle, AIAA J. 8, 1989-98 (1970).
- [3] M. M. Ibricu and F. A. Williams, Comb. Flame 24, 185-198 (1975).
- [4] S. F. Son and M. Q. Brewster, Comb. Sci. Tech. 107, 127-154 (1995).
- [5] F. A. Williams, AIAA J. 11, 1328-1330 (1973).
- [6] M. J. Ward, S. F. Son, and M. Q. Brewster, Comb. Flame 114, 556-568 (1998a).
- [7] M. J. Ward, S. F. Son, and M. Q. Brewster, Combust. Theory Modeling, 2, 293-312 (1998b).
- [8] F. A. Williams, Combustion Theory, 2nd ed. Addison-Wesley, Reading, MA, 1985.
- [9] M. Q. Brewster, M. J. Ward, and S. F. Son, Combust. Sci. Tech., 154, 1-30 (2000).
- [10] O. K. Rice and R. Ginell, J. Phys. (& Colloid) Chem. 54:885 (1950).
- [11] M. S. Miller, Combust. Flame 46:51 (1982).
- [12] R. G. Parr and B. L. Crawford, Jr., J. Phys. (& Colloid) Chem. 54:929 (1950).
- [13] M. Q. Brewster, M. J. Ward, and S. F. Son, AIAA 97-3333, 33rd J. Prop. Conf., Seattle, WA (1997).
- [14] A. Linan and F. A. Williams, Fundamental Aspects of Combustion. Oxford, 22-27 (1993).
- [15] M. W. Beckstead, AIAA J. 18, 980-985 (1980).
- [16] M. W. Beckstead, 26th JANNAF Combustion Mtg., CPIA Publ. 529, IV:255-268 (1989).

- [17] J. D. Buckmaster and G. S. S. Ludford, *Theory of Laminar Flames*. SIAM, Philadelphia, 58-78 (1982).
- [18] R. W. Hart, R. A. Farrell, and R. H. Cantrell, *Comb. Flame* 10, 367-380 (1966).
- [19] F. E. C. Culick, *Astronautica Acta* 13, 221-237 (1967).
- [20] F. E. C. Culick, *AIAA J.* 6, 2241-2255 (1968).
- [21] S. F. Son and M. Q. Brewster, *J. Prop. Power* 9, 222-232 (1993).
- [22] M. Q. Brewster and S. F. Son, *Comb. Flame* 103, 11-26 (1995).
- [23] A. A. Zenin, in *Prog. in Astro. and Aero.*, L. De Luca, E. W. Price and M. Summerfield, (eds.), AIAA, 143, 197-214 (1992).
- [24] M. S. Miller and A. J. Kotlar, 23rd JANNAF Comb. Mtg., CPIA Publ. 457, II:213-223 (1986).
- [25] G. Lengelle, A. Bizot, J. Duterque, and J. F. Trubert, in *Prog. in Astro. and Aero.*, K. K. Kuo and M. Summerfield, (eds.), AIAA, 90:389-393 (1984).
- [26] T. P. Parr and D. Hanson-Parr, CPIA Publ. 662, III:379-404 (1997).
- [27] A. A. Zenin, A., *J. Prop. Power* 11, 752-758 (1995).
- [28] T. Parr and D. Hanson-Parr, in *Non-Intrusive Combustion Diagnostics*, K. K. Kuo and T. P. Parr (eds.), Begell House Inc., New York, 586 (1994).
- [29] T. L. Boggs, J. L. Eisel, C. F. Price, and D. E. Zurn, 15th JANNAF Combustion Meeting, CPIA Publ. 297, I:241-251 (1979).
- [30] T. P. Parr, T. L. Boggs, C. F. Price, and D. M. Hanson-Parr, 19th JANNAF Combustion Meeting, CPIA, I:281-288 (1982).
- [31] T. L. Boggs, in *Fundamentals of Solid-Propellant Combustion*, K. K. Kuo and M. Summerfield, (eds.), *Prog. in Aero. Astro.*, AIAA, New York, 121-175 (1984).
- [32] B. V. Novozhilov, *Nonstationary Combustion of Solid Propellants*. Nauka, Moscow (English translation available from NTIS, AD-767945) (1973).
- [33] M. R. Denison and E. Baum, *ARS J.* 31-1112-1122 (1961).
- [34] L. De Luca, in *Challenges in Propellants and Combustion*, K. K. Kuo, (ed.), Begell House, 493-514 (1997).
- [35] M. D. Horton and E. W. Price, 9<sup>th</sup> Symposium (Int.) on Combustion, The Combustion Institute, 303-310 (1962).
- [36] M. M. Ibricu, "Experimental Studies on the Oscillatory Combustion of Solid Propellants," Naval Weapons Center, China Lake, CA, NWC TP 4393, (1969).
- [37] M. W. Beckstead and W. W. Erikson, 33rd JANNAF Combustion Mtg., CPIA Publ. 653, II:145-157 (1996).
- [38] J. C. Finlinson and R. A. Stalnaker, 34th JANNAF Comb. Mtg., CPIA Publ. 662, II:39-46 (1997).
- [39] G. N. Kudva and T. A. Litzinger, *J. Prop. Power* 18, 1218-1226 (2002).

## Chapter 9

# Modeling of Nitramine Propellant Combustion and Ignition

Eun. S. Kim, Rongjie Yang, and Vigor Yang\*

\*Department of Mechanical and Nuclear Engineering, The Pennsylvania State University, 104 Research Building East, University Park, PA 16802, United States of America

## NOMENCLATURE

$A$	cross-sectional area of propellant sample
$A_j$	pre-exponential factor of rate constant of $j$ th reaction
$A_{sp}$	specific surface area
$B_j$	temperature exponent in rate constant of $j$ th reaction
$C_i$	molar concentration of $i$ th species
$\dot{C}_{ij}$	rate of change in molar concentration of $i$ th species by $j$ th reaction
$c_{pi}$	constant-pressure heat capacity of $i$ th species
$D_i$	effective mass-diffusion coefficient of $i$ th species
$D_T$	thermal diffusion ratio of $i$ th species
$E_j$	activation energy of $j$ th reaction
$e$	internal energy
$f_g$	fraction of laser energy absorbed by gas phase
$H_{fus}$	molar heat of fusion
$H_{sub}$	molar heat of sublimation
$H_v$	molar heat of evaporation
$h$	enthalpy
$h_i$	enthalpy of $i$ th species
$h_{f,i}^\circ$	heat of formation of $i$ th species at standard condition
$k_j$	rate constant of $j$ th reaction

---

Corresponding Author. Email: [vigor@psu.edu](mailto:vigor@psu.edu)



$\dot{m}''$	mass flux
$N$	total number of species
$N_R$	total number of reactions
$p$	pressure
$p_{v,eq}$	equilibrium vapor pressure of RDX
$\dot{Q}_{laser}''$	external laser heat flux
$\dot{Q}_{rad}''$	volumetric absorption of laser energy
$R_u$	universal gas constant
$s$	sticking coefficient
$T$	temperature
$t$	time
$u$	bulk velocity
$V_{cor}$	correction velocity
$V_i$	diffusion velocity of $i$ th species
$W_i$	molecular weight of $i$ th species
$\dot{w}_i$	mass production rate of $i$ th species
$\dot{w}_{Rj}$	mass production rate of $j$ th reaction
$X_i$	mole fraction of $i$ th species
$x$	spatial coordinate
$Y_i$	mass fraction of $i$ th species

### Greek Symbols

$\beta$	absorption coefficient
$\kappa_i$	absorption cross section of $i$ th species
$\phi$	void fraction
$\rho$	density
$\lambda$	thermal conductivity
$\dot{\omega}$	molar production rate

### Subscripts

0+	gas-phase side of propellant surface
0-	subsurface side of propellant surface
bw	backward reaction
$c$	condensed phase
fw	forward reaction
$g$	gas phase
id	ignition delay
ini	initial condition
$l$	liquid phase

$l \rightarrow g$	from liquid to gas
$m$	melting
net	net value of evaporation rate minus condensation rate
$s$	solid phase
sur	surface
$t$	mass-averaged quantity in two-phase region
$v$	vapor

## 1. INTRODUCTION

Nitramines, including cyclotrimethylenetrinitramine (RDX) and cyclotetramethylenetetranitramine (HMX), are important oxidizer ingredients for solid propellants. These compounds are highly energetic and produce high impetus and specific impulse for gun and rocket propulsion applications. In comparison with ammonium perchlorate (AP), nitramines produce little smoke, toxicity, and corrosion. In order to meet the rising demand for various stringent performance and environmental requirements, the development of advanced energetic materials continues to be of strong interest to the solid-propellant community. Recently, attention has also been given to nitramine compounds with azide-containing energetic binder ingredients, such as glycidyl azide polymer (GAP), 3,3-bis(azidomethyl)oxetane (BAMO), and 3-azidomethyl-3-methyloxetane (AMMO), due to the unique characters of azide polymers. These highly energetic polymers have positive heats of formation but produce relatively low-temperature flames. Experimental and theoretical investigations of the complex processes involved in the combustion and ignition of nitramine monopropellants as well as nitramine/azide propellants have been a subject of extensive research.

In the past decade, a great deal of experimental diagnostic and analytical modeling efforts have been applied to obtain more accurate and reliable data for the thermal decomposition, thermophysical properties, and flame structures of these propellants [1-24]. Significant advancements have been made in the modeling of combustion and ignition of nitramine and nitramine/GAP propellants [25-41]. The work involved the treatment of self-sustained and laser-assisted combustion [25-39], as well as ignition transients [39,40], with detailed chemical kinetics and variable thermophysical properties. The results have provided direct insight into the underlying mechanisms dictating the entire combustion and ignition processes. The effects of propellant compositions and ambient conditions on burning characteristics and combustion wave structures were examined in detail.

This chapter is organized as follows. A short summary of various modeling efforts conducted in the past on nitramine and nitramine-composite propellant

combustion and ignition is first given. The state-of-the-art approaches recently developed in this subject area are then described along with a brief discussion of the numerical techniques. Finally, results of these modeling studies are summarized.

### 1.1. Modeling Development of Steady-State Combustion of Nitramine Propellants

The molecular structures of RDX, HMX, and GAP are shown in Fig. 1. Most of early theoretical analyses of steady-state combustion of nitramine propellants were based on global reaction schemes for gas-phase processes [42]. The first comprehensive model of RDX combustion, accommodating 23 species and 49 reactions in the gas phase, was initiated by Ermolin et al. [43]. The propellant surface conditions, however, were treated as input parameters in order to match experimentally measured species-concentration profiles. A substantial improvement was made by Melius [25] to relax this constraint. His formulation simultaneously took into account the thermal decomposition of RDX and the ensuing chemical reactions to an extent that the key heat-release mechanisms could be identified. Yetter et al. [26] refined Melius' model to include the sub-models of reactions among the major intermediate products such as  $\text{CH}_2\text{O}$ ,  $\text{NO}_2$ ,  $\text{N}_2\text{O}$ ,  $\text{H}_2$ ,  $\text{HCN}$ , and  $\text{NO}$ , but a significant amount of uncertainties still existed about the pathways of the reduction and associated rates of large fragments departing from the burning surface of these cyclic nitramines. By considering global reactions, Margolis, Williams, Li, and co-workers [27-29] developed an analytical approach, which included the presence of gas bubbles and liquid droplets in the two-phase region near the propellant surface by means of methods of matched asymptotic expansion. The model, however, provided limited information concerning the chemical processes. Prasad et al. also studied self-sustained and laser-assisted

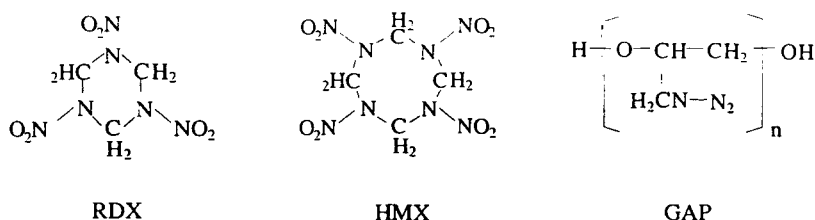


Fig. 1 Molecular structures of RDX, HMX, and GAP.

combustion of RDX and HMX [30,31]. Their model differed from the ones described in Refs. 25-29 in that bubble formation within the liquid layer was neglected. In general, these models of RDX and HMX combustion predicted burning rate, surface temperature, and melt-layer thickness reasonably accurately, although some disagreements with experimental data in the near-surface species profiles and the temperature sensitivity of propellant burning rate were noted. Recognizing the important role of the condensed phase, Liao and Yang developed a detailed model of RDX combustion accounting for the foam layer, which is the region between the gas and solid phases [33,34]. Such a foam layer consisted of two phases: liquefied RDX and bubbles containing gaseous RDX and its decomposition products. Davidson and Beckstead [35] further studied the near-surface temperature distribution and pressure sensitivity of burning rate. The similar approach was later extended to study the combustion behavior of HMX [36].

Studies on the physical properties, sublimation, decomposition, ignition, and self-deflagration of nitramine propellants conducted prior to 1984 are summarized by Boggs [44] and Fifer [45], and the state of understanding of steady-state combustion of nitramine propellants up to 1990 is given by Alexander et al. [46]. A summary of the latest development is covered in a volume edited by Yang et al. [47].

## **1.2. Modeling Development of Ignition of Nitramine Propellants**

Ignition of solid propellants and explosives involves an array of intricate physiochemical processes under energetic stimuli, and has been a subject of extensive research since 1950. A comprehensive review of the early work was conducted by Price et al. in 1966 [48]. The experimental and theoretical literature pertaining to the ignition of solid propellants over the period of 1966 through 1980 was reviewed by Kulkarni et al. [49] and Hermance [50]. The state of understanding in Russia up to 1989 was presented by Vilyunov and Zarko [51], giving a detailed examination of the various ignition models and related experimental approaches. In 1998, a review of laser and radiative ignition of 24 solid energetic materials, with emphasis on work performed in the Former Soviet Union, was provided by Strakouskiy et al. [52].

Many theoretical ignition models have been developed to study the ignition of solid propellants and explosives, which can be broadly divided into four categories: solid-phase (or reactive solid), heterogeneous, gas-phase, and multi-phase reaction models. The solid-phase reaction models [53-56] assume that exothermic reactions in the condensed phase are the dominant mechanism of ignition, while the effects of surface and gas-phase processes are secondary and can be neglected. Heterogeneous reaction models [57-65] assume that heterogeneous reactions at the propellant surface are responsible for ignition

due to the molecular diffusion of ambient oxidizer species to the propellant surface. The formulation takes into account the condensed-phase conservation equations of energy and species concentration along with interfacial boundary conditions. Unlike the previous two categories, the gas-phase reaction models [66-73] presume that exothermic gas-phase reactions and their heat feedback to the propellant surface are the primary mechanism of ignition. Conservation of energy and species concentration in the gas phase is of major concern, but the condensed-phase equations are also included for completeness. In spite of their contributions in correlating experimental data and providing qualitative understanding of ignition behavior, the solid-phase (or reactive solid), heterogeneous, and gas-phase reaction models [53-73] are semi-empirical in nature and do not provide predictive capability at scales sufficient to resolve the detailed ignition mechanisms and flame evolution. A prior understanding of the ignition process is usually required before modeling. This obstacle mainly results from the use of global kinetics schemes derived for steady-state combustion. Moreover, a simple pyrolysis law is often employed to describe the propellant gasification process in terms of propellant surface temperature along with prescribed condensed-phase heat release.

Recently, Liao, Kim, and Yang developed a multi-phase reaction model by extending the steady-state model described in [33,34] to include the transient development in the entire combustion zone, including the solid-phase, near-surface two-phase, and gas-phase regions [39,40]. The formulation accommodates detailed chemical kinetics and transport phenomena in the gas-phase region, as well as thermal decomposition and subsequent reactions in the two-phase region. Thermodynamic phase transition and volumetric radiant energy absorption are also considered for a complete description. The model is capable of treating the entire ignition process from surface pyrolysis to steady-state combustion, with the instantaneous burning rate and surface conditions treated as part of the solution [39,40]. A summary of the theoretical formulation and results of this multi-phase model is given in the following sections of the current chapter.

### **1.3. Modeling Development of Combustion of Nitramine/GAP Pseudo-Propellants**

Most of the early work on GAP decomposition and combustion was based on global decomposition pathways [74]. The physiochemical processes involved in the combustion of a cured GAP strand is schematically illustrated in Fig. 2. The entire combustion-wave structure can be segmented into three regions: solid-phase, near-surface two phase, and gas-phase regimes. In the solid phase, the extent of chemical reactions is usually negligible due to the low temperature and short residence time. Thermal decomposition and ensued

reactions, as well as phase transition, take place in the foam layer, generating gas bubbles and forming a two-phase region. Rapid gasification occurs at the burning surface, and further decomposition and oxidation continue to take place and release a significant amount of energy in the near-surface region. The burning surface temperature is greater than 700 K. No visible flame is observed

in the gas phase; instead, a large amount of fine powder is formed away from the burning surface and generates a cloud of intense smoke. The final flame temperature of GAP is around 1300-1500 K, which is significantly lower than those of nitramines ( $\sim 3000$  K).

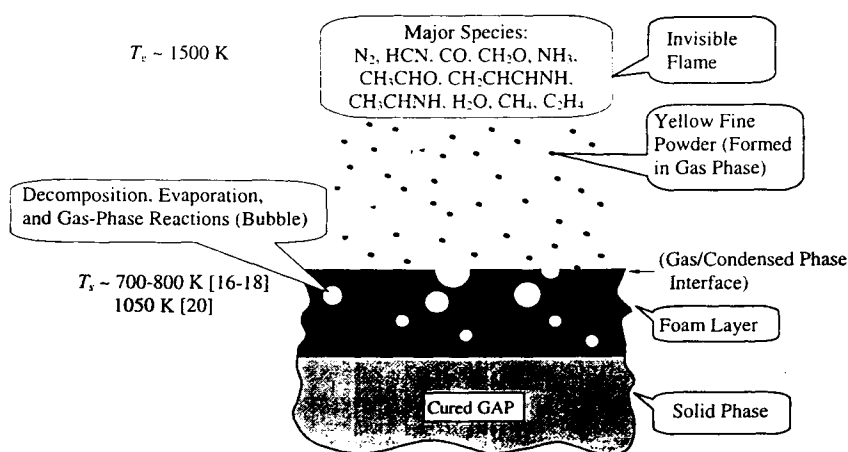


Fig. 2 Combustion-wave structure of GAP.

In recent years, Yang and coworkers [37-39] have established comprehensive numerical analyses of nitramine/GAP pseudo-propellant combustion to predict the propellant burning rate and detailed combustion wave structure over a broad range of pressure, laser intensity, and propellant composition. The steady-state model described in [33,34] was extended to include GAP binder in the nitramine combustion. The model takes into account various fundamental processes at scales sufficient to resolve the microscopic flame-zone physiochemistry. The thermochemical parameters of nitramine and GAP are deduced from existing experimental data. Four global decomposition reactions in the condensed phase as well as subsequent reactions are included. In the gas phase, a detailed chemical kinetics scheme involving 74 species and 532 reactions is employed to describe the heat-release mechanism. The key physiochemical processes dictating the propellant burning behavior and flame

structure were studied over a broad range of ambient pressure, preconditioned temperature, propellant composition, and impressed laser intensity.

The model approaches and results for HMX/GAP [37,39] and RDX/GAP [38] combustion will be briefly discussed in the current chapter.

## 2. THEORETICAL FORMULATION

Three physical problems are considered in this chapter: 1) steady-state combustion of nitramine propellants; 2) laser-induced ignition of RDX monopropellant; and 3) steady-state combustion of nitramine/GAP pseudo-propellants. During the past decade, Yang and co-workers [33,34,37-41] have developed a series of comprehensive numerical models for studying the key physiochemical processes involved in combustion and ignition of nitramine monopropellant and nitramine/GAP pseudo-propellants. These models accommodated detailed chemical kinetics and transport phenomena in the gas phase, as well as thermal decomposition and subsequent reactions in the condensed phase. The formation of gas bubbles in the molten surface layer due to molecular degradation and thermodynamic phase transition is also included to provide a complete description. The steady-state combustion models [33,34,37-39] are capable of resolving the combustion-wave structures in both the gas and condensed phases, with the instantaneous burning rate and surface temperature calculated as part of the solution. The analyses [33,34] were later extended to treat the entire ignition process from surface pyrolysis to steady-state combustion [39,40].

### 2.1. Steady-State Combustion of RDX Monopropellant

Figure 3 shows the physical model of concern, a strand of RDX monopropellant burning in a stagnant environment with or without the assistance of external laser heat flux. To facilitate formulation, the entire combustion-wave structure is conveniently segmented into three regions: 1) solid phase; 2) near-surface two phase, and 3) gas phase. During burning, the propellant remains thermally stable in the solid phase until the temperature approaches the melting point at which thermodynamic phase transition occurs as shown in Fig. 4. Molecular degradation and evaporation of RDX then take place in the liquid layer, generating bubbles and forming a two-phase region. The propellant subsequently undergoes a sequence of rapid evaporation and decomposition in the near field immediately above the foam layer. Oxidation reactions continue to occur and to release an enormous amount of energy in the gas phase, with the final temperature reaching the adiabatic flame temperature. A detailed description of the theoretical model can be found in Refs. 33 and 34.

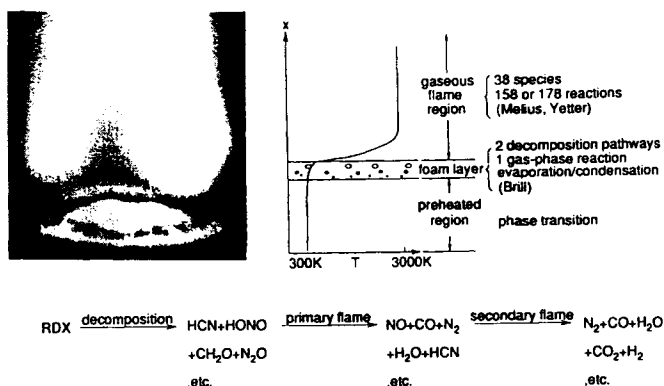


Fig. 3 Strand of RDX burning in a stagnant environment.

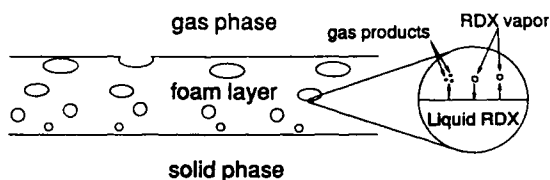


Fig. 4 Schematic diagram showing various regions in RDX combustion-wave structure.

## 2.2. Laser-Induced Ignition of RDX Monopropellant

The physical problem of concern is the ignition of a strand of RDX monopropellant induced by a continuous and radially uniform CO<sub>2</sub> laser. The physiochemical processes involved are schematically illustrated in Fig. 5. The propellant and the ambient gas are initially at room temperature. Once the laser is activated, volumetric absorption of laser energy in the solid phase takes place, as shown in Fig. 5a. In the gas phase, only certain gaseous species, such as vapor RDX, absorbs a noticeable amount of laser energy at the wavelength of 10.6  $\mu\text{m}$ ; thus, the gas-phase absorption is negligible during the inert heating period. When the solid reaches its melting temperature, the absorbed radiant energy can not further raise the temperature without first melting the solid. Since the radiant energy absorbed is insufficient for instantaneous melting of all of the solid in a short period, partial melting of the solid occurs, which leads to the formation of a mushy zone consisting of both solid and liquid (Fig 5b).



When a pure liquid layer is formed, the solid-liquid interface starts to move due to conductive and radiative heat transfer (Fig. 5c).

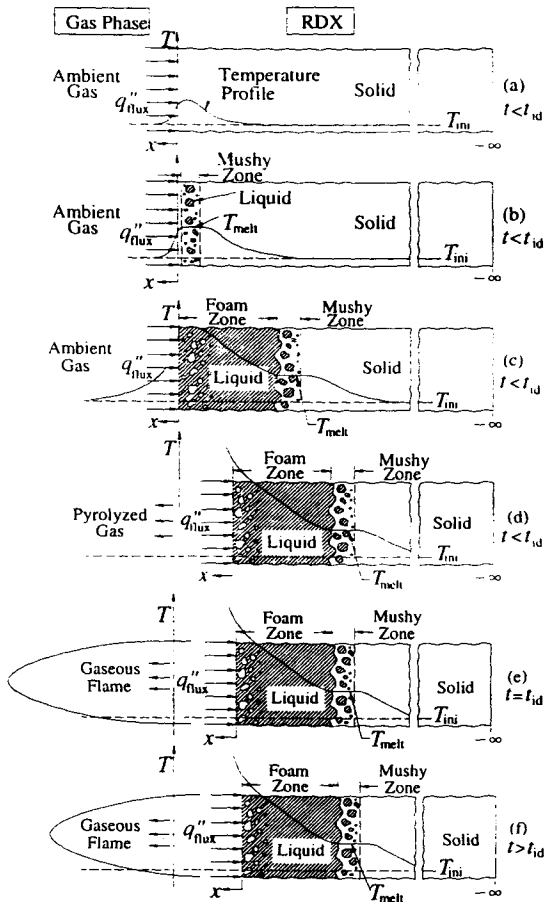


Fig. 5 Physiochemical processes involved in laser-induced ignition of RDX.

In the liquid, thermal decomposition and subsequent reactions, as well as phase transition, take place, generating gas bubbles and forming a two-phase region. The propellant then undergoes a sequence of rapid evaporation at the surface (Fig. 5d). Ignition occurs if the heat flux is sufficiently large to initiate the subsequent self-accelerated exothermic reactions which result in substantial heat release (in the gas phase) and emission of light. A luminous flame is

produced, regresses toward the surface, and finally reaches a stationary position corresponding to its steady-state condition. A brief description of the theoretical model is given in the Section 2.4, with detailed information available in Refs. 39 and 40.

### 2.3. Steady-State Combustion of Nitramine/GAP Pseudo-Propellants

Figure 6 shows schematically the physiochemical processes involved in the HMX/GAP pseudo-propellant combustion. A physical model for RDX/GAP pseudo-propellant combustion is available in Ref. 38. The entire combustion-wave structure is segmented into three regions: solid phase, near-surface

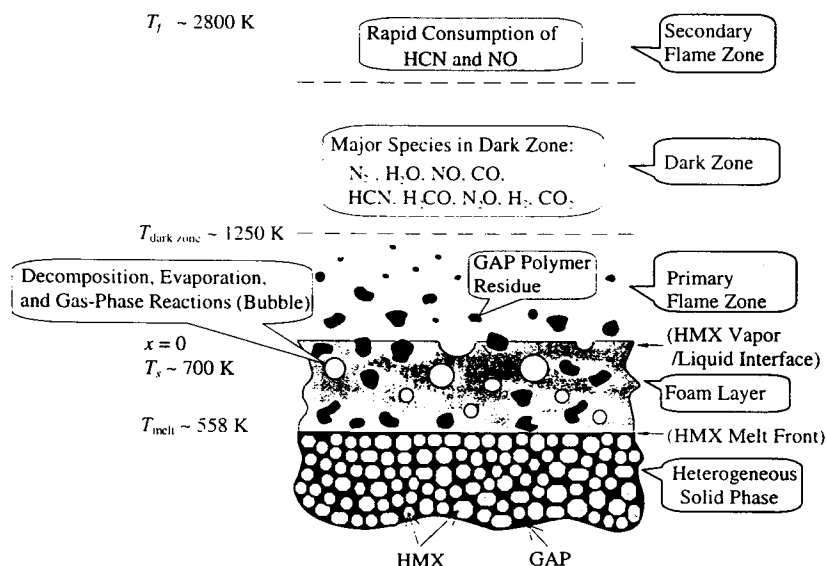


Fig. 6 Combustion-wave structure of HMX/GAP pseudo-propellant at 1 atm.

two phase, and gas phase. In the solid-phase region, HMX powder and GAP are physically mixed. The former melts at 558 K with negligible chemical reactions taking place, due to the low temperature and short residence time. Thermal decomposition and phase change of HMX occurs in the liquid phase to form a foam layer. The propellant surface ( $x = 0$ ) is defined herein as the interface between the foam layer and gas-phase region, at which rapid gasification of HMX prevails. Since the surface temperature of HMX/GAP pseudo-propellant ( $\sim 700$  K) is lower than that of pure GAP, GAP leaves the surface as aerosol surrounded with vapor HMX and its decomposed gaseous

products. In this region, GAP remains as a condensed species and continues to decompose. A significant amount of carbonaceous residue may be present on the surface during combustion. To facilitate analysis, the coordinate system is fixed at the propellant surface. A quasi one-dimensional model is formulated as a first approximation of the problem. Both the sub-surface and near-surface regions require a multi-phase treatment because of the presence of GAP and other condensed species in these zones. A detailed derivation of the theoretical model is available in Refs. 37 and 39. A similar model approach has been applied for studying RDX/GAP pseudo-propellant combustion [38].

## 2.4. Conservation Equations

A brief summary of the theoretical formulation of physicochemical processes in various regions during the laser-induced RDX ignition process [40] is given below. The model for steady-state combustion can be treated as a limiting case by neglecting all the time-varying terms.

### 2.4.1 Gas-Phase Processes

The formulation for the gas-phase region is based on the mass, energy, and species transport for a multi-component chemically reacting system of  $N$  species, and accommodates finite-rate chemical kinetics and variable thermophysical properties. If body force, viscous dissipation, and kinetic energy are ignored, the conservation equations for an isobaric flow can be written as follows.

*Mass*

$$\frac{\partial(\rho A)}{\partial t} + \frac{\partial}{\partial x}(\rho u A) = 0, \quad (1)$$

*Species concentration*

$$\rho A \frac{\partial Y_i}{\partial t} + \rho u A \frac{\partial Y_i}{\partial x} + \frac{\partial}{\partial x}(\rho A V_i Y_i) = A \dot{w}_i \quad (i = 1, 2, \dots, N), \quad (2)$$

*Energy*

$$\rho c_p A \frac{\partial T}{\partial t} - \frac{\partial(\rho A)}{\partial t} + \rho u c_p A \frac{\partial T}{\partial x} = \frac{\partial}{\partial x} \left( \lambda A \frac{\partial T}{\partial x} \right) - A \sum_{i=1}^N \left( \rho Y_i V_i c_{p_i} \frac{\partial T}{\partial x} + \dot{w}_i h_i \right) + A \dot{Q}_{\text{rad},g} \quad (3)$$

where subscript  $i$  denotes the  $i$ th species. The specific enthalpy  $h_i$  is defined by

$$h_i = \int_{T_{ref}}^T c_{p_i} dT + h_{f,i} \quad (4)$$

Standard notations in thermodynamics and fluid mechanics are used in Eqs. (1-4). The mass diffusion velocity  $V_i$  consists of contributions from both concentration (i.e., Fick's law) and temperature (i.e., Soret effect) gradients,

$$V_i = -D_i \frac{1}{X_i} \frac{\partial X_i}{\partial x} + D_i \frac{D_{T_i}}{X_i} \frac{1}{T} \frac{\partial T}{\partial x} + V_{\text{cor}} \quad (5)$$

where the correction velocity  $V_{\text{cor}}$  is employed to ensure that

$$\sum_{i=1}^N Y_i V_i = 0 \quad (6)$$

The ideal-gas law for a multicomponent system is derived to close the formulation.

$$p = \rho R_u T \sum_{i=1}^N \frac{Y_i}{W_i} \quad (7)$$

#### 2.4.2 Gas-Phase Chemical Kinetics

For a set of  $N_R$  elementary reactions involving  $N$  species, the reaction equations can be written in the following general form:



where  $\nu'_{ij}$  and  $\nu''_{ij}$  are the stoichiometric coefficients for the  $i$ th species appearing as a reactant in the  $j$ th forward and backward reactions, respectively, and  $M_i$  is the chemical symbol for the  $i$ th species. The reaction-rate constant  $k_j$  (either  $k_{fw,j}$  or  $k_{bw,j}$ ) is given empirically by the Arrhenius expression

$$k_j = A_j T^{B_j} \exp(-E_j / R_u T) \quad (9)$$

The rate of change in molar concentration of the  $i$ th species by the  $j$ th reaction is

$$\dot{C}_{ij} = (\nu'_{ij} - \nu''_{ij})(k_{fw,j} \prod_{i=1}^N C_i^{\nu'_{ij}} - k_{bw,j} \prod_{i=1}^N C_i^{\nu''_{ij}}) \quad (10)$$

The net rate of mass production of the  $i$ th species  $\dot{w}_i$  in Eq. (2) is then obtained by summing up the changes due to all reactions:

$$\dot{w}_i = W_i \sum_{j=1}^{N_R} \dot{C}_{ij} \quad (11)$$

It must be noted that the expression for chemical reaction rates, Eq. (10), is valid strictly for elementary reactions. If a global kinetics scheme is used, the exponents for molar concentrations may differ from their stoichiometric coefficients in order to match experimental data.

The detailed reaction mechanism proposed by Yetter [26] and augmented by Lin and co-workers [4] is employed to treat the gas-phase chemical kinetics. The model is developed based on a hierarchical approach for collecting kinetic

data and the specific chemical sub-models that are required to form the gas-phase combustion mechanism [26]. In particular, three kinetic sub-models of increasing complexity ( $\text{N}_2\text{O}$  decomposition,  $\text{H}_2/\text{NO}_2$  reaction, and  $\text{CH}_4/\text{N}_2\text{O}$  reaction) are established using the results from kinetics experiments over a broad range of temperature and pressure. When the initial decomposition steps of RDX proposed by Melius [25] are adopted, the overall scheme contains 38 species and 178 reactions. Here, the N-N bond cleavage is assumed to be the first step of the gas-phase decomposition process of RDX due to its weak bond energy of about 50 kcal/mol compared to ~ 60 kcal/mol for the C-N bond and ~ 90 kcal/mol for the C-H bond. Li and Williams [29], however, indicated that the initial dominant decomposition pathway might be concerted symmetric triple fission to produce three  $\text{H}_2\text{CNNO}_2$  fragments at high temperatures. At present, uncertainties still exist about the types of species formed and their associated rates, especially for regions in close proximity to the burning surface. More experimental investigation is needed to clarify the initial decomposition steps of RDX. In the past, detailed kinetics models have been implemented to simulate self-sustained and laser-induced combustion of RDX under steady-state conditions [33,34]. Reasonably good agreement was obtained with experimental data in terms of propellant burning rate and flame structure. Three deficiencies, however, were observed: 1) insufficient quantities of  $\text{N}_2$  and  $\text{NO}_2$  in the first stage of flame, 2) abundance of  $\text{CH}_2\text{O}$  at the end of the first stage, and 3) over-prediction of the ignition delay. Modifications were thus undertaken to circumvent these problems in three steps. First, a reaction allowing for the formation of  $\text{N}_2$  during the initial stage of reaction was added to the model. Second, the rate of thermal decomposition of  $\text{H}_2\text{CN}$  was increased to allow for greater H-radical generation and subsequently for faster consumption of  $\text{CH}_2\text{O}$ . Third, a reaction between  $\text{H}_2\text{CNNO}_2$  and  $\text{NO}_2$  was added to enhance the ignition process. Recently, Lin and coworkers [4] revised the near-surface combustion mechanism by adding more reactions involved in the consumption of  $\text{H}_2\text{CNNO}_2$ ,  $\text{H}_2\text{CNNO}$ ,  $\text{H}_2\text{CNO}$ ,  $\text{H}_2\text{CNOH}$ , and  $\text{H}_2\text{CN}$ . The kinetic rates of these added reactions were determined using high-level *ab initio* molecular orbital (MO) and statistical theory calculations [4]. The resulting kinetics scheme, containing 49 species and 250 reactions, can be found in Ref. 39.

#### 2.4.3 Subsurface Two-Phase Processes

The liquid and gas bubbles underneath the propellant surface are treated together and referred to as the subsurface two-phase region. The physiochemical processes in this region are extremely complicated, involving an array of intricacies such as thermal decomposition, evaporation, bubble formation, gas-phase reactions in bubbles, interfacial transport of mass and

energy between gas and condensed phases, etc. Taking full account of these processes is hardly practical, and many simplifications have been made to render the analysis manageable. A two-phase fluid dynamic model using a spatial averaging technique is employed to formulate the complicated phenomena in the two-phase region [33,34]. The mass diffusion velocities in the two-phase region  $V_{gi}$  and  $V_{ci}$  are assumed to be relatively small compared to their convective counterparts in the gas phase, and are ignored to simplify numerical calculations. The conservation equations for both the liquid phase and gas bubbles can be combined into the following form:

*Mass*

$$\frac{\partial[(1-\phi)\rho_l + \phi\rho_g]}{\partial t} + \frac{\partial[(1-\phi)\rho_l u_l + \phi\rho_g u_g]}{\partial x} = 0 \quad (12)$$

*Species concentration for liquid phase*

$$\frac{\partial[(1-\phi)\rho_l Y_{li}]}{\partial t} + \frac{\partial[(1-\phi)\rho_l u_l Y_{li}]}{\partial x} = \dot{w}_{li} \quad (i = 1, 2, \dots, N_l) \quad (13)$$

*Species concentration for gas phase*

$$\frac{\partial(\phi\rho_g Y_{gi})}{\partial t} + \frac{\partial(\phi\rho_g u_g Y_{gi})}{\partial x} = \dot{w}_{gi} \quad (i = 1, 2, \dots, N_g) \quad (14)$$

*Energy*

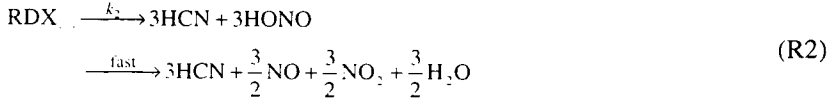
$$\begin{aligned} \rho_l c_{p,l} \frac{\partial T_l}{\partial t} + \rho_l u_l c_{p,l} \frac{\partial T_l}{\partial x} = \frac{\partial}{\partial x} \left( \lambda_l \frac{\partial T_l}{\partial x} \right) - \sum_{j=1}^{N_l} h_{lj} \dot{w}_{lj} - \sum_{j=1}^{N_g} h_{gj} \dot{w}_{gj} \\ + \sum_{j=1}^{N_g} h_{gj} Y_{gj} \dot{w}_{l \rightarrow g} \\ - \sum_{j=1}^{N_l} h_{lj} Y_{lj} \dot{w}_{l \rightarrow g} + \dot{Q}_{\text{rad},l} \end{aligned} \quad (15)$$

where subscript  $l$  denotes the mass-averaged quantity in the two-phase region. The source terms,  $\dot{w}_{li}$  and  $\dot{w}_{gi}$ , represent the mass production rates of the  $i$ th species in the liquid phase and gas bubbles, respectively, and  $\dot{w}_{l \rightarrow g}$  represents the mass conversion rate from liquid to gas.

#### 2.4.4 Subsurface Chemical Kinetics and Phase Transition

The global decomposition model of RDX proposed by Brill et al. [12], derived from a well-calibrated temperature-jump/Fourier transform infrared (T-

jump/FTIR) spectroscopy experiment, is adopted here. This mechanism includes two pathways as follows:



Reaction (R1) is an exothermic, low-temperature pathway, whereas reaction (R2) is an endothermic, high-temperature pathway. The reaction rates are obtained from a model of the T-jump/FTIR experiment [15], which takes into account the heat transfer of the filament and sample.

$$k_1 = 6.00 \times 10^{13} \exp\left(-\frac{36.0 \text{ kcal/mol}}{R_u T}\right) \text{ s}^{-1} \quad (16)$$

$$\dot{w}_{R1} = (1 - \phi) \rho_l k_1$$

$$k_2 = 1.60 \times 10^{17} \exp\left(-\frac{45.0 \text{ kcal/mol}}{R_u T}\right) \text{ s}^{-1} \quad (17)$$

$$\dot{w}_{R2} = (1 - \phi) \rho_l k_2$$

The two global decomposition reactions are nearly thermally neutral at temperatures around 600 K. Subsequent reactions among the products of (R1) and (R2) may occur and provide the energy to sustain pyrolysis. Brill [12] examined several plausible secondary reactions, such as  $\text{CH}_2\text{O} + \text{NO}_2$ ,  $\text{CH}_2\text{O} + \text{N}_2\text{O}$ , and  $\text{HCN} + \text{NO}_2$ , and their corresponding reaction rates. Results indicated that the following reaction



is probably the most important secondary reaction in the subsurface region. The reaction rate of (R3) has been determined from shock-tube experiments [16] and is given by

$$\begin{aligned} k_3 &= 8.02 \times 10^2 T^{2.77} \exp\left(-\frac{13.7 \text{ kcal/mol}}{R_u T}\right) \frac{\text{cm}^3}{\text{mol} \cdot \text{sec}} \\ \dot{w}_{R3} &= \phi k_3 \frac{\rho_g Y_{\text{CH}_2\text{O}}}{W_{\text{CH}_2\text{O}}} \frac{\rho_g Y_{\text{NO}_2}}{W_{\text{NO}_2}} \end{aligned} \quad (18)$$

In addition to the thermal decomposition and its subsequent reactions (R1-R3), thermodynamic phase transition from liquid to vapor RDX is considered to provide a complete description of the mass conversion process.



Based on gas-kinetic theory, the net evaporation rate is taken to be the difference between the evaporation and condensation rates [33] and is expressed as

$$\dot{m}_{\text{net}}^* = s \left( \frac{1}{4} \sqrt{\frac{8R_u T}{\pi W_{\text{RDX}}}} \right) \frac{p W_{\text{RDX}}}{R_u T} \left( \frac{p_{v,\text{eq}}}{p} - X_{\text{RDX}} \right) \quad (19)$$

Thus, the specific mass conversion rate due to evaporation becomes

$$\dot{w}_{R4} = A_{\text{sp}} \dot{m}_{\text{net}}^* \quad (20)$$

The specific surface area  $A_{\text{sp}}$  is a function of void fraction and number density of bubbles, and is derived as follows.

$$\begin{aligned} A_{\text{sp}} &= (36\pi n)^{1/3} \phi^{2/3}, & \phi < 1/2 \\ \text{or } (36\pi n)^{1/3} (1-\phi)^{2/3}, & \phi > 1/2 \end{aligned} \quad (21)$$

where  $n$  is the number density of gas bubbles to be determined empirically [33].

#### 2.4.5 Solid-Phase Processes

Since very little RDX decomposes in the solid phase, due to its low temperature conditions, only the energy conservation equation that includes both conductive and radiative heat transfer is required to model the solid-phase processes. The equation takes the form

$$\rho_s c_{p,s} \frac{\partial T_s}{\partial t} + \rho_s u_{s,c,p,s} \frac{\partial T_s}{\partial x} = \frac{\partial}{\partial x} \left( \lambda_s \frac{\partial T_s}{\partial x} \right) + \dot{Q}_{\text{rad},s} \quad (22)$$

where subscript  $s$  represents solid. The thermal properties of RDX were recently measured by Hanson-Parr and Parr [17]. Since the properties of liquid RDX, such as  $\lambda_l$  and  $c_{p,l}$ , are not available in the literature, the same values are used for both the liquid and solid RDX. The thermodynamic and transport properties of RDX used in this analysis are available in Ref. 39.

#### 2.4.6 Radiative Heat Transfer

The radiative heat transfer processes are complicated and difficult to model, usually including absorption, emission, and scattering of radiant energy in both the gas and condensed phases, as well as surface absorption, transmission, and reflection. In this work, the focus is on a CO<sub>2</sub> laser with a wavelength of 10.6  $\mu\text{m}$ . The following assumptions are made to render the analysis feasible. First, the CO<sub>2</sub> laser is treated as collimated irradiation and locally one-dimensional. Second, reflection at the propellant surface is not considered, since the normal reflectivity of RDX with a refractive index of 1.49 at 10.6  $\mu\text{m}$  was estimated to be only 0.047, using Fresnel's equation [18]. Third, the levels of scattering by and emission from the gas-phase, two-phase, and solid-phase regions are



assumed to be relatively small compared to that of absorption. Finally, Beer's law is employed to determine the volumetric absorption in the solid- and two-phase regions as follows.

The absorption in the solid and subsurface two-phase regions ( $x < 0$ ) is

$$\dot{Q}_{\text{rad},c} = (1 - f_g - \alpha_{\text{sur}})(1 - \phi)\beta_c e^{(1-\phi)\beta_c x} \dot{Q}_{\text{laser}}^* \quad (c = \text{liquid, solid}) \quad (23)$$

where  $f_g$  is the fraction of laser energy absorbed in the gas-phase region,  $\alpha_{\text{sur}}$  the fraction of laser heat flux absorbed by the propellant surface,  $\beta_c$  the absorption coefficient, and  $\dot{Q}_{\text{laser}}^*$  the laser heat flux. The absorption coefficient of solid RDX for a  $\text{CO}_2$  laser at a wavelength of  $10.6 \mu\text{m}$  has been measured by Isbell and Brewster [18] to be  $2800 \text{ cm}^{-1}$ . Since the absorption properties of many types of semi-transparent liquids are quite similar to those of solids [75], the absorption coefficients of solid and liquid RDX are assumed to be the same in this work. The fraction of laser energy absorbed in the gas-phase region  $f_g$  is defined by the following equation:

$$f_g = \frac{\int_0^\infty \dot{Q}_{\text{rad},g}^* dx}{\dot{Q}_{\text{laser}}^*} \quad (24)$$

where  $\dot{Q}_{\text{rad},g}^*$  is the gas-phase absorption of laser energy, and can be estimated by examining the infrared (IR) transmittance data. The vapor RDX IR spectrums obtained using both confined rapid thermolysis (CRT)/FTIR spectroscopy [13] and rapid-scanning FTIR spectroscopy [19] show strong, broad absorption bands of vapor RDX in a wavelength range of  $4.7$  to  $13.3 \mu\text{m}$ . The absorption characteristics of the gaseous decomposition products of RDX at  $10.6 \mu\text{m}$  can be readily studied from their corresponding individual IR spectra [76]. None of the major decomposition products exhibits a noticeable absorption at  $10.6 \mu\text{m}$ . It is clearly evident that of the species present, only vapor RDX absorbs a considerable amount of  $\text{CO}_2$  laser energy in the gas phase. Thus, volumetric absorption in the gas phase is given by

$$\dot{Q}_{\text{rad},g}^* = C_{\text{RDX}} A_v \kappa_{\text{RDX},g} \dot{Q}_{\text{laser}}^* \quad (25)$$

where  $C_{\text{RDX}}$  is the molar concentration of vapor RDX, and  $A_v$  Avogadro's constant. The absorption cross-section of vapor RDX,  $\kappa_{\text{RDX},g}$ , is defined as

$$\kappa_{\text{RDX},g} = \frac{\beta_c W_{\text{RDX}}}{\rho_{\text{RDX},c} A_v} \quad (26)$$

Since the absorption properties of vapor RDX are not available in the literature, the absorption coefficient  $\beta_c$  is used to estimate  $\kappa_{\text{RDX},g}$  with the assumption that

the characteristics of vibration-rotational bands of vapor RDX at the wavelength of interest are similar to those of intermolecular vibration bands of condensed RDX [75]. An IR transmittance spectrum for solid RDX, obtained from the measurement of RDX powder pressed in a KBr matrix [20] shows a strong absorption band of solid RDX at 10.6  $\mu\text{m}$ , similar to the absorption characteristics of vapor RDX. At present, the use of the same absorption properties for both condensed and vapor RDX seems to be reasonable, due to the lack of measured data. Note that a parametric study has also been performed by varying the absorption coefficient of vapor RDX by 20 % in order to investigate the effect of absorption properties on the overall ignition process.

#### 2.4.7 Boundary Conditions

The physical processes in the gas-phase and subsurface regions must be matched at the interface by requiring continuities of mass and energy fluxes. This procedure eventually determines propellant surface conditions and burning rate as the eigenvalues of the problem. The interfacial boundary conditions are expressed as follows:

##### Mass

$$(\rho u)_{0^-} = [(1-\phi)\rho_l u_l + \phi\rho_g u_g]_{0^-} \quad (27)$$

##### Species concentration

$$[\rho(u + V_i)Y_i]_{0^+} = [(1-\phi)\rho_l u_l Y_{li} + \phi\rho_g u_g Y_{gi}]_{0^-} \quad (28)$$

##### Energy

$$\left[ \lambda \frac{dT}{dx} \right]_{0^+} + \alpha_{\text{sur}} \dot{Q}_{\text{laser}} = \left[ \lambda \frac{dT}{dx} \right]_{0^-} + (1-\phi)\rho_l u_l \frac{H_v}{W_{\text{RDX}}} \quad (29)$$

where subscripts  $0^+$  and  $0^-$  represent conditions at the interface on the gas-phase and subsurface sides, respectively. Note that Eq. (27) is essentially the summation of mass fluxes of all species governed by Eq. (28), and thus can not be independently used for determining the eigenvalues. An additional condition is required. Here, the thermodynamic phase transition from liquid to vapor RDX is assumed to prevail at the interface, giving

$$(\rho_l u_l)_{0^-} = \dot{m}_{\text{net}}^* \quad (30)$$

Equations (28-30), coupled with the assumptions that  $T_g = T_l$  and  $\rho_g u_g = \rho_l u_l$  in the condensed phase, are sufficient to solve the set of unknowns ( $u_b$ ,  $T$ ,  $\phi$ ,  $Y_i$ ) at the propellant surface.

The far-field conditions for the gas phase require the gradients of flow properties to be zero at  $x \rightarrow \infty$ .

$$\frac{\partial \rho}{\partial x} = \frac{\partial u}{\partial x} = \frac{\partial Y_i}{\partial x} = \frac{\partial T}{\partial x} = 0 \text{ at } x \rightarrow \infty \quad (31)$$

The condition at the cold boundary for the solid phase ( $x \rightarrow -\infty$ ) is

$$T_s = T_{\text{ini}} \text{ at } x \rightarrow -\infty \quad (32)$$

Finally, the conditions for the phase transition from solid to liquid at the melting point ( $T_m = 478 \text{ K}$ ) are required.

$$T_s = T_l = T_m \text{ and} \quad (33)$$

$$k_s \left. \frac{\partial T_s}{\partial x} \right|_{x_m^-} = k_l \left. \frac{\partial T_l}{\partial x} \right|_{x_m^+} - \frac{\rho_s H_{\text{fus}}}{W_{\text{RDX}}} \left( \frac{dx_m}{dt} - u_{l,0} \right)$$

at  $x = x_m$ , where subscripts  $x_m^+$  and  $x_m^-$  represent conditions at the interface on the two-phase and solid-phase sides, respectively.

### 3. NUMERICAL METHOD

The theoretical formulation established in the preceding section requires a time-accurate analysis. A dual-time-stepping numerical integration method is employed to circumvent the computational difficulties associated with the rapid transients during the ignition process. The scheme includes artificial time derivatives, so that the solution converged in pseudo-time corresponds to a time-accurate solution in physical time. The physical time step is chosen to be around one hundredth of the estimated ignition delay, or even less, to obtain reasonable temporal resolution. When marching from one physical time level to the next, all the conservation equations and associated boundary conditions are solved by treating the propellant surface temperature  $T_{\text{sur}}$  and burning rate  $r_b$  as the eigenvalues. The iteration starts with guessed  $T_{\text{sur}}$  and  $r_b$ , which are bound by Eq. (30). The condensed- and gas-phase governing equations are solved with these guessed values and other boundary conditions. If the resulting temperature gradients do not satisfy the interfacial energy balance equation, Eq. (29) is used to correct the values of  $T_{\text{sur}}$  and  $r_b$  by means of a bisection method. The updated  $T_{\text{sur}}$  and  $r_b$  are then substituted into the governing equations for another solution of the temperature field. The iterative procedures are performed until  $T_{\text{sur}}$  and  $r_b$  converge, and Eq. (29) is satisfied. Finally, a solution at the physical time level is obtained when all the governing equations and associated boundary conditions are satisfied. In general, the gas-phase solver takes much more computational time than its counterpart for the condensed phase, due to the complexity of the chemical kinetics in the gas phase.

Calculations of chemically reacting flows often encounter numerical stiffness problems attributed to the wide variety of time and length scales associated with chemical reactions and transport processes. The problem can be effectively circumvented by using a combined Newton-iteration and (pseudo-) time-integration scheme originally developed by Kee et al. [77]. The Newton method works efficiently for linear systems but may fail to converge for nonlinear systems unless a reasonable initial guess is provided. Conversely, the (pseudo-) time-integration technique is more robust, but less efficient. To optimize the benefits of these two algorithms, computations usually start with the Newton method, and then switch to the time-integration scheme when the iteration fails to converge. After another trial solution is obtained with several time-marching steps, the Newton method is resumed to gain efficiency. The time step in the time-integration technique is sufficiently smaller than the physical time step in order to handle the numerical problems caused by the highly transient phenomena due to rapid chemical reactions. An adaptive-grid system is employed to further improve the convergence rate.

A four-step Runge-Kutta method is used for temporal integration of the condensed-phase conservation equations, along with a second-order central differencing scheme for spatial discretization. Calculations start with an estimate of the temperature profile, obtained by solving an inert energy equation. The conservation equations of mass and species concentration are then integrated with the given temperature profile. The energy equation is subsequently solved with the newly obtained void-fraction and species concentration profiles to update the temperature profile. Since these equations are solved sequentially, iteration is required to get a converged solution. Once the temperature reaches the melting temperature, the movement of the solid-liquid interface is determined from Eq. (31). The fixed-grid Eulerian method is employed for interface tracking.

#### 4. DISCUSSION OF MODEL RESULTS

The theoretical model and numerical method outlined in the above sections were implemented to study steady-state combustion of nitramine monopropellants [33,34], laser-induced ignition of RDX [39,40], and steady-state combustion of nitramine/GAP pseudo-propellants [37-39]. The analyses were carried out over a broad range of operating conditions. Various important burning and ignition characteristics were investigated systematically, with emphasis placed on the detailed flame structure and the effect of the subsurface two-phase layer on propellant deflagration.

#### 4.1. Steady-State Combustion of Nitramine Propellants

Figure 7 shows predicted temperature distributions at several ambient pressures using the gas-phase chemical kinetics mechanism proposed by Yetter et al. [26]. The temperature increases monotonically from its initial value of 293K, and levels off at a value close to the prediction by the chemical equilibrium analysis. The final flame temperature increases with increasing pressure, whereas the flame-standoff distance exhibits an opposite trend owing to enhanced chemical-reaction rates at high pressures. No evidence is obtained of the existence of a temperature plateau in the dark zone regardless of pressure, which is consistent with the experimental observations of self-sustained combustion of RDX monopropellant [41]. It is worth noting that a dark-zone temperature plateau (at  $T \sim 1500$  K) was present in the laser-assisted combustion of RDX, while the existence of the dark zone was not evident in the self-assisted combustion. Liao and Yang [41] indicated that the chemical preparation and fluid transport times of the intermediate species produced in the primary flame must be comparable in order to form a dark zone.

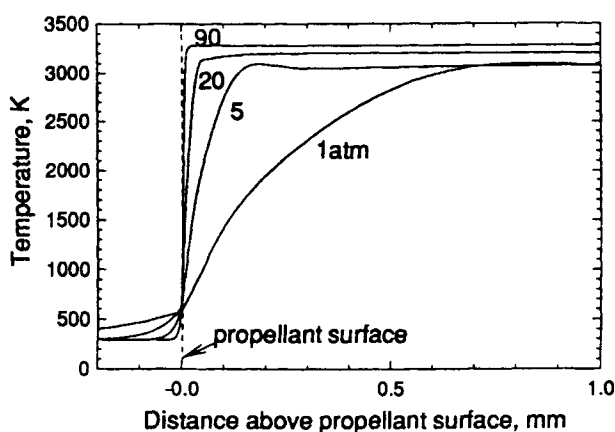


Fig. 7 Temperature profiles of self-sustained RDX combustion at various pressures

Figure 8 shows the burning rate as a function of pressure. Good agreement between predictions and measurements is obtained. A power law of the burning rate vs pressure is observed,

$$r_b = a p^n \quad (34)$$

where the pressure exponent  $n$  is about 0.83 (with  $p$  in atm), and the pre-exponential factor  $a$  equals to 0.3 cm/s for  $T_i = 293$ K. The increased burning

rate with pressure is attributed mainly to fast gas-phase exothermic reactions at high pressures and their influence on heat transfer to the condensed phase.

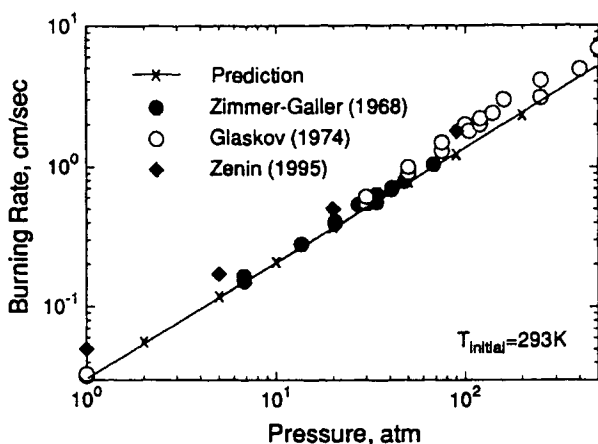


Fig. 8 Effect of pressure on strand burning rate of RDX monopropellant; self-sustained combustion.

The temperature sensitivity of burning rate defined in Eq. (35) is also examined, giving the result shown in Fig. 9.

$$\sigma_p = \left[ \frac{(\partial r_b) / r_b}{\partial T_i} \right]_p = \left[ \frac{\partial (\ln r_b)}{\partial T_i} \right]_p \quad (35)$$

The temperature sensitivity  $\sigma_p$  stays around  $0.0028 \text{ K}^{-1}$  for most cases. At elevated pressures, the heat feedback from the gas phase to the condensed phase is higher, and thus the effect of initial temperature on the interfacial energy balance becomes less important. A numerical analysis on the temperature sensitivity for low-pressure conditions was further performed by Beckstead and co-workers [35]. The predicted temperature sensitivity was determined to be too low compared to the measurements, mostly due to the uncertainties associated with the treatment of the condensed phase in the model.

A similar approach was applied to study the combustion characteristics of HMX monopropellant. A detailed description of the theoretical formulation and results is available in Ref. 37. Figure 10 shows the pressure sensitivity of the HMX burning rate. Good agreement was obtained with the experimental measurements by Zenin [11] and Atwood et al. [21]. The pressure exponent  $n$  in Eq. (34) was about 0.88, with the pre-exponential factor  $a$  equal to 0.35 for  $T_i = 293 \text{ K}$ . The temperature sensitivity of burning rate defined by Eq. (35) at various pressures is shown in Fig. 11. There were noticeable discrepancies

between the measured and predicted values at pressures below 20 atm, a phenomenon that may be attributed to the uncertainties in modeling the condensed-phase heat release process. More detailed understanding of the chemical kinetics in the condensed phase is required to improve model predictability, especially for low-pressure cases in which near-surface exothermic reactions play a more dominant role in determining propellant surface conditions than the heat feedback from the gas phase.

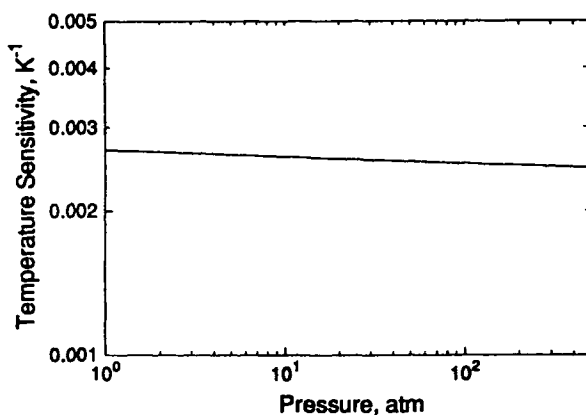


Fig. 9. Temperature sensitivity of RDX burning rate; self-sustained combustion.

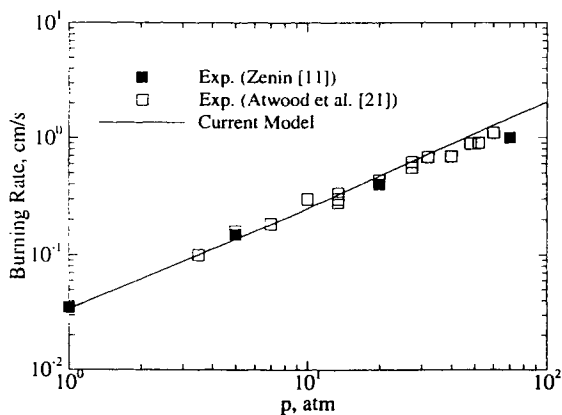


Fig. 10 Pressure dependence of burning rate of HMX monopropellant; self-sustained combustion.

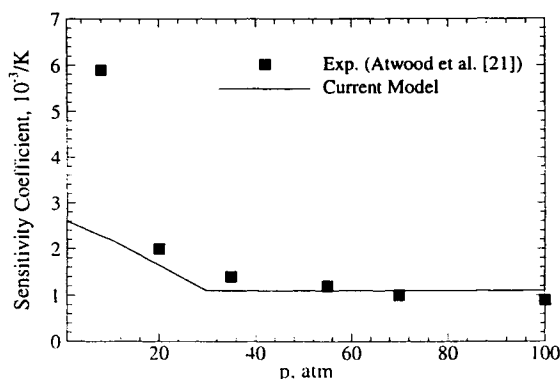


Fig. 11 Temperature sensitivity of burning rate of HMX monopropellant; self-sustained combustion.

In this chapter, the model results pertaining to the combustion-wave structure of RDX monopropellant are focused. A comprehensive description of theoretical formulation and results for combustion of HMX monopropellant can be found in Ref. 27. The calculated species-concentration profiles were validated against experimental data [22], which was obtained by means of a time-of-flight mass spectrometry technique at 0.5 atm, as shown in Fig. 12. Good agreement was obtained except for the region next to the surface. The discrepancy may arise from the ambiguity in determining the location of the propellant surface in experiments. Due to the limitation of the spatial resolution (500  $\mu\text{m}$ ), the diagnostic work defined the surface as the location where RDX was completely consumed. This analysis, however, predicted that an appreciable amount of RDX still existed at the surface since only limited RDX decomposition occurred in the subsurface region. If the spatial distribution of the calculated data was artificially shifted upward to the location where NO and HCN attained their peak values, then an improved agreement between the prediction and the measurement could be achieved. The species-concentration profiles revealed that the overall reaction mechanisms globally consist of three steps: (1) decomposition of RDX to  $\text{CH}_2\text{O}$ , HCN,  $\text{NO}_2$ , etc. near the surface, (2) first-stage oxidation which includes formation of NO and  $\text{H}_2\text{O}$  as well as removal of  $\text{NO}_2$ , and (3) second-stage oxidation which includes conversion of HCN and NO to the final products such as CO,  $\text{N}_2$ , and  $\text{H}_2$ . It is worth noting that the highly exothermic reductions of HCN and NO usually occur at elevated temperature ( $T \sim 2000$  K) owing to the large activation energies required to initiate these reactions, which provide the major heat source for raising the



flame temperature to its final adiabatic value. The calculated molar fractions of the final product species are quite consistent with the chemical-equilibrium predictions, with the deviation being less than 2%.

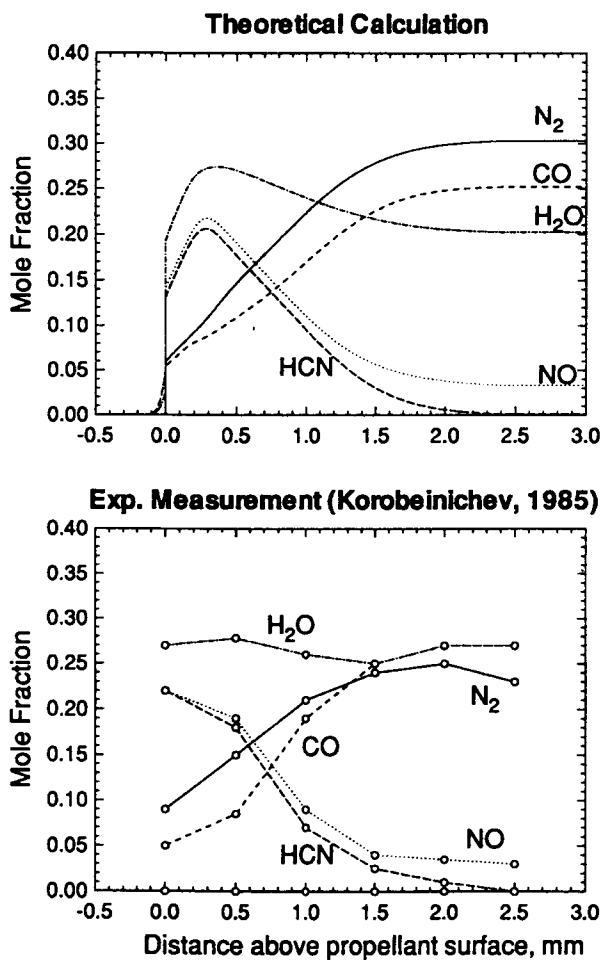


Fig. 12 Distributions of major species concentrations of self-sustained combustion of RDX at 0.5 atm.

The combustion wave structure at 100 atm is shown in Figs. 13 and 14, exhibiting a close similarity to that at 1 atm except for the shorter flame-standoff distance (6 vs. 600  $\mu\text{m}$ ) and molten-layer thickness (2.1 vs. 66  $\mu\text{m}$ ).

The major difference lies in a smaller void fraction. The shorter molten-layer thickness and higher burning rate yield a shorter residence time for condensed-phase reaction. Also, high pressure tends to retard the RDX evaporation, which dominates the gasification process in the two-phase layer. As evidenced by the large ratio of HCN to  $\text{CH}_2\text{O}$  mole fraction, the endothermic decomposition, (R2), appears more profound at high-pressure conditions. This can be attributed to the higher surface temperature and heat transfer into the condensed phase.

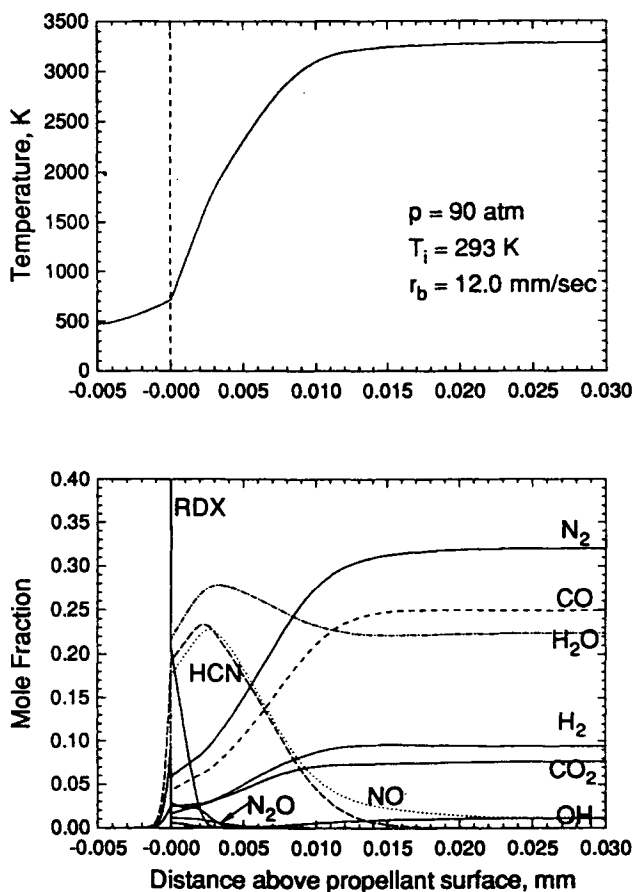


Fig. 13. Distributions of temperature and major species concentrations of self-sustained RDX combustion at 90 atm.

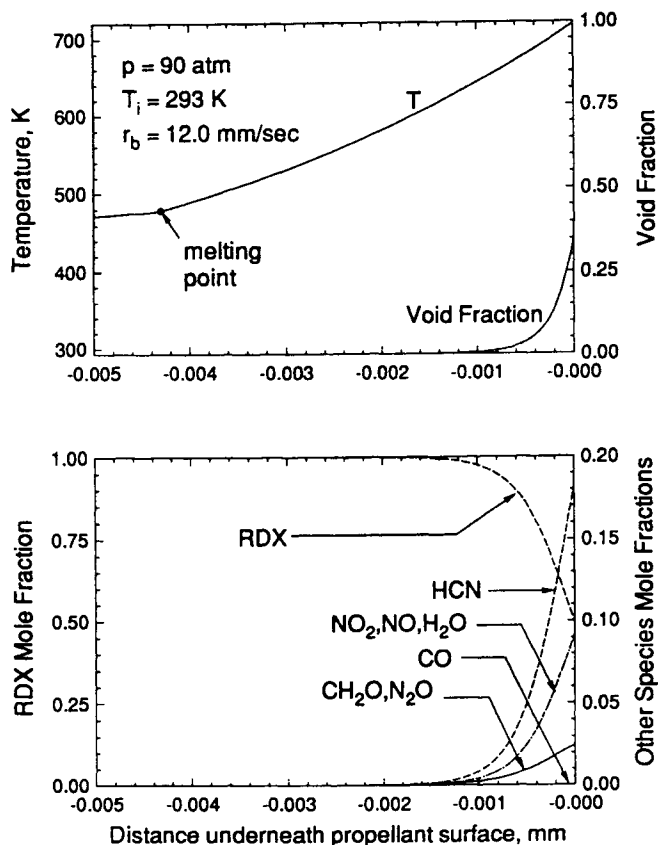


Fig. 14. Close-up view of temperature and species-concentration profiles in subsurface region at 90 atm.

#### 4.2. Laser-Induced Ignition of RDX Monopropellant

The entire laser-induced ignition process of RDX in an argon environment has been studied in detail [39,40]. Figure 15 shows the predicted temporal evolution of the temperature field at an incident laser heat flux of  $400 \text{ W/cm}^2$  under atmospheric pressure. The initial temperature is 300 K. The interface between the subsurface and gas-phase regions is set to be  $x = 0$ , with negative and positive values of the  $x$ -coordinate representing the subsurface and gas phase, respectively. The surface temperature is rapidly increased to 475 K within 1 ms, due to the high intensity of laser heat flux. The profiles for  $t < 1$

ms represent inert heating of the thin surface layer with conductive heat losses to both the solid- and gas-phase regions. The temperature rises in the gas phase at  $t = 2$  ms are primarily caused by radiant energy absorption rather than exothermic reactions, because the extent of RDX decomposition in the gas phase is very limited at this stage of the event. At  $t = 2.9$  ms, exothermic gas-phase reactions start to occur, and a flame appears near the propellant surface at  $t = 3$  ms. During the time period between 3 and 6 ms, the temperature continues to increase to around 1500 K, as a consequence of the heat release by exothermic reactions. As time further elapses, a luminous flame appears, and the temperature rises to its adiabatic temperature. The luminous flame is not stationary but regresses toward the surface. There is a time lag (about 4 ms) between the first appearances of the primary and secondary flames.

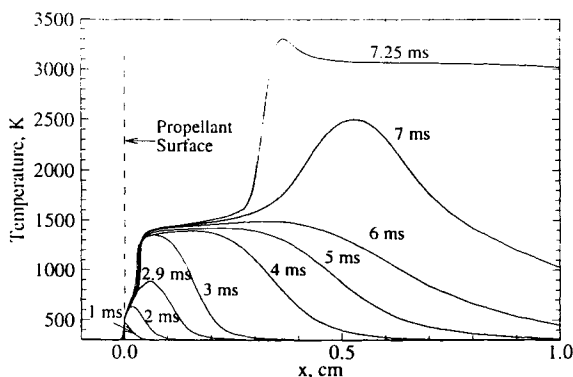


Fig. 15 Evolution of temperature field during laser-induced ignition of RDX in argon at  $p = 1$  atm and  $\dot{Q}_{\text{laser}}^{\prime\prime} = 400$  W/cm<sup>2</sup>.

Figure 16 shows a close-up view of the temperature evolution in the condensed phase near the propellant surface. The transient development of thermal-wave penetration into the subsurface region is clearly observed. The characteristic thickness of the thermal layer in the subsurface region is much thinner than that in the gas-phase region. Phase transition from solid to liquid can be indicated by the distinct change of temperature gradient at  $T_m = 478$  K. Since most of the CO<sub>2</sub> laser heat flux is absorbed by the thin surface layer due to the high absorption coefficient (2800 cm<sup>-1</sup>) of RDX at the wavelength of 10.6  $\mu\text{m}$ , the formation of the mushy zone can be safely ignored. However, some propellants, including RDX, are quite transparent to plasma irradiation in the UV/visible wavelength range; thus, the appearance of the mushy zone may be

evident in that situation. Figure 17 shows the distributions of void fraction and species concentrations in the subsurface two-phase region when ignition is achieved at  $t = 7$  ms. The extent of RDX decomposition in the condensed phase is very limited during the laser-induced ignition process up to 7 ms over the range of conditions studied, due to the short residence time and low temperature conditions. The molten layer in the subsurface region is not fully established within this time frame under atmospheric pressure. As indicated in the previous subsection, the steady-state combustion model predicts that the gas bubbles occupy about 45% of the volume at the surface under atmospheric pressure during self-sustained RDX combustion as a result of RDX evaporation and decomposition [34]. However, the surface void fraction during the self-sustained RDX combustion decreases significantly with increasing pressure [34].

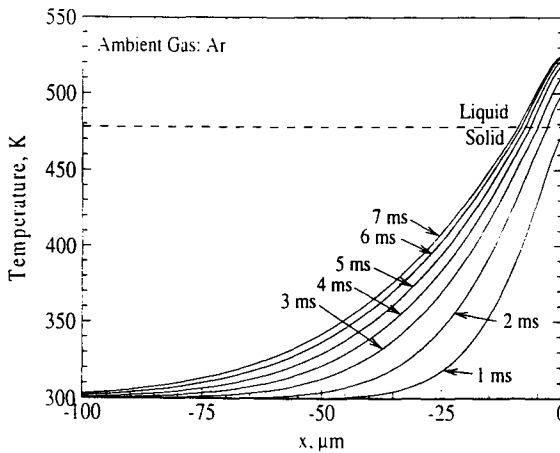


Fig. 16 Close-up view of temperature evolution in subsurface region during laser-induced ignition of RDX at  $p = 1$  atm and  $\dot{Q}_{\text{laser}} = 400 \text{ W/cm}^2$ .

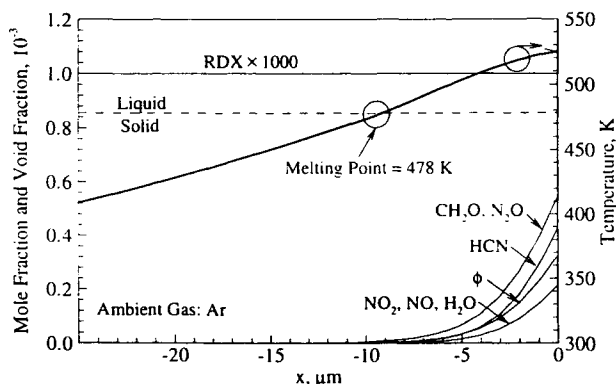
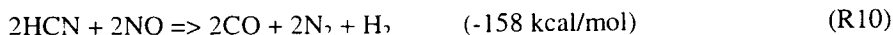


Fig. 17 Close-up view of temperature and species-concentration profiles in subsurface region at  $t = 7$  ms ( $p = 1$  atm and  $\dot{Q}_{\text{laser}}^* = 400$  W/cm<sup>2</sup>).

The overall gaseous RDX ignition process can be divided into five distinct stages: thermal decomposition, first oxidation, chemical preparation, second oxidation, and completion stages. In stage I, RDX decomposes to low-molecular weight species, such as  $\text{CH}_2\text{O}$ ,  $\text{N}_2\text{O}$ ,  $\text{NO}_2$ , HCN, and HONO. This decomposition process is slightly endo-/exo-thermic or thermally neutral depending on the initial temperature. In stage II, oxidation reactions occur and release a significant amount of energy with the temperature reaching about 1500 K. The dominant net reactions in stage II can be given as follows.



The heat release in stage II is mainly caused by the conversion of  $\text{CH}_2\text{O}$  and  $\text{NO}_2$  to  $\text{H}_2\text{O}$ ,  $\text{NO}$ , and  $\text{CO}$ , and to a lesser extent by the reactions of HCN and HONO. Stage III represents the chemical preparation time before the second oxidation reactions (stage IV) take place. The species formed in stage II are relatively stable, due to the high activation energies of their associated reactions, and require a finite time to oxidize further. The highly exothermic reactions occurring in stage IV may be attributed to the following net reactions.



The reduction of HCN and NO to  $\text{N}_2$ , CO,  $\text{H}_2\text{O}$ , and  $\text{H}_2$  is largely responsible for the heat release in stage IV. Finally, all the final products are formed; no further reactions occur in stage V.

Figures 18 - 23 show the temperature and species-concentration fields in the gas phase at various times. At  $t = 2$  ms, the gas temperature increases by more than 300 K, although only a small fraction (less than 10 %) of the laser energy is absorbed in the gas phase. This is not surprising, because the heat capacity of the gas mixture is much lower than that of the condensed mixture. At  $t = 2.9$  ms, small amounts of intermediate species, such as HCN, NO, HONO,  $\text{CH}_2\text{O}$ ,  $\text{N}_2\text{O}$ , and  $\text{NO}_2$ , result from thermal decomposition of RDX. The temperature rises to more than 800 K within 1 mm above the surface. Figure 10 shows the first appearance of the primary flame at  $t = 4$  ms. The aforementioned RDX decomposition products, especially  $\text{CH}_2\text{O}$  and  $\text{NO}_2$ , undergo rapid reactions, which leads to the formation of NO, HCN,  $\text{H}_2\text{O}$ , CO, and  $\text{N}_2\text{O}$  in the flame. The dominant net reactions in the primary flame zone can be given by (R4-R9). The temperature increases to about 1400 K. The species formed in the primary flame are relatively stable due to the high activation energies of their associated reactions, and require a finite time to oxidize further. At this stage, the fraction of laser absorption decreases significantly because of the rapid consumption of RDX, which is considered to be the only species absorbing a noticeable amount of laser energy in the gas phase. Figure 21 shows more details of the chemistry involved in the primary flame. The conversion of  $\text{CH}_2\text{O}$ ,  $\text{NO}_2$ , and HONO to NO, CO, HCN, etc. appears to be the major chemical mechanism releasing thermal energy. Figures 22 and 23 show the development of the secondary flame at  $t = 7$  and 7.25 ms, respectively. The temperature increases from 1500 to 3000 K at this stage, and the heat release can be largely attributed to (R10-R12). The conversion of HCN and NO to the final products seems to be the dominant net reaction in the secondary flame. Once the secondary flame appears, the intense energy release and heat transfer causes the flame to regress toward the propellant surface.

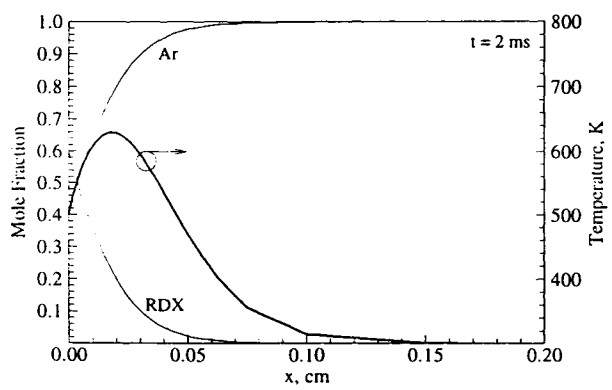


Fig. 18 Temperature and species-concentration profiles in gas phase at  $t = 2$  ms.

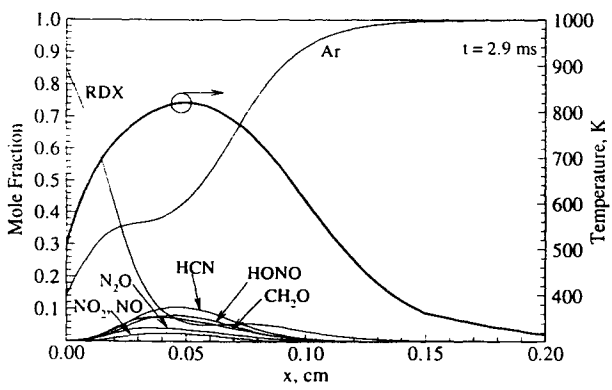


Fig. 19 Temperature and species-concentration profiles in gas phase at  $t = 2.9$  ms.



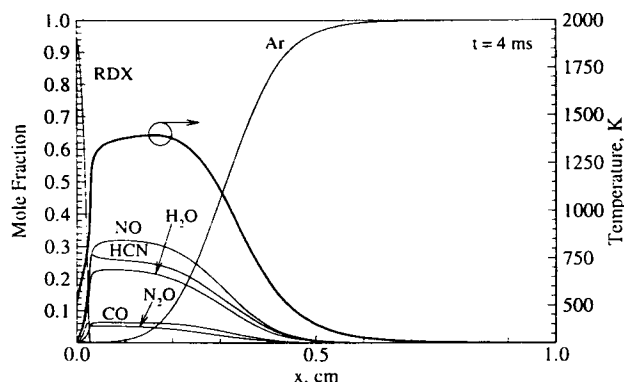


Fig. 20 Temperature and species-concentration profiles in gas phase at  $t = 4$  ms.

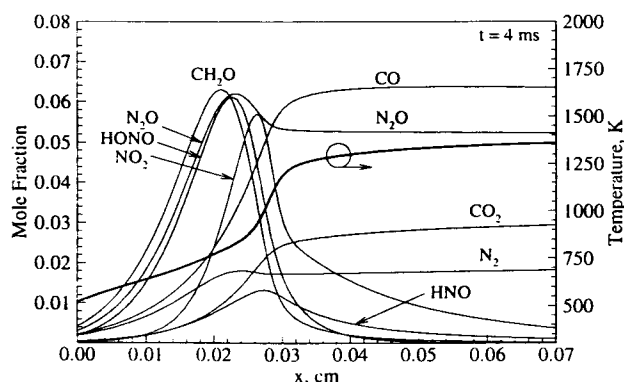


Fig. 21 Close-up view of temperature and species-concentration profiles in primary flame zone at  $t = 4$  ms.

A parametric study for investigating the effect of the absorption coefficient of vapor RDX on the overall ignition process has been performed by varying the absorption coefficient by 15 %. As shown in Fig. 18, the gas-phase temperature is rapidly increased by more than 300 K at  $t = 2$  ms, with a small amount of the laser energy absorbed by the gas phase. At  $t = 2.9$  ms, the gas-phase temperature rises to more than 800 K, caused by the heat release from the exothermic decomposition reactions in the gas phase. After the inert heating, the heat release from the exothermic reactions becomes much more pronounced than the laser energy absorbed by the gas phase. Since only a small amount of the laser energy was absorbed by the gas phase, a change by 15 % in absorption

coefficient did not influence the inert heating time significantly. Overall, the effect of the absorption coefficient of vapor RDX on the  $\text{CO}_2$  laser-induced ignition was not noticeable over the parameter range studied herein.

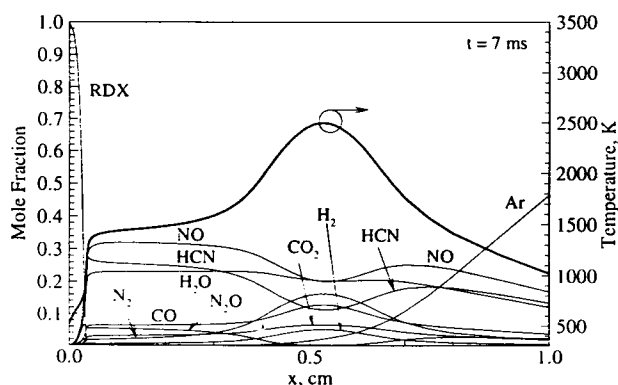


Fig. 22 Temperature and species-concentration profiles in gas phase at  $t = 7$  ms.

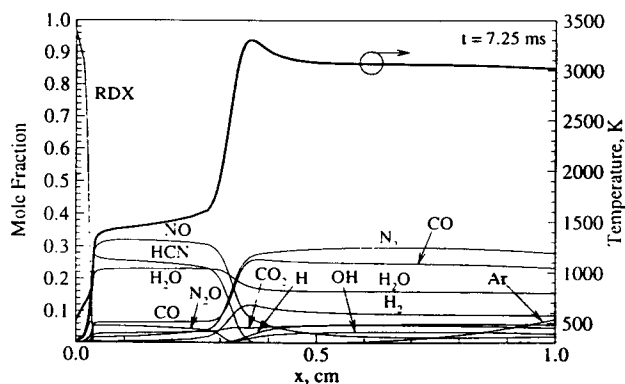


Fig. 23 Temperature and species-concentration profiles in gas phase at  $t = 7.25$  ms.

Figure 24 shows the evolution of the CN concentration field. A noticeable amount of CN is observed at  $t > 7$  ms. The concentrations of CN are usually small, except in the secondary flame, thereby serving as a good indication of the flame position. Parr and Hanson-Parr [23] conducted pioneering measurements of the transient flame structure of RDX using both UV-visible absorption and non-intrusive planar laser-induced fluorescence (PLIF). The experiments were

performed at three intensity levels of  $\text{CO}_2$  laser heat flux (i.e., 195, 402, and  $807 \text{ W/cm}^2$ ) under atmospheric pressure. Figure 25 shows the measured CN concentration profiles at various times for a laser flux of  $402 \text{ W/cm}^2$ . Comparison between Figs. 24 and 25 shows good agreement in terms of the CN concentration level. The measured ignition delay time (8.6 ms), however, is slightly longer than the predicted value ( $\sim 7 \text{ ms}$ ), whereas the predicted flame-standoff distance, defined as the location of the peak value of CN concentration profile, is slightly longer than the measurement.

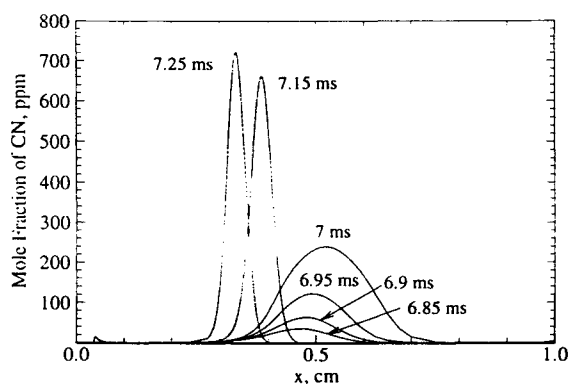


Fig. 24 Predicted concentration profiles of CN at various times.

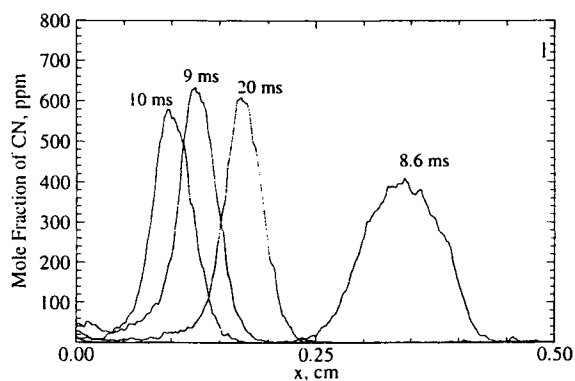


Fig. 25 Measured concentration profiles [23] of CN at various times.

Figure 26 shows the calculated and measured ignition delays of RDX induced by  $\text{CO}_2$  laser under atmospheric pressure. Excellent agreement is

achieved between the predicted and experimental data for laser intensities less than  $200 \text{ W/cm}^2$ . For  $400 \text{ W/cm}^2$ , the predicted ignition delay matches the measurements by Parr et al. [23] and Lee et al. [78]. However, the measured data of Vilyunov and Zarko [51] do not agree with the model prediction for laser intensities above  $200 \text{ W/cm}^2$ . Vilyunov and Zarko showed that the ignition delay increases with increasing laser intensity above  $200 \text{ W/cm}^2$ , whereas the results of the current model as well as Parr et al. [23] and Lee et al. [78] revealed the opposite trend. Vilyunov and Zarko [51] stated that the RDX ignition was controlled by the solid-phase kinetics at low laser intensities (below  $200 \text{ W/cm}^2$ ), whereas the gas-phase kinetics along with the liquid-phase decomposition governed the ignition process at high laser intensities. The current model, however, predicted that the gas-phase chemistry controlled the ignition process over the laser intensity range studied. Thus, the ignition delay became shorter at higher laser intensities, because the gasification rate at the propellant surface increased with increasing laser intensity. Vilyunov and Zarko [51] performed their experiment in both nitrogen and air under atmospheric pressure and found that the ignition delays were about the same within the measurement accuracy. Lee and Litzinger [78] utilized argon as an inert gas, whereas Parr and Hanson-Parr perform the experiment in air. The differences in ignition delay among these three sets of measured data, especially above  $200 \text{ W/cm}^2$ , can also be attributed to the variation in RDX sample preparation in each experiment. The RDX samples used by Parr and Hanson-Parr [23] and Lee and Litzinger [78] were pressed military-grade RDX. Information about the samples used by Vilyunov and Zarko [51] was not available.

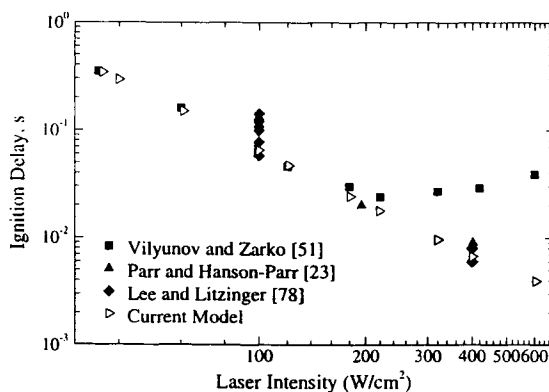


Fig. 26 Effect of  $\text{CO}_2$  laser intensity on ignition delay of RDX monopropellant.

In the experiment by Parr and Hanson-Parr [23], a significant time lag was obtained between the first light and go/no-go times (about 85 ~ 100 ms). First light was defined as the time when the luminous flame was first detected, whereas go/no-go was the time when a stable flame was achieved without the laser-assisted heating. The model predictions for the first light and go/no-go times, however, were about the same. In the experiments [23], the luminous flame progressed toward the surface immediately after the first light and moved away from the surface after the maximum temperature gradient was achieved near the surface. The model, however, did not predict this type of flame movement. The luminous flame continuously progressed toward the surface until steady-state deflagration was achieved. The discrepancy between model predictions and experimental observations may be attributed to the heat loss to the ambience. The entire ignition process was treated as adiabatic in the model, whereas heat losses from both the gas-phase flame and the condensed-phase region to the surrounding might be significant in the experiments, in which continuous laser heating was required in order to achieve self-sustained combustion by fully establishing the condensed flame. This suggests that during the ignition stage, heat loss in the condensed phase was too rapid compared to the heat transfer from the gas-phase flame to the surface.

The discrepancies among the existing experimental results may be attributed to the uncertainties associated with measurements under different types of experimental conditions. It is clearly evident that more measured data is needed for model validation. Nonetheless, the present model provides detailed insight into the key physiochemical processes involved in the laser-induced ignition of RDX, and can be effectively used to estimate ignition delay, heat release mechanisms, and flame structure.

#### **4.3. Steady-State Combustion of HMX/GAP and RDX/GAP Pseudo-Propellants**

Recently, Yang and co-workers performed numerical analyses to investigate the combustion characteristics of HMX/GAP and RDX/GAP pseudo-propellants over a broad range of pressure and laser intensity with various compositions [37-39]. Summaries of the model results for both HMX/GAP and RDX/GAP are given below.

##### **4.3.1 HMX/GAP Pseudo-Propellant**

Figure 27 shows the temperature and species-concentration profiles in the gas phase during HMX/GAP pseudo-propellant combustion at a CO<sub>2</sub> laser intensity of 100 W/cm<sup>2</sup> under atmospheric pressure. The ratio of HMX to GAP mass fraction is 8:2. Reasonable agreement was achieved with the experimental data reported in Ref. 3. The temperature rises rapidly from 677 K at the surface,

levels off around 1200-1600 K, and further increases to its final value at 2780 K. The flame can be divided into three regions: 1) the primary flame, 2) the dark zone, and 3) the secondary flame. The dark zone is a nonluminous region between the primary and the secondary flame, and is characterized with a temperature plateau. The concentrations of HCN, NO, and H<sub>2</sub>O in the dark zone appeared to be similar to those of pure nitramine propellants [3]. The rapid conversion of HCN and NO to N<sub>2</sub> and CO in the secondary flame zone were successfully predicted. The dominant net reactions in this stage are as follows.

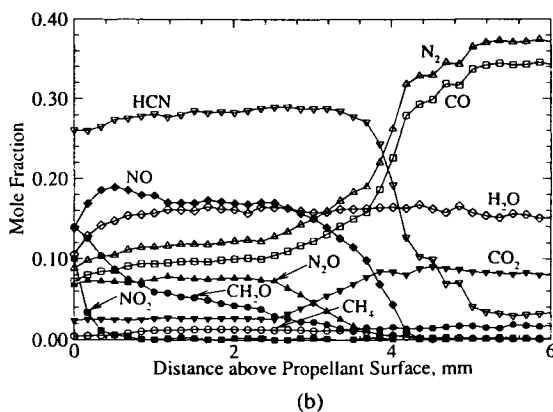
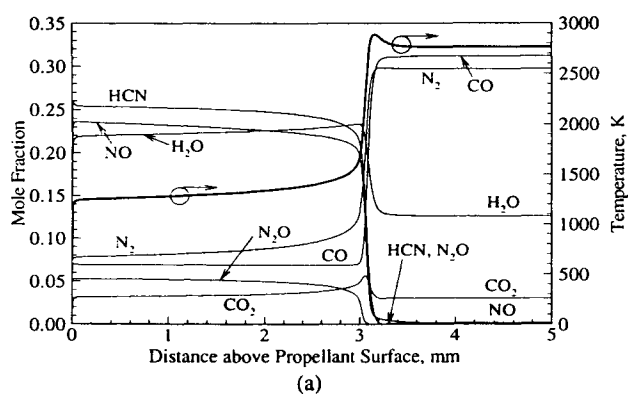


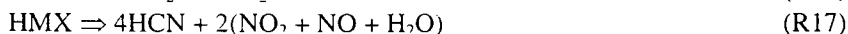
Fig.27 (a) Calculated and (b) measured [3] species-concentration profiles of gas-phase flame of HMX/GAP pseudo propellant (mass ratio 8:2) at 1 atm and laser intensity of 100 W/cm<sup>2</sup>.





These reactions are highly exothermic and usually take place at high temperatures due to their large activation energies. The predicted flame stand-off distance of 3 mm is slightly shorter than the measured value of 4 mm, partly because of the ambiguity in defining the propellant surface during experiments.

Figure 28 shows a close-up view of the primary flame immediately above the propellant surface, which extends over a length of 100  $\mu\text{m}$ . The dominant reactions in this oxidation stage are R16, R17, and R3.



The prediction of  $\text{N}_2\text{O}$  concentration was satisfactory compared with the measurement [3]; however,  $\text{NO}_2$  and  $\text{CH}_2\text{O}$  appear to be consumed too fast. Intermediate reactions forming  $\text{CH}_2\text{O}$  and  $\text{NO}_2$  are still lacking in the near-surface region in order to yield better agreement with experimental results. Conversion of GAP and  $\text{GAP}^*$  to  $\text{N}_2$ ,  $\text{HCN}$ ,  $\text{CO}$ ,  $\text{NH}_3$ ,  $\text{CH}_2\text{O}$ ,  $\text{CH}_3\text{CHO}$ ,  $\text{H}_2\text{O}$ ,  $\text{C}_2\text{H}_3\text{CHO}$ ,  $\text{C}_2\text{H}_4$ ,  $\text{CH}_3\text{CHNH}$ , and  $\text{CH}_2\text{CHCHNH}$  occurs in a very short distance ( $\sim 10 \mu\text{m}$ ). The GAP decomposition is a highly exothermic process releasing a significant amount of energy in the gas phase. However, at the same time, the heat feedback from the gas phase to the surface is reduced due to the dilution of reactive species by the GAP pyrolysis gases. The decomposed fuel fragments, such as  $\text{CH}_2\text{CHO}$ ,  $\text{C}_2\text{H}_3\text{CHO}$ ,  $\text{CH}_3\text{CHNH}$ , and  $\text{CH}_2\text{CHCHNH}$ , further react to form  $\text{CH}_3$ ,  $\text{HCO}$ ,  $\text{C}_2\text{H}_3$ , and  $\text{H}_2\text{CN}$ .

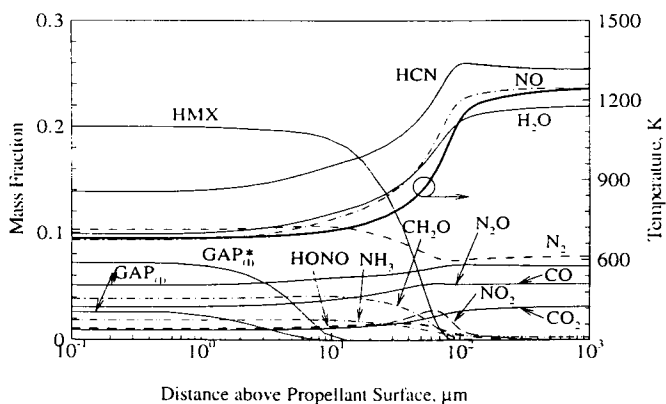


Fig. 28 Temperature and species-concentration profiles in near-surface region of HMX/GAP pseudo propellant (mass ratio 8:2) combustion at 1 atm and laser intensity 100  $\text{W}/\text{cm}^2$ .

The species-concentration and temperature profiles in the foam layer are shown in Fig. 29. An appreciable amount of HMX evaporates to form gas bubbles in this region, but the extent of decomposition through the pathways (R1) and (R2) appears to be limited. On the other hand, most of the GAP compound is consumed to become GAP\* and  $N_2$ , releasing heat to support pyrolysis in the condensed phase. Further decomposition of GAP\* according to (R4), however, is constrained due to the low temperature condition. The predicted surface temperature and foam-layer thickness are 677 K and 30  $\mu\text{m}$ , respectively.

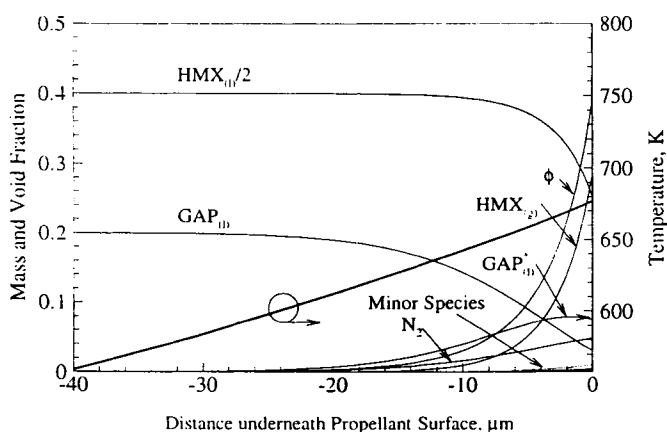


Fig. 29 Temperature and species-concentration profiles in subsurface of HMX/GAP pseudo propellant (mass ratio 8:2) combustion at 1 atm and laser intensity of 100 W/cm<sup>2</sup>.

Figure 30 presents the corresponding temperature sensitivity of burning rate, which appears to be independent of pressure and has a value twice greater than that of pure HMX. In general, the effect of preconditioned temperature on propellant burning rate diminishes with increasing pressure and impressed laser intensity. The enhanced heat transfer to the propellant surface due to large energy release and reduced flame standoff distance in the gas phase at elevated pressure overrides the influence of preconditioned temperature in determining the energy balance at the surface, and consequently decreases the temperature sensitivity of burning rate.

Figure 31 shows the effect of propellant composition on burning rate at various pressures. The burning rate in general decreases with the addition of GAP, which releases a substantial amount of  $N_2$  through the C-N<sub>3</sub> bond breaking in the near-surface region. Although the process is exothermic, the pressure of  $N_2$  and large fuel fragments dilute the concentrations of surface



reactive species, and consequently reduces the rate of energy release from HMX reactions. The heat feedback to the surface decreases accordingly, rendering a lower burning rate. Another factor contributing to this phenomenon is the blowing effect of the GAP compound, which tends to push the primary flame away from the surface. The situation is, however, different at high pressures. The burning rate of HMX/GAP pseudo-propellant with a mass ratio of 9:1 is greater than that of pure HMX for  $p > 30$  atm.

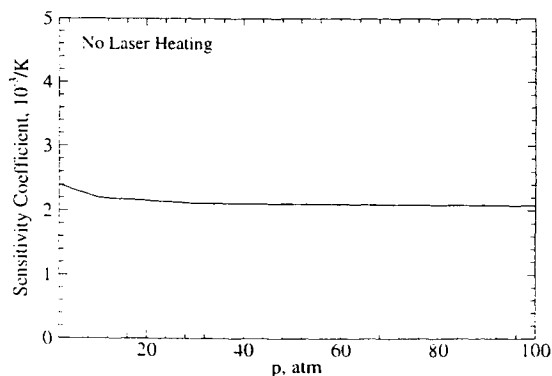


Fig. 30 Temperature sensitivity of burning rate of HMX/GAP pseudo propellant (mass ratio 8:2); self-sustained combustion.

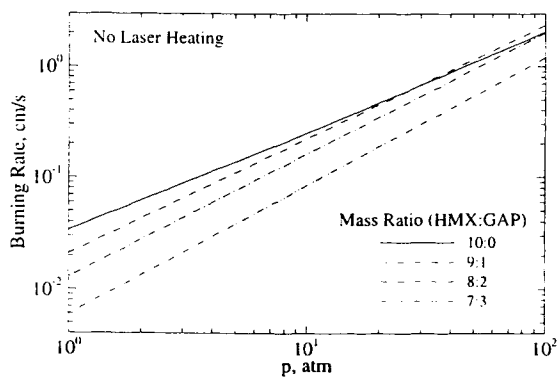


Fig. 31 Effect of propellant composition on burning rate at various pressures; self-sustained combustion.

Figures 32 and 33 show the effect of laser intensity on burning rate for several mixture ratios at 10 and 100 atm, respectively. At 10 atm, the burning

rate increases with increasing  $\text{CO}_2$  laser intensity. Although GAP decomposition is highly exothermic, the burning rate decreases with increasing GAP concentration since the fuel-rich pyrolysis products of GAP reduce the flame temperature and move the flame away from the surface. At a high pressure of 100 atm, the intensive heat transfer from the flame to the surface overrides the effect of surface radiant energy absorption. The burning rate thus appears to be insensitive to the impressed laser intensity. The influence of GAP concentration on burning rate exhibits a different trend from that at 10 atm due to the variation of surface temperature, a phenomenon that has been elaborated in connection with the discussion of Fig. 31.

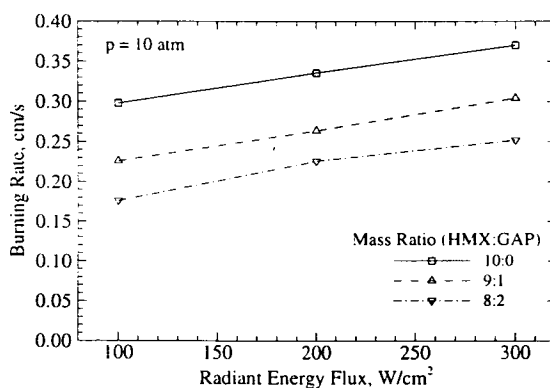


Fig. 32 Effect of propellant composition on burning rate at various  $\text{CO}_2$  laser intensities;  $p = 10$  atm.

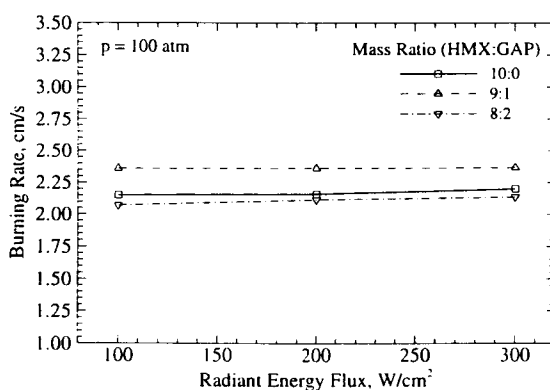


Fig. 33 Effect of propellant composition on burning rate at various  $\text{CO}_2$  laser intensities;  $p = 100$  atm.

The effects of laser heat flux and pressure on the burning rate of HMX/GAP pseudo-propellant (mass ratio 8:2) are shown in Fig. 34. The impressed laser flux causes a substantial increase in burning rate at low pressures (e.g., 1 and 10 atm). The effect, however, diminishes at high pressure, since the heat feedback from the gas phase overshadows the surface laser absorption in determining the energy balance at the surface, as shown in Fig. 35. The heat transfer to the burning surface increases almost linearly with pressure. Figure 36 shows the propellant surface temperature as a function of radiant heat flux at several pressures. The trend resembles that for the burning rate shown in Fig. 34.

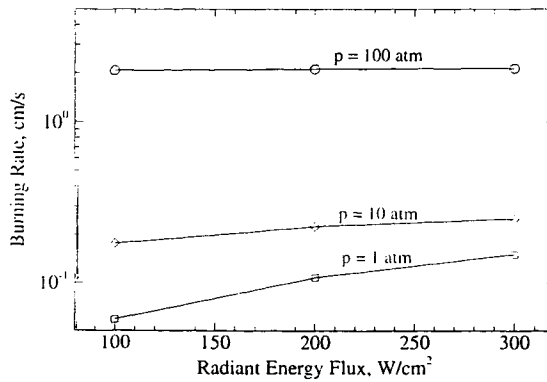


Fig. 34 Effect of pressure on burning rate at various  $CO_2$  laser intensities (HMX/GAP mass ratio 8:2).

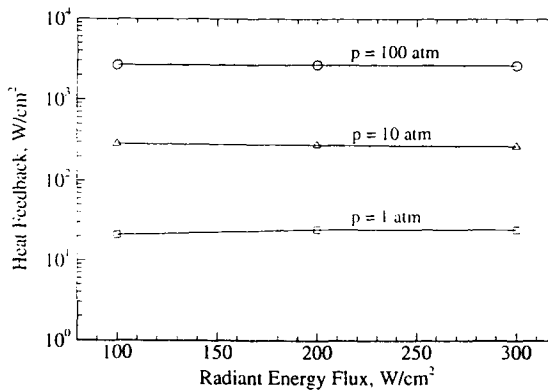


Fig. 35 Heat feedback to propellant surface at various  $CO_2$  laser intensities and pressures (HMX/GAP mass ratio 8:2).

The melt-layer thickness and surface void fraction are shown in Figs. 37 and 38, respectively. They both decrease with increasing radiant heat flux at low pressure, but remain almost fixed at high pressure. It should be noted that the bubble formation rate can be enhanced with increasing temperature, but may also be reduced by the decreased residence time resulting from the increased burning rate at high temperature. The present case shows a net decrease in the surface void fraction with increasing pressure.

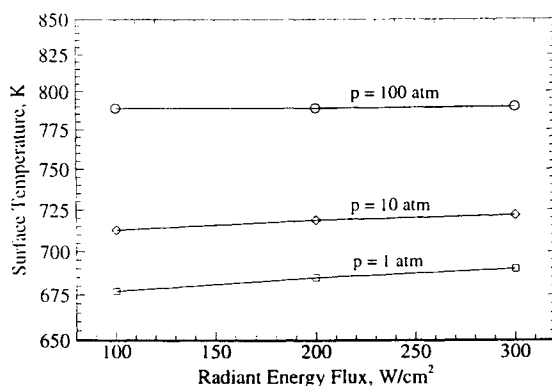


Fig. 36 Effect of  $\text{CO}_2$  laser intensity on surface temperature at various pressures (HMX/GAP mass ratio 8:2).

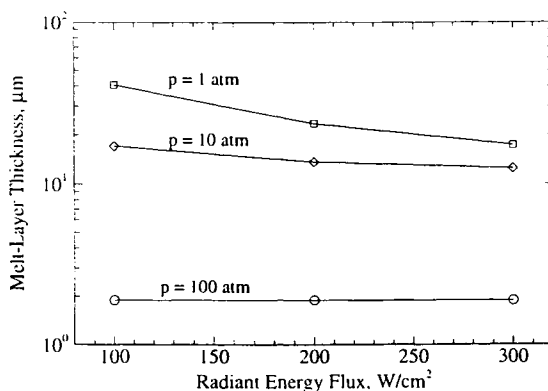


Fig 37 Effect of  $\text{CO}_2$  laser intensity on melt-layer thickness at various pressures (HMX/GAP mass ratio 8:2).

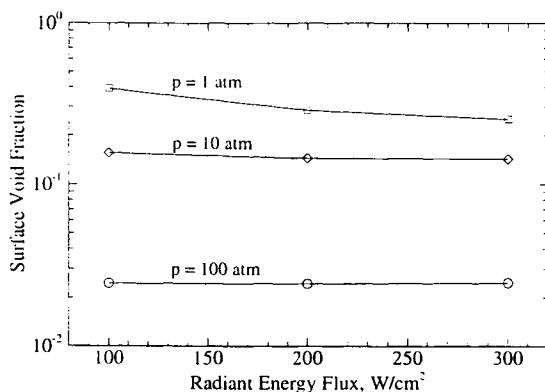
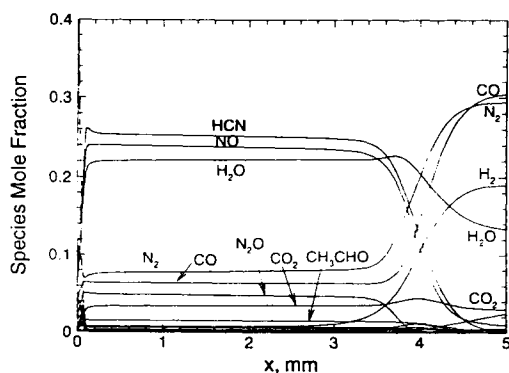


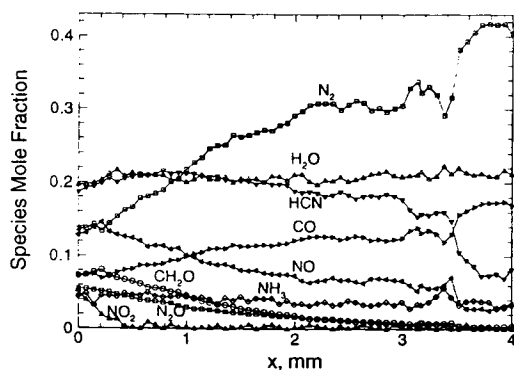
Fig. 38 Effect of  $\text{CO}_2$  laser intensity on surface void fraction at various pressures (HMX/GAP mass ratio 8:2).

#### 4.3.2 RDX/GAP Pseudo-Propellant

In general, the results from the RDX/GAP combustion model described in Ref. 38 show good agreement with the measured burning rates at atmospheric pressure. The measured burning rate of RDX/GAP pseudo propellant with a mass ratio 8:2 was 0.8 mm/s at 1 atm with a  $\text{CO}_2$  heat flux of  $100 \text{ W/cm}^2$ . The calculated value at the same condition was 0.88 mm/s. At  $300 \text{ W/cm}^2$ , the measured and predicted burning rates were 1.9 and 2.18 mm/s, respectively. The flame structure observed in experiments using TQMS [3] was also reasonably well predicted by the model. Figure 39 shows the predicted and measured [3] species concentration profiles in the gas phase at 1 atm and  $100 \text{ W/cm}^2$ . Similar to the HMX/GAP combustion, it is found that HCN, NO, and  $\text{H}_2\text{O}$  are the major intermediate products in the dark zone. The conversion of HCN and NO to  $\text{N}_2$  and CO dominates the luminous flame while the consumption of formaldehyde,  $\text{NO}_2$ , and  $\text{N}_2\text{O}$  accounts for the primary flame above the surface. In contrast to RDX combustion, a noticeable amount (1-2%) of  $\text{CH}_3\text{CHO}$  was observed near the surface. Here, the agreements between the predicted and measured concentration profiles of CO,  $\text{CO}_2$ , and formaldehyde are not as good as the others. Chemical equilibrium calculation was also performed. This calculation result matches the model output but not the experimental data. Even though the agreement between measured and computed burning rates is reasonably good, further investigations into the combustion wave are suggested to resolve the discrepancy in flame structure.



(a)



(b)

Fig. 39 (a) Calculated and (b) measured [3] species profiles of the gas-phase flame of RDX/GAP pseudo propellant (mass ratio 8:2) at 1 atm and laser intensity  $100 \text{ W/cm}^2$ .

In the foam layer, Fig. 40 shows that the predicted temperature rises from the melt point of RDX at 478 K to around 590 K at the propellant surface. The mass fraction of liquid RDX originates at 0.8 and decreases slightly mostly through evaporation and partially through decomposition. The void fraction increases from 0 to almost 9 % due to the formation of bubbles containing vapor RDX and a small amount of decomposed gases. Consistent with the condensed-phase kinetics, the extent of GAP decomposition is negligible at temperatures lower than 600 K. The mass fraction of GAP remains at 0.2 throughout the foam layer, and then evolves into the gas phase. Figure 41 shows the predicted temperature, void fraction, and condensed species

concentration profiles in the region immediately above the propellant surface. GAP starts to decompose in the gas phase when the temperature reaches 700 K. At this stage,  $\text{GAP}^*$  is immediately formed due to the elimination of  $\text{N}_2$  and reaches its maximum concentration within a short distance (less than 0.004 cm). The peak value of  $\text{GAP}^*$  mass fraction is less than 10%. The calculated concentration of carbon residue in this case is negligible. If the propellant surface is defined as the location where all condensed species are gasified, the surface temperature would be around 1000 K, consistent with GAP combustion.

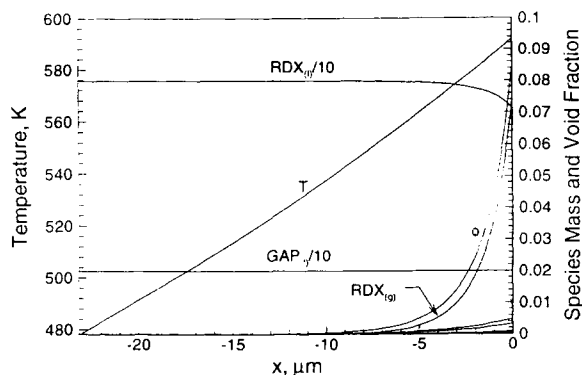


Fig. 40 Predicted flame structure in the foam layer of RDX/GAP pseudo propellant (mass ratio 8:2) at 1 atm and laser intensity  $100 \text{ W/cm}^2$ .

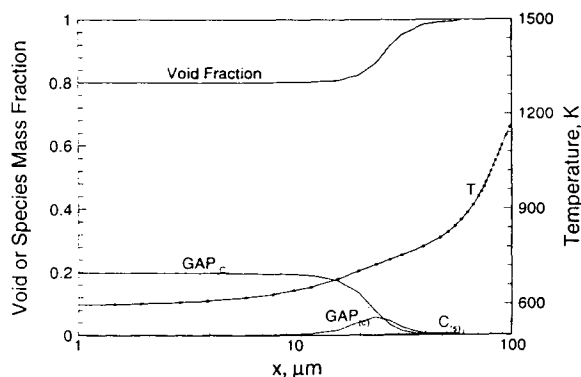


Fig. 41 Predicted temperature, void fraction, and condensed species concentration profiles in the near surface region of RDX/GAP pseudo propellant (mass ratio 8:2) at 1 atm and laser intensity  $100 \text{ W/cm}^2$ .

Figure 42 shows the predicted pressure dependence of burning rate for a RDX/GAP pseudo-propellant with a mass ratio of 8:2. It is found that the burning rate-pressure relation follows a power law which is applicable to many propellants with the exponent  $n = 1$ , whereas  $n = 0.83$  for pure RDX. The exponent value  $n = 1$  indicates that the addition of GAP does alter the combustion characteristics of RDX. Figure 43 shows the temperature sensitivity defined in Eq. (35) of burning rate at various pressures. The temperature sensitivity of burning rate decays at high pressures since the heat feedback is more profound than the effect of initial temperature on the burning rate.

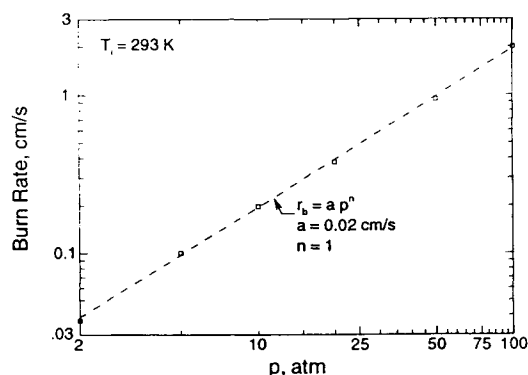


Fig. 42 Predicted pressure dependence of burning rate of RDX/GAP pseudo propellant (mass ratio 8:2).

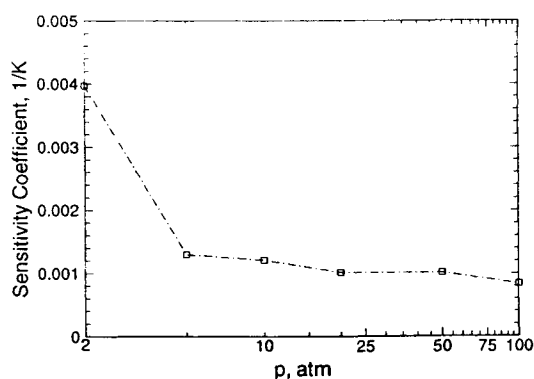


Fig. 43 Predicted temperature sensitivity of burning rate of RDX/GAP pseudo propellant (mass ratio 8:2).



Similar to results of the HMX/GAP analysis, the combustion characteristics of RDX/GAP pseudo-propellant at various pressures and initial temperatures were investigated [38]. The surface temperature increases linearly with increasing pressure on the logarithmic scale, but it is not very sensitive to the initial temperature. This is understandable because the surface temperature is resolved by an energy balance, and the heat flux is strongly dependant on the pressure but not the initial temperature. The adiabatic flame temperature increases with both increasing pressure and initial temperature. The increase is not linear due to the limitation of grid resolution and the non-linearity of chemical kinetics. The melt-layer thickness decreases with increasing pressure but is not sensitive to the initial temperature. In general, the melt-layer thickness decreases with increasing burning rate, but increases with the higher values of thermal conductivity of the propellant. As shown in Fig. 42, the burning rate is linearly dependant on pressure, and thus the pressure dependence of melt-layer thickness is also linear. The initial temperature of propellant does not exhibit a strong effect on the melt-layer thickness, because both the burning rate and thermal conductivity are not very sensitive to the initial temperature. The surface void fraction decreases with increasing pressure, but increases with increasing initial temperature. It is not surprising because the bubble formation strongly depends on the evaporation process, which is retarded at high pressures but enhanced at high initial temperatures.

The effects of laser heat flux on the burning rate, surface heat flux, surface temperature, melt-layer thickness, and surface void fraction at pressure levels of 1, 10, and 100 atm were numerically investigated. The burning rate and surface temperature increase with increasing laser heat flux. The effect decays with increasing pressure because the heat feedback from the gas phase increases with increasing pressure. The melt-layer thickness exhibits an opposite trend; it decreases with increasing burning rate, and its decreasing rate is consistent with the increasing rate of burning rate. In contrast to the heat feedback from the gas phase at high pressures, the laser heat flux increases bubble formation, up to 50% at the surface at 1 atm and  $300 \text{ W/cm}^2$ .

The final set of results show the effects of binder mass fraction on combustion characteristics over a broad range of pressure and initial temperature. Here, it is possible to utilize the model to describe experimental observations. For example, the burning rate of pure GAP is higher than that of HMX, but the addition of GAP into HMX lowers the burning rate [24]. In contrast, recent measurements [3] show the enhancement of burning rate by adding GAP into RDX or HMX. Both observations have been reproduced by the model. Figure 44 shows the effects of initial composition and pressure on the burning rate of RDX/GAP pseudo propellants. The burning rate decreases in the case of higher GAP composition because GAP decomposition produces

inert gases that dilute the concentrations of surface reactive species, and thus retard the heat feedback from the gas phase, as shown in Fig. 45.

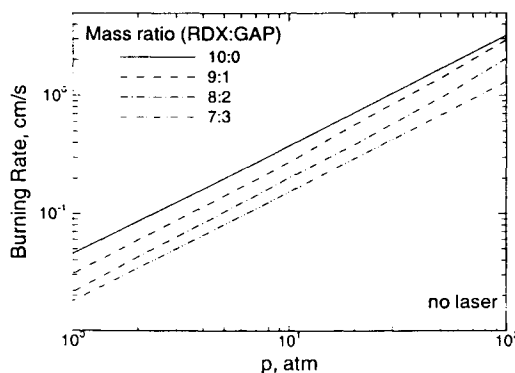


Fig. 44 Predicted effect of propellant formulation on burning rate at various pressures.

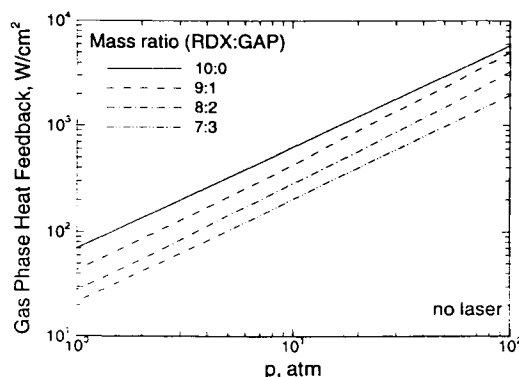


Fig. 45 Calculated gas-phase heat feedback to propellant surface at various composition and pressure levels.

It is evident that the heat feedback is a controlling factor for the burning rate in all the cases without laser, because the pressure dependence of burning rate follows the same trend as that of heat feedback. The addition of GAP modifies the slopes (pressure dependencies) in Figs. 44 and 45, but not in a consistent manner. A small amount of GAP (10% by weight) increases the slope and makes the system unstable, while more GAP (30% by weight) restores the slope to the pure RDX case but reduces the burning rate by more than 50%. Figure

46 shows the burning rates at 10 atm with various compositions and laser levels. The profiles of mass ratios 10:0 and 9:1 are very close, indicating the burning-rate change due to the addition of a small amount of GAP is negligible for laser heat fluxes ranging from 100 to 300 W/cm<sup>2</sup>. For higher GAP compositions (20 and 30 % by weight), the burning rates decrease at 100 W/cm<sup>2</sup>, but increase at 200 and 300 W/cm<sup>2</sup>. The effect is more profound at low pressures since the conductive heat feedback from the gas phase is of less importance in the case of laser-assisted combustion. More experimental data, however, is required for model validation as well as an improved chemical kinetics mechanism of GAP decomposition.

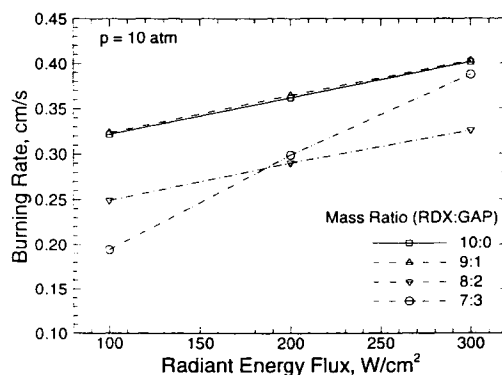


Fig. 46 Predicted effect of propellant formulation on burning rate at various laser and composition levels.

## CONCLUDING REMARKS

Comprehensive analyses have been developed and performed to investigate the steady-state combustion and transient ignition behavior of nitramine monopropellants and nitramine/GAP pseudo-propellants. The combustion-wave structures of these propellants were numerically studied over a wide range of operating conditions. These models accommodate detailed chemical kinetics and transport phenomena in the gas phase, and thermal decomposition and phase transition in the condensed phase. Parametric studies were carried out to investigate the propellant burning characteristics and chemical pathways, with special attention given to the effects of the subsurface two-phase region on the flame behavior. In general, good agreement between the measured and predicted burning rates as well as their temperature and pressure sensitivities was achieved. The calculated species profiles matched reasonably well with the measurements. The steady-state combustion model was extended to simulate

the entire laser-induced ignition process of RDX monopropellant. Emphasis was placed on the ignition delay and key physiochemical processes responsible for achieving ignition. The predicted ignition delay shows good agreement with experimental data. The propellant gasification rate increases with increasing laser intensity, which in turn gives rise to a shorter ignition delay. In spite of the accomplishments achieved so far, several challenges remains to be circumvented. One major difficulty in both experimental and theoretical investigations lies in the treatment of the two-phase near-surface region, which includes an array of intricacies such as thermal decomposition, subsequent reactions, evaporation, bubble formation and interaction, and interfacial transport of mass and energy between the gas and condensed phases. Nonetheless, the existing models provide a solid basis for investigating various underlying processes involved in the combustion and ignition of energetic materials.

## ACKNOWLEDGEMENTS

This work was supported partly by the Pennsylvania State University, partly by the Army Research Office under Contract DAAL 03-92-G-0118, and partly by the California Institute of Technology Multidisciplinary University Research Initiative under ONR Grant No. N00014-95-1-1338. The authors are indebted to Dr. Yeong Cherng (John) Liao for his contributions in developing the RDX ignition and combustion models.

## REFERENCES

- [1] T.P. Parr and D.M. Hanson-Parr, in *Solid Propellant Chemistry, Combustion, and Motor Interior Ballistics*, (V. Yang, T. B. Brill, and W. Z., Ren, Eds.), Vol. 185, Progress in Astronautics and Aeronautics, AIAA, Reston, VA, 2000 pp. 381-411.
- [2] O.P. Korobeinichev, in *Solid Propellant Chemistry, Combustion, and Motor Interior Ballistics*, (V. Yang, T. B. Brill, and W. Z., Ren, Eds.), Vol. 185, Progress in Astronautics and Aeronautics, AIAA, Reston, VA, 2000, pp. 335-354.
- [3] T.A. Litzinger, Y.-J. Lee, and C.-J. Tang, in *Solid Propellant Chemistry, Combustion, and Motor Interior Ballistics*, (V. Yang, T. B. Brill, and W. Z., Ren, Eds.), Vol. 185, Progress in Astronautics and Aeronautics, AIAA, Reston, VA, 2000, pp. 355-379.
- [4] D. Chakraborty, D. and M.C. Lin, in *Solid Propellant Chemistry, Combustion, and Motor Interior Ballistics*, (V. Yang, T. B. Brill, and W. Z., Ren, Eds.), Vol. 185, Progress in Astronautics and Aeronautics, AIAA, Reston, VA, 2000, pp. 33-71.
- [5] T. B. Brill, M. C. Beckstead, J. E., Flanagan, M. C. Lin, T. A. Litzinger, R. H. W. Waesche, and C. A. Wight, *J. Prop. Power*, No. 18 (2002) 824.
- [6] B.C. Beard, *Propellants, Explosives, and Pyrotechnics*, Vol. 16 (1991) 81.

- [7] H.H. Krause, N. Eisenreich, and A. Pfeil, *Propellants, Explosives, and Pyrotechnics*, Vol. 17 (1992) 179.
- [8] R. Behrens, Jr. and S.N. Bulusu, *J. Phys. Chem.*, Vol. 96 (1992) 8877.
- [9] C.A. Wight and T.R. Botcher, *J. Amer. Chem. Soc.*, Vol. 114 (1992) 8303.
- [10] R.R. Botcher and C.A. Wight, *J. Phys. Chem.*, Vol. 97 (1993) 9149.
- [11] A. Zenin, *J. Prop. Power*, Vol. 11 (1995) 752.
- [12] T.B. Brill, *J. Prop. Power*, Vol. 11 (1995) 740.
- [13] E.S. Kim, H.S. Lee, C.F. Mallery, and S.T. Thynell, *Combust. Flame* Vol. 110 (1997) 239.
- [14] T.A. Litzinger, B.L. Fetherolf, Y.-J. Lee, and C.-J. Tang, *J. Prop. Power*, Vol. 11, (1995) 698.
- [15] S.T. Thynell, P.E. Gongwer, and T.B. Brill, *J. Prop. Power*, Vol. 12 (1996) 933.
- [16] C.Y. Lin, H.I. Wang, M.C. Lin, and C.F. Williams, *Intern. J. Chem. Kinetics*, Vol. 22 (1990) 455.
- [17] D.M. Hanson-Parr and T.P. Parr, *J. Energetic Materials*, Vol. 17 (1999) 1.
- [18] R.A. Isbell and M.Q. Brewster, *Propellants, Explosives, and Pyrotechnics*, Vol. 23 (1998) 218.
- [19] T.B. Brill, *Prog. Energy Combust. Sci.*, Vol. 18 (1992) 91.
- [20] R.A. Isbell and M.Q.J. Brewster, *Thermophysics and Heat Transfer*, Vol. 11 (1997) 65.
- [21] A.I. Atwood, T.L. Boggs, P.O. Curran, T.P. Parr, and D.M. Hanson-Parr, *J. Prop. Power*, Vol. 15 (1999) 740.
- [22] O.P. Korobeinichev, L.V. Kuibida, V.N. Orlov, A.G. Tereshchenko, K.P. Kutsenogii, R.V. Mavliev, N.E. Ermolin, V.M. Fomin, and I.D. Emel'yanov, *Mass-Spektrom. Khim. Kinet.*, (1985) 73.
- [23] T.P. Parr and D.M. Hanson-Parr, *Twenty-Seventh Symp. (International) on Combust.*, The Combust. Institute, Pittsburgh (1998) 2301.
- [24] N. Kubota and T. Sonobe, *Twenty-Third Symp. (International) on Combust.* (1990) 1331.
- [25] C.F. Melius, in *Chemistry and Physics of Energetic Materials* (S. Bulusu, Ed.), Kluwer Academic, Norwell, MA, 1990, pp.21-78.
- [26] R.A. Yetter, F.L. Dryer, M.T. Allen, and J.L. Gatto, *J. Prop. Power*, Vol. 11 (1995) 666.
- [27] S.C. Li, F.A. Williams, and S.B. Margolis, *Combust. Flame*, Vol. 80 (1990) 329.
- [28] S.B. Margolis and F.A. Williams, *J. Prop. Power*, Vol. 11 (1995) 759.
- [29] S.C. Li and F.A. Williams, *J. Prop. Power*, Vol. 12 (1996) 302.
- [30] K. Prasad, R.A. Yetter, and M.D. Smooke, *Combust. Sci. Tech.*, Vol. 124 (1997) 35.
- [31] K. Prasad, M. Smooke, and R.A. Yetter, *Combust. Flame*, Vol. 115 (1998) 406.
- [32] M.S. Miller and W.R. Anderson, in *Solid Propellant Chemistry, Combustion, and Motor Interior Ballistics*, (V. Yang, T. B. Brill, and W. Z., Ren, Eds.), Vol. 185, *Progress in Astronautics and Aeronautics*, AIAA, Reston, VA, 2000, pp. 501-531.
- [33] Y.-C. Liao, The Pennsylvania State University, Department of Mechanical Engineering, Ph.D. Diss., 1996.
- [34] Y.-C. Liao, and V. Yang, *J. Prop. Power*, Vol. 11 (1995) 729.
- [35] J.E. Davidson and M.W. Beckstead, *J. Prop. Power*, Vol. 13 (1997) 375.
- [36] J.E. Davidson and M.W. Beckstead, *Twenty-Sixth Symp. (International) on Combust.*, The Combust. Institute (1996) 1989.
- [37] E.S. Kim, V. Yang, and Y.-C. Liao, *Combust. Flames*, Vol. 131 (2002) 227.
- [38] Y.-C Liao, V. Yang, and S.T. Thynell, in *Solid Propellant Chemistry, Combustion, and Motor Interior Ballistics*, (V. Yang, T. B. Brill, and W. Z., Ren, Eds.), Vol. 185, *Progress in Astronautics and Aeronautics*, AIAA, Reston, VA, 2000, pp. 477-500.

- [39] E.S. Kim, The Pennsylvania State University, Department of Mechanical Engineering, Ph.D. Diss., 2000.
- [40] Y.-C. Liao, E.S. Kim, and V. Yang, *Combust. Flames*, Vol. 126 (2001) 1680.
- [41] Y.-C. Liao and V. Yang, *AIAA Paper* 97-0589, 1997.
- [42] M. Benreuen, L.H. Caveny, R.J. Vichnevetsky, and M. Summerfield, *Sixteenth Symp. (International) on Combust., The Combust. Institute* (1976) 1223.
- [43] N.E. Ermolin, O.P. Korobeinichev, L.V. Kuibida, and V.M. Formin, *Fizika Goreniya i Vzryva*, Vol. 22, (1986) 54.
- [44] T.L. Boggs, in *Fundamentals of Solid Propellant Combustion*, (K.K. Kuo and M. Summerfield, Eds.), Vol. 90, *Progress in Astronautics and Aeronautics*, 1984, pp.121-175.
- [45] R.A. Fifer, in *Fundamentals of Solid Propellant Combustion*, (K.K. Kuo and M. Summerfield, Eds.), Vol. 90, *Progress in Astronautics and Aeronautics*, 1984, pp.177-237.
- [46] M.H. Alexander, P.J. Dagdigian, M.E. Jocox, C.E. Kolb, C.F. Melius, H. Rabitz, M. Smooke, and W. Tsang, *Prog. in Energy Combust. Sci.*, Vol. 17 (1991) 263.
- [47] V. Yang, T.B. Brill, and W.Z. Ren. (Eds.), *Solid Propellant Chemistry, Combustion, and Motor Interior Ballistics*, Vol. 185, *Progress in Astronautics and Aeronautics*, AIAA, Reston, VA. 2000. 990 pages.
- [48] E.W. Price, H.H. Bradley, G.L. Dehority, and M.M. Ibricu, *AIAA J.* Vol. 4 (1966) 1153.
- [49] A.K. Kulkarni, M. Kumar, and K.K. Kuo, *AIAA J.* Vol. 20 (1982) 243.
- [50] C.E. Hermance, in *Fundamentals of Solid Propellant Combustion*, (K. Kuo and M. Summerfield, Eds.), Vol. 90, *Progress in Astronautics and Aeronautics*, 1984, pp. 239-304.
- [51] V.N. Vilyunov and V.E. Zarko, *Ignition of Solids*, Elsevier Science Publishers, NY, 1989.
- [52] L. Strakouskiy, A. Cohen, R. Fifer, R. Beyer, and B. Forch, *Laser Ignition of Propellants and Explosives*, ARL-TR-1699, Army Research Laboratory, Aberdeen Proving Ground, MD, 1998.
- [53] S.D. Baer and N.W. Ryan, *AIAA J.*, Vol. 6 (1968) 872.
- [54] H.H. Bradley, *Combust. Sci. Technol.*, Vol. 2 (1970) 11.
- [55] A. Linan, and F.A. Williams, *Combust. Sci. Technol.*, Vol. 3 (1971) 91.
- [56] A. Linan, and F.A. Williams, *Combust. Flame*, Vol. 18 (1972) 85.
- [57] F.A. Williams, *AIAA J.*, Vol. 4 (1966) 1354.
- [58] C.H. Waldman and M. Summerfield, *AIAA J.*, Vol. 7 (1969) 1359.
- [59] C.H. Waldman, *Combust. Sci. Technol.*, Vol. 2 (1970) 81.
- [60] H.H. Bradley and F.A. Williams, *Combust. Sci. Technol.*, Vol. 2 (1970) 41.
- [61] W.H. Andersen, *Combust. Sci. Technol.*, Vol. 2 (1970) 23.
- [62] W.H. Andersen, *Combust. Sci. Technol.*, Vol. 5 (1972) 43.
- [63] W.H. Andersen, *Combust. Sci. Technol.*, Vol. 5 (1972) 75.
- [64] A. Linan, and A. Crespo, *Combust. Sci. Technol.*, Vol. 6 (1972) 223.
- [65] T. Niioka, *Combust. Sci. Technol.* Vol., 18 (1978) 207.
- [66] C.E. Hermance, R. Shinnar, and M. Summerfield, *Astronautica Acta*, Vol. 12 (1966) 95.
- [67] T. Kashiwagi, B.W. MacDonald, H. Isoda, and M. Summerfield, *Thirteenth Symp. (International) on Combust., Combust. Institute, Pittsburgh* (1971) 1073.
- [68] C.E. Hermance and R.K. Kumar, *AIAA J.*, Vol. 8 (1970) 1551.
- [69] R.K. Kumar and C.E. Hermance, *AIAA J.*, Vol. 9: (1971) 615.
- [70] R.K. Kumar and C.E. Hermance, *Combust. Sci. Technol.*, Vol. 4 (1972) 191.

- [71] R.K. Kumar and C.E. Hermance, *Combust. Sci. Technol.*, Vol. 14 (1976) 169.
- [72] M. Kindelan, and F.A. Williams, *Combust. Sci. Technol.*, Vol. 16 (1977) 47.
- [73] S. Ritchie, S. Thynell, and K.K Kuo, *J. Prop. Power*, Vol. 13 (1997) 367.
- [74] K. Puduppakkiam and M.W. Beckstead, 37<sup>th</sup> JANNAF Combust. Subcomm. Meeting, CPIA Publ. 2000.
- [75] M.F. Modest, *Radiative Heat Transfer*, McGraw-Hill, New York, 1993, pp. 438-449.
- [76] C.J. Pouchert, *The Aldrich Library of FT-IR Spectra*, Aldrich Chemical Co., Wisconsin, Vols. 1-3, 1997.
- [77] R.J. Kee, J.F. Grcar, M.D. Smooke, and J.A. Miller, A Fortran Program for Modeling Steady, Laminar, One-Dimensional, Premixed Flames, Sandia Report SAND85-8240, Sandia National Laboratories, Albuquerque, NM, 1985.
- [78] Y.J. Lee and T.A. Litzinger, Private Communication, The Pennsylvania State University, University Park, PA, 1995.

## *Chapter 10*

# **Use of Kinetic Models for Solid State Reactions in Combustion Simulations**

***J. Wang and C. A. Wight***

Department of Chemistry, University of Utah, 315 S. 1400 E., Salt Lake City, Utah, United States

## **1. INTRODUCTION**

Combustion of energetic materials usually involves a complex interaction between the solid, which generates gaseous reactants, and the gas phase flame, which generates most of heat required to sustain the combustion. All current combustion simulations of energetic materials make the assumption that the first step is a zero-order conversion of condensed phase to gas phase chemical intermediates. However, most propellants are complex composite mixtures of oxidizer, fuel, binder, cross-linker and plasticizers, each of these components react in different temperature range. The natural consequence of this is to give the burning surface a dynamic structure, in which the high-temperature components of the propellant will tend to aggregate at the surface, while lower-temperature components will tend to be burned out of the sub-surface layers as they are heated by the flame. Even for monopropellants, the burning surface is complicated physically and chemically. Scanning electron micrographs show that HMX crystals become highly porous during decomposition below the melting point [1, 2]. This porosity leads to an increase in the surface area of the crystal available for reaction and accounts for the apparently autocatalytic nature of the reaction, which means that a zero-order reaction model is a simplifying assumption. Because the choice of reaction model may have a significant influence on surface structure and energy feedback from the flame, it is desirable to determine the proper kinetic rate laws for condensed phase propellant reactions and incorporate them into combustion simulations in order to obtain valid results.

To accomplish this goal, we chose to construct a transient combustion model. Although the formulation of time-dependent combustion models involves considerably more effort than steady models, we felt that the extra effort was



required because steady-state combustion models are often “self-correcting” with respect to kinetic parameters. That is, the parameters are often flexible enough to provide the appropriate rate of gas formation at the surface, and the combustion properties are relatively insensitive to other features such as temperature profile in the solid. Conversely, time-dependent numerical models of solid propellant combustion are more sensitive to the use of the proper kinetic parameters, and this provides a means of testing many time-dependent characteristics of combustion of energetic materials (*e.g.*, ignition/extinction, unstable oscillatory combustion, deflagration-to-detonation transition, combustion stability).

### 1.1. Steady combustion models vs. Unsteady combustion models

The detailed study of propellant combustion presents an experimental challenge because this process involves complex interactions that can occur very rapidly and can be difficult to detect. As a result, simulation studies of propellant combustion have become increasingly common for more than 30 years. All numerical models of solid-propellant combustion fall into two major categories: steady-state burning models and non-steady or transient combustion models. Although phenomenological models, which are parameterized via mass burning rate measurements, can often adequately describe steady-state deflagration, the accurate predication of non-steady or transient combustion requires a more detailed knowledge of the chemistry and kinetics involved. A steady-state combustion model always contains enough user-defined parameters to obtain the desired results (*e.g.*, burn rate). However, extension of the model to more kinetically controlled environments such as unstable or transient combustion is error prone if the correct kinetic information is not included. Fully nonlinear numerical models of solid propellant burning must be retained if one wishes to accurately predict transient burning and in particular “critical” situations such as ignition or extinction. This means that we must account for temperature-dependent thermal properties and chemical reactions and use the proper kinetic models in both the surface and gas phase reactions.

Kuo and Gore have written a good, general introduction to solid propellant transient burning [3]. Radiation-driven combustion has been used extensively to study different aspects of solid-propellant combustion dynamics [4]. This experimental method requires a term accounting for radiation penetration in the condensed-phase energy equation. A rigorous formulation of such a term should include the complete optical characteristics of the condensed phase and of the external radiation source [5]. For the ideal case of monochromatic radiation and negligible scattering, the term reduces to an exponential form (Beer’s law).

For several classes of solid propellants, including 1,3,5,7-tetranitro-1,3,5,7-tetrazocine (HMX), there is evidence that chemical reactions take place in a thin

layer just beneath the burning surface [6]. One-dimensional models for simulating solid-propellant combustion are based on the condensed-phase energy conservation equation.

The most widely used approach of simulating unsteady solid-propellant combustion is to start with computing the condensed-phase steady temperature profiles both to determine the initial condition required to start most transient computations and to provide a basis for nonlinear combustion stability analysis. The next step is to choose its specific flame structure [7] obtained from experimental measurements to couple the condensed-phase burning. The gas phase is typically a premixed flame (diffusion phenomena are ignored). This approach is good for transients such as depressurization tests, self-sustained or externally excited oscillatory combustion regimes, and extinction tests, but are not as efficient and accurate for simulating ignition since there is no real flame prior to the ignition. An alternative way to model ignition is to make some changes in the gas phase computation. Zarko, *et al.* have described a model that takes into account heat propagation, diffusion and gas phase reactions, which gives better physics in the gas phase [8].

## 1.2. Surface reaction kinetics

For computational studies of HMX-based propellants, progress in the development of increasingly detailed and accurate models has better accounted for the underlying combustion chemistry and physics. As a result, increasingly accurate models fall into four categories: global kinetic models, semi-global models, development of detailed kinetic mechanisms and multi-phase models with reactions [9, 10]. Two common assumptions in these models are steady-state combustion and zero-order conversion from the condensed (liquid or solid) phase to gas phase chemical intermediates. Applying the second assumption to HMX would suggest that vaporization of HMX is more important than condensed phase reaction. However, the vapor pressure of HMX is rather low and combustion is generally rapid relative to vaporization. These two properties are consistent with Thermogravimetric Analysis (TGA) and Differential Scanning Calorimetry (DSC) experiments conducted in our laboratory, which showed that HMX combustion is not rate-limited by vaporization [11]. A list of 13 reaction models that are commonly employed to describe solid-state reaction kinetics can be found in previous works [12, 13]. The results of a simple model of HMX combustion using the zero-order and first-order conversion assumptions is presented in this paper to assess the importance of the choice of reaction mechanism of the condensed phase reaction.

In the longer term, the usual types of  $n$ th-order kinetic models used for gas phase and solution phase reactions will not suffice to describe the solid or liquid phase reactions at a burning surface. This is because the generally accepted

method of defining a reaction progress variable in solid-state reactions is to use the extent of reaction (*e.g.*, fraction of mass conversion or heat evolution). Such a measure does not have a basis in the fundamental chemical and physical processes that underlie the chemistry. A robust numerical technique, model-free isoconversional analysis method, has been developed for extracting reliable kinetic parameters for solid-state reactions, particularly with respect to thermal decomposition of energetic materials [14-21].

First, we should explain exactly what is meant by the reaction model in this context. The overall rate of a condensed phase reaction can be written in terms of temperature-dependent rate constant,  $k(T)$ , and a reaction model,  $f(\alpha)$ ,

$$\frac{d\alpha}{dt} = k(T)f(\alpha) \quad (1)$$

where  $\alpha$  represents a reaction progress variable, and  $t$  is time. In gas phase kinetics, the reaction progress variable is a measure of reactant concentration or partial pressure, so the reaction model is a description of how the reaction rate depends on reactant concentrations (*e.g.*, zero-order, first-order or *n*th-order kinetics). However, the concept of concentration is not particularly meaningful for condensed phase reactants, so the physical interpretation of  $\alpha$  is usually a measure of mass fraction of reactant consumption or fraction of heat release. It is known that many condensed phase reactions exhibit a dependence of the rate on the extent of reaction, as measured by bulk mass loss or overall heat release. Therefore it makes sense to speak of the dependence of the rate on extent of reaction in terms that are analogous to the familiar expressions used for gas phase reactions.

If the rate of reaction does not depend on the extent of reaction, then  $f(\alpha)=1$ . This is the case for a zero-order reaction. A first-order reaction has  $f(\alpha)=1-\alpha$ , which is a statement that the rate of reaction is proportional to the fraction of unreacted material remaining in the sample. Likewise, a second-order reaction has  $f(\alpha)=(1-\alpha)^2$ . In our combustion model,  $\alpha$  is dimensionless and takes on a value equal to  $1-V_s$ , where  $V_s$  is the volume fraction of solid.

The temperature dependence of the rate constant  $k(T)$  is usually assumed to have the form of the Arrhenius Law

$$k(T) = Ae^{\frac{-E}{RT}} \quad (2)$$

where  $A$  is the pre-exponential factor,  $E$  is the activation energy,  $R$  is the gas constant, and  $T$  is temperature. Under non-isothermal conditions, the temperature varies with time in an arbitrary manner, and the overall temperature-dependent reaction rate is

$$\frac{d\alpha}{dt} = A e^{\frac{-E}{RT(t)}} f(\alpha) \quad (3)$$

Methods of kinetic analysis that involve fitting of experimental data to assumed forms of the reaction model (first-order, second order, etc.) normally result in highly uncertain Arrhenius parameters. This is because errors in the form of the assumed reaction model can be masked by compensating errors in the values of  $E$  and  $A$ . The isoconversional technique eliminates the shortcomings associated with model-fitting methods. It assumes the unknown integrated form of the reaction model,  $g(\alpha)$ , as shown in Eq. (4), to be the same for all experiments.

$$g(\alpha) = \int_0^\alpha \frac{d\alpha}{f(\alpha)} = A \int_0^{t_\alpha} e^{\frac{-E_\alpha}{RT(t)}} dt = A I(E_\alpha, t_\alpha) \quad (4)$$

where  $E_\alpha$  and  $t_\alpha$  are the activation energy and time at  $\alpha$ , respectively.

Because  $g(\alpha)$  and  $A$  are independent of the heating rate, any experiments conducted at different heating rates should have a constant value of the Arrhenius integral,  $I(E_\alpha, t_\alpha)$ . Therefore, for a series of  $n$  experiments conducted at different heating rates, the activation energy can be evaluated by determining the minimum of the kinetic variance function<sup>19</sup>

$$S^2(E_\alpha) = \frac{1}{n(n-1)} \sum_{i=1}^n \sum_{j=1}^n \left( \frac{I(E_\alpha, t_{\alpha,i})}{I(E_\alpha, t_{\alpha,j})} - 1 \right)^2 \quad (5)$$

From this, it follows that  $S^2(E_\alpha)$  should have an  $F$ -distribution.

$$F(E_\alpha) = \frac{S^2(E_\alpha)}{S_{\min}^2} \quad (6)$$

where  $S_{\min}^2$  is the minimum value of all calculated  $S^2(E_\alpha)$  values obtained from Eq. (5). This enables the confidence limits for  $E_\alpha$  to be found by estimating the confidence limits for the variance  $S_{\min}^2$ .

An advantage of the advanced isoconversional method is that it can be applied to study the kinetics under arbitrary temperature programs such as distorted linear (e.g., self-heating/cooling) or purposely nonlinear heating (e.g., temperature modulation). To more adequately account for a strong variation of

the activation energy with the extent of reaction, the isoconversional method also allows for piecewise evaluation of the Arrhenius integral as

$$J[E_\alpha, T_i(t_\alpha)] \equiv \int_{t_{\alpha, m-1}}^{t_{\alpha, m}} \exp\left[\frac{-E_\alpha}{RT_i(t)}\right] dt \quad (7)$$

where  $m$  varies from 1 to the number of the equidistant values of  $\alpha$  chosen for the analysis. In this way, experimental data can be analyzed to yield activation energies for any number of discrete segments of the reaction. The Arrhenius integrals (7) are utilized in Eqs. (5) and (6) to map out the dependence of activation energy on the extent of reaction, including robust estimates of the uncertainty in  $E_\alpha$ . Once these are obtained, the values of  $Af(\alpha)$  are computed, and this information can be used to predict the kinetics of the reaction for any temperature program.

A logical next step is to incorporate these numerical models into combustion simulations. Ultimately, though, it will be necessary to develop new kinetic paradigms for condensed phase reaction kinetics that are firmly grounded in the underlying molecular properties.

## 2. MODEL

The numerical model of HMX combustion is formulated as a one-dimensional representation of a reactive solid phase coupled to a two-dimensional axial-symmetric representation of a reactive gas phase. It simulates the whole process of laser-initiated combustion that is sustained by diffusive heat transfer from the gas phase flame back to the solid material. This model employs a simplified global gas phase chain reaction kinetic mechanism originally proposed by Ward, Son and Brewster [22, 23], which we will refer to as the WSB model. The reason we chose the WSB model is that it is the simplest combustion model that includes explicit chemical reactions that gives good agreement with combustion validation data (mass burning rate, surface temperature, flame structure, etc.) for steady burning. The simplicity is important for large-scale simulations like the one currently carried on in Center for the Simulation of Accidental Fires and Explosions (C-SAFE) at University of Utah [24], where computation of the energetic material combustion can be only a small portion of the overall simulation.

The reaction sequence involves two steps. The first is a condensed phase reaction,  $A(\text{solid}) \rightarrow B(\text{gas})$ , an irreversible decomposition that produces B, the gaseous intermediate species (such as  $\text{CH}_2\text{O}$ ,  $\text{N}_2\text{O}$ ,  $\text{HCN}$ , or  $\text{NO}_2$ ). The second is a bimolecular irreversible gas phase reaction:  $B + M \rightarrow C + M$ , where species C represents a final product and M represents a free radical chain reaction carrier.

This reaction is assumed to be second order overall and first order with respect to B. In their analytical model, WSB used zero-order reaction kinetics for the first reaction and obtained the steady state solution to the resulting set of algebraic equations by iteration using both reactions. However, our model starts from igniting the pure HMX solid by a constant (simulated laser) heat flux, and we have experimented with different types of kinetics for the first (condensed phase) reaction. This strategy allows us to represent the solid-gas interface as a structured region in one dimension, as opposed to a discontinuous boundary.

In this model, the condensed phase and gas phase are one-dimensional and two-dimensional, respectively, as shown in Figure 1. Non-uniform meshes are used in both condensed phase and gas phase to provide a fine grid structure near burning surface (less than a micron in length) and course grid structure for other ends to save computational time. Laser energy is transmitted according to Beer's Law and absorbed by the surface of the solid. Condensed phase reaction occurs and in consequence the volume fraction of condensed phase grids reduces. Grids

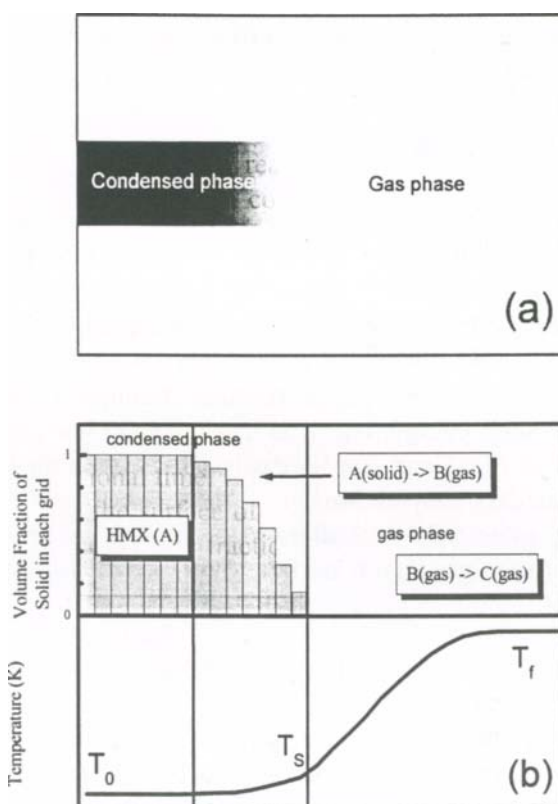


Fig. 1. Schematic diagram of HMX combustion model.

in the condensed phase are shifted towards the surface if any surface grids are consumed, *i.e.*, when the volume fraction is lower than a critical value, so that no grids in condensed phase become gas phase. Surface temperature and mass flux across the condensed phase/gas phase interface are obtained and used as inputs for the gas phase simulation. The gas phase part of the simulation is conducted with FLUENT®, a commercial Computational Fluid Dynamics software. A segregated implicit solver is used in this tool. For less computational efforts and better validation of WSB model, a laminar finite-rate model was chosen, which computes the chemical source terms using Arrhenius expressions, and ignores the effects of turbulent fluctuations.

The two phases are coupled explicitly with mass flux and energy flux preserved. Thermal radiation from gas phase reaction is neglected in this model; only laser radiation and conductive heat feedback from adjacent gas phase grids are taken into account as energy source terms for the condensed phase, which is critical to realize the pressure dependence of the mass burning rate.

We neglect effects such as body forces, viscous effects, energy loss via radiation and we assume ideal gas behavior of all gaseous products. We calculate the physical properties of solid region and gas phase separately using the finite-difference method (FDM). In the solid region (including the burning surface), only the energy equation needs to be solved:

$$\frac{dT}{dt} = \frac{\lambda}{C_{ps}\rho_s} \frac{d^2T}{dx^2} + \frac{Q_c}{C_{ps}\rho_s} A_c e^{-\frac{E_c}{RT}} \quad (8)$$

where  $\lambda$  is the thermal conductivity,  $C_{ps}$  is the heat capacity of solid HMX,  $\rho_s$  is the density of condensed phase,  $Q_c$  is the heat release in condensed phase reaction,  $A_c$  is the condensed phase reaction frequency factor,  $E_c$  is the corresponding activation energy, and  $R$  is the universal gas constant. This is a tridiagonal system in FDM and can be easily solved with an implicit method, given the initial boundary temperatures.

The governing inviscid flow equations of continuity, energy, and momentum (in conservation form) in gas region are Euler Equations (9)-(11):

$$\frac{\partial \rho}{\partial t} + \frac{\partial(\rho u)}{\partial x} = 0 \quad (9)$$

$$C_p \frac{\partial(\rho T)}{\partial t} + C_p \frac{\partial(\rho u T)}{\partial x} = \dot{Q} \quad (10)$$

$$\frac{\partial(\rho u)}{\partial t} + \frac{\partial(\rho u^2 + P)}{\partial x} = 0 \quad (11)$$

where  $u$  is the velocity of species,  $r$  is the rate of gas phase reaction,  $q$  is the heat input from the gas phase reaction, and  $C_p$  is the heat capacity of gaseous products.

The ideal gas equation of state is

$$P = \rho RT \quad (12)$$

The initial conditions are set to be

$$T(x,0) = T_0 \quad (13)$$

$$P(x,0) = P_0 \quad (14)$$

The boundary conditions are

$$T(x_{se}, t) = T_0 \quad (15)$$

$$P(x_{ge}, t) = P_0 \quad (16)$$

where  $T_0$  and  $P_0$  are the initial temperature and initial pressure, respectively,  $x_{se}$  and  $x_{ge}$  denote the cold ends of the solid region and gas region, respectively.

From the energy balance, the temperature at the burning surface,  $T_s$ , is given by

$$-\lambda \frac{\partial T}{\partial x} = q_{g,s} + J_L + r_b Q_s \quad (17)$$

where  $q_{g,s}$  is the heat flux from the gas phase flame to the burning surface,  $J_L$  is the heat flux from external radiation (simulated continuous wave CO<sub>2</sub> laser source),  $r_b$  is the mass burning rate, and  $Q_s$  is the heat released from solid surface reaction. In each simulation, however, the laser is turned off after ignition, when the heat release from exothermic reactions becomes much more pronounced. This enables the model to simulate full self-sustained HMX combustion in order to make direct comparisons with the WSB model. Condensed phase HMX is treated as a semi-transparent material and the spatial profile of the laser energy absorption is described by Beer's Law, with an absorption coefficient of 1/ $\mu\text{m}$  [25, 26] at the CO<sub>2</sub> laser wavelength (10.6 $\mu\text{m}$ ). Condensed phase surface reflection of the laser irradiation and the laser absorption by gas-phase species are neglected.



3. RESULTS AND DISCUSSION

3.1. Validation of the steady state combustion with WSB model

The first stage of this work was to carry out a simulation of steady combustion using the WSB steady state combustion model as a point of validation. In this validation, the simulation was done with no condensed phase reaction, but with fixed surface temperature and mass flux from solid HMX into the gas phase computational domain. The activation energy of the gas phase reaction is 0.11 kcal/mol, which was determined to be the best value by WSB model<sup>23</sup>. Figure 2 shows the 2D axisymmetric HMX flame at steady state combustion with all WSB parameters. This model successfully reproduced all results from WSB model, especially HMX combustion at 20 atm, which was the validation point WSB model used to match by adjusting kinetic parameters of two above-mentioned reactions (Table 1). The predicted final flame temperature at 20 atm is slightly lower than WSB result, due to adiabatic expansion of hot gas perpendicular to the flame direction. The final flame temperature at 1 atm is not compared with WSB model because the corresponding mass burning rate and flame temperature were not given in Ref. 23.

The stand-off distance characterizes the thickness of the gas phase reaction zone, and it is defined in this work as the distance from the solid surface to the point where 85% of the final temperature is achieved. Fig. 3 shows the mole

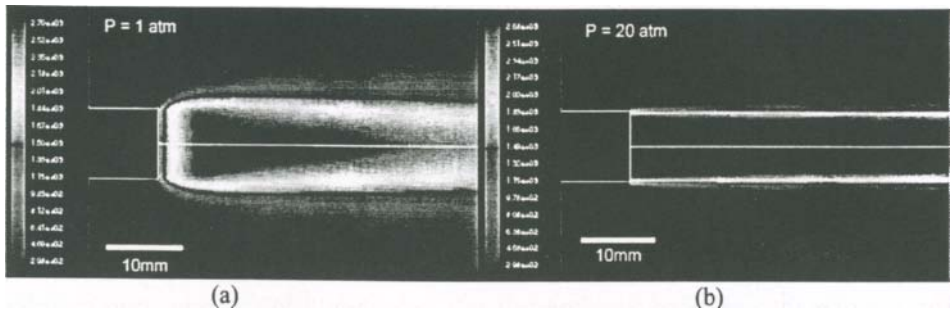


Fig.2. 2D axisymmetric HMX flame at steady state combustion with WSB parameters. (a) P = 1 atm; (b) P = 20 atm.

Table 1  
Validation of WSB model.

	P = 1 atm		P = 20 atm	
	This model	WSB model	This model	WSB model
Surface Temperature (K)	650	650	733	733
Burn rate (g/cm <sup>2</sup> -s)	0.061	n/a	6.8	6.8
Flame temperature (K)	2745	n/a	2676	2700
Stand-off distance (mm)	3.7	3.8	0.11	< 0.2

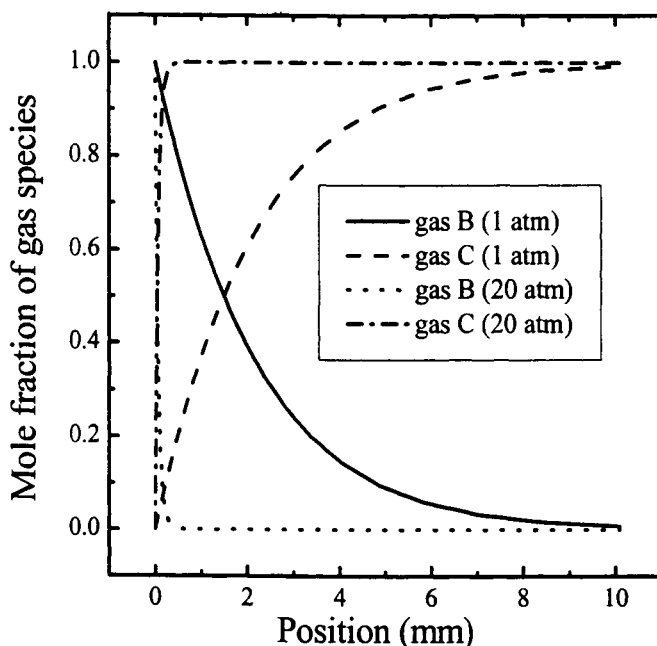


Fig. 3. Mole fraction of gas species in gas phase reaction zone.

fraction of gas B and C in gaseous phase. In this model (and WSB), most of the reactive heat release occurs in the  $B \rightarrow C$  reaction. Therefore, at higher pressures where the flame standoff distance becomes shorter, there is greater heat feedback from the flame. This accounts entirely for the pressure-dependence of the burn rate because radiative heat transfer is not treated explicitly.

### 3.2 Ignition time

The dependence of ignition time on simulated  $\text{CO}_2$  laser intensity was investigated at four different values of the heat flux (10, 20, 30, 50  $\text{cal/cm}^2/\text{sec}$ ) at the surface of the HMX monopropellant. Simulated ignition delays are somewhat longer than experimental values [27], as shown in Fig. 4. This is mainly due to the use of a constant absorption coefficient for laser energy, which in reality is varying as a function of surface structure, as shown by Ali et. al [28]. Another possibility is that the constant solid phase heat capacity used in this model (and also used by WSB), is somewhat higher than known value of the solid heat capacity at room temperature. As a consequence, the temperature rise is smaller in each time step in the early period of heating before ignition. The

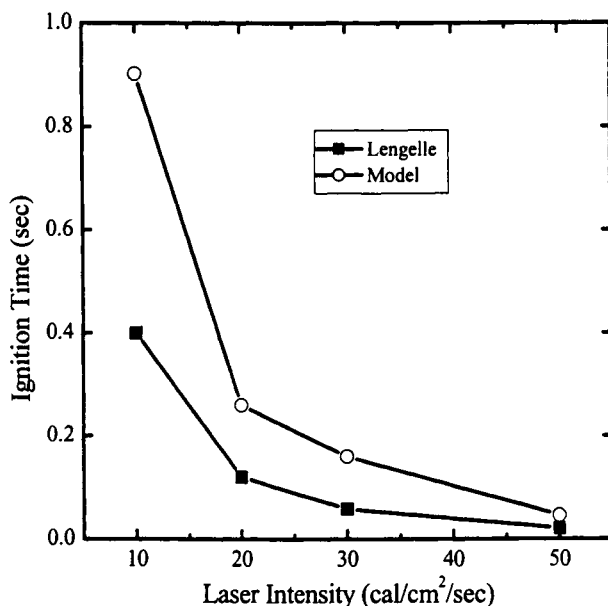


Fig. 4. Effect of CO<sub>2</sub> laser intensity on ignition time of HMX.

neglect of the  $\beta \rightarrow \delta$  phase transition, melting and evaporation of solid HMX during surface heating may also be part of the reason.

### 3.3. Pressure sensitivity and surface temperature

Experimental measurements of mass burning rate ( $r_b$ ) are frequently expressed in terms of a "ballistic law" for steady state combustion,

$$r_b = aP^n \quad (18)$$

where  $a$  is a constant and  $n$  is the pressure sensitivity. The values of  $a$  and  $n$  are known to be nearly constant for any given initial HMX temperature.

As shown in Fig. 5, unsteady burning of HMX during ignition consists of three regimes: the heating of inert HMX by external radiation, ignition delay (or flame setup) and steady-state burning. The initial pressure does not affect the simulated ignition time because this feature is dependent mostly on the heat flux and thermal diffusivity of the solid. The simulated HMX steady-state burning rate increases as  $P_0$  increases; this is because the higher the total pressure is, the greater the rate of the gas phase B  $\rightarrow$  C flame reaction.

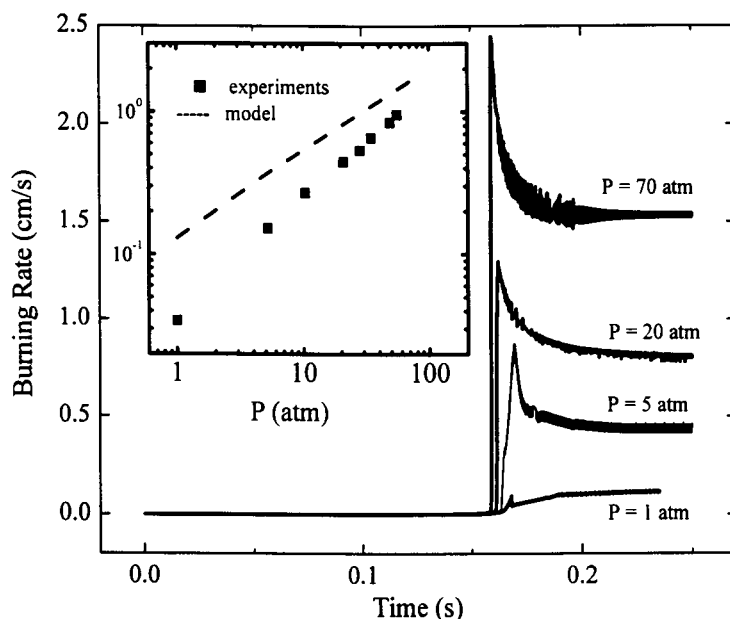


Fig.5. Pressure sensitivity of HMX combustion. (Laser intensity = 30cal/cm<sup>2</sup>/sec; P = 20atm)

The most interesting behavior happens in the intermediate regime. For small  $P_0$ , the burning rate increases monotonically (except for a small transient associated with turning the laser off), and levels off as steady-state burn rate. However, ignition at high pressure leads to an overshooting of burning rate and subsequent decrease toward steady burning. These results are consistent with previous reports [29, 30]. Our physical interpretation of the effect is that the flame comes to equilibrium with the solid surface more rapidly at high pressure than at low pressure. At high  $P$ , the mass-burning rate overshoots the steady value because the flame burns through a region of solid that was preheated by the laser ignition source. At low pressures, the flame equilibration time is slow enough that the preheated zone is consumed during flame setup; therefore, no overshoot occurs.

The mass-burning rate predicted by this model is higher than experimental values. This results in a difference between this model and WSB model. The analytical WSB solution assumes that the solid phase reaction only occurs at a "lengthless" surface. In this model, however, condensed phase reaction occurs in multiple grids; therefore, the mass loss is an integral over all burning grids.

The pressure dependence of the mass burning rate is also shown in Fig. 5. The pressure sensitivity  $n$  of this model is 0.59, somewhat lower than

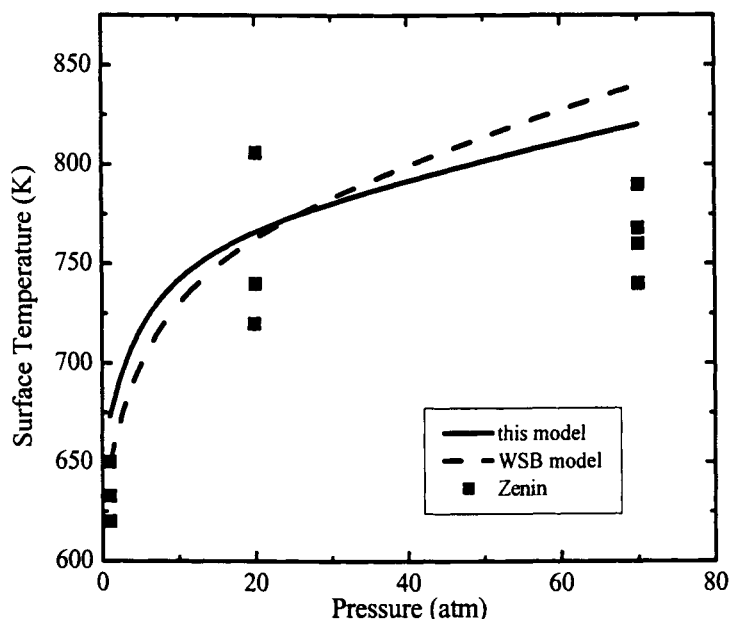


Fig. 6. Surface temperature of burning HMX vs. pressure.

experimental data [31-36], which is 0.81 in this pressure range. This is due to the method used to couple the gas phase region to the solid, which features a multi-grid burning surface structure (Fig. 1). The current implementation of the code does not allow the gas phase  $B \rightarrow C$  flame reaction to occur within grid elements where the solid is partially burned. This approximation is of little consequence at low pressures, where the flame standoff distance is large compared with the depth of the burning surface structure. However, at high pressures, the flame is extended too far from the surface and as a result, the heat feedback and mass burning rates are somewhat lower than the experimental values.

The predicted surface temperature as a function of pressure is compared with the WSB model and Zenin's data [36] in Fig. 6. It's in fairly good agreement with WSB model, especially at 20 atm.

### 3.4. Temperature sensitivity

Temperature sensitivity is the dependence of the steady burn rate on the initial (bulk) temperature of the HMX. The sensitivity coefficient is defined as

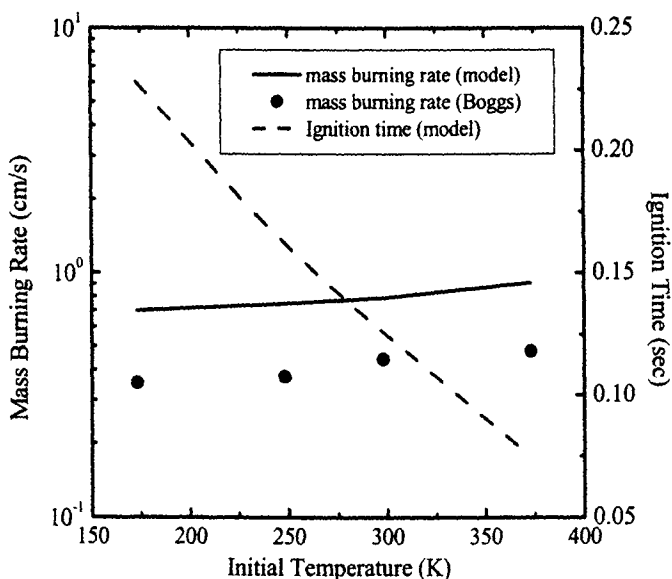


Fig. 7. Predicted temperature sensitivity of burning rate and ignition time vs. initial HMX temperature. (Laser intensity =  $30\text{cal/cm}^2/\text{sec}$ ;  $P = 20\text{atm}$ )

$$\sigma_P = \frac{\partial(\ln r_b)}{\partial T_{\text{ini}}} \quad (19)$$

The predicted temperature sensitivity of burn rate of HMX and ignition time as function of initial solid temperature are shown in Figure 7. The predicted mass burning rates are somewhat higher than experimental values, but the temperature sensitivity is basically the same as measured in experiments.

Ignition time decreases as the initial temperature increases, because higher initial temperatures in the solid require smaller temperature gradients at the solid surface, therefore requiring less heat transfer into the bulk solid. Therefore, it requires less time for the solid surface to reach a critical ignition temperature.

Surface temperatures are slightly higher for higher initial temperatures, but the difference is no more than a few degrees. The reason why surface temperature is not sensitive to initial temperature is that surface temperature is resolved by an energy balance between the burning surface and adjacent gas phase flame, and the heat flux is much more strongly dependent on pressure.

### 3.5. Effect of kinetic models

#### 3.5.1 First-order reaction model

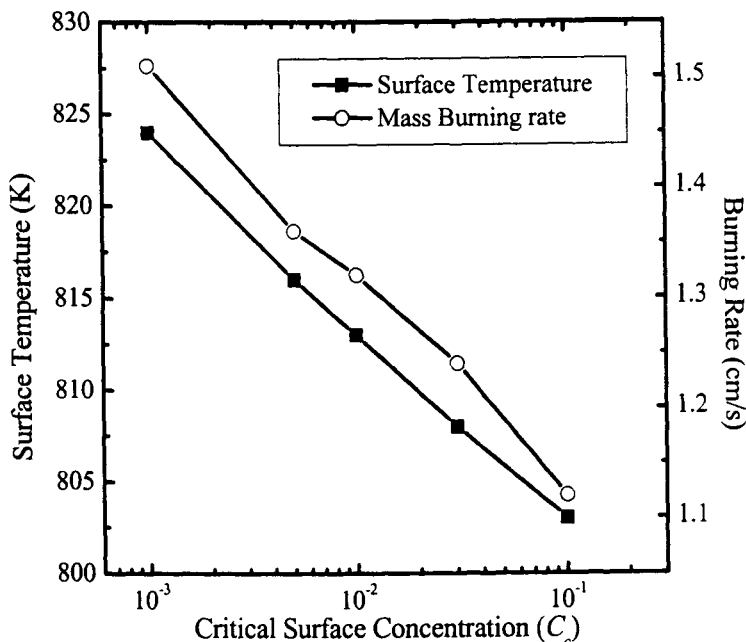


Fig.8. Surface temperature and mass burning rate as a function of critical surface concentration in each grid for first-order reaction.

The main purpose of this study is to investigate the effects of using kinetic models for the condensed phase reaction that are different from the usual zero-order kinetics assumed by other combustion simulations. In a first-order reaction, the reaction rate is proportional to the mass fraction of solid remaining in each grid element. When  $\alpha \rightarrow 1$  in a grid,  $f(\alpha) = 1 - \alpha \rightarrow 0$ , and the rate of reaction becomes infinitesimally small. In principle, an infinite amount of time is required to burn out all solid in that grid, and consequently this grid will never complete and the surface does not regress. Therefore, we set a critical value for the grid concentrate  $C_c$  which, when reached triggers the program to transfer all remaining mass to the next deeper element and translate the surface forward (toward the gas-solid interface). Fig. 8 shows the surface temperature and burning rate of HMX as a function of  $C_c$  in order to demonstrate the effects on the simulation for different choices of this parameter. It is noted that even with the highest  $C_c$  in this study ( $C_c = 0.1$ ), the burn rate (1.1 cm/s) is higher than that in zero-order reaction model (0.8 cm/s). Even higher values of  $C_c$  are not desired because it makes the model less realistic. Better solutions to this problem must be found, and this is the subject of future investigations.

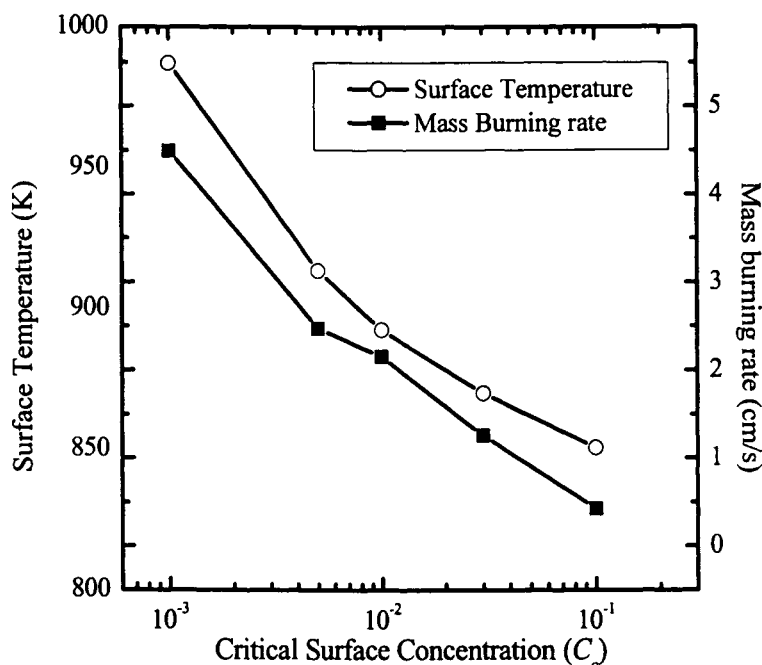


Fig.9. Surface temperature and mass burning rate as a function of critical surface concentration in each grid for second-order reaction.

The surface temperature and burning rate of HMX increase as  $C_c$  decreases. This is because the smaller the value of  $C_c$ , the longer time it takes to eliminate that grid. However in the meantime, heat feed back from gas phase keeps raising the temperature of that grid and grids next to it. When this grid is finally burned out, successive grids have already reached very high temperatures and burned a significant amount of mass in them, which can leave only a small amount of mass, even comparable with  $C_c$ , so they'll soon be eliminated too in very few successive time steps. The overall burning rate, therefore, exceeded that of the zero-order reaction, which burns HMX at a constant rate and never slows down as first-order reactions do at low concentrations (high extents of reaction).

### 3.5.2. Second-order reaction model

Similarly, the rate of second-order reaction in a grid also decreases as  $\alpha \rightarrow 1$ , and even faster. As a result, the choosing of  $C_c$  is more critical. Fig. 9 shows the effect of  $C_c$  on surface temperature and burning rate of HMX. Compared with the burn rates using the first-order reaction model, as shown in Fig. 8, the burn rates for second-order reaction are higher at low  $C_c$  values, (e.g., 5.5 cm/s for



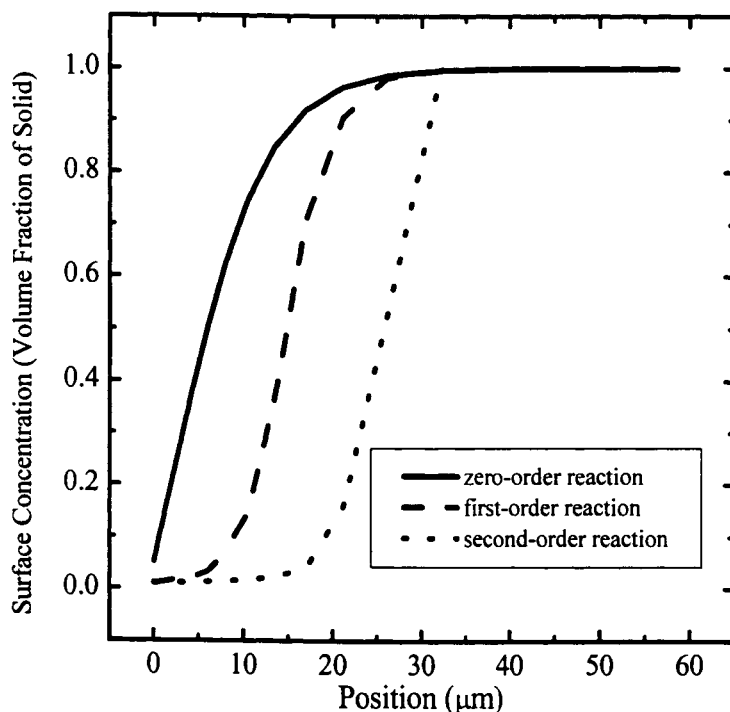


Fig. 10. Surface structure of burning HMX as a function of reaction models. ( $C_c=0.01$ )

second-order reaction versus 1.5 cm/s for first-order reaction at  $C_c = 0.001$ ). The burn rate for second-order reaction drops much faster than that in first-order reaction model as  $C_c$  increases. At  $C_c = 0.1$ , first-order and second-order reaction model reach the same burn rate, thus no difference exists between the two reaction models for higher values of  $C_c$  in terms of burn rate.

Fig. 10 shows the typical profiles of  $C_c$  at burning HMX surface for different reaction models. Zero-order reaction has a convex  $C_c$  profile, as a result of combustion at constant rate. First-order and second-order reactions lead to considerably lower concentrations at the burning surface. Because the first grid always “holds” the surface position and thus allows unrealistic heat penetration from gas phase into inner solid grids, first-order and second-order reaction have apparent higher surface temperature and mass burning rate. Choosing more realistic critical surface concentrations may solve this problem. Allowing the  $B \rightarrow C$  flame reaction gaseous reaction to propagate back to inside the solid surface should improve the model as well.

Finally we note that as expected, the ignition time is not sensitive to solid phase reaction models, because the surface structure does not change significantly during the initial heating period.

#### 4. CONCLUSION

A simple unsteady-state model using the WSB mechanism and parameters is used to study the effects of condensed phase reaction models on combustion of energetic material. Firstly, the steady state combustion of WSB mechanism is successfully validated in this 2D axial symmetric model. The ignition time, temperature profile, standoff distance, and mass burning rate are in good agreement with Ward, et al. However, the WSB model fails in this transient combustion model, in ignition delay for all cases, and in mass burning rate and surface temperature for most cases.

The choice of reaction model does make a difference in the modeling of HMX combustion. Different reaction models generate different burning surface structure, surface temperature and as a result, the burning rate of energetic materials. A critical concentration is introduced to the model to deal with the special problem that first-order and second-order reaction have. The effect of choosing this critical concentration turns out to be a very important factor to determine how well the model can simulate the combustion.

The use of grids in the solid phase is a simple and efficient way to model complicated burning surface structure. The limitations of this model, however, are also evident. It creates some inevitable artificial treatment of surface reaction and heat transfer.

#### 5. ACKNOWLEDGMENTS

This research is supported by the Center for Simulation of Accidental Fires and Explosions (C-SAFE) at the University of Utah, under LLNL subcontract B341493.

#### REFERENCES

- [1] J. Simons, *J. of Phys. Chem. B*, Vol. 103(41) (1999) 8650.
- [2] R. Behrens, S. Mack, and J. Wood, 17th JANNAF Propulsion Systems Hazards Subcommittee Meeting, CPIA, Vol. 1 (1998) 21.
- [3] K.K. Kuo and J.P. Gore, *Prog. Astronaut. Aeronaut.*, Vol. 90 (1984) 599.
- [4] C.E. Hermance, *Prog. Astronaut. Aeronaut.*, Vol. 90 (1984) 239.
- [5] L. De Luca, *Meccanica*, Vol. 13(2) (1978) 71.
- [6] K. Kishore, V.R.P. Verneker, and M.N.R. Nail, *AIAA Journal*, Vol. 13(9), (1975) 1240.

- [7] L. De Luca, L. Galfetti, G. Colombo, C. Grimaldi, C. Zanotti, and M. Liperi, Symposium on Commercial Opportunities in Space, Taiwan, China, (1987) 19.
- [8] V.E. Zarko, L.K. Gusachenko, A.D. Rychkov, Challenges in Propellants and Combustion 100 Years after Nobel, Begell House Inc., NY, 1997, pp. 1035-1045.
- [9] R.L. Hatch, 24th JANNAF Combustion Meeting, Vol. 1 (1987) 383.
- [10] W.W. Erikson and M.W. Beckstead, JANNAF 35th Combustion Subcommittee Meeting, Vol. 1 (1998) 415.
- [11] P. Lofy and C.A. Wight, JANNAF 35th Combustion Subcommittee and 17th Propulsion Systems Hazards Subcommittee Meeting, Joint Sessions, (1998) 137.
- [12] M.E. Brown, D. Dollimore, and A.K. Galwey, Comprehensive Chemical Kinetics, Vol. 22, Elsevier, Amsterdam, 1980, 340.
- [13] J. Sestak, Comprehensive Chemical Kinetics, Vol. 12D, Elsevier, Amsterdam, 1984, 440.
- [14] S. Vyazovkin and A. I. Lesnikovich, Thermochim. Acta, 203 (1992) 177.
- [15] S. Vyazovkin and D. Dollimore, J. Chem. Info. Comp. Sci., 36 (1996) 42.
- [16] S. Vyazovkin and C.A. Wight, Annu. Rev. Phys. Chem., 48 (1997) 125.
- [17] S. Vyazovkin, J. Therm. Anal., 49 (1997) 1493.
- [18] G. I. Senum, and R.T. Yang, J. Therm. Anal., 11 (1979) 445.
- [19] S. Vyazovkin, and C.A. Wight, Anal. Chem., 72 (2000) 3171.
- [20] S. Vyazovkin, Int. J. Chem. Kinet., 28 (1996) 95.
- [21] S. Vyazovkin, and C.A. Wight, Thermochim. Acta, 340(1) (1999) 53.
- [22] M. J. Ward, S.F. Son, and M.Q. Brewster, Combust. Theory Model., 2(3) (1998) 293.
- [23] M. J. Ward, S.F. Son, and M.Q. Brewster, Combust. Flame, Vol. 114(3/4) (1998) 556.
- [24] T.C. Henderson, P.A. McMurtry, P.J. Smith, G.A. Voth, C.A. Wight, and D.W. Pershing, Comput. Sci. Eng., Vol. 2(2) (2000) 64.
- [25] D.M. Hanson-Parr and T. Parr, 25th Symposium on Combustion, The Combustion Institute, (1994) 1281.
- [26] K. Prasad, R.A. Yetter, and M.D. Smooke, Combust. Flame, 115(3) (1998) 406
- [27] G. Lengelle, et al., AGARD-CP-391 on Smokeless Propellants, (1985) 8-1.
- [28] A.N. Ali, S.F. Son, B.W. Asay, R.K. Sander, and M.Q. Brewster, 36th JANNAF Combustion Subcommittee Meeting, CPIA, Vol. 1 (1999) 51.
- [29] A. Bizot, Challenges in Propellants and Combustion: 100 Years after Nobel, Begell House Inc., NY, 1997, pp. 1046-1061.

- [30] G. Lengelle, *Challenges in Propellants and Combustion: 100 Years after Nobel*, Begell House Inc., NY, 1997, pp. 515-548
- [31] T.L. Boggs, J.L. Eisel, C.F. Price, and D.E. Zurn, 15th JANNAF combustion Meeting, CPIA, (1979) 241.
- [32] T.L. Boggs, *Prog. Astronaut. Aeronaut.*, Vol. 90 (1984) 121.
- [33] T.P. Parr, T.L. Boggs, C.F. Price, and D.M. Hanson-Parr, 19th JANNAF Combustion Meeting, CPIA, (1982) 281.
- [34] A.I. Atwood, T.L. Boggs, P.O. Curran, T.P. Parr, D.M. Hanson-Parr, C.F. Price, and J. Wiknich, *J. Prop. Power*, 15(6) (1999) 740.
- [35] A.I. Atwood, T.L. Boggs, P.O. Curran, T.P. Parr, D.M. Hanson-Parr, C.F. Price, and J. Wiknich, *J. Prop. Power*, 15(6) (1999) 748.
- [36] A.A. Zenin, *J. Prop. Power*, 11 (1995) 752.

This Page Intentionally Left Blank

## *Chapter 11*

# **Towards reliable prediction of kinetics and mechanisms for elementary processes: Key combustion initiation reactions of ammonium perchlorate**

**R. S. Zhu and M. C. Lin**

Department of Chemistry, Emory University, Atlanta, GA, 30322, USA

A series of  $\text{ClO}_x$  reactions relevant to the combustion initiation of ammonium perchlorate has been studied. The reactions include the decomposition of  $\text{ClO}_x$  ( $x = 2 - 4$ ) and  $\text{HOClO}_y$  ( $y = 2 - 3$ ), the bimolecular reactions of  $\text{HO} + \text{X}$  ( $\text{X} = \text{ClO}, \text{OClO}, \text{HOClO}_3$ ),  $\text{ClO} + \text{Y}$  ( $\text{Y} = \text{O}, \text{ClO}, \text{OClO}$ ),  $\text{H} + \text{HOClO}_3$  and some of their reverse processes. The geometries of the reactants, intermediates, transition states and products involved in these reactions were optimized at the B3LYP/6-311+G(3df, 2p) or PW91PW91/6-311+G(3df, 2p) level and final energies were refined at the modified Gaussian - 2 (G2M) level. Rate constants for major product channels have been predicted and compared with the available experimental data. Detailed mechanisms for these reactions have been discussed on the basis of predicted potential energy surfaces. The rate constant calculations were carried out by the conventional transition state theory (TST) or Rice-Ramsperger-Kassel-Marcus (RRKM) theory for reactions with well-defined transition states and variational TST or RRKM theory for those channels which occur barrierlessly.

The results show that our predicted energies and rate constants are quite satisfactory and in good agreement with available experimental data. For practical applications, the molecular parameters and heats of formation of key species, and the rate constants for all the major reactions discussed under different conditions have been recommended.

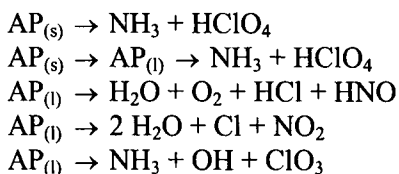
## 1. INTRODUCTION

Recent development of various effective *ab initio* molecular orbital computational schemes, such as G2 [1], G3 [2], CBS [3], and other G2-like methods, for example, G2Q [4] and G2M [5], allows us to predict molecular and thermochemical properties of complex species to within experimental accuracies (e.g.,  $\pm 2$  kcal/mol for heats of formation). Such improvement in energy prediction, aided by the continuing decrease in computational cost, as well as the progress made recently in treating barrierless radical-radical association processes [6-9] and reactions with multi-product channels [10-18], has provided chemical kineticists for the first time a powerful tool to calculate realistically rate constants for combustion reactions, which are dominated prevalently by the interaction of free radicals at high temperatures. Our recent success in interpreting complex kinetic data for combustion processes such as the new prompt NO formation mechanism [10, 11], the oxidation of CHO [12], CH<sub>3</sub> [13] and C<sub>2</sub>H<sub>3</sub> [14] by molecular oxygen, the reaction of OH radicals with CO [15], HONO [16] and HNO<sub>3</sub> [17], and a series of reactions involving NH<sub>x</sub> and CH<sub>2</sub>N with NO<sub>x</sub> relevant to the combustion of ADN, AP and RDX/HMX as summarized in a recent review [18], has amply demonstrated the potential and opportunity provided by the aforementioned progress in computational techniques.

We have recently extended the computational studies for elucidation of the complex chemistry of ClO<sub>x</sub> reactions, for which no successful attempts have been made to date to predict rate constants by direct first-principles calculations for combustion or atmospheric applications. ClO<sub>x</sub> species are known to have played a central role in the destruction O<sub>3</sub> in the earth's stratosphere by Freons; they are also believed to be the key chain carriers in the combustion of AP in its incipient stages. Their rapid exothermic oxidation of NH<sub>x</sub> species in the gas-phase leads to the formation of NO and NO<sub>2</sub> in the early stage of the AP combustion reaction.

Despite extensive studies on the mechanism for the decomposition and combustion of AP over the past few decades experimentally and computationally, as summarized in detail in overviews by Jacobs and Whitehead [19], and Tanaka and Beckstead [20, 21], many questions still remain regarding the key controlling initiation processes within and/or near the burning surface. Tanaka and Beckstead reviewed various assumed initiation reactions; they also put forth a three-phase combustion model to account for the observation of Brill et al. [22] acquired from a time-resolved FTIR measurement at high pressure and that of Ermolin and coworkers [23]

for species detected by mass-spectrometry near a burning AP surface. The mechanism includes the following initiation processes in the solid, liquid and gas phases:



These semi-global processes are followed by various radical-radical reactions in the gas phase involving  $\text{ClO}_x$  ( $x = 0 - 4$ ) which can be formed by reactions of molecular and radical species in the system.

As most of the rate constants for the reactions invoked are unknown, to fully substantiate the 3-phase combustion model requires a systematic study of the chemistries occurring in each of the three phases by high-level quantum-chemical calculations for the key processes involved. They include in particular the determination of the dissociative sublimation rate,  $\text{AP}_{(s)} \rightarrow \text{NH}_3 + \text{HClO}_4$ , the chain initiation reaction rate,  $\text{HClO}_4 \rightarrow \text{OH} + \text{ClO}_4$ , as a function of temperature and pressure, and the rates of ensuing chain reactions involving  $\text{ClO}_x$  ( $x = 0 - 4$ ),  $\text{NH}_y$  and  $\text{NO}_y$  ( $y = 1 - 3$ ) and  $\text{HO}_z$  ( $z = 1, 2$ ). The goal of the present study lies in the establishment of realistic kinetic database from reliable *ab initio* MO and statistical-theory calculations as alluded to above beginning from the gas phase. The results from a recent series of studies on  $\text{ClO}_x$  radical reactions, including their formation from the decomposition of  $\text{HClO}_x$  ( $x = 3, 4$ ) and their unimolecular decomposition and bimolecular reactions with OH and  $\text{HO}_2$ , are summarized in this chapter of review.

## 2. COMPUTATIONAL METHODS

### 2.1. *Ab initio* calculations

Reliable potential energy surfaces (PES's) are prerequisite to obtaining accurate rate constants for chemical reactions. With the significant progress made in the field of quantum chemical methods in recent years as alluded to in the introduction, scientists not only can reproduce experimental thermochemical data but also can make accurate predictions on rate constants for which experimental data are unknown or uncertain. The Gaussian-X (GX) ( $X = 1, 2, 3$ ) series of methods and the most recent new family of G3 methods, referred to as G3X, developed Pople et al. [24] and



Curtiss et al. [1, 2, 25] and are widely used to predict PES's of interesting reactions. The objective of these approaches was to develop a general calculative procedure to be applied in any molecular systems at a modest cost. These methods can now reproduce known experimental data to an accuracy within 1 – 2 kcal/mol. For the G1 – G3 theory, an initial equilibrium structure was optimized at the Hartree-Fock, HF/6-31G(d) level of theory to obtain the zero point energy (ZPE) and then the structure was refined at the MP2 (FU)/6-31G (d) level (second-order Møller-Plesset perturbation). Based on the optimized structures obtained at the MP2 (FU)/6-31G (d) level, a series of single-point energy calculations are carried out at higher levels of theory including diffuse function corrections, higher polarization function corrections and larger basis set corrections, etc.

From a technical viewpoint, the density function (DFT) method can reliably reproduce experimental molecular parameters when a sufficient basis set is employed [26-28]. To improve the accuracy for the calculated species, various modifications of GX (X = 2, 3) methods have been proposed [4, 5, 25]. In the modified G3 method (G3X) [25], the structure and ZPE obtained at the B3LYP/6-31G(2df, p) level are used.

In our recent studies, we employed the modified G2 (G2M) scheme [5]. The geometries of the reactants, products, intermediates and transition states in the related reactions have been fully optimized by using the hybrid density functional B3LYP method (Becke's three-parameter nonlocal exchange functional [29-30] and the correlation functional of Lee, Yang, and Parr [31]) with the 6-311+G(3df, 2p) basis set. We also employed the PW91PW91/6-311+G(3df) method with Perdew-Wang [32] functionals for exchange and correlation (PW91PW91), which can provide more reliable structures for systems with larger spin contaminations. Vibrational frequencies employed to characterize stationary points and for ZPE corrections have also been calculated at these levels of theory. All the stationary points have been positively identified for local minima (with the number of imaginary frequencies NIMAG = 0) and transition states (with NIMAG = 1). Intrinsic reaction coordinate (IRC) calculations [33] have been performed to confirm the connection of each transition state with designated intermediates.

For the total energy prediction with G2M, two versions of the method scheme [5] were used in this work depending on the size of the molecules involved in the reactions. They are represented as follows and will be indicated for a specific system in the related sections:

*Version 1*

$$E[(G2M(CC2))] = E_{\text{bas}} + \Delta E(+) + \Delta E(2\text{df}) + \Delta E(\text{CC}) + \Delta' + \Delta E(\text{HLC}, \text{CC2}) \\ + \text{ZPE}(3\text{df}, 2\text{p})$$

$$E_{\text{bas}} = E[\text{PMP4/6-311G}(\text{d}, \text{p})]$$

$$\Delta E(+) = E[\text{PMP4/6-311+G}(\text{d}, \text{p})] - E_{\text{bas}}$$

$$\Delta E(2\text{df}) = E[\text{PMP4/6-311G}(2\text{df}, \text{p})] - E_{\text{bas}}$$

$$\Delta E(\text{CC}) = E[\text{CCSD}(\text{T})/6-311\text{G}(\text{d}, \text{p})] - E_{\text{bas}}$$

$$\Delta' = E[\text{UMP2/6-311} + \text{G}(3\text{df}, 2\text{p})] - E[\text{UMP2/6-311 G}(2\text{df}, \text{p})] - E[\text{UMP2/6-} \\ 311+\text{G}(\text{d}, \text{p})] - E[\text{UMP2/6-311G}(\text{d}, \text{p})]$$

$$\Delta E(\text{HLC}, \text{CC2}) = -5.78n_{\beta} - 0.19n_{\alpha} \text{ in units of mhartree.}$$

*Version 2*

$$E[\text{G2M}(\text{CC5})] = E[\text{CCSD}(\text{T})/6-311\text{G}(\text{d}, \text{p})] + \Delta E(+3\text{df}, 2\text{p}) + \Delta E(\text{HLC}) + \\ \text{ZPE}(3\text{df}, 2\text{p})$$

$$\Delta E(+3\text{df}, 2\text{p}) = E[\text{MP2/6-311} + \text{G}(3\text{df}, 2\text{p})] - E[\text{MP2/6-311G}(\text{d}, \text{p})].$$

$$\Delta E(\text{HLC}) = -0.00530 n_{\beta} - 0.00019 n_{\alpha};$$

where  $n_{\alpha}$  and  $n_{\beta}$  are the numbers of valence electrons,  $n_{\alpha} \geq n_{\beta}$ . All calculations were carried out with the Gaussian 98 package [34].

**2.2. Rate constant calculations**

The rate constants were calculated with the transition state theory (TST) for direct abstraction reactions and the Rice-Ramsperger-Kassel-Marcus (RRKM) theory for reactions occurring via long-lived intermediates. For reactions taking place without well-defined TS's, the Variflex [35] code and the ChemRate [36] code were used for one-well and multi-well systems, respectively, based on the variational transition-state theory approach

discussed below. Potential energy surfaces computed by the G2M (CC2) or G2M (CC5) methods were used in the calculation.

For the calculation using Variflex, the number of a variational transition quantum states,  $N_{\text{EJ}}^{\dagger}$ , was given by the variationally determined minimum in  $N_{\text{EJ}}(R)$ , as a function of the bond length along the reaction coordinate  $R$ , which was calculated by the method developed by Wardlaw-Marcus [6, 7] and Klippenstein [8]. The basis of their methods involves a separation of modes into conserved and transitional modes. With this separation, one can evaluate the number of states by Monte Carlo integration for the convolution of the sum of vibrational quantum states for the conserved modes with the classical phase space density of states for the transitional modes.

The pressure dependence was treated by solving 1-D master equation [37, 38] using the Boltzmann probability of the complex for the  $J$  distribution. The exponential down model is employed for the energy transfer coefficients. The master equation was solved by eigenvector based routine [37, 38] for the multichannel reactions and inversion-based approach for single channel calculations [37, 38]. In order to achieve convergence in the integration over the energy range, an energy grain size of  $100 \text{ cm}^{-1}$  was used for  $\text{N}_2$ , Ar,  $\text{SF}_4$  or  $\text{SF}_6$  as a third body and  $40 \text{ cm}^{-1}$  was used for He.

The Morse potential,

$$E(R) = D_e [1 - e^{-\beta(R - R_e)}]^2$$

evaluated by *ab initio* calculations, typically with the B3LYP or PW91PW91 methods, was used to represent the potential energy along the minimum energy path of each individual reaction coordinate. In the above equation,  $R$  is the reaction coordinate (i. e., the distance between the two bonding atoms);  $D_e$  is the bond energy excluding ZPE and  $R_e$  is the equilibrium value of  $R$ . For the tight transition states, the numbers of states were evaluated with the rigid-rotor harmonic-oscillator approximation. More details about the implementation of the variational reaction coordinate approach and related RRKM analysis are available in refs. [6-9].

The ChemRate program [36] provides the computational means, based on energy conserved one-dimensional master equation, coupling chemical activation, isomerization, decomposition and collisional energy transfer processes involved in the reactions occurring via multiple intermediates. In the present work, the energy increment,  $10 \text{ cm}^{-1}$ , was used for all sum- and density-of-state calculations which were performed using the modified Beyer-Swinehart algorithm [39]. The energy bin size of  $\delta E = 100 \text{ cm}^{-1}$  was

used in the master equation computations. Again, the exponential down model was employed for the energy transfer. For the calculations by the ChemRate program, the transition state parameters for the barrierless association and decomposition processes were evaluated canonically for each temperature and critical separation,  $r^\#(T)$ , based on the maximum Gibbs free energy criterion [12, 40].

### 3. RESULTS AND DISCUSSION

#### 3.1. Unimolecular decomposition of $\text{HClO}_4$ and $\text{HClO}_3$

Four low energy isomers have been located on the  $\text{HClO}_4$  hypersurface at the B3LYP/6-311+G(3df, 2p) level; their structures are shown in Fig. 1. The relative stability of  $\text{HClO}_4$  isomers is predicted to be:  $\text{HOClO}_3 > \text{HOOCIO}_2 \approx \text{HOOOCl} > \text{HOOCIO}$  at the G2M(CC5)/B3LYP/6-311+G(3df, 2p) level [41]. The most stable  $\text{HOClO}_3$  isomer lies below  $\text{HO} + \text{ClO}_3$  by 52.9 kcal/mol, which is close to the value of 50.3 kcal/mol predicted by Francisco [42] and the values, 53.0, 54.0 and 41.0 kcal/mol predicted by Jalbout et al. [43] at the MP2/CBSB3, MP4/CBSB4, and B3LYP/6-311++G(3df, 3pd) levels, respectively. For  $\text{HOOCIO}_2$ , Francisco [42] predicted it to be 1.4 kcal/mol less stable than  $\text{HO}_2 + \text{OClO}$ . However, our result shows that it is 12.5 kcal/mol more stable than  $\text{HO}_2 + \text{OClO}$ , which is close to the value of 10.8 kcal/mol obtained by Thomas et al. [44] at the CASSCF(CASPT2)/cc-pVTZ level. The difference in the stability of  $\text{HOOCIO}_2$  between our result and those reported in refs. [42] and [44] probably arises from the inclusion of the f-basis function in our calculation. For  $\text{HOOOCl}$ , our predicted value lies 11.1 kcal/mol below  $\text{HO}_2 + \text{OClO}$ , comparing with  $5.1 \pm 3$  kcal/mol at the G2 level of theory [42]. The most unstable intermediate,  $\text{HOOCIO}$ , lies 2.5 kcal/mol above  $\text{HO}_2 + \text{OClO}$  according to our calculation. The schematic energy diagram of the  $\text{HO}-\text{ClO}_3$  system computed at the G2M(CC5)/B3LYP/6-311+G(3df, 2p) level is shown in Fig. 2.

Based on this energy diagram and the molecular parameters obtained at the B3LYP/6-311+G(3df, 2p) level, variational TST and RRKM calculations have been carried out for the unimolecular decomposition and the reverse bimolecular association reaction rate constant of the  $\text{HO}-\text{ClO}_3$  system.

The theoretically predicted dissociation rate constant is compared with the experimental values in Fig. 3. The figure shows that our theoretically predicted rate constant at 1 atm agrees well with those obtained from flow-

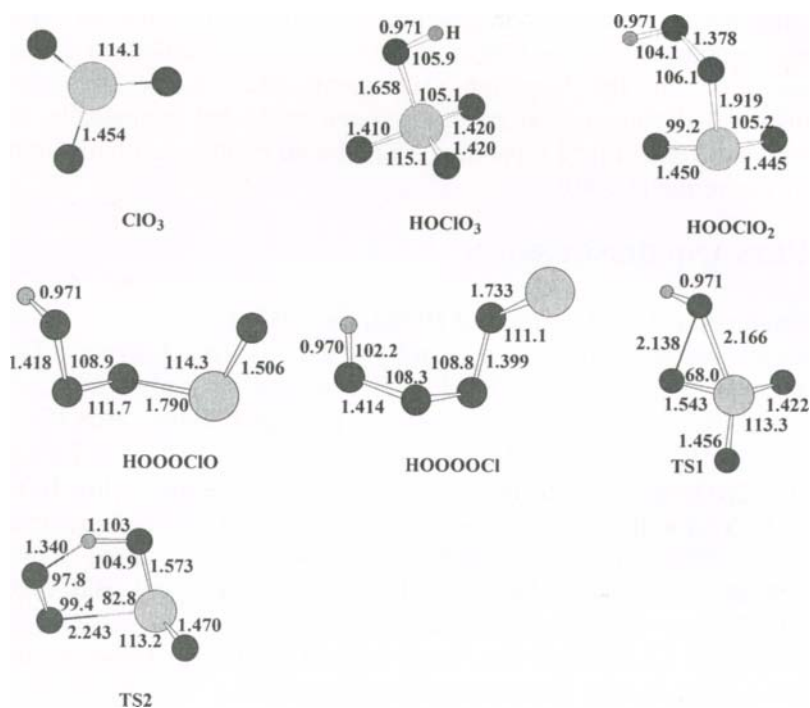


Fig. 1. The optimized geometries of the reactants, intermediates, transition states computed at the B3LYP/6-311+G(3df, 2p) level for the  $\text{HOClO}_3$  system (Ref. 41).

reactor studies [45,46] above 600 K, above which the reaction is believed to take place homogeneously with minimum heterogenous surface contributions noted at lower temperatures [45]. The rate constant at 1 atm with Ar as the third body for the decomposition reaction



can be expressed as:

$$k_1 = 5.0 \times 10^{-51} T^{-11.64} \exp(-30700 / T) \text{ s}^{-1}$$

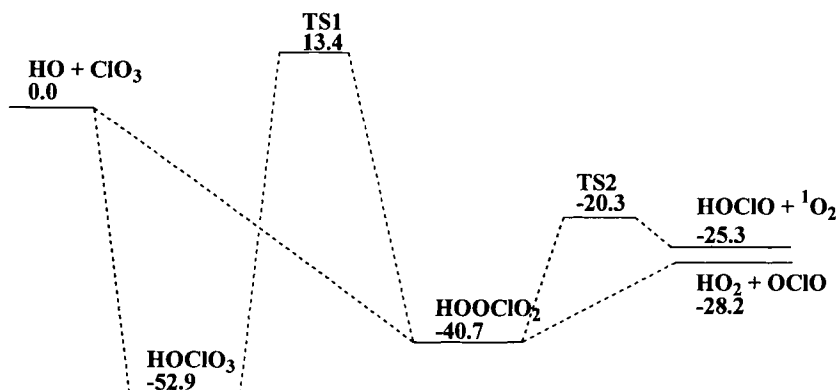


Fig. 2. Schematic energy diagram of the HO-ClO<sub>3</sub> system computed at the G2M (CC5)/B3LYP/6-311+G(3df, 2p) level (Ref. 41).

in the temperature range of 300 – 2500 K. The predicted low- and high-pressure limiting rate constants can be expressed by:

$$k_1^0 = 1.69 \times 10^{55} T^{-11.2} \exp(-29418/T) \text{ cm}^3 \text{ mol}^{-1} \text{ s}^{-1}$$

$$k_1^\infty = 1.45 \times 10^{17} \exp(-26500/T) \text{ s}^{-1}$$

in the temperature range of 300 - 2500 K. The large *A*-factor reflects the very loose transition structure for the barrierless dissociation process.

A similar calculation has been carried out for the unimolecular decomposition of chloric acid, HOClO<sub>2</sub>, employing the energetic parameters for the HO + OClO reaction (vide infra).



The predicted low- and high-pressure limiting rate constants can be expressed by:

$$k_2^0 = 7.59 \times 10^{40} T^{-7.60} \exp(-17738/T) \text{ cm}^3 \text{ mol}^{-1} \text{ s}^{-1}$$

$$k_2^\infty = 4.07 \times 10^{21} T^{-1.62} \exp(-17383/T) \text{ s}^{-1}$$

for the temperature range of 300 - 2500 K with N<sub>2</sub> as the third-body.

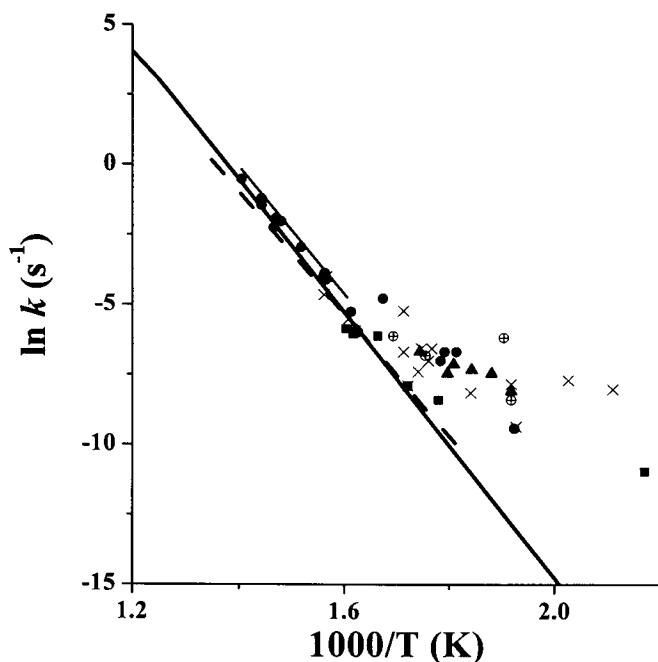


Fig. 3. Comparison of the predicted and experimental decomposition rate constants for  $\text{HOClO}_3 \rightarrow \text{HO} + \text{ClO}_3$  at atmospheric pressure. Solid line is the calculated result at 1 atm; thin solid and dashed lines are from the experimental values given the equations in refs. [45] and [46], respectively. Symbols are the experimental data of Levy [45] at 1 atm under different conditions, which were described in detail in Ref. [41].

### 3. 2. Reactions of H and HO with $\text{HClO}_4$

The kinetics and mechanisms for reactions of H and HO with  $\text{HClO}_4$ , important elementary processes in the early stages of the AP combustion reaction, have not been studied experimentally or theoretically. The mechanisms for these reactions and their rate constants are presented below.

#### 3.2.1. $\text{H} + \text{HClO}_4$ reaction

The possible channels for the  $\text{H} + \text{HClO}_4$  reaction are:

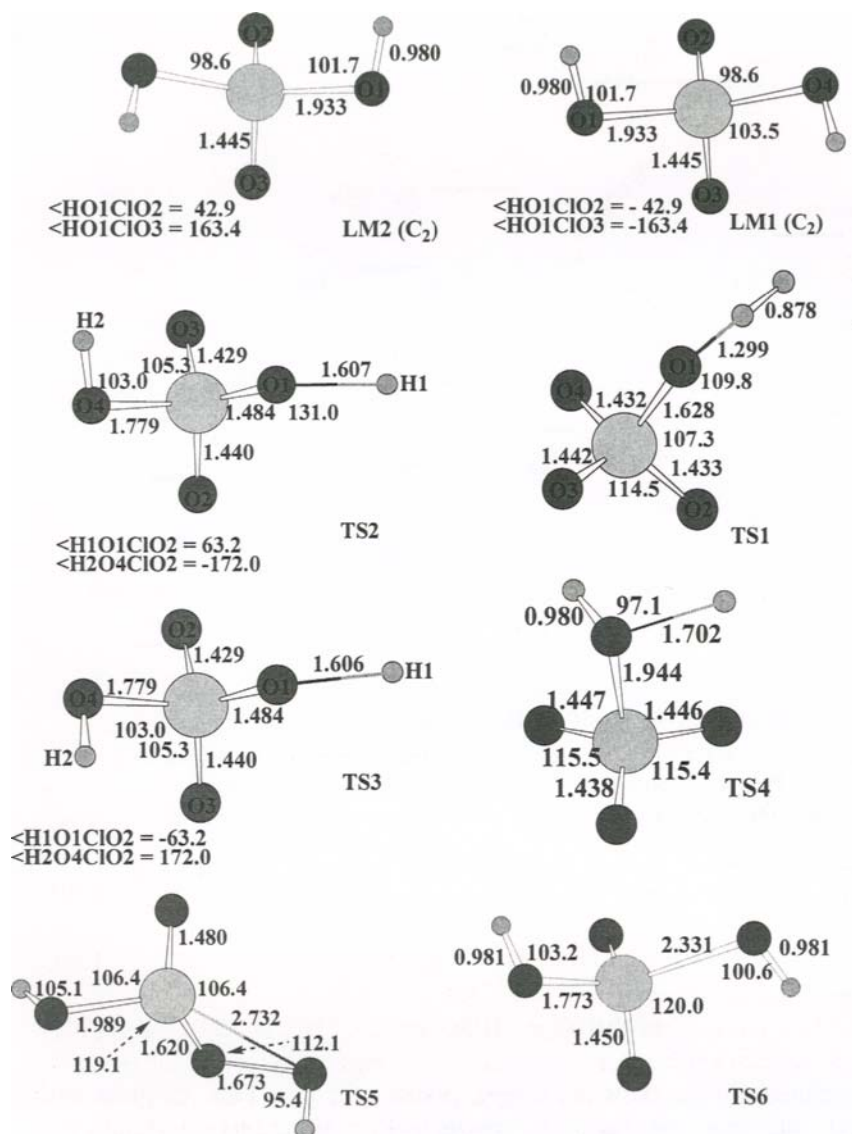


Fig. 4. The optimized geometries of intermediates, transition states computed at the PW91PW91/6-311+G(3df, 2p) level for the H-HClO<sub>4</sub> system.



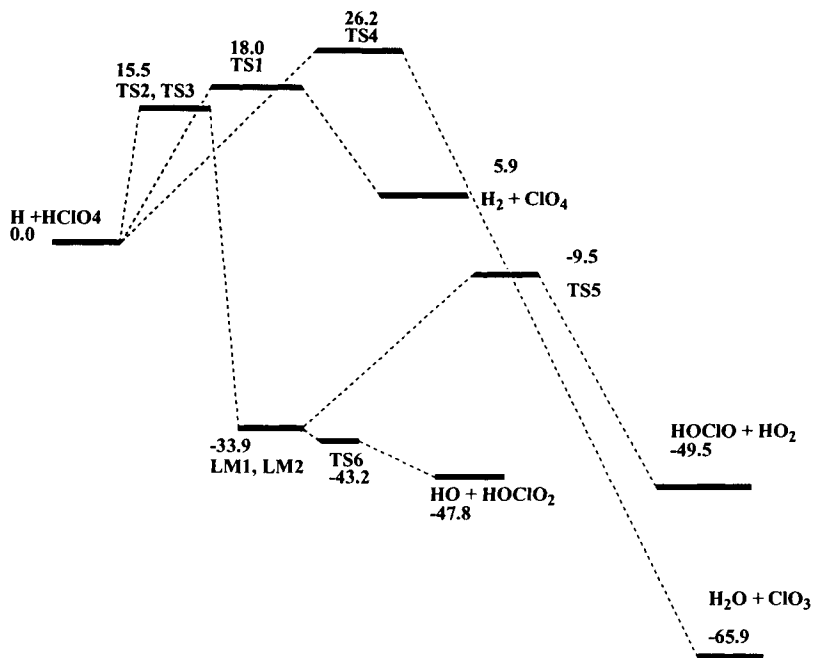
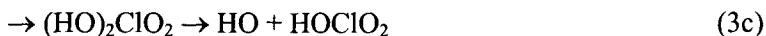


Fig. 5. Schematic energy diagram of the H-HClO<sub>4</sub> system computed at the



The structures of the key stationary points and the PES diagram are displayed in Figs. 4 and 5, respectively. For this system, the G2M(CC5)/PW91PW91/6-311+G(3df, 2p) method was employed. The results show that the direct H<sub>2</sub> and H<sub>2</sub>O elimination reactions need high barrier, 26.2 and 18.0 kcal/mol corresponding to channels 3 (a) and 3(b), respectively. The H-abstraction barrier is close to that in the H + HNO<sub>3</sub> reaction [47], 17.6 kcal/mol at the G2M level. Formation of intermediates, (HO)<sub>2</sub>ClO<sub>2</sub> (LM1), and its isomers LM2 has higher barrier, 15.5 kcal/mol,

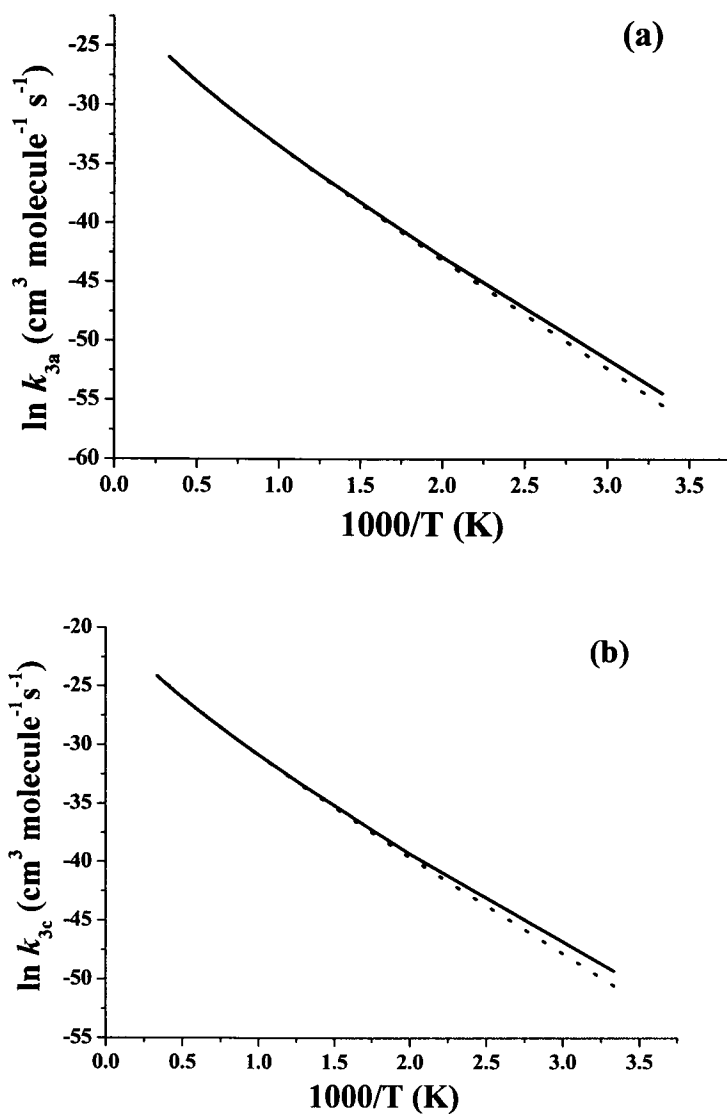


Fig. 6. Predicted rate constants for the formation of (a)  $\text{H}_2 + \text{ClO}_4$  and (b)  $\text{HO} + \text{HOClO}_2$  in the  $\text{H} + \text{HClO}_4$  reaction. Solid lines are the rate constants with tunneling corrections.

compared with the entrance barrier of forming  $(\text{HO})_2\text{NO}$  in the  $\text{H} + \text{HNO}_3$  system, 9.5 kcal/mol [47]. The results show that  $(\text{HO})_2\text{ClO}_2$  isomers are not stable and they can decompose readily to  $\text{HO} + \text{HOClO}_2$  and  $\text{HOClO} + \text{HO}_2$ . The elimination of  $\text{HO}$  from LM1 (LM2) has only 0.1 kcal/mol barrier height at the PW91PW91/6-311+G(3df, 2p) level, but at the G2M level, the transition state (TS6 in Fig. 5) lies below the  $(\text{HO})_2\text{ClO}_2$  intermediate, indicating that it is unstable and readily decomposes. It is a dominant channel with TS2 and TS3 as the controlling steps. The rate constants with parabolic tunneling corrections for the lower energy channels 3(a) and 3(c) can be represented by the following expressions in units of  $\text{cm}^3 \text{ molecule}^{-1} \text{ s}^{-1}$  in the temperature range of 300 – 3000 K.

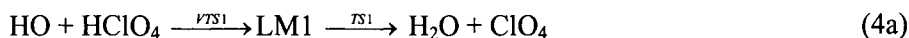
$$k_{3a} = 1.47 \times 10^{-18} T^{2.03} \exp(-7959/T)$$

$$k_{3c} = 3.33 \times 10^{-18} T^{2.02} \exp(-6878/T)$$

Both  $k_{3a}$  and  $k_{3c}$  are pressure independent, the rate constants including the tunneling effect at 300 K are 2.7 and 3.4 times higher than those without tunneling corrections as shown in Figs. 6 (a) and (b). These rate constants may be used for kinetic simulation of the AP decomposition and combustion reaction.

### 3.2.2 $\text{HO} + \text{HClO}_4$ reaction

The products of the bimolecular reaction can be formed according to the following reaction scheme:



The key complexes and transition states and the corresponding PES of the system are presented in Figs. 7 and 8, respectively. The energy profile is

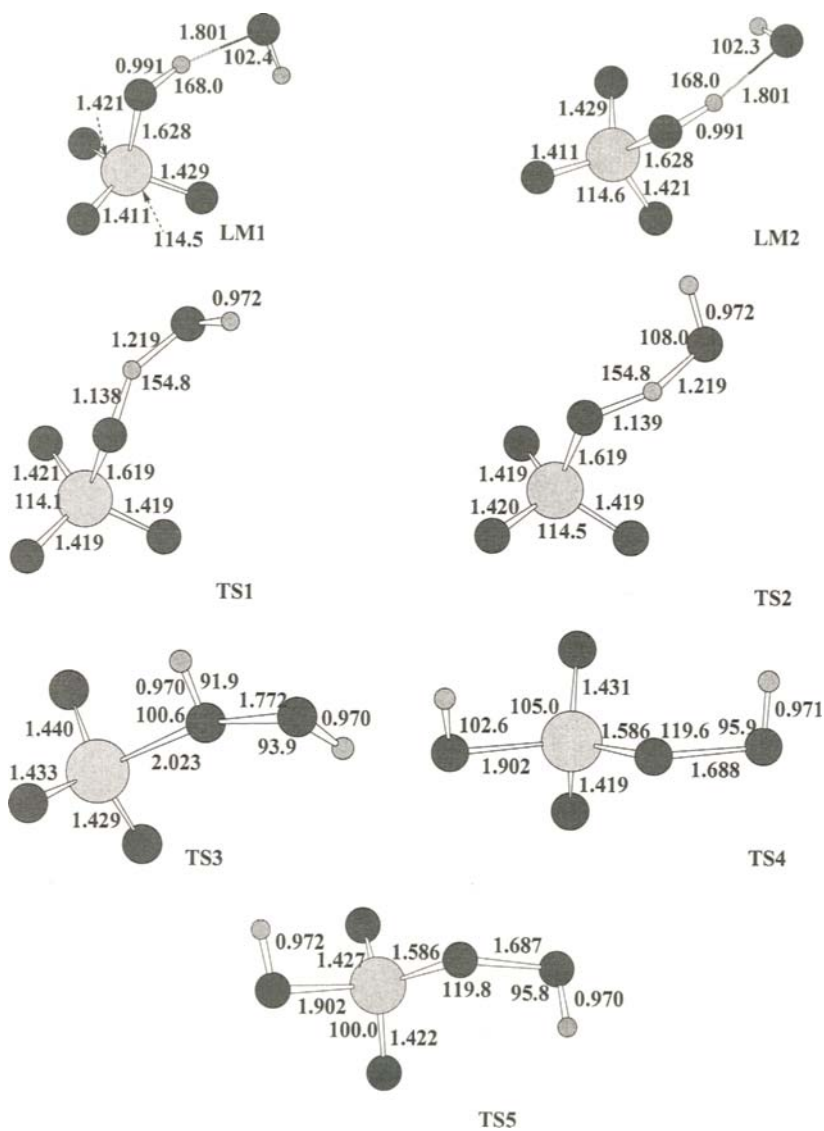


Fig. 7. The optimized geometries of the intermediates and transition states computed at the B3LYP/6-311+G(3df, 2p) level for the HO-HClO<sub>4</sub> system.

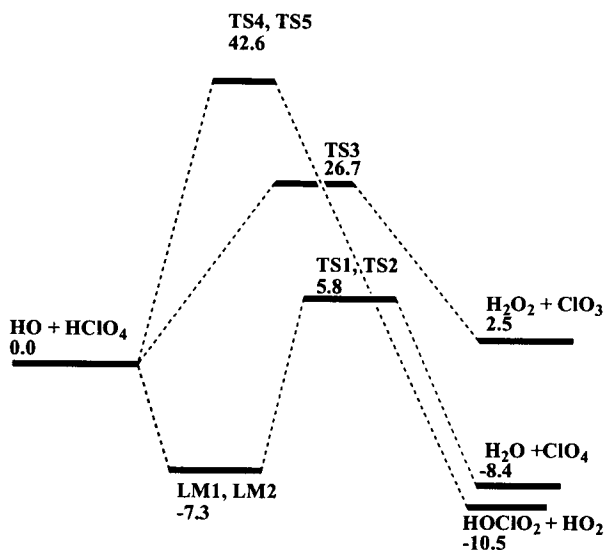


Fig. 8. Schematic energy diagram of the HO-HClO<sub>4</sub> system computed at the G2M (CC5)/B3LYP/6-311+G(3df, 2p) level.

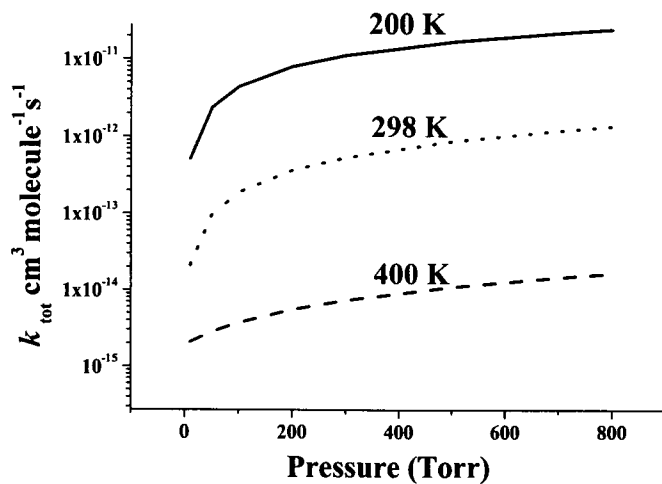


Fig. 9. Predicted total rate constants for the HO + HClO<sub>4</sub> reaction as a function of pressure Ar pressure.

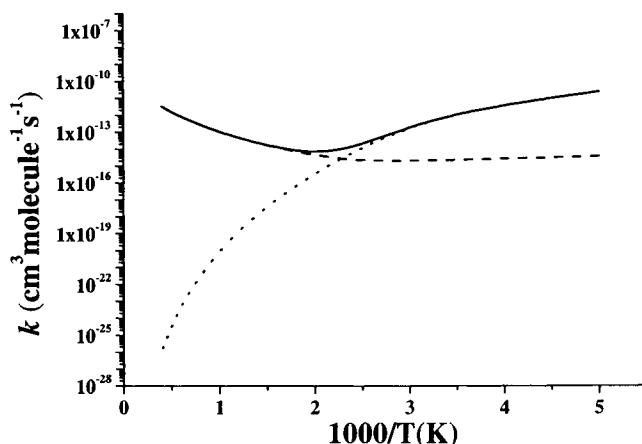


Fig. 10. Predicted individual and total rate constants as a function of temperature in the temperature of 200 – 2500 K at 1 atm. Dotted and dashed lines represent the rate constants for the formation of the HO-HClO<sub>4</sub> complex and H<sub>2</sub>O + ClO<sub>4</sub>, respectively. Solid line is the total rate constant.

similar to that of the HO + HNO<sub>3</sub> reaction [17], including the formation of the HO···HClO<sub>4</sub> complex and its dissociation energy, 7.3 kcal/mol at the G2M (CC5)//B3LYP/6-311+G(3df, 2p) level, which is close to 7.4 to 8.1 kcal/mol for that of HO···HONO<sub>2</sub> [17] complex at the G2M (cc3)//B3LYP/6-311G(d, p) level. The barrier for the direct formation of H<sub>2</sub>O<sub>2</sub> from the HO + HClO<sub>4</sub> reaction, 26.6 kcal/mol, is close to 24.4 kcal/mol corresponding to the H<sub>2</sub>O<sub>2</sub> formation in the HO + HNO<sub>3</sub> reaction [17].

The total rate constants computed as a function of pressure at 200, 298 and 400 K using Variflex [35], with Ar as a bath gas are shown in Fig. 9. The temperature dependent rate constant at 1 atm was shown in Fig. 10. The results presented in these figures indicate that the HO + HClO<sub>4</sub> reaction exhibits strong negative temperature and positive pressure effects at lower temperatures (< 500 K). The former effect can be attributed to the fact that the association reaction is barrierless and the exit channels (4a, 4b) with 5.8 kcal/mol barriers have negligible contributions at lower temperatures. The well depth of the stable complexes are 7.3 kcal/mol, which are responsible for the predicted pressure effect. The positive temperature dependence at higher temperatures apparently arises from the decomposition of LM1 and LM2 via TS1 and TS2, respectively. Over 500 K, the total rate constant appears to be pressure-independent and dominated by the decomposition processes. At 1 atm in Ar, the individual and total rate constants given in

units of  $\text{cm}^3 \text{ molecule}^{-1} \text{ s}^{-1}$  can be presented by:

$$k_{(4a+4b)} = 3.95 \times 10^{-23} T^{3.3} \exp(-930/T) \text{ for } 500 - 2500 \text{ K.}$$

$$k_{\text{tot}} = 3.27 \times 10^{-98} T^{26.2} \exp(14191/T) \text{ for } 200 - 500 \text{ K}$$

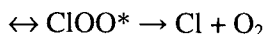
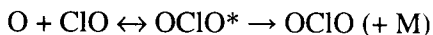
$$k_{\text{tot}} = 1.27 \times 10^{-23} T^{3.4} \exp(-747/T) \text{ for } 500 - 1000 \text{ K.}$$

### 3. 3. Unimolecular decomposition of $\text{ClO}_x$ ( $x = 2 - 4$ )

#### 3. 3 .1. *ClOO and OClO*

Both chlorine peroxy radical ( $\text{ClOO}$ ) and chlorine dioxide molecule ( $\text{OClO}$ ) play a pivotal role in the destruction of  $\text{O}_3$  and in the combustion of AP [20-21]. They can be formed by the reactions of Cl and ClO radical reactions with  $\text{O}_2$  and s- $\text{ClO}_3$ .  $\text{OClO}$  is also a potential intermediate in the  $\text{O} + \text{ClO}$  reaction under high-pressure conditions, although such a possibility has not been assumed in most studies under normal laboratory experimental conditions.

Theoretically, the decomposition of  $\text{OClO}$  and  $\text{ClOO}$  can take place by the following processes



The PES calculated at the G2M (CC2)//PW91PW91/6-311+G(3df) level is shown in Fig. 11. The key structures of species involved in this reaction are shown in Fig. 12. TS1 is the transition state for the  $\text{OClO} \leftrightarrow \text{ClOO}$  isomerization reaction with a barrier of 63.3 kcal/mol, whereas TS2 is that for the  $\text{ClO}'\text{O}'' \leftrightarrow \text{ClO}''\text{O}'$  isomerization with a barrier of 61.5 kcal/mol. Predicted rate constants for the production of  $\text{O} + \text{ClO}$  and  $\text{Cl} + \text{O}_2$  resulted directly from the unimolecular decomposition processes with no contributions from the isomerization reactions. Comparison of the predicted  $\text{ClOO}$  decomposition rate with experimentally available values is shown in Fig. 13. The low- and high-pressure rate constants for  $\text{OClO}$  and  $\text{ClOO}$  dissociations can be expressed by:

$$k_{\text{d}(\text{OClO})}^0 = 9.89 \times 10^{-24} T^{11.0} \exp(-16648/T) \text{ cm}^3 \text{ mol}^{-1} \text{ s}^{-1}$$

$$k_{\text{d}(\text{OClO})}^\infty = 1.11 \times 10^{16} T^{-0.28} \exp(-29567/T) \text{ s}^{-1}$$

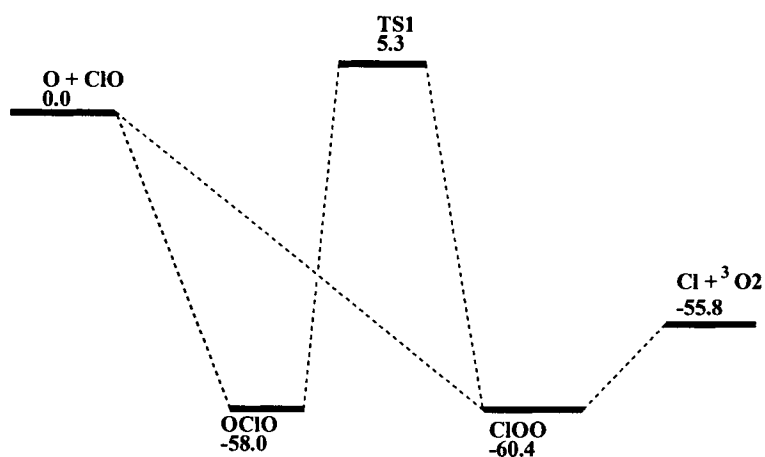


Fig. 11. Schematic energy diagram of the OCIO - ClOO system computed at the G2M (CC2)/PW91PW91/6-311+G(3df, 2p) level.

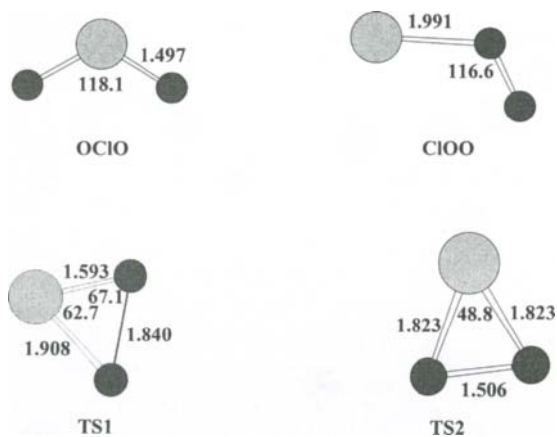


Fig. 12. The optimized geometries of intermediates, transition states computed at the PW91PW91/6-311+G(3df, 2p) level for the O-ClO system.



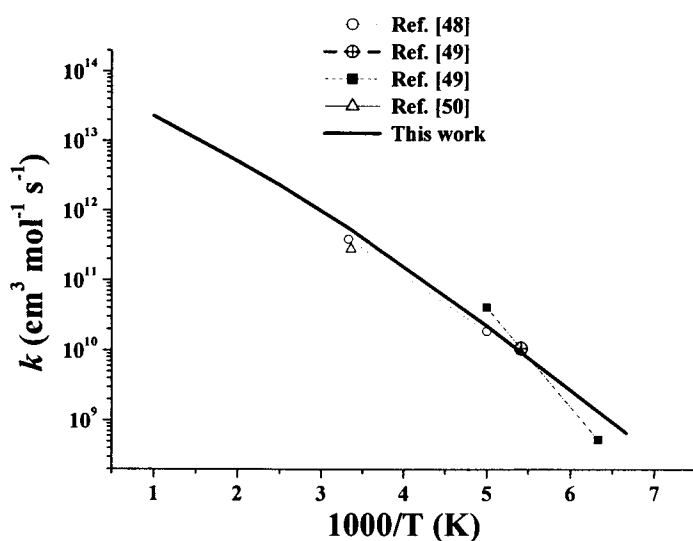


Fig. 13. Comparison of the predicted and experimental decomposition rate constants for  $\text{ClOO} + \text{M} \rightarrow \text{Cl} + \text{O}_2 + \text{M}$ . Solid line is the calculated result for  $\text{N}_2$  as the third body.

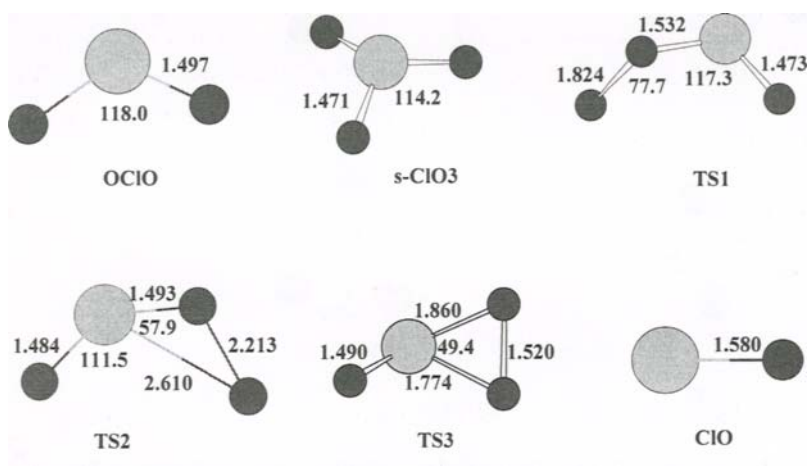


Fig. 14. The optimized geometries of reactants, intermediates, transition states computed at the PW91PW91/6-311+G(3df, 2p) level for the s-ClO<sub>3</sub> system.

$$k_{\text{d(CIOO)}}^0 = 2.81 \times 10^{15} T^{-0.41} \exp(-1897/T) \text{ cm}^3 \text{ mol}^{-1} \text{ s}^{-1}$$

$$k_{\text{d(CIOO)}}^\infty = 4.87 \times 10^{15} T^{-0.59} \exp(-2585/T) \text{ s}^{-1}$$

in the temperature range of 200 – 2500 K with N<sub>2</sub> as a third body.

### 3. 3. 2. *s*-ClO<sub>3</sub>

Although the *s*-ClO<sub>3</sub> system has been theoretically studied by several investigators [41, 51-56], its decomposition mechanism presented in this section had not been reported until our recent work on the system [57]. According to our calculation, there are two channels forming the commonly assumed products ClO + <sup>3</sup>O<sub>2</sub>. In the first channel, one of the Cl-O bond in *s*-ClO<sub>3</sub> lengthens to 2.610 Å via TS2 (see Fig. 14) and the departing O atom abstracts another O atom to give the ClO + O<sub>2</sub> products. TS2 has a looser structure with the predicted energy lying 5.6 kcal/mol above the <sup>3</sup>O + OCIO reactants at the G2M(CC2)//PW91PW91/6-311+G(3df) level. In the second channel, *s*-ClO<sub>3</sub> dissociates to form ClO + <sup>3</sup>O<sub>2</sub> via a tight transition state TS3 in which two of the Cl-O bonds break concurrently. The breaking bonds lengthen by 0.389 and 0.303 Å compared with those in *s*-ClO<sub>3</sub>. TS3 lies 16.9 kcal/mol above the reactants at the G2M(CC2)//PW91PW91/6-311+G(3df) level. This transition state has higher barrier because of the simultaneous involvement of two breaking bonds. Therefore, this dissociation channel is kinetically unimportant. The production of ClO + <sup>3</sup>O<sub>2</sub> is exothermic by 59.2 kcal/mol at the G2M//PW91PW91/6-311+G(3df) level. Apparently, the dominating channel is the formation of <sup>3</sup>O + OCIO without a well defined TS. The energy diagram is shown in Fig. 15. The predicted high- and low-pressure limiting rate constants for the decomposition reaction,



can be expressed by:

$$k_4^\infty = 1.5 \times 10^{20} T^{-1.1} \exp(-18360/T) \text{ s}^{-1}$$

$$k_4^0 = 3.76 \times 10^{25} T^{-3.28} \exp(-13890/T) \text{ cm}^3 \text{ mol}^{-1} \text{ s}^{-1}$$

in the temperature range of 500 – 2500 K.

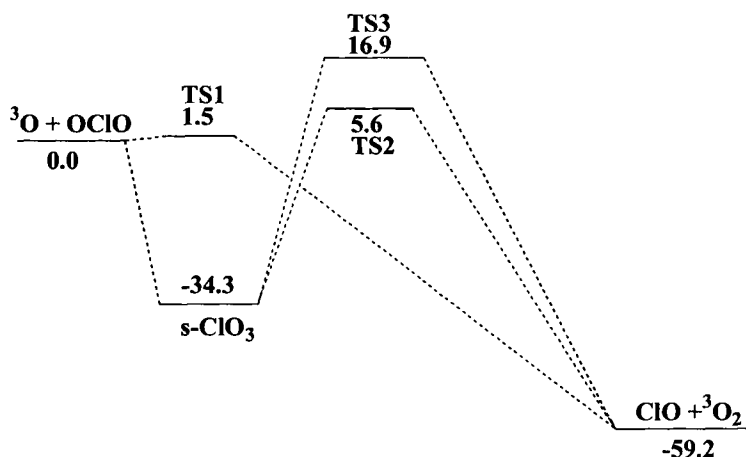
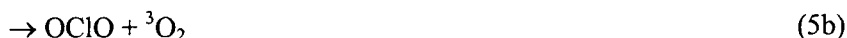


Fig. 15. Schematic energy diagram of the  $\text{O} + \text{OClO}$  system computed at the G2M (CC2)//PW91PW91/6-311+G(3df, 2p) level [57].

### 3. 3. 3. $\text{ClO}_4$

The structure of  $\text{ClO}_4$  with  $\text{C}_{2v}$  symmetry has been studied by Beltrá et al. [55] at the B3LYP/6-311+G(3df) level of theory, in agreement with our result obtained at the PW91PW91/6-311+G(3df) level. Its decomposition mechanism has not been reported theoretically or experimentally. Based on our calculation, the possible dissociation channels are:



The first channel is a barrierless process, whereas the second one has a tight transition state. The key structures and the energy diagram obtained at the G2M (CC5)//PW91PW91/6-311+G(3df) level are shown in Fig. 16.

The Variflex program [35] was employed to calculate the dissociation rate constants. The predicted high- and low-pressure limiting rate constants for the decomposition reaction  $\text{ClO}_4 \rightarrow \text{s-ClO}_3 + {}^3\text{O}$  can be expressed by:

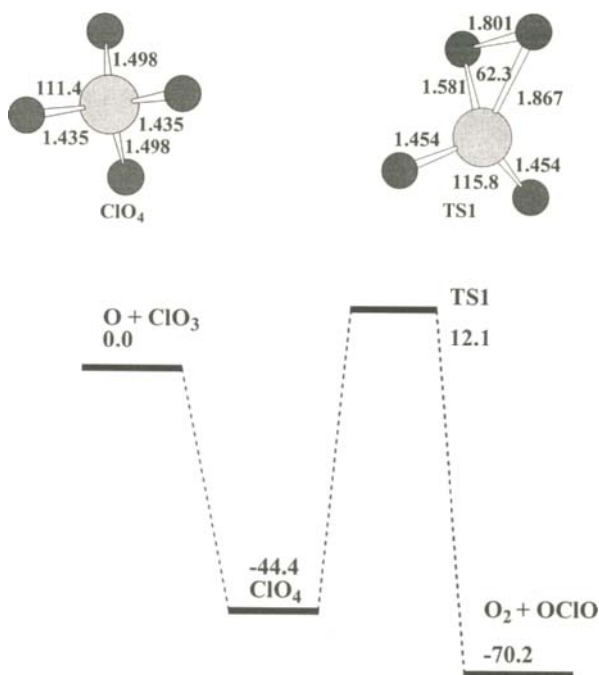


Fig. 16. Key species structures and the schematic energy diagram for  $\text{ClO}_4$  decomposition calculated at the G2M (CC2)//PW91PW91/6-311+G(3df, 2p) level.

$$k_{5a}^{\infty} = 5.2 \times 10^{20} T^{-1.3} \exp(-23215/T) \text{ s}^{-1}$$

$$k_{5a}^0 = 9.60 \times 10^{46} T^{-9.0} \exp(-24266/T) \text{ cm}^3 \text{ mol}^{-1} \text{ s}^{-1}$$

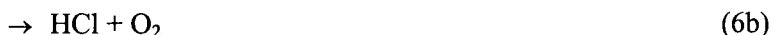
in the temperature range of 500 – 2500 K for Ar as a diluent. Comparing with the  $\text{ClO}_4 \rightarrow \text{s-ClO}_3 + {}^3\text{O}$  channel, the rate constant for production of molecular products  $\text{OCIO} + {}^3\text{O}_2$  can be neglected owing to its high barrier and tight transition state (see Fig. 16).

### 3. 4. Bimolecular reactions of $\text{ClO}_x$ ( $x = 1\text{-}3$ )

#### 3. 4. 1. $\text{HO} + \text{ClO}$

For this reaction, there have been numerous studies on its rate constants at the pressures of interest to the stratospheric chemistry [58-68]. The

reaction may occur by the following mechanism with the two key product channels:



HOOC1 has been assumed to be the key intermediate leading to the formation of these two sets of products [69]. Reaction (6a) has been shown to be the major channel in the reaction [58-61]. In these studies, the branching ratio  $k_{6b}/(k_{6a} + k_{6b})$  was reported in the range of 6.5 - 10 % at 243 - 298 K; but the products of reaction (6b) were not directly measured. More recently there are several measurements of HCl or DCl yields: the branching ratio for the 6(b) product channel has been determined. Lipson et al. [64-65] reported  $k_{6b}/(k_{6a} + k_{6b}) = 7 \pm 3\%$  for HO + ClO and  $5 \pm 2\%$  for DO + ClO reactions, respectively; Bedjania et al. [67] obtained  $k_{6b}/(k_{6a} + k_{6b}) = 3.5 \pm 1\%$  for the HO + ClO reaction. A direct measurement of the concentration of [HCl] and [HO] in the reaction by Wang and Keyser [68] found that the yield of HCl from the HO + ClO reaction given by  $[\text{HCl}]/[\text{HO}]_0$  was  $9.0 \pm 4.8\%$ , independent of temperature between 218 and 298 K at 1 Torr pressure.

Theoretically, the stability of HOOC1 intermediate and its structural isomers have been studied by Franciso et al. [70], and Lee and Rendell [71]. Sumathi and Peyerimhoff [72] calculated the potential energy surface (PES) of the reaction and concluded that reaction (6b) was less important because of the high barrier. Dubey et al. [73] performed a box-model sensitivity analysis using the recommended value [74] of  $k_{6a}$  and found that the transition state (see TS5 in Fig.17 later) for HCl production must lie at least 2 kcal/mol below the reactants for the HCl yield to exceed 5%; Lipson et al. [64, 65] performed a statistical theory calculation by adjusting the energy of TS5 to reproduce their results; they arrived at the conclusion that TS5 should locate at  $\sim 1.2$  kcal/mol below the reactants.

In our study, the complete PES for the system has been mapped out and the total rate constant and branching ratio were calculated for this reaction on the basis of the computed PES using a variational statistical method. The results of this study are presented below.

The geometry of the reactants, intermediates and products optimized at the B3LYP/6-311+G(3df, 2p) level is shown in Fig.17, while those of the transition states optimized at the same level are displayed in Fig.18. The singlet and triplet potential energy diagrams obtained at the G2M (CC2)//-

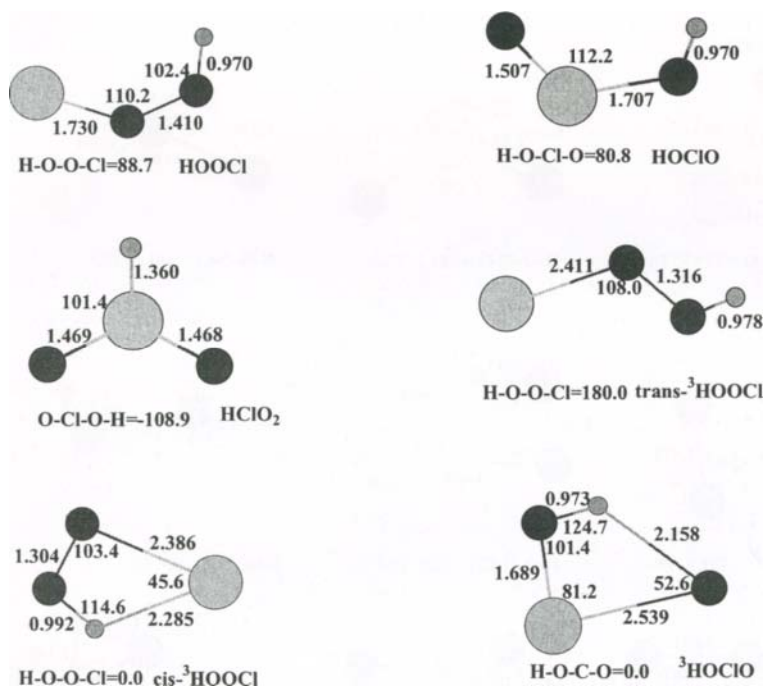


Fig. 17. The optimized geometries of the reactants and intermediates computed at the B3LYP/6-311+G(3df, 2p) level for the HO-ClO system [75].

B3LYP/6-311+G(3df, 2p) level are presented in Figs. 19 (a) and 19 (b), respectively.

The reaction was shown to take place primarily over the singlet surface by two main channels producing  $\text{HO}_2 + \text{Cl}$  and  $\text{HCl} + {}^1\text{O}_2$ , with the former being dominant. The Variflex program was used for the rate constant calculation. The predicted total rate constant,

$$k_t = 5.27 \times 10^{-9} T^{-1.03} \exp(-40/T) \text{ cm}^3 \text{ molecule}^{-1} \text{ s}^{-1},$$

and product branching ratios in the temperature range 200 - 500 K at  $P < 200$  atm agree satisfactorily with experimental values. The computed branching ratios,  $k_{6b}/(k_{6b} + k_{6a}) = 0.073$  for  $\text{HCl} + {}^1\text{O}_2$  and 0.045 - 0.048 for  $\text{DCI} + {}^1\text{O}_2$  in the temperature range 200 - 500 K based on the recent

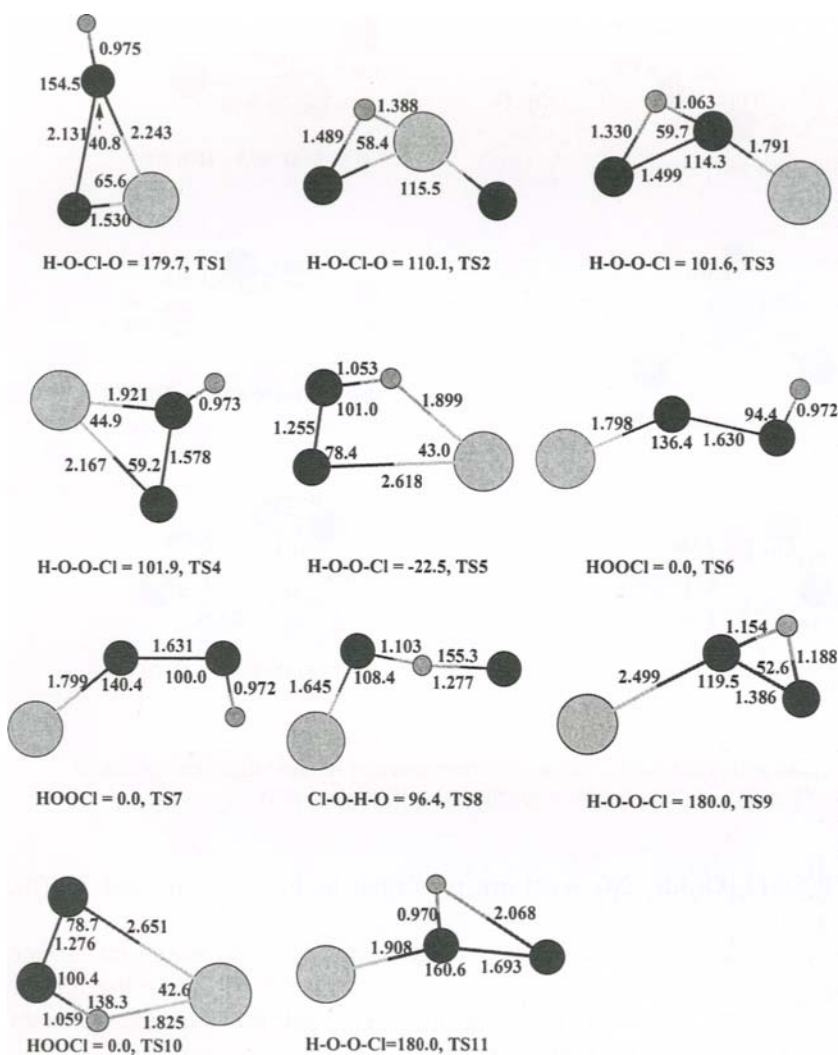


Fig. 18. The optimized geometries of transition states computed at the B3LYP/6-311+G(3df, 2p) level for the HO-ClO system [75].

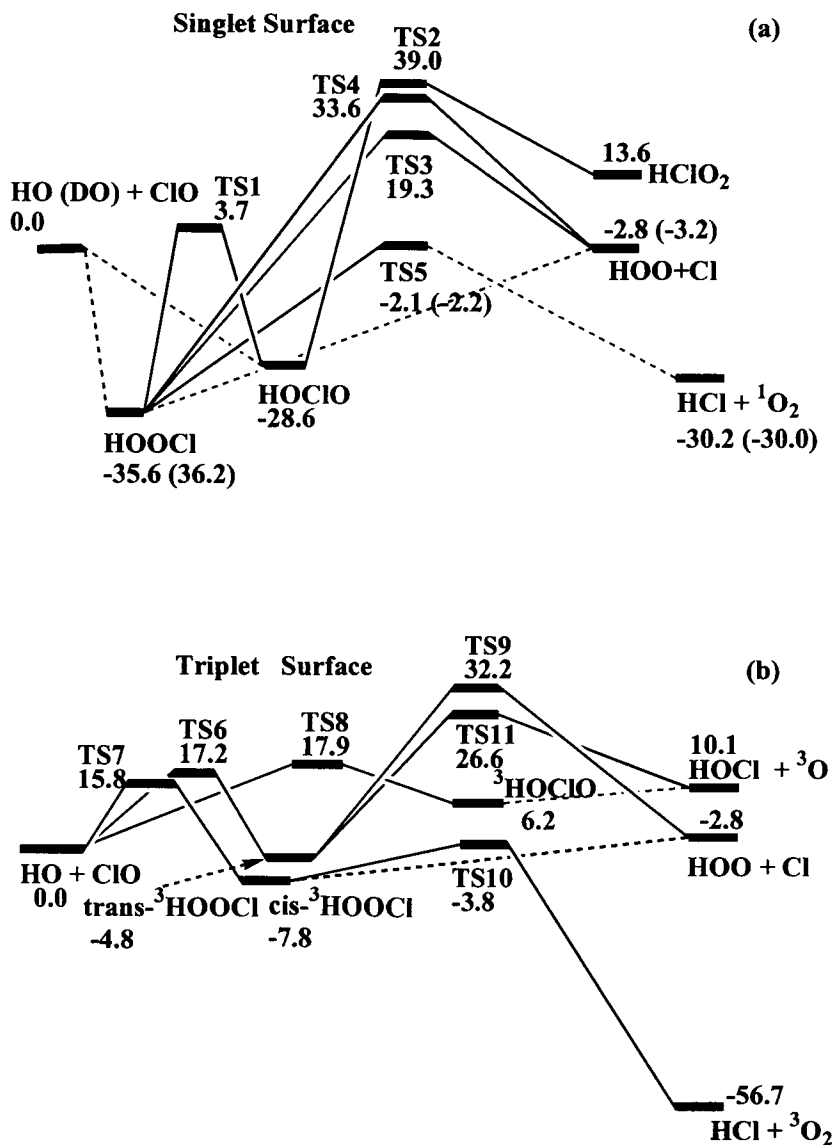


Fig. 19. Schematic energy diagram of the HO + ClO system [75] computed at the G2M (CC2)/B3LYP/6-311+G(3df, 2p) level.



experimental heat of formation for HO<sub>2</sub> ( $4.0 \pm 0.8$  kcal/mol) compare closely with the experimental values,  $0.07 \pm 0.03$  and  $0.05 \pm 0.02$ , respectively. At higher temperatures (1000 – 2500 K), the branching ratios increase slightly to 0.084 – 0.137 and 0.061 – 0.111 for the OH and OD reactions, respectively. The rate constant for HO<sub>2</sub> + Cl and HCl + O<sub>2</sub> production from OH + ClO in the temperature range, 500 – 2500 K, can be given by:

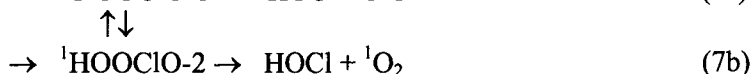
$$k_{6a} = 3.4 \times 10^{-13} T^{0.3} \exp(725/T)$$

$$k_{6b} = 5.85 \times 10^{-19} T^{1.67} \exp(1926/T)$$

in units of cm<sup>3</sup> molecule<sup>-1</sup> s<sup>-1</sup>, respectively. Comparison of the predicted total rate constants with the experimental values was shown in Fig. 20.

### 3. 4. 2. HO + OCIO reaction

Base on the ab initio MO calculations [76] made with the G2M (CC2)//B3LYP/6-311+G(3df, 2p) method, three key product channels, all located on the singlet PES have been identified as:



The singlet and triplet PES calculated at the G2M (CC2)//B3LYP/6-311+G(3df, 2p) level for the HO + OCIO reaction are presented in Figs. 21 (a) and (b); the corresponding structures can be found in Ref. [76]. Because of the high entrance barriers of all triplet channels, their contributions to the HO + OCIO reaction are negligible kinetically and are not calculated in this work.

The rate constant for the association reaction channel (7c) was calculated in the temperature range from 200 to 2500 K and the pressure range from  $1 \times 10^{-5}$  to  $7.6 \times 10^7$  Torr with the Variflex code [35], whereas those for channels (7b) and (7c) were computed with the ChemRate program [36] coupling all intermediates involved in the forward and reverse reactions as shown below:

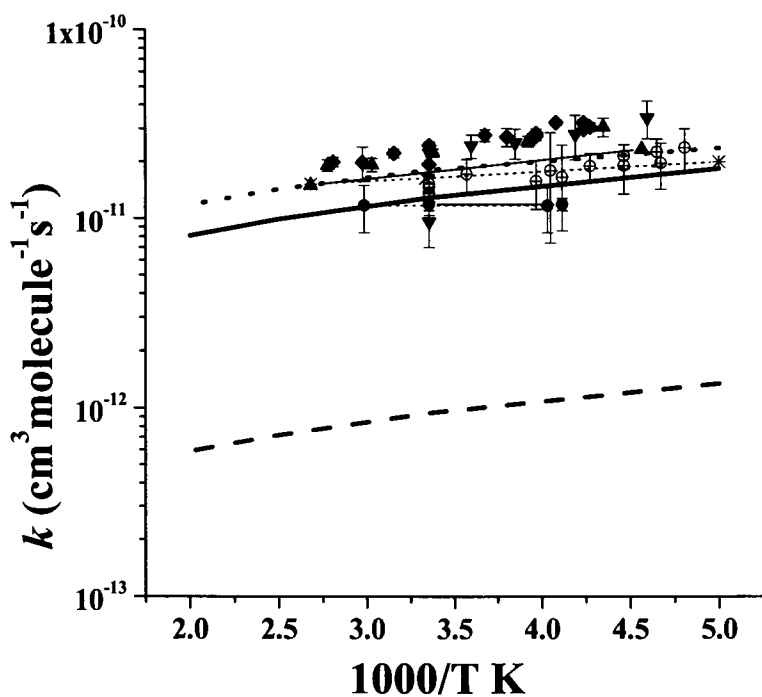
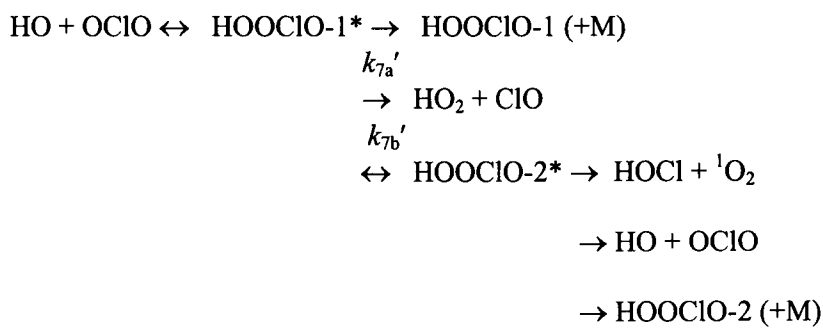


Fig. 20 All experimental points and symbols are described in Fig. 5 of ref. 75.

*Scheme 1:*



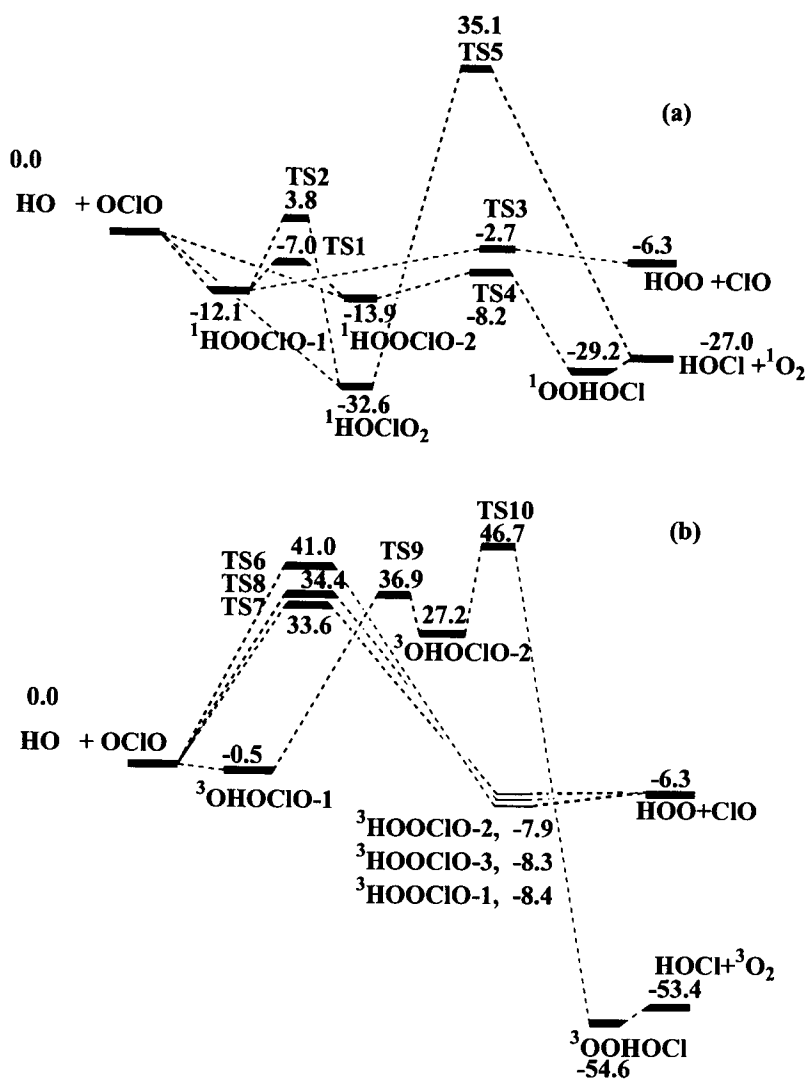
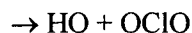
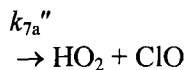
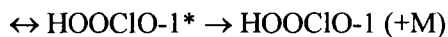
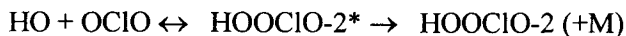


Fig. 21. Schematic energy diagram of the HO + OCIO system [76] computed at the G2M (CC2)/B3LYP/6-311+G(3df, 2p) level.

Scheme 2:



The calculated results show that the rate constants for channels (7a) and (7b) are pressure-independent up to 1000 atm and that for channel (7c) is strongly pressure dependent. Below 1000 K, all rate constants were found to vary negatively with temperature. Comparison of the predicted total rate constant with the available experimental values (Ref. 77) is drawn in Fig. 22. The agreement between theory and experiment is excellent.

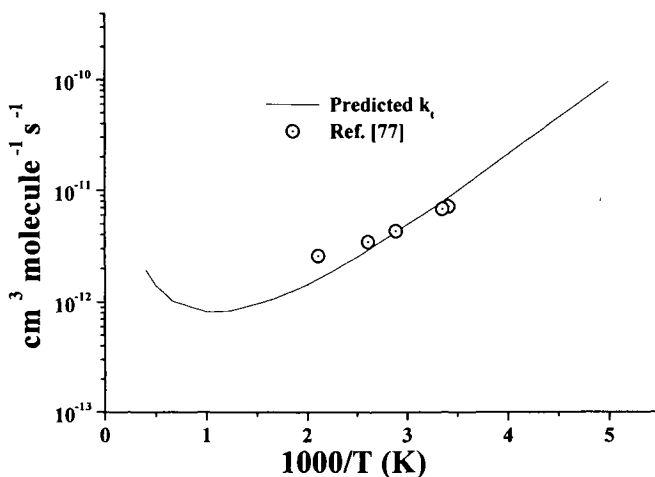


Fig. 22. Comparison between the predicted total rate constant and the available experimental values (Ref. 77) for the reaction of HO + OCIO.

The predicted rate constants over the temperature range of 200 - 1000 K at 1 Torr He pressure for the three product channels can be expressed in units of  $\text{cm}^3 \text{ molecule}^{-1} \text{ s}^{-1}$  by:

$$k_{7a} = 1.22 \times 10^{-22} T^{2.75} \exp(1682/T)$$

$$k_{7b} = 5.47 \times 10^{-20} T^{2.07} \exp(2064/T)$$

$$k_{7c} = 1.37 \times 10^{-4} T^{-6.61} \exp(-536/T) \text{ for } 200 - 500 \text{ K}$$

$$k_{7c} = 4.99 \times 10^{-34} T^{-22.36} \exp(-9807/T) \text{ for } 500 - 1000 \text{ K}$$

$$k_{\text{tot}} = 1.78 \times 10^{-20} T^{2.25} \exp(2100/T)$$

For AP combustion applications, the high- and low- pressure limits of the rate constant for the formation of  $\text{HClO}_3$  from  $\text{HO} + \text{OClO}$ ,  $k_{7c}$ , with  $\text{N}_2$  as the third-body are given below:

$$k_{7c}^{\infty} = 3.24 \times 10^{-11} T^{0.28} \exp(-18/T) \text{ cm}^3 \text{ molecule}^{-1} \text{ s}^{-1} \text{ in } 200 - 2500 \text{ K},$$

$$k_{7c}^0 = 1.28 \times 10^{-13} T^{-6.36} \exp(-635/T) \text{ cm}^6 \text{ molecule}^{-2} \text{ s}^{-1} \text{ in } 200 - 1000 \text{ K},$$

$$k_{7c}^0 = 2.91 \times 10^{-13} T^{-8.4} \exp(-11500/T) \text{ cm}^6 \text{ molecule}^{-2} \text{ s}^{-1} \text{ in } 1000 - 2500 \text{ K}.$$

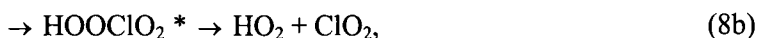
At atmospheric  $\text{N}_2$  pressure,  $k_{7c}$  can be represented by the expression in units of  $\text{cm}^3 \text{ molecule}^{-1} \text{ s}^{-1}$ :

$$k_{7c}^{1 \text{ atm}}(T) = 1.33 \times 10^9 T^{-7.36} \exp(-1182/T) \text{ in } 200 - 1000 \text{ K},$$

$$k_{7c}^{1 \text{ atm}} = 3.89 \times 10^{10} T^{-9.76} \exp(-10860/T) \text{ in } 1000 - 2500 \text{ K}.$$

### 3. 4. 3. $\text{HO} + \text{ClO}_3$

As shown in Fig. 2, the main channels of this reaction are:



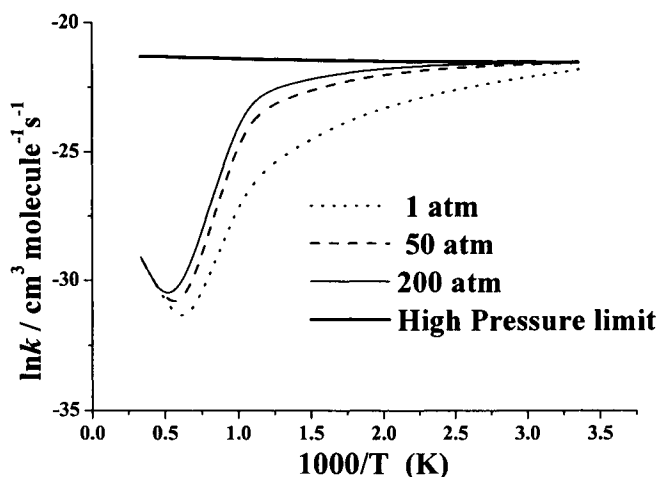


Fig. 23. Predicted pressure-dependent bimolecular rate constants for the combination reaction,  $\text{HO} + \text{ClO}_3 \rightarrow \text{HOClO}_3$ .

On the basis of the energies obtained at the G2M(CC5)//B3LYP/6-311+G(3df, 2p) level (Fig. 2), their rate constants were calculated with the Variflex program. The calculated pressure-dependent association reaction rate constants for  $\text{HO} + \text{ClO}_3 \rightarrow \text{HOClO}_3$  are displayed in Fig. 23. The result shows that the association process has a strong positive-pressure dependence from 0 – 200 atm and a strong, negative temperature dependence from 800 – 1500 K with a small positive – temperature effect above 1500 K (due to the onset of the isomerization reaction producing  $\text{HOOCLO}_2$ ). At the high-pressure limit, the association rate constant was predicted to have a slight positive-temperature effect resulting from the large entropic contribution to the dissociation process. The reaction of  $\text{HO} + \text{ClO}_3 \rightarrow \text{HO}_2 + \text{ClO}_2$  via  $\text{HOOCLO}_2$  was predicted to be pressure-independent up to 200 atm. At the low- and high-pressure limit, the rate constants for the bimolecular reactions,  $\text{HO} + \text{ClO}_3 \rightarrow \text{HOClO}_3$  and  $\text{HO} + \text{ClO}_3 \rightarrow \text{HO}_2 + \text{OCLO}$ , in the temperature range of 300 - 3000 K were found to be comparable and could be represented by:

$$k_{8a}^0 = 1.81 \times 10^2 T^{-10.4} \exp(-2201/T) \text{ cm}^6 \text{ molecule}^{-2} \text{ s}^{-1}$$

$$k_{8a}^\infty = 3.2 \times 10^{-10} T^{0.07} \exp(-25/T) \text{ cm}^3 \text{ molecule}^{-1} \text{ s}^{-1}$$

$$k_{8b}^0 = k_{8b}^\infty = 2.1 \times 10^{-10} T^{0.09} \exp(-18/T) \text{ cm}^3 \text{ molecule}^{-1} \text{ s}^{-1},$$

respectively. Under the atmospheric pressure condition, the production of  $\text{HO}_2 + \text{ClO}_2$  is dominant with the following predicted rate constants given in units of  $\text{cm}^3 \text{ molecule}^{-1} \text{ s}^{-1}$ :

$$k_{8a} = 1.94 \times 10^{36} T^{-15.3} \exp(-5542/T) \text{ in } 300 - 1500 \text{ K}$$

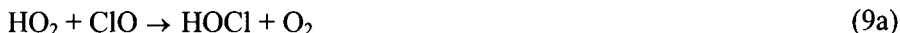
$$k_{8a} = 6.7 \times 10^{-21} T^{2.3} \exp(-4168/T) \text{ in } 500 - 3000 \text{ K}$$

$$k_{8b} = k_{8b}^\infty = 2.1 \times 10^{-10} T^{0.09} \exp(-18/T) \text{ in } 500 - 3000 \text{ K}.$$

We have also examined the possible formation of  $\text{HOOClO}$  from  $\text{OH} + \text{ClO}_3$  via  $\text{HOOCLO}_2$ . The reaction was found to be too slow to be competitive with the  $\text{HO}_2 + \text{OClO}$  product channel. Under the more favorable, higher temperature condition, for instance, at 1 atm and 2000 K, the predicted  $\text{HOOClO}$  formation rate constant,  $5.4 \times 10^{-14} \text{ cm}^3 \text{ molecule}^{-1} \text{ s}^{-1}$ , is 3 orders of magnitude lower than for  $\text{HO}_2 + \text{OClO}$  formation via  $\text{HOOCLO}_2$  under the same condition. Accordingly, the contributions of  $\text{HOOClO}$  and  $\text{HOOOCl}$  (via  $\text{HOOClO}$ ) to the  $\text{HO} + \text{ClO}_3$  reaction are insignificant under all accessible experimental conditions.

### 3. 4. 4. $\text{HO}_2 + \text{ClO}$

The reaction of  $\text{HO}_2 + \text{ClO}$  may in principle take place by a number of pathways by direct abstraction or by indirect association/decomposition processes involving excited intermediates:





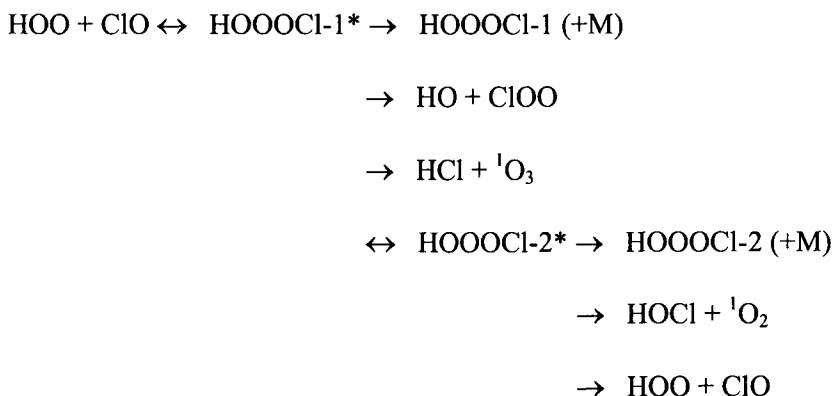
Experimentally, the kinetics of this important reaction have been extensively studied by several groups using a variety of techniques [78-85]. Theoretically, there are four papers on the mechanism and kinetics of the reaction. In 1986, Mozurkewich [86] proposed that the reaction proceeded via a  $\text{HO}_2\text{ClO}$  intermediate and calculated the rate constants by RRKM theory. Toohey and Anderson [87] reported in 1989 a transition state, connecting the reactants with the  $\text{HOCl}$  and  $\text{O}_2$  products on a triplet surface, at the HF and MP2 levels of theory with the 6-31G(d, p) basis set. They suggested a dual mechanism dominated by direct hydrogen abstraction at high temperatures and by elimination from a stable cyclic- $\text{OCIOOH}$ -intermediate at lower temperatures. In 1994, Buttar and Hirst [88] studied the reaction via both the triplet and singlet reaction paths. The geometries were optimized at the MP2/6-31G(d,p) level and the barriers were determined at the MP4/6-311G(d,p) level. They indicated that the  $\text{HO}_2 + \text{ClO}$  reaction proceeded via a multi-step reaction mechanism on the singlet surface and via a direct hydrogen-abstraction mechanism on the triplet surface. In addition to their experimental work, Nickolaissen and co-workers [84] also studied the reaction theoretically; they optimized the minima and saddle points of the reaction on the singlet surface at the B3LYP/6-311++G(3df,3pd) level and on the triplet surface at both MP2/6-31G(d) and CCSD(T)/6-31G(d) levels. They confirmed that the direct hydrogen-abstraction reaction proceeded mainly through a weak hydrogen-bonded intermediate on the triplet surface and that the rather stable  $\text{HOOOC}\text{I}$  intermediate might play an important role in the overall kinetics. To date, no successful attempts have been made to predict the total rate constant and the relative importance of the direct abstraction vs the stabilization of the potentially stable  $\text{HOOOC}\text{I}$  intermediate whose photochemistry may be relevant to the global  $\text{O}_3$ -destruction process.

In our recent work [89], the reaction of  $\text{HO}_2$  with  $\text{ClO}$  has been investigated by *ab initio* molecular orbital and variational transition state theory calculations. The geometric parameters of the reaction system  $\text{HO}_2 + \text{ClO}$  were optimized at the B3LYP and BH&HLYP levels of theory with the basis set, 6-311+G(3df,2p), which can be found in Ref. [89]. Both singlet and triplet potential energy surfaces were predicted by the G2M method, as shown in Fig. 24.

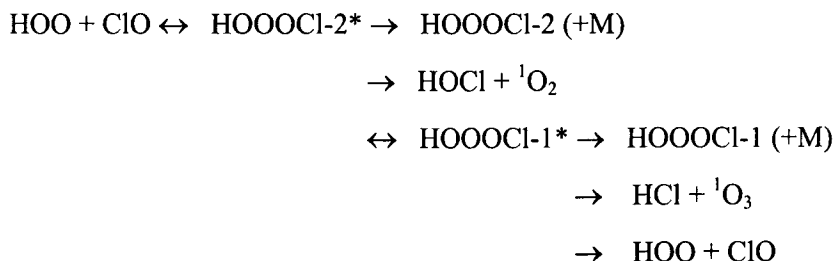


The rate constants for the product channels taking place via the HOOCl-1 and HOOCl-2 were computed with the ChemRate code [36] coupling all intermediates involved in the forward and reverse reactions as shown below.

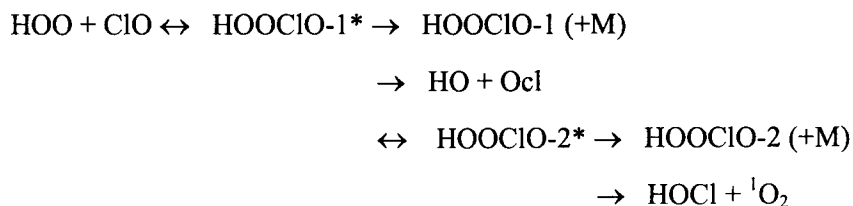
*Scheme 1:*



*Scheme 2:*



*Scheme 3:*



On the singlet surface, the reaction forms two HOOCl isomers lying below the reactants by 20 kcal/mol. Their stabilization contributes significantly to the observed overall  $\text{HO}_2 + \text{ClO}$  rate constant at low temperatures. The predicted high- and low-pressure association rate constants for the 150 – 600 K range can be represented by:

$$k^\infty = 9.04 \times 10^{-17} T^{1.22} \exp(897/T) \text{ cm}^3 \text{ molecule}^{-1} \text{ s}^{-1}$$

$$k^0 = 9.33 \times 10^{-24} T^{-3.45} \exp(472/T) \text{ cm}^6 \text{ molecule}^{-2} \text{ s}^{-1}$$

for  $\text{N}_2$  as the third-body. Dissociation of these excited HOOCl intermediates produces  $\text{HO} + \text{ClOO}$ ,  $\text{HCl} + {}^1\text{O}_3$ ,  $\text{HOCl} + {}^1\text{O}_2$  and  $\text{HO} + \text{OCIO}$  as minor products via multi-step mechanisms. On the triplet surface, formation of  $\text{HOCl} + {}^3\text{O}_2$  dominates; it occurs via a long-lived  $\text{O}_2\text{H}\cdots\text{OCl}$  complex with 3.3 kcal/mol binding energy. The complex decomposes to give the product pairs with a small (0.1 kcal/mol) barrier. The predicted rate constant can be represented by:

$$k(\text{HOCl} + {}^3\text{O}_2) = 1.64 \times 10^{-10} T^{-0.64} \exp(107/T) \text{ cm}^3 \text{ molecule}^{-1} \text{ s}^{-1}$$

in the temperature range 150 – 1000 K. The total rate constants predicted for 1 – 760 Torr  $\text{N}_2$  pressure exhibit a strong negative temperature dependence below 1000 K. In the 200 – 400 K range, where most kinetic data have been obtained, the agreement between theory and experiment is excellent as shown in Fig. 25. For practical combustion applications, the rate constants for these bimolecular product channels have been evaluated in units of  $\text{cm}^3 \text{ molecule}^{-1} \text{ s}^{-1}$  for the 500 – 2500 K temperature range:

$$k_{9a} = 1.30 \times 10^{-20} T^{2.37} \exp(-2572/T)$$

$$k_{(9b+9e)} = 1.39 \times 10^{-21} T^{2.26} \exp(226/T)$$

$$k_{9c} = 7.60 \times 10^{-21} T^{2.05} \exp(-855/T)$$

$$k_{9d} = 7.61 \times 10^{-19} T^{1.80} \exp(-1065/T)$$

$$k_{9f} = 2.22 \times 10^{-21} T^{2.32} \exp(-2566/T)$$

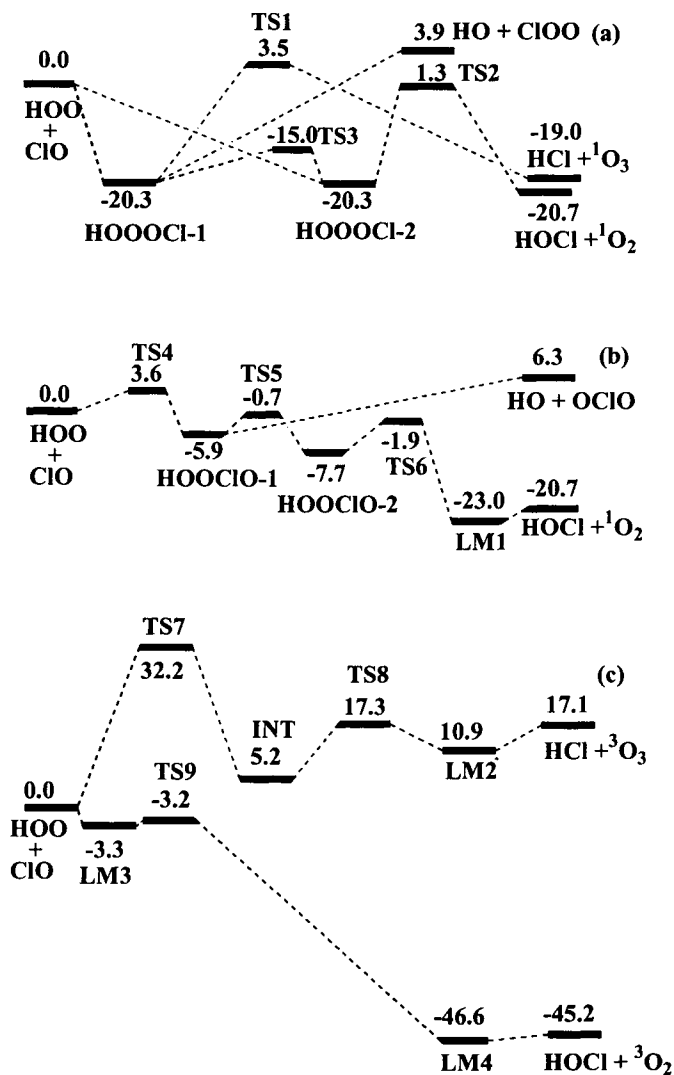


Fig. 24. Schematic energy diagram of the HOO + ClO system [89] at the G2M//B3LYP/6-311+G(3df, 2p) Level, with the exception of the reaction channel of TS9 which was calculated at the G2M//BH&HLYP/6-311+G(3df, 2p) level.  
a) and (b): singlet state PES's. (c): triplet state PES's.

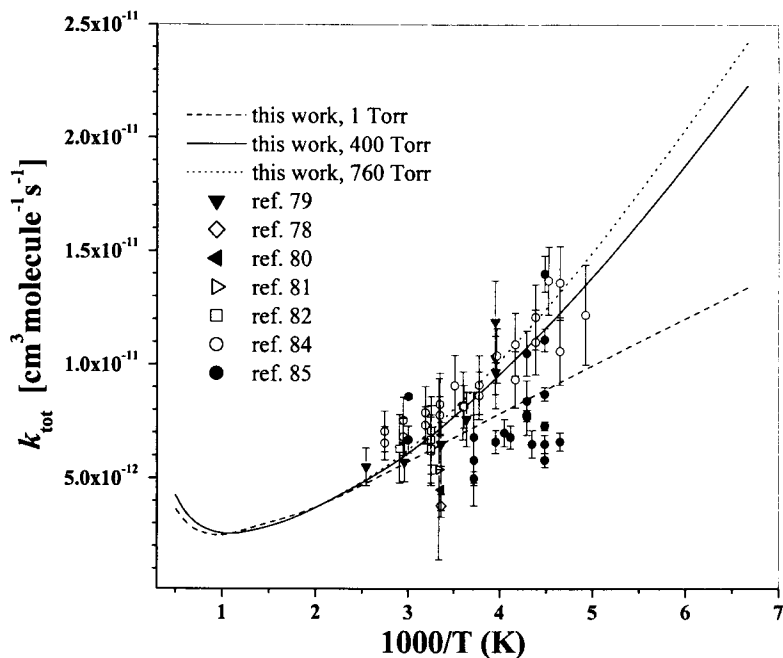


Fig. 25. Comparison of the predicted total rate constants with the experimental data in the temperature range from 150 to 2000 K.

### 3. 4. 5. $HO_2 + OCIO$

Based on the PES shown in Fig. 2, the rate constants of the following channels have been calculated with the Variflex code:



The low- and high-pressure rate constants for the association process can be expressed by:

$$k_{10a}^0 = 14.4 \times T^{-13.1} \exp(-963/T) \text{ cm}^6 \text{ molecule}^{-2} \text{ s}^{-1}$$

$$k_{10a}^\infty = (3.5 \pm 0.5) \times 10^{-10} \text{ cm}^3 \text{ molecule}^{-1} \text{ s}^{-1}$$

in the temperature range of 300 – 2500 K with Ar as the third-body. The individual and total rate constants at 1 atm for channels (10a) – (10c) are plotted in Fig. 26. The results show that below 600 K, formation of  $\text{HOOCIO}_2$  is dominant; over 600 K formation of  $\text{HOClO} + \text{O}_2$  becomes dominant; over 1000 K, for formation of  $\text{HO} + \text{ClO}_3$  is competitive. The rate constants at 1 atm can be in units of  $\text{cm}^3 \text{ molecule}^{-2} \text{ s}^{-1}$  by :

$$k_{10a}^{1\text{atm}} = 8.4 \times 10^{-20} T^{-13.5} \exp(-629/T)$$

$$k_{10b}^{1\text{atm}} = 1.0 \times 10^{-26} T^{3.6} \exp(-1056/T)$$

$$k_{10c}^{1\text{atm}} = 1.42 \times 10^{-14} T^{0.93} \exp(-14718/T)$$

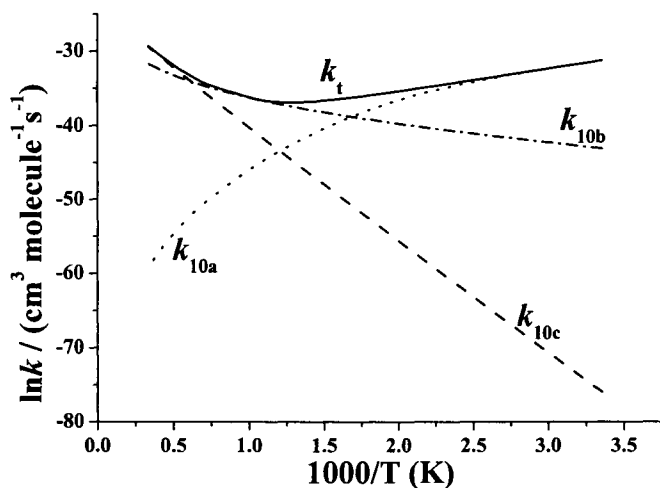
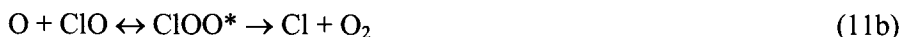


Fig. 26. Predicted individual and total rate constants for the  $\text{HO}_2 + \text{OCIO}$  reaction.

### 3. 4. 6. $O + ClO$ and its reverse reaction, $Cl + O_2$

As shown in Fig. 11,  $O + ClO$  can directly form  $OCIO$  and  $ClOO$  intermediates, the latter dissociates to  $Cl + O_2$ . The isomerization from  $OCIO$  to  $ClOO$  needs a very high barrier, 63.3 kcal/mol; it is not crucial to the measured kinetics of these reactions. The comparison of the total rate constants with experimental data is shown in Fig. 27. The results show that  $O + ClO \rightarrow Cl + {}^3O_2$  channel is pressure independent and dominant; formation of  $OCIO$  is pressure dependent and has some contribution to the total rate constants at lower temperatures and higher pressures as shown in the figure. The low- and high- pressure rate constants for the reactions,



can be represented by:

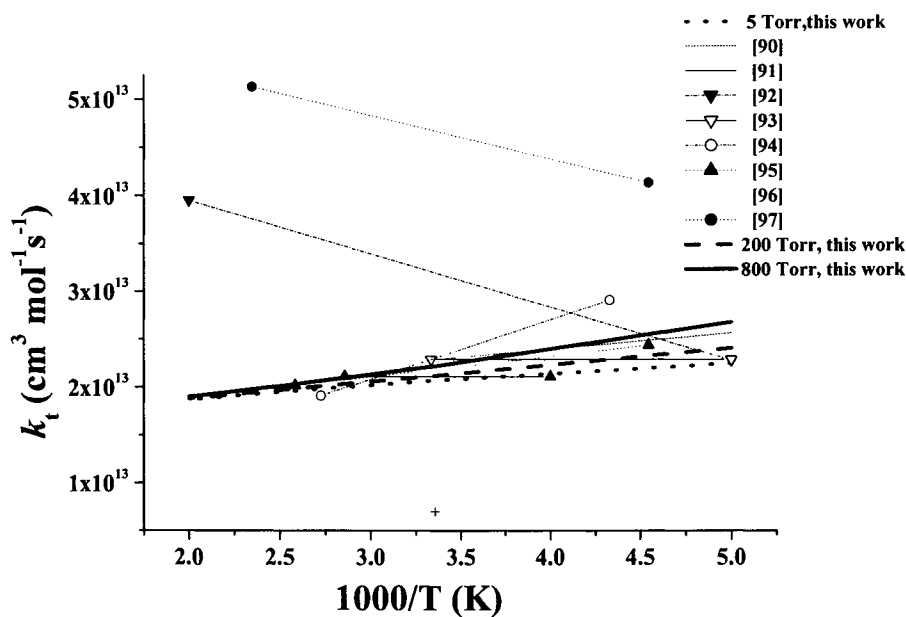


Fig. 27. Comparison of predicted and experimental total rate constants for the  $O + ClO$  reaction.

$$k_{11a}^0 = 3.12 \times 10^{27} T^{-4.1} \exp(-420/T) \text{ cm}^6 \text{ mol}^{-2} \text{ s}^{-1}$$

$$k_{11a}^\infty = 2.61 \times 10^{13} T^{-0.03} \exp(43/T) \text{ cm}^3 \text{ mol}^{-1} \text{ s}^{-1}$$

$$k_{11b}^0 = k_{11b}^\infty = 2.48 \times 10^{13} T^{-0.06} \exp(42/T) \text{ cm}^3 \text{ mol}^{-1} \text{ s}^{-1}$$

in the temperature range of 200 – 1000 K with N<sub>2</sub> as the third body.

In addition, we also calculated the reverse rate constants of reaction (11 b), forming stabilized ClOO by collisional deactivation; the results are in reasonable agreement with experimental values as shown in Fig. 28. The low- and high- pressure rate constants for this process can be expressed as:

$$k_{\text{Cl} + \text{O}_2}^0 = 8.63 \times 10^{27} T^{-4.92} \exp(-617/T) \text{ cm}^6 \text{ mol}^{-2} \text{ s}^{-1}$$

$$k_{\text{Cl} + \text{O}_2}^\infty = 4.0 \times 10^{13} T^{0.004} \exp(-8.0/T) \text{ cm}^3 \text{ mol}^{-1} \text{ s}^{-1}$$

in the temperature of 150 to 1000 K in N<sub>2</sub>.

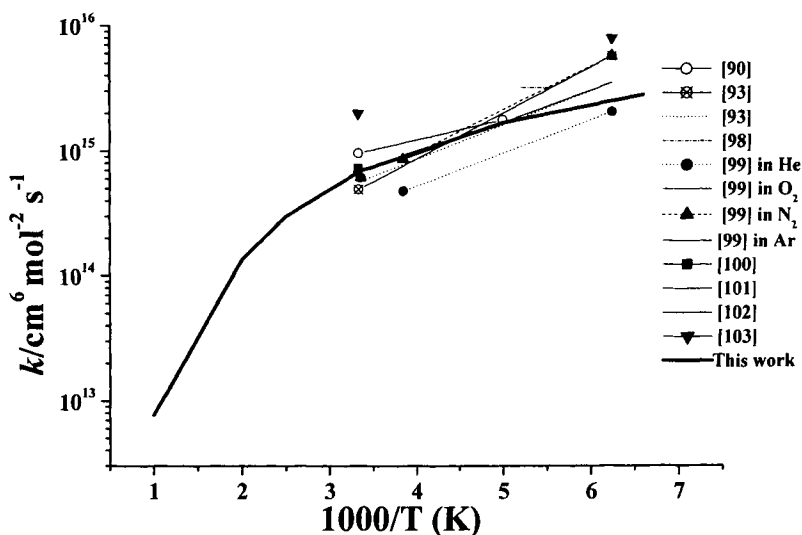
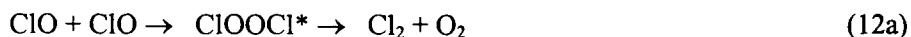


Fig. 28. Comparison of the predicted and experimental third-order association rate constants for Cl + O<sub>2</sub> reaction with N<sub>2</sub> as the third body.

### 3. 4. 7. $\text{ClO} + \text{ClO}$

The recombination and disproportionation reactions of  $\text{ClO}$  radicals have been investigated extensively on account of their relevance to the  $\text{O}_3$ -destruction chemistry in the stratosphere [104 - 118]. The reactions are expected to play a significant role in AP combustion also due to the potential high concentration of the  $\text{ClO}$  radical. In principle, the reactions may take place via at least two long-lived intermediates; viz.



Potentially, a third intermediate,  $\text{ClClO}_2$ , may be formed in the reverse  $\text{Cl} + \text{OC}\text{ClO}$  reaction, analogous to the association of  $\text{HO}$  with  $\text{OC}\text{ClO}$ , in which chloric acid ( $\text{HOClO}_2$ ) may be a major product, depending on the pressure of the system [76].

Under higher-pressure conditions, particularly at low temperatures, collisional deactivation of excited association products producing  $\text{ClOOC}\text{Cl}$  and  $\text{ClOC}\text{ClO}$  may be important kinetically. In fact for the most stable intermediate,  $\text{ClOOC}\text{Cl}$ , its formation is the dominant process under the stratospheric condition [107, 108, 112, 114, 116]. On the other hand, the disproportionation processes producing  $\text{ClOO}$  and  $\text{OC}\text{ClO}$  by (12b) and (12c), respectively, are endothermic by 3 - 4 kcal/mol [119]; accordingly, they cannot compete effectively with the recombination reaction in the stratosphere (with low temperature and medium pressure). These endothermic reactions may, however, become dominant processes in the combustion of the AP propellant.

In this work, both singlet and triplet potential energy surfaces were predicted at the  $\text{G2M}(\text{CC2})/\text{B3LYP}/6\text{-}311\text{+G}(3\text{df})$  level [119]. The corresponding energy diagrams and key structures are shown in Figs. 29 and 30, and Figs. 31 and 32, respectively.

Variational TST and RRKM calculations have been carried out for the following reaction channels:



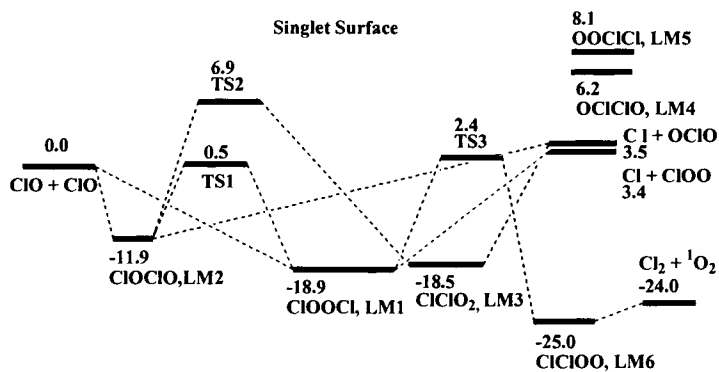


Fig. 29. Singlet energy diagram of the ClO + ClO system computed at the G2M (CC2)//B3LYP/6-311+G(3df) level.

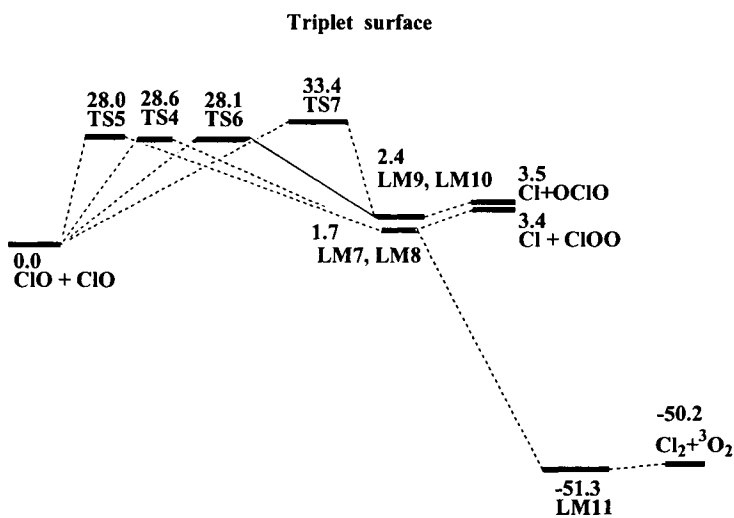
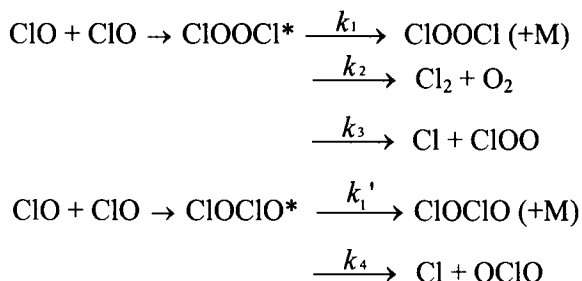
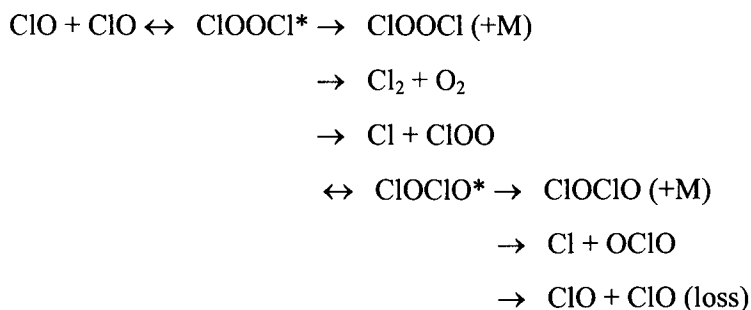


Fig. 30. Triplet energy diagram of the ClO + ClO system computed at the G2M (CC2)//B3LYP/6-311+G(3df) level.

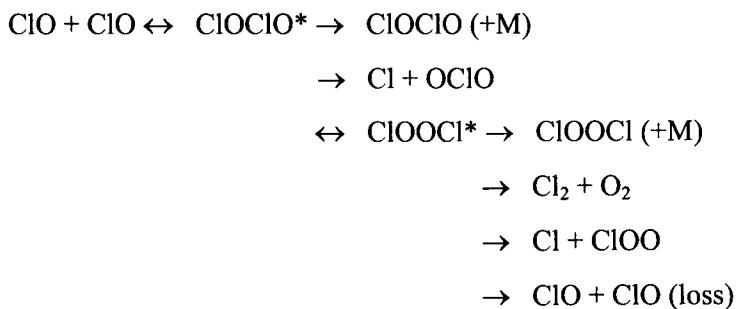


The rate constants for the dominant association reactions ( $k_1$  and  $k_1'$ ) were calculated with the Variflex code [35], whereas those for the disproportionation reactions,  $k_2$ ,  $k_3$  and  $k_4$ , were computed with the ChemRate code [36] coupling all intermediates involved in the forward and reverse reactions according to Scheme 1 and Scheme 2 :

*Scheme 1:*



*Scheme 2:*



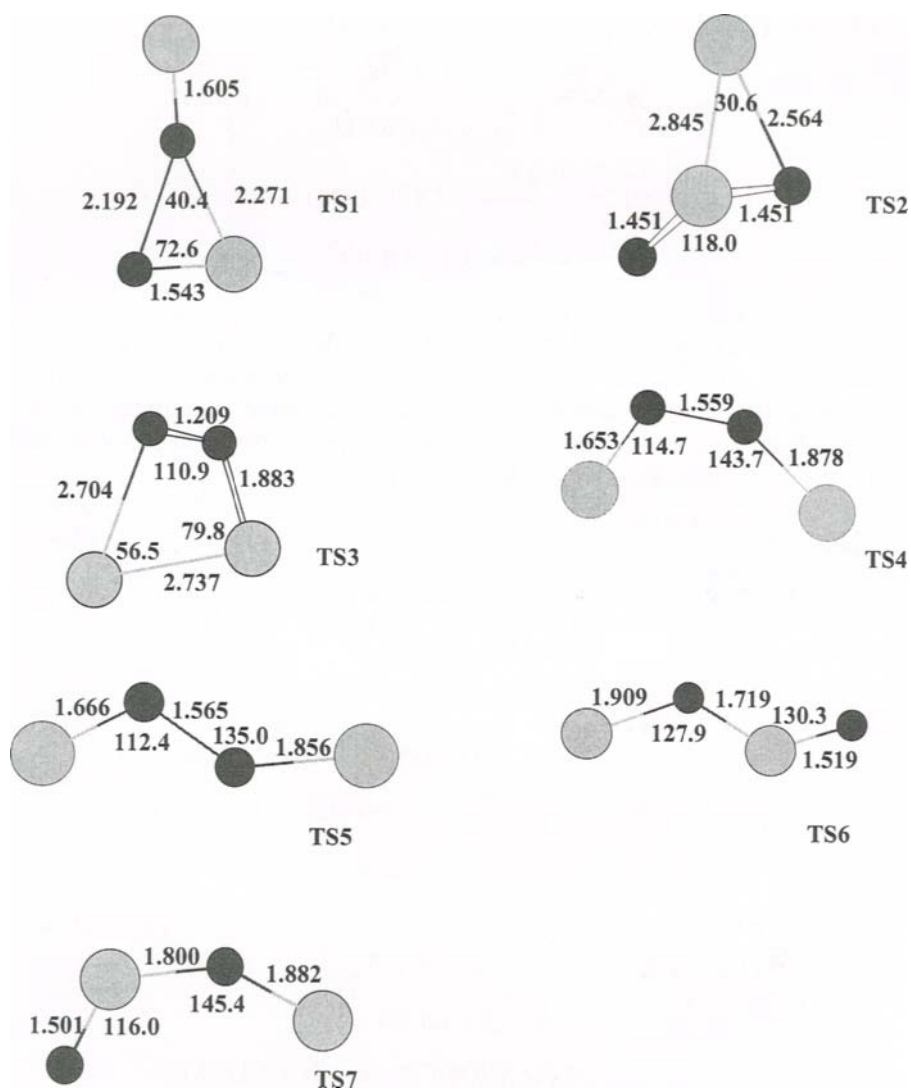


Fig. 31. The optimized geometries of transition states computed at the B3LYP/6-311+G(3df, 2p) level for the ClO-ClO system.

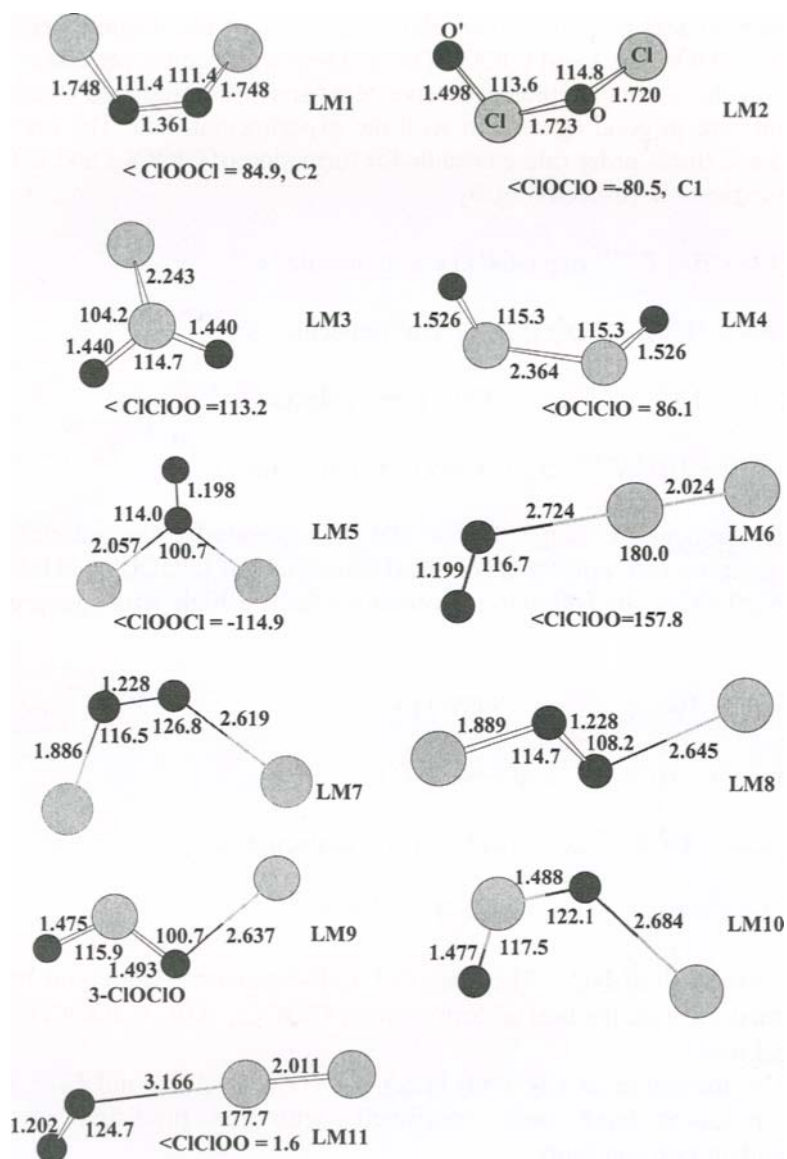


Fig. 32 The optimized geometries of intermediates computed at the B3LYP/6-311+G(3df, 2p) level for the ClO-ClO system.

The reaction was shown to take place mainly over the singlet surface by forming ClOOCl ( $k_1$ ) and ClOClO ( $k_1'$ ). These association processes were found to be strongly pressure-dependent and the predicted total rate constants are in good agreement with the experimental data. The predicted second and third-order rate constants for formation of ClOOCl and ClOClO can be expressed, respectively, by

$$k_1^\infty = 1.6 \times 10^{-9} T^{-0.67} \exp(-64/T) \text{ cm}^3 \text{ molecule}^{-1} \text{ s}^{-1}$$

$$k_1'^\infty = 6.4 \times 10^{-9} T^{-0.78} \exp(-76/T) \text{ cm}^3 \text{ molecule}^{-1} \text{ s}^{-1}$$

$$k_1^0 = 8.31 \times 10^{-20} T^{-4.96} \exp(-336/T) \text{ cm}^6 \text{ molecule}^{-2} \text{ s}^{-1}$$

$$k_1'^0 = 1.72 \times 10^{-14} T^{-6.99} \exp(-926/T) \text{ cm}^6 \text{ molecule}^{-2} \text{ s}^{-1}$$

for the temperature range 180 - 500 K. Similarly, the unimolecular decomposition rate constants for the dissociation of ClOOCl and ClOClO can be given by the following expressions for the high- and low-pressure limits:

$$k_{-1}^\infty = 6.3 \times 10^{19} T^{-1.32} \exp(-9999/T) \text{ s}^{-1}$$

$$k_{-1}'^\infty = 5.99 \times 10^{20} T^{-1.63} \exp(-6474/T) \text{ s}^{-1}$$

$$k_{-1}^0 = 4.64 \times 10^8 T^{-5.2} \exp(-10159/T) \text{ cm}^3 \text{ molecule}^{-1} \text{ s}^{-1}$$

$$k_{-1}'^0 = 6.81 \times 10^6 T^{-4.9} \exp(-6488/T) \text{ cm}^3 \text{ molecule}^{-1} \text{ s}^{-1}.$$

for N<sub>2</sub> as the third-body. The observed T, P-dependent data could be best accounted for with the heat of formation of ClOOCl,  $\Delta_f H_0^\circ$  (ClOOCl) = 29.4  $\pm$  1 kcal/mol.

The formation of Cl<sub>2</sub> + O<sub>2</sub> (12a), Cl + ClOO (12b) and Cl + OClO (12c) products have been confirmed, with the predicted pressure-independent rate constants:

$$k_{12a} = 1.09 \times 10^{-13} T^{0.66} \exp(-1892/T)$$

$$k_{12b} = 1.36 \times 10^{-13} T^{0.77} \exp(-2168/T)$$

$$k_{12c} = 6.26 \times 10^{-11} T^{0.005} \exp(-2896/T),$$

respectively, in units of  $\text{cm}^3 \text{ molecule}^{-1} \text{ s}^{-1}$ , covering the temperature range 200 – 1500 K. These results are also in reasonable agreement with exiting experimental kinetic data as shown in Figs. 33 - 35.

For practical applications, we have analyzed our theoretical fall-off curves in terms of the following empirical equations to obtain broadening parameters ( $F_c$ ) [120-121] :

$$k = a[b/(1+b)]F$$

$$\log F = \log F_c/[1 + (\log b)^2]$$

using the predicted high- and low-pressure limits for  $\text{N}_2$  as the third body. For the  $\text{ClOCl}$  association path, we obtained  $F_c = 0.24, 0.22, 0.22$ , and  $0.27$  at 200, 263, 298 and 400 K, respectively. In the fitting,  $a = k^\infty = 3.40$ ,

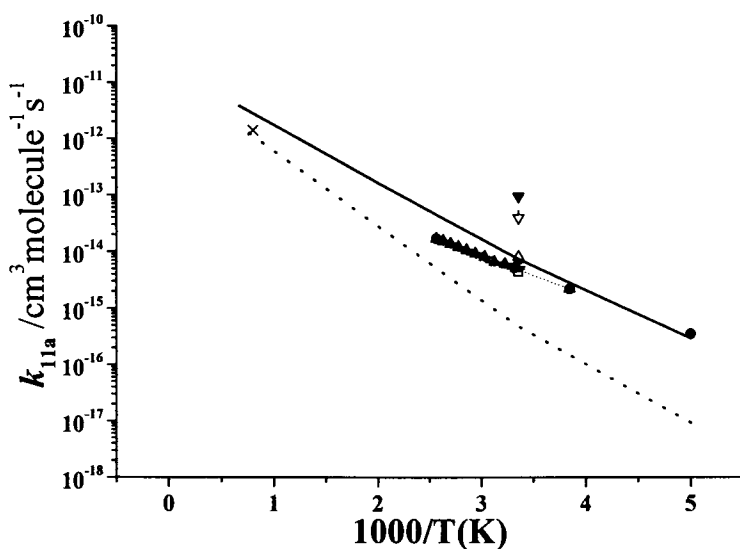


Fig. 33. Comparison of the predicted bimolecular reaction rate constant for  $\text{ClO} + \text{ClO} \rightarrow \text{Cl}_2 + \text{O}_2$  with the experimental values. Solid line is the predicted total value coupling Schemes 1 and 2; dotted line is the contribution from Scheme 2. Symbols are the experimental values as described in Ref. 119.

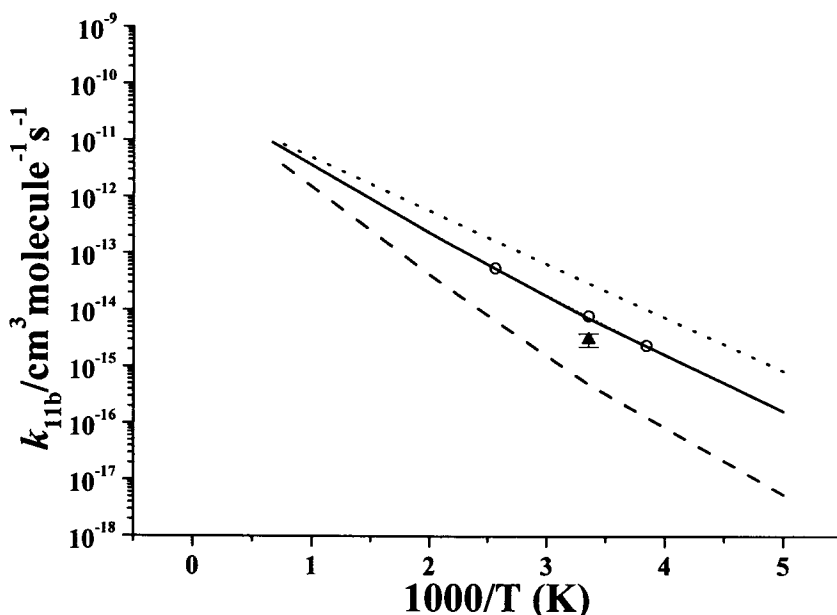


Fig. 34. Comparison of the predicted bimolecular reaction rate constant for  $\text{ClO} + \text{ClO} \rightarrow \text{Cl} + \text{ClOO}$  with the experimental values. Dotted and solid lines are calculated by using predicted 23.1 and experimental 23.8 kcal/mol for the heat of formation for ClOO, respectively. Dashed line is the contribution from Scheme 2 using the experimental heat of formation for ClOO.  $\circ$ —, Ref. 116;  $\blacktriangle$ —, Ref. 108.

3.07, 2.90, and 2.51 in units of  $10^{-11} \text{ cm}^3 \text{ molecule}^{-1} \text{ s}^{-1}$ , and  $b = k^0[\text{M}]/k^\infty$  with  $k^0 = 6.19, 2.35, 1.47$ , and  $0.464$  in units of  $10^{-32} \text{ cm}^6 \text{ molecule}^{-2} \text{ s}^{-1}$ , respectively. For the ClOClO association path,  $F_c = 0.72, 0.74, 0.75$  and  $0.83$  at 200, 263, 298 and 400 K with  $a = k^\infty = 6.97, 6.19, 5.80$ , and  $4.90$  in units of  $10^{-11} \text{ cm}^3 \text{ molecule}^{-1} \text{ s}^{-1}$  and  $k^0 = 14.5, 5.94, 3.83$ , and  $1.23$  in units of  $10^{-33} \text{ cm}^6 \text{ molecule}^{-2} \text{ s}^{-1}$ , respectively.

Figures 36 and 37 show the comparison of the predicted pressure dependent (in  $\text{N}_2$ ) and temperature dependent rate constants with the experimental values. The results of  $\text{O}_2$  and He as third body and the products branching compared with experimental data are available in Ref. [119].

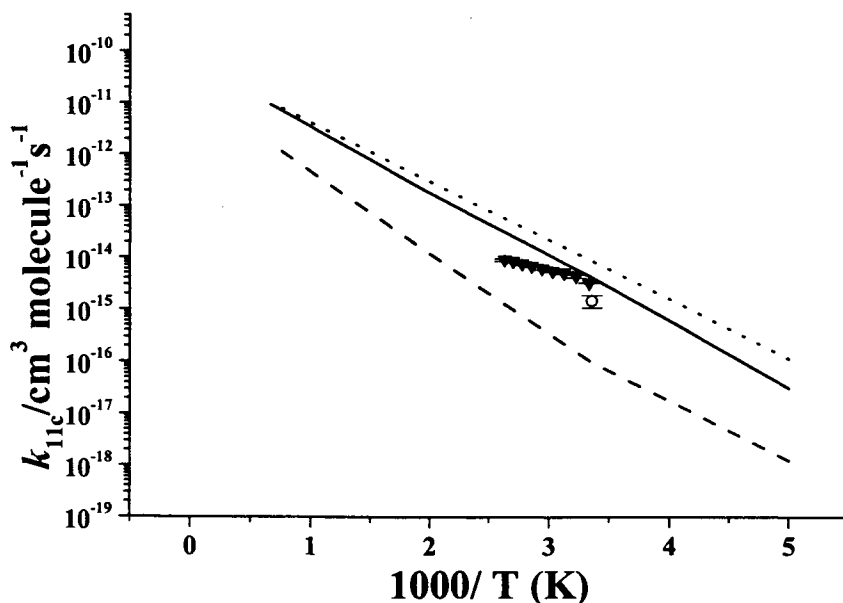


Fig. 35. Comparison of the predicted bimolecular reaction rate constant for  $\text{ClO} + \text{ClO} \rightarrow \text{Cl} + \text{OClO}$  with the experimental values. Dotted and solid lines are calculated by using predicted 23.2 and experimental 23.7 kcal/mol for the heat of formation for  $\text{ClOO}$ , respectively. Dashed line is the contribution from Scheme 1 using the experimental heat of formation for  $\text{ClOO}$ . -▼-, Ref. 116; -○-, Ref. 108.

### 3. 4. 8. $\text{ClO} + \text{OClO}$

Both  $\text{ClO}$  and  $\text{OClO}$ , and their higher oxides of chlorine have been implicated in the formation of  $\text{O}_3$ -hole in the antarctic stratosphere [122-135] at low temperatures, one of the major products of the reaction of  $\text{ClO}$  with  $\text{OClO}$  is  $\text{Cl}_2\text{O}_3$ , which may have several stable isomers under the stratospheric condition [131-135]. The stability of at least 3 isomers of  $\text{Cl}_2\text{O}_3$  (see below) have been predicted to be theoretically stable at low temperatures by several authors using different computational methods [136-



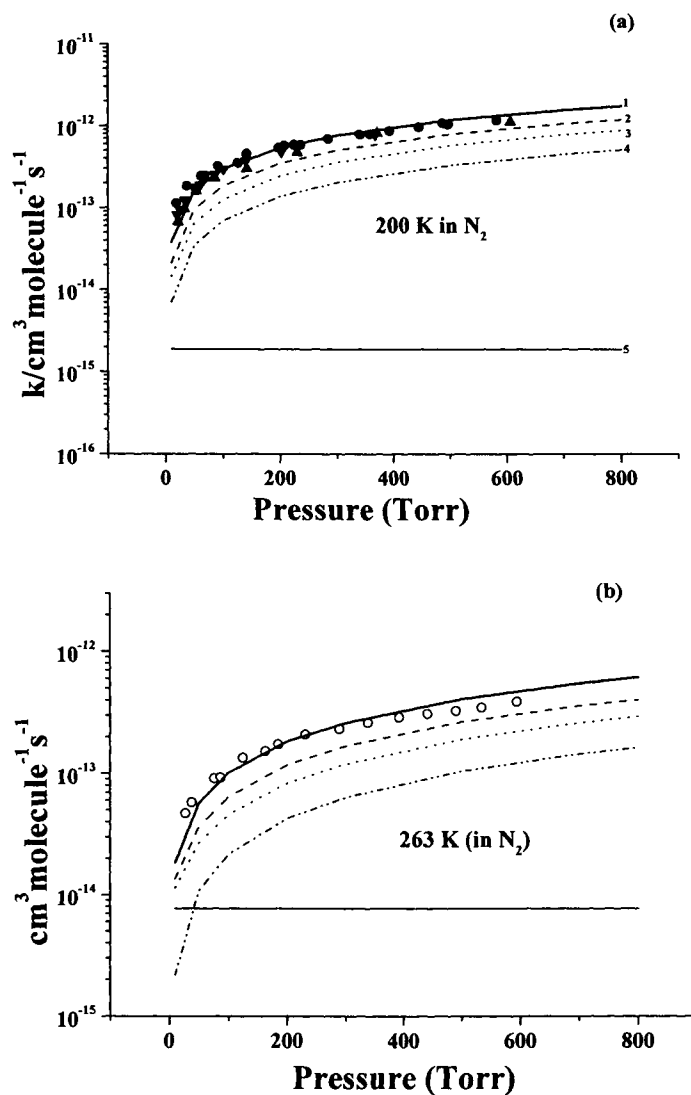


Fig. 36. Comparison of predicted and experimental pressure dependent association rate constants of  $\text{ClOOCl}$  and  $\text{ClOClO}$ . The meaning of lines and symbols can be found in detail in Ref. 119.

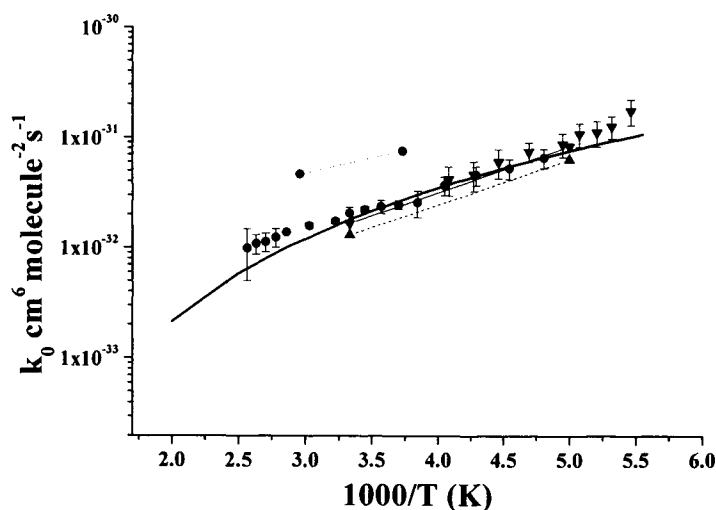
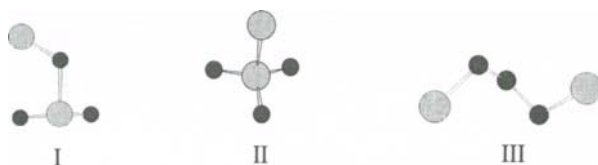


Fig. 37. Comparison of predicted and experimental third order association rate constants for  $\text{ClO} + \text{ClO}$  reaction. The meaning of lines and symbols can be found in detail in Ref. 119.

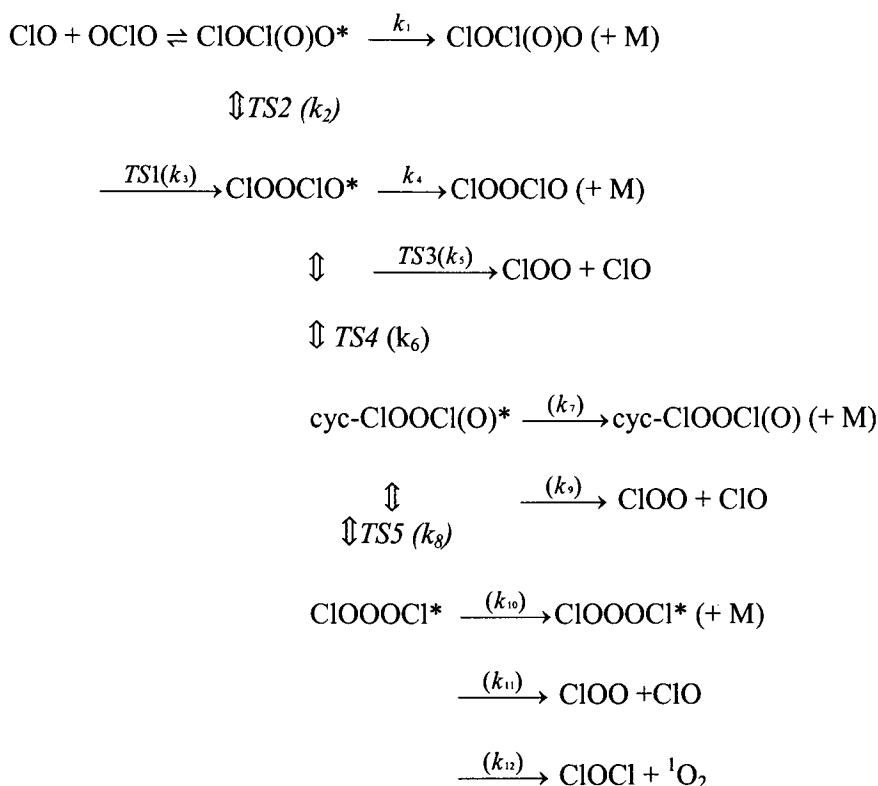


139]. Among these isomers, structure (I) has been shown to be most stable and (II), which cannot be directly formed by  $\text{ClO} + \text{OCIO}$ , was shown to be least stable. Another potential reaction intermediate,  $\text{ClOOCIO}$ , was reported to be unstable; its role in the  $\text{ClO} + \text{OCIO}$  reaction is unclear. Under AP combustion conditions, decomposition products such as  $\text{ClOCl} + \text{O}_2$  may be significant kinetically.

The mechanism for the reaction  $\text{ClO} + \text{OCIO}$  has been investigated by *ab initio* molecular orbital and transition state theory calculations [140]. Nine stable isomers of  $\text{Cl}_2\text{O}_3$  (including optical isomers) are located at the B3LYP/6-311+G(3df) level. The transition states between pairs of isomers

are explored and the stability of the isomers and their dissociation mechanisms are discussed. The energy diagram of possible channels was shown in Fig. 38 and the corresponding structures were displayed in Figs. 39 and 40. The relative stability predicted by the G2M(CC2)//B3LYP/6-311+G(3df) level is  $\text{ClOCl(O)O} > \text{ClOOCl(C}_2\text{)} > \text{ClOOCl(C}_s\text{)} > \text{ClClO}_3\text{(C}_{3v}\text{)} > \text{cyc-ClOOCl(O)} > \text{ClOOCIO}$ .

Variational TST and RRKM calculations have been carried out for the following reaction channels using Variflex [35] and ChemRate [36] codes :



In the ChemRate calculation, which couples all accessible channels, the transition state parameters for the barrierless association and decomposition processes were evaluated canonically for each temperature and critical separation,  $r^\#(\text{T})$ , based on the maximum Gibbs free energy as described in previously section.

For prediction of the formation of  $\text{ClOCl(O)O}$  by the barrierless  $\text{ClO} + \text{OCIO}$  association, we used the Variflex code [35], for which variational

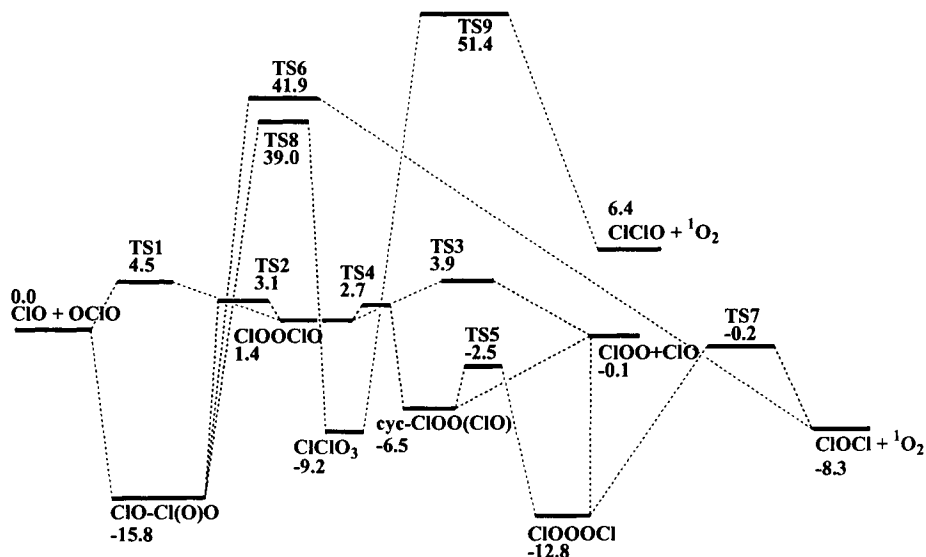


Fig. 38. Energy diagram of the ClO + OCIO system computed at the G2M (CC2)//B3LYP/6-311+G(3df) level.

treatment was employed to obtain the dissociation potential energy function by varying the breaking O-Cl bond from 2.133 to 4.533 Å at an interval of 0.1 Å. The detailed vibrational frequencies and rotational constants parameters can be obtained in Ref. [140].

Figures 41 (a) and (b) show the predicted and experimental rate coefficients at different temperatures as a function of N<sub>2</sub> pressure. In these figures, the solid lines represent the calculated results using the predicted  $\Delta H^\circ_0 = -15.8$  kcal/mol; the dotted and dashed lines represent the results using experimentally estimated  $\Delta H^\circ_0 = -14.8$  [130] and  $-11.1$  [131] kcal/mol, respectively; the dash-dot-dotted line is the results based  $\Delta H^\circ_0 = -17.7$  kcal/mol which is the upper-limit reported by Hayman and Cox [130]. Symbols are experimental results [130, 131, 141]. Apparently, the pressure-dependent rate constants are strongly sensitive to  $\Delta H^\circ_0$  for the low-dissociation energy process; our predicted values based on  $\Delta H^\circ_0 = -15.8$  kcal/mol are in good agreement with experimental data.

In Fig. 42, the predicted and experimental third-order rate constants for the association process in N<sub>2</sub> as a function of temperature are plotted and

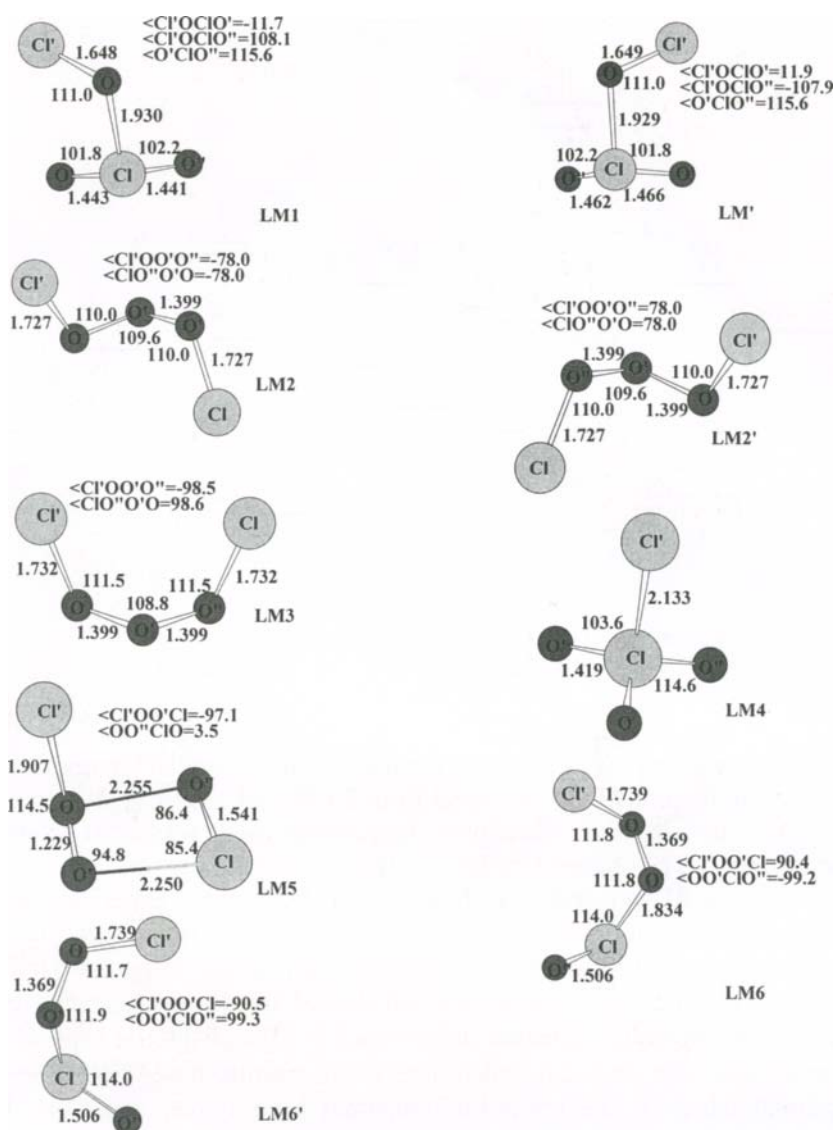


Fig. 39. The optimized geometry of intermediates computed at the B3LYP/6-311 + G(3df) level for the ClO + OClO reaction.

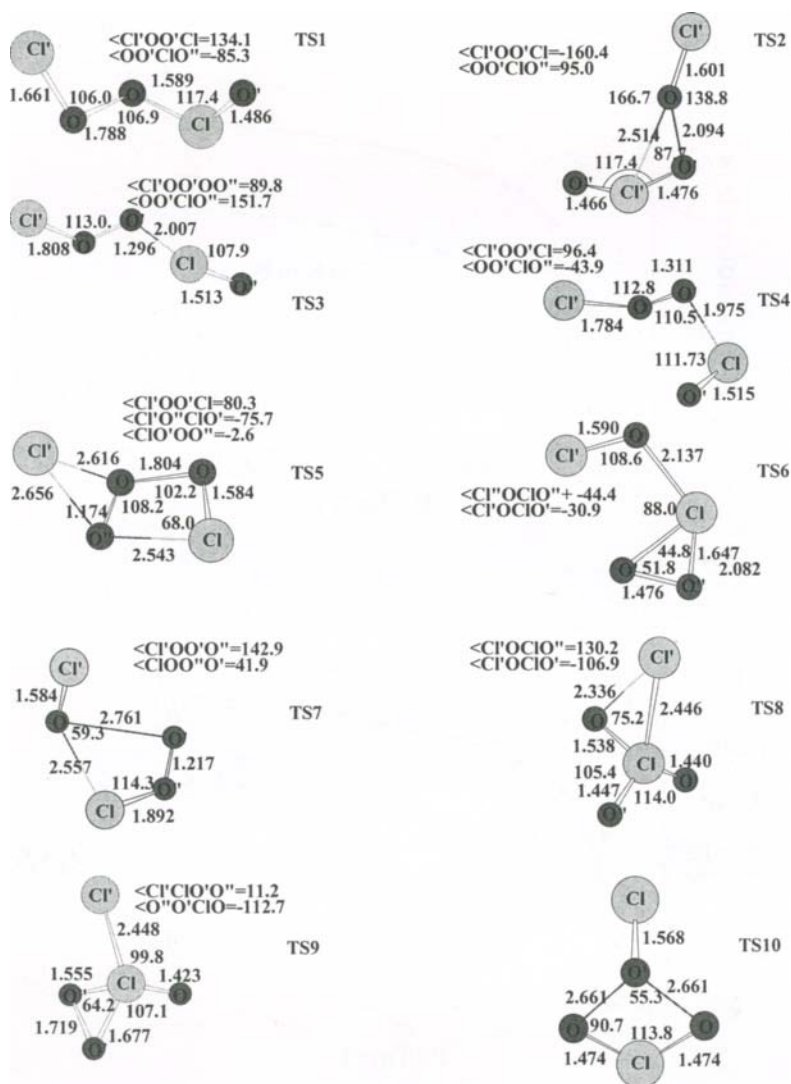


Fig. 40. The geometry of the transition states involved in the  $\text{ClO} + \text{OClO}$  reaction optimized at the B3LYP/6-311+G(3df) level.

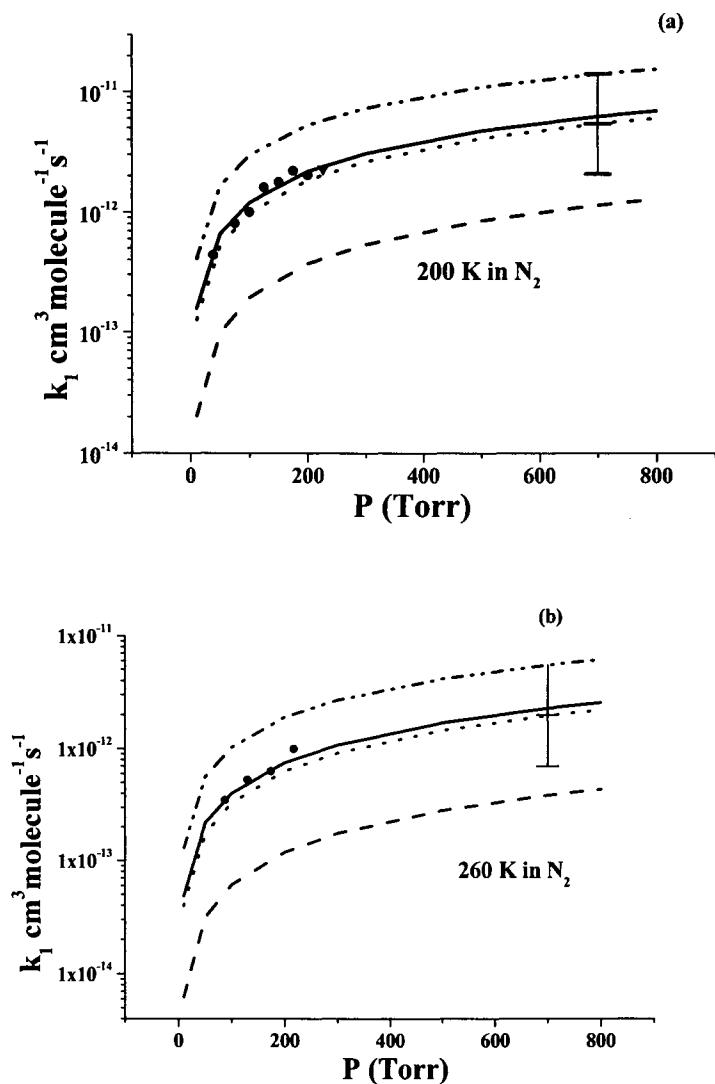


Fig. 41. Comparison of the predicted rate constants for the  $\text{ClO} + \text{OClO}$  association with the experimental values at (a) 200 K, (b) 260 K in  $\text{N}_2$ . The solid, dotted, dashed and dash-double-dotted curves represent the calculated results using the  $\Delta H^0$ , 15.8 (predicted in this work), 14.8 (Ref.130), 11.1 (Ref.131) and 17.7 kcal/mol (the upper-limit given by Ref. 130), respectively. ●, ref. 131; △, ref. 141; the error bar represents the range of results based on the  $\Delta H^0 = 14.8 \pm 2.9$  kcal/mol (Ref. 130).

compared. In the figure, the thick solid, dotted, dashed and dashed-dot-dotted lines represent the results obtained with different values of  $\Delta H^\circ_0$  as defined in Fig. 41. Symbols and dot-dashed line are experimentally extrapolated data. The predicted third- and second-order rate constants in the temperature range 200 - 400 K for the formation of ClOCl(O)O can be expressed by

$$k_1^0 = 1.10 \times 10^{-17} T^{-5.5} \exp(-398/T) \text{ cm}^6 \text{ molecule}^{-2} \text{ s}^{-1}$$

$$k_1^\infty = 2.98 \times 10^{-10} \text{ cm}^3 \text{ molecule}^{-1} \text{ s}^{-1}.$$

It can be seen that the rate constants of  $k_1^0$  for the formation of ClOCl(O)O computed with our predicted dissociation energy (15.8 kcal/mol) is in good agreement with experimental results given by Burkholder et al. [132] and Parr et al. [141]. However, the predicted high-pressure-limit rate constant at 300 K is about 1 order of magnitude greater than the extrapolated value, presumably due to the insufficient extrapolation of limited experimental data at higher pressures as we discussed above. Similar results were also found for the association of  $\text{O} + \text{OCIO} \rightarrow \text{ClO}_3$  [57].

Figure 43 displays the second-order rate coefficient for the association/decomposition processes at 200 Torr in the temperature range of 500 – 2500 K. The results show that below 570 K, the association process is dominant; over 570 K, ClOO and ClO become the main products and the formation of  $\text{ClOCl} + {}^1\text{O}_2$  is also competitive at high temperatures. The total rate constant for ClOO formation,  $(k_5 + k_9 + k_{11})$  and that for ClOCl formation,  $k_{12}$ , can be represented by:

$$k_{\text{ClOO}} = 1.03 \times 10^{-22} T^{2.76} \exp(-78/T)$$

$$k_{\text{ClOCl}} = 9.63 \times 10^{-22} T^{2.40} \exp(-1665/T)$$

in units of  $\text{cm}^3 \text{ molecule}^{-1} \text{ s}^{-1}$ , respectively, in the temperature range of 500 – 2500 K.



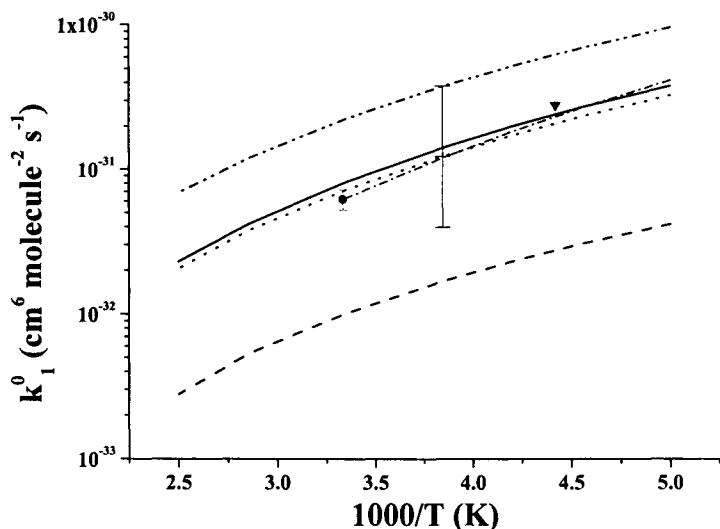


Fig 42. Comparison of the predicted low- pressure limit constant (in  $N_2$ ) with experimental values in the temperature range of 200 – 400 K. The meanings of thick lines are the same as those in Fig. 41. The dash-dotted line is taken from the equation given in Ref. 131. ●, Ref. 131; ▼, Ref. 141; the error bar represents the range of results based  $\Delta H_0^0 = 14.8 \pm 2.9$  kcal/mol (Ref. 130).

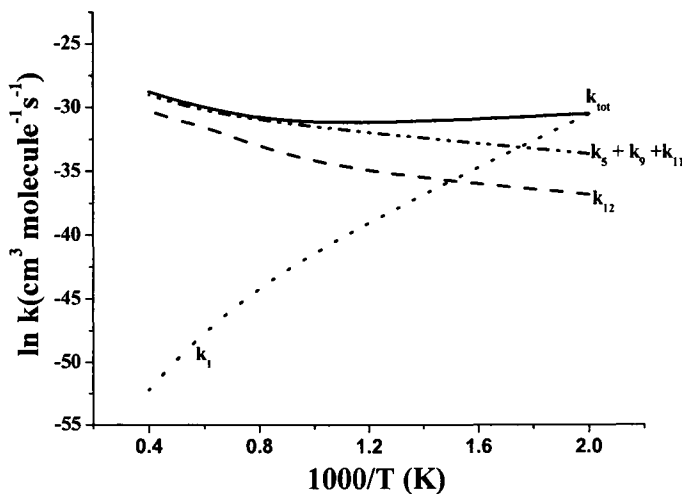


Fig. 43. Predicted second-order rate constants for the association/dissociation processes. Dotted, dashed, dash-double-dotted and solid lines represent the formation of  $ClOCl(O)O$  ( $k_1$ ),  $ClOCl + {}^1O_2$  ( $k_{12}$ ),  $ClOO + ClO$  ( $k_5 + k_9 + k_{11}$ ) and  $k_{tot}$ , respectively, in the temperature range of 500 – 2500K.

Table 1  
Molecular parameters and heats of formation of key species.

Species	$I_a, I_b, I_c$ (a.u.)	Frequencies ( $\text{cm}^{-1}$ )	$\Delta H_{f,0}^0$ (kcal/mol)
OCIO	35.3, 182.4, 217.7	451, 966, 1117	23.2 [119], 24.7 [57], 25.3 [75], $23.7 \pm 1.9$ [142]
ClOO	24.0, 410.7, 434.7	113, 326, 1594	23.1 [119], 23.5 [75], $23.8 \pm 0.7$ [142]
s-ClO <sub>3</sub>	179.4, 179.4, 340.1	472, 472, 564, 921 1078, 1078	$48.6 \pm 0.02$ [57], $47.2 \pm 2.7$ [53]
ClO <sub>4</sub>	297.6, 318.5, 342.3	376, 385, 418, 550 573, 650, 903, 1161 1259	
ClOOCl	133.8, 788.9, 881.2	127, 326, 443, 551 638, 844	29.4 [119], 29.4 [143], $32.6 \pm 3.2$ [144], 34.2 [145], 29.7 [116], 32.1 [112]
ClClO <sub>2</sub>	191.7, 521.7, 666.1	243, 264, 441, 524 1061, 1229	29.8 [119], 33.8 [144], 35.1 [145], 37.1 [143]
Cl <sub>2</sub> O <sub>3</sub>	238.1, 843.6, 966.62	53, 185, 257, 368 434, 1231, 1061, 764 540	32.3 [140], 36.5 [136] $33.9 \pm 2.9$ [130], 33.6 [146]
HOCl	2.9, 120.3, 123.2	739, 1262, 3786	-16.8 [76], $-17.1 \pm 0.5$ [142] $-16.7 \pm 0.6$ [147]
HOOC1	35.6, 297.1, 326.7	375, 429, 640, 896 1419, 3715	
HOClO <sub>2</sub>	194.9, 214.8, 362.1	97, 373, 409, 534 619, 1059, 1137 1237, 3742	0.1 [76]
HOClO <sub>3</sub>	327.3, 345.9, 350.6	200, 404, 415, 545 568, 575, 705, 1046 1208, 1256, 1328, 3726	$3.2 \pm 2.7$ [41]

**Table 2**Predicted rate constants for reactions discussed in this chapter<sup>a</sup>.

Reaction	T (K)	P (Torr)	$\Delta H_{f,0}^0$ (kcal/mol)
$\text{HOClO}_3 \rightarrow \text{ClO}_3 + \text{HO}$ (Ar) <sup>b</sup>	300 – 2500	0	$2.81 \times 10^{31} T^{-11.2} \exp(-29418/T)$
		$\infty$	$1.45 \times 10^{17} \exp(-26500/T)$
		760	$5.0 \times 10^{51} T^{-11.64} \exp(-30700/T)$
$\text{HOClO}_2 \rightarrow \text{OCIO} + \text{OH}$ (N <sub>2</sub> )	300 - 2500	0	$1.26 \times 10^{17} T^{-7.60} \exp(-17738/T)$
		$\infty$	$4.07 \times 10^{21} T^{-1.62} \exp(-17383/T)$
$\text{H} + \text{HOClO}_3 \rightarrow \text{H}_2 + \text{ClO}_4$ (Ar)	300 - 3000	$\infty$	$1.47 \times 10^{-18} T^{2.03} \exp(-7959/T)$
$\text{H} + \text{HOClO}_3 \rightarrow \text{HO} + \text{HOClO}_2$ (Ar)	300 - 3000	$\infty$	$3.33 \times 10^{-18} T^{2.02} \exp(-6878/T)$
$\text{HO} + \text{HOClO}_3 \rightarrow \text{H}_2\text{O} + \text{ClO}_4$ (Ar)	500 - 2500	c	$3.95 \times 10^{-23} T^{3.3} \exp(-930/T)$
$\text{OCIO} \rightarrow \text{O} + \text{ClO}$ (N <sub>2</sub> )	200 - 2500	0	$1.64 \times 10^{-47} T^{11.0} \exp(-16648/T)$
		$\infty$	$1.11 \times 10^{16} T^{-0.28} \exp(-29567/T)$
$\text{ClOO} \rightarrow \text{Cl} + \text{O}_2$ (N <sub>2</sub> )	200 - 2500	0	$4.67 \times 10^{15} T^{-0.41} \exp(-1897/T)$
		$\infty$	$4.87 \times 10^{15} T^{-0.59} \exp(-2585/T)$
$\text{ClO}_3 \rightarrow {}^3\text{O} + \text{OCIO}$ (Ar)	500 - 2500	0	$6.24 \times 10^1 T^{-3.28} \exp(-13890/T)$
		$\infty$	$1.5 \times 10^{20} T^{-1.1} \exp(-18360/T)$
$\text{ClO}_4 \rightarrow \text{s-ClO}_3 + {}^3\text{O}$ (Ar)	500 - 2500	0	$1.59 \times 10^{23} T^{-9.0} \exp(-24266/T)$
		$\infty$	$5.2 \times 10^{20} T^{-1.3} \exp(-23215/T)$
$\text{HO} + \text{ClO} \rightarrow \text{HOCl}$ (He, total <i>k</i> )	200 - 500	$\infty$	$5.27 \times 10^{-9} T^{-1.03} \exp(-40/T)$
$\text{HO} + \text{ClO} \rightarrow \text{HO}_2 + \text{Cl}$ $\rightarrow \text{HCl} + \text{O}_2$	500 - 2500	$\infty$	$3.4 \times 10^{-13} T^{0.3} \exp(725/T)$
		$\infty$	$5.85 \times 10^{-19} T^{1.67} \exp(1926/T)$
$\text{HO} + \text{OCIO} \rightarrow \text{HOClO}_2$ (N <sub>2</sub> )	200 - 1000	c	$1.78 \times 10^{-20} T^{2.25} \exp(2100/T)$
$\text{HO} + \text{OCIO} \rightarrow \text{HOO} + \text{ClO}$ $\rightarrow \text{HOCl} + {}^1\text{O}_2$ $\rightarrow {}^1\text{HOClO}_2$	200 - 1000	l	$1.22 \times 10^{-22} T^{2.75} \exp(1682/T)$
	200 - 1000	c	$5.47 \times 10^{-20} T^{2.07} \exp(2064/T)$
	200 - 500	c	$1.37 \times 10^4 T^{-6.61} \exp(-536/T)$
	500 - 1000	c	$4.99 \times 10^{34} T^{-22.36} \exp(-9807/T)$

**Table 2**Predicted rate constants for reactions discussed in this chapter <sup>a</sup> (continued).

Reactions	T (K)	P (Torr)	k
$\text{HO} + \text{OCIO} \rightarrow {}^1\text{HOCIO}_2 (\text{N}_2)^b$	200 - 2500	$\infty$	$3.24 \times 10^{-11} T^{0.28} \exp(-18/T)$
	200 - 1000	0	$1.28 \times 10^{-13} T^{-6.36} \exp(-635/T)$
	1000 - 2500	0	$2.91 \times 10^{-13} T^{-8.42} \exp(-11500/T)$
$\text{HO} + \text{ClO}_3 \rightarrow \text{HOCIO}_3$ $\rightarrow \text{HO}_2 + \text{ClO}_2, (\text{Ar})$	300 - 3000	$\infty$	$3.2 \times 10^{-10} T^{0.07} \exp(-25/T)$
		$\infty$	$2.1 \times 10^{-10} T^{0.09} \exp(-18/T)$
$\text{HO}_2 + \text{ClO} (\text{N}_2)$	150 - 600	$\infty$	$9.04 \times 10^{-17} T^{1.22} \exp(897/T)$
		0	$9.33 \times 10^{-24} T^{3.45} \exp(472/T)$
$\text{HO}_2 + \text{ClO} \rightarrow \text{HOCl} + {}^3\text{O}_2$	150 - 1000	760	$1.64 \times 10^{-10} T^{-0.64} \exp(107/T)$
$\text{HO}_2 + \text{ClO} \rightarrow \text{HOCl} + {}^3\text{O}_2$ $\rightarrow \text{HOCl} + {}^1\text{O}_2$ $\rightarrow \text{HO} + \text{ClOO}$ $\rightarrow \text{HO} + \text{OCIO}$	500 - 2500	760	$1.30 \times 10^{-20} T^{2.37} \exp(-2572/T)$
		760	$1.39 \times 10^{-21} T^{2.26} \exp(226/T)$
		760	$7.61 \times 10^{-19} T^{1.80} \exp(-1065/T)$
		760	$2.22 \times 10^{-21} T^{2.32} \exp(-2566/T)$
$\text{HO}_2 + \text{OCIO} \rightarrow \text{HOOCIO}_2 (\text{Ar})$	300 - 2500	0	$14.4 \times T^{-13.1} \exp(-963/T)$
		$\infty$	$(3.5 \pm 0.5) \times 10^{-10}$
$\text{HO}_2 + \text{OCIO} \rightarrow \text{HOOCIO}_2$ $\rightarrow \text{HOCIO} + \text{O}_2$ $\rightarrow \text{HO} + \text{ClO}_3$	300 - 2500	760	$8.4 \times 10^{-20} T^{-13.5} \exp(-629/T)$
		760	$1.0 \times 10^{-26} T^{3.6} \exp(-1056/T)$
		760	$1.4 \times 10^{-14} T^{0.93} \exp(-14718/T)$
$\text{O} + \text{ClO} \rightarrow \text{OCIO} (\text{N}_2)$	200 - 1000	0	$8.6 \times 10^{-21} T^{-4.1} \exp(-420/T)$
		$\infty$	$4.33 \times 10^{-11} T^{-0.03} \exp(43/T)$
$\text{O} + \text{ClO} \rightarrow \text{O}_2 + \text{Cl} (\text{N}_2)$	200 - 1000	$\infty$	$4.12 \times 10^{-11} T^{-0.06} \exp(42/T)$
$\text{Cl} + \text{O}_2 \rightarrow \text{ClOO} (\text{N}_2)$	150 - 1000	0	$2.38 \times 10^{-20} T^{-4.92} \exp(-617/T)$
		$\infty$	$6.64 \times 10^{-11} T^{0.004} \exp(-8.0/T)$
$\text{ClO} + \text{ClO} \rightarrow \text{ClOOC} (\text{N}_2)$	180 - 500	0	$8.31 \times 10^{-20} T^{-4.96} \exp(-336/T)$
		$\infty$	$1.6 \times 10^{-9} T^{-0.67} \exp(-64/T)$
$\text{ClO} + \text{ClO} \rightarrow \text{ClOC} (\text{N}_2)$	180 - 500	0	$1.72 \times 10^{-14} T^{-6.99} \exp(-926/T)$
		$\infty$	$6.4 \times 10^{-9} T^{-0.78} \exp(-76/T)$

**Table 2**Predicted rate constants for reactions discussed in this chapter<sup>a</sup> (continued).

Reaction	T (K)	P (Torr)	$\Delta H_{f,0}^0$ (kcal/mol)
$\text{ClOOCI} \rightarrow \text{ClO} + \text{ClO} (\text{N}_2)^b$	180 - 500	0	$4.64 \times 10^8 T^{-5.2} \exp(-10159/T)$
		$\infty$	$6.3 \times 10^{19} T^{-1.32} \exp(-9999/T)$
$\text{ClOClO} \rightarrow \text{ClO} + \text{ClO} (\text{N}_2)$	180 - 500	0	$6.81 \times 10^6 T^{-4.9} \exp(-6488/T)$
		$\infty$	$5.99 \times 10^{20} T^{-1.63} \exp(-6474/T)$
$\text{ClO} + \text{ClO} \rightarrow \text{Cl}_2 + \text{O}_2$ $\rightarrow \text{Cl} + \text{ClOO}$ $\rightarrow \text{Cl} + \text{OCIO}$	200 - 1500	c	$1.09 \times 10^{-13} T^{0.66} \exp(-1892/T)$
		c	$1.36 \times 10^{-13} T^{0.77} \exp(-2168/T)$
		c	$6.26 \times 10^{-11} T^{0.005} \exp(-2896/T)$
$\text{ClO} + \text{OCIO} \rightarrow \text{ClOCl(O)O} (\text{N}_2)$	200 - 400	0	$1.10 \times 10^{-17} T^{-5.5} \exp(-398/T)$
		$\infty$	$2.98 \times 10^{-10}$
$\text{ClO} + \text{OCIO} \rightarrow \text{ClOO} + \text{ClO}$	500 -2500	c	$1.03 \times 10^{-22} T^{2.76} \exp(-78/T)$
$\text{ClO} + \text{OCIO} \rightarrow \text{ClOCl} + \text{O}_2$	500 -2500	c	$9.63 \times 10^{-22} T^{2.40} \exp(-1665/T)$

a. Rate constants are given in units of  $\text{s}^{-1}$  and  $\text{cm}^3 \text{ molecule}^{-1} \text{ s}^{-1}$  for unimolecular reactions in the first-order and second-order, and in units of  $\text{cm}^3 \text{ molecule}^{-1} \text{ s}^{-1}$  and  $\text{cm}^6 \text{ molecule}^{-2} \text{ s}^{-1}$  for bimolecular reactions in the second-order and third-order, respectively.

b. Third body employed in the calculations.

c. Pressure-independent.

#### 4. CONCLUDING REMARKS

This chapter summarizes the results of our recent theoretical studies on a series of  $\text{ClO}_x$  reactions relevant to the combustion of ammonium perchlorate in its incipient stages. The kinetics and mechanisms for reactions of key species following the decomposition of  $\text{HClO}_4$  have been elucidated by means of detailed potential energy surface mapping at the G2M level of theory based on the geometries optimized with the hybrid density functional theory using a large 6-311+G(3df,2p) Gaussian basis set which is required

for the  $\text{ClO}_x$  systems. Rate constant calculations have been carried out using well-established statistical theories pertinent to each specific type of processes: the conventional TST or RRKM theory for reactions with well-defined transition states and variational TST or RRKM theory for reactions which occur barrierlessly. In the RRKM calculations for processes taking place via long-lived intermediates, the coupling of isomerization, decomposition and collisional deactivation of excited intermediates were handled with the Variflex code [35] for single intermediate systems and with the ChemRate program [36] for systems with multiple intermediates, typically by solving one dimensional master equations.

The results obtained to date have been quite satisfactory. Thermochemically, our predicted heats of formation for species which have been determined experimentally, for example,  $\text{OClO}$ ,  $\text{ClOO}$ ,  $\text{HOCl}$  and  $s\text{-ClO}_3$ , agreement between theory and experiment is typically better than  $\pm 2$  kcal/mol. Kinetically, effectively all rate constants for  $\text{ClO}_x$  reactions which have been measured to date in conjunction with stratosphere  $\text{O}_3$ -destruction chemistry can be accounted for within  $\pm 1$  kcal/mol of predicted transition state energies. Our results represent the first direct quantitative prediction of the kinetics and mechanisms for  $\text{ClO}_x$  reactions by first-principles calculations from PES mapping to rate constant computations over a wide range of temperature and pressure conditions.

Obviously what we have accomplished to date represents only a small fraction of the monumental work which must be completed before a realistic computer simulation of AP combustion can be carried out. For the gas-phase chemistry alone, much remains to be done. For example, the oxidation of  $\text{NH}_x$  by  $\text{ClO}_x$ , which rapidly generates  $\text{NO}_x$ ,  $\text{H}_2\text{O}$ ,  $\text{HCl}$  and  $\text{HOCl}$ , with the early release of chemical energy near the burning surface, should be fully investigated. Similarly the cross bimolecular reactions of  $\text{ClO}_x$  and  $\text{NO}_x$  have to be studied because of their high concentrations during the early stages of combustion. Furthermore, according to the three-phase model of Tanaka and Beckstead [20, 21], many reactive species may be generated in the liquid and solid phases which require completely different types of theoretical approaches for mechanistic elucidation as well as kinetic predictions for the processes involved.

For future combustion simulations, we have listed in Table 1 the molecular parameters and heats of formation of key species involved in the reactions studied. Table 2 summarizes the predicted rate constants calculated for varying experimental conditions covering those relevant to the stratosphere  $\text{O}_3$ -destruction and AP combustion chemistry for applications by scientists in both research communities.

## ACKNOWLEDGMENT

This work is sponsored by the Office of Naval Research under contract no. N00014 - 02- 1- 0133, Dr. J. Goldwasser program manager.

## REFERENCES

- [1] L. A. Curtiss, K. Raghavachari, J. A. Pople, *J. Chem. Phys.* 103 (1995) 4192.
- [2] L. A. Curtiss, K. Raghavachari, P. C. Redfern, V. Rassolov, J. A. Pople, *J. Chem. Phys.* 109 (1998) 7764.
- [3] (a) G. A. Petersson and M. A. Al-Laham, *J. Chem. Phys.* 94 (1991) 6081; (b) G. A. Petersson, Y. Tensfeldt, and J. A. Montgomery, *ibid.* 94 (1991) 6091.
- [4] J. L. Durant, Jr. and C. M. Rohlfing, *J. Chem. Phys.* 98 (1993) 8031.
- [5] A. M. Mebel, K. Morokuma, M. C. Lin, *J. Chem. Phys.* 103 (1995) 7414.
- [6] D. M. Wardlaw, R. A. Marcus, *Chem. Phys. Lett.* 110 (1984) 230.
- [7] D. M. Wardlaw, R. A. Marcus, *J. Chem. Phys.* 83 (1985) 3462.
- [8] S. J. Klippenstein, *J. Phys. Chem.* 98 (1994) 11459; *J. Chem. Phys.*, 98 (1991) 6994.
- [9] S. H. Robertson, A. F. Wagner, and D. M. Wardlaw, *Faraday Disc. Chem. Soc.* 102 (1995) 65.
- [10] L. V. Moskaleva, W. S. Xia, M. C. Lin, *Chem. Phys. Lett.* 331 (2000) 269.
- [11] L. V. Moskaleva, M. C. Lin, *Proc. Combust. Instit.* 28 (2000) 2393.
- [12] C. - C. Hsu, A. M. Mebel, M. C. Lin, *J. Chem. Phys.* 105 (1996) 2346.
- [13] R. S. Zhu, C. - C. Hsu, M. C. Lin, *J. Chem. Phys.* 115 (2001) 195.
- [14] A. M. Mebel, E. W. G. Diau, M. C. Lin, K. Morokuma, *J. Am. Chem. Soc.* 118 (1996) 9759.
- [15] R. S. Zhu, E. G. W. Diau, M. C. Lin, A. M. Mebel, *J. Phys. Chem.* 105 (2001) 11249.
- [16] W. S. Xia, M. C. Lin, *PhysChemComm*, 2 (2000).
- [17] W. S. Xia, M. C. Lin, *J. Chem. Phys.* 114 (2001) 4522.
- [18] D. Chakraborty, M. C. Lin, in *Solid Propellant Chemistry, Combustion and Motor Interior Ballistics*, V. Yang, T. B. Brill, W. Z. Ren, eds., *Prog. Astro. Aeron.*, Vol. 185, pp. 33-72, AIAA, Inc., Reston, Virginia, (2000).
- [19] P. W. M. Jacobs, and H. M. Whitehead, *Chem. Rev.* 69 (1969) 551.
- [20] M. Tanaka, M. W. Beckstead, *Kayaku Gakkaishi*, 58 (1997) 245.
- [21] M. Tanaka, M. W. Beckstead, "A Three Phase Combustion Model of Ammonium Perchlorate", unpublished
- [22] T. B. Brill, P. J. Brush, D. G. Patil, *Combustion and Flame*, 94 (1993) 70.
- [23] N. E. Ermolin, O. P. Korobeinichev, A. G. Tereshchenko, V. M. Fomin, *Fizika Goreniyai Vzryva*, 18 (1982) 46.
- [24] J. A. Pople, M. H. Gordon, D. J. Fox, K. Raghavachari, L. A. Curtiss, *J. Chem. Phys.* 90 (1989) 5622.
- [25] L. A. Curtiss, P. C. Redfern, K. Raghavachari, J. A. Pople, *J. Chem. Phys.* 114 (2001) 108.
- [26] B. G. Johnson and M. J. Frisch, *J. Chem. Phys.* 100 (1994) 7429.
- [27] T. J. Van Huis, H. F. Schaefer III., *J. Chem. Phys.* 106 (1997) 4028.
- [28] B. G. Johnson and M. J. Frisch, *Chem. Phys. Lett.* 216 (1993) 133.

- [29] A. D. Becke, *J. Chem. Phys.* 98 (1993) 5648.
- [30] A. D. Becke, *J. Chem. Phys.* 96 (1992) 2155 *ibid*, 97 (1992) 9173.
- [31] C. Lee, W. Yang, R. G. Parr, *Phys. Rev.*, 37B, (1988) 785.
- [32] (a) K. Burke, J. P. Perdew, Y. Wang, In *Electronic Density Functional Theory: Recent Progress and New Direction*; Dobson, J. F., Vignale, G., Das, M. P., Eds.; Plenum: New York, 1998. (b) J. P. Perdew, in *Electronic Structure of Solids* '91; Ziesche, P., Eschrig, H., Eds.; Akademie Verlag: Berlin, 1991; p11. (c) J. P. Perdew, J. A. Chevary, S. H. Vosko, K. A. Jasckson, M. R. Pederson, D. J. Singh, C. Fiolhais, *Phys. Rev. B* 46 (1992) 6671. (d) J. P. Perdew, K. Burke, Y. Wang, *Phys. Rev. B* 54 (1996) 16533.
- [33] C. Gonzalez, H. B. Schlegel, *J. Phys. Chem.*, 90 (1989) 2154.
- [34] M. J. Frisch, G. W. Trucks, H. B. Schlegel, P. M. W. Gill, B. G. Johnson, M. A. Robb, J. R. Cheeseman, T. Keith, G. A. Petersson, J. A. Montgomery, K. Raghavachari, M. A. Al-Laham, V. G. Zakrzewski, J. V. Ortiz, J. B. Foresman, J. Cioslowski, B. B. Stefanov, A. Nanayakkara, M. Challacombe, C. Y. Peng, P. Y. Ayala, W. Chen, M. W. Wong, J. L. Andres, E. S. Replogle, R. Gomperts, R. L. Martin, D. J. Fox, J. S. Binkley, D. J. Defrees, J. Baker, J. P. Stewart, M. Head-Gordon, C. Gonzalez and J. A. Pople, *GAUSSIAN 98, REVISION A.1*; Gaussian, Inc., Pittsburgh PA, 1998.
- [35] S. J. Klippenstein, A. F. Wagner, R. C. Dunbar, D. M. Wardlaw, and S. H. Robertson, *VARIFLEX: VERSION 1.00*, 1999.
- [36] Mokrushin, V.; Bedanov, V.; Tsang, W.; Zachariah, M. R.; Knyazev, V. D. *ChemRate*, Version 1.19; National Institute of Standards and Technology: Gaithersburg, MD 20899, 2002.
- [37] R. G. Gilbert, S. C. Smith, *Theory of Unimolecular and Recombination Reactions*, Blackwell Scientific, Carlton, Australia, 1990.
- [38] K. A. Holbrook, M. J. Pilling, and S. H. Robertson, *Unimolecular Reactions*, Wiley, 1996.
- [39] D. C. Astholz, J. Troe, W. Wieters, *J. Chem. Phys.* 70 (1979) 5107.
- [40] D. Chakraborty, C.-C. Hsu, and M. C. Lin, *J. Chem. Phys.* 109 (1998) 8889.
- [41] R. S. Zhu, M. C. Lin, *PhysChemComm*, 25 (2001) 1.
- [42] J. S. Francisco, *J. Phys. Chem.* 99 (1995) 13422.
- [43] A. F. Jalbout, F. N. Jalbout, H. Y. Alkahby, *J. Mol. Struct. (Theochem)*, 89 (2001) 546.
- [44] S. Thomas, N. Bengt, B. Anders and K. Gunnar, *J. Phys. Chem. A* 103 (1999) 4432.
- [45] J. B. Levy, *J. Phys. Chem.*, 66 (1962) 1092.
- [46] R. Gilbert, P. W. M. Jacobs, *Combust. Flame*, 17 (1971) 343.
- [47] J. W. Boughton, S. Kristyan, M. C. Lin, *Chem Phys. Lett.* 214 (1997) 219.
- [48] R. Atkinson, D. L. Baulch, R. A. Cox, R. F. Jr. Hampson, J. A. Kerr, M. J. Rossi, J. Troe, *J. Phys. Chem. Ref. Data* 26 (1997) 521.
- [49] J. M. Nicovich, K. D. Kreutter, C. J. Shackelford, P. H. Wine, *Chem. Phys. Lett.* 179 (1991) 367-373.
- [50] H. S. Johnston, E. D. Jr. Morris, J. Van den Bogaerde, *J. Am. Chem. Soc.*, (1969).
- [51] T. Rathmann, R. N. Schindler, *Bunsenges, Ber. Phys. Chem.* 96 (1992) 421.



- [52] A. Rauk, E. Tschuikow-Roux, Y. H. Chen, M. P. McGrath, and L. Radom, L. J. Phys. Chem. 97 (1993) 7947.
- [53] M. A. Workman, J. S. Francisco, Chem. Phys. Lett. 297 (1997) 158.
- [54] R. Janoschek, J. Mol. Stru. (Theochem), 423 (1998) 219.
- [55] A. Beltrán, J. Andrés, S. Noury, B. Silvi, J. Phys. Chem. A 103 (1999) 3078.
- [56] M. Alcamí, O. Mó, M. Yáñez, I. L. Cooper, J. Chem. Phys. 112 (2000) 6131.
- [57] R. S. Zhu, M. C. Lin, J. Phys. Chem. A, 106 (2002) 8386.
- [58] M. T. Leu, C. L. Lin, Geophys. Res. Lett. 6 (1979) 425.
- [59] J. P. Burrows, T. J. Wallington, R. P. Wayne, J. Chem. Soc. Faraday Trans. 2, 80 (1984) 957.
- [60] A. J. Hills, C. J. Howard, J. Chem. Phys. 81 (1984) 4458.
- [61] G. Poulet, G. Laverdet, G. Le Bras, G., J. Phys. Chem. 90 (1986) 159.
- [62] A. R. Ravishankara, F. L. Eisele, P. H. Wine, P. H. J. Chem. Phys. 78 (1983) 1140.
- [63] R. Atkinson, D. L. Baulch, R. A. Cox, R. F. Jr. Hampson, J. A. Kerr, J. Phys. Chem. Ref. Data 26 (1997), 521.
- [64] J. B. Lipson, M. J. Elrod, T. W. Beiderhase, L. T. Molina, M. J. Molina, J. Chem. Soc. Faraday Trans., 93 (1997) 2665.
- [65] J. B. Lipson, T. W. Beiderhase, L. T. Molina, and M. J. Molina, M. Olzmann, J. Phys. Chem. A, 103 (1999) 6540.
- [66] C. S. Kegley-Owen, M. K. Gilles, J. B. Burkholder, and A. R. Ravishankara, J. Phys. Chem. A, 103 (1999), 5040.
- [67] Y. Bedjanian, V. Riffault, G. Le Bras, Int. J. Chem. Kinet. 33 (2001), 587.
- [68] (a) J. J. Wang, L. F. Keyser, J. Phys. Chem. A, 105 (2001) 6479; (b) J. Phys. Chem. A, 105 (2001) 10544.
- [69] J. P. Burrows, D. I. Cliff, G. W. Harris, B. A. Thrush, J. P. T. Wilkinson, Proc. R. Soc. London A 368 (1979) 463.
- [70] J. S. Francisco, S. P. Sander, T. J. Lee, A. P. Rendell, J. Phys. Chem. 98 (1994) 5644.
- [71] T. J. Lee, A. P. Rendell, J. Phys. Chem. 97 (1993) 6999.
- [72] R. Sumathi, and S. D. Peyerimhoff, J. Phys. Chem. A, 103 (1999) 7515.
- [73] M. K. Dubey, M. P. McGrath, G. P. Smith, and F. S. Rowland, J. Phys. Chem. A 102 (1998) 3127.
- [74] W. B. DeMore, S. P. Sander, D. M. Golden, R. F. Hampson, M. J. Kurylo, C. J. Howard, A. R. Ravishankara, C. E. Kolb, M. J. Molina, Chemical Kinetics and Photochemical Data for Use in Stratospheric Modeling; Jet Propulsion Laboratory: Pasadena, CA, 1997.
- [75] R. S. Zhu, Z. F. Xu, M. C. Lin, J. Chem. Phys. 116 (2002) 7452.
- [76] Z. F. Xu, R. S. Zhu, M. C. Lin, J. Phys. Chem. In press (2003).
- [77] G. Poulet, H. Zagogianni, G. Le Bras, Int. J. Chem. Kinet., 847 (1986) 18.
- [78] B. Reimann, F. Kaufman, J. Chem. Phys., 69 (1978) 2925.
- [79] R.M. Stimpfle, R. A. Perry, C. J. Howard, J. Chem. Phys., 71 (1979) 5183.
- [80] T. J. Leck, Jac-E L. Cook, J. W. Birks, J. Chem. Phys., 72 (1980) 2364.
- [81] J. Burrows, R. A. Cox, J. Chem. Soc. Faraday Trans. 1. 77 (1981) 2465.
- [82] F. C. Cattell, R. A. Cox, J. Chem. Soc. Faraday Trans. 2. 82 (1986) 1413.
- [83] M. Finkbeiner, J. N. Crowley, O. Horie, R. Mueller, G. K. Moortgat, P. J. Crutzen, J. Phys. Chem. 99 (1995) 16264.

- [84] S. L. Nickolaisen, C. M. Roehl, L. K. Blakeley, R. R. Friedl, J. S. Francisco, R. Liu, S. P. Sander, *J. Phys. Chem. A*, 104 (2000) 308.
- [85] G. P. Knight, T. Beiderhase, F. Helleis, G. K. Moortgat, J. N. Crowley, *J. Phys. Chem. A*, 104 (2000) 1674.
- [86] M. Mozurkewich, *J. Phys. Chem.* 90 (1986) 2216.
- [87] D. W. Toohey, J. G. Anderson, *J. Phys. Chem.* 93 (1989) 1049.
- [88] D. Buttar, D. M. Hirst, *J. Chem. Soc. Faraday Trans.* 90 (1994) 1811.
- [89] Z. F. Xu, R. S. Zhu, M. C. Lin, *J. Phys. Chem.* Submitted.
- [90] W. B. DeMore, S. P. Sander, D. M. Golden, R. F. Hampson, M. J. Kurylo, C. J. Howard, A. R. Ravishankara, C. E. Kolb, M. J. Molina, JPL Publication 97-4, (1997).
- [91] J. J. Schwab, D. W. Toohey, W. H. Brune, J. G. Anderson, *J. Geophys. Res.* 89 (1984) 9581.
- [92] D. L. Baulch, J. Duxbury, S. J. Grant, D. C. Montague, *J. Phys. Chem. Ref. Data* 10, Suppl (1981).
- [93] R. Atkinson, D. L. Baulch, R. A. Cox, R. F. K. Jr. Hampson, J. A. Kerr, M. J. Rossi, J. Troe, *J. Phys. Chem. Ref. Data* 26 (1997) 521.
- [94] J. M. Nicovich, P. H. Wine, A. R. Ravishankara, *J. Chem. Phys.* 89 (1998) 5670.
- [95] A. P. Ongstad, J. W. Birks, *J. Chem. Phys.* 85 (1986) 3359.
- [96] N. Basco, S. K. Dogra, *Proc. R. Soc. London A*: 323 (1971) 29.
- [97] M. A. A. Clyne, W. S. Nip, *J. Chem. Soc. Faraday Trans.* 1: 72 (1976) 2211.
- [98] J. M. Nicovich, K. D. Kreutter, C. J. Shackelford, P. H. Wine, *P.H. Chem. Phys. Lett.* 179 (1991) 367.
- [99] S. Baer, H. Hippler, R. Rahn, M. Siefke, N. Seitzinger, J. Troe, *J. Chem. Phys.* 95 (1991) 6463.
- [100] Patrick, R.; Golden, D. M. *Int. J. Chem. Kinet.* 15 (1983) 1189.
- [101] H. S. Johnston, E. D. Jr. Morris, J. Van den Bogaerde, *J. Am. Chem. Soc.*, (1969)
- [102] J. E. Nicholas, R. G. W. Norrish, *Proc. R. Soc. London A*: 307 (1968) 391.
- [103] M. A. A. Clyne, J. A. Coxon, *Proc. R. Soc. London A*: 303 (1968) 207.
- [104] R. S. Stolarski, R. J. Cicerone, *Can. J. Chem.* 52 (1974) 1610.
- [105] F. S. Rowland, M. J. Molina, *Rev. Geophys. Space Phys.* 78 (1975) 5341; F. S. Rowland, *Annu. Rev. Phys. Chem.*, 42 (1991) 731. H. S. Johnston, *ibid*, 43 (1992), 1.
- [106] (a) M. A. A. Clyne, D. J. McKenney, R. T. Watson, *J. Chem. Soc., Faraday Trans. I*, 71 (1975), 322; (b) M. A. A. Clyne, D. J. McKenney, R. T. Watson, *J. Chem. Soc., Faraday Trans. I*, 73 (1977) 1169.
- [107] N. Basco, J. Hunt, *Int. J. Chem. Kinet.* 11 (1979), 649.
- [108] R. A. Cox, R. G. Derwent, *J. Chem. Soc., Faraday Trans. I* 75 (1979) 1635.
- [109] J. P. Burrows, R. A. Cox, *J. Chem. Soc., Faraday Trans. I* 77 (1981) 2465.
- [110] G. D. Hayman, J. M. Davies, R. A. Cox, *Geophys. Res. Lett.* 13 (1986) 1347.
- [111] L. T. Molina, L. J. Molina, *J. Phys. Chem.* 91 (1987) 43743.
- [112] R. A. Cox, G. D. Hayman, *Nature* 332 (1988), 796.
- [113] S. P. Sander, R. Friedl, Y. L. Young, *Science* 245 (1989), 1095.
- [114] M. Trolrier, R. L. III Mauldin, A. R. Ravishankara, *J. Phys. Chem.* 94 (1990),

- 4896.
- [115] F. G. Simon, W. Schneider, G. K. Moortgat, J. P. Burrows, J. Photochem. Photobiol. A. Chem. 94 (1990) 4896.
  - [116] S. L. Nikolaisen, R. R. Friedl, S. P. Sander, J. Phys. Chem. 98 (1994), 155.
  - [117] A. Horowitz, J. N. Crowley, G. K. Moortgat, J. Phys. Chem. 98 (1994) 11924.
  - [118] W. J. Bloss, S. L. Nikolaisen, R. J. Salawitch, R. R. Friedl and S. P. Sander, J. Phys. Chem. A 105 (2001) 11226.
  - [119] R. S. Zhu, M. C. Lin, J. Chem. Phys. In press (2003).
  - [120] J. Troe, J. Phys. Chem. 83 (1979) 114.
  - [121] J. Troe, Ber. Bunsen-Ges. Phys. Chem. 87 (1983) 161; R. G. Cilbert., K. Luther, J. Troe, Ber. Bunsen-Ges. Phys. Chem., 87 (1983) 169.
  - [122] S. Solomon, Rev. Geophys. 26, 131 (1988).
  - [123] L. T. Molina, M. J. Molina, J. Phys. Chem. 91, 433 (1987).
  - [124] J. G. Anderson, W. H., Brune, S. A. Lloyd, D. W. Toohey; S. P. Sander, W. L. Starr, M. Loewenstein, J. R. Podolske, J. Geophys. Res, 94, 1148 (1989).
  - [125] P. M. Solomon, B. Conner, R. L. de Zafra, A. Parrish, J. Barrett, M. Jaramillo, Nature, 328 (1987).
  - [126] S. Solomon, G. H. Mount, R. W. Sanders, A. L. Schmeltekopf, J. Geophys. Res. 92, 8329 (1987).
  - [127] S. Solomon, R. W. Sanders, M. A. Carroll, A. L. Schmeltekopf, J. Geophys. Res. 94, 11393 (1989).
  - [128] J. C. Farman, B. G. Gardiner and J. D. Shanklin, Nature 315, 207 (1985).
  - [129] R. S. Stolarski, A. J. Krueger, M. R. Schoeberl, R. D. McPeters, P. A. Newman and J. C. Alpert, Nature, 322, 808 (1986).
  - [130] G. D. Hayman, R. A. Cox, Chem. Phys. Lett. 155, 1 (1989).
  - [131] J. B. Burkholder, R. L. Mauldin III, R. J. Yokelson, S. Solomon, and A. R. Ravishankara, J. Phys. Chem. 97, 7597 (1993).
  - [132] B. M. Cheng, Y. P. Lee, J. Chem. Phys. 11, 5930 (1989).
  - [133] F. Zabel, Ber. Bunsen-Ges. Phys. Chem. 95, 893 (1991).
  - [134] R. R. Friedl, M. Birk, J. J. Oh, E. A. Cohen, J. Mol. Spectrosc. 170, 383 (1995).
  - [135] A. J. Colussi, R. W. Redmond, J. C. Scaiano, J. Phys. Chem. 93 (1989) 4783.
  - [136] J. Clark, J. S. Francisco, J. Phys. Chem. A, 101 (1997) 7145.
  - [137] R. Flesch, B. Wassermann, B. Rothmund, E. Rühl, J. Phys. Chem. 98 (1994) 6263.
  - [138] K. H. Kim, Y. K. Han, Y. S. Lee, J. Mol. Struct. (Theochem), 19 (1999) 460.
  - [139] W. K. Li, K. C. Lau, C. Y. Ng, H. Baumgärted, K. M. Weitzel, J. Phys. Chem. A, 104 (2000) 3197.
  - [140] R. S. Zhu, M. C. Lin, J. Chem. Phys. Submitted.
  - [141] A. D. Parr, R. P. Wayne, G. D. Hayman, M. E. Jenkin, R. A. Geophys. Res. Letts. 17 (1990) 2357.
  - [142] M. W. Chase, Jr. NIST-JANAF Thermochemical Tables, Fourth Edition, Woodbury, New York, (1998).
  - [143] J. F. Stanton, C. M. L. Rittby, R. J. Bartlett, and D. W. Toohey, J. Phys. Chem. 95 (1991), 2107.
  - [144] M. P. McGrath, K. C. Clemitshaw, F. S. Rowland, and W. J. Hehre, Geophys. Res. Lett. 15, 883 (1988).
  - [145] T. J. Lee, C. M. Rohlfling, J. E. Rice, J. Chem. Phys. 97 (1992) 6593.

- [146] S. Abramowitz, M. W. Chase, Jr. *Pure Appl. Chem.* 63 (1991) 1449.
- [147] Barnes, R. J.; Sinha, A. J. *Chem. Phys.* 107 (1997) 3730.

This Page Intentionally Left Blank

## Index for Parts 1 and 2

### A

additivity, atom and group volumes:  
 1: 185-188  
 ADN: see ammonium dinitramide  
 aluminum combustion: 1: 259-261  
 ammonium dinitramide (ADN):  
 combustion: 1: 398,399 2: 374  
 decomposition: 1: 29,30,33,  
 394-396,398,399,401,402  
 general: 1: 23,28,29,389-403  
 simulations: 1: 164,165  
 ammonium nitrate (AN):  
 decomposition: 1: 30,32  
 general: 1: 6,23,27,28,393,394,  
 398-400  
 simulations: 1: 164,165  
 ammonium perchlorate (AP):  
 combustion: 2: 290,297,374,375,  
 379-437  
 decomposition: 1: 29 2: 374,  
 375,379-437  
 general: 1: 23,28,29,342,390,  
 398-400 2: 127,131,297,  
 374-437  
 potential energy surface:  
 2: 375-377,379-437  
 AN: see ammonium nitrate  
 AP: see ammonium perchlorate

### B

band gap: see band structure  
 band structure:  
 general: 1: 173,174,327-339  
 2: 72-77,80,86,87,146

and initiation: 2: 72,73  
 boron combustion: 1: 259-261  
 burning rate, combustion:  
 2: 250-258,273-285,  
 299-347,360,363-368

### C

Chapman-Jouguet pressure: see  
 detonation pressure  
 Chapman-Jouguet state: 1: 168,169  
 2: 136,137,193,194,198,220,221  
 CL-20 (HNIW):  
 decomposition: 1: 19  
 general: 1: 16,18,19,22,152,398  
 2: 6,34,36  
 simulation: 1: 153-159  
 combustion:  
 aluminum: 1: 259-261  
 ammonium dinitramide (ADN):  
 1: 398,399 2: 374  
 ammonium perchlorate (AP):  
 2: 290,374,375,379-437  
 boron: 1: 259-261  
 burning rate: 2: 250-258,  
 273-285,299-347,360,363-368  
 flame structure: 2: 226,228,239,  
 249-258,273-285  
 foam layer: 2: 299-347  
 GAP: 2: 297-306,332-347  
 HMX: 2: 267-272,285-288,290,  
 297-306,317-319,332-340,344,  
 356-369,374  
 ignition: 2: 297-347  
 nitrate esters: 2: 259-269,285,286

RDX: **2**: 297-332,340-347,374  
 reaction zone:  
   condensed phase:  
     **2**: 227-234,243-258,  
       273-285,299-347,  
       353-369  
   gas phase: **2**: 227,228,  
     234-258,273-285,299-347,  
     356-369  
   multi-phase: **1**: 126  
     **2**: 299-347  
 simulation: **2**: 227,249-288,  
   297-347,351,356-369  
 steady: **2**: 227,249-273,298-347,  
   352,353,356-369  
 surface: **2**: 227-290,299-347,  
   351,353-369  
 unsteady (quasi-steady):  
   **2**: 273-288,352,353,362-369  
 wave: **2**: 226  
 compression effects: **1**: 147-150,155,  
   169,170,173,174,307-316 **2**: 73,  
   77-87,102,105,106,118,128,  
   139-142,147-153  
 crystal and molecular packing:  
   **1**: 150-161,164,165,188-211,  
   216-226,302,303  
 crystal plastic deformation:  
   **2**: 47,101-121,133  
 crystal surface distortion: **2**: 101-121  
 crystal volume, effective: **1**: 186-188

## D

DADNE: see FOX-7

DATB:

  decomposition: **2**: 26  
   general: **2**: 30,40,41  
 decomposition:  
   ammonium dinitramide (ADN):

**1**: 29,30,33,394-396,398,399,  
     401,402  
   ammonium nitrate (AN): **1**: 32  
   ammonium perchlorate (AP):  
     **1**: 29 **2**: 374,375,379-437  
 CL-20: **1**: 19  
 DATB: **2**: 26  
 difluoramines: **1**: 26,27  
 dimethylnitramine (DMNA):  
   **1**: 140-142  
 EDNA: **2**: 45  
 FOX-7 (DADNE): **1**: 56-60,  
   91-106  
 GAP: **2**: 297-306,332-347  
 general: **1**: 13,30-34,62-83,131,  
   132 **2**: 5-18,25-27,35-48,  
   53-69,143,144,228-234,374,375  
   table: **1**: 13  
 hexanitrostilbene: **1**: 72,73  
 HMX: **1**: 16-19,32,53-60,82,83,  
   93,94,139,140 **2**: 7,45,87-97,  
   297-306,317-319,332-340  
 methylene nitramine: **1**: 144-146  
   **2**: 53,64-69  
 nitrate esters: **1**: 8-10  
   **2**: 259-269,285,286  
 nitro/*aci*-tautomerism: **1**: 61-83  
   **2**: 35,36  
 nitroguanidine (NQ): **1**: 25,56-60  
 nitromethane (NM): **1**: 14,15,  
   64-69,142-144  
 NTO: **1**: 21,24,25,32-34,78-81  
 PETN: **1**: 8-10,30  
 picric acid (PA): **1**: 11-14,72,73  
 polynitrogen systems: **1**: 409-413,  
   422-433,441-452  
 RDX: **1**: 16-19,30,32,51-60,  
   81-83,131-139 **2**: 26,45,46,  
   54,55,69,91,297-332,340-347,  
   374

TACOT: **1**: 72  
 TATB: **1**: 11-14,72,73 **2**: 7,  
 10-12,26  
 Tetryl: **1**: 11-14,72,73  
 TNAZ: **1**: 20,21,32,33  
 TNT: **1**: 11-14,30,32,33,72,73,  
 75 **2**: 7,9,10,26,40,42  
 1,3,5-trinitrobenzene (TNB):  
**2**: 40  
 defects, lattice: see lattice defects  
 deflagration: **2**: 139,140  
 deformation, crystal:  
**2**: 47,101- 121,133  
 deformation density: **1**: 215,  
 225-230,241,242,246  
 density: **1**: 150,161-163,185-188,393  
 table: **1**: 22,23,27,29,209,210  
 detonation:  
 and initiation: **1**: 1,77,127,  
 168-172,341 **2**: 1,5-12,  
 25-27,35,36,40,45-48,53-72,  
 119,120,125,135-181  
 and initiation, simulation:  
**1**: 146-150,171-173  
**2**: 161-163,168-175,180,181,  
 209,210  
 detonation energy: see energy release  
 detonation pressure: **1**: 27,93,185  
**2**: 135-141,147  
 table: **1**: 27  
 detonation velocity: **1**: 22,23,93,185  
**2**: 10,27-32,40,41,43,119,120,  
 135-141,176  
 table: **1**: 22,23 **2**: 28-32  
 2,4-diamino-1,3,5-trinitrobenzene: see  
 DATB  
 difluoramines:  
 decomposition: **1**: 26,27  
 general: **1**: 26,27,199,208,209,  
 260-270

dimethylnitramine (DMNA):  
 decomposition: **1**: 140-142  
 general: **1**: 262,282,283,289-292  
 simulation: **1**: 140-142,163,164,  
 289-292  
 dinitramides: **1**: 23,28-30,33,164,165,  
 228,229,240-243,389-403 **2**: 374  
 dinitraminic acid: **1**: 262,389-397  
 direction-dependence, initiation and  
 shock propagation: **1**: 147,148  
**2**: 77,81,131,141,149,167  
 dissipation of energy: **2**: 7,8,11,12,  
 103,109-121  
 DMNA: see dimethylnitramine

## E

EDNA:  
 decomposition: **2**: 45  
 general: **1**: 23 **2**: 33  
 effective crystal volume: **1**: 186-188  
 electronic deformation density:  
**1**: 215,225-230,241,242,246  
 electronic density: **1**: 215-243  
**2**: 12  
 electronic excitation: **1**: 169,173,174,  
 327-339,435-437 **2**: 10,73,74,  
 80,86,143-148  
 electrostatic potential: **1**: 215,235,  
 236,249,258,259 **2**: 12-18  
 energy density: **1**: 236-241  
**2**: 115-118  
 energy dissipation: **2**: 7,8,11,12,103,  
 109-121  
 energy release: **1**: 1,2,6,58,59,62,  
 166-173,247,260,261,265-270,405,  
 406,415-417,422-424 **2**: 1,2,5,7,  
 8,11,12,53-69,127,135,136,151,  
 176-179,193,229,249,250,278-285,



301-347

table: **1:** 59,265-270,416**2:** 248,249

enthalpy of formation: see heat of formation

enthalpy of sublimation: see heat of sublimation

enthalpy of vaporization: see heat of vaporization

equations of state: **2:** 194-197, 200-210,221

ethylene dinitramine: see EDNA

explosives:

primary: **1:** 341 **2:** 127secondary: **1:** 341,342 **2:** 127**F**flame structure: **2:** 226,228,239, 249-258,273-285,353,360foam layer: **2:** 299-347force fields: **1:** 129,130,146-174, 194,197-199,281-292 **2:** 103, 108-112,167,195-207,213-215,378

FOX-7 (DADNE):

decomposition: **1:** 56-60,91-106general: **1:** 19,20,23,50,51,77,78, 92,158,159,266simulation: **1:** 54-60,158,159tautomerism: **1:** 102**G**

GAP:

combustion: **2:** 297-306,332-347decomposition: **2:** 297-306, 332-347general: **2:** 297**H**heat of formation: **1:** 247-271, 393,441,449,451table: **1:** 29,262-264,265-270, 447,449,451heat of sublimation: **1:** 149,152-159, 164,165,199-210,249,258-261, 271,306 **2:** 15table: **1:** 209,210,304heat of vaporization: **1:** 162,249, 258-261,271,294

heat release: see energy release

hexanitrostilbene:

decomposition: **1:** 72,73general: **1:** 22,72 **2:** 32

high-nitrogen systems: see polynitrogen systems

HMX:

combustion: **2:** 267-272,285-288, 290,297-306,317-319,332-340, 344,356-369,374compression effects: **1:** 307-316decomposition: **1:** 16-19,32, 53-60,82,83,93,94,139,140 **2:** 7,45,87-97,297-306,317-319,332-340elasticity: **1:** 316-320general: **1:** 16,22,23,26,27,50,51, 77,78,93,187,199,202,219,220, 225,227-230,235,236,279-323, 341-343,371,397 **2:** 6,8,34, 72,87,113,127,135,136,141, 144,147,151,160-163,174,175, 210,211,220,226,227,234,241, 242,257,297,351-353heat of sublimation: **1:** 306

potential energy surface:

**1:** 282-288pressure effects: **1:** 307-316,

320,321  
 simulations: 1: 54-60,153-159,  
 163,164,292-320 2: 90-97  
 tautomerism: 1: 82,83  
 thermal conductivity: 1: 298-302  
 thermal expansion coefficient:  
 1: 303-305  
 HNIW: see CL-20  
 HOMO, LUMO (also see band  
 structure): 2: 75-77,83-86,141  
 hot spots:  
 and defects: 1: 147-149  
 2: 7,8,168-172  
 general: 1: 127,147-149,172,320  
 2: 7-12,71,102,109-121,  
 137-142,153,163-165,168-172,  
 177-179  
 and initiation: 2: 7,8,71,72,102,  
 109-121,168-172  
 and strain: 1: 147 2: 7-9  
 Hugoniot relation: 1: 130,168,169  
 2: 125,128,133-137,170,197-211  
 hydrazine: 1: 398-401  
 hydrogen bonding: 1: 20,65-77,92,  
 158,159,240-243 2: 11,142

## I

ignition:  
 combustion: 2: 297-347  
 simulation: 2: 299-332,346,347  
 initiation:  
 and band structure: 2: 72,73  
 and detonation: 1: 1,77,127,  
 168-172,341 2: 1,5-12,  
 25-27,35,36,40,45-48,53-72,  
 119,120,125,135-181  
 and detonation, simulation:  
 1: 146-150,171-173  
 2: 161-163,168-175,180, 181,

209,210  
 direction dependence: 1: 147,148  
 2: 77,81,131,141,149,167  
 and hot spots: 2: 7,8,71,72,102,  
 109-121,168-172  
 and lattice defects: 1: 127,  
 147-149 2: 7,8,38,71,72,  
 108,109,138,140,153,163,  
 168-172  
 models: 1: 146-150,166-173  
 2: 72,73  
 and plastic deformation: 2: 47,  
 101-121  
 stimuli: 1: 1,128,341 2: 1,5,  
 25-34,36-48,71,101-121  
 intrinsic propellant stability:  
 2: 288-290

## L

lattice defects:  
 effects on initiation: 1: 127,147-  
 149,172 2: 7,8,38,71,72, 108,  
 109,138,140,153,163,168-172  
 formation: 1: 147 2: 38  
 and hot spots: 1: 147-149  
 2: 7,8  
 vacancies, voids: 1: 172  
 2: 7,8,81-86  
 lattice deformation: see deformation,  
 crystal  
 lattice energy: see heat of sublimation  
 lattice structure:  
 general: 1: 150-161,164,165,  
 188-211,216-226,302,303  
 NTO: 1: 217-219,222-225  
 table: 1: 218  
 lattice vibrations: 1: 128,148,149  
 2: 8,9,42,55-57,68,72,110,111,  
 119,120,145-168,181,211

**M**

methylene nitramine:

decomposition: **1**: 144-146

**2**: 45,53,64-69

simulation: **1**: 145,146

molecular and crystal packing:

**1**: 150-161,164,165,188-211,216-

226,302,303

**N**

nanoenergetic materials: **2**: 126,

151-153,175-181

NC: see nitrate esters

NG: see nitrate esters

nitrate esters:

combustion: **2**: 259-269,285,286

decomposition: **1**: 8-10

**2**: 259-269,285,286

general: **1**: 6-10,22,342 **2**: 226,

227,234,240-242

simulations: **1**: 162,163

nitrocellulose (NC): see nitrate esters

nitroglycerine (NG): see nitrate esters

nitroguanidine (NQ):

decomposition: **1**: 25,56-60

general: **1**: 23,50,51,77,78,342

simulations: **1**: 54-60

nitromethane (NM):

decomposition: **1**: 14,15,64-69,

142-144

general: **1**: 22 **2**: 73-87,127,

139-141,154-157,167,174,220

potential energy surface: **2**: 73,74

tautomerism: **1**: 63-69

simulations: **1**: 143,144,160-162

nitronic acids: **1**: 61-83

NMR chemical shifts: **2**: 27-34,36-47

NQ: see nitroguanidine

NTO:

decomposition: **1**: 21,24,25,32-34,78-81

general: **1**: 23,77-79,217-219,

222-225,228,230-240,265

**2**: 14,16,142

lattice structure: **1**: 217-219,

222-225

table: **1**: 218

tautomerism: **1**: 78-81

**O**

octanitrocubane (ONC): **1**: 15,199,

209,210,261,268 **2**: 16

ONC: see octanitrocubane

**P**

PETN:

decomposition: **1**: 8-10,30

general: **1**: 9,22,23,77,78,327,

332-335,338,342,399

**2**: 73,127,139-141,167,209,21

simulations: **1**: 155-159,163

phonons: see lattice vibrations

picramide: **1**: 22,74,76,77 **2**: 30

picric acid:

decomposition: **1**: 11-14,72,73

general: **1**: 6,11,22,72,73,76,77,

342 **2**: 16,30

plastic crystal deformation: **2**: 47,

101-121,133

pollution:

general: **1**: 2,343-346,380 **2**: 2

interactions with soil: **1**: 344-380

simulations: **1**: 347,348,351-366,

371-380

## polynitrogen systems:

decomposition: 1: 409-413,

422-433,441-452

general: 1: 406-418,421-437,

441-452

potential energy surface:

1: 409-413,422-429

## potential energy:

functions: 1: 129,130,146-174,

194,197-199,281-292 2: 103,

108-112,167,195-207,213-215,

378

surface:

ammonium perchlorate (AP):

2: 375-377,379-437

FOX-7: 1: 97,101

general: 1: 76 2: 53-69,

143,144,149

HMX: 1: 282-288

nitromethane: 2: 73,74

polynitrogen systems:

1: 409-413,422-429

pressure effects: 1: 155-161,173,

174,307-316,320,321 2: 75,78,

79,83,85-87,117-120,136,139,

140,174,213-215,218,219,221,

234-290,362-364

primary explosives: 1: 341 2: 127

propellant intrinsic stability: 2: 288-

290

propellant reaction zone: see

combustion reaction zone

pyrolysis equations: 2: 233,234

## R

## RDX:

combustion: 2: 297-332,340-

347,374

decomposition: 1: 16-19,30,32,

51-60,81-83,92-94,131-139

2: 26,45,46,54,55,69,297-332,

341-348

general: 1: 6,16,20,22,23,50,77,

78,92,93,131,187,327,328,332,

333,336-338,341-343,371,

396-400 2: 6-8,33,73,86,89,

94,103-108,112-115,127,138,

141,144,160,163,167,174,175,

220,226,234,241,242,297

simulations: 1: 54-60,134-139,

152-159

tautomerism: 1: 81-83

reaction zone, propellant: see

combustion reaction zone

rigid molecule approximation:

1: 150-159

## S

secondary explosives: 1: 341,342

2: 127

sensitivity:

correlations: 1: 58,59,247

2: 5-18,25,36-40,43,44,72,

141,162,163

factors determining: 1: 397

2: 5-18,102,141,142,153,

160-165,168-172

and nitro, *aci*-nitro tautomerism:

1: 61-83

table: 1: 22,23,59,78,397

2: 28-34

shock wave:

direction-dependence: 1: 147,148

2: 77,81,131,141,149,167

general: 1: 1 2: 1,71,125,

128-137

simulation: 1: 128-131,168-172

- 2: 161-163,168-175,180,181, 197-211
- simulation:
- ammonium dinitramide (ADN):
    - 1: 164,165
  - ammonium nitrate (AN):
    - 1: 164,165
  - CL-20: 1: 153-159
  - combustion: 2: 227,249-288, 297-347,351,356-369
  - dimethylnitramine (DMNA):
    - 1: 140-142,163,164,289-292
  - force fields: 1: 129,130,146-174, 194,197-199,281-292 2: 103, 108-112,167,195-207,213-215, 378
  - FOX-7 (DADNE): 1: 54-60,158, 159
  - HMX: 1: 54-60,153-159,163,164, 292-320 2: 90-97
  - ignition: 2: 299-332,346,347
  - initiation and detonation:
    - 1: 146-150,171-173
    - 2: 161-163,168-175, 180, 181, 209,210
  - methodology: 1: 51,53,54, 128-131,347,348 2: 161-163
  - methylene nitramine: 1: 145,146
  - nitrate esters: 1: 162,163
  - nitroguanidine (NQ): 1: 54-60
  - nitromethane (NM): 1: 143,144, 160-162
  - PETN: 1: 155-159,163
  - pollution (interactions with soil):
    - 1: 347,348,351-366,371-380
  - RDX: 1: 54-60,134-139,152-159
  - shock wave: 1: 128-131,168-172 2: 161-163,168-175,180,181, 197-211
  - TNT: 1: 155
  - specific impulse: 1: 93,400,401,408
    - table: 1: 27,401
  - state equations: 2: 194-197,200-210, 221
  - surface distortion, crystal:
    - 2: 101-121
- T**
- TACOT:
- decomposition: 1: 72
  - general: 1: 22,72
- TATB:
- decomposition: 1: 11-14,72,73 2: 7,10-12,26
  - general: 1: 11,22,72-74 2: 10-12,30,72,127,141,142, 162,174,210,211
  - thermal conductivity: 2: 11
- tautomerism:
- general: 1: 61,62
  - nitro, *aci*-nitro: 1: 61-83 2: 35,36
  - and sensitivity: 1: 61-83
- 1,3,5,7-tetranitro-1,3,5,7-tetraazacubane: 1: 261,268
- Tetryl:
- decomposition: 1: 11-14,72,73
  - general: 1: 11,22,72,342 2: 34
- thermal conductivity:
- HMX: 1: 298-302
  - TATB: 2: 11
- TNAZ:
- decomposition: 1: 20,21,32,33
  - general: 1: 16,20,21,265 2: 16,33
- TNB: see 1,3,5-trinitrobenzene
- TNT:
- decomposition: 1: 11-14,30,32,

33,72,73,75 . 2: 7,9,10,26,35,  
 40,42  
 general: 1: 6,11,22,23,72-77,  
 341-343,370,371,400  
 2: 16,29,141  
 simulation: 1: 155  
 toxicity: 1: 2,342,398-401 2: 2  
 table: 1: 401  
 2,4,6-triamino-1,3,5-trinitrobenzene:  
 see TATB  
 trigger linkage: 2: 8-14  
 2,4,6-trinitroaniline: see picramide  
 1,3,3-trinitroazetidine: see TNAZ  
 1,3,5-trinitrobenzene (TNB):  
 decomposition: 2: 40  
 general: 1: 22,369,371-380  
 2: 28  
 2,4,6-trinitrophenol: see picric acid  
 2,4,6-trinitroresorcinol: 1: 22  
 2: 30,40,41  
 2,4,6-trinitrotoluene: see TNT

## V

vibrational energy, molecular:  
 1: 136,137,141,146,148, 149,172,  
 249 2: 7-12,42,53-69,72,74,102,  
 109-121,143-181  
 vibrational excitation: see vibrational  
 energy, molecular  
 vibrons: see vibrational energy,  
 molecular  
 volume:  
 additivity: 1: 185-188  
 atom: 1: 185-188  
 crystal (effective): 1: 186-188  
 group: 1: 185-188

This Page Intentionally Left Blank